

Theory of Quantum Transport in Metallic and Hybrid Nanostructures

Edited by

Andreas Glatz, Veniamin I. Kozub
and Valerii M. Vinokur

NATO Science Series

II. Mathematics, Physics and Chemistry – Vol. 230

Theory of Quantum Transport in Metallic and Hybrid Nanostructures

NATO Science Series

A Series presenting the results of scientific meetings supported under the NATO Science Programme.

The Series is published by IOS Press, Amsterdam, and Springer in conjunction with the NATO Public Diplomacy Division.

Sub-Series

I. Life and Behavioural Sciences	IOS Press
II. Mathematics, Physics and Chemistry	Springer
III. Computer and Systems Science	IOS Press
IV. Earth and Environmental Sciences	Springer

The NATO Science Series continues the series of books published formerly as the NATO ASI Series.

The NATO Science Programme offers support for collaboration in civil science between scientists of countries of the Euro-Atlantic Partnership Council. The types of scientific meeting generally supported are "Advanced Study Institutes" and "Advanced Research Workshops", and the NATO Science Series collects together the results of these meetings. The meetings are co-organized by scientists from NATO countries and scientists from NATO's Partner countries – countries of the CIS and Central and Eastern Europe.

Advanced Study Institutes are high-level tutorial courses offering in-depth study of latest advances in a field.

Advanced Research Workshops are expert meetings aimed at critical assessment of a field, and identification of directions for future action.

As a consequence of the restructuring of the NATO Science Programme in 1999, the NATO Science Series was re-organized to the four sub-series noted above. Please consult the following web sites for information on previous volumes published in the Series.

<http://www.nato.int/science>

<http://www.springer.com>

<http://www.iospress.nl>



Series II: Mathematics, Physics and Chemistry – Vol. 230

Theory of Quantum Transport in Metallic and Hybrid Nanostructures

edited by

Andreas Glatz

Argonne National Laboratory,
IL, U.S.A.

Veniamin I. Kozub

Ioffe Institute,
RAS, St. Petersburg, Russia

and

Valerii M. Vinokur

Argonne National Laboratory,
IL, U.S.A.



Published in cooperation with NATO Public Diplomacy Division

Proceedings of the NATO Advanced Research Workshop on
Theory of Quantum Transport in Metallic and Hybrid Nanostructures
St. Petersburg, Russia
25-29 August 2003

A C.I.P. Catalogue record for this book is available from the Library of Congress.

ISBN-10 1-4020-4778-9 (PB)
ISBN-13 978-1-4020-4778-7 (PB)
ISBN-10 1-4020-4777-0 (HB)
ISBN-13 978-1-4020-4777-0 (HB)
ISBN-10 1-4020-4779-7 (e-book)
ISBN-13 978-1-4020-4779-9 (e-book)

Published by Springer,
P.O. Box 17, 3300 AA Dordrecht, The Netherlands.

www.springer.com

Printed on acid-free paper

All Rights Reserved
© 2006 Springer

No part of this work may be reproduced, stored in a retrieval system, or transmitted in any form or by any means, electronic, mechanical, photocopying, microfilming, recording or otherwise, without written permission from the Publisher, with the exception of any material supplied specifically for the purpose of being entered and executed on a computer system, for exclusive use by the purchaser of the work.

Printed in the Netherlands.

Preface

A new science emerges at the intersection of modern physics, computer science, and material science. The struggle to further miniaturize is putting nanotechnology to the verge of creating single-electron and/or single-spin devices that operate by moving a single electron (spin) and can serve as transistors, memory cells, and for logic gates. These devices take advantage of quantum physics that dominates nanometer size scales. The devices that utilize metal-based hybrid nanostructures may possess significant advantages over those exploiting purely semiconducting materials. First, the chemistry of metals is typically simpler than that of semiconductors. Second, the electric properties of metals are much less sensitive to the structural defects and impurities than those of semiconductors. Next, metallic devices allow better electric and thermal contacts. Another important plus point is that in metals the electron de Broglie wavelength is smaller by many orders of magnitude as compared to that in semiconductors. This makes metallic devices more promising with respect to their size - down to the size of an atom. Further, high bulk and interface thermal conductance in metallic devices are beneficial for the heat withdraw. And, last but by no means the least, the high electron velocity in metals promises to accelerate enormously operation rates with respect to those in semiconductor-based devices. The final note is that metals can exhibit strong ferromagnetism and/or superconductivity. While ferromagnetism provides a new possibility for information storage and processing associated via utilizing spin transfer and storage (the corresponding approach is often referred to as spintronics), the superconductivity offers unique opportunities for completely novel class of devices based on quantum coherence.

These devices allow utilizing new computational algorithms based on quantum superposition of states, allowing simultaneous representing many different numbers (so-called quantum computation). In a quantum computer information is loaded as a string of "qubits" (quantum mechanical representation of bits), which are quantum objects that can occupy different quantum states. A material implementation of qubits requires finding a medium, which can keep superpositional states from the destruction by interaction with the

environment (decoherence effect), i.e. the medium which has a long enough characteristic decoherence time. On the other hand, interaction effects are crucial for reading off the result of computation. Hence, the main problem is to find physical systems allowing coherent operation and a switchable interaction with the environment. In this sense the superconductor devices exhibiting properties of a single macroscopic quantum state are of prime interest.

The abovementioned aspects of nanoscale physics focusing along the properties of metallic and hybrid nanostructures became the focus of the NATO Advanced Research Workshop held in St.-Petersburg, August 24 - 29, 2003; the scientific contributions of this workshop are presented in this volume.

Significant attention is paid to hybrid nanostructures on the base of ferromagnets and superconductors including ferromagnet-superconductors hybrid systems. In the latter systems the role of proximity effects is discussed in detail. The possible developments in spintronics are demonstrated by studies of current-induced magnetization switching in multilayered nanopillars and by studies spin-dependent transport of electrons in shuttle-structures and magnetic point contacts. Important and unexpected results are presented for single electron transport through the vortex core levels and for domain wall superconductivity in ferromagnetic superconductors and hybrid S/F structures. Widely discussed are correlation effects in nanostructures; in particular, the problem of the metal-insulator transition in 2D electron systems which - since the existence of such a transition contradicts to conventional expectations of scaling theory of localization is addressed. New realizations of two-channel Kondo effect in single electron transistor and ratchet effects in Luttinger liquids are reported.

A special attention is paid to the noise phenomenon in nanostructures. In particular, non-Gaussian shot noise, higher cumulants of noise, shot noise in transport through localized states were considered. It is demonstrated that the detailed studies of noise, in particular studies of the shot noise, can provide important information about the electron system involved. Several issues concerning peculiarities of transport in nanostructures and nanoscale devices are widely discussed in this volume: magnetoresistance caused by non-Markovian effects, transport properties of granular metals at low temperatures, and persistent currents in interacting Aharonov-Bohm interferometers under acoustic radiation can be mentioned to name the few. To summarize, the investigations reported in this volume, will, by no doubts, signify the important step towards further understanding mechanisms of quantum transport in nanoscale devices.

St. Petersburg,
June 2004

*Andreas Glatz
Veniamin Kozub
Valerii Vinokur*

Contents

Preface	v
List of Contributors	xi

Part I Coherence and Correlation Effects

Phase Measurements in Closed Aharonov-Bohm Interferometers <i>Amnon Aharony, Ora Entin-Wohlman, and Yoseph Imry</i>	3
Berry Phase with Environment: Classical versus Quantum <i>Robert S. Whitney, Yuriy Makhlin, Alexander Shnirman, and Yuval Gefen</i>	9

Part II Quantum Mesoscopic Phenomena

Electron Transport in Granular Metals <i>I.S. Beloborodov, K.B. Efetov, A.V. Lopatin, and V.M. Vinokur</i>	27
Studies of Current-Driven Excitations in Co/Cu/Co Trilayer Nanopillars <i>S. Urazhdin, Norman O. Birge, W.P. Pratt, Jr., and J. Bass</i>	39
Nanomechanical Effects in Suspended Carbon Nanotubes <i>Ya.M. Blanter</i>	47
Transport through Ferromagnet/Superconductor Interfaces <i>Zhigang Jiang, José Aumentado, Wolfgang Belzig, and Venkat Chandrasekhar</i>	57
Anomalous Negative Magnetoresistance Caused by Non-Markovian Effects <i>Vadim V. Cheianov, A. P. Dmitriev, and V. Yu. Kachorovskii</i>	67

Persistent Currents in Interacting Aharonov-Bohm Interferometers <i>Ora Entin-Wohlman, Yoseph Imry, and Amnon Aharony</i>	77
Experimental Implementations of the Superconductor-Insulator Transition <i>V.F. Gantmakher</i>	83
Thermal Fluctuations in One-Dimensional Disordered Quantum Systems <i>Andreas Glatz</i>	91
Coulomb Drag between Quantum Wires: Effect of Small Momentum Transfer <i>L.I. Glazman, M. Pustilnik, E.G. Mishchenko, and A.V. Andreev</i>	119
Signatures of Spin-Charge Separation in Double-Quantum-Wire Tunneling <i>Yaroslav Tserkovnyak, Bertrand I. Halperin, Ophir M. Auslaender, and Amir Yacoby</i>	129
Transport of Interacting Electrons through a Double Barrier <i>I.V. Gornyi, and D.G. Polyakov</i>	141
Ratchet Effects in Luttinger Liquids <i>D.E. Feldman, S. Scheidl, and V.M. Vinokur</i>	147
<hr/>	
Part III Superconductivity in Nanostructures	
<hr/>	
Ferromagnetic-Superconducting Hybrid Systems <i>J.Y. Gu, Ya.B. Bazaliy, S.D. Bader, and C.Y. You</i>	159
STM Spectroscopy of the Local Density of States in Normal Metal - Superconductor Systems <i>L. Crétinon, A. Gupta, N. Moussy, B. Pannetier, and H. Courtois</i>	173
Quantum Tunneling between Paramagnetic and Superconducting States of a Nanometer-Scale Superconducting Grain Placed in a Magnetic Field <i>A.V. Lopatin, and V.M. Vinokur</i>	187
Domain Wall Superconductivity in Ferromagnetic Superconductors and Hybrid S/F Structures <i>A.Yu. Aladyshkin, A.I. Buzdin, A.A. Fraerman, A.S. Mel'nikov, D.A. Ryzhov, and A.V. Sokolov</i>	209

Rasba Spin-Orbit Interaction in a Ballistic Josephson Junction	
<i>I.V. Krive, L.Y. Gorelik, R.I. Shekhter, and M. Jonson</i>	215
Manifestation of Triplet Superconductivity in Superconductor-Ferromagnet Structures	
<i>F.S. Bergeret, A.F. Volkov, and K.B. Efetov</i>	229
<hr/>	
Part IV Noise and Fluctuation Phenomena	
<hr/>	
Phase Dependent Current Statistics in a Short-Arm Andreev Interferometer	
<i>E.V. Bezuglyi, E.N. Bratus, V.S. Shumeiko, and V.M. Vinokur</i>	241
Semiclassical Theory of Higher Cumulants of Noise	
<i>K.E. Nagaev</i>	257
Josephson Junctions as Threshold Detectors for Full Counting Statistics	
<i>Jens Tobiska, and Yuli V. Nazarov</i>	263
Energy Dependence of Current Noise in Superconducting/Normal Metal Junctions	
<i>M. Houzet, and F. Pistolesi</i>	271
Measurement of the Third Moment of Voltage Fluctuations in a Tunnel Junction	
<i>B. Reulet, J. Senzier, L. Spietz, C.M. Wilson, and D.E. Prober</i>	277
Shot Noise in Mesoscopic Transport Through Localised States	
<i>A.K. Savchenko</i>	283
<hr/>	
Part V Single Electron Physics	
<hr/>	
Single Particle Transport in Disordered Andreev Wires	
<i>N.B. Kopnin, A.S. Mel'nikov, and V.M. Vinokur</i>	291
Two-Channel Kondo Effect in a Modified Single Electron Transistor	
<i>Yuval Oreg</i>	297
Spin-Dependent Transport of Electrons in a Shuttle Structure	
<i>L.Y. Gorelik, S.I. Kulinich, R.I. Shekhter, M. Jonson, and V.M. Vinokur</i>	307
Index	321

List of Contributors

Amnon Aharony

School of Physics and Astronomy
Tel Aviv University
69978 Tel Aviv
Israel
aharony@post.tau.ac.il

Samuel D. Bader

Argonne National Laboratory
Materials Science Division
9700 South Cass Ave
Argonne, IL 60439
USA
bader@anl.gov

Igor S. Beloborodov

Argonne National Laboratory
Materials Science Division
9700 South Cass Ave
Argonne, IL 60439
USA
beloborodov@anl.gov

Eugene V. Bezuglyi

Institute for Low Temperature
Physics
and Engineering
Kharkov 61103
Ukraine
eugene@fy.chalmers.se

Norman O. Birge

Dept. of Physics and Astronomy,
Center for Fundamental
Materials Research, and Center for
Sensor Materials
Michigan State University
East Lansing, MI 48824-2320
USA
birge@pa.msu.edu

Yaroslov M. Blanter

Department of NanoScience and
DIMES
Delft University of Technology
Lorentzweg 1
2628CJ Delft
The Netherlands
blanter@tnntw14.tn.tudelft.nl

Venkat Chandrasekhar

Department of Physics and Astron-
omy
Northwestern University
2145 Sheridan Road
Evanston, IL 60208
USA
v-chandrasekhar@northwestern.edu

Vadim V. Cheianov

NORDITA
Blegdamsvej 17

Copenhagen, DK 2100
Denmark
cheianov@nordita.dk

Hervé Courtois
Centre de Recherches sur les Très
Basses Températures - C.N.R.S.
and Université Joseph Fourier
25 Avenue des Martyrs
38042 Grenoble
France
courtoih@grenoble.cnrs.fr

Ora Entin-Wohlman
School of Physics and Astronomy,
Tel Aviv University,
69978 Tel Aviv
Israel
entin@post.tau.ac.il

Dmitri E. Feldman
Department of Physics
Brown University
184 Hope Street
Providence, RI 02912
USA
Dmitri.Feldman@brown.edu

Vsevolod F. Gantmakher
Institute of Solid State Physics
RAS
143432, Chernogolovka, Moscow
Russia
gantm@issp.ac.ru

Yuval Gefen
Department of Condensed Matter
Physics
The Weizmann Institute of Science
Rehovot 76100
Israel
yuval.gefen@weizmann.ac.il

Andreas Glatz
Argonne National Laboratory
Materials Science Division
9700 South Cass Ave
Argonne, IL 60439
USA
glatz@anl.gov

Leonid I. Glazman
William I. Fine Theoretical Physics
Institute
School of Physics and Astronomy
University of Minnesota
116 Church Street SE
Minneapolis, MN 55455
USA
glazman@umn.edu

Bertrand I. Halperin
Lyman Laboratory of Physics
Harvard University
17 Oxford Street
Cambridge, MA 02138
USA
halperin@physics.harvard.edu

Nikolai B. Kopnin
Low Temperature Laboratory
Helsinki University of Technology
PO BOX 2200
02015 TKK
Finland
kopnin@boojum.hut.fi

Andrei V. Lopatin
Argonne National Laboratory
Materials Science Division
9700 South Cass Ave
Argonne, IL 60439
USA
lopatin@anl.gov

Alexander S. Melnikov
Institute for Physics of Microstruc-
tures

Russian Academy of Sciences
603950, Nizhny Novgorod, GSP-105
Russia
melnikov@ipm.sci-nnov.ru

Kirill E. Nagaev
Institute of Radioengineering and
Electronics
Russian Academy of Sciences
Mokhovaya ulica 11
125009 Moscow
Russia
nag@cplire.ru

Yuli V. Nazarov
Department of NanoScience
Delft University of Technology
2628 CJ Delft
The Netherlands
Y.V.Nazarov@tn.tudelft.nl

Yuval Oreg
Department of Condensed Matter
Physics
The Weizmann Institute of Science
Rehovot 76100
Israel
yuval.oreg@weizmann.ac.il

Fabio Pistolesi
Laboratoire de Physique et
Modélisation des Milieux Condensés
CNRS-UJF B.P. 166
F-38042 Grenoble
France
fabio.pistolesi@grenoble.cnrs.fr

Dmitri G. Polyakov
Institut für Nanotechnologie
Forschungszentrum Karlsruhe

76021 Karlsruhe
Germany
polyakov@int.fzk.de

Daniel E. Prober
Departments of Applied Physics and
Physics
Yale University
New Haven, CT 06520
USA
daniel.prober@yale.edu

Alexander K. Savchenko
School of Physics
University of Exeter
Stocker Road, Exeter, EX4 4QL
United Kingdom
A.K.Savchenko@ex.ac.uk

Stefan Scheidl
Institut für Theoretische Physik
Universität zu Köln
Zùlpicher Straße 77
50937 Köln
Germany
sts@thp.uni-koeln.de

Robert I. Shekhter
Department of Applied Physics
Chalmers University of Technology
and Göteborg University
SE-412 96 Göteborg
Sweden
shekhter@fy.chalmers.se

Anatoly F. Volkov
Theoretische Physik III
Ruhr-Universität Bochum
44780 Bochum
Germany
volkov@tp3.ruhr-uni-bochum.de

Coherence and Correlation Effects

Phase Measurements in Closed Aharonov-Bohm Interferometers

Amnon Aharony¹, Ora Entin-Wohlman¹, and Yoseph Imry²

¹ School of Physics and Astronomy, Raymond and Beverly Sackler Faculty of Exact Sciences, Tel Aviv University, Tel Aviv 69978, Israel
aharony@post.tau.ac.il

² Department of Condensed Matter Physics, The Weizmann Institute of Science, Rehovot 76100, Israel

Summary. We discuss measurements of the resonant quantum transmission amplitude $t_{QD} = -i|t_{QD}|e^{i\alpha_{QD}}$ through a quantum dot (QD), as function of the plunger gate voltage V . Mesoscopic solid state Aharonov-Bohm interferometers (ABIs) have been used to measure the “intrinsic” phase, α_{QD} , when the QD is placed on one of the paths. In a “closed” interferometer, connected to two terminals, the conductance $\mathcal{G} = \frac{2e^2}{h}|t_{QD}|^2$ through the ABI is an even function of the magnetic flux $\Phi = \hbar c\phi/e$ threading the ABI ring. Therefore, fits of \mathcal{G} to the 2-slit formula $A + B \cos(\phi + \beta)$ allow only jumps of β between 0 and π . Here we include the many reflections of the electrons within the ABI ring, and replace the 2-slit formula by a new formula, which allows to extract *both* $|t_{QD}|$ and α_{QD} from the closed ABI data. Also, the relation $|t_{QD}|^2 \propto \sin^2(\alpha_{QD})$ allows a direct measurement of $\alpha_{QD}(V)$, without interferometry.

1 Introduction and Review of Experiments

Mesoscopic quantum dots (QDs) represent artificial atoms with experimentally controllable properties [1, 2, 3]. Connecting a QD via two one-dimensional (1D) ‘metallic’ leads to electron reservoirs, one can vary the attraction of electrons to the QD by the ‘plunger gate voltage’, V . Measurements of the conductance \mathcal{G} through the QD, as function of V , show peaks whenever the Fermi energy ϵ_F of the electrons crosses a bound state on the QD. The quantum information on the resonant tunneling through the QD is contained in the *complex* transmission amplitude, $t_{QD} = -i\sqrt{\mathcal{T}_{QD}}e^{i\alpha_{QD}}$. It is thus of great interest to measure the V -dependence of both the magnitude \mathcal{T}_{QD} and the phase α_{QD} .

Model calculations (e.g. [4]) predict that \mathcal{T}_{QD} exhibits resonances at the bound state energies of the QD, while α_{QD} exhibits an interesting variation

between 0 and π , growing gradually through each resonance, and dropping sharply between consecutive resonances. The resonant dependence of \mathcal{T}_{QD} on V has been confirmed by many experiments [1, 2], which measure the conductance and take advantage of the Landauer formula [5], $\mathcal{G} = \frac{2e^2}{h} \mathcal{T}_{QD}$. However, the experimental measurement of α_{QD} has only become accessible since 1995 [6, 7], using the Aharonov-Bohm interferometer (ABI) [8].

The simplest method to measure the phase of a wave is based on the *two-slit interferometer* [9]. In this geometry, a coherent electron beam is split between two paths, going through two slits, and one measures the distribution of electrons absorbed on a screen behind the two slits. Assuming that each electron goes through one of the slits only *once*, without any reflection from the slits or from the screen, and assuming complete coherence, the distribution of electrons on the screen is given by $\mathcal{T} = |t|^2$, where $t = t_1 + t_2$ is the sum of the (complex) amplitudes of the waves which went via the two slits.

In the two-slit ABI, a magnetic flux Φ in the area surrounded by the two electronic paths creates a difference $\phi = e\Phi/\hbar c$ between the phases of the wave functions in the two branches of the ring [10], yielding $t = t_1 e^{i\phi} + t_2$. (Gauge invariance allows one to attach the AB phase ϕ to either branch). Writing $t_i = |t_i| e^{i\alpha_i}$, one thus has the ‘2-slit formula’, $\mathcal{T} = A + B \cos(\phi + \alpha)$, where $\alpha = \alpha_1 - \alpha_2$.

Placing a QD on one path, and changing its plunger gate voltage V , would vary the corresponding phase $\alpha_1 \equiv \alpha_{QD}$. If the 2-slit formula were valid, it would allow the determination of the dependence of α_{QD} on V . This was the motivation of Yacoby *et al.* [6], who placed a QD on one path of a closed mesoscopic ABI. Indeed, the measured conductance was periodic in ϕ , and the detailed dependence of \mathcal{G} on ϕ varied with V . However, close to a resonance the data did not fit the simple 2-slit formula; they required more harmonics in ϕ , e.g. of the form

$$\mathcal{T} = A + B \cos(\phi + \beta) + C \cos(2\phi + \gamma) + \dots, \quad (1)$$

with the conventions $B, C > 0$. Furthermore, the fitted phase β did not follow the continuous variation with V (as would be implied from the 2-slit scenario, where $\beta = \alpha_{QD} + \text{const}$). Instead, β exhibited discrete jumps by $\pm\pi$.

These jumps follow from the Onsager relations. Unlike the 2-slit geometry, the closed ABI requires many reflections of the electron waves from the ‘forks’ connecting the ring with the leads. Each such reflection adds a term to the interference sum of amplitudes, and modifies the simple 2-slit formula. In fact, unitarity (conservation of current) and time reversal symmetry imply that $\mathcal{G}(\phi) = \mathcal{G}(-\phi)$ [11], and therefore β (as well as γ etc.) *must* be equal to 0 or π . The additional reflections also explain the need for higher harmonics near resonances. Below we include these many reflections, and replace the 2-slit formula by a new one – which can be used to extract α_{QD} from the closed interferometer data [12].

Later experiments [7] opened the interferometer, by adding ‘lossy’ channels which break unitarity. Indeed, fitting the conductance to Eq. (1) yielded a phase $\beta(V)$ which was qualitatively similar to the calculated ‘intrinsic’

$\alpha_{QD}(V)$. However, it turns out that β depends on the details of the coupling to the open channels [13]; 2-slit conditions are recovered only after a careful tuning of the relevant parameters! Although such tuning is possible [4], it requires systematic studies of many configurations, and it leaves only a small fraction of the original current through the ABI. Therefore, it is desirable to have alternative ways to measure α_{QD} , as discussed below.

2 Model for the QD

We model the QD by a site D on a tight binding 1D chain [14]. All the on-site energies are zero, except $\epsilon_D \equiv V$ on the QD. Electron-electron interactions are included only via an on-site Hubbard interaction U on the QD. The hopping matrix elements $J_{i,i+1}$ on the chain are all equal to J , except on the bonds connected to the QD, where they are $J_{-1,D} = J_L$ and $J_{D,1} = J_R$. For $\epsilon_D = 0$, $U = 0$ and $J_L = J_R = J$, one has the simple wave eigenstates $|n\rangle = e^{ikna}$, with eigenenergies $\epsilon_k = -2J \cos ka$ (a is the lattice constant).

Following Ref. [14], the transmitted wave for $n > 1$ is $|n\rangle = t_{QD}e^{ikna}$, and (at $T = 0$) [12]

$$t_{QD} = -i\gamma_D \sin \alpha_{QD} e^{i\alpha_{QD}} \equiv 2i \sin |k| a J_L J_R g_D(\epsilon_k) / J, \quad (2)$$

with the QD asymmetry factor $\gamma_D = 2J_L J_R / (J_L^2 + J_R^2)$ and the ‘‘intrinsic’’ Green function on the QD, $g_D(\epsilon_k) = 1/[\epsilon_k - \epsilon_D - \Sigma_D(\epsilon_k)]$. Here, $\Sigma_D(\epsilon_k)$ is the self-energy on the QD, which contains contributions from the leads, $\Sigma_{D,ext} = -e^{i|k|a} (J_L^2 + J_R^2) / J$ and from the electron-electron interactions on the QD, $\Sigma_{D,int}$. As $\epsilon_D \equiv V$ increases, α_{QD} grows gradually from zero, through $\pi/2$ (at the resonance), towards π .

Interestingly, for this one-dimensional model, normalizing the measured

$$\mathcal{T}_{QD} = |t_{QD}|^2 = \gamma_D^2 \sin^2(\alpha_{QD}) \quad (3)$$

by its (V -independent) maximum $\max[\mathcal{T}_{QD}] \equiv \gamma_D^2$ relates α_{QD} with the measured \mathcal{T}_{QD} . Assuming coherence, this method for measuring α_{QD} directly from \mathcal{T}_{QD} eliminates the need for any complicated interferometry! Interestingly, this conclusion holds for any Breit-Wigner-like resonance, with an energy-independent width. It also holds for a multi-level QD, with many resonances. In the next section we discuss ways of extracting α_{QD} indirectly, from the closed AB interferometer measurements. Comparing results from $\sin^2(\alpha_{QD}) = \mathcal{T}_{QD} / \gamma_D^2 \equiv \mathcal{T}_{QD} / \max[\mathcal{T}_{QD}]$, from the closed interferometer [12] and from the open one [4] (all with the same QD) should serve as consistency checks for this conclusion.

3 Model for the closed AB interferometer

Our ABI is modeled by two paths between two ‘forks’: one path contains the QD, with the bonds hoppings J_L and J_R , and the other path contains

an interaction-free ‘reference’ site B , with bond hoppings $J_{-1,B} = I_L$ and $J_{B,1} = I_R$ and with a site energy $\epsilon_0 \equiv V_0$, controlled by the gate voltage V_0 . A magnetic flux Φ inside the AB ring is included by the replacement $J_R \rightarrow J_R e^{i\phi}$. As explained in Ref. [12], one can use the equation-of-motion method to derive the new fully “dressed” Green function on the QD, $G_D(\omega) = 1/[\omega - \epsilon_D - \Sigma(\omega)]$, with the dressed self-energy $\Sigma = \Sigma_{int} + \Sigma_{ext}$. Both terms in Σ differ from their counterparts in the “intrinsic” Σ_D , by contributions due to the reference path. The resulting transmission amplitude is

$$t = A_D t_{QD} e^{i\phi} + A_B t_B, \quad (4)$$

where $A_D = g_B(\epsilon_k - \epsilon_0)G_D(\epsilon_k)/g_D(\epsilon_k)$ and $A_B = 1 + G_D(\epsilon_k)\Sigma_{ext}(\epsilon_k)$. Also, $t_B = -i\gamma_B \sin \delta_B e^{i\delta_B} = 2i \sin |k| I_L I_R g_B / J$ is the transmission amplitude of the “reference” path (when $J_L = J_R = 0$, or $|\epsilon_D| \rightarrow \infty$), with the bare reference site Green function $g_B = 1/[\epsilon_k - \epsilon_0 + e^{i|k|}(I_L^2 + I_R^2)/J]$, and the asymmetry factor $\gamma_B = 2I_L I_R / (I_L^2 + I_R^2)$. Equation (4) looks like the 2-slit formula. However, each of the terms is now *renormalized*: A_D contains all the additional processes in which the electron “visits” the reference site, and A_B contains the corrections to t_B due to “visits” on the dot.

The Onsager relations, which require that \mathcal{T} depends on ϕ only via $\cos \phi$, imply that the ratio $K \equiv A_B t_B / (A_D t_{QD}) \equiv \tilde{x}[G_D(\epsilon_k)^{-1} + \Sigma_{ext}(\epsilon_k)]$, with the real coefficient $\tilde{x} = I_L I_R / [J_L J_R (\epsilon_k - \epsilon_0)]$, must be real. This implies that $\Im[G_D(\epsilon_k)^{-1} + \Sigma_{ext}(\epsilon_k)] \equiv \Im \Sigma_{int} \equiv 0$, namely that the width of the resonance, $\Im G_D(\epsilon_k)^{-1}$, is *fully determined by the non-interacting self-energy* $\Im \Sigma_{ext}(\epsilon_k)$.

An explicit calculation gives $\Sigma_{ext}(\epsilon_k) = \Sigma_{D,ext}(\epsilon_k) + \Delta_{ext}$, where $\Delta_{ext} = e^{2i|k|} g_B (J_L^2 I_L^2 + J_R^2 I_R^2 + 2J_L J_R I_L I_R \cos \phi) / J^2$. The term proportional to $\cos \phi$ comes from the electron clock- and counterclockwise motion around the AB “ring”. Similarly, one can write $\Sigma_{int}(\epsilon_k) = \Sigma_{D,int}(\epsilon_k) + \Delta_{int}$, and thus $G_D(\epsilon_k)^{-1} = g_D(\epsilon_k)^{-1} - \Delta$, with $\Delta = \Delta_{ext} + \Delta_{int}$. Hence, $t = A_D t_D (e^{i\phi} + K)$. Writing also $A_D = C/[1 - g_D(\epsilon_k)\Delta]$, with $C = (\epsilon_k - \epsilon_0)g_B$, we find

$$\mathcal{T} = |C|^2 \mathcal{T}_D \frac{1 + K^2 + 2K \cos \phi}{1 - 2\Re[g_D \Delta] + |g_D \Delta|^2}. \quad (5)$$

Although the numerator in Eq. (5) looks like the 2-slit formula, with $\beta = 0$ or π (depending on $\text{sign} K$), the new physics is contained in the denominator – which becomes important in the vicinity of a resonance. The central term in this denominator depends explicitly on the phase of the complex number g_D . Since this number is directly related to t_{QD} , via Eq. (2), one may expect to extract α_{QD} from a fit to Eq. (5), taking advantage of the dependence of the denominator on $\cos \phi$.

For $\Delta \approx \Delta_{ext}$, Eq. (5) becomes

$$\mathcal{T} = |C|^2 \mathcal{T}_{QD} \frac{1 + K^2 + 2K \cos \phi}{1 + 2P(z + \cos \phi) + Q(z + \cos \phi)^2}, \quad (6)$$

where $z = (J_L^2 I_L^2 + J_R^2 I_R^2)/(2J_L J_R I_L I_R)$, $P = \Re[vt_B t_{QD}]$, $Q = |vt_B|^2 \mathcal{T}_{QD}$, and $v = e^{2i|k|a}/(2\sin^2|k|a)$ depends only on the Fermi wavevector k , independent of any detail of the interferometer. A 5-parameter fit to the explicit ϕ -dependence in Eq. (6) for given values of V and V_0 then yields $|C|^2 \mathcal{T}_{QD}$, K , z , P and Q , and thus $\cos(\alpha_{QD} + \delta_B + 2|k|a) = P/\sqrt{Q}$, from which one can extract the V -dependence of α_{QD} . Since the V -dependence of \mathcal{T}_{QD} can also be extracted from the fitted values of either $|C|^2 \mathcal{T}_{QD}$ or Q , we end up with several consistency checks for the determination of α_{QD} . Additional checks arise from direct measurements of \mathcal{T}_{QD} and $\mathcal{T}_B = |t_B|^2$, by taking the limits $|V_0| = |\epsilon_0| \rightarrow \infty$ or $|V| = |\epsilon_D| \rightarrow \infty$.

For small \mathcal{T}_B , or large $|V_0| = |\epsilon_0|$, it is reasonable to conjecture that Δ_{int} is dominated by single visits of the electron at the reference site B . In that case, we expect the proportionality $\Delta_{int} \approx w(z + \cos \phi)$, with a real coefficient w . This yields the same dependence of \mathcal{T} on $\cos \phi$ as in Eq. (6), with a shifted coefficient v . If w depends only weakly on V , then this shift has little effect on the determination of α_{QD} .

Interestingly, a plot of Eq. (6) versus V and ϕ [12] looks very similar to the experimental plots in Ref. [17]. It would be very interesting to attempt detailed quantitative fits of data to our predictions.

4 Concluding remarks

Basically, we presented three methods to measure the intrinsic scattering phase of a quantum dot. The first method is based on Eq. (3), and does not involve interferometry. The second is based on Eq. (6), which allows one to extract information from measurements on the closed ABI. The third method, described in Ref. [4], uses the open ABI, but requires conditions under which this ABI behaves as a two-slit interferometer. As stated, a convincing approach would be to use more than one method, with the same QD, and to obtain consistent results.

Although Eq. (6) was justified only for non-interacting electrons or for the limit of small \mathcal{T}_B , we expect it to be qualitatively correct over a broader range. We emphasize that *a successful fit of the ϕ -dependence to Eq. (6) justifies the above assumptions*. If the various procedures to determine α_{QD} from Eq. (6) yield the same V -dependence, this would again confirm our assumptions. A failure of this check, or a more complicated dependence of the measured \mathcal{T} on $\cos \phi$, would require a more detailed treatment of the interactions.

Acknowledgements.— We thank B. I. Halperin, M. Heiblum, Y. Levinson, A. Schiller, H. A. Weidenmüller and A. Yacoby for helpful conversations. This project was carried out in a center of excellence supported by the Israel Science Foundation, with additional support from the Albert Einstein Minerva Center for Theoretical Physics at the Weizmann Institute of Science, and from the German Federal Ministry of Education and Research (BMBF) within the Framework of the German-Israeli Project Cooperation (DIP).

References

1. L. P. Kouwenhoven *et al.*, *Mesoscopic Electron Transport*, NATO Advanced Study Institute, Series E: Applied Science, Vol. **345**, edited by L. L. Sohn, L. P. Kouwenhoven and G. Schön (Kluwer, Dordrecht, 1997), p. 105.
2. Y. Imry, *Introduction to Mesoscopic Physics* (Oxford University Press, Oxford 1997; 2nd edition, 2002).
3. M. A. Kastner, *Physics Today* **46**(1) (1993) 24.
4. A. Aharony, O. Entin-Wohlman, B. I. Halperin and Y. Imry, *Phys. Rev.* **B66** (2002) 115311.
5. R. Landauer, *Phil. Mag.* **21** (1970) 863.
6. A. Yacoby, M. Heiblum, D. Mahalu and H. Shtrikman, *Phys. Rev. Lett.* **74** (1995) 4047.
7. R. Schuster *et al.*, *Nature* **385** (1997) 417.
8. Y. Gefen, Y. Imry and M. Ya. Azbel, *Phys. Rev. Lett.* **52** (1984) 129.
9. R. P. Feynmann, R. B. Leighton and M. Sands, *The Feynmann Lectures on Physics*, Vol. III, Chap. 1 (Addison-Wesley, Reading 1970).
10. Y. Aharonov and D. Bohm, *Phys. Rev.* **115** (1959) 485.
11. L. Onsager, *Phys. Rev.* **38** (1931) 2265; H. B. G. Casimir, *Rev. Mod. Phys.* **17** (1945) 343; M. Büttiker, *Phys. Rev. Lett.* **57** (1986) 1761.
12. A. Aharony, O. Entin-Wohlman and Y. Imry, *Phys. Rev. Lett.* **90** (2003) 156802.
13. O. Entin-Wohlman, A. Aharony, Y. Imry, Y. Levinson and A. Schiller, *Phys. Rev. Lett.* **88** (2002) 166801.
14. T. K. Ng and P. A. Lee, *Phys. Rev. Lett.* **61** (1988) 1768.
15. O. Entin-Wohlman, C. Hartzstein and Y. Imry, *Phys. Rev.* **B34** (1989) 921.
16. H. A. Weidenmüller, *Phys. Rev.* **B65** (2002) 245322.
17. K. Kobayashi, H. Aikawa, S. Katsumoto, and Y. Iye, *Phys. Rev. Lett.* **88**, (2002) 256806.

Berry Phase with Environment: Classical versus Quantum

Robert S. Whitney¹, Yuriy Makhlin^{2,3}, and Alexander Shnirman²,
and Yuval Gefen⁴

¹ Département de Physique Théorique, Université de Genève, CH-1211 Genève 4, Switzerland

² Institut für Theoretische Festkörperphysik, Universität Karlsruhe, 76128 Karlsruhe, Germany

³ Landau Institute for Theoretical Physics, Kosygin st. 2, 117940 Moscow, Russia

⁴ Department of Condensed Matter Physics The Weizmann Institute of Science, Rehovot 76100, Israel yuval.gefen@weizmann.ac.il

Summary. We discuss the concept of the Berry phase in a dissipative system. We show that one can identify a Berry phase in a weakly-dissipative system and find the respective correction to this quantity, induced by the environment. This correction is expressed in terms of the symmetrized noise power and is therefore insensitive to the nature of the noise representing the environment, namely whether it is classical or quantum mechanical. It is only the spectrum of the noise which counts. We analyze a model of a spin-half (qubit) anisotropically coupled to its environment and explicitly show the coincidence between the effect of a quantum environment and a classical one.

1 Introduction

Three papers published independently in 1932 by Zener, Landau and Stueckelberg [7, 22, 14] have introduced the phenomenon known today as Landau-Zener tunneling. The idea is to consider a 2-level system, where the energy of each level varies linearly with a classical variable (which, in turn, is varied linearly in time). As function of time, t , the energy levels should intersect but for the inter-level coupling Δ which gives rise to an “avoided crossing” in the spectrum, cf. Fig. 1. Using the spin notation, one can write the Hamiltonian as $\hat{\mathcal{H}} = \alpha t S_z + \Delta S_x$. Here $\mathbf{S} = \boldsymbol{\sigma}/2$, and σ_z, σ_x are Pauli spin-1/2 operators; α is the rate of change of the energy of the pseudo-spin at asymptotic

times. The avoided crossing gap is Δ . The probability of transition from, say, the lower level at time $-\infty$, to the upper level at time $+\infty$ is given by $P_{\text{LZ}} = \exp[-(\pi/2)\Delta^2/\alpha]$.

Besides being ubiquitous in physics and chemistry, the Landau-Zener framework appears to suggest a natural definition for the notion of adiabaticity. The adiabatic limit is approached when $P_{\text{LZ}} \ll 1$, i.e., $\alpha \ll \Delta^2$. The latter inequality involves a comparison of the rate of change (of the time dependent term in the Hamiltonian) with the gap in the spectrum, Δ . This notion of the adiabatic limit has become widespread. A closer look suggests that, in general, adiabaticity **cannot** be associated with comparing the rate of change to the gap. Indeed, on one hand any finite, discrete-spectrum system is coupled, however weakly, to the rest of the universe. Hence the emerging spectrum is, at least in principle, always continuous and gapless. The naive view would then imply that the adiabatic limit cannot be approached. This, on the other hand cannot be correct: if we consider a finite system with a discrete spectrum, for which adiabaticity is well defined, it is inconceivable that an infinitesimal coupling to the continuum (rendering the overall spectrum continuous) will change its physics in a dramatic way. The resolution of this problem is provided by the observation that the criterion for adiabaticity involves not only spectral properties but also the **matrix elements** of the system-environment coupling.

To gain some insight into this problem we focus here on the analysis of the Berry phase [1] in a weakly dissipative system. It is particularly timely to address this issue now given the recent experimental activities in realization of controlled quantum two-level systems (qubits), and in particular, the interest in observing a Berry phase (BP) (see, e.g., [5]). For instance, the superconducting qubits have a coupling to their environment, which is weak but not negligible [10, 15, 4], and thus it is important to find both the conditions under which the Berry phase can be observed and the nature of that Berry phase.

In this paper we appeal to a simple analysis of the problem. We first, in Section 3, consider a quantum-mechanical framework, where a perturbative approach is taken. When the environment is replaced by a single oscillator, a second-order perturbation analysis is straightforward and produces a result which allows for a simple interpretation. We then generalize the calculation for a host of environmental modes. In Section 4 we consider a toy model where the environment is replaced by a **classical** stochastic force. The quantities of interest, the Lamb shift and the Berry phase, are then calculated, and simple heuristic arguments are given to interpret the results. To complete the analogy with the analysis of the previous section, here the “single-oscillator environment” is replaced by a simple periodic classical force (of random amplitude). In Section 5 we summarize the relation between the quantum mechanical approach and the classical model in more general terms.

2 The system: spin + environment

We begin in the conventional way by writing the Hamiltonian for the “universe” (system + environment) as

$$\hat{\mathcal{H}} = \hat{\mathcal{H}}_{\text{sys}} + \hat{\mathcal{H}}_{\text{env}} + \hat{\mathcal{V}}_{\text{coupling}} \quad (1)$$

The system is defined as the set of those quantum degrees of freedom that one is interested to control and measure; the environment consists of all the rest, namely those degrees-of-freedom we can neither control nor measure. The coupling between the system and environment is $\mathcal{V}_{\text{coupling}}$. The properties of the environment are controlled by macroscopic parameters, such as temperature. Our treatment below applies to a reservoir at either zero or a finite temperature.

For our purposes it is sufficient to represent the environment by a single operator X which couples to a spin. The Hamiltonian then becomes

$$\hat{\mathcal{H}} = -\frac{1}{2} \mu g \mathbf{B} \cdot \hat{\boldsymbol{\sigma}} - \frac{1}{2} X \sigma_z + \hat{\mathcal{H}}_{\text{env}}. \quad (2)$$

Hereafter we put $\mu g = 1$. Below we express our results in terms of the statistical properties (correlators) of the environment’s noise, $X(t)$. Depending on the physical situation at hand, one can choose to model the environment via a bath of harmonic oscillators [6, 3]. In this case the generalized coordinate of the reservoir is defined as $X = \sum \lambda_i x_i$, where $\{x_i\}$ are the coordinate operators of the oscillators and $\{\lambda_i\}$ are the respective couplings. Eq. 2 is then referred to as the spin-boson Hamiltonian [8]. Another example of a reservoir could be a spin bath [11]⁵. However, in our analysis below we do not specify the type of the environment. We will only assume that the reservoir gives rise to markovian evolution on the time scales of interest. More specifically, the evolution is markovian at time scales longer than a certain characteristic time τ_c , determined by the environment⁶. We assume that τ_c is shorter than the dissipative time scales introduced by the environment, such as the dephasing or relaxation times and the inverse Lamb shift (the scale of the shortest of which we denote as T_{diss} , $\tau_c \ll T_{\text{diss}}$). We further assume that $\tau_c \ll t_P$, the

⁵ For any reservoir in equilibrium the fluctuation-dissipation theorem provides the relation between the symmetrized and antisymmetrized correlators of the noise: $S_X(\omega) = A_X(\omega) \coth(\omega/2T)$. Yet, the temperature dependence of S_X and A_X may vary depending on the type of the environment. For an oscillator bath, A_X (also called the spectral density $J_X(\omega)$) is temperature-independent, so that $S_X(\omega) = J_X(\omega) \coth(\omega/2T)$. On the other hand, for a spin bath S_X is temperature-independent and is related to the spins’ density of states, while $A_X(\omega) = S_X(\omega) \tanh(\omega/2T)$.

⁶ This time may be given by the correlation time of the fluctuations, but in general is a more subtle characteristic of the spectrum related to its roughness near qubit’s frequencies. Note further that for singular spectra τ_c may be ill defined and the perturbative analysis may fail. See, e.g., [2, 12, 13, 9, 21, 19].

characteristic variation time of the field $\mathbf{B}(t)$. Moreover, under these conditions we may consider only lowest-order (in the system-environment coupling) contributions to the quantities of interest: energy shifts, BP and relaxation rates. Indeed, if one divides the evolution time interval into short domains ($\ll t_P$), longer than τ_c but shorter than T_{diss} , fluctuations at different domains are uncorrelated and their effect can be analyzed separately. At the same time, for each domain ($\ll T_{\text{diss}}$) the effect of the noise is weak. Thus, to the leading order corrections to the dynamics may be described as corrections to the rates (energies) of the spin dynamics, which may be estimated perturbatively. We also consider an underdamped spin, with the dissipative times longer than the period of the coherent dynamics, $T_{\text{diss}} \gg 1/B$. This implies that the time windows alluded to above consist of numerous oscillations, in other words they are $\gg 1/B$.

We have chosen an anisotropic spin-environment coupling, $\propto \sigma_z$. This is a realistic model, e.g., for many designs of solid-state qubits, where the different components of the “spin” are influenced by entirely different environmental degrees of freedom [10, 15, 4]. While our analysis can be generalized to account for multiple-directional fluctuating fields [20], here we focus on unidirectional fluctuations (along the z axis).

Another remark to be made concerns the possibility to observe a (weak) dissipative correction to Berry phase in spite of the dephasing and relaxation phenomena. While the respective time scales (T_1 , T_2 and the inverse of the correction to the Berry phase) scale similarly with the strength of fluctuations (inversely proportionally to the noise power), they are dominated by different frequency domains. Indeed, the dephasing and relaxation are known to be dominated by resonant fluctuations with frequencies close to B (for the relaxation and the corresponding contribution to dephasing) and 0 (for the pure dephasing), cf. Eq. (15) below. In contrast, as we shall see below, the Lamb shift and the correction to the Berry phase accumulate contribution from the entire range of frequencies. Thus, one may think of (engineering) a system with an environment whose fluctuations at $\nu \sim B$ and $\nu \sim 0$ are suppressed. In this case, one can easily observe an observable correction to the Berry phase at times when the dephasing and relaxation are still negligible.

3 Quantum-mechanical analysis

In this section we consider a two-level system coupled to an environment which we treat as a quantum-mechanical system. We begin with a discussion of the Lamb shift and then show, in Subsection 3.3, how the results for the Lamb shift may be used to find the environment-induced correction to the Berry phase and the relaxation times.

3.1 Lamb shift as level repulsion

Consider first, for illustration, a simple system of the spin coupled to a single oscillator, with the Hamiltonian

$$\mathcal{H} = -\frac{1}{2}B\sigma_z - \frac{1}{2}c\sigma_x(a^\dagger + a) + \omega_0 a^\dagger a, \quad (3)$$

where c is the coupling constant. Let $|n\rangle$ denote the n -th level of the oscillator; the second-order corrections to the energies of the states $|\uparrow, 0\rangle$ and $|\downarrow, 0\rangle$ are

$$E_\uparrow^{(2)} = -\frac{|\langle \uparrow, 0 | \mathcal{V} | \downarrow, 1 \rangle|^2}{\omega_0 + B} = -\frac{1}{4} \frac{c^2}{\omega_0 + B}, \quad (4)$$

and

$$E_\downarrow^{(2)} = -\frac{|\langle \downarrow, 0 | \mathcal{V} | \uparrow, 1 \rangle|^2}{\omega_0 - B} = -\frac{1}{4} \frac{c^2}{\omega_0 - B}, \quad (5)$$

where $\mathcal{V} \equiv (c/2)\sigma_x(a^\dagger + a)$ is the perturbation. This results in the following correction to the level spacing $E_\downarrow - E_\uparrow$:

$$E_\downarrow^{(2)} - E_\uparrow^{(2)} = \frac{c^2}{2} \frac{B}{B^2 - \omega_0^2}. \quad (6)$$

This correction (the Lamb shift) has different signs for fast ($\omega_0 > B$) and slow ($\omega_0 < B$) oscillators. As one can see from Eqs. (4), (5), this result can be understood in terms of the level repulsion [21]: the perturbation couples the level $|\uparrow, 0\rangle$ to $|\downarrow, 1\rangle$ and $|\downarrow, 0\rangle$ to $|\uparrow, 1\rangle$. The levels of the latter pair are closer, and the coupling has a stronger effect on their energies. They repel each other due to the coupling, thus reducing the distance between $|\uparrow, 0\rangle$ and $|\downarrow, 0\rangle$ for $\omega_0 > B$ and increasing it for $\omega_0 < B$.

3.2 Second-order perturbative analysis

In this section we find the Lamb shift using the lowest-, second-order perturbative analysis. In the Hamiltonian (2) we treat the coupling term $\mathcal{V} = -\frac{1}{2}X\sigma_z$ as a perturbation: $\mathcal{H} = \mathcal{H}_0 + \mathcal{V}$. The eigenstates of \mathcal{H}_0 are $|\alpha, i\rangle$, where $\alpha = \uparrow_B / \downarrow_B$ denotes the eigenstates of the spin without dissipation, with the spin direction parallel or antiparallel to the field \mathbf{B} , and i denotes eigenstates of the environment. The perturbation theory gives for the corrections to their eigenenergies:

$$E_{\alpha, i}^{(2)} = -\sum_{\beta, j} \frac{|\langle \alpha, i | \mathcal{V} | \beta, j \rangle|^2}{E_\beta^{(0)} + E_j^{(0)} - E_\alpha^{(0)} - E_i^{(0)} - i0}. \quad (7)$$

For $\mathcal{V} = -\frac{1}{2}X\sigma_z$ we notice that $\langle \uparrow_B | \sigma_z | \uparrow_B \rangle^2 = \langle \downarrow_B | \sigma_z | \downarrow_B \rangle^2 = \cos^2 \theta$ and $\langle \uparrow_B | \sigma_z | \downarrow_B \rangle^2 = \langle \downarrow_B | \sigma_z | \uparrow_B \rangle^2 = \sin^2 \theta$, and find for the environment-averaged

quantities $E_\alpha^{(2)} \equiv \sum_i \rho_i E_{\alpha,i}^{(2)}$ (see the discussion of these quantities at the end of this subsection):

$$E_\uparrow^{(2)} = -\frac{\cos^2 \theta}{4} \sum_{i,j} \frac{\rho_i |\langle i|X|j\rangle|^2}{E_j^{(0)} - E_i^{(0)} - i0} - \frac{\sin^2 \theta}{4} \sum_{i,j} \frac{\rho_i |\langle i|X|j\rangle|^2}{B + E_j^{(0)} - E_i^{(0)} - i0}. \quad (8)$$

The correction to E_\downarrow is obtained by substituting $B \rightarrow -B$ into the above equation. Now using the identity

$$\frac{1}{E - i0} = i \int_0^\infty dt e^{-i(E-i0)t}, \quad (9)$$

we rewrite Eq. (8) as

$$E_\uparrow^{(2)} = -\frac{i}{4} \int_0^\infty dt \langle X(t)X(0) \rangle (\cos^2 \theta + \sin^2 \theta e^{-iBt}) e^{-0t}, \quad (10)$$

where we have used the relation

$$\langle X(t)X(0) \rangle = \sum_{i,j} \rho_i \langle i|X|j\rangle \langle j|X|i\rangle e^{-i(E_j - E_i)t}. \quad (11)$$

In terms of the the Fourier transform $\langle X_\nu^2 \rangle \equiv \int dt \langle X(t)X(0) \rangle e^{i\nu t}$ we obtain

$$E_\uparrow^{(2)} = -\frac{1}{4} \cos^2 \theta \int \frac{d\nu}{2\pi} \frac{\langle X_\nu^2 \rangle}{\nu - i0} - \frac{1}{4} \sin^2 \theta \int \frac{d\nu}{2\pi} \frac{\langle X_\nu^2 \rangle}{\nu + B - i0}. \quad (12)$$

For the Lamb shift $E_{\text{Lamb}}^{(2)} \equiv \Re(E_\downarrow^{(2)} - E_\uparrow^{(2)})$ this gives a principal value integral

$$E_{\text{Lamb}}^{(2)} = \frac{1}{2} \sin^2 \theta \mathcal{P} \int \frac{d\nu}{2\pi} \frac{S_X(\nu)}{B - \nu} = B \sin^2 \theta \mathcal{P} \int_0^\infty \frac{d\nu}{2\pi} \frac{S_X(\nu)}{B^2 - \nu^2}, \quad (13)$$

where

$$S_X(\nu) \equiv \frac{1}{2} (\langle X_\nu^2 \rangle + \langle X_{-\nu}^2 \rangle) = \frac{1}{2} \int dt \langle [X(t), X(0)]_+ \rangle e^{i\nu t}. \quad (14)$$

Thus the Lamb shift is expressed in terms of the symmetrized correlator S_X and is insensitive to the antisymmetric part of the noise spectrum.

As one can see from Eq. (13), in agreement with the discussion in the previous section, the high-frequency noise ($\nu > B$) reduces the energy gap between the spin states [8], while the low frequency modes ($\nu < B$) increase the energy gap.

Similarly, from Eq. (12) one can evaluate the dephasing time:

$$\frac{1}{T_2} = -\Im(E_\uparrow^{(2)} + E_\downarrow^{(2)}) = \frac{\cos^2 \theta}{4} S_X(\nu = 0) + \frac{\sin^2 \theta}{4} S_X(\nu = B). \quad (15)$$

This expression correctly reproduces the contribution of the transverse fluctuations ($\propto \sin^2 \theta$) to the dephasing rate, but underestimates the longitudinal contribution ($\propto \cos^2 \theta$) by a factor of two (cf. Ref. [2, 12, 16]). One can show that an accurate evaluation of this contribution, as well as the analysis of the relaxation, requires taking into account corrections to the eigenstates, and not only to the eigenenergies (7). More precisely, our calculation of the corrections to the eigenenergies in this subsection corresponds to evaluation only of the four left diagrams in Fig. 7 of Ref. [9]; the term $i0$ in the denominators allows one to find also the outgoing transition rates *from* the eigenstates (and the respective contribution, $\propto \sin^2 \theta$, to dephasing) but only the part of the ‘pure-dephasing’ rate, $\propto \frac{1}{4} \cos^2 \theta$. Analysis of the two remaining diagrams in Fig. 7 and those in Fig. 6 allows one to find also the pure dephasing rate (as well as the incoming transition rates, the latter though do not require an extra evaluation due to probability conservation).

3.3 From Lamb shift to Berry phase

So far we have analyzed the environment-induced correction to the level splitting (the Lamb shift). Using the results above one can evaluate also the environment-induced correction to the Berry phase for a slow cyclic variation of the magnetic field \mathbf{B} [17, 18, 20, 19].

Indeed, consider the simplest case of conic variations of the field around the z -axis (to which the environment is coupled), as shown in Fig. 1: the field varies at a constant rate, with the low angular velocity ω_B , and traverses the circle after the period $t_P \equiv 2\pi/\omega_B$. The analysis of the spin dynamics is considerably simplified by going to the frame, rotating with the angular velocity $\omega_B \hat{z}$, where \hat{z} is the unit vector along the z -axis. In this frame the spin is subject to the fluctuating field $X\hat{z}$ and the field $\mathbf{B} + \omega_B \hat{z}$, which is *stationary*. Thus, in this frame one can use the results of the analysis above to obtain the Lamb shift, if one substitutes \mathbf{B} by $\mathbf{B} + \omega_B \hat{z}$. In other words, the correction to the Lamb shift associated with the variation of the field \mathbf{B} in time, is given by taking the derivative $\omega_B \partial_{B_z}$ of the Lamb shift (13) and multiplying by the period of variation, t_P . After a full period the basis of the rotating frame makes a complete circle and returns to its initial position, i.e. coincides with the laboratory frame’s basis. Hence the phases accumulated in the rotating and laboratory frames coincide, and it is sufficient to evaluate it in the rotating frame. Thus, one finds the environment-induced correction to the Berry phase to be

$$\delta\Phi_{BP} = 2\pi \frac{\partial E_{\text{Lamb}}(\mathbf{B})}{\partial B_z}. \quad (16)$$

Taking the derivative of Eq. (13), we find:

$$\delta^{(2)}\Phi_{BP} = \cos \theta \sin^2 \theta \mathcal{P} \int d\nu \frac{S_X(\nu)(2\nu - 3B)}{2B(B - \nu)^2}. \quad (17)$$

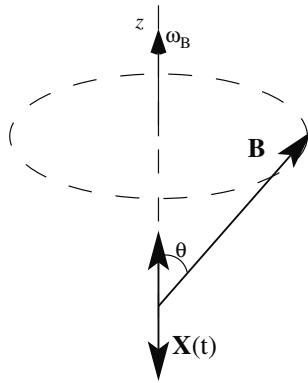


Fig. 1. Conic variations of the field around the z -axis (to which the environment is coupled). (see text)

(Notice the convention: this expression gives the correction to the relative Berry phase between the spin-up and spin-down states, rather than to the phases of each of these states.) As for the Lamb shift, the contributions of the high- and low-frequency fluctuations are of opposite signs. For the Berry phase the contribution changes sign at $\nu = 3B/2$.

In passing we note that this analysis can be generalized to an arbitrary (but adiabatic) path $\mathbf{B}(t)$, this enables one to see that the correction to the Berry phase is geometric, but that its geometric nature is very different from the Berry phase of an isolated spin-half [20].

In Section 4 we shall find exactly the same expression for the Lamb shift and therefore for the Berry phase in the case of classical environment.

3.4 High-frequency noise: renormalization of the transverse B -field

Consider now the influence of the high-frequency fluctuations in the environment only ($\nu \gg B$). Since the frequencies of the fluctuations are much higher than the typical spin-dynamics frequencies, one may eliminate these high-frequency fluctuations using the adiabatic (Born-Oppenheimer) approximation, as described, e.g., by Leggett et al. [8].

Indeed, consider the spin-boson model, with the Hamiltonian

$$\mathcal{H} = -\frac{1}{2}(\mathbf{B} + X\hat{z})\boldsymbol{\sigma} + \mathcal{H}_{\text{env}}, \quad (18)$$

where $X = \sum_i c_i (a_i^\dagger + a_i)$ and $\mathcal{H}_{\text{env}} = \sum_i \omega_i a_i^\dagger a_i$. Let us ignore the low-frequency oscillators and focus on those at high frequencies $\nu \gg B$. These fast oscillators adjust almost instantaneously to the slowly varying spin state. For the last two terms of the Hamiltonian (18) two lowest-energy states are $|\tilde{\uparrow}\rangle = |\uparrow\rangle \prod_i |g_i^\uparrow\rangle$ and $|\tilde{\downarrow}\rangle = |\downarrow\rangle \prod_i |g_i^\downarrow\rangle$. Here $|g_i^\uparrow\rangle$ denotes the ground state of the i th oscillator corresponding to the spin state $|\uparrow\rangle$, i.e. the ground state of

$\omega_i a_i^\dagger a_i + c_i (a_i^\dagger + a_i)$, and $|g_i^\downarrow\rangle$ is defined similarly; further eigenstates of the last two terms are separated by a gap $\sim \nu$.

Consider now the matrix elements of the first term $-\frac{1}{2}\mathbf{B}\boldsymbol{\sigma}$ in this two-state low-energy subspace; one finds that its transverse component is suppressed by the factor

$$\prod_i \langle g_i^\uparrow | g_i^\downarrow \rangle = \prod_i \exp(-c_i^2/2\omega_i^2) = \exp\left(-\int_0^\infty \frac{d\nu}{2\pi} \frac{J_X(\nu)}{\nu^2}\right), \quad (19)$$

where $J_X(\nu) \equiv \pi \sum_i c_i^2 \delta(\nu - \omega_i)$ is the spectral density of the oscillator bath. At a finite temperature T each high-frequency oscillator remains in its thermal equilibrium state (subject to the spin state), rather than the ground state, and on the rhs of Eq. (19) the spectral density $J_X(\nu)$ is replaced by the thermal noise power $S_X(\nu) = J_X(\nu) \coth(\nu/2k_B T)$.

Thus the role of the high-frequency oscillators is to suppress the transverse field component (in other words, the transverse g -factor). If we are interested only in the contribution to the level spacing (the Lamb shift), one should consider only the longitudinal ($\parallel \mathbf{B}$) part of the renormalization, i.e. multiply the result by $\sin \theta$, to obtain Eq. (13).

3.5 Effective-action analysis

One can study the spin dynamics integrating out the environment and using the effective action for the spin. We derive the effective action using the Feynman-Vernon-Keldysh technique. For the interaction $-X s_z$ with the z -component of the spin, the effective action (the influence functional) reads

$$i\Phi_{\text{infl}} = -\frac{1}{2} \int_{C_K} dt \int_{C_K} dt' s_z(t) \cdot s_z(t') [iG_X(t, t')], \quad (20)$$

where we assumed the Gaussian statistics of X , and defined the Green function G_X as $iG_X(t, t') = \langle T_{C_K} X(t) X(t') \rangle$. The time ordering here refers to the Keldysh time contour C_K , and in Eq. (20) we integrate over C_K ; accordingly each of the time dependent variables assumes a ‘Keldysh index’ u, d indicating the upper/lower branch of this contour.

After the Keldysh rotation one obtains the influence functional in terms of the classical and quantum components, $s_z^c \equiv (s_z^u + s_z^d)/2$ and $s_z^q \equiv s_z^u - s_z^d$:

$$\Phi_{\text{infl}} = - \int dt dt' \left[s_z^q(t) G_X^R(t-t') s_z^c(t') + \frac{1}{4} s_z^q(t) G_X^K(t-t') s_z^q(t') \right], \quad (21)$$

in terms of the retarded and Keldysh Green functions, $G_X^R \equiv -i\theta(t-t') \langle [X(t), X(t')]_- \rangle$ and $G_X^K \equiv -i\langle [X(t), X(t')]_+ \rangle = -2iS_X(t-t')$.

For classical noise X the commutator in the definition of G^R vanishes, and one finds

$$\Phi_{\text{infl}}^{\text{class}} = \frac{i}{2} \int dt \int dt' s_z^q(t) S_X(t-t') s_z^q(t'). \quad (22)$$

The results (13), (17) for the Lamb shift and the Berry phase involve only S_X and not the antisymmetrized correlator. Hence for the analysis of these quantities it should be sufficient to use the functional (22). Alternatively, one may consider a problem with a classical random field $\mathbf{X}(t)$ to reproduce these results. In the next section we perform the corresponding analysis.

4 The Classical Model

In this section we analyze the dynamics of a spin subject to a classical random field and derive the equation of motion for the spin dynamics (the spin-evolution operator), averaged over the fluctuations. Following the discussion of the case with quantum fluctuations, we first analyze the dynamics in a stationary field \mathbf{B} and a random field; exactly as in the quantum case one can reduce the analysis of the dissipative corrections to the Berry phase accumulated over a conic loop to the problem with a stationary field by going over to a rotating frame.

As we have demonstrated above, in the quantum problem the results for the corrections to the phase and dephasing, associated with the controlled dynamics of the magnetic field, involve only the symmetric part of the noise correlator, one expects that the results for these quantities in the classical problem, expressed in terms of the noise power, would coincide with the quantum results. Indeed, we find this relation below.

Specifically, we analyze the following problem: a spin \mathbf{S} is coupled to a controlled magnetic field \mathbf{B} (stationary for now, but to be varied slowly in a Berry-phase experiment) and a randomly fluctuating field $\mathbf{X}(t)$, which we treat as a random variable with the correlation function given by $S_X(t)$. Its dynamics is governed by the Larmor equation:

$$\dot{\mathbf{S}} = [\mathbf{B} + \mathbf{X}(t)] \times \mathbf{S}. \quad (23)$$

This equation can be used to describe the dynamics of either a classical spin or the average spin value (i.e. the density matrix) of a spin-1/2.

As we discussed in the Introduction, we assume that the noise is weak and short-correlated, i.e., that considerable dissipative contributions to the spin dynamics arise on time scales much longer than the typical correlation time τ_c of the noise. Below we discuss the influence of the low- and high-frequency fluctuations on the (classical) spin dynamics and recover the results of the quantum analysis above. Further, using the result for the low-frequency contribution we obtain the correction to the Berry phase from the environmental fluctuations at all frequencies.

4.1 Low-frequency noise: Lamb shift

Consider first the effect of a slowly fluctuating random field $\mathbf{X} = X\hat{z}$. Similar to the quantum-mechanical analysis in Section 3 we begin with the case of harmonic fluctuations (of random amplitude) and purely transverse noise ($\mathbf{B} = B\hat{x}$, i.e. $\theta = \pi/2$). Consider fluctuations $X = c_\nu \cos(\nu t)$ at a low frequency $\nu \ll B$, during a time interval δt . To evaluate the evolution operator, we analyze the dynamics in a reference frame $(\hat{\xi}, \hat{\eta}, \hat{\zeta})$ fluctuating together with the field (with the ζ -axis along $\mathbf{B} + \mathbf{X}(t)$ and the η -axis, for instance, orthogonal to \mathbf{B} and \mathbf{X}). Since the fluctuating angular velocity of this frame's rotation is negligible, $\sim c_\nu \nu / B \ll c_\nu$, the effective magnetic field in this frame $|\mathbf{B} + \mathbf{X}(t)|\hat{\zeta}$ points along the ζ -axis. Thus the dynamics reduces to rotation about this axis by the angle $\phi(t) = \int_t^{t+\delta t} d\tau |\mathbf{B} + \mathbf{X}(\tau)| \approx \int_t^{t+\delta t} d\tau (B + X^2(\tau)/2B)$, where $B = |\mathbf{B}|$. Averaging the transverse spin component $S_x + iS_y \propto e^{i\phi(t)}$ one finds a lowest-order contribution to the phase factor, $\delta t \langle X^2 \rangle / 2B$, i.e. a Lamb shift $c_\nu^2 / 4B$ (we assumed δt much longer than the period of oscillations, $1/\nu$).

In principle, the evolution in the laboratory frame differs from that in the rotation frame. Transformation to/from the rotation frame at the beginning and the end of the time interval introduces corrections to the evolution operator of order c_ν / B . This is however a negligible boundary contribution. Indeed, for a sufficiently long time interval $\delta t \gg 1/c_\nu$ the phase shift due to the Lamb shift, of order $c_\nu^2 \delta t / B$, is much larger (but still small, as long as $\delta t \ll B/c_\nu^2$).

Similar results hold for more general low-frequency fluctuations, non-harmonic and with arbitrary direction θ . Indeed, in the same rotating frame the dynamics reduces to rotation about the ζ -axis by the angle $\phi(t) = \int_t^{t+\delta t} d\tau |\mathbf{B} + \mathbf{X}(\tau)| \approx \int_t^{t+\delta t} d\tau (B + X_\parallel(\tau) + X_\perp^2(\tau)/2B)$, where $X_\parallel = X \cos \theta$, $X_\perp = X \sin \theta$ are the longitudinal and transverse components of \mathbf{X} (relative to \mathbf{B}). Averaging the transverse spin component $\propto e^{i\phi(t)}$ one finds, apart from dephasing, a lowest-order contribution to the phase factor, $\delta t \langle X_\perp^2 \rangle / 2B$, and hence the Lamb shift

$$\delta E = \sin^2 \theta \int \frac{d\nu}{4\pi} \frac{S_X(\nu)}{B}, \quad (24)$$

where θ is the angle between \mathbf{B} and the direction \hat{z} of the noise. This result coincides with the low-frequency contribution in Eq. (13).

4.2 From low frequencies to all frequencies

The expression (24) and the symmetry of the problem suggests a way to find the contribution of all, not only slow, modes in the environment to the Lamb shift (and later to the Berry phase). Indeed, we discuss weak short-correlated noise, i.e. such that its contribution to the dynamics on time scales of order τ_c is small. Contributions from different time intervals $\sim \tau_c$ are uncorrelated and add up independently. Hence in the evaluation of the (real and imaginary) contribution of such a short interval to the evolution frequencies (the Lamb

shift, the dephasing and relaxation rates) it is enough to consider the lowest non-vanishing, i.e. second order.

The symmetry of the problem can be used to analyze the structure of such a second-order contribution. The spin-rotational symmetry (about the \mathbf{B} -field's direction) and the time-translational symmetry imply that (i) the longitudinal and transverse fluctuations, X_{\perp} and X_{\parallel} , do not interfere and may be considered separately; (ii) it is convenient to expand the transverse fluctuating field in circularly polarized harmonic modes, and the latter contribute independently.

The longitudinal noise gives rise to the pure dephasing (and only the low frequencies $\lesssim 1/T_2$ contribute), without affecting the level splitting. As for the transverse noise, for a single circularly polarized mode at frequency ν it is convenient to analyze its contribution in the spin frame, rotating at frequency ν around the field \mathbf{B} . In this frame the Larmor field is $B - \nu$ in the direction of \mathbf{B} , and the fluctuating circularly polarized mode is slow. Applying to this mode Eq. (24), going back to the laboratory frame and adding up contributions of all modes we arrive at the expression for the correction to the Larmor frequency:

$$\delta E = \sin^2 \theta \mathcal{P} \int \frac{d\nu}{4\pi} \frac{S(\nu)}{B - \nu}. \quad (25)$$

It is thus this result which needs to be compared with the quantum correction (Lamb shift) of the previous section. Symmetrization of the integral in Eq. (25) w.r.t. to ν brings it to the form of Eq. (13). Notice that regularization of this expression via the introduction of $+i0$ in the denominator allows us also to recover the imaginary part of the Lamb shift, i.e. a contribution to the dephasing rate.

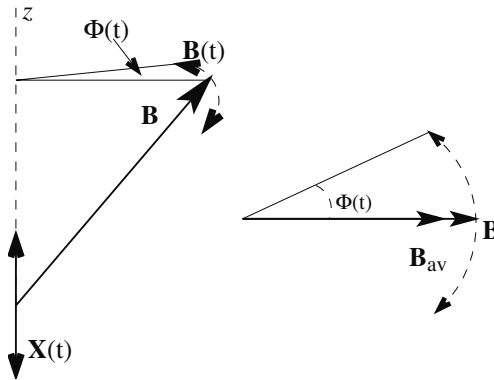


Fig. 2. (see text)

4.3 High frequencies

Although Eq. (25) describes the contribution of all frequencies, it is interesting to discuss specifically the limit of high frequencies. In this subsection we provide an argument which parallels the result of subsection 3.4: the high-frequency fluctuations ($\nu \gg B$) suppress the transverse ($\perp \hat{z}$) component of the \mathbf{B} -field.

Indeed, to solve for the dynamics in the presence of high-frequency fluctuations in a fixed direction, $X(t)\hat{z}$, and the static field \mathbf{B} , let us analyze the dynamics in the frame that rotates about the \hat{z} -axis with angular velocity $X(t)$, i.e. differs from the lab frame by a rotation by the fluctuating angle $\Phi(t) = \int_0^t X(\tau)d\tau$. The rotation of this frame is chosen to exactly compensate for the field $X(t)\hat{z}$, and the Larmor field $\mathbf{B}(t)$ in this frame is just the \mathbf{B} -field, but now fluctuating due to the frame's rotation as shown in Fig. 2. The spin dynamics is governed by the Larmor equation $\dot{\mathbf{S}} = \mathbf{B}(t) \times \mathbf{S}$, and the value of the spin changes considerably only on time scales of order $1/B$, during which many fluctuations occur. Looking at the dynamics on intermediate time scales, between $1/\nu$ and $1/B$, one finds that the spin dynamics is governed by the value of the \mathbf{B} -field averaged over fast fluctuations. The averaging affects only the horizontal (orthogonal to z) component of the \mathbf{B} -field. The direct evaluation shows that the horizontal component is suppressed exactly by the factor $\exp[-\int_0^\infty (d\nu/2\pi)S_X(\nu)/\nu^2]$ (cf. Eq. (19)). For instance, for a single mode at frequency ν we have $X(t) = 2X_\nu \cos(\nu t)$ and $\Phi(t) = 2X_\nu \sin(\nu t)/\nu$; then the transverse component of the field is suppressed by the factor $1 - \langle \Phi^2 \rangle / 2$, and $\langle \Phi^2 \rangle / 2 = \langle X_\nu^2 \rangle / \nu^2$. This evaluation of the dynamics in the rotating frame relies on the small parameter B/ν .

The spin-evolution operator (before averaging) $\hat{O}_{\text{lab}}(t, t')$ in the laboratory frame is related to that in the rotating frame, $\hat{O}_{\text{lab}}(t, t') = \hat{O}_z(-\Phi(t))\hat{O}_{\text{rot}}(t, t')\hat{O}_z(\Phi(t'))$, via the transformation $O_z(\Phi(t))$ from the lab frame to the rotating frame. However, this transformation $\hat{O}_z(\Phi(t))$ at the beginning and at the end of the evolution is close to the identity operator, and taking it into account adds only a boundary effect, which does not grow with the size of the time interval and is therefore negligible.

4.4 Berry phase under classical noise

To find a dissipation-induced correction to the Berry phase we may use the same approach as in Section 3.3: first, we find the Lamb shift for a stationary field \mathbf{B} and then evaluate the Berry phase using the relation (16). In this way we find the same expression (17) for the Berry phase.

5 Conclusions

In this paper we have derived expressions for the environment-induced correction to the Berry phase, for a spin coupled to an environment. On one hand, we presented a simple quantum-mechanical derivation for the case when the environment is treated as a separate quantum system. On the other hand, we analyzed the case of a spin subject to a random classical field. The quantum-mechanical derivation provides a result which is insensitive to the antisymmetric part of the random-field correlations. In other words, the results for the Lamb shift and the Berry phase are insensitive to whether the different-time values of the random-field operator commute with each other or not. This observation gives rise to the expectation that for a random classical field, with the same noise power, one should obtain the same result. For the quantities at hand, our analysis outlined above involving classical randomly fluctuating fields has confirmed this expectation.

Furthermore, we provided simple arguments, which allow one to understand the contribution of fluctuations in various frequency ranges (below and above the Larmor frequency).

Acknowledgements. — We thank M. Chlascinski, R. Chhajlany, G. Schön for discussions. This work was supported by the German-Israeli foundation (GIF), by the Minerva foundation, by the Israel Science Foundation (ISF) of the Israel Academy, by the Center for Functional Nanostructures (CFN) of the DFG, and by the Landesstiftung BW. R.W. was also supported by EPSRC fellowship GR/R44836/01 during the latter part of this work. Y.M. was supported by the S. Kovalevskaya award of the Humboldt foundation, the BMBF, and the ZIP programme of the German government.

References

1. Berry, M. V. (1984). Quantal phase factors accompanying adiabatic changes. *Proc. R. Soc. Lond.*, 392:45.
2. Bloch, F. (1957). Generalized theory of relaxation. *Phys. Rev.*, 105:1206.
3. Caldeira, A. O. and Leggett, A. J. (1983). Quantum tunneling in a dissipative system. *Ann. Phys. (NY)*, 149:374.
4. Chiorescu, I., Nakamura, Y., Harmans, C. J. P. M., and Mooij, J. E. (2002). Coherent quantum dynamics of a superconducting flux qubit. *Science*, 299:1869.
5. Falci, G., Fazio, R., Palma, G. H., Siewert, J., and Vedral, V. (2000). Detection of geometric phases in superconducting nanocircuits. *Nature*, 407:355–358.
6. Feynman, R. P. and Vernon, F. L. (1963). The theory of a general quantum system interacting with a linear dissipative system. *Ann. Phys. (NY)*, 24:118.
7. Landau, L. D. (1932). Zur Theorie der Energieübertragung II. *Physik. Z. Sowjet.*, 2:46. [A theory of energy transfer. II, *Collected Papers of L. D. Landau*, Pergamon and Gordon & Breach, 1965, p. 63].
8. Leggett, A. J., Chakravarty, S., Dorsey, A. T., Fisher, M. P. A., Garg, A., and Zwerger, W. (1987). Dynamics of the dissipative two-state system. *Rev. Mod. Phys.*, 59:1.

9. Makhlin, Yu., Schön, G., and Shnirman, A. (2003). Dissipation in Josephson qubits. In Fazio, R., Gantmakher, V. F., and Imry, Y., editors, *New directions in mesoscopic physics (towards nanoscience)*. Kluwer, Dordrecht.
10. Nakamura, Y., Pashkin, Yu. A., and Tsai, J. S. (1999). Coherent control of macroscopic quantum states in a single-Cooper-pair box. *Nature*, 398:786.
11. Prokof'ev, N. and Stamp, P. (2000). Theory of the spin bath. *Rep. Prog. Phys.*, 63:669.
12. Redfield, A. G. (1957). On the theory of relaxation processes. *IBM J. Res. Dev.*, 1:19.
13. Slichter, C. (1978). *Principles of Magnetic Resonance*. Springer, Berlin, 2nd edition.
14. Stueckelberg, E. C. G. (1932). Theorie der unelastischen Stöße zwischen Atomen. *Helv. Phys. Acta*, 5:369.
15. Vion, D., Aassime, A., Cottet, A., Joyez, P., Pothier, H., Urbina, C., Esteve, D., and Devoret, M. H. (2002). Manipulating the quantum state of an electrical circuit. *Science*, 296:886.
16. Weiss, U. (1999). *Quantum dissipative systems*. World Scientific, Singapore, 2nd edition.
17. Whitney, R. and Gefen, Y. (2001). Does Berry phase exist for a system coupled to its environment? In *Electronic correlations: from Meso- to Nano-physics*, Proceedings of XXXVIth Rencontres de Moriond. cond-mat/0107359.
18. Whitney, R. and Gefen, Y. (2003). Berry phase in a non-isolated system. *Phys. Rev. Lett.*, 90:190402.
19. Whitney, R. and Gefen, Y. (2004). *in preparation*.
20. Whitney, R., Makhlin, Yu., Shnirman, A., and Gefen, Y. (2004). *in preparation*.
21. Wilhelm, F. K., Kleff, S., and von Delft, J. (2004). The spin-boson model with a structured environment: A comparison of approaches. *Chem. Phys.*, 296:345.
22. Zener, C. (1932). Non-adiabatic crossing of energy levels. *Proc. R. Soc. London A*, 137:696.

Quantum Mesoscopic Phenomena

Electron Transport in Granular Metals

I. S. Beloborodov¹, K. B. Efetov^{2,3}, A. V. Lopatin¹, and V. M. Vinokur¹

¹ Materials Science Division, Argonne National Laboratory, Argonne, Illinois 60439, USA beloborodov@anl.gov

² Theoretische Physik III, Ruhr-Universität Bochum, 44780 Bochum, Germany

³ L. D. Landau Institute for Theoretical Physics, 117940 Moscow, Russia

Summary. We investigate transport in a granular metallic system at large tunneling conductance between the grains, $g_T \gg 1$. We show that at low temperatures, $T \leq g_T \delta$, where δ is the single mean energy level spacing in a grain, the coherent electron motion at large distances dominates the physics, contrary to the high temperature ($T > g_T \delta$) behavior where conductivity is controlled by the scales of the order of the grain size. The conductivity of one and two dimensional granular metals, in the low temperature regime, decays with decreasing temperature in the same manner as that in homogeneously disordered metals, indicating thus an insulating behavior. However, even in this temperature regime the granular structure remains important and there is an additional contribution to conductivity coming from short distances. Due to this contribution the metal-insulator transition in three dimensions occurs at the value of tunnel conductance $g_T^C = (1/6\pi) \ln(E_C/\delta)$, where E_C is the charging energy of an isolated grain, and not at the generally expected $g_T^C \propto 1$. Corrections to the density of states of granular metals due to the electron-electron interaction are calculated.

1 Introduction

A great deal of research in the current mesoscopic physics focuses on understanding properties of granular metals (see [1, 2, 3]). The interest is motivated by the fact that while their properties are generic for a wealth of strongly correlated systems with disorder, granular metals offer a unique experimentally accessible tunable system where both the interaction strength and degree of disorder can be controlled.

The key phenomenon revealing the most of the underlying physics is transport, where the effects of interactions play a crucial role. The processes of electron tunneling from grain to grain that govern electron transfer, are

accompanied by charging the grains involved after each electron hop to another grain. This may lead to a Coulomb blockade, and one justly expects this effect to be of the prime importance at least in the limit of weak coupling. It makes it thus clear, on a qualitative level, that it is the interplay between the the grain-to-grain coupling and the electron-electron Coulomb interaction that controls transport properties of granular metals; yet, despite the significant efforts expended, a quantitative theory of transport in metallic granular systems is still lacking.

A step towards formulation such a theory was made recently in [[3]]. It was shown that depending on the dimensionless tunneling conductance g_T one observes either exponential-, at $g_T \ll 1$, or logarithmic, at $g_T \gg 1$ temperature dependence of conductivity. The consideration in [[3]] was based on the approach developed by Ambegaokar, Eckern and Schön (AES) [5] for tunnel junctions. This technique however, as shown in [4], applies only at temperatures $T > g_T \delta$, where δ is the mean energy level spacing in a single grain. At low temperature region, $T \leq g_T \delta$, the effects of the electron coherent motion at distances much exceeding the single grain size a must be included; this important regime is not described by the AES approach [4].

Although experimentally the low temperature regime is well within the experimental reach [1, 2], it has never been addressed theoretically so far. The important question whether the system is a metal or becomes an insulator, in other words, whether the conductivity of the granular metals at large conductances remain finite in the limit of $T \rightarrow 0$ is still open.

In this paper we investigate the low-temperature conductivity of granular samples focusing on the case of large tunneling conductance between the grains, $g_T \gg 1$. To this end we develop a technique that goes beyond the AES approach and includes effects of coherent electron motion at distances larger than the size of the grain. Without the Coulomb interaction the granular system would be a good metal in the limit, $g_T \gg 1$, and our task is to include the charging effects into the theory. We find that at temperatures, $T \leq g_T \delta$ properties of the granular metal depend on the dimensionality of the array, and corrections to the conductivity and density of states due to the effects of Coulomb interaction are similar to those obtained in Ref. [7] for a homogeneous metal. Thus at low temperatures the systems behaves essentially as a homogeneous metal contrasting the case of large temperatures, $T \gg g_T \delta$ considered in Ref. [3].

This in particular means that at large conductances the 3D system is a good metal. On the other hand, at $g_T \ll 1$ a granular sample is in the insulating state. Therefore a 3D system should exhibit a metal-insulator transition at the critical value of the conductance g_T , such that samples with conductances $g_T > g_T^C$ are metals and their conductivity remains finite at $T \rightarrow 0$ while samples with $g_T < g_T^C$ are insulators and their conductivity vanishes at $T \rightarrow 0$.

2 Results

The main results of our work are as follows: (i) We find the critical value g_T^C of the tunnel conductance at which the metal-insulator transition in $3D$ occurs

$$g_T^C = (1/6\pi) \ln(E_C/\delta), \quad (1)$$

where E_C is the charging energy of an isolated grain. (ii) We find the expression for the conductivity of a granular metal that includes corrections due to Coulomb interaction and holds for all temperatures as long as these corrections are small. The corresponding answer can be conveniently written separating the correction due to the contribution from the large energy scales $\varepsilon > g_T\delta$ from that coming from the low energy scales $\varepsilon < g_T\delta$. Denoting corrections as $\delta\sigma_1$ and $\delta\sigma_2$ respectively we have

$$\sigma = \sigma_0 + \delta\sigma_1 + \delta\sigma_2, \quad (2)$$

where $\sigma_0 = 2e^2g_Ta^{2-d}$, with a being the size of a single grain is the classical Drude conductivity for a granular metal (spin included). Correction $\delta\sigma_1$ in Eq. (2) contains the dimensionality of the array d only as a coefficient and is given by the following expression [3],

$$\frac{\delta\sigma_1}{\sigma_0} = -\frac{1}{2\pi dg_T} \ln \left[\frac{g_T E_C}{\max(T, g_T\delta)} \right]. \quad (3)$$

On the contrary the correction $\delta\sigma_2$ in Eq. (2) that is important only at temperatures $T < \delta g_T$ strongly depends on the dimensionality of the array

$$\frac{\delta\sigma_2}{\sigma_0} = \begin{cases} \frac{\alpha}{12\pi^2 g_T} \sqrt{\frac{T}{g_T\delta}} & d = 3, \\ -\frac{1}{4\pi^2 g_T} \ln \frac{g_T\delta}{T} & d = 2, \\ -\frac{\beta}{4\pi} \sqrt{\frac{\delta}{Tg_T}} & d = 1. \end{cases} \quad (4)$$

Here $\alpha = \int_0^\infty dx x^{-1/2} [1 - \coth(x) + x/\sinh^2(x)] \approx 1.83$ and $\beta = \int_0^\infty dx x^{-3/2} [\coth(x) - x/\sinh^2(x)] \approx 3.13$ are the numerical constants. For a $3d$ granular system a temperature independent term of the order $1/g_T$ has been subtracted in the first line in Eq. (4).

Corrections $\delta\sigma_1$ and $\delta\sigma_2$ are of a different origin: the correction $\delta\sigma_1$ comes from the large energy scales, $\varepsilon > g_T\delta$ where the granular structure of the array dominates the physics. On the other hand, correction $\delta\sigma_2$ in Eq. (4) is similar to that obtained for homogeneous metals long ago [7] and comes from the low energy scales, $\varepsilon \leq g_T\delta$, where the coherent electron motion on the scales larger than the grain size a dominates the physics.

It is important to note that in the low temperature regime all temperature dependence of conductivity comes from the correction $\delta\sigma_2$. At the same time, in this regime the correction $\delta\sigma_1$, though being temperature independent, still exists and can be even larger than $\delta\sigma_2$.

When deriving Eqs. (2) we neglected possible weak localization corrections that may originate from quantum interference of electron waves. This approximation is legitimate if a magnetic field is applied as in Ref. [1] or dephasing is strong due to inelastic processes.

3 Model and Derivation

Now we turn to the description of our model and the derivation of Eqs. (2): We consider a d -dimensional array of metallic grains with the Coulomb interaction between electrons. The motion of electrons inside the grains is diffusive and they can tunnel from grain to grain. In principle, the grains can be clean such that electrons scatter mainly on grain surfaces. We assume that the sample in the absence of the Coulomb interaction would be a good metal. For large tunneling conductance we may also neglect the nonperturbative charging effects (discreteness of the electron charge) [6], which are exponentially small (as $\exp(-\#g_T)$). Although we assume that the dimensionless tunneling conductance g_T is large, it should be still smaller than the grain conductance, g_0 , such that $g_T < g_0$. This inequality means that the granular structure is still important and the main contribution to the macroscopic resistivity comes from the contacts between the grains.

The system of weakly coupled metallic grains can be described by the Hamiltonian

$$\hat{H} = \hat{H}_0 + \hat{H}_c + \sum_{ij} t_{ij} [\hat{\psi}^\dagger(r_i) \hat{\psi}(r_j) + \hat{\psi}^\dagger(r_j) \hat{\psi}(r_i)], \quad (5)$$

where t_{ij} is the tunneling matrix element corresponding to the points of contact r_i and r_j of i -th and j -th grains. The Hamiltonian \hat{H}_0 in Eq. (5) describes noninteracting isolated disordered grains. The term \hat{H}_c describes the Coulomb interaction inside and between the grains. It has the following form

$$\hat{H}_c = \frac{e^2}{2} \sum_{ij} \hat{n}_i C_{ij}^{-1} \hat{n}_j, \quad (6)$$

where C_{ij} is the capacitance matrix and \hat{n}_i is the operator of electron number in the i -th grain. In the regime under consideration one can neglect the coordinate dependence of a single grain diffusion propagator. The electron hopping between the grains can be included using the diagrammatic technique developed in Refs. [8, 4], which we outline below.

The electron motion in a random impurity potential within a single grain can be considered using the standard diagrammatic techniques described, for example in Ref. [9]. Electron hopping between the grains can be considered in a similar way assuming that tunneling matrix elements between neighboring grains are random variables obeying the Gaussian statistics and correlated as



Fig. 1. Self energy of the electron Green function averaged over impurity potential inside the grains and over tunneling elements between the grains. Averaging over the impurity potential is represented by the dotted line (a) while tunneling elements are represented by crossed circles (b).

$$\langle t_{k_1, k_2} t_{k_3, k_4} \rangle = t^2 (\delta_{k_1, k_3} \delta_{k_2, k_4} + \delta_{k_1, k_4} \delta_{k_2, k_3}), \quad (7)$$

where t is related to the average intergranular conductance as $g_T = 2\pi t^2 / \delta^2$. The average electron Green function is defined by the Dyson equation where the self energy, shown on Fig. 1 has two contributions: The first contribution (a) corresponds to scattering inside a single grain while the second (b) is due to processes of scattering between the neighboring grains. Both these processes result in a similar contribution $\sim \text{sign}(\omega)$ to the electron self-energy, thus on the level of single particle electron Green function intergranular scattering results only in a small renormalization of the relaxation time τ

$$\tau^{-1} = \tau_0^{-1} + 2dg_T\delta, \quad (8)$$

where τ_0 is the electron mean free time in a single grain.

The next step is to consider the diffusion motion of electron through a granular metal: Diffusion motion inside a single grain is given by the usual ladder diagram that results in the diffusion propagator

$$D_0(\Omega) = \frac{1}{|\Omega|}, \quad (9)$$

where Ω is the Bosonic Matsubara frequency. Coordinate dependence in (9) was neglected since we assume the zero dimensional limit for a single grain. Tunneling between the grains is accounted for in a similar way, such that the total diffusion propagator is given by the ladder diagrams shown on Fig 2a. This results in the following expression:

$$D(\Omega, q) = \frac{1}{|\Omega| + \delta\varepsilon_q}, \quad (10)$$

where $\varepsilon_q = 2g_T \sum_{\mathbf{a}} (1 - \cos \mathbf{q}\mathbf{a})$ with \mathbf{a} being the lattice vectors. For small quasimomenta $q \ll a^{-1}$ we have $\varepsilon_q \rightarrow g_T \delta a^2 q^2$ such that the diffusion propagator (10) describes the diffusion motion on the scales much larger than the granular size with effective diffusion coefficient $D = g_T a^2 \delta$.

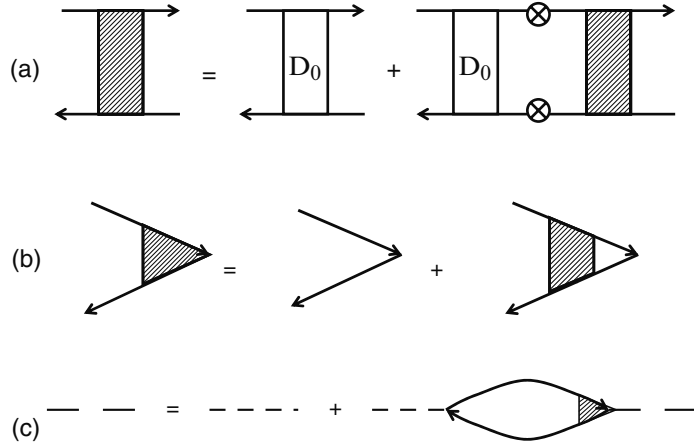


Fig. 2. These diagrams represent (a) Dyson equation for diffusion propagator, (b) interaction vertex dressed by impurity and intergranular scattering, (c) Screened Coulomb interaction.

Similar ladder diagrams describe the dressing of interaction vertex as it shown in Fig. 2b. The dressed vertex can be used to obtain the polarization operator, that defines effective dynamically screened Coulomb interaction (Fig 2c):

$$V(\Omega, q) = \left[\frac{C(q)}{e^2} + \frac{2\varepsilon_q}{|\Omega| + \delta\varepsilon_q} \right]^{-1}. \quad (11)$$

The conductivity of the granular metals is given by the analytical continuation of the Matsubara current-current correlator. In the absence of the electron-electron interaction the conductivity is represented by the diagram (a) in Fig. 3 that results in high temperature (Drude) conductivity σ_0 which is defined below Eq. (2). First order interaction corrections to the conductivity are given by the diagrams (b-e) in Fig. 3. These diagrams are analogous to ones considered in Ref. [7] for the correction to the conductivity of homogeneous metals. We consider the contributions from diagrams (b,c) and (d,e) separately: The sum of the diagrams (b,c) results in the following correction to the conductivity

$$\frac{\delta\sigma_1}{\sigma_0} = -\frac{1}{2\pi dg_T} \text{Im} \sum_{\mathbf{q}} \int d\omega \gamma(\omega) \varepsilon_{\mathbf{q}} \tilde{V}(\omega, \mathbf{q}). \quad (12)$$

where $\gamma(\omega) = \frac{d}{d\omega} \omega \coth \frac{\omega}{2T}$, and the potential $\tilde{V}(\omega, \mathbf{q})$ is the analectic continuation of the screened Coulomb potential with dressed interaction vertices attached at both ends

$$\tilde{V}(\omega, \mathbf{q}) = \frac{2E_C(\mathbf{q})}{(\varepsilon_{\mathbf{q}}\delta - i\omega)(4\varepsilon_{\mathbf{q}}E_C(\mathbf{q}) - i\omega)}. \quad (13)$$

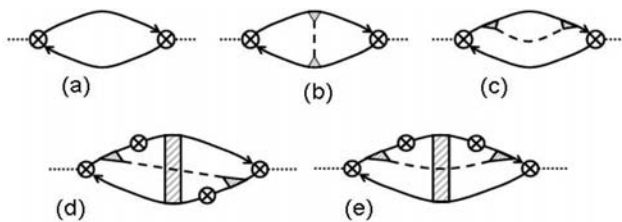


Fig. 3. Diagrams describing the conductivity of granular metals: the diagram (a) corresponds to σ_0 in Eq. (2) and it is the analog of Drude conductivity. Diagrams (b)-(e) describing first order correction to the conductivity of granular metals due to electron-electron interaction. The solid lines denote the propagator of electrons and the dashed lines describe effective screened electron-electron interaction. The sum of the diagrams (b) and (c) results in the conductivity correction $\delta\sigma_1$ in Eq. (2). The other two diagrams, (d) and (e) result in the correction $\delta\sigma_2$.

The above expression was simplified using that the charging energy $E_C(\mathbf{q}) = e^2/2C(\mathbf{q})$, expressed in terms of the Fourier transform of the capacitance matrix $C(\mathbf{q})$ is much larger than δ . Performing the integration over the frequency and summing over the quasimomentum \mathbf{q} in Eq. (12) with the logarithmic accuracy we obtain the correction (3). One can see from Eq. (12) that the contribution $\delta\sigma_1$ in Eq. (3) comes from the large energy scales, $\varepsilon > g_T\delta$ such that at low temperatures the logarithm is cut off on the energy scale of the order of $g_T\delta$.

To obtain the total correction to the conductivity of granular metal the two other diagrams, (d) and (e) in Fig. 3 should be taken into account. These diagrams result in the following contribution to the conductivity

$$\frac{\delta\sigma_2}{\sigma_0} = -\frac{2g_T\delta}{\pi d} \sum_{\mathbf{q}} \int d\omega \gamma(\omega) \text{Im} \frac{\tilde{V}(\omega, \mathbf{q}) \sum_{\mathbf{a}} \sin^2(\mathbf{q}\mathbf{a})}{\varepsilon_{\mathbf{q}}\delta - i\omega}. \quad (14)$$

In contrast to the contribution $\delta\sigma_1$ in Eq. (12), the main contribution to the sum over the quasimomentum \mathbf{q} in Eq. (14) comes from the low momenta, $q \ll 1/a$. In this regime the capacitance matrix, $C(\mathbf{q})$ in Eqs. (13) and (14) has the following asymptotic form

$$C^{-1}(\mathbf{q}) = \frac{2}{a^d} \begin{cases} \ln(1/qa) & d = 1, \\ \pi/q & d = 2, \\ 2\pi/q^2 & d = 3. \end{cases} \quad (15)$$

Using Eqs. (13-15), we obtain the result for the correction $\delta\sigma_2$ in Eq. (4). This correction has a physical meaning similar to that of the Altshuler-Aronov correction [7] derived for homogeneous disordered metals.

Comparing our results in Eqs. (2) with those obtained in Ref. [3] using the AES functional we see that the correction to the conductivity obtained in Ref. [3] is equivalent to the correction $\delta\sigma_1$ in Eq. (2), which corresponds in our approach to the sum of diagrams (b) and (c) in Fig. 3. The correction

$\delta\sigma_2$ in Eq. (2) becomes important only at low temperatures, $T < g_T\delta$ where AES functional is not applicable. While in our approach both corrections to the conductivity must be small $\delta\sigma_1, \delta\sigma_2 \ll \sigma_0$ the method of Ref. [3] gives a possibility to show that for $T \gg g_T\delta$ the dependence of the conductivity is logarithmic so long as $\sigma/e^2 a^{2-d} \gg 1$.

It follows from Eq. (4) that at low temperatures, $T < g_T\delta$, for a $3d$ granular array, there are no essential corrections to the conductivity coming from the low energies since the correction $\delta\sigma_2$ is always small. This means that the result for the renormalized conductance, \tilde{g}_T of Ref. [3] (see also [10]) for $3D$ samples within the logarithmic accuracy can be written as

$$\tilde{g}_T(T) = g_T - \frac{1}{6\pi} \ln \left[\frac{g_T E_C}{\max(\tilde{g}_T \delta, T)} \right], \quad (16)$$

such that it is valid for *all* temperatures as long as the renormalized conductance, $\tilde{g}_T \gg 1$. One can see from Eq. (16) that for bare conductance, $g_T \gg (1/6\pi) \ln(g_T E_C/\delta)$ the renormalized conductance, \tilde{g}_T is always large and the system remains metallic down to zero temperatures. In the opposite limit $g_T < (1/6\pi) \ln(g_T E_C/\delta)$, the system flows when decreasing the temperature to the strong coupling regime, $\tilde{g}_T \sim 1$ that indicates the onset of the insulating phase. We see that with the logarithmic accuracy the critical value of the conductance g_T^C is given by Eq. (1).

The result for the bare critical conductance in Eq. (1) agrees with the estimate for g_T^C that follows from the consideration of Coulomb blockade phenomena in a single grain [12]: the contribution of Coulomb blockade to thermodynamic quantities in the regime of strong coupling is controlled by the factor $\sim \exp[-\pi g(T)]$, where $g(T) = g_T - (1/Z\pi) \ln(g_T E_C/T)$ with Z being the number of contacts. Coulomb blockade effects become strong at $g(T) \sim 1$. Taking $T \sim g_T\delta$ and $Z = 6$ we estimate the bare conductance as $g_T^C \sim (1/6\pi) \ln(g_T E_C/T)$ that coincides with Eq. (1).

Corrections to the density of states (DOS) can be obtained in a similar way by considering the diagrams shown on Fig 4. The diagram (b) results only in the energy shift, and therefore is not important, while the diagram (a) results in the following contribution

$$\frac{\delta\nu(\varepsilon)}{\nu_0} = -\frac{1}{4\pi} \sum_{\mathbf{q}} \text{Im} \int d\omega \frac{\tanh[(\varepsilon - \omega)/2T]}{(\varepsilon_{\mathbf{q}}\delta - i\omega)[\varepsilon_{\mathbf{q}} - i\omega/4E_C(\mathbf{q})]}. \quad (17)$$

Here ν_0 is the DOS for noninteracting electrons, $\varepsilon_{\mathbf{q}}$ and $E_C(\mathbf{q})$ were defined below Eqs. (12) and (13) respectively. Using Eq. (17) for a $3D$ granular array we obtain

$$\frac{\delta\nu_3}{\nu_0} = -\frac{A}{2\pi g_T} \ln \left[\frac{E_C g_T}{\max(\tilde{\varepsilon}, g_T\delta)} \right], \quad (18)$$

where $A = g_T a^3 \int d^3q / (2\pi)^3 \varepsilon_{\mathbf{q}}^{-1} \approx 0.253$ and $\tilde{\varepsilon} = \max\{T, \varepsilon\}$. For $\tilde{\varepsilon} \gg g_T\delta$ the correction to the DOS (18) coincides with the one obtained in Ref. [3]

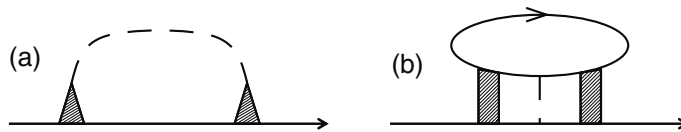


Fig. 4. Diagrams representing the first order corrections to the single particle density of states $\nu(\epsilon)$.

using AES approach. It follows from Eq. (18) that for a $3D$ array of grains, as in case with conductivity, the main contribution to the DOS comes from the large energy scales, $\epsilon > g_T \delta$.

Using Eq. (17) for a $2d$ array we obtain the following result for the correction to the DOS

$$\frac{\delta \nu_2}{\nu_0} = -\frac{1}{16g_T \pi^2} \begin{cases} 2 \ln^2(g_T E_C / \tilde{\epsilon}) & \tilde{\epsilon} \gg g_T \delta, \\ \ln \frac{g_T \delta}{\tilde{\epsilon}} \ln \frac{g E_C^4}{\tilde{\epsilon} \delta^3} + 2 \ln^2 \frac{E_C}{\delta} & \tilde{\epsilon} \ll g_T \delta. \end{cases} \quad (19)$$

Using the relation between the tunneling conductance, g_T and the diffusion coefficient, $D = g_T a^2 \delta$ one can see that the temperature (energy) dependence of the DOS for $\tilde{\epsilon} \ll g_T \delta$ given by Eq. (19) coincides up to the constant term with the result for the correction to the DOS of the homogeneous metal [7].

The logarithmic behavior (3) of the conductivity is in a good agreement with experimental findings [1, 2]. It would be very interesting to extend the resistivity measurements to the low temperature regime where we predict the temperature dependence (4). A similar logarithmic dependence of resistivity on temperature was recently found in high- T_c compounds $La_{2-y}Sr_yCuO_4$ and $Bi_2Sr_{2-x}La_xCuO_{6+\delta}$ in a very strong magnetic field [11, 13]. A possible granularity of these samples was suggested in Ref. [3]. Recently the microscopic granularity was directly experimentally observed in the superconducting state of $Bi_2Sr_2CaCu_2O_{8+\delta}$ by the STM probe [14]. If we accept that samples studied in [11, 13] are indeed microscopically granular, we can compare the results of the experiments with our predictions. When doing so it is convenient to scale three dimensional conductivity to the conductivity of CuO planes, σ_{plane} . According to our predictions

$$d\sigma_{plane}/d \ln T = (e^2/\pi \hbar) k, \quad (20)$$

where the coefficient $k = 1/2\pi$ in the low temperature- and $k = 1/d$ in the high temperature regimes. While in the low temperature regime the application of Eq. (20) is legitimate only under the assumption that electrons in different CuO plane are incoherent, in the high temperature regime the behavior of conductivity according to Eq. (3) is logarithmic for any dimension. In this regime the real dimensionality d should be replaced by $d = Z/2$, where Z is

the (average) number of the contacts of each grain with all the adjacent grains. Describing the data shown in Fig. 3 of Ref. [13] by our log dependencies at temperature $T \approx 5K$ we extract $k \simeq 0.4$, for Sr concentration of $y = 0.08$ for $La_{2-y}Sr_yCuO_4$ [15]; for the $Bi_2Sr_{2-x}La_xCuO_{6+\delta}$ compound we find $k \simeq 0.2$ for $x = 0.84$ La concentration, and $k \simeq 0.3$ for $x = 0.76$. For each particular curve the values k extracted from Fig. 3 of Ref. [13] increase with temperature (especially in case of $LSCO$), this is in a complete agreement with our results provided that the “coherent-incoherent” crossover occurs at about $T \sim 5K$. At higher temperatures k noticeably exceeds $1/2\pi$, supporting the idea of a granularity of doped cuprates.

4 Conclusions

In conclusion, we have investigated transport properties of granular metals at large tunneling conductance and obtained corrections to the conductivity, Eqs. (2,3,4) and DOS, Eqs. (18,19) due to electron-electron interaction. We have shown that at temperatures, $T > g_T\delta$ the granular structure of the array dominates the physics. On the contrary at temperatures, $T \leq g_T\delta$ the large-scale coherent electron motion is crucial. Comparison our results with experimental data supports the assumption about a granular structure of doped high- T_c cuprates.

Acknowledgements. — We thank A. Andreev, A. Koshelev, A. Larkin and K. Matveev for useful discussion of the results obtained. K. E. thanks German-Israeli programs DIP and GIF for a support. This work was supported by the U.S. Department of Energy, Office of Science through contract No. W-31-109-ENG-38 and by the A.P. Sloan and the Packard Foundations.

References

1. A. Gerber *et al.*, Phys. Rev. Lett. **78**, 4277 (1997).
2. R. W. Simon *et al.*, Phys. Rev. B **36**, 1962 (1987).
3. K. B. Efetov and A. Tschersich, Europhys. Lett. **59**, 114 (2002); Phys. Rev. B **67**, 174205 (2003).
4. I. S. Beloborodov *et al.*, Phys. Rev. B **63**, 115109 (2001).
5. V. Ambegaokar, U. Eckern, and G. Schön, Phys. Rev. Lett. **48**, 1745 (1982).
6. I. S. Beloborodov and A. V. Andreev, in preparation.
7. B. L. Altshuler and A. G. Aronov, in *Electron-Electron Interaction in Disordered Systems*, ed. by A. L. Efros and M. Pollak, North-Holland, Amsterdam (1985).
8. I. S. Beloborodov and K. B. Efetov, Phys. Rev. Lett. **82**, 3332, (1999).
9. A. A. Abrikosov, L. P. Gorkov, I. E. Dzyaloshinski, *Methods of quantum field theory in statistical physics*, Dover Publications, New York
10. J. M. Kosterlitz, Phys. Rev. Lett. **37**, 1577 (1976);
11. Y. Ando *et al.*, Phys. Rev. Lett. **75**, 4662, (1995); G. S. Boebinger *et al.*, Phys. Rev. Lett. **77**, 5417 (1996).

12. I. S. Beloborodov, A. V. Andreev and A. I. Larkin, Phys. Rev. B **68**, 024204 (2003).
13. S. Ono *et al.*, Phys. Rev. Lett. **85**, 638 (2000).
14. K. M. Lang *et al.*, Nature. **415**, 412 (2002).
15. This curve for $Bi_2Sr_{2-x}La_xCuO_{6+\delta}$, $x = 0.15$ shows a very wide crossover at about 20K extending to low temperatures. Thus there are just a very few points in the narrow temperature interval 1-3K where our approach is applicable. This invalidates the comparison the data with our results for this particular curve.

Studies of Current-Driven Excitations in Co/Cu/Co Trilayer Nanopillars

S. Urazhdin, Norman O. Birge, W.P. Pratt, Jr., and J. Bass

Dept. of Physics and Astronomy, Center for Fundamental Materials Research, and
Center for Sensor Materials, Michigan State University, East Lansing, MI 48824,
USA birge@pa.msu.edu

Summary. We measure the dynamic resistance of a Co/Cu/Co trilayer nanopillar at varied magnetic field H and current I . The resistance displays the usual behavior, almost symmetric in H , both when magnetization switching is hysteretic at small I, H , and reversible at larger I, H . We show differences in the I, H magnetization stability diagram measured by holding I fixed and varying H and vice versa. We also show how the peak in dV/dI associated with telegraph noise in the reversible switching regime, is calculated from the telegraph noise variations with I . Lastly, we show data for a similar sample that displays behavior asymmetric in H , and a negative reversible switching peak instead of a usual positive one.

1 Introduction

Current-induced switching of magnetization has generated much excitement due to its potential for magnetic random access memory. In spite of the apparent success of the spin-torque model [1] in describing many of the experiments, the basic physical processes involved in the switching are not yet fully understood. Most experimental studies of current-driven magnetization switching in magnetic nanopillars have been made on Co/Cu/Co trilayers at room temperature (295 K) [2, 3, 4, 5, 6, 7, 8, 9, 10]. For magnetically uncoupled samples, switching at low current I and magnetic field H is hysteretic, but becomes reversible at large enough I in one direction. This reversibility is associated with telegraph noise switching [11]. In this paper we examine several subtleties of switching in Co/Cu/Co that have not been previously described. First, the I vs. H switching (magnetization stability) diagrams are slightly different when measured by varying H while holding I fixed and vice versa. Second, we show how the reversible switching peak can be calculated from the measurements of telegraph noise dwell times vs. I . Third, we show

data for an unusual sample, where a positive reversible switching peak is replaced by a negative one.

2 Measurements and Results

Our samples were fabricated with a multistep process described elsewhere [10]. The samples had structure Co(20)/Cu(10)/Co(2.5), where thicknesses are in nm. To minimize dipolar coupling between the Co layers, only the Cu(10)/Co(2.5) layers were patterned into a nanopillar with approximate dimensions 140×70 nm. We measured differential resistance, dV/dI , at 295 K with four-probes and lock-in detection, adding an ac current of amplitude $20 \mu\text{A}$ at

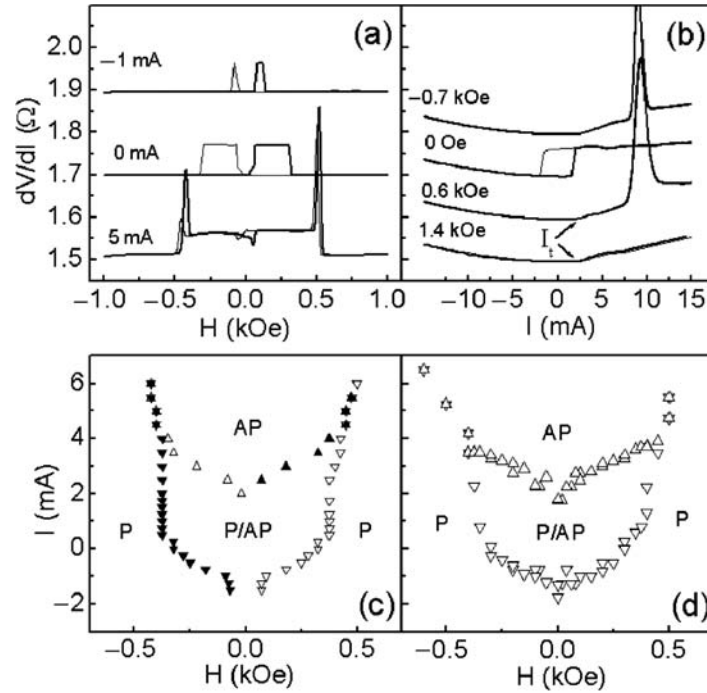


Fig. 1. Data for sample 1. (a) H -dependence of dV/dI at specified values of I ; (b) I -dependence of dV/dI at specified values of H . I_t denotes the excitation threshold current. In (a),(b), thick curves: scan from left to right, thin curves: scan in opposite direction, and curves are offset for clarity. (c) Magnetization stability diagram extracted from H scans such as shown in (a). Upward(downward) triangles: $P \rightarrow AP$ ($AP \rightarrow P$) switching. Open symbols: scan from left to right, solid symbols: reverse scan direction. (d) Magnetization stability diagram extracted from I scans such as shown in (b). Upward(downward) triangles: $P \rightarrow AP$ ($AP \rightarrow P$) switching. In (c),(d) AP, P denote the stability region of the respective configurations, P/AP is a bistable region.

8 kHz to the dc current I . Positive current flows from the extended to the patterned Co layer. H is in the film plane along the easy axis of the nanopillar.

Figs. 1(a,b) show field- and current-switching data, consistent with prior studies [2, 10, 11]. Starting, for example, at $I = 0$ and large negative H , the magnetizations of the thick and thin Co layers are parallel (P). As H is increased from a large negative value, the magnetization of Co(20) switches first at small positive H into a high resistance antiparallel (AP) state, and the patterned Co(2.5) switches at larger switching field, $H_s(I = 0)$, determined by its shape anisotropy. For $I = -1$ mA, Fig. 1(a) shows reduced $H_s(I)$, and the hysteretic switching disappears at $I < -1$ mA. $I > 0$ increases the range of H for the AP configuration. At $I > 4$ mA, the hysteretic switching steps in dV/dI turn into reversible peaks ($I = 5$ mA shown). Fig. 1(b) shows that hysteretic asymmetric current-driven switching between the AP state at $I > 0$ and the P state at $I < 0$ at $H = 0$, changes to reversible peaks both at large $H > 0$ and $H < 0$. These peaks are the same as those in Fig. 1(a) at large $I > 0$. The P state resistance grows above a threshold I_t , marked on the $H = 0.6, 1.4$ kOe curves. A similar, more pronounced threshold in Py/Cu/Py nanopillars has been associated with the onset of large amplitude magnetic excitations [11]. At small H , the switching from P to AP state occurs at $I_s \approx I_t$. The small variation of I_t between 0.6 kOe and 1.4 kOe in Fig. 1(b) is determined by the balance between the current-driven excitation and weakly H -dependent magnetic damping rate.

Figs. 1(c,d) show the Co(2.5) nanopillar magnetization stability diagrams extracted from H and I scans such as those in Figs. 1(a,b), respectively. (We show only the switching of the thin Co layer in Fig. 1(c), to avoid clutter and facilitate comparison with Fig. 1(d).) Both scan directions give similar stability regions, with a minor difference in the line separating the bistable and P-stable regions. At small $I > 0$, the stability line in Fig. 1(c) is almost vertical, giving a sharp knee at $I = 0$, whereas in Fig. 1(d) it curves smoothly at $I \approx 0$. Vertical lines are poorly reproduced by I -scans, so Fig. 1(c) better captures the singular behavior at $I \approx 0$. This knee has been attributed to the effect of spontaneous current-driven magnon emission, generally small compared to stimulated emission [12].

The reversible switching peaks in dV/dI that at large I, H replace the hysteretic steps, are due to random telegraph noise switching between the P and AP states [11]. Fig. 2(a) shows the variations of average dwell times $\tau_P(\tau_{AP})$ in the P(AP) state with I . τ_P decreases as I increases, but τ_{AP} increases. For a fixed H , $\tau_{AP} \ll \tau_P$ at small I , so dV/dI is close to the resistance of the P state, R_P , and $\tau_{AP} \gg \tau_P$ at large I , giving $dV/dI \approx R_{AP}$, the resistance in the AP state. We now show how the variations in Fig. 2(a) give a peak in the differential resistance at $\tau_P \approx \tau_{AP}$. For a given H , the average voltage across the sample is

$$V(I) = I \left[\frac{R_{AP}\tau_{AP} + R_P\tau_P}{\tau_P + \tau_{AP}} \right], \quad (1)$$

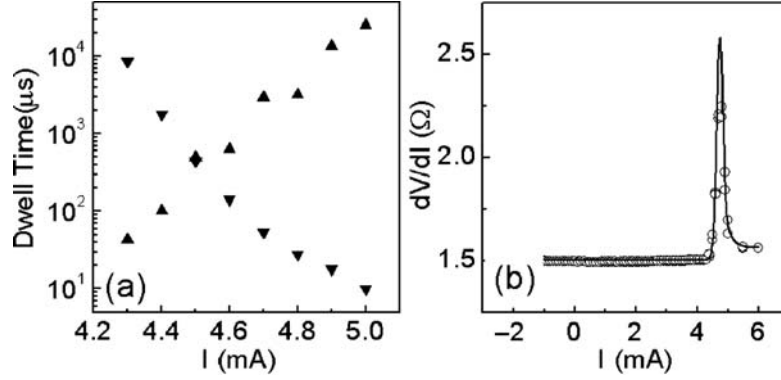


Fig. 2. Data for sample 1. (a) Variation of the average dwell times in the AP state τ_{AP} (upward triangles) and P state τ_P (downward triangles) with I at $H = 0.48$ kOe, (b) Circles: dV/dI vs. I at $H = 0.5$ kOe. Solid curve: a calculation, as described in the text.

where $\tau_P(I) \approx \tau_0 \exp[-\alpha(I - I_0)]$, $\tau_{AP}(I) \approx \tau_0 \exp[\beta(I - I_0)]$, as follows from Fig. 2(a). I_0 , τ_0 are defined by $\tau_{AP}(I_0) = \tau_P(I_0) = \tau_0$. Differentiating Eq. 1 with respect to I , we find

$$\frac{dV}{dI} \approx \frac{\tau_{AP}R_{AP} + \tau_P R_P}{\tau_P + \tau_{AP}} + I(\alpha + \beta)(R_{AP} - R_P) \frac{\tau_P \tau_{AP}}{(\tau_P + \tau_{AP})^2}.$$

The first term on the right is just the resistance V/I , giving a step for the reversible transition from the P to the AP state. The second term has a maximum value $I_0(\alpha + \beta)(R_{AP} - R_R)/4$ at $\tau_P = \tau_{AP}$. This term gives rise to a peak in dV/dI at $I = I_0$, which can be much higher than R_{AP} . The solid line in Fig. 2(b) is calculated from the data in Fig. 2(a), and Eq. 2, for $I_0 = 4.8$ mA, and $\alpha + \beta = 19.2$ mA⁻¹ extracted from fig. 2(a). The calculation agrees well with the data shown as circles.

From the above analysis, we conclude that the reversible switching peak positions characterize the points (H, I) where $\tau_P = \tau_{AP}$, thus giving an indirect measure for telegraph noise variation with I, H [13]. We have shown [11] that the telegraph noise period decreases approximately exponentially when I is increased and H is adjusted to remain along the reversible switching line. The presence of telegraph noise near the reversible switching line means that both AP and P states are unstable in that region. Thus, the stability diagrams, Figs. 1(c,d), should be modified to include this unstable region. This instability is indirectly manifested in the rise of R_P at $I > I_t$. However, the measurements of dV/dI at I above the reversible switching peak give values very close to R_{AP} . Fig. 2 and our analysis show that, because τ_P is exponentially smaller than τ_{AP} , the resistance can become close to R_{AP} , even though the AP state is unstable.

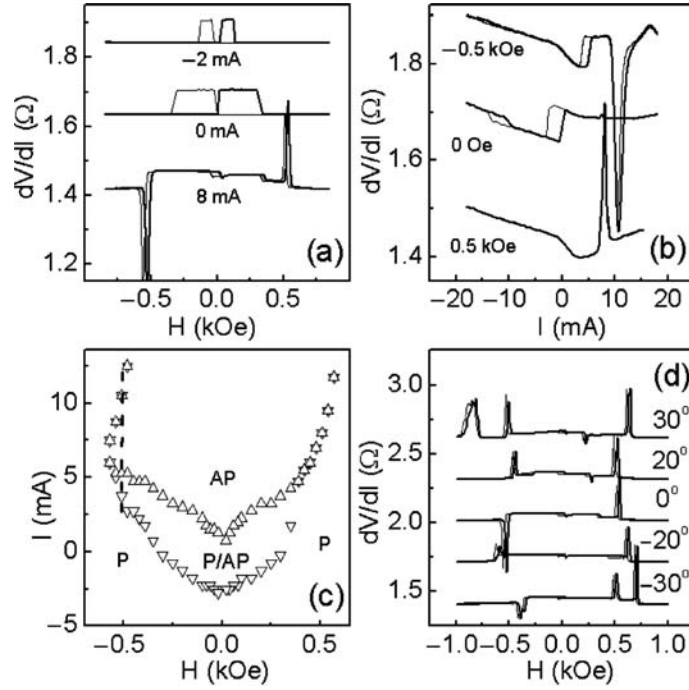


Fig. 3. Data for sample 2. (a) H -dependence of dV/dI at specified values of I , (b) I -dependence of dV/dI at specified values of H . (c) Magnetization stability diagram extracted from I scans such as shown in (b). Upward(downward) triangles: $P \rightarrow AP$ ($AP \rightarrow P$) switching. A $H = -0.5$ kOe section shown with dashed line, (d) MR curves at $I = 8$ mA, at the specified in-plane angles between H and the nominal easy axis of the nanopillar. AP, P denote the stability region of the respective configurations, P/AP is a bistable region. In (a),(b),(d), thick curves: scan from left to right, thin curves: scan in opposite direction, curves are offset for clarity.

In most samples, both I and $|H|$ increase along the reversible switching line close to the transition from hysteretic to reversible switching. The behavior at larger I varies: in some samples, the reversible switching peak disappears, or splits into several peaks. These peaks are usually asymmetric in H , showing the importance of inhomogeneous and tilted magnetization states, affected both by sample imperfections and the Oersted field of the current. Fig. 3 shows data for a sample nominally identical to that of Fig. 1. The hysteretic MR at $I = 0$, and current-driven switching at $H = 0$ (Figs. 3(a,b)), are similar to those in Figs. 1(a,b). The $I = 8$ mA MR curve in Fig. 3(a) is asymmetric, showing a positive peak at $H > 0$ like those in the 5 mA curve in Fig. 1(a), but a negative peak at $H < 0$. Similarly, in the current scans of Fig. 3(b), the peak at $H = 0.5$ kOe is consistent with those at $-0.7, 0.6$ kOe in Fig. 1(b), while the -0.5 kOe scan shows a small hysteresis in current switching with a negative peak at larger I . By comparing the 8 mA resistances to the left of the negative

peak and to the right of the positive peak in Fig. 3(a), we conclude that the negative peak corresponds to complete AP \rightarrow P switching. The resistance increase to the right of the negative peak in Fig. 3(b) is consistent with the previously noted current-driven excitations in the P state [11]. Fig. 3(c) shows the stability diagrams extracted from I scans such as those in Fig. 3(b), where we mark both the positive and negative peaks as reversible switching points. This plot clearly shows the asymmetry of behaviors with respect to reversal of H . For $H > 0$ the stability diagram is similar to those of Figs. 1(c,d). For $H < 0$ in Fig. 3(c), the reversible switching line has a positive slope, i.e. the negative peaks appear at decreasing I as the magnitude of H is increased. A dashed $H = -0.5$ kOe line crosses both a bistable region (hysteretic switching), and a reversible switching line. The positive slope of the reversible line is consistent with $\alpha + \beta < 0$, giving a negative peak in Eq. 2.

Fig. 3(d) shows H -scans at $I = 8$ mA with varied angles θ between the nominal easy nanopillar axis and H directed in the sample plane. The $\theta = 0$ curve has a positive peak at $H > 0$ and negative peak at $H < 0$. The peaks in the $\theta = \pm 20^\circ$ curves are nearly symmetric, and positive for both directions of H . The $\theta = \pm 30^\circ$ curves are asymmetric again, and have double peaks for one of H directions. These data show that the details of switching are sensitive to the sample shape defects, misalignment of the nanopillar easy axis with H , and are also affected by the Oersted field of the current and magnetization pinning. We note that only the last two factors (possibly in combination with the first two) give asymmetry between the behaviors at $H < 0$ and $H > 0$.

3 Conclusions

To summarize, we focused on four phenomena in Co/Cu/Co nanopillars at 295 K. First, we provided evidence (although not as clear as in Py/Cu/Py [11]) of a threshold current I_t for excitations that occur in the reversible switching regime, but at lower I than the reversible switching peak. Second, we showed that the sharp knee at $I = 0$, visible in a magnetization switching diagram obtained by fixing I and varying H , is lost in a similar plot obtained by fixing H and varying I . Third, we showed that the reversible switching peak shape can be derived from measurements of the variation of telegraph noise with I . Fourth, in Fig. 3 we showed an example of a switching diagram asymmetric in H , more complex than the symmetric one in Fig. 1. We attribute the complexity to a combination of sample shape asymmetry, the Oersted field, and possible misalignment of H . Of particular interest in Fig. 3(b) is the negative peak, associated with re-entrance of the P state at high $I > 0$.

Acknowledgements.— We acknowledge support from the MSU CFMR, CSM, the MSU Keck Microfabrication facility, the NSF through Grants DMR 02-02476, NSF-EU 98-09688, and NSF-EU 00-98803, and Seagate Technology.

References

1. J. Slonczewski, *J. Magn. Magn. Mater.* **159**, L1 (1996).
2. F.J. Albert, J.A. Katine, R.A. Buhrman, and D.C. Ralph, *Appl. Phys. Lett.* **77**, 3809 (2000).
3. J.A. Katine, F.J. Albert, R.A. Buhrman, E.B. Myers, and D.C. Ralph, *Phys. Rev. Lett.* **84**, 3149 (2000).
4. F.J. Albert, N.C. Emley, E.B. Myers, D.C. Ralph, and R.A. Buhrman, *Phys. Rev. Lett.* **89**, 226802 (2002).
5. E.B. Myers, F.J. Albert, J.C. Sankey, E. Bonet, R.A. Buhrman, and D.C. Ralph, *Phys. Rev. Lett.* **89**, 196801 (2002).
6. F.B. Mancoff and S.E. Russek, *IEEE trans.* **38**, 2853 (2002).
7. J.Z. Sun, D.J. Monsma, T.S. Kuan, M.J. Rooks, D.W. Abraham, B. Oezylmaz, A.D. Kent, and R.H. Koch, *J. Appl. Phys.* **93**, 6859 (2003).
8. J. Grollier, V. Cros, H. Jaffres, A. Hamzie, J.M. George, G. Faini, J. Ben Youssef, H. Le Gall, and A. Fert, *Phys. Rev. B* **67**, 174402 (2003).
9. B. Oezylmaz, A.D. Kent, D. Monsma, J.Z. Sun, M.J. Rooks, and R.H. Koch, *Phys. Rev. Lett.* **91**, 067203 (2003).
10. S. Urazhdin, H. Kurt, W.P. Pratt, Jr., and J. Bass, *Appl. Phys. Lett.* **83**, 114 (2003).
11. S. Urazhdin, N.O. Birge, W.P. Pratt, Jr., and J. Bass, *Phys. Rev. Lett.* **91**, 146803 (2003).
12. S. Urazhdin, *cond-mat/0308320*.
13. If we follow the reversible switching peak to very large I and H , the dwell times τ_P and τ_D extrapolate to values smaller than any plausible microscopic attempt time. At that point the magnetization dynamics no longer produce telegraph noise, but become more complicated.

Nanomechanical Effects in Suspended Carbon Nanotubes

Ya. M. Blanter

Department of NanoScience and DIMES, Delft University of Technology,
Lorentzweg 1, 2628CJ Delft, The Netherlands blanter@tntw14.tn.tudelft.nl

Summary. The interplay between electrical and mechanical properties of suspended, doubly clamped carbon nanotubes in the Coulomb blockade regime is studied theoretically. In this geometry, the capacitance between the nanotube and the gate depends on the distance between them. We find that the tube position changes in discrete steps every time an electron tunnels onto it. Edges of Coulomb diamonds acquire a (small) curvature. Eigenfrequencies are modified by Coulomb blockade in a discrete fashion.

1 Introduction

Recently, a great interest appeared in nanoelectromechanical systems (NEMS), which convert electrical current into mechanical motion on a nanoscale and vice versa. The ultimate goal of the NEMS research is development of commercial applications like sensors and actuators at a nanoscale. Currently, the fundamental side of NEMS is being extensively explored, with new physical phenomena being revealed.

The development follows two main lines. One is shuttling mechanism for transport, proposed by the Gothenburg group [1] and subsequently developed further [2, 3, 4]. One considers a single-electron transistor with the mobile central island. In the original proposal, the island moves due to electrostatics interaction with the electrodes and transports charge in a discrete fashion. In the subsequent experimental realizations [5, 6] the island was attached to a cantilever and moved under the external ac perturbation. The experiments [6], in which the role of the island was taken by a fullerene molecule, were especially influential, and generated much of theoretical interest to the subject. Very unusual behavior, in particular, negative differential resistance, was observed and has become a subject for the subsequent theoretical research

[7, 8]. A number of other questions not yet accessible experimentally, like destruction of the quantum-mechanical coherence in the moving island [9] and a possibility of superconducting phase coherence across the shuttle [10] is at the focus of theoretical research.

Another direction is represented by suspended structures. Doubly-clamped suspended single- and multi-wall carbon nanotubes have been previously fabricated, and their transport [11], acoustoelectric [12], thermal [13], elastic [14], and emission [15] properties have been measured. Recently, experiments in the Coulomb blockade regime started. Coulomb blockade regime is interesting since it gives access to the quantum properties of the system and probes non-equilibrium phenomena. In Delft, Jarillo-Herrero *et al.* [16] fabricated suspended single-wall carbon nanotubes (SWNT) over a back-gate and measured the Coulomb stability diagram. LeRoy and Lemay [17] performed STM measurements on SWNT suspended over a trench. Höhberger *et al.* [18] presented Coulomb blockade measurements in suspended silicon quantum dots. Although the experiments are still under way, and the results are at this stage inconclusive, some resonances were observed which could be identified with inelastic processes due to vibrations of the structures. For this reason, it necessary to analyze the properties of suspended structures in Coulomb blockade regime. In this article, which is based on Ref. [19], we start such an analysis by discussing the ground state properties of suspended SWNT. Current in this system is essentially non-linear and thus requires a consideration of non-equilibrium situation. This will be done elsewhere [20].

This article is organized as follows: Next Section describes the model with inclusion of the influence of initial stress. We concentrate on the case where the junction capacitances are zero so that analytical expressions are obtained. We then describe the influence of nanoelectromechanical effects on Coulomb blockade. Section 4 discusses the eigenmodes and the influence on the initial strain on them. We end with some remarks on the limitations of our model.

2 Displacement, stress, and energy

2.1 Equilibrium position

We consider a SWNT (modeled as a rod of length L along the x -axis), freely suspended between source and drain electrodes, in the vicinity of a gate (see Fig. 1). The nanotube is attached to the electrodes via tunneling contacts. An electrostatic force (gate voltage) bends the tube; the deviation from a straight line is denoted by $z(x)$ with $0 < x < L$. The elastic energy of the bent tube is [21]

$$W_{el}[z(x)] = \int_0^L dx \left\{ \frac{EI}{2} z''^2 + \left[\frac{T_0}{2} + \frac{ES}{8L} \int_0^L z'^2 dx \right] z'^2 \right\}, \quad (1)$$

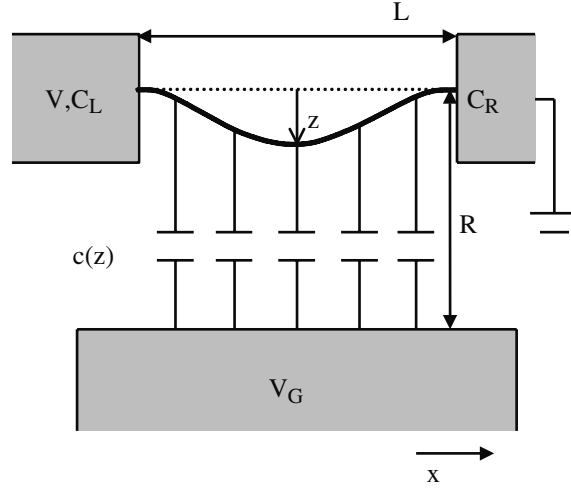


Fig. 1. A schematic drawing of a suspended nanotube capacitively coupled to a gate and clamped on both sides to metal pads that serve as tunnel contacts. A voltage V is applied to the left pad.

where E , $I = \pi r^4/4$, and $S = \pi r^2$ are the elastic modulus, the inertia moment and the cross-section, respectively. Here, r is the (external) radius of the tube. The first term in Eq. (1) is the energy of an unstressed bent rod; the two other terms describe the effect of the stress force $\tilde{T} = T_0 + T$. Here T_0 is the residual stress which may result *e.g.* from the fabrication, and the induced stress T is due to the elongation of the tube caused by the gate voltage,

$$T = \frac{ES}{2L} \int_0^L z'^2 dx. \quad (2)$$

To write down the electrostatic energy, we consider the case when the capacitance of the tube to the gate dominates those of the barriers (see Fig. 1), $C_L, C_R \ll C_G$. The capacitance to the gate per unit length is $c(z)$. Approximating the gate by an infinite plane at a distance R from the nanotube, we obtain

$$c(z) = \frac{1}{2 \ln \frac{2(R-z)}{r}} \approx \frac{1}{2 \ln \frac{2R}{r}} + \frac{z(x)}{2R \ln^2 \frac{2R}{r}}, \quad (3)$$

where the Taylor expansion restricts validity to $z \ll R$. The electrostatic energy of the system reads

$$W_{est}[z(x)] = \frac{(ne)^2}{2C_G[z]} - neV_G \approx \frac{(ne)^2 \ln \frac{2R}{r}}{L} - \frac{(ne)^2}{L^2 R} \int_0^L z(x) dx - neV_G. \quad (4)$$

For a moment, we assume $T_0 = 0$. Minimizing the energy,

$$W_n[z(x)] = W_{el}[z(x)] + W_{est}[z(x)],$$

with respect to z , one finds the equation determining the tube position [21],

$$IEz'''' - Tz'' = K_0 \equiv \frac{(ne)^2}{L^2R}, \quad (5)$$

where K_0 is the electrostatic force per unit length, which we approximate by a constant. Higher-order terms are small for $z \ll R$. To solve Eq. (5) we have to assume that the stress force T is constant, and find it later from the self-consistent condition (Eq. (2)).

The solution of Eq. (5) with the appropriate boundary conditions (for the doubly-clamped rod $z(0) = z(L) = z'(0) = z'(L) = 0$) has the form

$$z_n(x) = \frac{K_0L}{2T\xi} \left[\frac{\sinh \xi L}{\cosh \xi L - 1} (\cosh \xi x - 1) - \sinh \xi x + \xi x - \xi \frac{x^2}{L} \right], \quad (6)$$

with $\xi = (T/EI)^{1/2}$. Substituting this into Eq. (2), a relation between the stress T and the external force K_0 is obtained. In the limiting cases, it reads

$$T = \begin{cases} K_0^2 L^6 S / (60480 EI^2), & T \ll EI/L^2, \\ (ES/24)^{1/3} (K_0 L)^{2/3}, & T \gg EI/L^2. \end{cases} \quad (7)$$

The first line corresponds to weak bending of the tube: The energy associated with the bending exceeds the energy of the stress. Generally, it is realized for $z < r$. The second line describes strong bending, when the tube displacement is large ($r < z \ll R, L$).

For the displacement of the tube center $z_n^{max} = z_n(L/2)$ we find

$$\begin{aligned} z_n^{max} &= 0.003 \frac{(ne)^2 L^2}{Er^4 R}, & T \ll \frac{EI}{L^2} & \left(n \ll \frac{Er^5 R}{e^2 L^2} \right); \\ z_n^{max} &= 0.24 \frac{(ne)^{2/3} L^{2/3}}{E^{1/3} r^{2/3} R^{1/3}}, & T \gg \frac{EI}{L^2} & \left(n \gg \frac{Er^5 R}{e^2 L^2} \right). \end{aligned} \quad (8)$$

For a SWNT with $r = 0.65$ nm, $E = 1.25$ TPa, $L = 500$ nm and $R = 100$ nm (to be referred to as the E-nanotube) the crossover from weak to strong bending, $T \sim EI/L^2$, occurs already at $n \sim 5 \div 10$. In the strong-bending regime, the displacement of the E-nanotube is (in nanometers) $z_n^{max} = 0.24n^{2/3}$. For the same setup in the situation when the role of a gate is taken by an STM-tip ($R \sim 5$ nm) and addition of *one* electron drives the tube into the strong-bending regime. Note that state-of-the-art silicon submicron devices always stay in the weak-bending limit.

2.2 Charge and energy

For comparison with experiments, we have to relate the charge ne to the gate voltage by minimizing the energy. The expression for the energy (elastic plus electrostatic) of the tube at equilibrium in the limiting cases reads

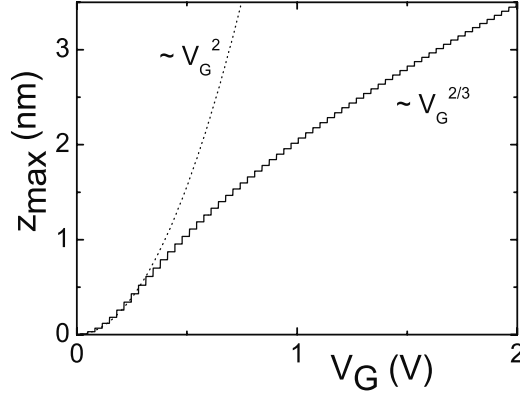


Fig. 2. Calculated displacement as a function of gate voltage for the E-nanotube: $r = 0.65$ nm, $E = 1.25$ TPa, $L = 500$ nm and $R = 100$ nm. At $V_G \approx 0.5V$, there is a crossover from weak bending with a V_G^2 -dependence to strong bending with a $V_G^{2/3}$ dependence.

$$W_n^{eq} \equiv W_{st} - \delta W = \frac{(ne)^2}{L} \ln \frac{2R}{r} - neV_G \quad (9)$$

$$- \begin{cases} 0.0009(ne)^4 L / (Er^4 R^2), & T \ll EI/L^2; \\ 0.08(ne)^{8/3} / (Er^2 R^4 L)^{1/3}, & T \gg EI/L^2. \end{cases}$$

The first two terms represent the electrostatic energy of a straight tube, and the third one is due to the elastic degrees of freedom (stress, bending, and change of C_G due to displacement). This nonlinear, *nanomechanical term* for E-nanotube is a small correction: It becomes of the same order as W_{st} if $n \sim 3000$ in which case Eq. (3) is not valid anymore. However, for the STM-setup ($R = 5nm$) the nanomechanical term becomes essential already at $n \sim 10$. Thus, for this set-up nanomechanical corrections have to be taken into account even for the ground state energy.

The negative sign of the nanomechanical contribution is easily understood: As the gate voltage changes, the movable tube adjusts not only its charge, but also its position, which leads to a lower energy as compared to the fixed-position system.

The value of n which minimizes the energy is

$$n = \text{Int} \left(\frac{V_G L}{2e \ln(2R/r)} + \frac{1}{2} + \delta n \right),$$

with Int denoting the integer part of the expression. The small correction δn in the strong-bending regime is proportional to $V_G^{5/3}$. Thus, the tube displacement z_{max} changes in discrete steps when V_G is varied as shown in Fig. 2. The envelope is proportional to V_G^2 (weak bending) or $V_G^{2/3}$ (strong bending).

2.3 Thermal fluctuations

The preceding considerations are restricted to the case of zero temperature. To understand the role of the temperature, we now evaluate the effect of thermal fluctuations on the equilibrium position of the tube.

The variance of the position of the tube center at a given charge n can be generally represented as a functional integral,

$$\begin{aligned} \text{var } z_n &\equiv \left\langle [z(L/2) - z_n(L/2)]^2 \right\rangle \\ &= \frac{\partial^2}{\partial J^2} \int Dz(x) \exp [-W_n[z]/k_B\Theta + Jz(L/2)] \Big|_{J=0} \\ &\quad \times \left[\int Dz(x) \exp (-W_n[z]/k_B\Theta) \right]^{-1}, \end{aligned} \quad (10)$$

where Θ is the temperature. Except for $n = 0$, the functional integral in Eq. (10) is not Gaussian and has to be linearized around the equilibrium solution $z_n(x)$, Eq. (6). The remaining Gaussian integral can be calculated, and we arrive at

$$\text{var } z_n = k_B\Theta\zeta(L/2), \quad (11)$$

where $\zeta(x)$ solves the equation

$$EI\zeta'''' - \frac{ES}{2L} \int z_n'^2 dx \zeta'' - \frac{ES}{L} z_n'' \int \zeta' z_n' dx = \delta(x - L/2). \quad (12)$$

In the two limiting cases of weak and strong bending, the solution of Eq. (12) yields

$$\text{var } z_n = \begin{cases} k_B\Theta L^3/192EI, & n = 0 \\ k_B\Theta L/8T, & n \gg Er^5R/e^2L^2, \end{cases} \quad (13)$$

where the stress T is still given by the lower line of Eq. (7). Thus, the fluctuations in the tube position are expected to grow linearly with temperature. However, their magnitude is small. For the E-nanotube, at 100K the fluctuations in the $n = 0$ state are of the order of 0.1 nanometer, and at least an order of magnitude less in the strong-bending regime.

Thermal fluctuations in the position of a suspended carbon nanotube were recently measured in Ref. [22].

3 Coulomb effects

Since the nanotube is attached to the electrodes by tunneling contacts, it is in the Coulomb blockade regime. We define the energy to add the n th electron to the tube as $S_n = W_n - W_{n-1}$. Then, if the nanotube contains $n > 0$ electrons, the conditions that current can not flow (is Coulomb blocked) are

$S_n < 0, eV < S_{n+1}$. In quantum dots, S_n depends linearly on the bias V and gate V_g voltages. Thus, in the $V_G - V$ plane regions with zero current are confined within Coulomb diamonds, that are identical diamond-shape structures repeating along the V_G -axis.

In a suspended carbon nanotube, in addition to the purely Coulomb energy, we also have the nanomechanical corrections. Generally, these corrections make the relations between V and V_G , which describe the boundaries of Coulomb blockade regions, non-linear. Consequently, the Coulomb “diamonds” in suspended nanotubes are not diamonds any more, but instead have a curvilinear shape (with the exception of the case $C_L = C_R = 0$). Their size is also not the same and decreases with $|V_G|$. Thus, the mechanical degrees of freedom *affect* the Coulomb blockade diamonds. However, since these effects originate from the nanomechanical term which is typically a small correction, its influence on Coulomb diamonds is small as well. For the E-nanotube, these effects do not exceed several percents for typical gate voltages.

4 Eigenmodes

The eigenfrequency of a particular eigenmode is a directly measurable [12] property. In future experiments on suspended tubes we expect that the eigenmodes influence tunneling (“phonon-assisted tunneling”) in a similar way as observed for a single C_{60} molecule [6]. Below, we demonstrate that the effect of the electrostatic interactions on the elastic properties (specifically, eigenfrequencies) is strong and changes the behavior qualitatively.

To find the eigenmodes, we apply a gate voltage with a large dc (single gate) and a small ac component. The displacement $z(x, t)$ is time-dependent, which provides an external force $-\rho S \ddot{z}$ to Eq. (5), where ρ equals 1.35 g/cm^3 . Eq. (5) must be solved first with a constant stress, and then the stress is found self-consistently. The tube displacement has a small ac component δz on top of a large static one. The self-consistency procedure is essentially the same and again leads to Eq. (7). Thus, the dc component of the gate voltage determines the stress T and it therefore controls the eigenmodes.

The frequencies of the (transverse) eigenmodes are found from the requirement that the equation

$$IE\delta z'''' - T\delta z'' - \rho S\omega^2\delta z = 0 \quad (14)$$

with the boundary condition $\delta z(0) = \delta z(L) = \delta z'(0) = \delta z'(L) = 0$ has a non-zero solution. This yields the following equation for the frequency ω ,

$$\cosh y_1 \cos y_2 - \frac{1}{2} \frac{y_1^2 - y_2^2}{y_1 y_2} \sinh y_1 \sin y_2 = 1, \quad (15)$$

$$y_{1,2} = \frac{L}{\sqrt{2}} \left(\sqrt{\xi^4 + 4\lambda^2} \pm \xi^2 \right)^{1/2}, \quad \lambda = \sqrt{\frac{\rho S}{EI}} \omega.$$

In the following, we restrict ourselves to the fundamental (lowest frequency) eigenmode ω_0 . In the limiting cases, the solutions of Eq. (15) are

$$\omega_0 = \sqrt{\frac{EI}{\rho S}} \begin{cases} 22.38L^{-2} + 0.28\xi^2, & \xi L \ll 1; \\ \pi\xi L^{-1} + 2\pi L^{-2}, & \xi L \gg 1. \end{cases} \quad (16)$$

The second terms on the rhs represent small corrections to the first ones.

The frequency dependence $\omega_0 \propto L^{-2}$ is associated with a loose string, while $\omega_0 \propto L^{-1}$ means that the string is tied like in a guitar. Our results show that the behavior of the tube crosses over from “loose” to “tied” as V_G increases. For the fundamental mode, the crossover occurs at $\xi L \sim 1$, corresponding to the crossover from weak to strong bending. The middle curve in Fig. 3 shows the frequency of the fundamental mode as a function of gate voltage (zero residual stress). The arrow denotes the cross-over from weak to strong bending.

The gate voltage dependence of the frequency is a stepwise function, as shown in the inset of Fig. 3. Steps occur whenever an additional electron tunnels onto the tube. For the E-nanotube, their height is ~ 5 MHz, which is measurable. Note, that the present submicron silicon devices are always in the weak-bending regime so that corrections due to the second term in Eq. (16) are too small to be measured. Furthermore, one should realize that frequency quantization is only observable if the frequency itself is greater than the inverse tunneling time for electrons.

We now consider the effect of a residual stress ($T_0 \neq 0$). First, we obtain the stress by solving Eqs. (2), (5) (in the latter, T is replaced by $T + T_0$). In particular, for a negative stress $T + T_0 < 0$, $T_0 \sim -EI/L^2$, Eq. (2) acquires several solutions. This signals *Euler instability*: the tube bends in the absence of an external force.

If the residual stress is large, $T_0 \gg EI/L^2$, the tube always acts like a tied string (upper curve in Fig. 3). The frequency depends weakly on V_G for low voltages, and above $T \sim T_0$ (denoted with the arrow) grows with an envelope $\propto V_G^{2/3}$. For negative T_0 the picture is qualitatively different (lower curve in Fig. 3). Whereas for large gate voltages the envelope is still proportional to $V_G^{2/3}$, the frequency dives below the value for an unstressed tube ($22.38(EI/\rho S)^{1/2}L^{-2}$, represented by the thin solid line in Fig. 3), when the overall stress becomes negative. It further drops to zero at the Euler instability threshold.

The qualitative difference between the various regimes means that by measuring the gate voltage dependence of ω_0 one can determine the sign of T_0 and get a quantitative estimate. On the other side, the gate effect can be used to tune the eigenfrequencies. We also mention that in the absence of charging effects, the steps vanish but the overall shape of the curves in Fig. 3 remains the same.

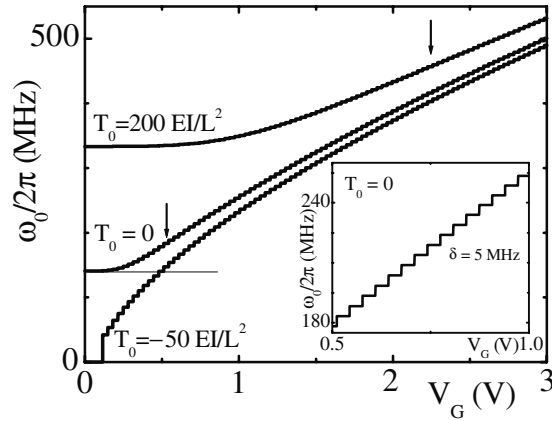


Fig. 3. Gate voltage dependence of the frequency ω_0 of the fundamental mode for three different values of the residual stress. Numbers are taken for the E-nanotube (see Fig. 2). The fundamental mode of an unstressed tube is 140 MHz (thin horizontal line). The inset is an enlargement of the $T_0 = 0$ curve of the main figure showing step-wise increases of ω_0 whenever an additional electron tunnels onto the tube.

5 Discussion

The presented model is simplified in many respects. Mechanical degrees of freedom are introduced via classical theory of elasticity: The nanotube (modeled by a rod) is considered as incompressible and without internal structure. This is justified, since so far the theory of elasticity has described all existing experiments on carbon nanotubes well. Creation of defects in SWNT starts at deformations of order of ten percents. We have neglected damping, which is also expected to originate from the creation of the defects and to be irrelevant in this range. We also disregarded quantum effects (cotunneling and finite spacing of quantum levels of electrons in the tube). These issues need to be clarified for a detailed comparison with the experimental data, and will be a subject for future research.

Our main result is that the nanotube can be manipulated by the gate voltage, which determines its deformation and stress, and modifies the eigenmodes. Though the eigenmodes of nanotube ropes have been measured in Ref. [12] four years ago, the *strain dependence* of the eigenmodes was only recently reported in Ref. [15]. It demonstrates this effect for singly-clamped multi-wall carbon nanotubes. We expect that our predictions will soon be tested in experiments on doubly-clamped SWNTs.

Acknowledgements.— Collaboration with S. Sapmaz, L. Gurevich, H. S. J. van der Zant, and O. Usmani on Refs. [19, 20] is appreciated. This work was supported by the Netherlands Foundation for Fundamental Research on Matter (FOM).

References

1. L. Y. Gorelik, A. Isacsson, M. V. Voinova, B. Kasemo, R. I. Shekhter, and M. Jonson, *Phys. Rev. Lett.* **80**, 4526 (1998).
2. C. Weiss and W. Zwerger, *Europhys. Lett.* **47**, 97 (1999).
3. D. Boese and H. Schoeller, *Europhys. Lett.* **54**, 668 (2001).
4. T. Nord, L. Y. Gorelik, R. I. Shekhter, and M. Jonson, *Phys. Rev. B* **65**, 165312 (2002).
5. M. T. Tuominen, R. V. Krotkov, and M. L. Breuer, *Phys. Rev. Lett.* **83**, 3025 (1999); A. Erbe, C. Weiss, W. Zwerger, and R. H. Blick, *Phys. Rev. Lett.* **87**, 096106 (2001).
6. H. Park, J. Park, A. K. L. Lim, E. H. Anderson, A. P. Alivisatos, and P. L. McEuen, *Nature* **407**, 57 (2000).
7. K. D. McCarthy, N. Prokof'ev, and M. T. Tuominen, *Phys. Rev. B* **67**, 245415 (2003).
8. A. Mitra, I. Aleiner, and A. J. Millis, cond-mat/0302132; cond-mat/0311503.
9. A. Romito, F. Plastina, and R. Fazio, cond-mat/0212414.
10. A. Isacsson, L. Y. Gorelik, R. I. Shekhter, Yu. M. Galperin, and M. Jonson, *Phys. Rev. Lett.* **89**, 277002 (2002).
11. T. W. Tomblor, C. Zhou, L. Alexseyev, J. Kong, H. Dai, L. Liu, C. S. Jayanthi, M. Tang, and S.-Y. Wu, *Nature* **405**, 769 (2000); J. Nygård and D. H. Cobden, *Appl. Phys. Lett.* **79**, 4216 (2001); P. A. Williams, S. J. Papadakis, M. R. Falvo, A. M. Patel, M. Sinclair, A. Seeger, A. Helser, R. M. Taylor II, S. Washburn, and R. Superfine, *ibid* **80**, 2574 (2002); N. R. Franklin, Q. Wang, T. W. Tomblor, A. Javey, M. Shim, and H. Dai, *ibid* **81**, 913 (2002).
12. B. Reulet, A. Yu. Kasumov, M. Kociak, R. Deblock, I. I. Khodos, Yu. B. Gorbatov, V. T. Volkov, C. Journet, and H. Bouchiat, *Phys. Rev. Lett.* **85**, 2829 (2000).
13. P. Kim, L. Shi, A. Majumdar, and P. L. McEuen, *Phys. Rev. Lett.* **87**, 215502 (2001).
14. G.-T. Kim, G. Gu, U. Waizmann, and S. Roth, *Appl. Phys. Lett.* **80**, 1815 (2002).
15. S. T. Purcell, P. Vincent, C. Journet, and Vu Thien Binh, *Phys. Rev. Lett.* **89**, 276103 (2002).
16. P. Harillo-Herrero *et al.*, unpublished.
17. B. LeRoy and S. Lemay (unpublished).
18. E. M. Höhberger, R. H. Blick, F. W. Beil, W. Wegscheider, M. Bichler, and J. P. Kotthaus, *Physica E* **12**, 487 (2002); E. M. Höhberger *et al.* (unpublished).
19. S. Sapmaz, Ya. M. Blanter, L. Gurevich, and H. S. J. van der Zant, *Phys. Rev. B* **67**, 235414 (2003).
20. O. Usmani and Ya. M. Blanter (unpublished).
21. L. D. Landau and E. M. Lifshits, *Theory of Elasticity* (Pergamon, Oxford, 1986).
22. B. Babič, J. Furer, S. Sahoo, Sh. Farhangfar, and C. Schönenberger, *Nanoletters* **3** 1577 (2003).

Transport through Ferromagnet/ Superconductor Interfaces

Zhigang Jiang¹, José Aumentado², Wolfgang Belzig³, and Venkat Chandrasekhar¹

¹ Department of Physics and Astronomy, Northwestern University, 2145 Sheridan Road, Evanston, IL 60208, USA v-chandrasekhar@northwestern.edu

² National Institute of Science and Technology, 325 Broadway, Boulder, CO 80305, USA

³ Department of Physics and Astronomy, University of Basel, Klingelbergstr. 82, CH-4056 Basel, Switzerland

Summary. The differential resistance of submicron-size ferromagnet/superconductor interface structures shows asymmetries as a function of the current through the ferromagnet/superconductor interface. These asymmetries are a consequence of spin-polarized electron transport from the ferromagnet to the superconductor, coupled with the Zeeman-splitting of the superconducting quasiparticle density of states. They are sensitive to the orientation of the magnetization of the ferromagnet, as the magnetic field required to spin-split the quasiparticle density of states can be provided by the ferromagnetic element itself.

1 Introduction

There has been continuing interest in the past few years in heterostructures that combine ferromagnetic (F) and superconducting (S) elements. This interest can be broadly divided into two categories: the superconducting proximity effect in ferromagnets, and spin-polarized electron transport between ferromagnets and superconductors. In the first category are included earlier work on FS multilayers [1], more recent work on critical currents in SFS junctions [2], and long-range superconducting proximity effects in ferromagnets adjacent to superconductors [3, 4]. Some of this work is discussed in other contributions in this volume. In the second category is included spectroscopic studies of FS point contacts [5], extending the pioneering work of Tedrow and Meservey [6] in FS junctions mediated by an insulating tunnel barrier (I) to systems with higher transparency FS interfaces. Point contact FS spectroscopy has

been used to determine the degree of spin-polarization P in the ferromagnet by examining in detail the differential conductance of the FS junction as a function of the voltage bias applied across it [7], and analyzing the results in terms of a spin-polarized extension of the Blonder, Tinkham, Klapwijk (BTK) [8] theory of transport across a normal-metal/superconductor junction. Other theoretical studies have focused on the excess resistance of FS junctions associated with spin accumulation at the interface [9, 10].

In the work of Tedrow and Meservey on FIS junctions, a magnetic field was applied to the thin film device in order to Zeeman-split the quasi-particle density of states in the superconductor. The finite spin-polarization P in the ferromagnet showed up directly as different peak heights in the FIS tunneling characteristics. In the more recent work on point contact FS spectroscopy, a large magnetic field could not be applied, as this would rapidly suppress superconductivity in the bulk superconductors used in the experiments, so that the analysis of the current-voltage characteristics depends on a subtle interplay between P and the FS interface transparency. This restriction does not apply to mesoscopic FS devices made from thin films, where a magnetic field can be applied parallel to the plane of the superconducting thin film as in the original experiments of Tedrow and Meservey, splitting the quasi-particle density of states without substantially suppressing superconductivity in the film. As in the FIS case, the finite spin-polarization in the ferromagnet is expected to show up as asymmetric peaks in the differential conductance as a function of voltage bias, as recently discussed by Mélin [11].

In this paper, we report measurements of the low temperature differential resistance of mesoscopic FS junctions. We observe asymmetries in the differential resistance even in the absence of an external magnetic field. These asymmetries are associated with spin-polarized tunneling into the superconductor, with the splitting of the quasi-particle density of states in the superconductor arising from the magnetic field generated by the ferromagnetic elements.

2 Sample fabrication and measurement

The samples for our experiments were fabricated by multi-level electron-beam lithography onto oxidized silicon substrates. A number of samples corresponding to two different geometries were measured, but we present here results on only a few representative samples. Figure 1(a) and (b) show scanning electron micrographs of our samples corresponding to the first and second types. The first device type (Fig. 1(a)) consists of an elliptical Ni particle in contact with a superconducting Al film. The shape and size of the Ni particle, which was patterned and deposited first, ensures that it is single-domain, and that its magnetization lies along the major axis of the ellipse, as we have shown in previous experiments [12]. Four Au wires were then deposited to make contact with the Ni particle, and allowed us to make four-terminal measurements of the resistance of the Ni particle to characterize its electrical and magnetic properties. The Al film was then deposited in the final lithography step. Two

of the Au probes were placed within 20-50 nm of the FS interface, enabling us to measure the resistance of the interface by itself, with very little contribution from the ferromagnet. All interfaces were cleaned with an ac Ar^+ etch prior to deposition of the Au and Al films. The thickness of the Ni films was ~ 30 nm, and the Al and Au films ~ 50 -60 nm. Control samples of Ni, Al and Ni/Al interfaces were also fabricated in order to characterize the properties of the films and interfaces. From low temperature measurements on these samples, the resistivity of the Ni film was estimated to be $\rho_{\text{Ni}} \sim 6.6 \mu\Omega\text{cm}$, and that of the Al film $\rho_{\text{Al}} \sim 8.4 \mu\Omega\text{cm}$, corresponding to electronic diffusion coefficients $D_{\text{Ni}} \sim 76 \text{ cm}^2/\text{s}$ and $D_{\text{Al}} \sim 26 \text{ cm}^2/\text{s}$ respectively. The second set of samples (Fig. 1(b)) were simple FS crosses, that enabled us to measure the four-terminal resistance of the FS interface directly. In this second device type, both Ni and permalloy (NiFe) were used as the ferromagnet.

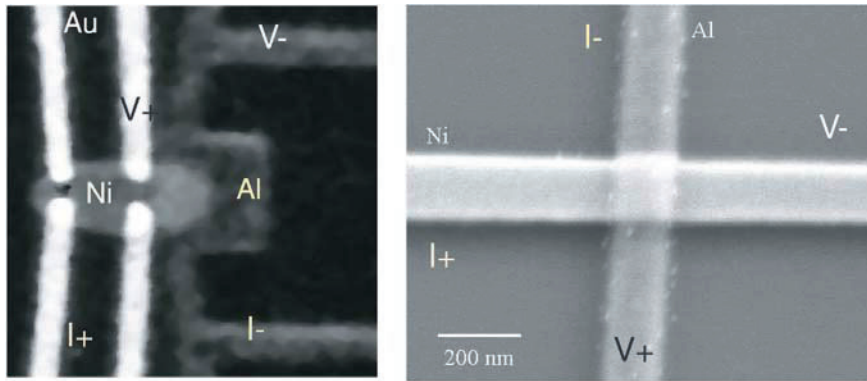


Fig. 1. Scanning electron micrographs of representative device of the first type (a), and the second type (b). (a) is scaled to $1\mu\text{m}\times 1\mu\text{m}$. The leads used to measure the four-terminal resistance are marked. The current leads were used to send both the ac and dc current.

The measurements were performed down to 0.26 K in a ^3He sorption insert with standard ac lock-in techniques. The insert was placed in a dewar with a superconducting split-coil magnet, which allowed us to apply a magnetic field in the plane of the Ni particle, along its easy axis in the case of the first device type, and along the length of the ferromagnetic wire in the case of the second device type. The application of the field in this direction has two advantages: first, the critical field of the superconductor is much greater than if the field were to be applied perpendicular to the plane of the sample, and second, the field direction is along the easy axis of magnetization of the ferromagnet. We concentrate here on the differential resistance and conductance of the FS interfaces as a function of bias current; the temperature dependence of the resistance of these devices has been described in detail in an earlier publication [4], and will not be discussed here. In order to measure the differential resistance of a low resistance FS interface, we use a four-terminal

configuration with the probe configurations as shown in Fig. 1, with a small ($\sim 10 - 50$ nA) ac current superposed on a dc bias current.

3 Experimental results and discussion

Figure 2 shows the differential resistance of a permalloy/Al (Py/Al) cross similar to that shown in Fig. 1(b) at a temperature of $T = 290$ mK, as a function of the dc current through the FS junction, at two different values of magnetic field. As the current is increased from $|I_{dc}| = 0$, the resistance first increases, reaches a peak at a current of $|I_{dc}| \simeq 1 \mu\text{A}$, and then shows two dips in the resistance before approaching the normal state resistance at higher values of I_{dc} . The dips in dV/dI , corresponding to peaks in the differential conductance dI/dV , are asymmetric, in that the amplitude of the dips is different. As the applied external field H is increased, the features become *sharper*, and more symmetric. At larger values of H (not shown in Fig. 2), the positions of the peaks and dips move down to lower values of $|I_{dc}|$. Note that this behavior is strikingly different from what is observed in the FS point contact experiments. Indeed, apart from the absence of the multiple peak structure, the resistance of the devices goes *down* rather than up as one moves away from $I_{dc} = 0$.

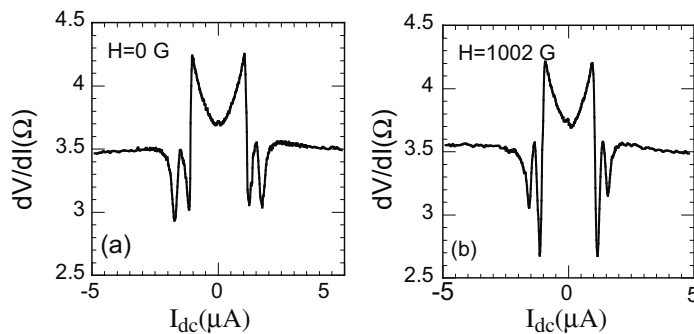


Fig. 2. Differential resistance dV/dI of a Py/Al cross, similar to the one in Fig. 1(b), as a function of dc current I_{dc} , at an external magnetic field of (a) $H = 0$, and (b) $H = 0.1002$ T. $T = 290$ mK.

In order to understand this behavior, we consider charge transport across the FS junction in the framework of a spin-polarized BTK model [5, 7]. In the conventional BTK model [8], the current across a NS junction with a voltage V applied across it is given by

$$I_{NS} = 2N(0)ev_F S \int_{-\infty}^{\infty} [f(E - eV) - f(E)] [1 + A(E) - B(E)] dE, \quad (1)$$

where $N(0)$ is the density of states at the Fermi energy, v_F is the Fermi velocity of the electrons, S is the cross-sectional area of the interface, f is the Fermi function, and $A(E)$ and $B(E)$ are the BTK coefficients that represent the probability for Andreev reflection and normal reflection of electrons from the NS interface. Their functional forms have been discussed in detail by BTK [8], and we shall not reproduce them here. We only note that $A(E)$ and $B(E)$ depend on the transparency of the NS interface, characterized by the BTK parameter Z . $Z=0$ corresponds to a perfectly transparent interface, while $Z \rightarrow \infty$ corresponds to a tunnel barrier. For $Z=0$, $A(E)=1$ for $E < \Delta$, the energy gap of the superconductor, and gradually reduces to zero as Z increases.

The process of Andreev reflection involves a spin-up electron of energy E coupling with a spin-down electron of energy $-E$ to form a Cooper pair in the superconductor. If the normal metal is replaced by a ferromagnet with a finite polarization P , not all electrons of one spin species will be able to find a corresponding electron of the opposite spin species in order to form Cooper pair. Hence, the probability of Andreev reflection will be reduced by a factor of $(1-P)$, where we define the polarization P by

$$P = \frac{N_{\uparrow}(E_F) - N_{\downarrow}(E_F)}{N_{\uparrow}(E_F) + N_{\downarrow}(E_F)}, \quad (2)$$

$N_{\uparrow}(E_F)$ and $N_{\downarrow}(E_F)$ being the density of states for the up-spin electrons and down-spin electrons respectively [13]. The equation of BTK can then be modified to [7]

$$\begin{aligned} I_{NS} = 2N(0)ev_F S \int_{-\infty}^{\infty} [f(E - eV) - f(E)] \\ ((1 - P) [1 + A_u(E - g\mu H) - B_u(E - g\mu H)] \\ + P [1 - B_p(E + g\mu H)]) dE, \end{aligned} \quad (3)$$

where the original BTK coefficients $A(E)$ and $B(E)$ are modified to unpolarized (A_u, B_u) and polarized (A_p, B_p) versions, with $A_p=0$. This modification is required to maintain current conservation across the FS interface [7], and involves a simple renormalization of the coefficients. In addition to the formulation of Ref. [7], we have also added the contribution to the energy of the quasiparticles from Zeeman splitting due to an external field H .

Figure 3(a) shows the results of our calculations of the normalized differential resistance using Eqn.(3) with $H = 0$, for a number of different combinations of Z and P . For $Z = 0$ and $P = 0$, we recover the usual BTK result, in that the resistance at zero bias drops to half the normal state value. For $Z = 0$ and $P = 0.5$, the resistance at zero bias is exactly the same as the normal state resistance, while for $Z = 0.5$ and $P = 0$, it is slightly larger. As both Z and P are increased, the resistance of the sample rises above the normal state resistance R_N , but Z and P affect the differential resistance in different ways

at higher bias. It is clear that the zero bias resistance is sensitive to both Z and P , so one cannot determine both independently by examining only the zero bias resistance; the entire curve needs to be fit. Figure 3(b) shows the results of similar calculations, but now with an applied magnetic field $H = 0.2\Delta$. The effect of the finite field is to cause a splitting in the structure of dV/dI near $V \simeq \Delta/e$ due to the Zeeman effect. The splitting can be seen even for $P = 0$, but results in a substantial asymmetry of the curve when $P \neq 0$.

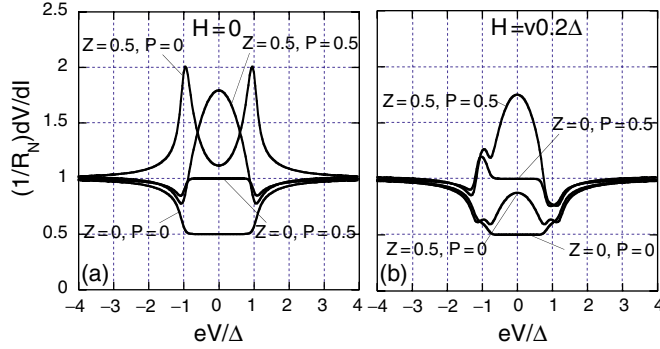


Fig. 3. Numerical simulations of the differential resistance of a FS interface, from the theory described in the text. (a) $H = 0$, (b) $H = 0.2\Delta$. The values for Z and P are noted in the figure, and the temperature is $T = 0.05\Delta$.

Comparing the results of these simulations to the data from the Py/Al cross shown in Fig. 2, we note that there are some similarities, but substantial differences in even the qualitative behavior. First, the resistance in the simulations invariably decreases as the bias is shifted from 0, except for the case $Z = 0$. In the experiment, the trend is opposite; the resistance *increases* as the bias is shifted from 0. This behavior is also reflected in the zero-bias resistance as a function of temperature in this sample, where a large increase in resistance is observed as one cools to below the transition temperature. Second, at higher bias, two sharp dips appear in the data, which are not symmetric. These are similar to the dips seen in Fig. 3(b), which are associated with Zeeman splitting of the quasi-particle density of states. However, in the experiment, this structure is seen even at zero applied external field. On the other hand, it should be noted that the field H can result from a combination of the externally applied field and the self-field of the ferromagnet, which can be substantial near the ferromagnet. At the superconductor, the direction of the externally applied field may be opposite that of the self-field of the ferromagnet, resulting in a decrease in H as the external field is increased. This apparently is the case for the sample of Fig. 2; as the external field is increased from 0 to 0.1 T, the two dips in dV/dI become sharper and the

spacing between them decreases, exactly as one would expect if the actual field at the superconductor decreased. We have seen similar behavior in other devices as well.

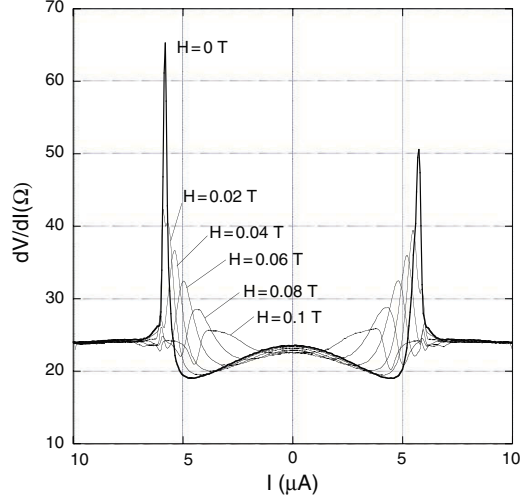


Fig. 4. Differential resistance dV/dI of the sample shown in Fig. 1(a), as a function of dc current I_{dc} , at different values of the applied magnetic field H . The temperature $T = 300$ mK.

The data shown in Fig. 2 was taken using the probe configuration shown in Fig. 1(b), and corresponds to a four-terminal measurement of the differential resistance of the FS interface alone. Figure 4 shows the differential resistance dV/dI of the sample of Fig. 1(a) as a function of dc current I_{dc} at six different values of the external magnetic field H , applied along the major axis of the elliptical Ni particle, at $T = 300$ mK. Unlike the FS crosses, the four-terminal probe configuration used to measure this device (shown in Fig. 1(a)) includes a small portion of the Ni as well as the Al. All the curves show an initial decrease in resistance as I_{dc} is increased in either direction from zero, then an increase at $|I_{dc}| \simeq 5 \mu\text{A}$, and finally, all curves approach the normal state resistance R_N at larger values of $|I_{dc}|$. For low values of H , the peaks in dV/dI are very sharp. As H is increased, the peaks decrease in amplitude, and move to lower values of $|I_{dc}|$. In other devices we have measured, the peaks increase in amplitude and move to higher values of $|I_{dc}|$ as H is increased from 0 initially, and then decrease in amplitude and move to lower values of $|I_{dc}|$ as H is increased further. This is simply due to the fact that the externally applied field can either add to or subtract from the field generated by the ferromagnetic element at the superconductor. It should be noted that the peaks, especially at low magnetic fields, are not symmetric with respect to

the applied current; the peak at negative current is higher than the peak at positive current. This asymmetry is a manifestation of the injection of spin-polarized carriers into the superconductor.

The nature of the peaks is qualitatively different from those seen in the FS crosses, and in the simulations shown in Fig. 3, in that they are much sharper. In fact, such peaks can be seen in the FS cross devices if one includes a portion of the superconductor in the four-terminal measurement. Similar peaks have been observed in NS devices as well [14], where they are associated with an excess resistance from a non-equilibrium charge imbalance in the superconductor. Injection of quasiparticles into the superconductor results in a difference between the quasiparticle chemical potential μ_{qp} and the Cooper pair chemical potential μ_{cp} . μ_{cp} rises to its bulk value within a superconducting coherence length ξ_S of the interface; μ_{qp} relaxes to μ_{cp} over a much longer length scale λ_{Q^*} , called the charge imbalance length. In diffusive systems, $\lambda_{Q^*} = \sqrt{D\tau_{Q^*}}$, where D is the diffusion coefficient. Near T_c , the charge imbalance time τ_{Q^*} is given by [15]

$$\tau_{Q^*} = \frac{4k_B T}{\pi\Delta(T, H)} \sqrt{\frac{\tau_{in}}{2\Gamma}}, \quad (4)$$

where τ_{in} is the inelastic scattering time, and Γ is given by

$$\Gamma = \frac{1}{\tau_s} + \frac{1}{2\tau_{in}} \quad (5)$$

and τ_s gives the contribution from orbital pair breaking. The excess resistance arises from the difference between μ_{cp} and μ_{qp} . If the superconducting probe is placed a distance x from the interface, an excess resistance ΔR will be measured, where $\Delta R = (\lambda_{Q^*} - x)\rho_S$, ρ_S being the resistance per unit length of the superconductor. λ_{Q^*} diverges when $\Delta \rightarrow 0$, and this divergence gives rise to the peak in resistance seen in NS structures just below T_c .

For a particle with an energy E , the effective gap seen is $\Delta - E$. At low temperatures, we can take into account the excess resistance due to charge imbalance by introducing an effective *voltage* dependent charge imbalance time $\tau_{Q^*} \simeq T/(\Delta - eV)$, and adding a resistance $R_{Q^*} = \rho_{Al}\lambda_{Q^*}$ to the resistance calculated in the spin-polarized BTK model described above.

The solid line in Fig. 5 shows the result of our calculation including both spin-polarized BTK in a finite magnetic field as described above, and charge imbalance. For comparison, we also show the result for only spin-polarized BTK. These numerical calculations were performed by calculating the current through the FS interface for a particular voltage V_0 , adding the charge imbalance voltage V_{ci} , and taking the derivative $d(V_0 + V_{ci})/dI$ numerically. The numerical calculations reproduce the large peaks seen in dV/dI at currents corresponding to the gap, i.e., $I \simeq (\Delta/eR_N)$. Unlike the BTK case, no splitting of the peaks near the gap is observed in the solid line in Fig. 5 (the dashed line, which shows the BTK case, does have a small splitting at

negative I that is difficult to observe because of the scale of the plot). Closer examination of the position of the charge-imbalance peaks, however, shows that the peak at positive current is slightly greater than Δ/eR_N , while the peak at negative current is slightly less than $-\Delta/eR_N$; the shift corresponds to the Zeeman splitting of the quasiparticle density of states. Only one spin species gives rise to a peak for positive current; the other spin species gives rise to the corresponding peak for negative current. Thus, the difference in the height of the peaks is an indication of the degree of spin polarization in the ferromagnet. If we take the difference between the two peaks heights, divided by the sum of heights of the peaks taken from the normal state resistance, we obtain a value of 0.25, which is close to the value of $P = 0.3$ used in the simulation. A similar analysis performed on the experimental data of Fig. 4 gives a spin polarization of $P=0.23$, in good agreement with the expected value of the spin polarization for Ni.

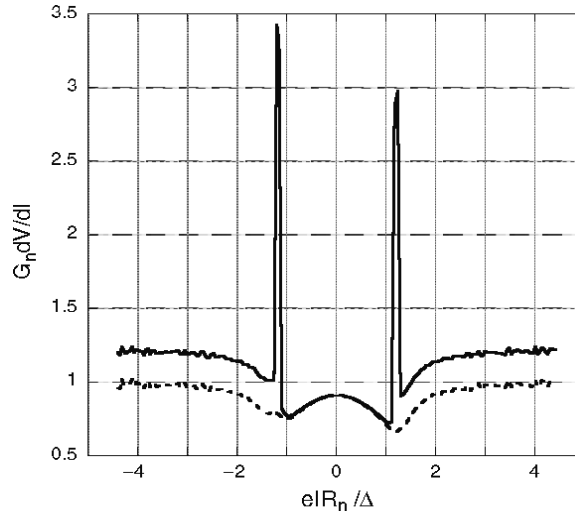


Fig. 5. Numerical simulation of the differential resistance of a FS interface, including charge imbalance, as described in the text. Solid line, spin-polarized BTK model with charge-imbalance; dashed line, spin-polarized BTK model without charge imbalance. The other parameters used in the simulation are $P = 0.3$, $Z = 0.3$, and $H = 0.1\Delta$.

4 Conclusions

The differential resistance of mesoscopic ferromagnet/superconductor junctions shows a number of features associated with the injection of spin-polarized carriers into the superconductor. In particular, large peaks are observed at currents corresponding to the superconducting gap voltage. These peaks are

not symmetric with respect to the current, in that their amplitudes are different. The peaks are associated with the excess resistance arising from quasiparticle charge imbalance in the superconductor, and the difference in their heights is directly related to the degree of spin polarization in the ferromagnet.

Acknowledgements.— This work was supported by the US National Science Foundation under grant number DMR-0201530.

References

1. K. Kawaguchi and M. Sohma, Phys. Rev. B **46**, 14722 (1992); J.S. Jiang *et al.*, Phys. Rev. Lett. **74**, 314 (1995).
2. T. Kontos *et al.*, Phys. Rev. Lett. **86**, 304 (2001); V.V. Ryazanov *et al.*, Phys. Rev. Lett. **86**, 2427 (2001).
3. M. Giroud *et al.*, Phys. Rev. B **58**, R11872 (1998); M.D. Lawrence and N. Giordano, J. Phys.: Condens. Matter **11**, 1089 (1999); V. Petrashov *et al.*, Phys. Rev. Lett. **83**, 3281 (1999).
4. J. Aumentado and V. Chandrasekhar, Phys. Rev. B **64**, 54505 (2001).
5. R.J. Soulen *et al.*, Science **282** 85 (1998); S.K. Upadhyay *et al.*, Phys. Rev. Lett. **81**, 3247 (1998).
6. P.M. Tedrow and R. Meservey, Phys. Rev. Lett. **26**, 192 (1971); Phys. Rev. B **7**, 318 (1973).
7. G.J. Strijkers *et al.*, Phys. Rev. B **63**, 104510 (2001); B. Nadgorny *et al.*, Phys. Rev. B **63**, 184433 (2001); I.I. Mazin, A.A. Golubov, and B. Nadgorny, J. Appl. Phys. **89**, 7576 (2001); Y. Ji *et al.*, Phys. Rev. Lett. **86**, 5585 (2001); C.H. Kant *et al.*, Phys. Rev. B **66**, 212403 (2002).
8. G.E. Blonder, M. Tinkham, and T.M. Klapwijk, Phys. Rev. B **25**, 4515 (1982).
9. H.L. Zhao and S. Hershfield, Phys. Rev. B **52**, 3632 (1995); F.J. Jedema *et al.*, Phys. Rev. B **60**, 16549 (1999).
10. W. Belzig *et al.*, Phys. Rev. B **62**, 9726 (2000).
11. R. Mélin, Europhys. Lett. **51**, 202 (2000).
12. J. Aumentado and V. Chandrasekhar, Appl. Phys. Lett. **74**, 1898 (1999).
13. Another way to P takes into account the Fermi velocities of the up spin and down spin electrons as well. Since we use P as a phenomenological fitting parameter, the detailed definition of P is not of concern here.
14. C.-J. Chien and V. Chandrasekhar, Phys. Rev. B **60**, 3655 (1999).
15. A. Schmid and G. Schön, J. Low Temp. Phys. **20**, 207 (1975).

Anomalous Negative Magnetoresistance Caused by Non-Markovian Effects

Vadim V. Cheianov¹, A. P. Dmitriev², and V. Yu. Kachorovskii²

¹ NORDITA, Blegdamsvej 17, Copenhagen, DK 2100, Denmark
cheianov@nordita.dk

² A.F. Ioffe Physical-Technical Institute, 26 Polytechnicheskaya str., Saint
Petersburg, 194021, Russia

Summary. A theory of recently discovered anomalous low-field magnetoresistance is developed for the system of two-dimensional electrons scattered by hard disks of radius a , randomly distributed with concentration n . For small magnetic fields the magnetoresistance is found to be parabolic and inversely proportional to the gas parameter, $\delta\rho_{xx}/\rho \sim -(\omega_c\tau)^2/na^2$. With increasing field the magnetoresistance becomes linear $\delta\rho_{xx}/\rho \sim -\omega_c\tau$ in a good agreement with the experiment and numerical simulations.

1 Introduction

It is well known that in the Boltzmann-Drude approach the longitudinal resistivity ρ_{xx} of a degenerate two-dimensional (2D) electron gas does not depend on the transverse magnetic field B . Therefore, the known mechanisms of magnetoresistance (MR) involve either quantum interference effects or classical non-Markovian memory effects, which are not captured in the Boltzmann picture. The MR, arising from quantum effects was discussed in a great number of works (see for review Ref. [1]). The role of classical memory effects was underappreciated for a long time, though several theoretical works pointed out at the importance of such effects for magnetotransport [2, 3, 4]. The interest to the problem of classical MR has sharply increased in recent years, starting with Ref. [5], where it was shown that effects of "classical localization" may lead to the exponential suppression of electron diffusion at large B . This work was followed by a series of works [6, 7, 8, 9, 10, 11, 12, 13, 14], discussing different aspects of classical 2D magnetotransport in strong magnetic fields.

In this paper we focus on a mechanism of low field classical MR specific for systems of strong scatterers. This mechanism is connected to the

memory effects due to backscattering events. The corresponding corrections to the conductivity are small in the parameter a/l , where a is the characteristic size of the scatterers and l is the mean free path. Nevertheless, the dependence of these corrections on the magnetic field turns out to be very sharp, resulting in the MR anomaly. The anomaly was discovered in recent numerical simulations [15] where the MR in a system of 2D electrons scattering on randomly distributed hard disks was studied. This system is usually referred to as the Lorenz gas and is the simplest model of the 2D electron gas with strong scatterers. In the following we restrict our considerations to this model. The generalization of our results to other models of strong disorder is straightforward. Magnetotransport in the Lorenz gas is characterized by two dimensionless parameters: $\beta = \omega_c \tau$, and the gas parameter $\beta_0 = a/l = 2na^2$. Here a is the disk radius, n is disks' concentration, ω_c is the cyclotron frequency, $\tau = l/v_F$ is the mean free time and $l = 1/2na$ is the mean free path. The anomaly was observed in the case $\beta \ll 1$, $\beta_0 \ll 1$. Both the numerical simulations and the qualitative analysis of [15] indicated that at zero temperature, T , the MR can be expressed in terms of a dimensionless function $f(z)$ via

$$\frac{\delta\rho_{xx}}{\rho} = -\beta_0 f\left(\frac{\beta}{\beta_0}\right), \quad (1)$$

where ρ is the resistivity for $B = 0$. Numerical results [15] suggest that $f(z) \sim z$ as $z \rightarrow 0$, yielding $\delta\rho_{xx}/\rho \sim -|\omega_c|\tau$. The latter expression is in a very good agreement with experimental measurements of MR in a random antidot arrays [16]. It is anomalous in two senses. First, it has a non-analytic dependence on the magnetic field. Second, it does not vanish in the limit of vanishing β_0 , which is normally regarded as the expansion parameter for the corrections to the Drude-Boltzmann picture. This intriguing behavior calls for a rigorous analytical theory of the effect, which would establish Eq. 1 and enable one to derive the analytical expression for function f . In this letter we present a theory of the anomaly and give an expression for $f(z)$. We find that for $z \lesssim 1$, $f(z)$ is linear in agreement with numerical experiment, but at very small $z \lesssim 0.05$ crosses over to a quadratic dependence. Thus, for $\beta \rightarrow 0$, Eq. 1 yields $\delta\rho_{xx}/\rho \sim -\beta^2/\beta_0$. The limit $\beta_0 \rightarrow 0$ should be taken with care. While the small β expansion seems to be singular as a function of β_0 , the region of β where this expansion is valid shrinks as $\beta_0 \rightarrow 0$. For $z \rightarrow \infty$, f saturates at some constant value. Therefore, the full variation of $\delta\rho_{xx}/\rho$ is of the order β_0 . In other words, the anomalous MR is strong but it exists in a small region of magnetic fields.

In [15] a mechanism of MR connected with memory effects arising in backscattering events was proposed. It has a close relation to the well known non-analyticity of the virial expansion of transport coefficients [17, 18, 19, 20, 21], which we briefly recall. For $B = 0$ the leading nonanalytic correction to resistivity, $\delta\rho$, is due to the processes of return to a scatterer after a single collision with another scatterer [Fig. 1(a)]. The relative correction, $\delta\rho/\rho$, is proportional to the corresponding backscattering probability, given by the product of $e^{-r/l} d\phi dr/l$ (which is the probability to reach scatterer 2

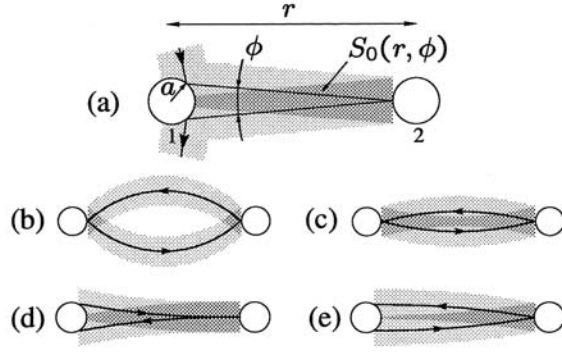


Fig. 1. Backscattering process responsible for leading nonanalytic contribution to the resistivity at $B = 0$ (a). For $B \neq 0$, the overlap area, S_B , between two corridors is small at large B (b). For $\phi = 0$, S_B decreases with B (c). For $\phi \neq 0$ and small B the values of $S_B - S_0$ for time reversed trajectories have opposite signs (d,e).

without collision and scatter in the angle $d\phi$) and the probability p to return without collisions from 2 to 1 (here l is the mean free path). Assuming $p = \exp(-r/l)$ and integrating over intervals $0 < \phi < a/r$, $a < r < \infty$, one obtains [17, 18, 19, 20, 21] $\delta\rho/\rho \sim \beta_0 \ln(1/2\beta_0)$.

In Ref. [15] it was shown that the probability p is actually larger than $\exp(-r/l)$ because the passage of a particle from 1 to 2 ensures the existence of a corridor of width $2a$ free of the centers of the disks. This reduces the scattering probability on the way back, yielding $p(r, \phi) = \exp(-r/l + nS_0(r, \phi))$, where $S_0(r, \phi) = 2ar - r^2|\phi|/2$ is the area of the overlap of the two corridors [Fig. 1(a)]. For example, for $\phi = 0$, we have $S_0 = 2ar$ and $p = 1$. Physically, this means that the particle is unable to scatter, since it travels back along the same path. Taking into account the effect of “empty corridor”, we get

$$\frac{\delta\rho}{\rho} \sim \int_a^\infty \frac{dr}{l} \int_0^{a/r} d\phi e^{-(2r/l) + nS_0} \approx \beta_0 \ln\left(\frac{C}{2\beta_0}\right), \quad (2)$$

where C is a constant of the order of unity. Thus, for $B = 0$ this effect simply changes the constant in the argument of the logarithm.

The key idea suggested in [15] was that for $B \neq 0$ the area of the overlap of the two corridors, S_B , sharply depends on B , resulting in the observed MR. Indeed, it is seen from Fig. 1(b) that for $\beta \gtrsim \beta_0$, $S_B \rightarrow 0$, resulting in sharp negative MR

$$\frac{\delta\rho_{xx}}{\rho} \sim \int_0^\infty \frac{dr}{l} \int_0^{a/r} d\phi e^{-2r/l} (e^{nS_B} - e^{nS_0}). \quad (3)$$

The following qualitative explanation of the observed linear MR was presented in Ref. [15]. The value $n(S_B - S_0)$ was estimated for $\phi = 0$ [Fig. 1(c)] to the

first order in B as $-nr^3/R_c = -r^3/2alR_c$, where R_c is the cyclotron radius. Assuming that this estimate also works at $\phi \neq 0$ and expanding $e^{nS_B} - e^{nS_0}$ to the first order in B , one gets $\delta\rho_{xx}/\rho \sim -l/R_c = -\omega_c\tau$.

In fact, the physical picture of the phenomenon is more subtle. The contribution of any trajectory with $\phi \neq 0$ is cancelled in the first order in B by the contribution of the time-reversed trajectory, since the values of $S_B - S_0$ are opposite for these paths [Fig. 1(d), (e)]. The cancellation does not occur only at very small $\phi \sim \beta$. The integration in Eq. 3 over $\phi < \beta$ yields $\delta\rho_{xx}/\rho \sim -\beta^2/\beta_0$. Larger values of ϕ also give a quadratic in β contribution to the MR. This contribution is positive and comes from the second order term in the expansion of $e^{nS_B} - e^{nS_0}$ in B . It follows from our results [Eqs. (1),(9)] that the contribution of small angles is dominant resulting in a negative parabolic MR [22]. We find that the parabolic MR crosses over to linear at very small $\beta \approx 0.05\beta_0$, which explains why the parabolic MR was not seen in numerical simulations [15] and experiment [16].

2 Calculations

Next we sketch our calculations. We consider the Lorentz gas at $T = 0$, assuming that $\beta \ll 1$, $\beta_0 \ll 1$. In this case [23], $\delta\rho_{xx}/\rho = -(D - D_0)/D_0$, where $D_0 = v_F l_{tr}/2$ is the Drude diffusion coefficient for $B = 0$, $l_{tr} = 3l/4 = 3/8na$ is the momentum relaxation length and D is given by

$$D = \frac{1}{2} \int_0^\infty dt \langle \mathbf{v}(0)\mathbf{v}(t) \rangle = \frac{1}{2} \int d\mathbf{r} d\mathbf{v} \langle G \rangle \mathbf{v}\mathbf{v}_0. \quad (4)$$

Here $G = G(\mathbf{v}, \mathbf{v}_0, \mathbf{r})$ is the Fourier transform (at $\omega = 0$) of the retarded Green's function of the Liouville equation and $\langle \dots \rangle$ stands for the averaging over the positions of the disks. The equation for G reads

$$\left(\hat{L}_0 - \hat{T}_- - \hat{T}_+ \right) G = \delta(\mathbf{r})\delta(\mathbf{v} - \mathbf{v}_0), \quad (5)$$

where $\hat{L}_0 = \mathbf{v}\partial/\partial\mathbf{r} - \omega_c[\mathbf{v} \times \partial/\partial\mathbf{v}]$ is the Liouville operator of the free motion in the magnetic field. The interaction with disks is written in Eq. 5 in the form of a collision integral [18, 24]. The scattering operators \hat{T}^\pm transform arbitrary function $f(\mathbf{r}, \mathbf{v})$ as follows,

$$\begin{aligned} \hat{T}^+ f(\mathbf{r}, \mathbf{v}) &= p_F \int d\mathbf{v}' \sigma(\varphi) \delta(\epsilon - \epsilon') n^+ f(\mathbf{r}, \mathbf{v}'), \\ \hat{T}^- f(\mathbf{r}, \mathbf{v}) &= -p_F \int d\mathbf{v}' \sigma(\varphi) \delta(\epsilon - \epsilon') n^- f(\mathbf{r}, \mathbf{v}'), \end{aligned} \quad (6)$$

where $n^\pm = \sum_i \delta(\mathbf{r} - \mathbf{R}_i \pm \mathbf{a})$. Here \mathbf{R}_i are the positions of the disks, delta-function $\delta(\epsilon - \epsilon')$ provides the energy conservation, p_F is the Fermi momentum, $\sigma(\varphi) = (a/2)|\sin(\varphi/2)|$ is the differential cross-section of one disk and φ is the

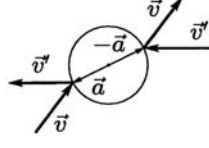


Fig. 2. Scattering of a particle on a hard disk.

angle between \mathbf{v}' and \mathbf{v} . The vector $\mathbf{a} = \mathbf{a}(\mathbf{v}', \mathbf{v}) = a(\mathbf{v}' - \mathbf{v})/\sqrt{2(v^2 - \mathbf{v}'\mathbf{v})}$ is pointing from the center of a disk to the scattering point at the disk surface [Fig. 2]. Physically, operator \hat{T}^+ describes influx of particles with velocity \mathbf{v} at the point $\mathbf{R}_i - \mathbf{a}$, while operator \hat{T}^- describes the outflux of particles with velocity \mathbf{v} at the point $\mathbf{R}_i + \mathbf{a}$. The Boltzmann equation is obtained from Eq. 5 by averaging the Liouville operator over the positions of the disks, yielding $\langle \hat{T}^+ \rangle f(\mathbf{r}, \mathbf{v}) = p_F n \int d\mathbf{v}' \sigma(\mathbf{v}, \mathbf{v}') \delta(\epsilon - \epsilon') f(\mathbf{r}, \mathbf{v}')$, $\langle \hat{T}^- \rangle = -1/\tau$. Here $n = \langle n^\pm \rangle$ is the concentration of the disks and $1/\tau = nv2a$ is the inverse full scattering time. Introducing now $\delta\hat{T}^\pm = \hat{T}^\pm - \langle \hat{T}^\pm \rangle$ and writing a formal solution of (5), $\hat{G} = (\delta + \hat{L}_0 - \hat{T}^- - \hat{T}^+)^{-1}$ as a series in $\delta\hat{T}^\pm$, we get

$$\langle \hat{G} \rangle = \hat{G}_0 + \sum_{\alpha, \gamma = \pm} \hat{G}_0 \langle \delta\hat{T}^\alpha \hat{G}_0 \delta\hat{T}^\gamma \rangle \hat{G}_0 + \dots, \quad (7)$$

where $\hat{G}_0 = (\delta + \hat{L}_0 + 1/\tau - \langle \hat{T}^+ \rangle)^{-1}$ is the Green's function of the Boltzmann operator (here $\delta \rightarrow 0$). Eq. 7 gives a regular way to calculate correlations, which are absent in the Boltzmann picture.

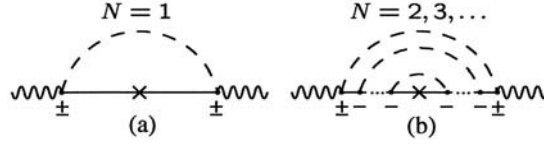


Fig. 3. Diagrams, corresponding to the process shown in Fig. 1(a). Diagram (a) does not take into account effect of “empty corridor” and should be renormalized by (b).

Consider first the case $B = 0$. Substituting the first term in the right hand side of Eq. 7 into Eq. 4, we get $D = D_0$. The second term in Eq. 7 describes the memory-effect due to diffusive returns. As discussed above, the main contribution comes from returns after a single scattering. This process is described by the diagram Fig. 3(a). The dashed line corresponds to the pairings $\langle \delta\hat{T}^\alpha \delta\hat{T}^\gamma \rangle$ ($\alpha, \gamma = \pm$), external wavy lines to the diffusion propagators \hat{G}_0 . The internal line corresponds to the Boltzmann propagator truncated at one scattering $\hat{G}_- \langle \hat{T}^+ \rangle \hat{G}_-$, where $\hat{G}_- = (L_0 + 1/\tau)^{-1}$ is the ballistic propagator and $\langle \hat{T}^+ \rangle$ stands for one scattering event (G_- are shown by solid lines and

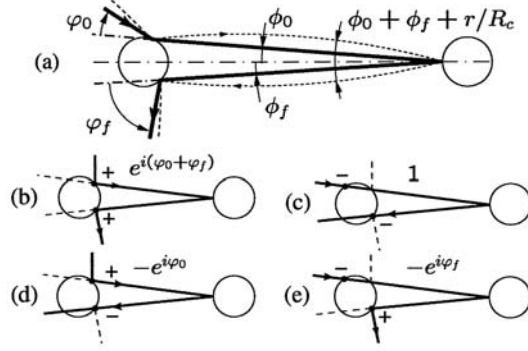


Fig. 4. Backscattering process is parameterized by the angles φ_0, φ_f . The magnetic field changes the backscattering angle $\phi = \phi_0 + \phi_f + r/R_c$. The solid (dashed) line in (a) represents electron trajectory for $B = 0$ ($B \neq 0$). Different processes contributing to MR are shown in (b)-(e).

$\langle \hat{T}^+ \rangle$ by the cross). This diagram yields $\delta\rho/\rho = -\delta D/D = (2\beta_0/3) \ln(1/2\beta_0)$ [17, 18, 19, 20, 21]. The terms of the N -th order in Eq. 7 contain N pairings (N dashed lines) and are typically small as β_0^N . However, there is a series of diagrams, shown in Fig. 3(b), whose contribution is of the order β_0 [19]. The internal dashed lines in this series only contain pairings $\langle \delta\hat{T}^+ \delta\hat{T}^- \rangle$. Summing the diagrams Fig. 3(b) together with Fig. 3(a), one gets an exact equation

$$\frac{\delta\rho}{\rho} = \frac{nl_{\text{tr}}}{4l} \text{Re} \int_a^\infty \frac{dr}{r} e^{-2r/l} \int_0^{2\pi} d\varphi_0 \int_0^{2\pi} d\varphi_f \sigma(\varphi_0) \sigma(\varphi_f) (1 - e^{i\varphi_0})(1 - e^{i\varphi_f}) e^{nS_0(r, \phi_0 + \phi_f)} = \frac{2\beta_0}{3} \ln\left(\frac{C}{2\beta_0}\right), \quad (8)$$

instead of qualitative estimate Eq. 2. Here φ_0, φ_f are the scattering angles [Fig. 4(a)], $\phi_0 \approx (a/r) \cos(\varphi_0/2)$, $\phi_f \approx (a/r) \cos(\varphi_f/2)$ and $C \approx 1.8$. Thus, addition of the series Fig. 3(b) to Fig. 3(a) leads to the following renormalization: $\ln(1/2\beta_0) \rightarrow \ln(C/2\beta_0)$. Physically, the series Fig. 3(b) accounts for the effect of the “empty corridor”. The N -th order term in this series corresponds to $N - 1$ term in the Taylor expansion of the $\exp(nS_0)$ in Eq. 8. Four terms in the product $(1 - e^{i\varphi_0})(1 - e^{i\varphi_f}) = 1 - e^{i\varphi_0} - e^{i\varphi_f} + e^{i(\varphi_0 + \varphi_f)}$ correspond to four combinations of (\pm, \pm) at the ends of external dashed lines in the diagrams shown in Fig. 3. They are connected with four different types of correlation at a given point \mathbf{r} . The diagram $(+, +)$ [Fig. 4(b)] corresponds to the process, where an electron has two real scatterings on a disk placed at point \mathbf{r} . The diagram $(-, -)$ [Fig. 4(c)] does not correspond to any real scattering at point \mathbf{r} . It just allows us to calculate correctly the probability for an electron to pass twice the region of the size a around point \mathbf{r} without scattering. To interpret the diagram $(+, -)$, note that in the Boltzmann picture, which neglects correlations, the following process is allowed. An electron

scatters on a disk and later on passes through the region occupied by this disk without a scattering [Fig. 4(d)] The diagrams (+, -) correct the Boltzmann result by subtracting the contribution of such unphysical process. Analogous consideration is valid for diagram (-, +) shown in Fig. 4[e].

3 Results

For $B \neq 0$ the sum of diagrams shown in Fig. 3 can be expressed as an integral over angles φ_0, φ_f (scattering angles for $B = 0$). The only difference from Eq. 8 is that one should replace $S_0 \rightarrow S_B$. For $\beta \ll 1$ the overlap area can be calculated as $S_B(r, \phi) = \int_0^r dx h(x)$, where $h(x) \approx (2a - |\phi x - x^2/R_c|) \theta(2a - |\phi x - x^2/R_c|)$, θ is the Heaviside step function and $\phi = \phi_0 + \phi_f + r/R_c$ [Fig. 4(a)]. The value of $\delta\rho_{xx}/\rho$ is obtained from Eq. 8 by replacing e^{nS_0} to $e^{nS_B} - e^{nS_0}$. Introducing dimensionless variables $T = r/l$, $z = \beta/\beta_0$ we get Eq. 1, where function $f(z)$ is given by

$$f(z) = \frac{3}{32} \int_0^\infty \frac{dT}{T} e^{-2T} \int_0^{2\pi} d\varphi_0 \int_0^{2\pi} d\varphi_f \cos\left(\frac{\varphi_0 + \varphi_f}{2}\right) \sin^2\left(\frac{\varphi_0}{2}\right) \sin^2\left(\frac{\varphi_f}{2}\right) (e^{s_z} - e^{s_0}). \quad (9)$$

Here

$$s_z = \int_0^T dt \left(1 - \left|\zeta t - \frac{zt^2}{2}\right|\right) \theta\left(1 - \left|\zeta t - \frac{zt^2}{2}\right|\right), \\ \zeta = \frac{\cos(\varphi_0/2) + \cos(\varphi_f/2)}{2T} + \frac{zT}{2}, \quad s_0 = s_{z \rightarrow 0}. \quad (10)$$

Function $f(z)$ has the following asymptotics

$$f(z) = \begin{cases} 0.33z^2 & \text{for } z \lesssim 0.05 \\ 0.032(z - 0.04) & \text{for } 0.05 \lesssim z \lesssim 2 \\ 0.39 - 1.3/\sqrt{z} & \text{for } z \rightarrow \infty. \end{cases} \quad (11)$$

Note that there is a parametrically small nonanomalous correction to Eq. 1 due to returns after multiple scatterings, $\delta\rho'_{xx}/\rho \approx -0.2\beta_0\beta^2$ [15]. To compare the results of simulations [15] with the theoretical results in a wider region of parameters β, β_0 , we subtract $\delta\rho'_{xx}/\rho$ from the numerical curves. Theoretical and numerical [15] results are plotted in Fig. 5. in the universal units, $\delta\rho_{xx}/\rho\beta_0$ versus $z = \beta/\beta_0$. It is seen, that the theoretical and numerical results are in a very good agreement. The comparison with the experiment [16] is more difficult, because of the 50% uncertainty in the sizes of the antidots. However, a good agreement with the experiment can be achieved by appropriate choice of a in the uncertainty interval [15].

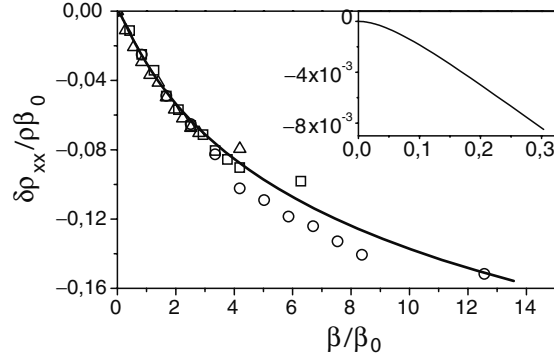


Fig. 5. The value of $\delta\rho_{xx}/\rho\beta_0$ from Eqs. (1), (9) (solid line) shown as a function of β/β_0 together with the results of numerical simulations [15] presented for different values of β_0 (triangles for $\beta_0 = 0.09$, boxes for $\beta_0 = 0.06$, circles for $\beta_0 = 0.03$). Data for all numerical curves are shown for $\beta < 0.3$. Inset: The crossover from quadratic to a linear dependence at $\beta/\beta_0 \sim 0.05$. This crossover was not resolved in numerical simulations.

Note finally that we fully neglected quantum effects. This is possible when $a \gg \sqrt{\lambda_F l}$ (λ_F is a Fermi wavelength). This criterion ensures that diffraction effects on the edges of the disks are not relevant at the scales of the order of l . In the opposite case, $a \ll \sqrt{\lambda_F l}$, the diffraction should destroy the “corridor effect”, does suppressing the anomalous MR. The detailed analysis of quantum effects will be presented elsewhere.

4 Conclusions

In summary, we have proposed a theory of the negative anomalous MR in the Lorenz gas. The analytical expression for the MR [Eqs. (1), (9), (11)] has been derived.

Acknowledgements.— We thank M.I. Dyakonov for insightful discussions and R. Jullien for providing us with the numerical data. We are also grateful to I.V. Gornyi and D.G. Polyakov for useful comments. The work was partially supported by RFBR and INTAS.

References

1. P.A. Lee and T.V. Ramakrishnan, *Rev. Mod. Phys.*, **57**, 287 (1985).
2. E.M. Baskin, L.N. Magarill, and M.V. Entin, *Sov. Phys. JETP* **48**, 365 (1978).
3. D. Polyakov, *Sov. Phys. JETP* **63**, 317 (1986).
4. A.V. Bobylev, F.A. Maaø, A. Hansen, and E.H. Hauge, *Phys. Rev. Lett.* **75**, 197 (1995).

5. M. Fogler, A. Dobin, V. Perel, and B. Shklovskii, Phys. Rev. B **56**, 6823 (1997).
6. M.M. Fogler and B.I. Shklovskii, Phys. Rev. Lett. **80**, 4749 (1998).
7. A.V. Bobylev, F.A. Maaø, A. Hansen, and E.H. Hauge, J. Stat. Physics, **87**, 1205 (1997).
8. E.M. Baskin and M.V. Entin, Physica B, **249**, 805 (1998).
9. A. Kuzmany and H. Spohn, Phys. Rev. E, **57**, 5544 (1998).
10. A.D. Mirlin, J. Wilke, F. Evers, D.G. Polyakov, and P. Wolfle, Phys. Rev. Lett. **83**, 2801 (1999).
11. A.D. Mirlin, D.G. Polyakov, F. Evers, and P. Wolfle, Phys. Rev. Lett. **87**, 126805 (2001).
12. D.G. Polyakov, F. Evers, A.D. Mirlin, and P. Wolfle, Phys. Rev. B **64**, 205306 (2001).
13. D.G. Polyakov, F. Evers, and I.V. Gornyi Phys. Rev. B, **65**, 125326 (2002).
14. A. Dmitriev, M. Dyakonov, and R. Jullien, Phys. Rev. B **64**, 233321 (2001).
15. A. Dmitriev, M. Dyakonov, and R. Jullien, Phys. Rev. Lett. **89**, 266804 (2002).
16. G. Gusev, P. Basmaji, Z. Kvon, L. Litvin, Yu. Nastaushev, and A. Toporov, Surface Science, **305**, 443 (1994).
17. J. Dorfman and E. Cohen, Phys. Lett. **16**, 124 (1965).
18. J. Van Leeuwen and A. Weiland, Physica, **36**, 457 (1967).
19. J. Van Leeuwen and A. Weiland, Physica, **38**, 35 (1968).
20. E.H. Hauge, in *Transport Phenomena*, edited by G. Kirczenow and J. Marro, Lecture Notes in Physics, No.31 (Springer, New York, 1974), p. 337.
21. R. Peierls, *Surprises in Theoretical Physics* (Princeton University, Princeton, 1979).
22. For very small β contribution of Lyapunov trajectories becomes important. This contribution is parametrically small compared to Eq.(1) for $\beta \gtrsim \beta_0^2$.
23. For $\beta \ll 1$ one can neglect the off-diagonal part of the conductivity tensor.
24. R. Zwanzig, Phys.Rev. B, **129**, 486, (1963).

Persistent Currents in Interacting Aharonov-Bohm Interferometers

Ora Entin-Wohlman^{1,2}, Yoseph Imry², and Amnon Aharony¹

¹ School of Physics and Astronomy, Raymond and Beverly Sackler Faculty of Exact Sciences, Tel Aviv University, Tel Aviv 69978, Israel

entin@post.tau.ac.il

² Albert Einstein Minerva Center for Theoretical Physics at the Weizmann Institute of Science, Rehovot 76100, Israel

³ Department of Condensed Matter Physics, The Weizmann Institute of Science, Rehovot 76100, Israel

Summary. The orbital magnetic moment of electrons, (proportional to the persistent current I_{pc}), arising from interference on an Aharonov-Bohm ring, is reviewed when the electrons are also subject to an external radiation. Two cases are analyzed: (i) An isolated ring, where special doubly-resonant electron-boson processes contribute to I_{pc} a term additional to the Debye-Waller exponent, which arises only at non-zero temperatures T , and whose T -dependence is *non-monotonic*. (ii) A ring opened to external electron reservoirs, where the electronic levels acquire a finite life-time, and the modification of I_{pc} (beyond that of the Debye-Waller exponent) exists even at $T = 0$. It is suggested that by controlling the intensity of the radiation in a certain frequency range, the magnitude of these unique contributions to the orbital moment can be tuned.

1 Introduction

The “ring current” driven by a constant magnetic field has been invoked as early as 1936, [1] to explain the large orbital magnetic response of π electrons moving on a benzene-type molecules. This ‘persistent current’, I_{pc} , results from the modifications of the electronic interference pattern caused by an Aharonov-Bohm phase, acquired by electrons moving on rings threaded by a magnetic flux, and can be related to the orbital magnetic moment. The analogy with the Josephson effect has been expanded in Refs. [2], whose discussion of possible realizations of I_{pc} in small rings has sparked much interest and led to a considerable experimental effort. [3] Much recent interest is focused on

non-equilibrium, or time-dependent properties, [4] and attempts [5] to relate this coherence effect with dephasing due to coupling to an equilibrium bath.

Indeed, when electrons are coupled to a boson source, the naive expectation is that I_{pc} will diminish due to loss of coherence, as is manifested by the overall Debye-Waller exponent. However, it is not the whole effect: The coupling leads to an additional term. [6] At thermal-equilibrium this term reduces further I_{pc} . However, at non-equilibrium, its magnitude may be tuned by controlling the intensity of the boson field in a certain frequency range, which is experimentally feasible. [7] I.e., by coupling the electrons to an *out-of-equilibrium* radiation source, one may control their orbital magnetic response. Such a relation between the radiation intensity and the magnetic moment opens interesting possibilities for future nanodevices.

Although the term ‘electron-phonon coupling’ is used here, the discussion applies equally to coupling with an electro-magnetic source. In any event, in order to retain the coherence of the electrons at the given T , the system has to be sufficiently small. At the same time, the strength of the acoustic source is assumed to be such that the additional decoherence it causes is not detrimental. The precise parameter windows in which this can be achieved will be sensitive to acoustic mismatch, details of the sample geometries, etc.

2 The Holstein process

The effect of electron-phonon coupling on I_{pc} of an *isolated* ring has been studied [6] by applying the Holstein theory of the Hall effect in hopping conduction. [8] He proposed that in order to capture this effect, which is odd in the magnetic field, it is necessary to consider the interference of tunneling amplitudes involving doubly-resonant electronic transitions. The mechanism can be explained in terms of *transition probabilities*. Let P_{ij} be the transition probability from the electronic state localized around i (of energy ϵ_i) to that localized around j . It is obtained by squaring the absolute value of the corresponding *transition amplitude*, J_{ij} (which in the absence of the field can be always chosen to be real). In the presence of a magnetic field, J_{ij} is multiplied by the magnetic phase acquired along the path $i-j$. However, P_{ij} due to direct hopping alone is then independent of the field. Upon adding to J_{ij} the amplitude for indirect tunneling, e.g., along the path $i-\ell-j$, where ℓ denotes an intermediate site, the resulting P_{ij} becomes field-dependent. The dependence is on the total (gauge-invariant) magnetic flux enclosed by the two paths, Φ (measured in units of the flux quantum). However, it is an *even* dependence and hence cannot lead to a dc Hall conduction. Hence, a phase $\pi/2$ is required in the interference term, to yield an odd dependence on Φ in P_{ij} .

Where will this phase come from? Holstein [8] argued that when electron-phonon processes are included, the amplitude for the indirect path is

$$J_{i-\ell-j} \sim \sum_{\mathbf{q}''} \frac{\langle i\mathbf{q}|V|\ell\mathbf{q}''\rangle \langle \ell\mathbf{q}''|V|j\mathbf{q}'\rangle}{\epsilon_i - \epsilon_\ell \pm \omega_{\mathbf{q}''} + i\eta}, \quad \eta \rightarrow 0^+, \quad (1)$$

where ω_q is the boson energy, and V is a matrix element that transfers the electron between sites, and also may change the phonon states. As now the intermediate state lies in a continuum, η leads to *finite* contribution when there is a real, energy-conserving transition [9] between the initial and intermediate states, which will appear with the required phase $\pi/2$. At least two resonant electron-phonon processes are required, because the three electronic energies are in general different: One phonon is needed to supply the energy difference $\epsilon_i - \epsilon_j$ between the initial and final electronic states, and the second appears in the intermediate process.

Since P_{ij} includes a term odd in Φ , detailed balance is broken even at thermal equilibrium, $P_{ij} - P_{ji} \neq 0$, and is *odd* in Φ . E.g., in a triad of three sites, i, j , and ℓ , P_{ij} , (which includes also the indirect processes via ℓ), and $P_{i\ell}$, (also through j), are such that $P_{ij} + P_{i\ell} = P_{ji} + P_{\ell i}$, so that charge balance is maintained at i . However, since $P_{ij} \neq P_{ji}$, there will be a net current circulating around the triad, proportional to $P_{ij} - P_{ji}$, and therefore arising from the Holstein process. That current is additional to the persistent current flowing in this system in the absence of the coupling to the phonon source. In fact, [6] it is always flowing in the reverse direction to the one with no phonons! (The direction of the current is determined by delicate effects like the location of the Fermi level with respect to the site energies, etc.) It has been therefore termed ‘counter-current’, I_{cc} . The doubly-resonant processes can be analyzed also from the view-point of coherence. One of the two phonons is common to both interfering paths, thus retaining their coherence, [6, 10] while the other is absorbed and re-emitted by one of the paths, again retaining coherence with the second. Hence, although the mechanism involves real, energy-conserving, electron-phonon transitions, it still contributes in a non-trivial way to I_{pc} . It necessitates ‘real’ phonon modes, namely, non-zero temperatures, T . Thus, I_{cc} will initially *increase* with T , and then, because of the Debye-Waller factor, will decrease.

Taking the phonon source out of equilibrium at a certain frequency range may lead to enhancement in I_{pc} . On a speculative level, one may visualize shining the electrons with a high intensity beam of non-equilibrium phonons with a narrow frequency range around, say, ω_0 . I_{cc} , resulting from resonant transitions, will be significantly affected only when ω_0 is close to the differences $|\epsilon_i - \epsilon_j|$ or $|\epsilon_i - \epsilon_\ell|$. The effect on the Debye-Waller factor will be small for a narrow-band beam. In this way, I_{cc} will initially increase with the intensity of this radiation, until decoherence effects will take over and I_{pc} will disappear.

3 The persistent current in an ‘open’ ring

When the electronic system is ‘open’ the energy levels acquire a finite lifetime, and the the transitions no longer conserve the sum of electronic and radiation energies. Nonetheless, the radiation introduces again a unique effect, which goes beyond that of the Debye-Waller exponent. [11] Imagine an

Aharonov-Bohm ring, connected to two external electron reservoirs, kept at slightly different chemical potentials μ_ℓ and μ_r , (i.e., the system is in the *linear response regime*). On one of the ring's arms we place a 'site' denoted as 'quantum dot' at which the electrons are coupled to the radiation source. A second, 'reference' site is placed on the other arm of the ring. The current flowing into the ring splits into I_1 (in the upper arm) and I_2 (in the lower), and the *circulating* current is defined as $2I_{pc} = (I_1 - I_2)|_\Phi - (I_1 - I_2)|_{-\Phi}$, to avoid spurious currents caused by asymmetries.

When the electrons are free of any interactions except on the dot, I_{pc} is given in terms of the dot exact Green function, G_d , which includes all effects of the problem. One finds [11]

$$I_{pc} = \int \frac{d\omega}{i\pi} \frac{f_\ell(\omega) + f_r(\omega)}{2} \left[\frac{\partial \Sigma_{\text{ext}}^A}{\partial \Phi} G_d^A(\omega) - cc \right], \quad (2)$$

where $f_{\ell,r}$ is the electron distribution on the two reservoirs. The superscripts A (R) refer to the advanced (retarded) Green functions, and Σ_{ext} is the self-energy part of G_d that comes *solely* from the coupling of the dot to the electron reservoirs. Both Σ_{ext}^A and G_d^A are even in Φ , and hence I_{pc} is odd in Φ .

When the interactions are confined to the dot alone, Σ_{ext} can be obtained straightforwardly since it pertains to non-interacting electrons. It is useful to consider first the interaction-free case, in which $G_d^0(\omega) = (\omega - \epsilon_d - \Sigma_{\text{ext}}(\omega))^{-1}$, where ϵ_d is the dot energy level. By connecting to the electron reservoirs that level becomes a resonance, with a finite width (inverse life-time) given by $\Im \Sigma_{\text{ext}}$. In that case, [12]

$$I_{pc}^0 = \int \frac{2d\omega}{\pi} \frac{f_\ell(\omega) + f_r(\omega)}{2} \frac{\partial \delta^0(\omega)}{\partial \Phi}, \quad (3)$$

where δ^0 is the transmission phase of the dot, with $\tan \delta^0(\omega) = -\Im \Sigma_{\text{ext}}^R(\omega - \epsilon_d - \Re \Sigma_{\text{ext}}^R)^{-1}$. Hence, in a steady-state situation, I_{pc}^0 is related to the variation of δ^0 with Φ , replacing that of the eigenenergies at equilibrium.

However, this ceases to hold when G_d contains also the self-energy part due to interactions. Using an approximate solution [13] for G_d for an electron-phonon interaction linear in the boson coordinates, one finds [11] that to lowest-order in the electron-phonon coupling $|\alpha_{\mathbf{q}}|^2$, $I_{pc} = I_{pc}^0 + \Delta I_{pc}$, with

$$\begin{aligned} \Delta I_{pc} = & \int \frac{d\omega}{\pi} \frac{f_\ell(\omega) + f_r(\omega)}{2} \sum_{\mathbf{q}} \left[A_{\mathbf{q}}^- \frac{\partial}{\partial \Phi} \left(\delta^0(\omega + \omega_{\mathbf{q}}) - \delta^0(\omega - \omega_{\mathbf{q}}) \right) \right. \\ & \left. + A_{\mathbf{q}}^+ \frac{\partial}{\partial \Phi} \left(\delta^0(\omega + \omega_{\mathbf{q}}) + \delta^0(\omega - \omega_{\mathbf{q}}) - 2\delta^0(\omega) \right) \right], \quad (4) \end{aligned}$$

where $A_{\mathbf{q}}^+ = \frac{|\alpha_{\mathbf{q}}|^2}{\omega_{\mathbf{q}}^2} (1 + 2N_{\mathbf{q}})$, $A_{\mathbf{q}}^- = \frac{|\alpha_{\mathbf{q}}|^2}{\omega_{\mathbf{q}}^2} (2n_d - 1)$. Here n_d is the dot occupation and $N_{\mathbf{q}}$ is the boson occupation, not necessarily the thermal-equilibrium one. The acousto-induced current, ΔI_c , consists of a part which depends only

on n_d , and whose sign may change according to the relative location of ϵ_d with respect to the Fermi energy, and a part dominated by the phonon occupations via A_q^+ . [The term $-2\delta^0(\omega)$ there comes from the the Debye-Waller exponent.] By shining a beam of phonons of a specific frequency, the magnitude of that term can be controlled experimentally, as long as the temperature of the electrons and the intensity of the phonon source N_q are low enough to retain electronic coherence. Both the precise magnitude of these effects and their bounds depend on the detailed geometry of the dot and on the acoustic mismatch.

It is instructive to examine the transmission phase in a simple case. Characterizing the lower arm of the ring by its transmission (T_B) and reflection (R_B) coefficients, one has [11] $\Im\Sigma_{\text{ext}}^A = \Gamma_d^0[1 - T_B \cos^2(\Phi/2)]$ and $\Re\Sigma_{\text{ext}}^A = -\Gamma_d^0\sqrt{R_B T_B} \cos^2(\Phi/2)$, where Γ_d^0 is the width of the resonance level of the dot itself. This determines δ^0 : Unless at resonance itself, that phase, and consequently I_{pc} , scales with $\Gamma_d^0/|\epsilon_d|$. Moreover, ΔI_{pc} survives even at zero temperature. When the voltage drop on the ring vanishes, and ϵ_d is well below the Fermi level, i.e., $n_d = 1$, the square brackets of ΔI_{pc} contain $\delta^0(\omega + \omega_q) - \delta^0(\omega)$, reflecting processes which begin by the *emission* of bosons. This is quite different from the case of an isolated ring, where $\Gamma_d^0 = 0$, and only the resonances contribution remains, which vanishes at $T = 0$. Here the effect comes from a single, *virtual* phonon, and will disappear as $\Gamma_d^0/|\epsilon_d| \rightarrow 0$.

4 Conclusions

We have considered the effect of coupling the electrons to a boson source on their interference pattern in an Aharonov-Bohm ring, and in particular on the orbital magnetic response. Both in the isolated ring and the ‘open’ one, the naively-expected Debye-Waller exponent reduces the interference term (as well as the ‘classical’ term), and hence the persistent current, as T is raised. All boson modes contribute to that detrimental factor. In both cases, there is an additional contribution, arising from a bounded range of phonon energies which is dictated by the electronic energies. For an isolated ring, that contribution comes from boson modes whose frequencies satisfy the energy conservation required for the electronic transitions. In the open ring the electronic energies are broadened; a *single virtual* boson suffices to produce the new effect yielding a phonon-induced contribution to I_{pc} even at $T = 0$, which is lower in the electron-phonon coupling.

Because this novel contribution to I_{pc} comes from a limited range of boson frequencies, it is expected that by modulating the radiation intensity in that range, it will be possible to manipulate the magnitude of I_{pc} . This will require boson intensities low enough to retain coherence; However, since the unique effect arises from a rather narrow region of frequencies it is hoped that such an acousto-magnetic effect is feasible.

Acknowledgements. — We thank Y. Levinson and the late A. G. Aronov for helpful discussions. This project was carried out in a center of excellence supported by the Israel Science Foundation, and was partially supported by the German-Israeli Foundation (GIF) and by the German Federal Ministry of Education and Research (BMBF), within the framework of the German Israeli Project Cooperation (DIP).

References

1. L. Pauling, *J. Chem. Phys.* **4**, 673 (1936); F. London, *J. Phys. Radium* **8**, 397 (1937).
2. I. O. Kulik, *JETP Lett.* **11**, 275 (1970); M. Büttiker, Y. Imry, and R. Landauer, *Phys. Lett. A* **96**, 3365 (1985).
3. L. P. Lévy *et al.*, *Phys. Rev. Lett.* **64**, 2074 (1990); V. Chandrasekhar *et al.*, *ibid.* **67**, 3578 (1991); D. Mailly *et al.*, *ibid.* **70**, 2020 (1993); E. M. Q. Jariwala *et al.*, *ibid.* **86**, 1594 (2001); W. Rabaud *et al.*, *ibid.* **86**, 3124 (2001); R. Deblock *et al.*, *ibid.* **89**, 206803 (2002).
4. Y. Galperin and O. Entin-Wohlman, *Phys. Rev. B* **54**, 9346 (1996); V. E. Kravtsov and V. I. Yudson, *Phys. Rev. Lett.* **70**, 210 (1993); V. E. Kravtsov and B. L. Altshuler, *Phys. Rev. Lett.* **84**, 3394 (2000); O. L. Chalaev and V. E. Kravtsov, *Phys. Rev. Lett.* **89**, 176601 (2002); M. Moskalets and M. Büttiker, *Phys. Rev. B* **66**, 245321 (2002).
5. P. Mohanty, *Ann. Phys. (Leipzig)* **8**, 549 (1999); P. Schwab, *Eur. Phys. J.* **B18**, 189 (2000); P. Cedraschi, V. V. Ponomarenko and M. Büttiker, *Phys. Rev. Lett.* **84**, 346 (2000); P. Cedraschi and M. Büttiker, *Phys. Rev. B* **63**, 165312 (2001).
6. O. Entin-Wohlman, Y. Imry, A. G. Aronov, and Y. Levinson, *Phys. Rev. B* **51**, 11584 (1995).
7. S. A. Cavill *et al.*, *Phys. Rev. B* **66**, 235320 (2002).
8. T. Holstein, *Phys. Rev.* **124**, 1329 (1961).
9. A. Miller and E. Abrahams, *Phys. Rev.* **120**, 745 (1960).
10. A. Stern, Y. Aharonov, and Y. Imry, *Phys. Rev. A* **41**, 3436 (1990).
11. O. Entin-Wohlman, Y. Imry, and A. Aharony, *Phys. Rev. Lett.* **91**, 046802 (2003).
12. E. Akkermans, A. Auerbach, J. E. Avron, and B. Shapiro, *Phys. Rev. Lett.* **66**, 76 (1991).
13. L. I. Glazman and R. I. Shekhter, *Sov. Phys. JETP* **67**, 163 (1988).

Experimental Implementations of the Superconductor-Insulator Transition

V.F. Gantmakher

Institute of Solid State Physics RAS, Chernogolovka, Russia gantm@issp.ac.ru

Summary. Various experimental observations of the superconductor-insulator transition are described and compared with two theoretical models: one based on boson-vortex duality and the other where the superconducting fluctuations at low temperatures in the magnetic field are calculated. The latter shows that the superconducting fluctuations in dirty but homogeneous superconductor act as grains in a granular superconductor.

When superconductivity is destroyed by changing some of parameters, either intrinsic (carriers density, level of disorder) or extrinsic (magnetic field) ones, the material can turn not only into normal metal but into insulator as well. We'll discuss here magnetic-field-induced superconductor-insulator transitions (SIT). Magnetic field transfers the superconductor into insulator in the case when the carrier density in the material is low and the level of disorder is high, so that without the superconductivity the material would be in zero field on the insulating side of the metal-insulating transition. The main sign of SIT is the fan-like set of the resistance curves $R(T)$: they go down with decreasing of the temperature at fields below the critical, $B < B_c$, and go up at fields $B > B_c$.

The list of materials which displayed such type of behaviour contains amorphous $\text{Mo}_x\text{Ge}_{1-x}$ [1] and $\text{Mo}_x\text{Si}_{1-x}$ [2] films, amorphous InO_x films [3, 4], ultrathin films of Be [5], crystalline films of $\text{Nd}_{2-x}\text{Ce}_x\text{CuO}_{4+y}$ [6, 7]. Two typical examples of such sets of curves relevant to different limits are presented in Figs. 1 and 2. In $\text{Nd}_{2-x}\text{Ce}_x\text{CuO}_{4+y}$ (Fig. 1) the growth of the resistance with decreasing temperature on the non-superconducting side of the field-induced transition was below ten percent so that it reminded more a metal with quantum corrections to its conductivity than an insulator. In amorphous InO_x (Fig. 2), typical for insulator exponential temperature dependence of the resistance resulted in almost tenfold increase of the resistance.

All the above-listed experiments were interpreted as SIT in two-dimensional (2D) electron systems. This interpretation for those systems where the growth of the resistance was comparatively trifling was based on scaling hypothesis [8] which asserts that there is no non-superconducting metallic state at zero temperature in 2D. Hence any state of a film which does not display tendency to become superconducting, i.e. which has negative derivative $\partial R/\partial T < 0$, should be accepted as insulating.

The theoretical grounds for existence of 2D-SIT which was suggested in [9, 10] appealed to the boson-vortex duality model. It considered the superconducting phase as a condensate of Cooper pairs with localized vortices and the insulating phase as a condensate of vortices with localized Cooper pairs. The theory described only vicinity of the SIT and predicted existence of some critical region on the (T, B) -plane where the behavior of the system was

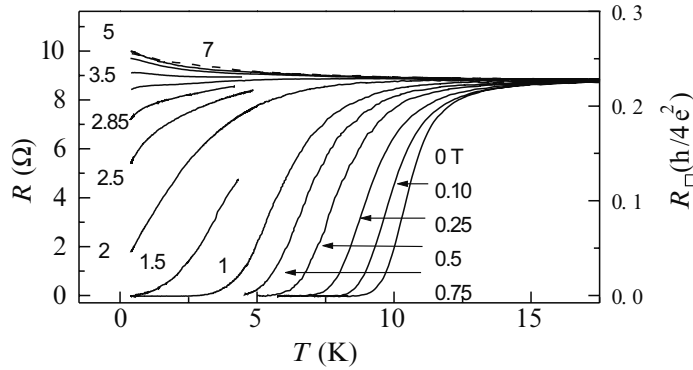


Fig. 1. Temperature dependence of the resistivity of $\text{Nd}_{2-x}\text{Ce}_x\text{CuO}_{4+y}$ films at different magnetic fields [7]. At high fields the resistivity changes lie in the range of 10%; two upper curves cross at low temperatures.

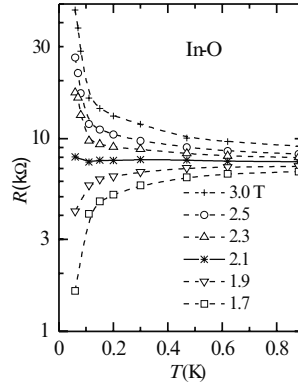


Fig. 2. Temperature dependence of the resistivity of amorphous InO_x films at different magnetic fields [4].

governed by competition of the quantum phase transition correlation length $\xi \propto (B - B_c)^{-\nu}$ and thermal length $L_T \propto T^{1/z}$ with z and ν being constants called the critical exponents. All relevant quantities in this region are supposed to be universal functions f of ratio of the lengths which can be written in the form of scaling variable $(B - B_c)/T^{1/z\nu}$. For the resistivity in two dimensions R_{\square} this dependence takes form [10]

$$R_{\square}(B, T) = R_c f[(B - B_c)/T^{1/z\nu}], \quad (1)$$

where the critical resistance R_c is a constant.

Experimenalists managed to confirm existence of this so called finite-size scaling practically in *all* cases when checking the existence of supposed SIT. Fig. 3 presents a typical example. The question is whether the possibility to depict the data by relation (1) is a cogent argument in favor of SIT.

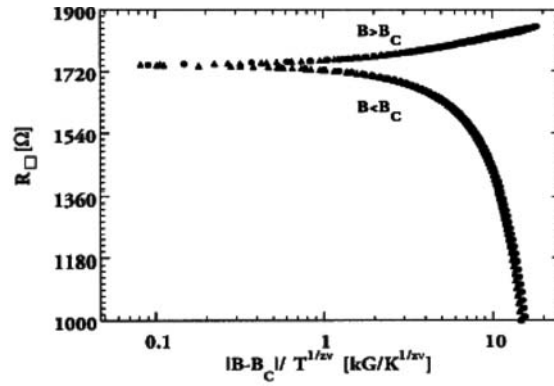


Fig. 3. Scaling of the function $R(T, B)$ for a sample $\text{Mo}_x\text{Ge}_{1-x}$ [1]; the changes in the upper branch lie within the range of 7%.

The insulating phase which appears as the result of such SIT is rather specific; it contains pair correlations between the localized electrons as the remnant of the superconducting pairing. Such insulator is called the Bose-insulator [11] and the correlated electrons are called localized electron pairs. Of course, existence of such phase should be confirmed experimentally.

In most cases, the fan-like shape of the set of $R(T, B = \text{const})$ curves is accompanied by the negative magnetoresistance in higher fields, on the insulating side of the SIT but far enough from the critical region (Figs. 4 and 5). This has a natural explanation. The pair correlations are done away with the strong magnetic field and this results in raising of the carrier mobility. Similar effect is well known for granular superconductors [12, 13]: when Josephson currents are absent by some reason so that the conductance is determined by one-particle tunneling between the grains then the superconductivity of the grains results in insulating behavior of the whole material. The magnetic field

destroys the superconducting gap in the grains and hence restores metallic properties of the material.

So, the localized pairs display themselves at the stage when they become decoupled and contribute to the conductance. The negative magnetoresistance serves as an indirect manifestation of the specific insulating state destroyed by the field. However, as the theory [9, 10] relates only to the vicinity of the SIT, the negative magnetoresistance happens beyond the range of its action.

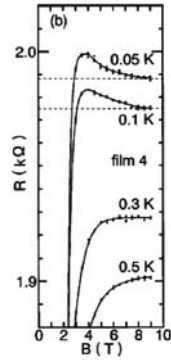


Fig. 4. Set of isotherms $R(T=\text{const}, B)$ of $\text{Mo}_x\text{Si}_{1-x}$ films [2].

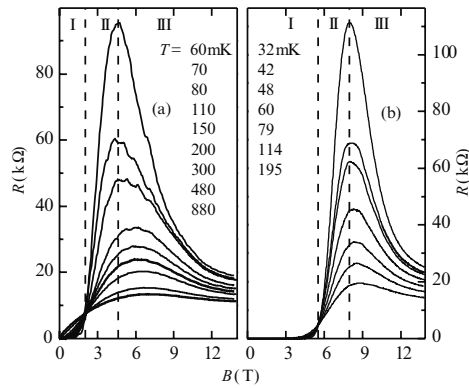


Fig. 5. Set of isotherms $R(T=\text{const}, B)$ of amorphous InO_x films [4]. (a) Magnetic field normal to the film; (b) magnetic field parallel to the film. In the fields region I the material remains superconducting, label III marks the region of negative magnetoresistance. The theory [9, 10] relates to the vicinity of the boundary between the regions I and II in the geometry (a).

Finally, the situation looks as follows. Experiments concentrate on three specific properties as signs of the SIT: fan-like temperature dependence; scaling relation (1); negative magnetoresistance. The latter is very important

indication of the pair localization but it does not follow from the theory [9, 10]. At the same time, the data which do not display explicitly the insulating behavior can be adjusted with this theory as well. Additional questions come from the observation in amorphous InO_x films [14] that all three crucial properties of the function $R(T, B)$ remain the same with magnetic field parallel to the film. This means that SIT is a kind of 3D-phenomenon in InO and should be explained without reference to the boson–vortex duality.

From here follow main goals in the SIT problem: to find theoretical models which would lead to the negative magnetoresistance; to trace how the specific SIT properties appear in the field-induced superconductor–normal metal transition while the normal metal is shifted toward the insulating state; to find out whether the low dimensions of the films is crucial or the SIT can happen in 3D materials; to find the explanation for the pair localization alternative to the boson–vortex duality. It seems that the first two goals are achieved.

The progress came from the recent paper by Galitski and Larkin [15]. They succeeded in extending calculations of the quantum corrections due to superconducting fluctuations for 2D superconductors to the low temperature $T \ll T_c(0)$ and high magnetic field $B \gtrsim B_{c2}(0)$. The corrections $\delta\sigma$ include Aslamazov–Larkin, Maki–Thompson and density-of-states (DOS) terms. In the dirty limit $\delta\sigma$ they can be written in explicit form by using digamma function $\psi(r)$

$$\delta\sigma = \frac{4e^2}{3\pi\hbar} \left[-\ln \frac{r}{b} - \frac{3}{2r} + \psi(r) + 4(r\psi'(r) - 1) \right], \quad (2)$$

where $r = (1/2\gamma')(b/t)$, $\gamma' = e^\gamma = 1.781$ is the exponential of Euler’s constant, and $t = T/T_{c0} \ll 1$ and $b = (B - B_{c2}(T))/B_{c2}(0) \ll 1$ are reduced temperature and magnetic field. The particular feature of this expression are the negative terms. They originate from the depression of DOS at the Fermi-level by fluctuative pairing of carriers. This becomes important if disorder and magnetic field make ineffective the transport by Cooper pairs and finally lead to the negative magnetoresistance.

Expression (2) can be compared with experiment. Fig. 6 presents such comparison made in [7]. One can see remarkable resemblance — there is separation between low-field curves which “bend down”, and high-field curves which “bend up”; there is also high field negative magnetoresistance at low temperature. Detailed analysis in [7] confirms that the fluctuations may explain all the main features of the transport in those materials where the effect is not too large and can be described in terms of the perturbation theory. In practice, almost all the materials except InO fall into this group. For them, superconducting fluctuations act as superconducting grains.

The theory [15] cannot be applied to InO directly. But just as the divergence of the weak localization quantum corrections point to the Anderson localization, quantum corrections here point to the SIT. This returns us to the problem of low dimensions. Fluctuations are larger in the systems with low dimensions, but the difference is only quantitative and we may expect SIT

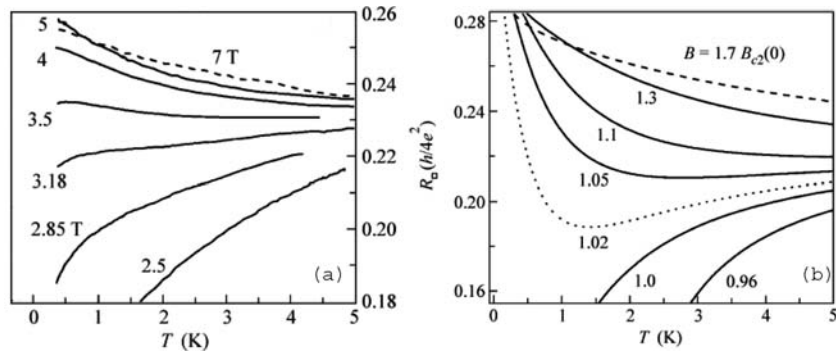


Fig. 6. Comparison from [7] of (a) the experimental set of curves for crystalline $\text{Nd}_{2-x}\text{Ce}_x\text{CuO}_{4+y}$ films and (b) the set calculated from the theory [15].

on the basis of fluctuations in 3D as well. These expectations are supported by the results of numerical simulations [16, 17]. According to [17], the attractive interaction leads to the insulating phase of localized pairs well within the metallic phase of single-particle 3D Anderson model.

The last comment is about the finite-size scaling equation (1) related to SIT. Certainly, expression (2) cannot be reduced to the form of equation (1) and no genuine scaling exists. However, in a restricted region of values of T and B representation of the theoretical curves in the form (1) can be done. This was demonstrated in [7]. This means that the scaling presentation cannot be the decisive argument in favor of a specific model.

Acknowledgements.— This work was supported by grant RFBR-02-02-16782 and by grants from Russian Ministry of Science.

References

1. A. Yazdani and A. Kapitulnik, Phys. Rev. Lett. **74**, 3037 (1995).
2. S. Okuma, T. Terashima, and N. Kokubo, Solid State Comm. **106**, 529 (1998).
3. A.F. Hebard and M.A. Paalanen, Phys. Rev. Lett. **65**, 927 (1990).
4. V.F. Gantmakher, M.V. Golubkov, V.T. Dolgoplov, G.E. Tszydynzhapov, and A.A. Shashkin. JETP Lett. **68**, 363 (1998).
5. E. Bielejec and W. Wu, Phys. Rev. Lett. **88**, 206802 (2002).
6. S. Tanda, S. Ohzeki, and T. Nakayama Phys. Rev. Lett. **69**, 533 (1992).
7. V.F. Gantmakher, S.N. Ermolov, G.E. Tszydynzhapov, A.A. Zhukov, and T.I. Baturina. JETP Letters **77**, 424 (2003).
8. E. Abrahams, P.W. Anderson, D.C. Licciardello, and T.V. Ramakrishnan, Phys. Rev. Lett. **42**, 673 (1979).
9. S.L. Sondhi, S.M. Girvin, J.P. Carini, and D. Shahar, Rev. Mod. Phys **69**, 315 (1997).
10. M.P.A. Fisher, Phys. Rev. Lett. **65**, 923 (1990).
11. M.A. Paalanen, A.F. Hebard, and R.R. Ruel, Phys. Rev. Lett. **69**, 1604 (1992).

12. V.F. Gantmakher, V.N. Zverev, V.M. Teplinskii, G.E. Tsydynhapov, and O.I. Barkalov, JETP **77**, 513 (1993).
13. I.S. Beloborodov and K.B. Efetov, Phys. Rev. B **82**, 3332 (1999).
14. V.F. Gantmakher, M.V. Golubkov, V.T. Dolgoplov, G.E. Tsydynzhapov, and A.A. Shashkin. JETP Lett. **71**, 473 (2000).
15. V.M. Galitski and A.I. Larkin, Phys. Rev. B **63**, 174506 (2001).
16. J. Lages and D.L. Shepelyansky, Phys. Rev. B **64**, 094502 (2001).
17. B. Srinivasan, G. Benenti, and D.L. Shepelyansky, Phys. Rev. B **66**, 172506 (2002).

Thermal Fluctuations in One-Dimensional Disordered Quantum Systems

Andreas Glatz

Materials Science Division, Argonne National Laboratory, Argonne, Illinois 60439, USA glatz@anl.gov

Summary. We study the low temperature phase diagram of one-dimensional weakly disordered quantum systems like charge or spin density waves and Luttinger liquids by a *full finite temperature* renormalization group (RG) calculation. In the classical region, for vanishing quantum fluctuations those results are supplemented by an *exact* solution of the model in the case of strong disorder, described by the ground state and the correlation function. Furthermore, by a mapping of the problem onto a *Burgers equation with noise*, in the case of weak disorder, we can derive an expression for the correlation length. At *zero* temperature we reproduce the (quantum) phase transition between a pinned (localized) and an unpinned (delocalized) phase for weak and strong quantum fluctuations, respectively, as found previously by Fukuyama [12] or Giamarchi and Schulz [16].

At *finite* temperatures the localization transition is suppressed: the random potential is wiped out by thermal fluctuations on length scales larger than the thermal de Broglie wave length of the phason excitations. The existence of a zero temperature transition is reflected in a rich cross-over phase diagram determined by the correlation functions. In particular we find four different scaling regions: a *classical disordered*, a *quantum disordered*, a *quantum critical*, and a *thermal* region. The results can be transferred directly to the discussion of the influence of disorder in superfluids. Finally we extend the RG calculation to the treatment of a commensurate lattice potential, which might lead to a new scenario for the unpinning (delocalization) transition at zero temperature.

1 Introduction

The collective behavior of condensed modulated structures like charge or spin density waves (CDWs/SDWs) [23, 22, 4], flux line lattices [2, 36] and Wigner crystals [4] in random environments has been the subject of detailed investigations since the early 1970s. These were motivated by the drastic influence

of disorder: without pinning CDWs would be ideal superconductors whereas type-II superconductors would show finite resistivity.

Here we study one-dimensional weakly disordered quantum systems like charge or spin density waves and Luttinger liquids at low temperatures. Disorder and quantum fluctuations in 1D CDWs at zero temperature have been considered previously (see, e.g., [12, 15, 16]) and an unpinning transition as a function of the interaction strength was found. Finite temperature effects were partially incorporated by truncating the renormalization group (RG) flow at the de Broglie wave length of the phason excitations [16]. However, for a complete study of the thermal to quantum crossover, quantum and thermal fluctuations have to be considered on an equal footing [6, 7], which is the main aim of this paper. Experimentally, quasi-1D behavior can be seen in real materials, e.g., in whiskers [5], hairlike single crystal fibers like NbSe₃, with a transverse extension smaller than the correlation length or in chain like crystals with weak interchain coupling. In the latter case there is a large crossover length scale up to which 1D behavior can be observed [23, 4]. The results obtained for the CDWs or SDWs have a large number of further applications on disordered quantum systems: they relate, e.g., to the localization transition of Luttinger liquids [12, 16], superfluids [3, 11, 37], tunnel junction chains [28], Josephson coupled chains of these systems, if the coupling is treated in mean-field theory [12], and CDWs in a lattice potential.

This paper is organized as follows: In section 2 we give a detailed introduction to our model and the used notation. We also briefly discuss the influence of Coulomb interaction on the properties of the system. In section 3 the influence of disorder is studied in detail. Using an anisotropic momentum shell renormalization group calculation, in which the full Matsubara sum over frequencies is performed, we obtain flow equations for the effective strength of the disorder, thermal and quantum fluctuations (i.e., the interaction strength in the case of Luttinger liquids). These are discussed first in the case of zero temperature and are in agreement with previously obtained results [12, 16]. At finite temperatures the disorder is always renormalized to zero. In the classical limit two more methods are applied: (i) at low temperatures and strong disorder the ground state of the model is calculated exactly. (ii) For weak disorder and strong thermal fluctuations a second RG calculation is applied which is based on the mapping onto a Burgers equation with noise. The main result of this paper is the calculation of the low temperature quantum crossover diagram for one-dimensional CDWs. Using all these findings, the complete phase diagram, including the crossover regions, of the system is studied in section 4 with help of the density-density correlation function.

The influence of a commensurate lattice potential on a free density wave is considered in section 5. The full finite temperature renormalization group flow equation for this sine-Gordon type model are derived and resulting phase diagram is discussed. Furthermore a qualitative picture of the combined effect of disorder and a commensurate lattice potential at zero temperature is presented in section 6, including the phase diagram.

2 Model

2.1 Charge and spin density

In this section we derive the effective Hamiltonian which will be the starting point for our further treatment. The strategy of the calculation is therefore separated into two steps. In the first step the system is treated in a mean-field-(MF) type approximation applied to a microscopic Hamiltonian. This leaves us with a slowly varying complex order parameter field for which we derive an effective Hamiltonian. The second step involves the consideration of the fluctuations of this order parameter.

Now we briefly summarize the result of the mean-field calculation. For a detailed review we refer to the book [23]: Well below the mean-field condensation temperature T_c^{MF} of the CDW, the underlying lattice will be periodically distorted with a period λ which is related to the Fermi wave vector k_F by $\lambda = \pi/k_F$. This distortion of the lattice leads to the formation of a gap in the dispersion relation at $k = \pm k_F$ which is (in one dimension) proportional to the amplitude of the lattice modulation. For small displacements (which are typically smaller than 1% of the interatomic spacing [42]), the increase of the elastic energy is smaller than the gain of electronic energy due to the formation of the gap and hence an instability is favored. The period of the CDW depends on the band filling factor (via $k_F = \pi/\lambda$) and is in general at arbitrary band filling incommensurate with the undistorted lattice (with lattice constant a).

In (quasi-)one-dimensional systems [22] also SDWs can be found, but in contrast to CDWs they arise due to electron-electron and not to electron-phonon interaction. A SDW can be considered to consist of two CDWs, one for spin-up and another for spin-down electrons (see, e.g., Fig. 5 in [22]). Therefore the spatial modulation of SDWs is characterized by a wave vector $Q = 2k_F$, as for CDWs.

The charge or spin density $\rho(x, t)$ can be written in the form [22, 9, 45]

$$\rho(x, t) = (1 + Q^{-1}\partial_x\varphi(x, t))[\rho_0 + \rho_1 \cos(p\varphi(x, t) + pQx)] \quad (1)$$

where $\rho_0 = Qf(T)/\pi$ and $\rho_1 = 2|\Delta|/(\pi g v_F)$. g is the dimensionless electron-phonon coupling constant and v_F the Fermi velocity. ρ_1 is proportional to $|\Delta|$, the CDW gap or the amplitude of the complex (mean field) order parameter

$$\Delta(x, t) = |\Delta(x, t)|e^{i\varphi(x, t)}. \quad (2)$$

f is the condensate density ($Y = 1 - f$ is the so-called *Yoshida function*) related to $|\Delta|$ by [9, 45]

$$f(T) = \frac{\pi T}{\hbar} \sum_{\omega_n} \frac{(|\Delta|/\hbar)^2}{(\omega_n^2 + (|\Delta|/\hbar)^2)^{3/2}}, \quad \omega_n = 2\pi nT/\hbar. \quad (3)$$

From this expression one finds that $f(T)$ approaches 1 for $T \rightarrow 0$ (by integration) and $f(T) \simeq 2(1 - T/T_c^{MF}) \sim |\Delta|^2$ for $T \rightarrow T_c^{MF}$. T_c^{MF} denotes the mean-field transition temperature. For quasi one-dimensional systems ρ_1 has an additional factor ζ^{-2} (the inverse area perpendicular to the chain).

Note, that (1) is correct for arbitrary band filling and, to be more precisely, is the particle density of the charge or spin carrying particles. Since $4k_F$ modulations of SDWs or CDWs are also possible [43], we introduce the factor p in the argument of the modulating cosine function, i.e., for CDWs and SDWs p is usually 1, but can also be 2 or greater.

In (1) we omitted higher harmonics proportional to $\cos(np(\varphi(x, t) + Qx))$ with $n \in \{2, 3, \dots\}$, since these more strongly oscillating terms give close to the zero temperature transition only small contributions in the renormalization process, compared to the leading $n = 1$ contribution. They will therefore be neglected throughout this paper. Note, that p is the integer describing the ground 'oscillation'. The particle current density j follows from (2) as $j = -\rho_0 \dot{\varphi}/Q$.

2.2 Hamiltonian

In the following we use a minimal model for the low energy, long wave length excitations of the condensed charge density wave. Since fluctuations in the amplitude $|\Delta|$ are suppressed, because they are massive, we take only fluctuations of the phase φ (cf. eq. 2) into account. Clearly, such an approach breaks down sufficiently close to the mean-field transition temperature T_c^{MF} . Neglecting fluctuations in $|\Delta|$, the Hamiltonian for our model is given by

$$\hat{\mathcal{H}} = \hat{\mathcal{H}}_0 + \hat{\mathcal{H}}_u + \hat{\mathcal{H}}_w \quad (4)$$

with

$$\hat{\mathcal{H}}_0 \equiv \int_0^L dx \frac{c}{2} \left[\left(\frac{v}{c} \right)^2 \hat{P}^2 + (\partial_x \hat{\varphi})^2 \right], \quad (4a)$$

$$\hat{\mathcal{H}}_u \equiv \int_0^L dx U(x) \rho(x), \quad U(x) = \sum_{i=1}^{N_{imp}} U_i \delta(x - x_i), \quad (4b)$$

$$\hat{\mathcal{H}}_w \equiv - \int_0^L dx W \cos(q\hat{\varphi}(x)), \quad (4c)$$

$\hat{\mathcal{H}}_0$ describes the phason excitations of the CDW, where $c = \frac{\hbar v_F}{2\pi} f(T)$ denotes the elastic constant. $v = v_F / \sqrt{1 + (2|\Delta|/\hbar\omega_{pQ})^2/(gf)}$ is the effective velocity of the phason excitations with ω_{pQ} the phonon frequency. For CDWs $(2|\Delta|/\hbar\omega_{pQ})^2/(gf) \gg 1$ is typically fulfilled and hence quantum fluctuations are weak.

\hat{P} is the momentum operator, corresponding to the phase $\hat{\varphi}$, with the standard commutation relation $[\hat{P}(x), \hat{\varphi}(x')] = \frac{\hbar}{i} \delta(x - x')$

$\hat{\mathcal{H}}_u$ results from the effects of impurities with random potential strength U_i and positions x_i . The potential strength is characterized by $\overline{U_i} = 0$ and $\overline{U_i U_j} \equiv U_{imp}^2 \delta_{i,j}$, and includes a forward and a backward scattering term proportional to ρ_0 and ρ_1 , respectively. The disorder average of the impurity potential $U(x)$ follows then to be given by $\overline{U(x)} = 0$ and

$$\overline{U(x)U(y)} = \frac{U_{imp}^2}{l_{imp}} \delta(x - y). \quad (5)$$

We will further assume, that the mean impurity distance $l_{imp} = L/N_{imp}$ is large compared with the wave length of the CDW and, in most parts of the paper, that the disorder is weak, i.e.,

$$1 \ll l_{imp}Q \ll cQ/(U_{imp}\rho_1). \quad (6)$$

In this case the Fukuyama–Lee length [13]

$$L_{FL} = \left(\frac{c\sqrt{l_{imp}}}{U_{imp}\rho_1 p^2} \right)^{2/3} \quad (7)$$

is large compared to the mean impurity distance l_{imp} .

The last term in (4), \mathcal{H}_w , includes the influence of a harmonic lattice potential. This term will be discussed section 5 in greater detail.

Our model (4) includes the four dimensionless parameters

$$t = T/\pi\Lambda c, \quad (8a)$$

$$K = \hbar v/\pi c, \quad (8b)$$

$$u^2 = \frac{(U_{imp}\rho_1)^2}{\Lambda^3 \pi c^2 l_{imp}}, \quad (8c)$$

$$w = W/\pi c \Lambda^2, \quad (8d)$$

which measure the strength of the thermal (t), quantum (K) and disorder fluctuations (u), and the periodic potential (w), respectively. $\Lambda = \pi/a$ is a momentum cut-off. Note, that for non interacting electrons, i.e., $v = v_F$, K takes the value 2 (and not 1 as in the usual Luttinger liquid notation). The classical region of the model is given by $K \ll t$ which can be rewritten as the condition, that the thermal de Broglie wave length of the phason excitations is small compared to a .

$$\lambda_T = \hbar\beta v = K/(t\Lambda) \quad (9)$$

At $T = 0$, K -values of the order 10^{-2} to 10^{-1} and 1, have been discussed for CDWs and SDWs, respectively [23, 32]. It has to be noted however, that the the expressions relating c and v to the microscopic (mean-field-like) theory lead to the conclusion that K and t diverge by approaching T_c^{MF} , whereas the ratio K/t remains finite.

2.3 Coulomb Interaction

We could also add a *Coulomb interaction* term to our model (4) which can be written as

$$\hat{\mathcal{H}}_c = \frac{1}{2} \int dx \int dx' \hat{\rho}(x) V_c(x-x') \hat{\rho}(x'), \quad (10)$$

where V_c is the Coulomb potential. In all dimensions the unscreened potential has the form e^2/r , in the sense that we are dealing with quasi-one-dimensional systems embedded in a 3D space. If we assume, that the quasi one-dimensional system has the finite width ζ , V_c can be written as [34, 40]

$$V_c^0(x) = \frac{e^2}{\sqrt{x^2 + \zeta^2}} = \frac{1}{L} \sum_k e^{ikx} V_c^0(k) \quad \text{with} \quad (11)$$

$$V_c^0(k) = 2e^2 K_0(|\zeta k|), \quad (12)$$

where K_0 is a modified Bessel function of second kind with $K_0(x) \approx -\ln(x)$ for $x \ll 1$.

In general the Coulomb potential is screened and can be written as [1]

$$V_c(k, \omega) = \frac{V_c^0(k)}{1 + V_c^0(k) \Pi(k, \omega)}, \quad (13)$$

with the momentum and frequency dependent polarization operator, defined by $\Pi(k, \omega) = \langle \rho(0, 0) \rho(k, \omega) \rangle$.

If we only consider the static case $\omega = 0$ we can distinguish two limiting cases: First, if the typical range λ_{eff} of the screened Coulomb potential V_c is much smaller than the mean electron distance, the potential can be assumed to be a delta distribution and \mathcal{H}_c can be approximated by

$$\hat{\mathcal{H}}_c \approx \frac{\hbar\chi}{2} \int dx \left(\frac{f(T)}{\pi} \partial_x \varphi(x) \right)^2 + \dots, \quad (14)$$

with $\chi = \frac{1}{\hbar} \int dx V_c(x)$. The cos-terms (...) from the density can be neglected due to strong fluctuations. Therefore the Coulomb interaction gives only an additional contribution to the elastic constant of the initial model: $c = \frac{\hbar v_F}{2\pi} f + \frac{\hbar\chi}{\pi^2}$. For $\chi > 0$ the Coulomb interaction is repulsive, which leads to an increase of c and therefore a decrease of the dimensionless parameter K , i.e., the quantum fluctuations will be reduced by repulsive Coulomb interaction. In the case $\chi < 0$ (attraction), K will be increased. Keeping this consideration in mind, we will not further include $\hat{\mathcal{H}}_c$ in the model explicitly.

In the other case – with weak screening – $V_c(k) \approx V_c^0(k)$ shows the dispersion given in (12) and in general, the details of the k -dependence are not only up to the transverse extension ζ of the quasi one-dimensional system under consideration but also to the screening length [3, 11, 46, 34].

However, the logarithmic k -dependence will only weakly affect our RG-analysis, but may suppress phase transitions, as discussed later in section 3.2.

Coulomb interaction is also important if one considers multi-channel systems [30, 18] or the effect of the non-condensated normal electrons.

3 Renormalization group treatment of disorder

3.1 Flow equations

In order to determine the phase diagram we adopt a standard Wilson-type renormalization group calculation, which starts from a path integral formulation of the partition function corresponding to the Hamiltonian (4). We begin with the renormalization of the disorder term and set $w = 0$ in the following. The system is transformed into a translational invariant problem using the replica method, in which the disorder averaged free energy is calculated, using

$$\overline{\mathcal{F}} = -T \overline{\ln \text{Tr} e^{-\mathcal{S}/\hbar}} \equiv -T \lim_{n \rightarrow 0} \frac{1}{n} \left(\text{Tr} e^{-\mathcal{S}^{(n)}/\hbar} - 1 \right), \quad (15)$$

which defines the replicated action $\mathcal{S}^{(n)}$. $\mathcal{S}^{(n)}$ is given by

$$\mathcal{S}^{(n)} = \sum_{\alpha, \nu} \int_{\tau} \left\{ \mathcal{L}_{0, \alpha} \delta_{\alpha \nu} + \frac{1}{2\hbar} \int_{\tau'} \overline{\mathcal{H}_u[\varphi_{\alpha}(\tau)] \mathcal{H}_u[\varphi_{\nu}(\tau')] } \right\}, \quad (16)$$

where \mathcal{L}_0 is the Lagrangian corresponding to $\hat{\mathcal{H}}_0$, $\int_{\tau} \equiv \int_0^{\hbar\beta} d\tau$ and α, ν are replica indices. Using (5) and consequently neglecting higher harmonics ($2pQ$ -modes) one finds

$$\overline{\mathcal{H}_u[\varphi_{\alpha}(\tau)] \mathcal{H}_u[\varphi_{\nu}(\tau')]} = \frac{U_{imp}^2 \rho_1^2}{2l_{imp}} \int_0^L dx \left\{ \cos p \left(\varphi_{\alpha}(x, \tau) - \varphi_{\nu}(x, \tau') \right) + \frac{2\rho_0^2}{Q^2 \rho_1^2} \partial_x \varphi_{\alpha}(x, \tau) \partial_x \varphi_{\nu}(x, \tau') \right\}. \quad (17)$$

Together with (16) one obtains the following form

$$\begin{aligned} \frac{\mathcal{S}^{(n)}}{\hbar} &= \frac{1}{2\pi K} \sum_{\alpha, \nu} \int_0^{L\Lambda} dx \int_0^{K/t} d\tau \left\{ \left[(\partial_x \varphi_{\alpha})^2 + (\partial_{\tau} \varphi_{\alpha})^2 \right] \delta_{\alpha \nu} - \right. \\ &\left. \frac{1}{2K} \int_0^{K/t} d\tau' \left[u^2 \cos p \left(\varphi_{\alpha}(x, \tau) - \varphi_{\nu}(x, \tau') \right) + \sigma \partial_x \varphi_{\alpha}(x, \tau) \partial_x \varphi_{\nu}(x, \tau') \right] \right\}, \end{aligned} \quad (18)$$

with $\sigma = 2u^2(\rho_0\Lambda/\rho_1Q)^2$.

Note, that we introduced dimensionless spatial and imaginary time variables,

$$\begin{aligned} \Lambda x &\rightarrow x, \\ \Lambda v \tau &\rightarrow \tau, \end{aligned}$$

which will be used throughout the paper - beginning here. Furthermore all lengths (e.g. correlation lengths, λ_T , L_{FL} , l_{imp} , and L), wave vectors (e.g. k , k_F , and Q) and Matsubara frequencies are dimensionless accordingly, from now on. Additionally we rescale the elastic constant for convenience to avoid the appearance of Λ .

$$\Lambda c \rightarrow c,$$

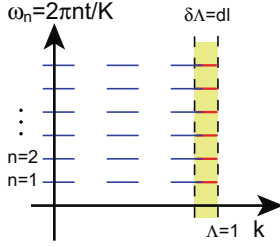


Fig. 1. Momentum “shell” in the space of (discrete) Matsubara frequencies (ω_n) and momenta (k). Only modes of the phase φ in the stripe $1/b \leq |k| \leq 1$ with $b = 1 + 0^+$ are integrate in one RG step.

Integrating over the high momentum modes of $\varphi(x, \tau)$ in a momentum shell of infinitesimal width $1/b \leq |k| \leq 1$ with the rescaling parameter $b = 1 + 0^+$, but arbitrary frequencies (see Fig. 1) and rescaling $x \rightarrow x' = x/b$, $\tau \rightarrow \tau' = \tau/b$, we obtain the following renormalization group flow equations (up to one loop):

$$\frac{dt}{dl} = t, \quad (19a)$$

$$\frac{dK}{dl} = -\frac{1}{2}p^4 u^2 K B_0 \left(p^2 K, \frac{K}{2t} \right) \coth \frac{K}{2t}, \quad (19b)$$

$$\frac{du^2}{dl} = \left[3 - \frac{p^2 K}{2} \coth \frac{K}{2t} \right] u^2, \quad (19c)$$

$$\frac{d\sigma}{dl} = \sigma, \quad (19d)$$

where $dl = \ln b$. For some more details on the RG calculation we relegate to [21, 20] where we have written the RG-flow also for dimensions $|d - 1| \ll 1$. The complete calculations can be found in [19]. Note, that the renormalization group equation for terms in the replica Hamiltonian which follow from higher order harmonics in the charge density look similar to those presented in (19c) with p replaced by np , $n > 1$, integer. Therefore these terms are negligible close to the quantum phase transition considered below. One should keep in mind though, that in the region where $K \ll 1$ at zero temperature, also those higher harmonics become relevant. But since this is also the parameter range where we leave the weak pinning regime, the RG breaks down anyways.

For legibility we have introduced the following functions:

$$B_i(\nu, y) = \int_0^y d\tau \int_0^\infty dx \frac{g_i(\tau, x) \cosh(y - \tau)}{\mathcal{T}(\tau, x) \cosh y}, \quad (20)$$

$$\mathcal{T}(\tau, x) = \left[1 + \left(\frac{y}{\pi} \right)^2 \left(\cosh \frac{\pi x}{y} - \cos \frac{\pi \tau}{y} \right) \right]^{\nu/4}, \quad (21)$$

with

$$g_0(\tau, x) = \delta(x) \tau^2.$$

Note, that $B_0(p^2 K, \frac{K}{2t}) \rightarrow 0$ for $K \rightarrow 0$ (see Fig. in appendix E1 of [20]).

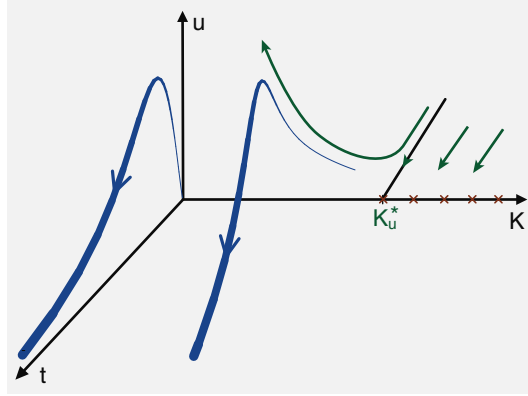


Fig. 2. Typical flow diagram for $w = 0$ in the three dimensional parameter space of K , u and t , proportional to the strength of quantum, disorder and thermal fluctuations, respectively.

The strength of the thermal fluctuations t is only rescaled, since there is no non-trivial renormalization of t (i.e., of the elastic constant c) because of a statistical tilt symmetry [39]. Note, that (18) is written in rescaled dimensionless parameters and the different renormalization of the kinetic and elastic term is reflected in the different renormalization of v and c , i.e., K and t , respectively.

From the flow equation for u^2 (19c) one directly sees that, depending on the sign of the prefactor, the behavior changes from increase for small t and K to decrease for high K or t .

There is no first order RG correction to σ and the change of σ with length scale is simply given by rescaling, see (19d). The two-loop contribution to σ is much more involved than the one-loop contributions for the other flow equations and gives no qualitatively different result for the flow of σ . As seen from (19d), the forward scattering amplitude always increases as $\sigma_0 e^l$ on larger length scales and is therefore not well controlled in the RG sense. But, since

the flow of σ does not feed back into the other flow equations it has only minor relevance for our considerations. And indeed, we can get rid of the forward scattering term $f/\pi U(x) \frac{\partial \varphi}{\partial x}$ by introducing the field $\hat{\varphi}_b(x)$ by [39]

$$\hat{\varphi}(x) = \hat{\varphi}_b(x) - \varphi_f(x), \quad \varphi_f(x) = \int_0^x dy c(y), \quad (22)$$

where $c(x) \equiv \frac{U(x)f}{\pi c\Lambda}$, with $\overline{c(x)} = 0$ and $\overline{c(x)c(x')} = \frac{\pi}{2} \sigma \delta(x-x')$. This can easily be verified by inserting this decomposition of $\hat{\varphi}(x)$ into the initial Hamiltonian (4) written in dimensionless units, and using (5) and the definition of σ for deriving the averages of $c(x)$. Note, that x is dimensionless. The typical flow described by the flow equations (19a) to (19c) is shown in Fig. 2, obtained by a numerical solution.

symbol here	Giamarchi and Schulz	Haldane
φ, \hat{j}	$\sqrt{2}\phi, \sqrt{2}/\pi \partial_\tau \phi$	$\theta - \pi \rho_0 x, \pi^{-1} \dot{\theta}$
\hat{P}	$\hbar \Pi / \sqrt{2}$	$-\frac{\hbar}{\pi} \nabla \varphi$
K	$2K_\rho$	$\sqrt{v_j/v_N}$
v	u_ρ	$\sqrt{v_j v_N}$
c	$\frac{\hbar u_\rho}{2\pi K_\rho}$	$\hbar v_N / \pi$
p	1	2

Table 1. Notation guide. Symbols used in this paper compared to the notation in Ref. [16] by Giamarchi and Schulz (charge operators) and Ref. [24] by Haldane.

3.2 Zero temperature - a review

The special case $t = 0$ was previously considered, e.g., in [16, 15] (for a better comparison see the *notation guide* listed in table 1).

The flow equations for K and u at zero temperature read:

$$\frac{dK}{dl} = -\frac{1}{2} p^4 u^2 K B_0(p^2 K, \infty), \quad (23a)$$

$$\frac{du^2}{dl} = \left[3 - \frac{p^2 K}{2} \right] u^2, \quad (23b)$$

with

$$B_0(\nu, \infty) = \int_0^\infty d\tau \tau^2 e^{-\tau} [1 + \tau^2/2]^{-\nu/4}. \quad (24)$$

The corresponding flow equation for K obtained in [16] deviates slightly from (23a), which can be traced back to the different RG procedures. In [16] the authors performed the RG at strictly zero temperature and used a symmetric, circular shape of the “momentum-shell”, i.e., treated the model as, effectively, isotropic in the 1+1-dimensional space-time.

This procedure may be a good approximation at zero temperature, but if one considers finite temperatures this does not hold anymore, since the extension in τ -direction is now finite. As a result, there is a region $\pi/L < |k| < \pi/\lambda_T$ where fluctuations are mainly one-dimensional and purely thermal. This region was disregarded in previous treatments. As we will see, fluctuations from this region have an important influence on the overall phase diagram.

The critical behavior is, however, the same: there is a Kosterlitz-Thouless (KT) transition at the phase boundary K_u between a disorder dominated, pinned and a free, unpinned phase which terminates in the fixed point $K_u^* = 6/p^2$. One can derive an implicit equation for K_u by combining (23a) and (23b) to a differential equation

$$\frac{du^2}{dK} = \frac{1}{p^2\eta K}(K - K_u^*), \quad (25)$$

which has the solution

$$u^2(K) - u_0^2 = \frac{K_u^*}{p^2\eta} \left(\frac{K - K_0}{K_u^*} - \ln \frac{K}{K_0} \right), \quad (26)$$

where u_0 and K_0 denote the bare values of the disorder and quantum fluctuation, respectively, and $\eta \equiv B_0(p^2 K_u^*, \infty)$. Then, K_u is implicitly given by

$$u^2(K_u) = \frac{K_u^*}{p^2\eta} \left(\frac{K_u - K_u^*}{K_u^*} - \ln \frac{K_u}{K_u^*} \right), \quad (27)$$

where the initial condition $u^2(K_0 = K_u^*) = u_0^2 = 0$ is used. The KT-flow equations at K_u^* can be recovered by defining

$$2\gamma \equiv \frac{p^2 K}{2} - 3,$$

$$2\chi^2 \equiv \frac{3}{2} p^4 \eta u^2$$

with $|\gamma| \ll 1$. This yields

$$\frac{d\gamma}{dl} = -\chi^2, \quad (28a)$$

$$\frac{d\chi^2}{dl} = -2\gamma\chi^2, \quad (28b)$$

which are exactly the flow equations obtained by Kosterlitz and Thouless [29].

Under the assumption, that a small deviation from the dimension $d = 1$ changes only the naive scaling dimensions of the fields, our results can be extended also to $d = 1 + \epsilon$ dimensions (For details see appendix [20]). The zero temperature phase diagram is modified and illustrated in Fig. 3. For $\epsilon < 0$ the fixed point at $(K = K_u^*, u = 0)$ is shifted to positive u -values (see left inset of Fig. 3), whereas for $\epsilon > 0$, K and u always flow to the

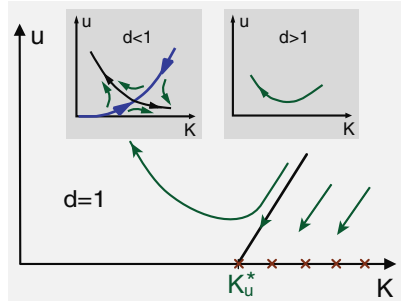


Fig. 3. Schematic zero temperature phase diagram in $d = 1$ and close to $d = 1$ dimensions (see text). u and K denote the strength of the disorder and quantum fluctuations, respectively.

strong pinning fixed point (at $K = 0$ and $u \rightarrow \infty$; right inset), i.e., quantum fluctuations are too weak to renormalize the random potential to zero. The zero temperature transition disappears therefore for $d > 1$, since the fixed point lies in the unphysical $u < 0$ region of the K - u parameter space. In general this discussion applies to the localization transition as well as to the Mott transition (see discussion of the the lattice potential in section 5). Note, that the flow for $d \neq 1$ is qualitatively different from that discussed in Ref. [25], because the model for superfluids in this paper [eq. (7) therein] is dual to our model. Since this mapping can only be done in strictly one dimension, one has to go back to the initial Hamiltonian for superfluids [24] to obtain the rescaling in $d = 1 + \epsilon$.

If one includes the effect of *Coulomb interaction* in $d = 1$ dimension, phase fluctuations of the free phase field increase only as ($T = 0$)

$$\langle (\varphi(x, 0) - \varphi(0, 0))^2 \rangle \sim K \ln^{1/2} |x|. \quad (29)$$

As a result, phase fluctuations are too weak to suppress the disorder even for large values of K and the system is always in the pinned phase. The phase diagram is therefore similar to that in $d > 1$ dimensions.

In the pinned phase the parameters K and u flow into the classical, strong disorder region: $K \rightarrow 0, u \rightarrow \infty$.

Integration of the flow equations gives for small initial disorder and $K \ll K_u^*$ an effective correlation or localization length at which u becomes of the order unity. This can be extracted from (23b), neglecting the flow of K .

$$\xi_u \approx L_{FL}^{(1-K/K_u^*)^{-1}}, \quad (30)$$

A better approximation of ξ_u , which takes also the flow of K into account, can be obtained by replacing u^2 in the flow equation for K (23a) by the expression given in (26). We still use the approximation, that K deviates not

much from the bare value K_0 which is the case, as long as $u_0^2 l \ll 1$. Then, the solution for $K(l)$ is given by

$$K(l) \approx K_0 \left(1 - \frac{p^4}{2} u_0^2 \eta l \right), \quad (31)$$

which yields a solution of (23b):

$$\ln \frac{u^2(l)}{u_0^2} \approx \left(3 - \frac{p^2}{2} K_0 \right) l + \frac{p^6}{8} \eta K_0 u_0^2 l^2. \quad (32)$$

With $u^2(\ln(\xi_u)) \approx 1$, the correlation length ξ_u is defined by

$$0 = \ln u_0^2 + \underbrace{\left(3 - \frac{p^2}{2} K_0 \right)}_{\equiv a} \ln(\xi_u) + \underbrace{\frac{p^6}{8} \eta K_0 u_0^2 (\ln(\xi_u))^2}_{\equiv b}, \quad (33)$$

which yields

$$\begin{aligned} \ln(\xi_u) &= \frac{\sqrt{a^2 - 4b \ln u_0^2} - a}{2b} \\ &\approx -\frac{\ln u_0^2}{3 - \frac{p^2 K_0}{2}} - \frac{p^6}{8} \eta K_0 u_0^2 \frac{(\ln u_0^2)^2}{\left(3 - \frac{p^2 K_0}{2} \right)^3}, \end{aligned} \quad (34)$$

where the first term of the right-hand side gives the result (30).

Close to the transition line, ξ_u shows KT behavior. For $K \geq K_u$, ξ_u diverges and $C(x, \tau) \sim K(l = \ln|z|) \ln|z|$ where $|z| = \sqrt{x^2 + \tau^2}$ (cf. section 4).

3.3 Strong pinning limit: Exact ground state

For large values of u our flow equations break down. Qualitatively the flow is towards large u and small K . We can, however, find the *asymptotic* behavior in this phase by solving the initial model in the *strong pinning limit exactly*. To find this solution we will assume strong pinning centers and weak thermal fluctuations:

$$U_{imp} \rightarrow \infty \quad \text{and} \quad c/(p^2 l_{imp}) \gg T. \quad (35)$$

To treat this case, we go back to the initial Hamiltonian (4) (with $W \equiv 0$ and the kinetic term also vanishes because of $K \rightarrow 0$). For strong disorder it is convenient to integrate out the phase field $\varphi(x)$ at all points which are not affected by the impurities. Then the effective Hamiltonian takes the form [10]

$$\mathcal{H}_{eff} = \sum_{i=1}^N \left\{ \frac{c}{2} \frac{(\varphi_{i+1} - \varphi_i)^2}{x_{i+1} - x_i} + U_i \rho(x_i) \right\}, \quad \varphi_i \equiv \varphi(x_i). \quad (36)$$

Under condition (35), φ_i only takes values obeying

$$p(\varphi_i + Qx_i) = 2\pi n_i + \pi \text{ with } n_i \in \mathbb{Z} \text{ integer} \quad (37)$$

which minimizes the backward scattering term. Defining h_i and ϵ_i by

$$n_{i+1} - n_i \equiv h_i + \left\lceil \frac{pQl_{imp}}{2\pi} \right\rceil, \quad x_{i+1} - x_i \equiv l_{imp} + \epsilon_i \quad (38)$$

with $0 \leq x_1 \leq x_2 \leq \dots \leq x_{N+1} \leq L$, the effective Hamiltonian can be rewritten as

$$\mathcal{H}_{eff} = \frac{c}{2p^2} \sum_i \frac{(2\pi)^2 \left(h_i - \frac{pQ\epsilon_i}{2\pi} - \gamma \right)^2}{l_{imp} + \epsilon_i}. \quad (39)$$

Here $[x]$ denotes the closest integer to x (*Gaussian brackets*):

$$[x] = m \text{ for } x \in \left[m - \frac{1}{2}, m + \frac{1}{2} \right], m \in \mathbb{Z} \quad (40)$$

and

$$\gamma \equiv \frac{pQl_{imp}}{2\pi} - \left\lceil \frac{pQl_{imp}}{2\pi} \right\rceil, \quad (41)$$

such that $|\gamma| \leq \frac{1}{2}$.

Because thermal fluctuations are small compared to the elastic energy, see (35), $(h_i - \frac{pQ\epsilon_i}{2\pi} - \gamma)$ takes on its minimal value, which is given by

$$h_i^0 = \left\lceil \frac{pQ\epsilon_i}{2\pi} + \gamma \right\rceil. \quad (42)$$

This defines the exact ground state of the classical model: If we use (38) one finds for the optimal value of the n_i 's

$$n_{i+1}^0 = n_i^0 + \left\lceil \frac{pQ}{2\pi} (\epsilon_i + l_{imp}) \right\rceil,$$

which leads, using (37), to the exact classical ground state

$$\varphi_i^0 = \frac{1}{p} \left(2\pi \left\{ n_1^0 + \sum_{j<i} \left\lceil \frac{pQ}{2\pi} (\epsilon_j + l_{imp}) \right\rceil \right\} + \pi \right) - Qx_i, \quad (43)$$

where n_1^0 has an arbitrary integer value (see Fig. 4).

3.4 Finite temperature and crossover diagram

At *finite temperatures* thermal fluctuations wipe out the random potential, which leads to the pinning of the CDW at $t = 0$ and $K < K_u$. Thus, there

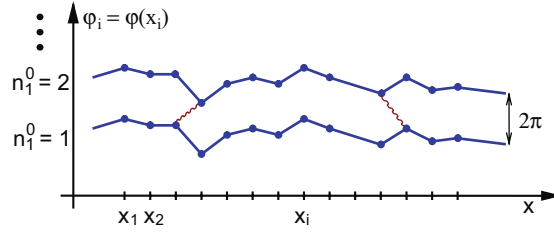


Fig. 4. Ground states in the strong pinning regime characterized by the integer number n_1^0 . The wavy lines show an excitation from one ground state forming an instanton configuration which could be a mechanism for quantum tunneling transport at low temperatures [35, 33].

is no phase transition anymore and the system is always in its delocalized phase, even if the disorder may still play a significant role on intermediate length scales.

In the special case $K \rightarrow 0$ the flow equation (19c) reduces to $\frac{du^2}{dt} = [3 - p^2 t] u^2$ with solution

$$u^2(l) = u_0^2 e^{3l - p^2 t_0 (e^l - 1)}. \quad (44)$$

If we write $t = t_0 e^l$, we may express l by t and hence, we may write u^2 as t -dependent function:

$$u^2(t) = u_0^2 (t/t_0)^3 e^{-p^2 (t - t_0)}, \quad (45)$$

which is plotted in Fig. 2 in the t - u plane.

One sees that the flow of the disorder has a maximum at $t = 3/p^2$ or $l = \ln(3/(p^2 t_0))$, if $t_0 < 3/p^2$. For finite K , the RG flow of u in the region $K < K_u$ first increases and then decreases. The region of increase in the K - t plane is implicitly defined by $\mathcal{M}_u \equiv \{(K, t) | K_u^* \geq K \coth \frac{K}{2t} \geq 0\}$, i.e., the positions of the maxima of $u^2[K, t]$ are located on the boundary of \mathcal{M}_u defined by $K_u^* = K \coth \frac{K}{2t}$.

The correlation length ξ can be found approximately by integrating the flow equations until the maximum of $u(l)$ and $t(l)/(1 + K(l))$ is of the order one (see discussion in section 4). This can be done in full generality only numerically (see Fig. 5).

It is however possible to discuss several special cases analytically. The zero temperature correlation length can still be observed as long as this is smaller than the thermal de Broglie wave length λ_T which can be rewritten for K not too close to K_u as $t \lesssim t_K \approx K t_u^{(1 - K/K_u)^{-1}}$ with $t_u \approx L_{FL}^{-1}$, where we defined t_K via $\xi_u \equiv \frac{K}{t_K}$, analogously to the definition of λ_T , and used (30). We call this domain the *quantum disordered region*.

For $K \geq K_u$ the correlation length ξ is given by λ_T which is larger than given by purely thermal fluctuations. For scales smaller than λ_T , the phase

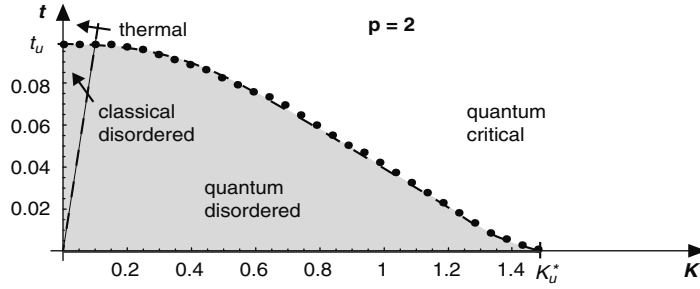


Fig. 5. The low temperature crossover diagram of a one-dimensional CDW. t and K are proportional to the temperature and the strength of quantum fluctuations, respectively. The amount of disorder corresponds to a reduced temperature $t_u \approx 0.1$. In the classical and quantum disordered region, respectively, essentially the $t = 0$ behavior is seen. The straight dashed line separating them corresponds to $\lambda_T \approx 1$, i.e., $K \approx t$, where λ_T is the de Broglie wave length. In the quantum critical region, the correlation length is given by λ_T . Pinning (localization) occurs only for $t = 0$, $K < K_u^*$.

correlation function still increases as $\sim \ln|z|$ with a continuously varying coefficient $K_{\text{eff}}(u_0)$, as will be discussed in detail in the next section. In this sense one observes *quantum critical behavior* in that region, despite of the fact, that the correlation length is now finite for all values of K [6, 7].

In the *classical disordered region* $t_K < t < t_u$ the correlation length is roughly given by L_{FL} as follows from previous studies [10, 44] or by solving $u^2(\ln(\xi)) \simeq 1$ using (44) for small t_0 yielding $\xi \approx u_0^{-2/3} e^{-p^2 t_0} \approx u_0^{-2/3} = L_{FL}(\pi p^4)^{1/3}$. Note, that $t_K \approx K$ for small K .

In the remaining region $t \gtrsim t_u$, the *thermal region*, we apply the mapping onto the Burgers equation (see section 4). In this case the RG-procedure applied to this equation becomes trivial, since there is only a contribution from a single momentum shell and one finds for the correlation length $\xi^{-1} \approx \frac{\pi}{2} f(T) t [1 + 1/2 [t_u / (\pi p^2 t)]^3] \Lambda$.

The phase diagram depicted in Fig. 5 is the result of the numerical integration of our flow equations and shows indeed the various crossovers discussed before.

In the *high temperature region* ($t \gg K$) the flow equations can be solved explicitly. For $u^2(l)$ we get the same result as given in (44) and the flow equation for K reduces to

$$\frac{dK}{dl} = -\frac{p^4}{2} u^2 \frac{K^4}{(2t)^3}, \quad (46)$$

where we used $B_0(p^2 K, \frac{K}{2t} \rightarrow 0) = (K/2t)^4$. The solution of this equation is given by

$$K(l) = \left[K_0^{-3} + \frac{3p^4 u_0^2}{16t_0^3} e^{p^2 t_0} \text{Ei}(p^2 t_0, p^2 t_0 e^l) \right]^{-1/3}, \quad (47)$$

with the incomplete exponential integral function $\text{Ei}(a, b)$ defined by

$$\text{Ei}(a, b) \equiv \int_a^b dt e^{-t}/t.$$

One observes that $K(l)$ saturates very quickly at a value $K(\infty) < K_0$.

4 Correlation functions

In this section we discuss the density-density and the phase correlation functions in more detail and summarize all correlation lengths in the various regimes – partly already used in the last two sections.

The (full) density-density correlation function is defined as

$$S(x, \tau) \equiv \langle \rho(x, \tau) \rho(0, 0) \rangle, \quad (48)$$

where $\rho(x, \tau)$ is given in (1). In the following we restrict our considerations to the (*charge*) *density wave order* part of S , which is the term proportional to ρ_1^2 , i.e.

$$S_1(x, \tau) = \rho_1^2 \langle \cos p(\varphi(x, \tau) + Qx) \cos p\varphi(0, 0) \rangle, \quad (49)$$

which defines the type of order of the density wave: If it decays algebraically we have quasi long-range order (QLRO), an exponential decay over a correlation length ξ corresponds to short-range order (SRO). The omitted parts of S decay faster than S_1 [17].

S_1 can be rewritten as

$$S_1(x, \tau) = \frac{\rho_1^2}{4} \left(e^{ipQx} \langle e^{ip(\varphi(x, \tau) - \varphi(0, 0))} \rangle + e^{-ipQx} \langle e^{-ip(\varphi(x, \tau) - \varphi(0, 0))} \rangle \right), \quad (50)$$

and using a gaussian approximation for the averages, which can be indeed *exact* in lowest order perturbation theory [8], we obtain

$$S_1(x, \tau) \simeq \rho_1^2 \cos(pQx) e^{-\frac{p^2}{2} \langle (\varphi(x, \tau) - \varphi(0, 0))^2 \rangle}. \quad (51)$$

From now on we focus on the *phase correlation function*

$$C(x, \tau) \equiv \langle (\varphi(x, \tau) - \varphi(0, 0))^2 \rangle, \quad (52)$$

and discuss it in various limits. Combining (51) and (52) we can extract a correlation length from the relation

$$\xi^{-1} = \lim_{x \rightarrow \infty} \frac{p^2}{2x} C(x, 0). \quad (53)$$

An overview of all different correlation lengths is shown in table 2.

4.1 Disorder-free case

We start with the most simple case $u = 0$. Then, the correlation function in dimensionless units follows directly from the action \mathcal{S}_0 written in momentum space:

$$C_0(x, \tau) = \frac{2\pi t}{L} \sum_{k,n} \frac{1 - e^{i(kx + \omega_n \tau)}}{\omega_n^2 + k^2}, \quad (54)$$

with Matsubara frequencies $\omega_n = 2\pi n/\lambda_T$ and momenta $k = k_m = 2\pi m/L$.

The sums over n and k (i.e., m) can be performed approximately for sufficiently large x and τ and one obtains [38]

$$C_0(x, \tau) \simeq \frac{K}{2} \ln \left(1 + \left(\frac{\lambda_T}{2\pi} \right)^2 \left[\cosh \left(\frac{2\pi x}{\lambda_T} \right) - \cos \left(\frac{2\pi \tau}{\lambda_T} \right) \right] \right). \quad (55)$$

The behavior of this function is considered in the following cases:

(i) At *zero temperature* ($\lambda_T \rightarrow \infty$) (55) reduces to

$$C_0(x, \tau) \simeq \frac{K}{2} \ln \left(\frac{1}{2} [x^2 + \tau^2] + 1 \right), \quad (56)$$

i.e., the correlation function has a logarithmic dependency on x and τ and leads to an algebraic decay of S_1 , i.e., the system shows QLRO.

(ii) At *finite temperatures* we can distinguish between length scales smaller and larger than λ_T .

In the first case $x \ll \lambda_T$ and $\tau \ll \lambda_T$ the cosh and cos term can be expanded to second order in the arguments and one gets the same logarithmic function as in the zero temperature case. In the opposite case $x \gg \lambda_T$, which is the usual case at high temperatures, the cosh term can be approximated by the exponential function and one finds a linear dependency on x :

$$C_0(x) \approx \pi t x = T x / c \quad \Longrightarrow \quad \xi = \frac{2}{p^2 \pi t} \equiv \xi_T, \quad (57)$$

i.e., S_1 decays exponentially (SRO) over a characteristic length $\xi \sim t^{-1}$. The same result is obtained for the limit $K \rightarrow 0$ at a fixed, finite temperature.

Note, that with this result we have neglected the algebraic decay for small $x < \lambda_T$. Therefore a better interpolation formula for the correlation length is $\xi \approx \frac{2}{p^2} (\xi_T + \lambda_T)$, which takes the slow decay for small x into account. In terms of the length-scale dependent $t(l)$ this rewrites to

$$t(l = \ln(\xi)) = K + 1, \quad (58)$$

i.e., the correlation length is reached, if $t(l)/(1 + K)$ is of order one.

The change from QLRO on small length scales $x < \xi$ to SRO on large length scales becomes clear if one considers the cylindric topology of the system in space-time at finite temperatures: As soon as one reaches length scales of the order of the perimeter of the cylinder, which is λ_T (see Fig. 6), starting from small scales, the system changes from two-dimensional to effectively one-dimensional behavior.

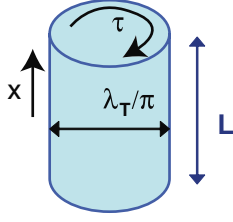


Fig. 6. Topology of the 1 + 1 dimensional system at finite temperature. Due to periodic boundary conditions in imaginary time direction the system has a cylinder topology with perimeter of the thermal de Broglie wave length λ_T .

4.2 Finite disorder

If u is finite, the action of the system has a forward and a backward scattering part. With the decomposition (22), the phase correlation function divides into two parts:

$$C(x, \tau) = C_b(x, \tau) + C_f(x) \quad (59)$$

and has therefore always a contribution $C_f(x) \sim |x|/\xi_f$ with $\xi_f^{-1} \sim \sigma(l = \ln|x|)$, i.e., the density wave order has always an exponentially decaying contribution and we can define

$$S_1(x, \tau) \equiv f_\rho(x) e^{-\frac{v^2}{2} C_b(x, \tau)}, \quad (60)$$

with $f_\rho(x) = \rho_1^2 \cos(pQx) e^{-\frac{v^2 \pi}{4} |x|/\xi_f}$. However, since $C_f(x)$ is not τ -dependent, it will not influence the dynamical properties of the system. Therefore all further remarks about phase correlations refer to $C_b(x, \tau)$ and consequently we will drop the subscript b in the following. Again we examine the $T = 0$ and finite temperature cases:

- (i) At *zero temperature* we have to distinguish between three K -regimes: For $K > K_u$ the disorder becomes irrelevant under the RG flow and we can use the zero temperature, disorder free result for the correlation function with the pre-factor K replaced by an effective quantity $K_{eff}(l = \ln z)$ on a length scale $z = \sqrt{x^2 + \tau^2}$, defined by the flow equation for K . This effective K saturates on large scales at a fixed point value $K_{eff}(u_0)$, which may be seen in Fig. 2. Therefore we have QLRO in this K region.

For $0 < K < K_u$ we integrate the flow of u until it reaches a value of order one, starting at small u_0 , which defines the localization length ξ_u (see section 3.2), i.e., the correlation function behaves like $C(x, \tau) \sim |x|/\xi_u$, i.e., we have an additional (to C_f) exponentially decaying contribution to S_1 .

The third case, $K = 0$, is discussed in the next section.

- (ii) At *finite temperatures* the parameter K saturates at an effective value $K_{eff}(u_0)$ on large length scales. Therefore the correlation function for small disorder is given by (55) with K replaced by $K(l = \ln z)$.

In the region \mathcal{M}_u of the K - t plane (see section 3.4), u still increases and we can find an effective correlation length by comparing the length scales

on which $u(l)$ or $t(l)/[1+K(l)]$ become of order one. Then, the correlation length is the smaller length of these two.

For $K=0$, high temperatures, but weak disorder we adopt an alternative method by mapping the (classical) one-dimensional problem onto the Burgers equation with noise [26]. With this approach one can derive an effective correlation length given by

$$\xi_B^{-1} \approx \xi_T^{-1} \left(1 + \frac{1}{2} \left[\frac{\xi_T}{2L_{FL}} \right]^3 \right) \quad (61)$$

where $\xi_T \ll L_{FL}$, which changes the prefactor of the free correlation function at high temperatures (57). The full calculation for this result can be found in [21, 20].

4.3 Strong disorder

In the last region $K=0$ for $T \ll c/(p^2 l_{imp})$ we come back to the *strong pinning case*, discussed in section 3.3 before, and calculate the pair correlation function *exactly*. Taking into account that the h_i 's are independent on different lattice sites, i.e., $\overline{h_i h_j} \propto \delta_{ij}$, the (discrete) phase correlation function is given by

$$\begin{aligned} \overline{\langle (\varphi_{n+1} - \varphi_1)^2 \rangle} &= \frac{4\pi^2}{p^2} \overline{\left\langle \left(h_i - \frac{pQ\epsilon_i}{2\pi} - \gamma \right)^2 \right\rangle} \cdot n \\ &= \frac{4\pi^2}{p^2} \overline{\left(\frac{pQ\epsilon_i}{2\pi} + \gamma - \left[\frac{pQ\epsilon_i}{2\pi} + \gamma \right] \right)^2} n, \end{aligned}$$

where we used (42) for the second equality. For evaluating the disorder average in this expression, one has to take into account the order statistics of the impurity distances ϵ_i . In the thermodynamic limit the probability density function for the ϵ_i 's can be rewritten as

$$p(\epsilon_i) \approx \frac{l_{imp}^{-1}}{e} e^{-l_{imp}^{-1} \epsilon_i}, \quad -l_{imp} \leq \epsilon_i < \infty. \quad (62)$$

A complete derivation of this expression can be found in [19].

Then, the correlation function can be explicitly written as

$$\overline{\langle (\varphi_{n+1} - \varphi_1)^2 \rangle} = \frac{4\pi^2}{p^2} \int_0^\infty dx e^{-x} \left(\frac{x}{2\alpha} - \left[\frac{x}{2\alpha} \right] \right)^2 n, \quad (63)$$

where we introduced the parameter $\alpha \equiv \frac{\pi}{pQ l_{imp}}$ and substituted $x = l_{imp}^{-1} \epsilon_i + 1$. This integral can be evaluated exactly, which leads to the following exact expression for the pair correlation function at zero temperature, written in a continuum version:

$$C(x, \tau) = \frac{2\pi}{p\alpha} \left(1 - \frac{\alpha}{\sinh \alpha}\right) |Qx| \equiv \frac{2x}{p^2\xi}, \quad \alpha = \frac{\pi}{pQl_{imp}}. \quad (64)$$

Finally, we want to give an interpolating expression for $C(x, \tau)$ from $T = 0$ to high temperatures $T \gg c/(l_{imp}p^2)$ starting with the result (64). In the latter case we may neglect the discreteness of h_i and hence

$$\begin{aligned} & \overline{\langle (\varphi_{n+1} - \varphi_1)^2 \rangle} \\ & \approx \frac{4\pi^2}{p^2 l_{imp}} \overline{\left(-\frac{\partial}{\partial \lambda_1} \ln \left(\int dh e^{-\sum_i \lambda_i h^2} \right) \right)} |x| \\ & = \frac{T}{c} |x| = \pi t |x|, \end{aligned} \quad (65)$$

with $\lambda_i = \frac{2\pi^2 c}{Tp^2(l_{imp} + \epsilon_i)}$.

A plausible interpolation formula is then given by

$$\overline{\langle (\varphi(x) - \varphi(0))^2 \rangle} \approx \left(2Q^2 l_{imp} \left(1 - \frac{\alpha}{\sinh(\alpha)}\right) + \frac{T}{c} \right) |x|, \quad (66)$$

and for $l_{imp} \gg Q^{-1}$, i.e., $\alpha \ll 1$:

$$\overline{\langle (\varphi(x) - \varphi(0))^2 \rangle} \approx \left(\frac{\pi^2}{3p^2} l_{imp}^{-1} - \frac{7\pi^4}{180p^4} \frac{l_{imp}^{-3}}{Q^2} + \frac{T}{c} \right) |x|. \quad (67)$$

Hence the correlation length acquires the form

$$\xi_{sp}^{-1} \approx p^2 Q^2 l_{imp} \left(1 - \frac{\alpha}{\sinh(\alpha)}\right) + \xi_T^{-1}. \quad (68)$$

Note, that $l_{imp}Q \geq 1$, i.e., $\alpha \leq \pi/p$ and $\xi_T \gg l_{imp}$. An approximate crossover to the weak pinning limit follows by choosing $l_{imp} \approx L_{FL}$.

length	description	eq.
ξ_B	weak pinning/high temp. length	(61)
ξ_f	forward scattering length	(59)
ξ_{sp}	strong pinning length	(68)
ξ_T	high temp./disorder free length	(57)
ξ_u	disorder localization length	(30)
ξ_w	lattice pot. correlation length	sec. 5

Table 2. Overview of the dimensionless correlation lengths.

For application of those results to other systems like superfluids, see [21, 20].

5 Influence of a commensurate lattice potential

If the wave length λ of the CDW modulation is commensurate with the period a ($= \pi$, due to dimensionless units) of the underlying lattice such that $n\lambda = qa$ with integers n and q , the umklapp term $-2\pi(w/K)\cos(q\varphi)$ appears in the Hamiltonian [23]. Therefore we switch on the lattice potential $w \neq 0$ now. In this section we consider the case $u = 0$, which leads to the sine-Gordon type model:

$$\frac{\mathcal{S}_{LPP}}{\hbar} = \int_0^L dx \int_0^{K/t} d\tau \left[\frac{1}{2\pi K} \{(\partial_x \varphi)^2 + (\partial_\tau \varphi)^2\} - \frac{w}{K} \cos(q\varphi) \right]. \quad (69)$$

The model has q degenerate classical ground states given by $\varphi_m = 2\pi m/q$ with $m = 0, \dots, q-1$. Performing a calculation analogous to the one above (but with $u = 0$) the RG-flow equations read

$$\frac{dK}{dl} = \frac{\pi}{2} q^4 w^2 B_2 \left(q^2 K, \frac{K}{2t} \right) \coth \frac{K}{2t}, \quad (70a)$$

$$\frac{dt}{dl} = \left[1 + \frac{\pi}{2} q^4 w^2 B_1 \left(q^2 K, \frac{K}{2t} \right) \coth \frac{K}{2t} \right] t, \quad (70b)$$

$$\frac{dw}{dl} = \left[2 - \frac{q^2}{4} K \coth \frac{K}{2t} \right] w, \quad (70c)$$

where $B_{1,2}$ are given in (20) with

$$g_1 = 2x^2 \cos x, \\ g_2 = (x^2 + \tau^2) \cos x.$$

Plots of the functions B_1 and B_2 can be found in [20]. A plot of the numerical solution of (70a) to (70c) is shown in Fig. 7.

At zero temperature (70a) and (70c) reduce to

$$\frac{dK}{dl} = \frac{\pi}{2} q^4 w^2 B_2 \left(q^2 K, \infty \right), \quad (71a)$$

$$\frac{dw}{dl} = \left[2 - \frac{q^2}{4} K \right] w, \quad (71b)$$

and we find, that the lattice potential becomes relevant (i.e., w grows) for $K < K_w$, where K_w is implicitly defined by

$$w^2(K_w) = \frac{K_w^{*2}}{2\pi q^2 \tilde{\eta}} \left(\frac{K_w}{K_w^*} - 1 \right)^2, \quad (72)$$

which follows from

$$\frac{dw}{dK} = -\frac{4}{q^4 \pi \tilde{\eta} w} \left(1 - \frac{K}{K_w^*} \right), \quad (73)$$

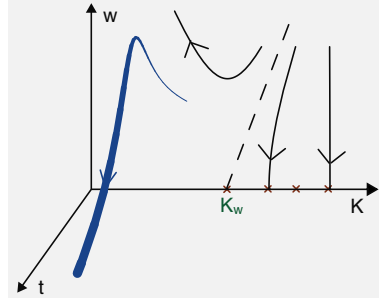


Fig. 7. Typical flow diagram for the disorder free model in the three dimensional parameter space of K , w and t . w denotes the strength of the commensurate lattice potential.

where we used (71a) and (71b) and the initial condition $w(K_w^* \equiv 8/q^2) = w_0 = 0$; $\tilde{\eta} = -B_2(q^2 K_w^*, \infty)$ (≈ 0.4 , for $q = 1$).

In this region the periodic potential stabilizes true long-range order of the CDW: the phase is everywhere close to one of the q classical ground states φ_m . The *depinning transition from the lattice* for $K \nearrow K_w$ is again of KT type. The correlation length ξ_w in the low- K ordered phase is defined by $w(\ln \xi_w) \approx 1$ and diverges at $K_w - 0$ [3, 11, 46]. This can be seen by considerations analogous to the disordered case. Defining

$$\gamma = 2 \frac{K}{K_w^*} - 2,$$

$$\chi^2 = \frac{\pi}{8} q^6 \tilde{\eta} w^2$$

(note that $\tilde{\eta} > 0$) leads for $|\gamma| \ll 1$, i.e., close to K_w^* , to the KT equations (28a) and (28b).

At finite temperatures we find a similar scenario as in the case where we considered the influence of the disorder: w first increases in a region in the K - t plane which is defined by $\mathcal{M}_w \equiv \{(K, t) | K_w^* \geq K \coth \frac{K}{2t} \geq 0\}$, i.e., when the right-hand side of (70c) is positive, but then decreases and flows into the region of large t and small w . Thus the periodic potential becomes irrelevant at finite temperatures. This can be understood as follows: at finite t the 1D quantum sine-Gordon model can be mapped on the Coulomb gas model on a torus of perimeter λ_T since periodic boundary conditions apply now in the τ -direction. Whereas the entropy of two opposite charges increases for separation $L \gg \lambda_T$ as $\ln(L\lambda_T)$, their action increases linearly with L . Thus, the charges remain bound. The one-dimensional Coulomb gas has indeed only an insulating phase [31].

6 Disorder and lattice potential

In this section we consider the combined influence of the disorder and the umklapp term at zero temperature. Although the RG calculation breaks down

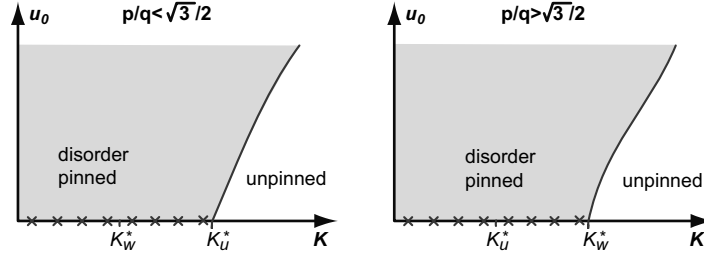


Fig. 8. Qualitative zero temperature phase diagram for a system with commensurate lattice potential and small disorder. One has to distinguish two cases: (i) $K_w^* < K_u^*$ (or $p/q < \sqrt{3}/2$) and (ii) $K_w^* > K_u^*$ (or $p/q > \sqrt{3}/2$). The phase boundaries can be estimated by Imry-Ma arguments (see text).

for $K < \max(K_u, K_w)$, the common influence of both the random and the commensurate potential can be estimated by combining the results obtained so far with Imry-Ma arguments [27]. We distinguish the following cases:

- (i) *Case:* $K > \max(K_u, K_w)$. Both disorder and the umklapp term become irrelevant and the system is asymptotically free. The order is of quasi-long-range type.
- (ii) *Case:* $K_u < K < K_w$ (i.e. $p > \frac{\sqrt{3}}{2}q$). This is the region where in the absence of the umklapp term the disorder would still become irrelevant. The umklapp term favors phase values $\varphi_m = 2\pi m/q$, $m = 0, \dots, q-1$, equally. We consider now the stability of one of these phases, say with $m = 0$, with respect to the formation of domains with $m \neq 0$ due to the disorder. Since the disorder is completely correlated in the τ -direction, it is clear that these domains - if they exist - are stripe-like with an infinite extension in this direction.

In the presence of weak disorder the free energy density of this stripe domain state is given by

$$f_{domain} = (qw^{1/2}L_x^{-1} - uL_x^{-1/2}), \quad (74)$$

where L_x denotes the extension of these domains. $qw^{1/2}$ is the surface tension of the domain wall. Minimizing f_{domain} leads to $L_x \simeq q^2w/u^2$. To determine whether the disorder or the lattice potential dominate in the considered K region, we study the behavior of L_x on larger length scales by using the flow equations

$$L_x(l) \propto \frac{w_{\text{eff}}(l)}{u_{\text{eff}}^2(l)} \approx \frac{\xi^{-2}w(l)}{\xi^{-3}u^2(l)} = \xi \frac{w(l)}{u^2(l)}, \quad (75)$$

where $\ln \xi = l$. The effective parameters follow from the unrescaled flow equations which are expressed by the renormalized and rescaled quantities as given in (75). At the correlation length ξ_w , where the renormalization stops ($w \approx 1$), L_x behaves like

$$L_x(\ln \xi_w) \equiv \xi_u = \text{const} \times \frac{\xi_w}{u^2(\ln \xi_w)} \quad (76)$$

and therefore $\xi_u > \xi_w$. We conclude that even though the disorder in the absence of the periodic potential is irrelevant for $K > K_u$, the decay of u is stopped due to the suppression of the φ fluctuations which in turn are due to w , and the ordered state $\varphi = \varphi_m = 2\pi m/q$ state is destroyed on the scale ξ_u by arbitrarily weak disorder. In the space direction the system decomposes into domains of extension ξ_u . Note, that there are still long-range correlations in the τ -direction since the disorder is frozen. For these reasons we expect only two phases, a free phase for $K > K_w$ and a pinned phase for $K < K_w$ (see right diagram in Fig. 8).

- (iii) *Case: $K_w < K < K_u$ (i.e. $p < \frac{\sqrt{3}}{2}q$) or $K < \min(K_u, K_w)$.* In this case the above considerations suggest that the disorder dominates the lattice potential even more, and we again expect only two phases (see Fig. 8).

This means that for $K < \max(K_u, K_w)$ disorder turns out to be always relevant with $\xi_u \approx \xi_w/u^2(\ln \xi_w)$.

7 Conclusions

To conclude we have shown, that in one-dimensional charge and spin density waves, Luttinger liquids, and superfluids, quantum phase transitions between a disordered (or locked-in) phase and an asymptotically free phase at zero temperature are destroyed by thermal fluctuations, leaving behind a rich crossover behavior. This was demonstrated by using a *full finite temperature* renormalization group (RG) calculation. The crossover regions were characterized by the behavior of the phase pair correlation functions. For vanishing quantum fluctuations our calculation was improved by an *exact* solution in the case of strong disorder and by a mapping onto the *Burgers equation with noise* in the case of weak disorder, respectively. Both methods gave an exponential decay of density correlations.

We have also briefly discussed, that the inclusions of Coulomb interaction may destroy the unpinning (localization) transition at zero temperature.

The finite temperature calculation, used in this paper, is also suited for treating the low frequency, low temperature behavior of dynamical properties

which may depend crucially on the ratio ω/T , e.g., the frequency dependent electric conductivity. This will be postponed to a forthcoming publication.

The combined effect of disorder and the lattice potential on the zero temperature phase diagram, i.e., the competition between unpinning (Anderson) and lock-in (Mott) transition, is still controversially discussed [41, 14] and cannot be explained by the RG-results presented here, since both perturbations become relevant for small K . However, using Imry-Ma arguments one finds, that as soon as K is below one of the two critical values (for the unpinning and lock-in transition) the disorder dominates the lattice potential and only two phases exist. This is in contrast to the proposed existence of a so-called intermediate *Mott-Glass* phase [14].

Acknowledgements. — I thank T. Nattermann, S. Scheidl, V. Vinokur, and I. Beloborodov for useful discussions. Support by the Deutsche Forschungsgemeinschaft through SFB 608 and the Forschungsstipendium program is acknowledged.

References

1. B. L. Altshuler and A. G. Aronov. *Electron-Electron Interaction in Disordered Conductors*, volume 10 of *Modern Problems in Condensed Matter Science*, page 1. North-Holland, Amsterdam, 1985.
2. G. Blatter, M. V. Feigel'man, V. B. Geshkenbein, A. I. Larkin, and V. M. Vinokur. *Rev. Mod. Phys.* **66**, 1125 (1994).
3. R. M. Bradley and S. Doniach. *Phys. Rev. B* **30**, 1138 (1984).
4. S. Brazovski and P. Monceau, editors. *Proceedings of the International Workshop on Electronic Crystals ECRYS 99*, volume 9 of *Journal de Physique IV Proceedings*. Societe Francaise de Physique, 1999.
5. J. D. Brock, D. A. DiCarlo, W. J. Prdulka, N. Sutton, E. Sweetland, and R. E. Thorne. *J. Phys. IV France* **3**, 115 (1993).
6. Sudip Chakravarty, Bertrand I. Halperin, and David R. Nelson. *Phys. Rev. Lett.* **60**, 1057 (1988).
7. Sudip Chakravarty, Bertrand I. Halperin, and David R. Nelson. *Phys. Rev. B* **39**, 2344 (1989).
8. Pierre Le Doussal and Kay Jörg Wiese. *Phys. Rev. E* **68**, 046118 (2003).
9. U. Eckern and A. Geier. *Z. Phys. B* **65**, 15 (1986).
10. M. Feigelman. *Sov. Phys. JETP* **52**, 555 (1980).
11. Matthew P. A. Fisher and G. Grinstein. *Phys. Rev. Lett.* **60**, 208 (1988).
12. H. Fukuyama. *Lect. Notes Phys.* **217**, 487 (1984).
13. H. Fukuyama and P. A. Lee. *Phys. Rev. B* **17**, 535 (1978).
14. T. Giamarchi, P. Le Doussal, and E. Orignac. *Phys. Rev. B* **64**, 245119 (2001).
15. T. Giamarchi and H. J. Schulz. *Europhys. Lett.* **3**, 1287 (1987).
16. T. Giamarchi and H. J. Schulz. *Phys. Rev. B* **37**, 325 (1988).
17. T. Giamarchi and H. J. Schulz. *Phys. Rev. B* **39**, 4620 (1989).
18. Thierry Giamarchi. *Quantum Physics in One Dimension*, volume 121 of *The International Series of Monographs on Physics*. Oxford Press, Oxford, 2003.
19. Andreas Glatz. *cond-mat/0302133* (2003).

20. Andreas Glatz. Disordered elastic systems: Fluctuations and AC-dynamics, 2004. ph.D. thesis, <http://kups.ub.uni-koeln.de/volltexte/2004/1312/>.
21. Andreas Glatz and Thomas Nattermann. *Phys. Rev. B* **69**, 115118 (2004).
22. G. Grüner. *Rev. Mod. Phys.* **66**, 1 (1994).
23. George Grüner. *Density Waves in Solids*, volume **89** of *Frontiers in Physics*. Addison-Wesley, 1994.
24. F. D. M. Haldane. *Phys. Rev. Lett.* **47**, 1840 (1981).
25. Igor F. Herbut. *Phys. Rev. B* **58**, 971 (1998).
26. David A. Huse, Christopher L. Henley, and Daniel S. Fisher. *Phys. Rev. Lett.* **55**, 2924 (1985).
27. Yoseph Imry and Shang keng Ma. *Phys. Rev. Lett.* **35**, 1399 (1975).
28. S. E. Korshunov. *Sov. Phys. JETP* **68**, 609 (1989).
29. J. M. Kosterlitz and D. J. Thouless. *J. Phys.: Condens. Matter* **6**, 1181 (1973).
30. P. A. Lee and H. Fukuyama. *Phys. Rev. B*, **17**, 542 (1978).
31. A. Lenard. *J. Math. Phys.* **2**, 682 (1961).
32. K. Maki. *Phys. Lett. A* **202**, 313 (1995).
33. Sergey V. Malinin, Thomas Nattermann, and Bernd Rosenow. *Phys. Rev. B* **70**, 235120 (2004).
34. H. Maurey and T. Giamarchi. *Phys. Rev. B* **51**, 10833 (1995).
35. Thomas Nattermann, Thierry Giamarchi, and Pierre Le Doussal. *Phys. Rev. Lett.* **91**, 056603 (2003).
36. Thomas Nattermann and Stefan Scheidl. *Adv. Phys.* **49**, 607 (2000).
37. Scot R. Renn and Ji-Min Duan. *Phys. Rev. Lett.* **76**, 3400 (1996).
38. Subir Sachdev. *Quantum Phase Transitions*. Cambridge University Press, 1999).
39. U. Schultz, J. Villain, E. Brezinand, and H. Orland. *J. Stat. Phys.* **51**, 1 (1988).
40. H. J. Schulz. *Phys. Rev. Lett.* **71**, 1864 (1993).
41. R. Shankar. *Int. J. Phys. B* **4**, 2371 (1990).
42. R. E. Thorne. *Phys. Today* **49**, 42 (1996).
43. Y. Tomio and Y. Suzumura. *J. Phys. Soc. Jap.* **70**, 2884 (2001).
44. J. Villain and J.F. Fernandez. *Z. Phys. B* **54**, 139, 1984).
45. C. R. Werner and U. Eckern. *Ann. Phys. (Leipzig)* **6**, 595 (1997).
46. Andrei D. Zaikin, Dmitrii S. Golubev, Anne van Otterlo, and Gergely T. Zimanyi. *Phys. Rev. Lett.* **78**, 1552 (1997).

Coulomb Drag between Quantum Wires: Effect of Small Momentum Transfer

L.I. Glazman¹, M. Pustilnik², E.G. Mishchenko³, and A.V. Andreev⁴

¹ Theoretical Physics Institute, University of Minnesota, Minneapolis, MN 55455, USA glazman@umn.edu

² School of Physics, Georgia Institute of Technology, Atlanta, GA 30332, USA

³ Department of Physics, University of Colorado, Boulder, CO 80390, USA

⁴ Bell Laboratories, Lucent Technologies, Murray Hill, NJ 07974, USA

Summary. We demonstrate that in a wide range of temperatures Coulomb drag between two weakly coupled quantum wires is dominated by processes with a small interwire momentum transfer. Such processes, not accounted for in the conventional Luttinger liquid theory, cause drag only because the electron dispersion relation is not linear. The corresponding contribution to the drag resistance scales with temperature as T^2 if the wires are identical, and as T^5 if the wires are different.

1 Introduction

Electrons moving in a conductor generate a fluctuating electric field around it. This field gives rise to an unusual transport phenomenon, Coulomb drag between two closely situated conductors [1]. The structure of the fluctuating field is determined by electron correlations within the conductors. Correlations are stronger in conductors of lower dimensionality. Tomonaga-Luttinger model captures some aspects of the correlations in the case of one-dimensional conductors (quantum wires). Within this model, the Coulomb drag was studied in [2, 3]. In a typical setup [4, 5] a dc current flows through the active wire 1, while the bias applied to the passive wire sets $I_2 = 0$, see Fig. 1. The *drag resistivity* (drag resistance per unit length of the interacting region) is then defined as

$$r = - \lim_{I_1 \rightarrow 0} \frac{e^2}{2\pi\hbar} \frac{1}{L} \frac{dV_2}{dI_1}. \quad (1)$$

The only source of drag in the Luttinger liquid is interwire backscattering, associated with a large momentum transfer between the wires. The model predicts a distinctive temperature dependence of the corresponding contribution

r_{2k_F} to the drag resistivity (1). In the case of identical wires $r_{2k_F} \propto l_{2k_F}^{-1} e^{\Delta/T}$ at the lowest temperatures [2, 3]. Here l_{2k_F} is the scattering length characterizing the interwire backscattering. At temperatures T above the gap Δ , this exponential dependence is replaced by a power-law, $r_{2k_F} \sim l_{2k_F}^{-1} (T/\epsilon_F)^{1-\gamma}$, where ϵ_F is the Fermi energy. The exponential temperature dependence of r_{2k_F} indicates a formation of a zig-zag charge order due to the $2k_F$ -component of the interwire interaction [2, 3]. To the contrary, the exponent $\gamma > 0$ in the power-law portion of the function $r_{2k_F}(T)$ is determined by the interactions within the wires; $\gamma = 0$ in the absence of interactions [6]. This renormalization of r_{2k_F} is similar in origin to the suppression of the conductance of a Luttinger liquid with an impurity [7]: in both cases repulsive interactions enhance the backscattering probability when temperature is lowered.

However, *forward* scattering between the wires also induces drag. To see this, one has to go beyond the Tomonaga-Luttinger model and account for the nonlinearity of the electronic dispersion relation. If the electron velocity depends on momentum, then even small (compared to $2k_F$) momentum transfer results in drag.

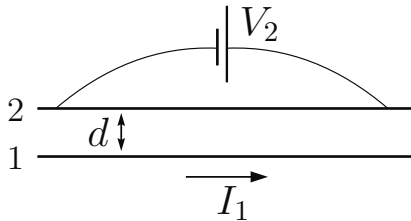


Fig. 1. Coulomb drag between quantum wires. A dc current I_1 flows through the active wire (1). A voltage bias V_2 is applied to the passive wire (2) in such a way that $I_2 = 0$.

The small (r_0) and large (r_{2k_F}) momentum transfer contributions to the drag are inversely proportional to the corresponding scattering lengths l_0 and l_{2k_F} , respectively. Their ratio $l_0/l_{2k_F} \propto e^{-4k_F d}$ depends strongly on the distance d between the wires. If the drag effect is employed to study the correlations within a wire, rather than the zig-zag order induced by interwire interaction, then d must be large: $k_F d > 1$. In this case the gap $\Delta \sim \epsilon_F (k_F l_{2k_F})^{-1/\gamma}$ becomes narrow, and the role of forward scattering increases.

In this paper we demonstrate that the drag resistivity between weakly coupled wires is dominated by the forward scattering in a wide temperature range. Even for identical wires, which is the most favorable for backscattering case, $r_0 \propto T^2$ wins over r_{2k_F} at all T above $T^* \sim \epsilon_F (l_0/l_{2k_F})^{1/(1+\gamma)}$. For different wires, r_{2k_F} is exponentially small at $T \lesssim u\delta n$, whereas r_0 has a power-law low-temperature asymptotics; here δn is the mismatch of the electron densities between the wires and u is the characteristic plasma velocity; hereafter we set $\hbar = 1$.

2 Drag Resistance in Terms of the Density-Density Correlation Function

The Hamiltonian of the system, $H = H_1 + H_2 + H_{12}$, is given by the sum of the Hamiltonians of the two isolated wires $i = 1, 2$,

$$\begin{aligned} H_i &= \int dx \psi_i^\dagger(x) \frac{\hat{p}^2}{2m} \psi_i(x) + H_{int}, \quad \hat{p} = -id/dx, \\ H_{int} &= \int dx dy \rho_i(x) U_{ii}(x-y) \rho_i(y), \end{aligned} \quad (2)$$

and of the Hamiltonian of the interwire interaction,

$$H_{12} = \int dx_1 dx_2 \rho_1(x_1) U_{12}(x_1 - x_2) \rho_2(x_2); \quad (3)$$

here $\rho_i(x) = \psi_i^\dagger(x) \psi_i(x)$.

We will assume that the interactions are screened by the nearby metallic gates. The screening length d_s is set by the distance to the gates and is typically [4, 5] of the order of the separation d between the wires, $d_s \sim d$. The short-distance cutoff d_{ij} of the Coulomb potential is provided by the wire width d_0 for $i = j$ or by the interwire distance d for $i \neq j$. The Fourier transforms $U_{ij}(k) = \int dx e^{ikx} U_{ij}(x)$ are rapidly decreasing functions of k with $U_{ij}(k) \propto e^{-|k|d_s}$ for $|k| \gg 1/d_s$, and $U_{ij}(k) \approx \text{const}$ for $|k| \ll 1/d_{ij}$. Note that $d_{ij} \sim d_s \sim d$ for interwire interaction $U_{12}(k)$. Thus, its k -dependence is characterized by a single scale $k_0 \sim 1/d$.

Because of the interaction H_{12} , electrons in the wire 2 experience a force [2] whose density is given by

$$\mathcal{F}_2 = \int dx (dU_{12}(x)/dx) \langle \rho_1(x) \rho_2(0) \rangle. \quad (4)$$

Since there is no current in the wire 2, this force must be balanced by an external electric field, $en_2 \mathcal{E}_2 + \mathcal{F}_2 = 0$, where $\mathcal{E}_2 = V_2/L$ and $n_i = \langle \rho_i \rangle$ is the concentration of electrons in the wire i . At $T \gg \Delta$ (see the discussion above) the correlation function in the r.h.s. of Eq. (4) can be evaluated in the first order in U_{12} ,

$$\frac{V_2}{L} = \frac{1}{en_2} \int \frac{dk d\omega}{(2\pi)^2} k U_{12}^2(k) \tilde{S}_1(k, \omega) \tilde{S}_2(-k, -\omega), \quad (5)$$

where $\tilde{S}_i(k, \omega)$ are the dynamic structure factors,

$$\tilde{S}_i(k, \omega) = \int dx dt e^{i\omega t - ikx} \langle \rho_i(x, t) \rho_i(0, 0) \rangle,$$

calculated in the presence of a finite current I_1 in the wire 1. The structure factor $\tilde{S}_2(k, \omega)$ in the wire 2 coincides with its equilibrium value, $S_2(k, \omega)$.

The electronic subsystem in the wire 1 is in equilibrium in the reference frame moving with the drift velocity $v_d = I_1/en_1$ in the direction of the current. Therefore the structure factor \tilde{S}_1 is obtained from the equilibrium value S_1 using the Galilean transformation: $\tilde{S}_1(k, \omega) = S_1(k, \omega - qv_d)$. Equations (1) and (5) then yield

$$r = \int dk d\omega \frac{k^2 U_{12}^2(k)}{8\pi^3 n_1 n_2} \frac{\partial S_1(k, \omega)}{\partial \omega} S_2(-k, -\omega). \quad (6)$$

Now we use the fluctuation-dissipation theorem,

$$S_i(k, \omega) = \frac{2A_i(k, \omega)}{1 - e^{-\omega/T}}$$

to further simplify Eq. (6),

$$r = \int_0^\infty dk \int_0^\infty d\omega \frac{k^2 U_{12}^2(k)}{4\pi^3 n_1 n_2 T} \frac{A_1(k, \omega) A_2(k, \omega)}{\sinh^2(\omega/2T)}. \quad (7)$$

Here A_i is the imaginary part of the retarded density-density correlation function; $A_i(k, \omega) = A_i(-k, \omega) = -A_i(k, -\omega)$. Equation (7) was derived by different means in [8]; similar expressions have been also obtained for noninteracting systems with disorder [9]. Here we demonstrated the validity of Eq. (7) for clean interacting systems.

3 Temperature Dependence of the Drag Resistance

We start with the evaluation of the drag resistivity for noninteracting electrons ($U_{ii} = 0$). Concentrating on the small momentum transfer contribution to r , we consider the limit $l_0/l_{2k_F} \rightarrow 0$, thus setting $r_{2k_F} = 0$. In this case the main contribution to the integral over k in Eq. (7) comes from small momenta $k \ll k_F$ and small energies $\omega \ll \epsilon_F$. At these values of k and ω , functions $A_i(k, \omega)$ are sharply peaked at $\omega_i = v_i k$, where $v_i = \pi n_i/m$ are the Fermi velocities in the two wires. For a given $k < 2k_F$ the widths of the peaks can be estimated as

$$\delta\omega(k, T) = \max \{k^2/m, kT/k_F\}. \quad (8)$$

Equation (8) and the exact f-sum rule,

$$\int_0^\infty d\omega \omega A_i(k, \omega) = \frac{\pi n_i}{m} \frac{k^2}{2}, \quad (9)$$

allow us to estimate the peak heights: $A_i \sim k/2\delta\omega$. If the difference between the Fermi velocities is small,

$$\delta v = |v_1 - v_2| \ll v_F = \pi n/m, \quad n = (n_1 + n_2)/2,$$

then Eq. (7) reduces to

$$r = \frac{1}{4\pi^3 n^2 T} \int_0^\infty dk \frac{k^2 U_{12}^2(k)}{\sinh^2(v_F k/2T)} \alpha(k, T), \quad (10)$$

$$\alpha(k, T) = \int_0^\infty d\omega A_1(k, \omega) A_2(k, \omega). \quad (11)$$

The function $\alpha(k, T)$ depends on δv . If the wires are identical ($\delta v = 0$), then Eq. (11) and the above estimates for A_i yield

$$\alpha(k, T) \approx \frac{k^2}{4\delta\omega(k, T)}. \quad (12)$$

There are two competing scales in the integrand of Eq. (10). The first scale, $k_0 \sim 1/d \ll k_F$, characterizes the k -dependence of the interwire interaction $U_{12}(k)$. The typical wave vector of thermally excited electron-hole pairs, T/v_F , defines the second scale. The two scales coincide at $T = T_0 = v_F k_0$. At $T \ll T_0$ one can replace $U_{12}(k)$ by $U_{12}(0)$ in Eq. (10). Furthermore, we use α in the form of Eq. (12) at $T = 0$, which results in

$$r = \frac{c_1}{l_0} \left(\frac{T}{\epsilon_F} \right)^2, \quad \frac{1}{l_0} = \left[\frac{U_{12}(0)}{2\pi v_F} \right]^2 n \quad (13)$$

with $c_1 = \pi^4/12$. Use of exact form of $A_i(k, \omega)$ in Eq. (11) changes only the numerical coefficient, $c_1 = \pi^2/4$.

The increase of temperature T above T_0 results in a saturation of the drag resistivity. Indeed, at $T_0 \ll T \ll \epsilon_F$ one can expand $\sinh(v_F k/2T)$ in Eq. (10) and use $\delta\omega = kT/k_F$ for the peak width in (12). This yields

$$r \sim \frac{1}{l_0} \int_0^\infty \frac{k dk}{n^2} \frac{U_{12}^2(k)}{U_{12}^2(0)} \sim \frac{1}{l_0} \left(\frac{T_0}{\epsilon_F} \right)^2. \quad (14)$$

Further increase of T leads to the decay of the drag,

$$r \propto l_0^{-1} (T_0/\epsilon_F)^2 (T/\epsilon_F)^{-3/2}, \quad T \gg \epsilon_F, \quad (15)$$

similar to the two-dimensional case [10].

We now consider wires with slightly different Fermi velocities $\delta v > 0$. In this case the peaks of $A_i(k, \omega)$ are separated in ω by $k\delta v$. We define a new temperature scale $T_1 = k_F \delta v$ by equating the separation to the peak width (8). We assume this scale is small, $T_1 \ll T_0$. The difference between velocities does not affect the drag at $T \gg T_1$. However, at $T \ll T_1$ the drag resistivity is suppressed exponentially. To obtain the leading asymptotics of $r(T)$ it is sufficient to use the $T = 0$ limit [11] of $A_i(k, \omega)$ in Eq. (11), $\alpha(k, 0) = (m/4k) (k - m\delta v) \theta(k - m\delta v)$. Equation (10) then results in

$$r = \frac{\pi^2/4}{l_0} \left(\frac{T_1}{\epsilon_F} \right)^2 \frac{T}{T_1} e^{-T_1/T}, \quad T \ll T_1. \quad (16)$$

The activation temperature dependence Eq. (16) holds for all $T \ll T_1$, because for noninteracting electrons at $T = 0$ the product $A_1(k, \omega)A_2(k, \omega)$ is exactly zero [11] at $k < m\delta v$. If electrons interact, some overlap of A_1 and A_2 exists even at small $k \ll m\delta v$. This yields a further contribution to r , that has a power-law temperature dependence. We will evaluate this contribution for weak intrawire interaction.

It is convenient to write $A(k, \omega)$ (we suppress the index i in the following) in the form $A(k, \omega) = [S(k, \omega) - S(-k, -\omega)]/2$ and use the Lehmann representation for the dynamic structure factor:

$$S(k, \omega) = \frac{2\pi}{L} \sum_n |\langle n | \rho_k | gs \rangle|^2 \delta(\omega - E_n + E_{gs}). \quad (17)$$

Here L is the system size, $|gs\rangle$ is the ground state, and $\rho_k = \sum_p \psi_{p+k}^\dagger \psi_p$. We evaluate the matrix element in Eq. (17) in the first order in the intrawire interaction. The nonvanishing at $\omega - v_F k \gg \delta\omega$ contribution results from the processes in which the unperturbed final state $|n\rangle$ in Eq. (17) has two electron-hole pairs: $|n\rangle^{(0)} = \psi_{p+q}^\dagger \psi_p \psi_{p'-q'}^\dagger \psi_{p'} |0\rangle$. This contribution is

$$\begin{aligned} \delta S(k, \omega) &= \frac{1}{\pi^2} \int dp dp' dq dq' \delta(q - q' - k) \\ &\times \delta(\omega - \xi_{p+q} + \xi_p - \xi_{p'-q'} + \xi_{p'}) \\ &\times f_p (1 - f_{p+q}) f_{p'} (1 - f_{p'-q'}) K^2(p, p', q, q', \omega), \end{aligned} \quad (18)$$

where f_p are the Fermi functions, $\xi_p = p^2/2m$, and

$$\begin{aligned} K &= \frac{U(q') - U(p - p' + q')}{\omega - \xi_{p+q} + \xi_{p+q'}} - \frac{U(q') - U(p - p' + q)}{\omega - \xi_{p+q-q'} + \xi_p} \\ &+ [p \leftrightarrow p', q \leftrightarrow -q']. \end{aligned}$$

Note that Eq. (18), unlike Eq. (17), accounts for a finite temperature. At $\omega \ll \epsilon_F$ and $k \ll k_F$, Eq. (18) yields the interaction-induced correction to $A(k, \omega)$,

$$\delta A(k, \omega) = \frac{\tilde{U}^2 k^4 \theta(\omega - v_F k)}{v_F m^2 \omega^2 - v_F^2 k^2}, \quad (19)$$

where $\tilde{U} = [U(0) - U(2k_F)]/2\pi v_F \ll 1$. This result is valid for $\omega \ll \epsilon_F$, $k \ll k_F$, $|\omega - v_F k| \gg \max\{\tilde{U} v_F k, \delta\omega(k, T)\}$, and describes $A(k, \omega)$ outside the interval Eq. (8). The limit of linear electron dispersion relation ($m \rightarrow \infty$) corresponds [12] to $\delta A(k, \omega) = 0$.

We use Eq. (19) to evaluate the interaction-induced correction δr to the drag resistivity between non-identical wires with $T_1 = k_F \delta v \gg \epsilon_F \tilde{U}$. At the lowest temperatures, Eqs. (10) and (11) yield

$$\delta r \sim \frac{\tilde{U}^2}{l_0} \left(\frac{T_1}{\epsilon_F} \right)^4 \left(\frac{T}{T_1} \right)^5. \quad (20)$$

With increasing temperature, the $r(T)$ dependence changes from Eq. (20) to the activation law (16). At $T \gg T_1$ the difference between wires does not affect $r(T)$.

We will argue now that intrawire interactions do not change the quadratic temperature dependence of $r(T)$ at $T_1 \ll T \ll T_0$, see Eq. (13). At these temperatures, an estimate equivalent to Eq. (13) reads $r \sim |U_{12}^2(0)|v_F^{-3}\delta\omega(k_T, T)$ and yields $r \propto T^2$; here $k_T \sim T/v_F \ll k_F$ is the wave vector of a typical electron-hole excitation. Interaction apparently does not affect the functional dependence of $\delta\omega$ on k and T ; the estimate (8) still can be used, although the coefficients $1/m$ and $1/k_F$ in it are affected by the interaction.

The Tomonaga-Luttinger model is insufficient for the evaluation of $\delta\omega$ in the presence of interaction: it implies linear electron spectrum, which yields [12] $\delta\omega = 0$. Accounting for the curvature of the electron spectrum complicates the treatment of the interaction greatly. The width $\delta\omega$ can be explicitly evaluated in the Calogero-Sutherland model which is characterized by a very specific interaction potential,

$$U_{ii}(x) = \frac{2\pi^2}{mL^2} \frac{\lambda(\lambda-1)}{\sin^2[\pi x/L]}. \quad (21)$$

The parameter λ here is related to the conventional interaction parameter g of the Luttinger liquid: $g = 1/\lambda$. This relation follows from the definition $g = v_F/u$ in terms of the velocity of the collective mode (plasmon) u , and its value $u = (\pi n/m)\lambda$ in the Calogero-Sutherland model [14, 13]. For the rational values of λ and at $T = 0$ the density-density correlation function is known exactly [14, 13]. Due to the integrability of the model, $A_i(k, \omega) \neq 0$ only in a finite interval of ω around $\omega = u_i k$ [15]. We found this interval for $k \leq 2\pi n_i$:

$$-(1/g)\frac{k^2}{2m} < \omega - u_i k < \frac{k^2}{2m}, \quad (22)$$

which yields for the width

$$\delta\omega(k, 0) = \frac{1+g}{2g} \frac{k^2}{m}. \quad (23)$$

In order to estimate r we note that Eq. (7) and the sum rule (9) remain valid in the presence of interactions within the wires. This allows us to follow the steps that led to Eq. (13). Replacing v_F by the plasma velocity u in Eq. (10) and using Eq. (23), we find

$$r = \frac{c_g}{l_0} \left(\frac{T}{\epsilon_F} \right)^2, \quad c_g \propto \frac{g^6}{1+g}, \quad (24)$$

which agrees with our expectation for the $r(T)$ dependence. We are not aware of a reliable theory of $A_i(k, \omega)$ beyond the exactly solvable case. However, the self-consistent Born approximation results [16] allow us to corroborate the estimate $\delta\omega \propto k^2/m$ for the peak width, so, apparently, the $r \propto T^2$ dependence is universal.

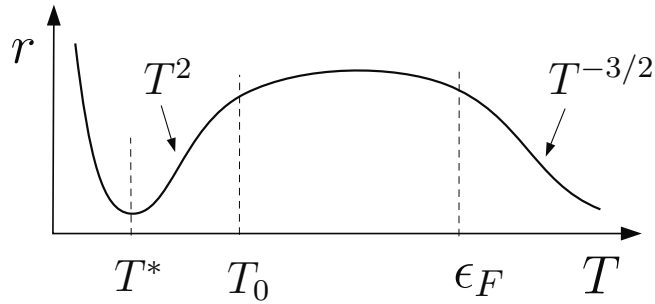


Fig. 2. Sketch of the temperature dependence of the drag resistivity between identical wires. The small momentum transfer contribution considered in this paper dominates at $T > T^*$; the ratio T^*/ϵ_F is exponentially small for $k_F d > 1$.

4 Conclusions

First observations of drag between ballistic quantum wires appeared recently [4, 5]. In a limited temperature interval, $0.2 \text{ K} < T < 0.9 \text{ K}$, a three-fold drop in the drag resistance was observed [4] with the increase of temperature. This drop was fit to a power-law $r \propto T^{-0.77}$ and interpreted as evidence of the Luttinger liquid behavior. However, the Fermi wave vector in the wires of Ref. [4] was estimated to be $k_F = 6 \times 10^4 \text{ cm}^{-1}$, which yields $\epsilon_F = \hbar^2 k_F^2 / 2m^* \approx 0.2 \text{ K}$ (we used here $m^* = 0.068 m_0$ known for GaAs). It thus appears that the measurements of Ref. [4] correspond to a non-degenerate or weakly degenerate regime incompatible with the Luttinger liquid description. An alternative explanation of the observations [4, 5] is provided by our theory. Indeed, using the values of k_F and $d = 200 \text{ nm}$ of [4], we find $k_F d = 1.2$. Under this condition the small momentum transfer contribution dominates at $T > T^*$, see Fig. 2. The observed [4, 5] behavior of $r(T)$ may correspond to the crossover regime between the limits $r(T) = \text{const}$ and $r(T) \propto T^{-3/2}$ presented by Eqs. (14) and (15).

To conclude, the small momentum transfer contribution dominates Coulomb drag at almost all temperatures if the distance between the wires exceeds the Fermi wavelength, see Fig. 2. Drag by small momentum transfer is possible because electron dispersion relation is not linear, and therefore can not be accounted for in the conventional Tomonaga-Luttinger model.

Acknowledgements. — We thank KITP, Santa Barbara, for hospitality, and K. Flensberg, A. Kamenev, S. Tarucha, and A. Tsvelik for discussions. This work was supported by NSF grants DMR97-31756, DMR-9984002, DMR02-37296, EIA02-10736, and by the Packard Foundation.

References

1. A.G. Rojo, J. Phys.: Cond. Matter **11**, R31 (1999).
2. Yu.V. Nazarov and D.V. Averin, Phys. Rev. Lett. **81**, 653 (1998).

3. R. Klesse and A. Stern, Phys. Rev. B **62**, 16912 (2000).
4. P. Debray *et al.*, J. Phys.: Cond. Matter **13**, 3389 (2001); P. Debray *et al.*, Semicond. Sci. Technol. **17**, R21 (2002).
5. M. Yamamoto *et al.*, Physica E **12**, 726 (2002).
6. B. Y.-K. Hu and K. Flensberg, in *Hot Carriers in Semiconductors*, edited by K. Hess *et al.* (Plenum, New York, 1996), p. 943.
7. C.L. Kane and M.P.A. Fisher, Phys. Rev. B **46**, 15233 (1992).
8. L. Zheng and A.H. MacDonald, Phys. Rev. B **48**, 8203 (1993).
9. A. Kamenev and Y. Oreg, Phys. Rev. B **52**, 7516 (1995); K. Flensberg *et al.*, Phys. Rev. B **52**, 14 761 (1995),
10. K. Flensberg and B.Y.-K. Hu, Phys. Rev. B **52**, 14796 (1995).
11. For noninteracting electrons at zero temperature $A_i(k, \omega) = (m/2k)\theta(k^2/2m - |\omega - v_i k|)$.
12. I.E. Dzyaloshinskii and A.I. Larkin, Zh. Eksp. Teor. Fiz. **65**, 411 (1973) [Sov. Phys. JETP **38**, 202 (1973)].
13. Z.N.C. Ha, Phys. Rev. Lett. **73**, 1574 (1994).
14. B.D. Simons, P.A. Lee, and B.L. Altshuler, Phys. Rev. Lett. **70**, 4122 (1993).
15. For a generic interaction $A_i(k, \omega)$ has a tail $\delta A_i(k, \omega)$ extending outside the interval (22), see Eq. (19). The corresponding contribution to the integral in Eq. (9) scales as k^4 at small k . Accordingly, the presence of the tail does not affect the estimate of the height of the peak in $A_i(k, \omega)$, and, therefore, the $r \propto T^2$ dependence.
16. K.V. Samokhin, J. Phys. Cond. Mat. **10**, L533 (1998).

Signatures of Spin-Charge Separation in Double-Quantum-Wire Tunneling

Yaroslav Tserkovnyak¹, Bertrand I. Halperin¹, Ophir M. Auslaender², and Amir Yacoby²

¹ Lyman Laboratory of Physics, Harvard University, Cambridge, Massachusetts 02138, USA halperin@physics.harvard.edu

² Dept. of Condensed Matter Physics, Weizmann Institute of Science, Rehovot 76100, Israel

Summary. We present evidence for spin-charge separation in the tunneling spectrum of a system consisting of two quantum wires connected by a long narrow tunnel junction at the edge of a GaAs/AlGaAs bilayer heterostructure. Multiple excitation velocities are detected in the system by tracing out electron spectral peaks in the conductance dependence on the applied voltage, governing the energy of tunneled electrons, and the magnetic field, governing the momentum shift along the wires. The boundaries of the wires are important and lead to a characteristic interference pattern in measurements on short junctions. We show that the experimentally observed modulation of the conductance oscillation amplitude as a function of the voltage bias can also be accounted for by spin-charge separation of the elementary excitations in the interacting wires.

1 Introduction

One-dimensional (1D) electronic systems are a very fertile ground for studying the physics of interacting many-body systems. Gapless electron gases in one dimension possess universal low-energy properties which can be mapped onto the exact solution of the Luttinger model.[1] Such 1D systems are collectively termed as Luttinger liquids (LL's). Despite a number of remarkable predictions for electronic and thermodynamic properties of LL's,[1] some made more than twenty years ago, direct experimental verification for many of them has remained a challenge. This mostly owes to the high quality of quasi-1D systems necessary to bridge the gap between the usual Landau Fermi-liquid (FL) physics in three spatial dimensions and the LL physics in one dimension.

An important prediction of LL theory is that the low-energy elementary excitations of a one-dimensional metal are not electronic quasiparticles, as

in the Landau FL theory of three-dimensional Fermi systems, but rather are separate spin and charge excitations that propagate at different velocities. An electron entering an LL will split into spin and charge excitations, and the electron propagator will have singularities corresponding to both velocities, in contrast to the case of a Landau FL where there is a simple pole at a single Fermi velocity. In this paper, we discuss evidence for spin-charge separation in tunneling between two parallel quantum wires at a cleaved edge of a double-quantum-well heterostructure. We use two approaches: one based on mapping out the elementary-excitation dispersions by measuring the conductance G as a function of the magnetic field B applied perpendicular to the plane connecting the wires and the voltage bias V , and the other focusing on the conductance oscillation pattern, in the (V, B) plane, arising due to the finite length of the tunnel junction.

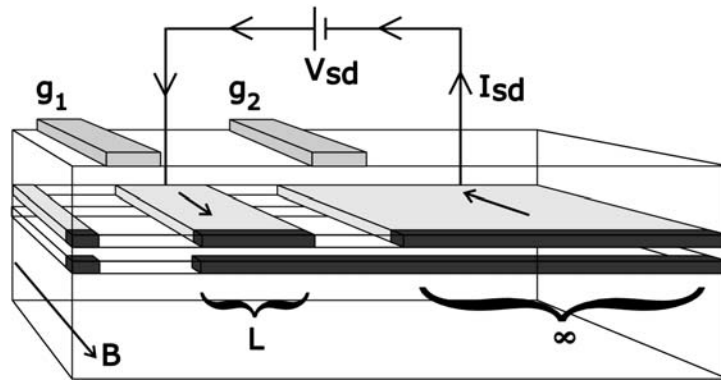


Fig. 1. Illustration of the sample and the contacting scheme. The sample is fabricated using the CEO method. The parallel 1D wires span along the whole cleaved edge (front side in the schematic). The upper wire (UW) overlaps the 2DEG, while the lower wire (LW) is separated from them by a thin AlGaAs barrier (the wires are shown in dark gray and the 2DEG is light gray). Contacts to the wires are made through the 2DEG. Several tungsten top gates can be biased to deplete the electrons under them: We show only g_1 , here biased to deplete the 2DEG and both wires, and g_2 , here biased to deplete only the 2DEG and the upper wire. The magnetic field B is perpendicular to the plane defined by the wires. The depicted configuration allows the study of the conductance of a tunnel junction between a section of length L of the upper wire and a semi-infinite lower wire.

2 Experimental Method

The two parallel 1D wires are fabricated by cleaved-edge overgrowth (CEO), see Fig. 1. Initially, a GaAs/AlGaAs heterostructure with two closely situated parallel quantum wells is grown. The upper quantum well is 20 nm wide, the lower one is 30 nm wide and they are separated by a 6 nm AlGaAs barrier

about 300 meV high. We use a modulation doping sequence that renders only the upper quantum well occupied by a two-dimensional electron gas (2DEG) with a density $n \approx 2 \times 10^{11} \text{ cm}^{-2}$ and mobility $\mu \approx 3 \times 10^6 \text{ cm}^2\text{V}^{-1}\text{s}^{-1}$. After cleaving the sample in the molecular beam epitaxy growth chamber and growing a second modulation doping sequence on the cleaved edge, two parallel quantum wires are formed in the quantum wells along the whole side of the sample. Both wires are tightly confined on three sides by atomically smooth planes and on the fourth side by the triangular potential formed at the cleaved edge.

Spanning across the sample are several tungsten top gates of width $2 \mu\text{m}$ that lie $2 \mu\text{m}$ from each other (two of these are depicted in Fig. 1). The differential conductance G of the wires is measured through indium contacts to the 2DEG straddling the top gates. While monitoring G with standard lock-in techniques (we use an excitation of $10 \mu\text{V}$ at 14 Hz) at $T = 0.25 \text{ K}$, we decrease the density of the electrons under a gate by decreasing the voltage on it (V_g). At $V_g = V_{2D}$, the 2DEG depletes and G drops sharply, because the electrons have to scatter into the wires in order to pass under the gate. For $V_{2D} > V_g > V_U$ the conductance drops stepwise each time a mode in the upper wire is depleted.[2] In this voltage range, the contribution of the lower wire to G is negligible because it is separated from the upper quantum well by a tunnel barrier. When $V_g = V_U$, the upper wire depletes and only the lower wire can carry electrons under the gate. This last conduction channel finally depletes at V_L and G is suppressed to zero.

The measurements are performed in the configuration depicted in Fig. 1. The source is the 2DEG between two gates, g_1 and g_2 in Fig. 1, the voltages on which are $V_1 < V_L$ and $V_L < V_2 < V_U$, respectively. The upper wire between these gates is at electrochemical equilibrium with the source 2DEG. This side of the circuit is separated by the tunnel junction we wish to study from the drain. The drain is the 2DEG to the right of g_2 (the semi-infinite 2DEG in Fig. 1) and it is in equilibrium with the right, semi-infinite, upper wire and with the whole semi-infinite lower wire in Fig. 1. Thus, any voltage difference (V) induced between the source and the drain drops on the narrow tunnel junction between the gates. In addition, we can shift the momentum of the tunneling electrons with a magnetic field B perpendicular to the plane defined by the wires. This configuration therefore gives us control over both the energy and the momentum of the tunneling electrons.

3 Dispersions of Elementary Excitations

The conductance for a spacing of $2 \mu\text{m}$ between gates g_1 and g_2 is shown in Fig. 2. The measured bright and dark curves in the plot can be interpreted as spectral peaks tracing out the dispersions of the elementary excitations in the wires.[3] In the case of noninteracting electrons, the curves are expected to map out parabolas defining the continua of electron-hole excitations across

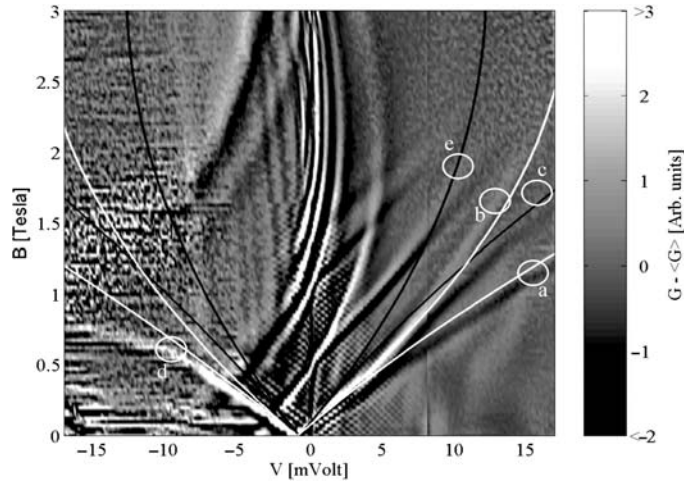


Fig. 2. Measurement of $G(V, B)$ for a $2 \mu\text{m}$ junction. Light shows positive and dark negative differential conductance. A smoothed background has been subtracted to emphasize the spectral peaks and the finite-size oscillations. The solid black lines are the expected dispersions of noninteracting electrons at the same electron densities as the lowest 1D bands of the wires, $|u_1\rangle$ and $|l_1\rangle$. The white lines are generated in a similar way but after rescaling the GaAs band-structure mass, and correspondingly the low-voltage slopes, by a factor of 0.7. Only the lines labeled by a , b , c , and d in the plot are found to trace out the visible peaks in $G(V, B)$, with the line d following the measured peak only at $V > -10$ mV.

the tunnel barrier for various pairs of 1D modes, one in the UW and the other in the LW. At small voltages, electron repulsion is predicted to split the curves into branches with slopes corresponding to different charge- and spin-excitation velocities, crossing at a point with $V = 0$ and magnetic field necessary to compensate for the Fermi wave-vector mismatch between the 1D modes (in the following referred to as the “crossing point”).[4, 5]

The 1D modes in the upper quantum well are coupled to the 2DEG via elastic scattering which ensures an Ohmic contact between the 2D well states and the states confined to the cleaved edge.[6] (This scattering is however weak on the scale of the junction length, not affecting the finite-size quantum-interference effects in tunneling.[7]) In addition to tunneling between the 1D states of the wires, there is a direct electron transfer from the 2DEG to the lower wire, when the extended states have an appreciable weight on the edge. Each of the quasi-1D wires carries several 1D modes. In our theoretical analysis, we will only consider the transition between the lowest 1D bands of the wires (i.e., the bands with the largest Fermi momentum), $|u_1\rangle \leftrightarrow |l_1\rangle$, which has a strong signal, as seen in Fig. 2, given by a family of curves crossing at the lowest magnetic field. Since other 1D modes have Fermi velocities smaller than $|u_1\rangle$ and $|l_1\rangle$ by at least 40%,[3] we can disregard their coupling to the

lowest bands,[8] keeping in mind, however, that the effective electron-electron interaction is affected by screening due to the nearby 2DEG and other 1D modes. Both the spin-orbit interaction and Zeeman splitting are negligible in comparison to the Fermi energy, so that the electron states are nearly spin degenerate in our heterostructure. In our theoretical discussion we therefore consider tunneling between two coupled spinful modes having some effective intrawire and interwire interaction. To this end, we use Luttinger-liquid formalism, [1] assuming sufficiently low temperature and voltage bias. It is important in our analysis that the measured densities of $|u_1\rangle$ in the UW and $|l_1\rangle$ in the LW happen to match to within several per cent,[3] so that the electronic excitations in the double-wire system are collective across the tunnel barrier as well as within each wire.

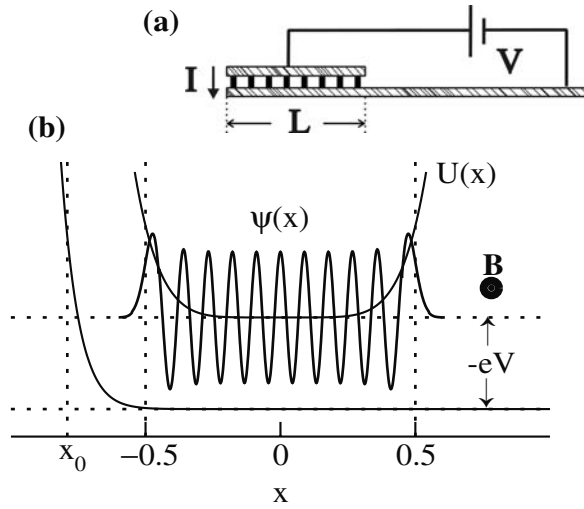


Fig. 3. Schematics of the circuit (a) and the model (b). A wire of length L runs parallel to a semi-infinite wire. The boundary of the upper wire is formed by potential $U(x)$ confining the one-electron wave function $\psi(x)$ along the wire. The energy and momentum of the tunneling electrons are governed by applied voltage V and magnetic field B .

The geometry for our theoretical description is shown in Fig. 3. The potential well $U(x)$ is felt by electrons in the upper quantum wire, which are confined to a region of finite length by potential gates at both ends (see the source region in Fig. 1). One of these gates (g_1) causes the electrons in the lower wire to be reflected at one end, but the other (g_2) allows them to pass freely under it. The effective tunneling region is determined by the length of the upper wire, which is approximately the region $|x| < L/2$ in Fig. 3. The magnetic field, B , gives a momentum boost $\hbar q_B = eBd$ along the x -axis to

the electrons tunneling from the upper to the lower wire. The current (for electrons with a given spin)

$$I = e|\lambda|^2 \int_{-\infty}^{\infty} dx dx' \int_{-\infty}^{\infty} dt e^{iq_B(x-x')} e^{ieVt/\hbar} C(x, x'; t), \quad (1)$$

is determined to lowest order in perturbation theory by the two-point Green function[4]

$$\begin{aligned} C(x, x'; t) &= \left\langle \left[\Psi_l^\dagger \Psi_u(x, t), \Psi_u^\dagger \Psi_l(x', 0) \right] \right\rangle \\ &= G_u^>(x, t; x', 0) G_l^<(x', 0; x, t) - G_u^<(x, t; x', 0) G_l^>(x', 0; x, t). \end{aligned} \quad (2)$$

The last equality in Eq. (2) is valid when the interwire electron-electron interactions vanish. Although it might not be a good approximation for our closely-spaced wires, for pedagogical reasons we will discuss this limit first. One-particle correlators are defined by the usual expressions: $G^>(x, t; x', t') = -i \langle \Psi(x, t) \Psi^\dagger(x', t') \rangle$ and $G^<(x, t; x', t') = i \langle \Psi^\dagger(x', t') \Psi(x, t) \rangle$. For $V > 0$ ($V < 0$), only the $G_u^> G_l^<$ ($G_u^< G_l^>$) term in Eq. (2) contributes to the current (1).

In the LL picture, we can distinguish between the left- and right-moving electronic excitations in a given 1D mode.[1] In long wires, each chirality contributes terms proportional to $e^{\pm ik_F(x-x')}$ to the one-particle Green functions (away from the boundaries), where $k_F = (\pi/2)n$ and n is the electron density in the mode. If the magnetic field is small enough, $q_B \ll k_F$, the edge-state chirality of the electrons cannot be changed during a tunneling event, and the total current is thus a sum of the right-moving and left-moving contributions. It is sufficient to calculate the tunneling rate of the right movers only, since it equals to that of the left movers under the magnetic-field reversal, $B \rightarrow -B$ (so that the total conductance is an even function of B). The corresponding zero-temperature one-particle Green functions for a gapless translation- and spin-rotation-invariant 1D gas of interacting electrons has a universal form

$$\begin{aligned} G^{>, <}(x, t; x', 0) &= \frac{\pm \psi(x) \psi^*(x')}{2\pi \sqrt{(z - v_s t \pm i0^+)(z - v_c t \pm i0^+)}} \times \\ &\quad \left[\frac{r_c}{\sqrt{z^2 - (v_c t \mp i r_c)^2}} \right]^\alpha, \end{aligned} \quad (3)$$

where $v_c = v_F/K$ is the charge-excitation velocity, which is enhanced with respect to the Fermi velocity v_F by electron repulsion, v_s is the spin-excitation velocity, which is close to v_F for vanishing backscattering rate and is determined by the exchange interaction of neighboring electrons for strong repulsion with a sizable backscattering, and $\alpha = (K + K^{-1} - 2)/4$ is a non-universal exponent. $K < 1$ is the compressibility normalized to that of the free-electron gas at the same density, $z = x - x'$, and r_c is a short-distance cut-off. $\psi(x) = e^{ik_F x}$ is the noninteracting-electron wave function for an infinite

wire at the Fermi level. Using Eq. (3) to calculate the two-particle Green function (2) and then performing the integration in Eq. (1), one shows that the interactions do not shift the position of the crossing point at $V = 0$ and $q_B = \Delta k_F$, the mismatch in the Fermi wave vectors of the wires, but are manifested by multiple peaks in the tunneling conductance $G(V, B)$, which intersect at the crossing point with slopes determined by different spin and charge velocities.[4, 5]

It turns out that in a symmetric double-wire structure, the interwire electron-electron interactions, do not change the two-point correlation function (2) apart from renormalizing the parameters entering Eq. (3).[5] The reason for this is that a tunneling event from the UW to the LW at a low magnetic field creates a long-lived exciton across the tunnel-barrier with the electron in the lower and hole in the upper wire, moving in the same direction. The exciton propagates freely, as an acoustic plasmon in a single wire but with the velocity v_c reduced by the electron-hole attraction (corresponding to a larger normalized compressibility K).[7] Similarly, v_s entering Eq. (3) should be thought of as the antisymmetric spin velocity of coupled antiferromagnetic Heisenberg chains, again reducing to v_F in the case of vanishing backscattering. For a symmetric double-wire structure, one therefore expects two velocities to be present at low magnetic-field and bias data: the antisymmetric spin- and charge-excitation velocities. The situation is more complicated at high magnetic fields capable of flipping the electron cleaved-edge chirality: A tunneled particle moves in the direction opposite to the hole left behind, decaying into a combination of symmetric and antisymmetric excitations across the tunnel barrier, even in the case of a perfectly symmetric double wire.[4] We will not discuss this regime here.

One can see a family of measured curves crossing at $V = 0$ and $B \approx 0.1$ T in Fig. 2, which constitute the signal from the $|u_1\rangle \leftrightarrow |l_1\rangle$ tunneling. We also draw in Fig. 2 as black solid lines the expected parabolic dispersions for non-interacting electrons at the same electron densities as $|u_1\rangle$ and $|l_1\rangle$; the white solid lines are generated in a similar way but after rescaling the GaAs band-structure mass, and correspondingly the low-voltage slopes, by a factor of 0.7. Remarkably, for positive voltages, we can fit the three visible experimental curves, a , b , and c , by such parabolas crossing at $V = 0$ with two different slopes. Such a fitting is a naive extrapolation of LL spectrum at small voltages, where the excitation dispersions can be linearized and the two visible low-voltage slopes can be associated with elementary 1D excitations. Understanding the high-voltage regime, where the dispersions acquire a curvature, requires going beyond LL theory, and for that matter beyond the scope of this paper. For negative voltages, fewer $G(V, B)$ peaks are visible after we subtract a large background signal due to the direct 2DEG-1D tunneling; in particular, only one curve, d , is visible for the $|u_1\rangle \leftrightarrow |l_1\rangle$ tunneling, which cannot be fitted by our naive procedure at $V < -10$ mV. It is important to point out that the observed curves a , b , and c in Fig. 2 rule out the noninteracting-electron picture for tunneling between two 1D modes with different Fermi velocities:

If the LW had the higher Fermi velocity, we would expect to see dispersions e and a in Fig. 2, and if the UW had the higher velocity, we would see only b and c , but not three curves.

The curve c slope is given by the Fermi velocity of the noninteracting electron gas, corresponding to the value of the electron density measured in Ref. [3]. The slope of a has the velocity enhanced by a factor of 1.4. Identifying the faster velocity with the charge mode and the slower with the spin mode, we arrive at the following LL parameters characterizing the system: $K \approx 0.7$ and $v_s \approx v_F$. This value of K indicates that the electron-electron interaction energy in the cleaved-edge quantum wires is comparable to the Fermi energy, resulting in a sizable effect on the correlation and thermodynamic properties. The closeness of the spin velocity v_s to the noninteracting Fermi velocity implies a small backscattering rate due to electron repulsion, as expected in our wide quantum wires.[4]

4 Finite-Size Effects

The momentum of the electrons tunneling through a window of finite length L is only conserved within an uncertainty of order $2\pi/L$, resulting in conductance oscillations away from the main dispersion peaks. We show in this section that another spectacular manifestation of spin-charge separation at small voltages can be tracked down in such oscillations, as those forming checkerboard-like patterns near the crossing points of various dispersion curves in Fig. 2a. We zoom into these oscillations in Fig. 4a. In order to understand them in detail, we now generalize our analysis to take into account the finite length of the upper wire.

Assuming that the electron density in each wire varies slowly on the length scale of k_F^{-1} (except for unimportant regions very close to the boundaries), we use the WKB wave function

$$\psi(x) = \frac{e^{ik_F x} e^{-is(x)}}{\sqrt{k(x)}}, \quad (4)$$

where $k(x) = k_F[1 - U(x)/E_F]^{1/2}$ and $s(x) = \int_0^x dx' [k_F - k(x')]$, for right-moving electrons in the UW in Eq. (3). $U(x)$ is the potential formed by the top gates defining the finite length of the UW, see Fig. 3. The right movers in the LW are taken to be propagatory, as in the infinite wire, assuming its left boundary is formed by the gate g_1 in the region where the UW is already depleted and assuming the gate g_2 potential in the LW is well screened. Additional assumptions required for using the WKB wave function (4) in the correlator of a finite interacting wire are discussed in Ref. [7].

Substituting Green functions (3) into integral (1), we obtain for the tunneling current at $V > 0$

$$I \propto \int_{-\infty}^{\infty} dx dx' e^{i(q_B - k_F)(x - x')} \psi_u(x) \psi_u^*(x') h(x - x'), \quad (5)$$

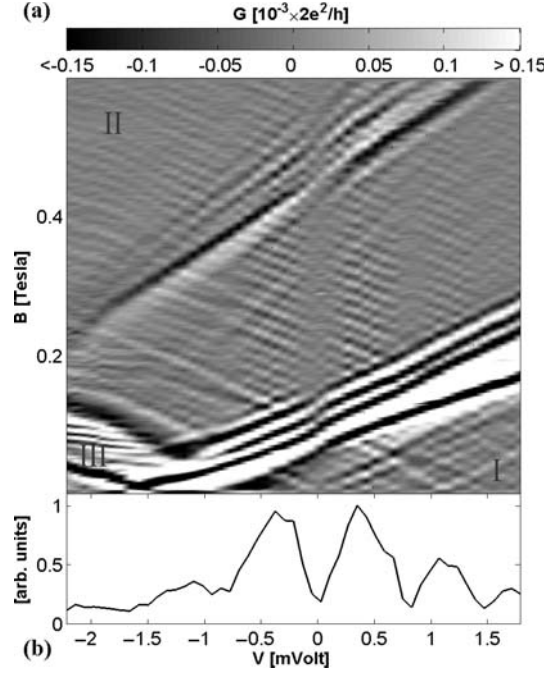


Fig. 4. Nonlinear conductance oscillations at low field from a 6 μm junction. (a) shows the oscillations as a function of both B and V . (A smoothed background has been subtracted to emphasize the oscillations.) The brightest (and darkest) lines, corresponding to tunneling between the lowest modes, break the V - B plain into regions I, II, and III. Additional positively-sloped bright and dark lines in II arise from other 1D channels in the wires and are disregarded in our theoretical analysis. Also present is a slow modulation of the strength of the oscillations along the abscissa. (b) Absolute value of the peak of the Fourier transform of the conductance at a fixed V in region II as a function of V . Its slow modulation as a function of V is easily discerned.

where

$$h(z) = - \int_{-\infty}^{\infty} dt \frac{e^{ieVt/\hbar}}{(z - v_s t + i0^+)(z - v_c t + i0^+)} \left[\frac{r_c^2}{z^2 - (v_c t - ir_c)^2} \right]^\alpha. \quad (6)$$

Here we have taken the two wires to have the same electron density and strength of the interactions. For not very strong interactions, $\alpha \ll 1$, the last term in Eq. (6) can be disregarded, away from the regime of the zero-bias anomaly.[7] The integrand in Eq. (6) then has two simple poles yielding

$$h(z) \approx -2\pi i \frac{e^{ieVz/(\hbar v_s)} - e^{ieVz/(\hbar v_c)}}{(v_c - v_s)(z + i0^+)}. \quad (7)$$

Combining this with Eq. (5), we finally find the differential conductance $G = \partial I / \partial V$:

$$G(V, B) \propto \frac{1}{v_c - v_s} \left[\frac{1}{v_s} |M(\kappa_s)|^2 - \frac{1}{v_c} |M(\kappa_c)|^2 \right], \quad (8)$$

where $\kappa_{s,c} = q_B + \Delta k_F + eV / (\hbar v_{s,c})$ (now including a small mismatch $\Delta k_F = k_{Fu} - k_{Fl}$ in the Fermi wave vectors of the UW and LW, respectively) and

$$M(\kappa) = \int dx \frac{e^{i\kappa x} e^{-is(x)}}{\sqrt{k(x)}} \quad (9)$$

$s(x)$ and $k(x)$ being the same as in Eq. (4). $M(\kappa)$ can be found analytically using the stationary-phase approximation (SPA): $M(\kappa)$ is evaluated near positions x^\pm ($x^+ > x^-$) where $k(x^\pm) = k_F - \kappa$ and the integrand in Eq. (9) has a stationary phase. In the case of a symmetric potential, $U(x) = U(-x)$ (so that, in particular, $x^- = x^+$), the SPA gives

$$M(\kappa) \propto \frac{\Theta(\kappa)}{\sqrt{\partial U(x^+) \partial x}} \cos [\kappa x^+ - s(x^+) - \pi/4], \quad (10)$$

where $\Theta(\kappa)$ is the Heaviside step function. The SPA approximation (10) can be shown to diverge for small values of κ , where we have to resort to a numerical calculation of the integral in Eq. (9). [9] The form of Eq. (10) shows that (1) the conductance is asymmetric in κ , vanishing for $\kappa < 0$ (in the SPA approximation), (2) it oscillates in magnetic field (and similarly in voltage) with period $\Delta q_B = 2\pi/x^+$, assuming x^+ to be a slow-varying function of κ and that (3) it is a superposition of two oscillating patterns in the (V, B) plane, the first (second) being constant-valued along line $\kappa_s = \text{const}$ ($\kappa_c = \text{const}$) and oscillating perpendicular to it, resulting in a moiré structure of $G(V, B)$. [Note that the conductance in Eq. (8) so far only includes the right-movers' contribution. In order to get the total conductance, one has to add the piece which is mirror symmetric to Eq. (8) around $B = 0$.] If the two velocities v_s and v_c are not very different, there are two voltage scales characterizing the conductance oscillation pattern:

$$\Delta V = \frac{2\pi\hbar v_c v_s}{ex^+(v_c + v_s)} \quad \text{and} \quad \Delta V_{\text{mod}} = \frac{\pi\hbar v_c v_s}{ex^+(v_c - v_s)}. \quad (11)$$

ΔV is the period of the “fast” oscillations, which would be present even in the absence of spin-charge separation, and ΔV_{mod} is the distance between consecutive minima in the oscillation power due to the moiré amplitude modulation in the voltage direction. The ratio between these two scales

$$\frac{\Delta V_{\text{mod}}}{\Delta V} = \frac{1}{2} \frac{v_c + v_s}{v_c - v_s} = \frac{1}{2} \frac{1 + v_s/v_c}{1 - v_s/v_c} \quad (12)$$

can be used to experimentally extract the ratio between the two velocities. We find

$$v_s/v_c = 0.67 \pm 0.07, \quad (13)$$

which is independent of the UW length L , while both ΔV and ΔV_{mod} scale roughly as $1/L$. This value is in agreement with the one found in Sec. 3.

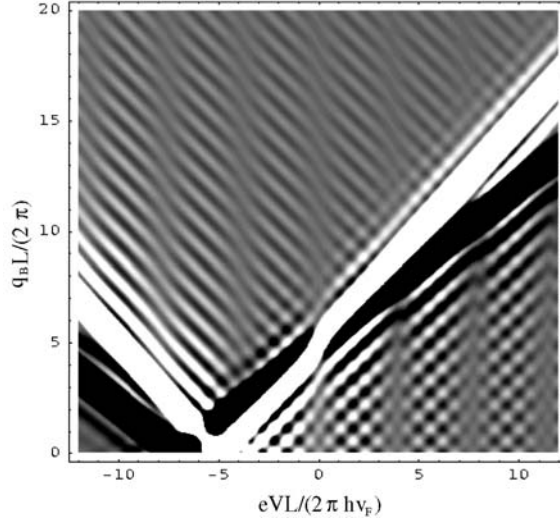


Fig. 5. The differential conductance interference pattern near the lower crossing point calculated using a smooth confining potential for the upper wire. $v_c = 1.4v_F$, $v_s = v_F$, and $\Delta k_F = 10\pi/L$.

Finally, we compare the interference pattern predicted by our theory, Eq. (8), with the experiment, Fig. 4(a). $G(V, B)$ calculated using a smooth confining potential given by $U(x) = E_F \exp[(L/2 - |x|)/10]$ at the boundaries of the upper wire is shown in Fig. 5. Many pronounced features observed experimentally—the asymmetry of the side lobes, a slow fall-off of the oscillation amplitude and period away from the principal peaks, an interference modulation along the V -axis, π phase shifts at the oscillation suppression stripes running parallel to the field axis—are reproduced by the theory. There is however one experimental finding which is not captured by the presented theory: In addition to the periodic modulation of the oscillations, there is an appreciable fall-off in amplitude in the voltage direction, as can be seen in Fig. 4(b). This dephasing can be due to the dispersion curvature which becomes appreciable with increasing voltage bias. Its discussion, however, requires going beyond the linearized LL theory, which we do not attempt here.

5 Conclusions

The two approaches to study the size of spin-charge separation, one by mapping out the dispersions, which are independent of the tunnel-junction length, and the other based on the finite-size conductance oscillations, the frequency of which scales linearly with the junction length, are found to be in excellent agreement, giving the LL parameter $K = v_F/v_c \approx 0.7$ for the antisymmetric (i.e., excitonic) collective charge excitations in the lowest modes of the double-wire structure, and $v_s \approx v_F$ for the antisymmetric spin velocity. Additional, complimentary information about the electron-electron interactions can be extracted by measuring the tunneling density-of-states exponent α in the regime of very small voltage bias and temperature, where the tunneling rate is suppressed as a power law (the so-called LL zero-bias anomaly).[7] We do not discuss this in the present paper.

Acknowledgements.— This work was supported in part by the US-Israel BSF, NSF Grant DMR 02-33773, and by a research grant from the Fufeld Research Fund. YT is supported by the Harvard Society of Fellows and OMA by a grant from the Israeli Ministry of Science.

References

1. For a review see, e.g., J. Voit, Rep. Prog. Phys., **57**, 977 (1994).
2. A. Yacoby, H. L. Stormer, N. S. Wingreen, L. N. Pfeiffer, K. W. Baldwin, and K. W. West, Phys. Rev. Lett. **77**, 4612 (1996).
3. O. M. Auslaender, A. Yacoby, R. de Picciotto, K. W. Baldwin, L. N. Pfeiffer, and K. W. West, Science **295**, 825 (2002).
4. D. Carpentier, C. Peca, and L. Balents, Phys. Rev. B **66**, 153304 (2002).
5. U. Zülicke and M. Governale, Phys. Rev. B **65**, 205304 (2002).
6. R. de Picciotto, H. L. Stormer, A. Yacoby, L. N. Pfeiffer, K. W. Baldwin, and K. W. West, Phys. Rev. Lett. **85**, 1730 (2000).
7. Y. Tserkovnyak, B. I. Halperin, O. M. Auslaender, and A. Yacoby, Phys. Rev. B **68**, 125312 (2003).
8. K. A. Matveev and L. I. Glazman, Phys. Rev. Lett. **70**, 990 (1993).
9. Y. Tserkovnyak, B. I. Halperin, O. M. Auslaender, and A. Yacoby, Phys. Rev. Lett. **89**, 136805 (2002).

Transport of Interacting Electrons through a Double Barrier

I.V. Gornyi^{1,2} and D.G. Polyakov^{1,2}

¹ Institut fuer Nanotechnologie, Forschungszentrum Karlsruhe, 76021 Karlsruhe, Germany polyakov@int.fzk.de

² A.F. Ioffe Physico-Technical Institute, St.Petersburg, 194021, Russia

Summary. We generalize the fermionic renormalization group method to describe analytically transport through a double barrier structure in a one-dimensional system. Focusing on the case of weakly interacting electrons, we investigate thoroughly the dependence of the conductance on the strength and the shape of the double barrier for arbitrary temperature T . Our approach allows us to systematically analyze contributions to the renormalized scattering amplitudes from scales absent for a single impurity, without restricting to the single-resonance model.

1 Introduction

Effects related to the Coulomb interaction between electrons become increasingly prominent in systems of lower spatial dimensionality as their size is made smaller. Recent experimental progress in controlled preparation of nanoscale devices has led to a revival of interest in the transport properties of one-dimensional (1D) quantum wires. A remarkable example of a correlated 1D electron phase is the Luttinger-liquid model (for a review see, e.g., Ref. [1]). In this model, arbitrarily weak interactions ruin the conventional Fermi liquid phenomenology, which leads to the striking transport properties of a Luttinger liquid in the presence of impurities. In particular, even a single impurity yields a complete pinning of a Luttinger liquid with repulsive interactions, which results in a vanishing conductance at zero temperature [2]. In addition to quantum wires, largely similar ideas apply to edge modes in a Hall bar geometry in the fractional quantum Hall regime, which are thought to behave as spatially separated chiral Luttinger liquids. Evidence has recently emerged pointing towards the existence of the Luttinger liquid in metallic single-wall carbon nanotubes [3]. Further technological advances have made possible the

fabrication of low-resistance contacts between nanotubes and metallic leads (see, e.g., Ref. [4] and references therein).

Two striking experimental observations have been reported recently. In Ref. [5], a resonant structure of the conductance of a semiconductor single-mode quantum wire was attributed to the formation (with reduction of electron density by changing gate voltage) of a single disorder-induced quantum dot. In Ref. [6], two barriers were created inside a carbon nanotube in a controlled way with an atomic force microscope. In both cases, the amplitude of a conductance peak G_p as a function of temperature T showed power-law behavior $G_p \propto T^{-\gamma}$ with the exponent γ noticeably different from $\gamma = 1$. The latter is the value of γ expected in the absence of interactions provided T lies in the range $\Gamma \ll T \ll \Delta$, where Γ is the width of a resonance in the transmission coefficient and Δ is the single-particle level spacing. The width of a conductance peak w followed a linear temperature dependence $w \propto T$ in both experiments.

On the theoretical side, resonant tunneling in a Luttinger liquid was studied previously in a number of papers [2, 7, 8]. In particular, the width $\Gamma \propto T^{\alpha_e}$ was shown [7] to shrink with decreasing temperature. The exponent α_e depends on the strength of interaction and describes tunneling into the end of a semi-infinite liquid. The dimensionless peak conductance (in units of e^2/h) obeys $G_p \sim \Gamma/T$ in the above range of T , which indeed leads to a smaller value of $\gamma = 1 - \alpha_e$. Surprisingly, in Ref. [6] both the amplitude G_p and the width w were reported to vanish with decreasing T , in sharp contrast to the non-interacting case. While such behavior is known to be possible for very strong repulsive interaction [7], the required strength of interaction would then be much larger than expected and indeed reported in carbon nanotubes.

It is thus desirable to examine the resonant tunneling in a Luttinger liquid in a broad range of temperature down to $T = 0$ and for various parameters of the barriers. Our purpose in this paper is to analyze transport through a double barrier of arbitrary strength, strong or weak, symmetric or asymmetric, within a general analytical method applicable to all these situations.

2 RG Equations for a Double Barrier

Consider two potential barriers located at $x = 0$ and $x = x_0$ and let the distance x_0 be much larger than the width of each of them. The spatial structure itself yields an energy dependence of the total (describing scattering on both impurities) transmission and reflection amplitudes, $t(\epsilon)$ and $r_{L,R}(\epsilon)$. Specifically, without interaction the energy $\Delta = \pi v_F/x_0$ gives a period of oscillations in the total scattering amplitudes with changing Fermi energy ϵ_F (v_F is the Fermi velocity).

A renormalization group (RG) description of a double barrier requires a generalization of the RG [9] to the case when the bare amplitudes are energy dependent. A question, however, arises if the total amplitudes generated by

RG transformations are expressed in terms of themselves only. The answer depends on the parameter Δ/D_0 , where $D_0 = \min\{\epsilon_F, v_F/d\}$, with d being the radius of interaction. If $\Delta \ll D_0$, the RG transformations generate more terms than are encoded in the total S -matrix, namely the amplitudes to stay inside the dot $A_{\mu,-\mu}(\epsilon)$ and those to escape from the dot to the left(right) $d_{\mu}^{\pm}(\epsilon)$ for right(left)-movers ($\mu = \pm$).

The system of one-loop RG equations for a double barrier reads

$$\frac{\partial t(\epsilon, D)}{\partial l_D} = \hat{I}_{\epsilon'}(\epsilon, D) \left\{ L_+(\epsilon, \epsilon'; D) + \theta(-\epsilon')t(\epsilon, D) \right. \\ \left. [r_R(\epsilon, D)r_R^*(\epsilon', D)\chi_{\epsilon-\epsilon'} + r_L(\epsilon, D)r_L^*(\epsilon', D)] \right\}, \quad (1)$$

$$\frac{\partial r_L(\epsilon, D)}{\partial l_D} = \hat{I}_{\epsilon'}(\epsilon, D) \left\{ L_-(\epsilon, \epsilon'; D) + \theta(\epsilon')r_L(\epsilon', D) + \theta(-\epsilon') \right. \\ \left. [t^2(\epsilon, D)r_R^*(\epsilon', D)\chi_{\epsilon-\epsilon'} + r_L^2(\epsilon, D)r_L^*(\epsilon', D)] \right\}, \quad (2)$$

and similar equations for other amplitudes. Here $l_D = \ln(D_0/D)$ [we introduced D dependent amplitudes],

$$L_{\mu}(\epsilon, \epsilon') = d_{-}^{-}(\epsilon)A_{+-}(\epsilon')d_{-}^{\mu}(\epsilon)(\chi_{\epsilon-\epsilon'} - 1) \\ + d_{+}^{-}(\epsilon)A_{-+}(\epsilon')d_{+}^{\mu}(\epsilon)(1 - \chi_{\epsilon'-\epsilon}), \quad (3)$$

$$\hat{I}_{\epsilon'}(\epsilon, D)\{\dots\} = -\frac{\alpha}{2 \ln \Lambda} \left[\int_D^{\Lambda D} + \int_{-\Lambda D}^{-D} \right] \frac{d\epsilon'}{\epsilon - \epsilon'} \{\dots\}, \quad (4)$$

$\Lambda \gg 1$ is restricted by the condition $\alpha \ln \Lambda \ll 1$ with α being the parameter characterizing the strength of the interaction, and $\chi_{\epsilon} = \exp(2\pi i\epsilon/\Delta)$.

3 Results

Integrating Eqs. (1),(2) we get renormalized transmission amplitudes and then obtain the amplitude $[G_p(T)]$ and the shape [width $w(T)$] of the conductance peak $G(\epsilon_0, T)$ by using the Landauer formalism (ϵ_0 is the resonance energy counted from ϵ_F).

For strong barriers (the bare transmission through the barriers may be high, but we assume that the barriers get strong before the RG flow parameter D equals Δ) we have a sharp peak of the transmission probability centered at $\epsilon = \epsilon_0$ whose width is $\max\{D_s, \Gamma(T)\} \ll \Delta$, where $D_s = \Gamma(\Delta)(D_s/\Delta)^{\alpha}$ is the zero- T width, $\Gamma(T) = \Gamma(\Delta)(T/\Delta)^{\alpha}$, and $\Gamma(\Delta)$ is determined by the renormalization on scales $\Delta < D < D_0$.

For $T \gg D_s$, the shape of the conductance peak is given by

$$G(\epsilon_0, T) = \frac{\zeta G_p}{\cosh^2(\epsilon_0/2T)}, \quad (5)$$

where the peak value of the conductance

$$G_p = \pi\lambda\Gamma(T)/8T, \quad (6)$$

with $\zeta = (\max\{|\epsilon_0|, T\}/T)^\alpha$ and $\lambda = 4\Gamma_1\Gamma_2/\Gamma^2(\Delta)$ ($\Gamma_{1,2}$ are the renormalized transmission rates for individual barriers at $D = \Delta$). The width of the conductance peak w is of order T , as for noninteracting electrons; however, the power-law behavior of $G_p(T)$ is seen to be modified by interaction, in accordance with the results derived in Ref. [7]. Note that the scaling of $G_p \propto T^{\alpha-1}$ is proportional to the single-particle density of states for tunneling into the end of a Luttinger liquid.

Let us now turn to low temperatures $T \ll D_s$, where processes of all orders in the tunneling amplitudes are important. Consider first the symmetric case: the shape of the conductance peak is a Lorentzian:

$$G(\epsilon_0, T) = \frac{\Gamma^2(T)}{\Gamma^2(T) + 4\epsilon_0^2}. \quad (7)$$

We see that $G_p = 1$ and

$$w = D_s(T/D_s)^\alpha \quad (8)$$

exhibits a power-law T dependence with an exponent depending on the strength of interaction. The vanishing of w as $T \rightarrow 0$ should be contrasted with the behavior of the transmission probability peak, whose width is D_s for low T . In the limit $T \rightarrow 0$, the conductance peak becomes infinitely narrow but the resonance at $\epsilon_0 = 0$ persists down to $T = 0$, in accordance with Ref. [2].

The renormalization in the asymmetric case is governed by the scale $D_- = D_s[|I_1 - I_2|/\Gamma(\Delta)]^{1/\alpha}$ which describes the degree of asymmetry. For $T \gg D_-$ the conductance is given by Eq. (7) for symmetric barriers with an overall factor of λ . For $T \ll D_-$ the transmission at ϵ_F falls off with decreasing T . As a result,

$$G(\epsilon_0, T) = \frac{\lambda(T/D_s)^{2\alpha}}{(D_-/D_s)^{2\alpha} + (2\epsilon_0/D_s)^2}, \quad (9)$$

which gives

$$G_p = \lambda \left(\frac{T}{D_-} \right)^{2\alpha}, \quad w = D_s \frac{|I_1 - I_2|}{\Gamma(\Delta)}. \quad (10)$$

Thus, G_p goes down as $T \rightarrow 0$, whereas w does not depend on T any longer.

Naively one could think that scattering on weak barriers cannot possibly yield a sharp peak in $G(\epsilon_0, T)$. Indeed, the transmission probability as a function of ϵ does not have any peak at $\epsilon = \epsilon_0$, in contrast to the case of resonant tunneling. At high T , $G(\epsilon_0, T)$ is a weakly oscillating (with a period Δ) function of ϵ_0 . The only difference with the non-interacting case is an enhanced amplitude of the oscillations. In fact, however, the interaction-induced vanishing of the transmission probability at ϵ_F for $T = 0$ does lead to a narrow Lorentzian peak of $G(\epsilon_0, T)$, provided that T is low enough and the barriers are not too asymmetric.

The thermal averaging of the transmission probability obtained from the RG equations (1),(2) for symmetric barriers yields

$$G(\epsilon_0, T) = \left[1 + \left(\frac{2\pi\epsilon_0}{\Delta} \right)^2 \left(\frac{D_r}{T} \right)^{2\alpha} \right]^{-1}, \quad (11)$$

which indeed describes a Lorentzian peak with the height $G_p = 1$ and the width

$$w = \frac{\Delta}{\pi} \left(\frac{T}{D_r} \right)^\alpha, \quad (12)$$

where $D_r = D_0 R^{1/2\alpha}$, $R = R_{1,2}$ is the bare reflection probability of individual barriers. The peak is narrow, $w \ll \Delta$, provided that $T \ll D_r$. In the limit $T \rightarrow 0$, the width of the peak is infinitesimally small.

Introducing a weak asymmetry $R_- = |R_1 - R_2| \ll R \simeq R_{1,2}$, we get for $T \ll \delta_- = D_r(R_-/2R)^{1/\alpha}$:

$$G(\epsilon_0, T) = \frac{R^2(T/D_r)^{2\alpha}}{R_-^2/4 + R^2(2\pi\epsilon_0/\Delta)^2}. \quad (13)$$

The height and the width of the peak are

$$G_p = \left(\frac{T}{\delta_-} \right)^{2\alpha}, \quad w = \frac{\Delta R_-}{2\pi R}. \quad (14)$$

Thus, the asymmetry leads to vanishing G_p at $T \rightarrow 0$ and the width is seen to saturate with decreasing T , similarly to Eq. (10). It is worth noting that the dependence of G_p on T is non-monotonic: $G_p \propto T^{2\alpha}$ grows with increasing T for $T \ll \delta_-$, continues to grow in the range $\delta_- \ll T \ll w$ according to $1 - G_p \propto T^{-2\alpha}$, but goes down for $w \ll T \ll \Delta$, where the correction behaves similarly to the case of symmetric barriers, $1 - G_p \propto T^{2(1-\alpha)}$. The conductance peak is narrow provided the asymmetry is weak. If the asymmetry is strong, the peak is completely destroyed.

4 Conclusions

In conclusion, we have thoroughly studied transport of weakly interacting spinless electrons through a double barrier. We have described a rich variety of different regimes depending on the strength of the barrier, its shape, and temperature [10]. We have developed a fermionic RG approach to the double barrier problem, which has enabled us to treat on an equal footing both the resonant tunneling and resonant transmission through weak impurities. In the latter case, we have demonstrated how the interaction-induced renormalization in effect creates a quantum dot with tunneling barriers with a pronounced resonance peak structure. Moreover, we have shown that even

very weak impurities, for which the renormalized transmission coefficient does not exhibit any peak, may give a sharp peak in the conductance as a function of gate voltage, provided that the double barrier is only slightly asymmetric. In contrast, the resonant structure is shown to be completely destroyed for a strongly asymmetric barrier. All the regimes we have studied may be characterized by three different types of behavior of the conductance peak height G_p and the peak width w on temperature T : (i) for high T , $G_p \propto T^{\alpha-1}$ and $w \propto T$; (ii) for lower T , depending on the shape of the barrier (whether it is symmetric or asymmetric), either G_p does not depend on T and $w \propto T^\alpha$ or (iii) $G_p \propto T^{2\alpha}$ and w is constant.

One can see that none of the regimes (i-iii) supports $G_p \propto T^{2\alpha-1}$ and $w \propto T$, as proposed in Ref. [6]. Further experiments would be useful to resolve the puzzle. Including spin and generalizing to the case of several channels (possibly with different Fermi wavevectors) within the framework of the present approach warrant further study.

Acknowledgements. — We thank V.V. Cheianov, F. Evers, L.I. Glazman, D.L. Maslov, A.D. Mirlin, Yu.V. Nazarov, and P. Woelfle for interesting discussions. This work was supported by SFB 195 and the Schwerpunktprogramm “Quanten-Hall-Systeme” of DFG, by GIF, and by RFBR.

References

1. J. Solyom, Adv. Phys. **28**, 201 (1979); J. Voit, Rep. Prog. Phys. **57**, 977 (1994).
2. C.L. Kane and M.P.A. Fisher, Phys. Rev. B **46**, 15233 (1992).
3. M. Bockrath *et al.*, Nature **397**, 598 (1999); Z. Yao *et al.*, Nature **402**, 273 (1999).
4. Z. Yao *et al.*, Phys. Rev. Lett., **84**, 2941 (2000); J. Nygard *et al.*, Nature **408**, 342 (2000); M. Bockrath *et al.*, Science **291**, 283 (2001); R. Krupke *et al.*, Appl. Phys. A **76**, 397 (2003).
5. O.M. Auslaender *et al.*, Phys. Rev. Lett. **84**, 1764 (2000).
6. H.W.Ch. Postma *et al.*, Science **293**, 76 (2001).
7. A. Furusaki and N. Nagaosa, Phys. Rev. B **47**, 3827 (1993); A. Furusaki, *ibid.* **57**, 7141 (1998).
8. Yu.V. Nazarov and L.I. Glazman, Phys. Rev. Lett. **91**, 126804 (2003).
9. K.A. Matveev, D. Yue, and L.I. Glazman, Phys. Rev. Lett. **71**, 3351 (1993); Phys. Rev. B **49**, 1966 (1994).
10. D.G. Polyakov and I.V. Gornyi, Phys. Rev. B **68**, 035421 (2003).

Ratchet Effects in Luttinger Liquids

D.E. Feldman^{1,2}, S. Scheidl³, and V.M. Vinokur⁴

¹ Department of Physics, Brown University, 182 Hope Street, Providence, RI 02912, USA

² Landau Institute for Theoretical Physics, Chernogolovka, Moscow region 142432, Russia Dima_Feldman@physics.brown.edu

³ Institut für Theoretische Physik, Universität zu Köln, Zùlpicher Strasse 77, 50937 Köln, Germany

⁴ Materials Science Division, Argonne National Laboratory, 9700 South Cass, Argonne, Illinois 60439, USA

Summary. We investigate the rectification of an ac bias in Luttinger liquids in the presence of an asymmetric potential (the ratchet effect). We show that strong repulsive electron interaction enhances the ratchet current in comparison with Fermi liquid systems, and the dc $I - V$ curve is strongly asymmetric in the low-voltage regime even for a weak asymmetric potential. At higher voltages the ratchet current exhibits an oscillatory voltage dependence.

1 Introduction

Asymmetric conductors have asymmetric $I - V$ curves. This phenomenon is known as the diode or ratchet effect and plays a major role in electronics. Recently much interest has been attracted by transport asymmetries in single-molecule devices and other mesoscopic systems [1]. The idea that asymmetric molecules can be used as rectifiers is rather old [2], however, it was implemented experimentally [3] only recently. Another experimental realization of a mesoscopic rectifier is an asymmetric electron waveguide constructed within the inversion layer of a semiconductor heterostructure [4]. The ratchet effect was observed in carbon nanotubes [5], and strongly asymmetric $I - V$ curves were recently reported for the tunneling in the quantum Hall edge states [6]. These experimental advances have stimulated much theoretical activity [7, 8, 9, 10, 11] with the main focus on the simplest Fermi-liquid systems [12].

Transport in one-channel quantum wires, where electrons form a Luttinger liquid, differs significantly from the Fermi liquid case. In particular, impurity effects are stronger in Luttinger liquids, and even a weak impurity potential

may render the linear conductance zero at low temperatures [13]. In this Letter we investigate the ratchet effect in Luttinger liquids. We show that strong repulsive electron interaction enhances the ratchet current, and the low-voltage part of the $I - V$ curve is strongly asymmetric even in quantum wires with weak asymmetric potentials.

We consider the ratchet effect in the presence of a weak asymmetric potential $U(x) \ll E_F$, where E_F is the band width. We calculate the ratchet current $I_r(V) = [I(V) + I(-V)]/2$ for a one-channel quantum wire with spin-polarized electrons. The ratchet current vanishes for systems with symmetric $I - V$ curves. It can be measured as the dc response to a low-frequency square voltage wave of amplitude V . First, we consider voltages $V < V_0 = \hbar v_F / (ea)$, where v_F is the Fermi velocity, e the electron charge, and a the size of the region containing the asymmetric potential. We find a weak ratchet effect in the interval $eV_0 > eV > \sqrt{UE_F}$ for both Fermi and Luttinger liquids, $I_r \sim (e/h)U^2(eV)^{2g}/E_F^{2g+1}$, where $g = 1$ for Fermi liquids and $g < 1$ for Luttinger liquids with repulsive interaction. However, at strong repulsive interaction (the Luttinger liquid parameter $g \ll 1$) and sufficiently low voltages, the ratchet current $I_r(V)$ grows as the voltage decreases until $I_r(V)$ becomes comparable with the total current $I(V)$ at $eV = eV^* \sim (UE_F^{-g})^{1/(1-g)}$. At $E_F \gg eV > eV_0$ the ratchet current oscillates as a function of the voltage and can become comparable with the total current $I(V)$ for any repulsive interaction strength. We also briefly discuss the ratchet effect in the presence of a strong asymmetric potential $U > E_F$. The complicated ratchet-current behavior is caused by the energy dependence of the effective impurity strength in Luttinger liquids [13]. This introduces an additional energy scale V^* absent in Fermi-liquid systems.

2 Model

One-channel quantum wires can be described by the Tomonaga-Luttinger model with the Hamiltonian

$$H = \int dx \left\{ -\hbar v_F [\psi_R^\dagger(x) i \partial_x \psi_R(x) - \psi_L^\dagger(x) i \partial_x \psi_L(x)] + U(x) \rho(x) + \int dy K(x-y) \rho(x) \rho(y) \right\}, \quad (1)$$

where ψ_R^\dagger and ψ_L^\dagger are the creation operators for right- and left-moving electrons, $\psi^\dagger = \psi_R^\dagger + \psi_L^\dagger$ gives the conventional electron creation operator, $\rho = \psi^\dagger \psi$ is the electron density, $U(x)$ is the asymmetric potential, and $K(x-y)$ the interaction strength. Our aim is to calculate the current I as a function of the applied voltage V . We assume that the long-range Coulomb interaction is screened by the gates so that $K(x-y)$ decreases rapidly for large $(x-y)$. Electric fields of external charges are also assumed to be screened. Thus, the

applied voltage reveals itself only as the difference of the electrochemical potentials E_L and E_R of the particles injected from the left and right reservoirs.

We assume that one lead is connected to the ground so that its electrochemical potential $E_R = E_F$ is fixed. The electrochemical potential of the second lead $E_L = E_F + eV$ is controlled by the voltage source. In such situation a symmetric potential $U(x)$ is sufficient for rectification. For example, in a non-interacting system $I(V) \sim \int_{E_R}^{E_L} [1 - R(E)] dE$, where $R(E)$ is the reflection coefficient. If the only relevant scale for the energy dependence of the reflection probability is the band width $\sim E_F$ then the ratchet current $I_r \sim \int_0^{eV} dE [R(E_F - E) - R(E_F + E)] \approx -2 \int_0^{eV} dE R'(E_F) E \sim R(E_F) (eV)^2 / E_F \sim U^2 (eV)^2 / E_F^3$ for small U and V , and any coordinate dependence $U(x)$.

A ‘not-trivial’ ratchet effect can be observed when the injected charge density is voltage-independent, $E_{L/R} = E_F \pm eV/2$. Symmetry considerations require an asymmetric $U(x)$ for a non-vanishing ratchet current in this case. Also an electron interaction must be present. Indeed, for free particles the reflection coefficient $R(E)$ is independent of the electron propagation direction [14] and hence $I(V) = -I(-V)$.

The ‘non-trivial’ ratchet effect is absent in the first two orders in $U(x)$. Indeed, in the lowest two orders the ratchet current $I_r^{(1,2)} = \int dx C(x) U(x) + \int dx dy D(x, y) U(x) U(y)$. $I_r^{(1,2)}$ must be zero for any symmetric potential. Substituting $U(x) = U \delta(x - x_0)$ we find that $C(x_0), D(x_0, x_0) = 0$. Substituting $U(x) = U \delta(x - x_1) + U \delta(x - x_2)$ we see that $D(x_1, x_2) + D(x_2, x_1) = 0$. Hence, $I_r^{(1,2)} = 0$ for any $U(x)$.

3 Hartree picture

We first consider the ‘non-trivial’ ratchet effect and then check what changes after the voltage dependence of the injected charge density is taken into account. Let us begin with a qualitative explanation before we make a rigorous calculation. The origin of the ratchet current can be understood from a simplified Hartree-Fock picture. In this approximation, electrons are backscattered off a combined potential $\tilde{U}(x) = U(x) + W(x)$, where $W(x)$ is a self-consistent electrostatic potential created by the average local charge density. To obtain $W(x)$ we use the following approximation in the last term of Eq. (1): $\rho(x)\rho(y) \approx (\psi_R^\dagger(x)\psi_R(x) + \psi_L^\dagger(x)\psi_L(x))(\psi_R^\dagger(y)\psi_R(y) + \psi_L^\dagger(y)\psi_L(y)) + [\langle \rho(x) \rangle \psi_R^\dagger(y)\psi_L(y) + \langle \rho(y) \rangle \psi_R^\dagger(x)\psi_L(x) + h.c.] + \text{const}$. Thus, the relation between W and ρ is linear. The combined potential $\tilde{U}(x)$ is different for the opposite voltage signs.

In the model (1) the electron interaction is short-ranged due to the screening gates, and hence, the relation between the potential $W(x)$ and the electron density $\rho(x)$ is local, $W(x) \sim \rho(x)$. The simplest choice of $U(x)$ is a two-impurity asymmetric potential $U(x) = U_1 \delta(x + a/2) + U_2 \delta(x - a/2)$. The charge density profile [16] in the presence of a two-impurity potential and

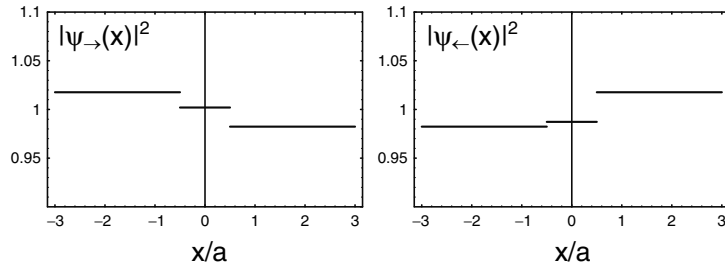


Fig. 1. Density profiles averaged over the period of Friedel oscillations for a potential with $U_1 < U_2$. The averaged densities show drops at the impurity positions. The amplitudes of the density drops depend on the direction of the incident wave.

the voltage drop V is sketched in Fig. 3. Depending on the voltage sign, the charge density decreases or grows as a function of the coordinate x . So does the electrostatic potential $W(x)$. Hence, $\tilde{U}(x)$ is different for the opposite voltage signs. The density is essentially independent of the coordinate between the impurities [16], as well as on the left and on the right of the impurities, since no backscattering occurs in those regions. The charge density and the electrostatic potential drop at the positions of the impurities. The magnitude of a drop is proportional to the electric charge backscattered off the impurity. Indeed, if the incident charge densities of the electrons approaching the impurity from the left and from the right are ρ_L^\rightarrow and ρ_R^\leftarrow , and the backscattered charge densities are ρ_L^\leftarrow and ρ_R^\rightarrow then the density drop across the impurity $\Delta\rho = (\rho_L^\rightarrow + \rho_L^\leftarrow + \rho_R^\leftarrow - \rho_R^\rightarrow) - (\rho_R^\leftarrow + \rho_R^\rightarrow + \rho_L^\rightarrow - \rho_L^\leftarrow) = 2(\rho_L^\leftarrow - \rho_R^\rightarrow) \sim I_{\text{bs}}$, where I_{bs} is the current backscattered off the impurity. Thus $W(x) = \tilde{U} - U \sim I_{\text{bs}}$. From Ref. [13] we know that for a weak potential U

$$I_{\text{bs}} \sim |U_{2k_F}|^2 |V|^{2g-1} \text{sign} V / E_F^{2g}, \quad (2)$$

where $U_{2k_F} \sim k_F \int dx \exp(2ik_F x) U(x)$, k_F is proportional to the mean electron density, and the dimensionless constant g characterizes the interaction strength, $g = 1$ for non-interacting electrons (in which case $W(x) = 0$).

Now we can substitute the renormalized potential $\tilde{U} = U + W$ for U in Eq. (2). The Fourier component W_{2k_F} is different for the opposite voltage signs. Hence, we obtain the asymmetric part of the $I - V$ characteristics $I_r \sim eU^3 |eV|^{4g-2} / (hE_F^{4g})$. The ratchet effect is strongest for $g \rightarrow 0$ when the ratchet current grows as the voltage decreases.

4 Bosonization

The above Hartree-Fock argument provides a qualitatively correct picture at small g but underestimates fluctuations in Luttinger liquids. As shown below, the ratchet current growth at small voltages differs from our estimate:

$I_r \sim U^3|V|^{6g-2}$, $E_F \gg V > V^* \sim (UE_F^{-g})^{1/(1-g)}$, $g \ll 1$. We will see that the growth terminates at $V = V^*$. At such voltage $I_r(V^*)/I(V^*) \sim [(V^*)^{3g+1}/E_F^{3g}]/[V^*] \sim (V^*/E_F)^{3g} \sim 1$ as $g \ll 1$. Fluctuations are less important in many-channel systems and the Hartree-Fock picture gives exact results for some two-channel systems and for Fermi liquids [15].

We use the bosonization technique [17] to calculate the ratchet current. After an appropriate rescaling of the time variable, the system can be described by the action [13]

$$S = \int dt dx \left\{ \frac{1}{8\pi} [(\partial_t \Phi)^2 - (\partial_x \Phi)^2] - \delta(x) \sum_{n \geq 1} 2\tilde{U}_{2nk_F} \cos(n\sqrt{g}\Phi + \alpha_n) \right\}, \quad (3)$$

where the bosonic field Φ is related to the charge density as $\rho = e(\sqrt{g}\partial_x \Phi + 2k_F)/(2\pi)$, and $\tilde{U}_{2nk_F} \exp(i\alpha_n)$ are of the order of the Fourier components of the asymmetric potential, $k_F \int \exp(2ink_F x) \tilde{U}(x) dx$. We assume that the charge density $\sim k_F$ is independent of the voltage. The operator $\cos(n\sqrt{g}\Phi + \alpha_n)$ describes scattering events involving n electrons. We assume that $\alpha_1 = 0$. Indeed, we can always set $\alpha_1 = 0$ by a constant shift of the bosonic field Φ . For a general asymmetric potential, α_n with $n > 1$ remain non-zero after this shift. On the other hand, for a symmetric potential $U(x) = U(-x)$ all $\alpha_n = 0$. In most problems it is sufficient to keep only the $n = 1$ term. The $n = 2$ contribution is relevant in the theory of resonant transmission in Luttinger liquids [13]. This term is also important for the ratchet effect.

We use the standard model [18, 19, 20] for Fermi-liquid leads adiabatically connected to the wire. We assume that the action (3) is applicable for $|x| < L$ only. At large $|x|$ the interaction strength $K(x-y)$, Eq. (1), is zero. This model can be interpreted as a quantum wire with electron interaction completely screened by the gates near its ends. Electric fields of external charges are assumed to be screened in all parts of the wire. A simple modification of this model describes electrically neutral leads [20]. All results coincide for our set-up and the model [20].

The current injected from the non-interacting 1D regions is given by the Landauer formula $I_0 = e^2 V/h$ [18]. Indeed, left-/right-movers entering the non-interacting region from the central part of the wire cannot affect the current of right-/left-movers in the non-interacting region. Hence, the current of right-/left-moving particles in the left/right non-interacting region is determined by the chemical potential of the left/right reservoir. The total current is the sum [19, 20] of the injected current and the current backscattered off the asymmetric potential: $I = I_0 + I_{\text{bs}}$. Only I_{bs} contributes to the ratchet effect. To find the backscattered current we employ the Keldysh formalism [21]. We assume that at $t = -\infty$ there is no backscattering in the Hamiltonian, and then the backscattering is gradually turned on. Thus, at the initial moment of time the numbers N_L and N_R of left- and right-moving electrons conserve separately. Hence, at $t = -\infty$ the system can be described by a partition function with two chemical potentials $\mu_R = E_F$ and $\mu_L = E_F + eV$ conjugated with

the particle numbers N_R and N_L . This initial state determines bare Keldysh Green functions.

We will consider only zero temperature. It is convenient to switch [19] to the interaction representation $H \rightarrow H - \mu_R N_R - \mu_L N_L$. This transformation induces time dependence in the electron creation and annihilation operators. As a result, $\sum_n 2\tilde{U}_{2nk_F} \cos(n\sqrt{g}\Phi + \alpha_n)$ in the action should be modified as $\sum_n 2\tilde{U}_{2nk_F} \cos(n\sqrt{g}\Phi + \alpha_n + nA(t))$, where $A(t) = eVt/\hbar$ [13, 19, 20]. The backscattered current operator equals [13, 20]

$$I_{\text{bs}}(t) = dN_L/dt = i[H, N_L]/\hbar = -\delta S/\delta A(t), \quad (4)$$

where we omit dimensional factors such as e , \hbar , and v_F for brevity. We need to calculate

$$\langle \hat{I}_{\text{bs}}(t=0) \rangle = \langle 0|S(-\infty; 0)\hat{I}_{\text{bs}}(0)S(0; -\infty)|0 \rangle, \quad (5)$$

where $|0\rangle$ denotes the initial state and S is the evolution operator. In the weak impurity case this can be done with the perturbation theory in \tilde{U}_{2nk_F} using the bare Green function [17] $\langle 0|\Phi(t_1, x_1=0)\Phi(t_2, x_2=0)|0 \rangle = -2\ln(\delta + i[t_1 - t_2])$, where δ is an infinitesimal positive constant.

If all $\alpha_k = 0$ then the ratchet current is zero. Indeed, at $\alpha_k = 0$ the action (3) is invariant under the transformation $\Phi \rightarrow -\Phi$, $V \rightarrow -V$ while the current operator (4) changes its sign. As discussed above, for an asymmetric potential we expect $\alpha_2 \neq 0$. Then a ratchet current I_r emerges in the order $\tilde{U}_{2k_F}^2 \tilde{U}_{4k_F}$. Before the calculation of I_r let us determine its voltage dependence with a heuristic argument similar to Ref. [13]. As one changes the energy scale E , the backscattering amplitudes \tilde{U}_{2nk_F} in the action (3) scale as $\tilde{U}_{2nk_F}(E) \sim \tilde{U}_{2nk_F} E^{n^2 g - 1}$ [13]. This renormalization stops at the energy scale V . Assuming that a scattering matrix approach could be applied for an estimation of the current, we write $I_{\text{bs}}(V) \sim V R_{\text{eff}}(V)$, where $R_{\text{eff}}(E) = \sum \text{const} \tilde{U}_{2nk_F}^2(E) + \sum \text{const} \tilde{U}_{2nk_F}(E) \tilde{U}_{2mk_F}(E) \tilde{U}_{2lk_F}(E) + \dots$ is an effective reflection coefficient. Quadratic terms do not contribute to the ratchet current. The leading contribution emerges in the order $\tilde{U}_{2k_F}^2 \tilde{U}_{4k_F}$. One gets $I_r \sim V \tilde{U}_{2k_F}^2(V) \tilde{U}_{4k_F}(V) \sim V^{6g-2}$. Below we obtain the same result rigorously from Eqs. (4,5).

Expanding Eq. (5) to the order $\tilde{U}_{2k_F}^2 \tilde{U}_{4k_F}$ gives

$$I_r = 2 \sin \alpha_2 \tilde{U}_{2k_F}^2 \tilde{U}_{4k_F} \left\{ \int_{-\infty}^0 dt_1 \int_{-\infty}^{t_1} dt_2 \cos(Vt_1 - 2Vt_2) P(t_1, t_2, t_2 - t_1) \right. \\ \left. + \int_{-\infty}^0 dt_1 \int_{t_1}^0 dt_2 \cos(Vt_1 - 2Vt_2) P(t_1, t_2, t_1 - t_2) \right.$$

$$\begin{aligned}
& - \int_{-\infty}^0 dt_1 \int_{-\infty}^0 dt_2 \cos(Vt_1 - 2Vt_2) P(-t_1, t_2 - t_1, t_2) \\
& - 2 \int_{-\infty}^0 dt_1 \int_{-\infty}^{t_1} dt_2 \cos(Vt_1 + Vt_2) P(t_2 - t_1, t_1, t_2) \\
& + \int_{-\infty}^0 dt_1 \int_{-\infty}^0 dt_2 \cos(Vt_1 + Vt_2) P(t_2 - t_1, -t_1, t_2) \Big\} + c.c., \quad (6)
\end{aligned}$$

where $P(t, s, q) = (\delta - it)^{2g} (\delta - is)^{-4g} (\delta - iq)^{-4g}$. Dimensional analysis shows that $I_r \sim V^{6g-2}$ in agreement with our previous estimate. It is convenient to change variables in the integrals with $\cos(Vt_1 - 2Vt_2)$ as $\tau_1 = t_2 - t_1$, $\tau_2 = t_2$. Then after tedious but straightforward manipulations Eq. (6) can be represented as

$$I_r = 2 \sin \alpha_2 \tilde{U}_{2k_F}^2 \tilde{U}_{4k_F} \left\{ \int_{-\infty}^{\infty} dt d\tau \cos[V(\tau - t)] P(-(t + \tau), -\tau, -t) - \int_{-\infty}^{\infty} dt d\tau \cos[V(\tau + t)] P(\tau - t, \tau, t) \right\}. \quad (7)$$

The first integral in (7) is zero as seen from the location of the branching points of the function P . The second integral yields

$$I_r = - \sin \alpha_2 \tilde{U}_{2k_F}^2 \tilde{U}_{4k_F} \cos(\pi g) \frac{2^{2+2g} \pi^{3/2} \Gamma(g + 1/2)}{\Gamma(4g) \Gamma(3g)} |V|^{6g-2}. \quad (8)$$

This expression becomes 0 at $g = 1/2$. We also get a zero ratchet current for non-interacting electrons, $g = 1$, because the Hamiltonian (1) is quadratic in Fermi-operators in the non-interacting case and hence no operators which backscatter more than one electron can appear, $\tilde{U}_{4k_F} = 0$.

At small g the ratchet current (8) is proportional to a negative power of the voltage. This means an unusual behavior: the dc response to an ac voltage grows as the ac voltage decreases.

So far we ignored the voltage dependence of the injected charge density. At $g \ll 1$, Eq. (8) gives the main contribution to the ratchet current only for $eV < \sqrt{UE_F}$. For g close to 1 the result (8) is always exceeded by another contribution. This contribution emerges in the second order in U and is related to the voltage dependence of the injected charge density. The density is proportional to k_F which enters the expression for U_{2k_F} in Eq. (2). At small $V \ll E_F$ the correction [22] to U_{2k_F} is a linear function of V . The substitution of this correction into Eq. (2) gives an additional ratchet current

$$I_r^{(\text{density})} \sim \frac{eU_{2k_F}^2 (eV)^{2g}}{hE_F^{2g+1}}. \quad (9)$$

For $g > 1/3$ and $V > V^*$ the contribution (9) always exceeds (8). At $g < 1/3$ the current (9) is greater than (8) above a threshold voltage that depends on U and g . As we already discussed, I_r (8) is comparable with the total current $I(V) \sim e^2V/h$ at small g near the border of the perturbatively accessible region $UV^{g-1}/E_F^g < 1$. On the other hand, Eq. (9) provides only a small correction to the total current for any g . Still a repulsive interaction of any strength enhances the ratchet effect as seen from the comparison of the current (9) for $g < 1$ and for the non-interacting case $g = 1$.

What happens beyond the perturbative region when $V < V^* \sim U^{1/(1-g)}$? As the energy scale decreases the effective impurity strength grows. Hence, we need to consider a strong $U > E_F$ limit. In this limit we have a weak tunneling between the left and right halves of the wire. The current $I(V) \sim t^2V^{(2/g)-1}/E_F^{2/g}$, where t is the tunneling amplitude [13]. Inserting the voltage dependence of the tunneling amplitude in the expression above we estimate $I_r(V) \sim V^{2/g}$.

A single impurity model (3) can be used only when the potential $U(x)$ is confined in a small space region of size $a < a_V \sim \hbar v_F/(eV)$. If the potential changes slowly at the scales $x > a_V \gg 1/k_F$ it cannot backscatter electrons since backscattering involves high momentum transfers, $\Delta k \geq k_F$. Interesting interference effects are possible for a two-impurity potential $U_1\delta(x) + U_2\delta(x-a)$ and other $U(x)$ which significantly change at the scale $1/k_F$ but are non-zero in a region of size $a \sim a_V$. In the two-impurity case the current oscillates as a function of the voltage bias [23]. For $U_1, U_2 \ll E_F$, $I - e^2V/h \sim [U_1^2 + U_2^2 + 2U_1U_2 \cos(2k_F a)H(geVa/[\hbar v_F])]|V|^{2g-1} \text{sign}V$, where $H(x) = \sqrt{\pi}\Gamma(2g)J_{g-1/2}(x)/[\Gamma(g)(2x)^{g-1/2}]$ and $J_{g-1/2}(x)$ is the Bessel function of the first kind [23]. The main contribution to the ratchet current at $a \sim a_V$ comes from the shift of k_F due to the change of the electrochemical potential of the left reservoir by eV . From the minimum of the quadratic part of the bosonized Hamiltonian one finds the charge density shift [24]. This gives $k_F = k_F^{(0)} + g^2eV/(2\hbar v_F)$. After the substitution to the expression for the total current I we find

$$I_r(V) \sim U_1U_2 \sin(2k_F^{(0)}a)|V|^{2g-1} \sin(g^2e|V|a/[\hbar v_F])H(geVa/[\hbar v_F]) \quad (10)$$

Thus, $I_r(V)$ oscillates. Notice that for $V \sim V^* \ll E_F$, $a \sim a_{V^*}$ the ratchet current (10) is of the order of the total current $\sim e^2V/h$.

5 Conclusions

In conclusion, we have found the ratchet current for strong and weak asymmetric potentials. It exhibits a set of universal power dependencies on the voltage and can grow as the voltage decreases. In Ref. [25] our analysis was extended to include the electron spin. This leads to a complicated phase diagram with several qualitatively different transport regimes for different interaction strengths.

Acknowledgements.— This work was supported by the US DOE Office of Science under contract No. W31-109-ENG-38.

References

1. Special issue on “Ratchets and Brownian motors: Basics, Experiments, and Applications”, Appl. Phys. A **75** (2002).
2. A. Aviram and M. A. Ratner, Chem. Phys. Lett. **29**, 277 (1974).
3. C. Joachim, J. K. Gimzewski, and A. Aviram, Nature **408**, 541-548 (2000).
4. H. Linke, T. E. Humphrey, A. Löfgren, A. O. Sushkov, R. Newbury, R. P. Taylor, and P. Omling, Science **286**, 2314 (1999); A. Löfgren, I. Shorubalko, P. Omling, and A. M. Song, Phys. Rev. B **67**, 195309 (2003).
5. H. W. C. Postma, T. Teepen, Z. Yao, M. Grifoni, and C. Dekker, Science **293**, 76 (2001).
6. S. Roddaro, V. Pellegrini, F. Beltram, G. Biasiol, L. Sorba, R. Raimondi, and G. Vignale, Phys. Rev. Lett. **90**, 046805 (2003).
7. P. Reimann, M. Grifoni, and P. Hänggi, Phys. Rev. Lett. **79**, 10 (1997).
8. J. Lehmann, S. Kohler, P. Hänggi, and A. Nitzan, Phys. Rev. Lett. **88**, 228305 (2002).
9. S. Scheidl and V. M. Vinokur, Phys. Rev. B **65**, 195305 (2002).
10. A. Komnik and A. O. Gogolin, Phys. Rev. B **68**, 235323 (2003).
11. B. Spivak and A. Zyuzin, cond-mat/0404408; D. Sanchez and M. Buttiker, Phys. Rev. Lett. **93**, 106802 (2004).
12. V. I. Belinicher and B. I. Sturman, Sov. Phys. Usp. **23**, 199 (1980).
13. C. L. Kane and M. P. A. Fisher, Phys. Rev. B **46**, 15233 (1992).
14. L. D. Landau and E. M. Lifshitz, *Quantum Mechanics* (Addison-Wesley, Reading, Massachusetts, 1965).
15. D. E. Feldman, S. Scheidl, and V. M. Vinokur, Phys. Rev. Lett. **94**, 186809 (2005).
16. We do not take Friedel oscillations into account since they do not change our estimate qualitatively [15].
17. A. O. Gogolin, A. A. Nersesyan, A. M. Tsvelik, *Bosonization and Strongly Correlated Systems* (Cambridge University Press, Cambridge, 1998)
18. D. L. Maslov and M. Stone, Phys. Rev. B **52**, R5539 (1995); V. V. Ponomarenko, *ibid.* **52**, R8666 (1995); I. Safi and H. J. Schultz, *ibid.* **52**, R17040 (1995).
19. D. E. Feldman and Y. Gefen, Phys. Rev. B **67**, 115337 (2003).
20. B. Trauzettel, I. Safi, F. Dolcini, and H. Grabert, Phys. Rev. Lett. **92**, 226405 (2004); e-print cond-mat/0409320.
21. J. Rammer and H. Smith, Rev. Mod. Phys. **58**, 323 (1986).
22. The applied voltage renormalizes other terms in the action too (for example, the Luttinger parameter g). Power counting shows that some of them could also give rise to ratchet current contributions of the order of $U^2 V^{2g} \ln^s V$, $s = \text{const}$.
23. C. de C. Chamon, D. E. Freed, S. A. Kivelson, S. L. Sondhi, and X. G. Wen, Phys. Rev. B **55**, 2331 (1997).
24. H. Grabert, cond-mat/0107175.
25. B. Braunecker, D. E. Feldman, and J. B. Marston, Rectification in one-dimensional electronic systems, *Phys. Rev. B* **72**, 125311 (2005).

Superconductivity in Nanostructures

Ferromagnetic-Superconducting Hybrid Systems

J.Y. Gu¹, Ya.B. Bazaliy¹, S.D. Bader¹, and C.Y. You²

¹ Materials Science Division, Argonne National Laboratory, Argonne, Illinois 60439, USA bader@anl.gov

² Department of Physics, Inha University, Incheon 402-751, South Korea

Summary. The interplay between superconductor (S) and ferromagnet (F) in hybrid structures consisting of S and F layers creates an exotic spin-triplet ordering in the vicinity of F/S boundaries, even though the S-layers are made of conventional BCS superconductors. We present experimental and theoretical studies of F/S/F trilayer hybrid systems, where the emergent spin-triplet correlations lead to the dependence of the superconducting transition temperature on the angle between the magnetization directions of the two ferromagnetic layers.

1 Introduction

Proximity effects between a superconductor (S) and a metallic ferromagnet (F) are a subject of much recent work. Apart from the regular suppression of superconductivity by an adjacent ferromagnet, many unusual phenomena were observed in experiments, such as, Josephson π -junctions in S/F/S systems,[1, 2, 3, 4] anomalous proximity effects, [5] oscillations of the superconducting transition temperature T_c as a function of layer thickness in S/F bilayers,[6, 7] and the superconducting switch, where T_c is controlled by the mutual orientation of the magnetizations in the F/S/F structure.[8] Other effects are predicted theoretically and await experimental realization.[9, 10]

In many practical cases, metals constituting the hybrid system are characterized by a small mean free path of electrons (“dirty limit”). The system can be then described by an appropriate generalization of the Usadel equations.[11, 10] Ferromagnetism is taken into account in the mean field approximation by introducing Zeeman fields \mathbf{h} , directed along the magnetization inside the F-layers, and the possibility of exotic correlations is allowed for by retaining the full form of the anomalous Green’s function with two spin indices:

$$f_{\sigma_1\sigma_2}(r, \omega_n) = \begin{vmatrix} f_{\uparrow\uparrow} & f_{\uparrow\downarrow} \\ f_{\downarrow\uparrow} & f_{\downarrow\downarrow} \end{vmatrix}, \quad (1)$$

where σ_1 and σ_2 , r and ω_n are the spin indices, spatial argument and Matsubara frequency, respectively. In the absence of ferromagnets, \hat{f} has a form, corresponding to spin-singlet Cooper pairs

$$f_{\sigma_1\sigma_2} = \begin{vmatrix} 0 & f_s(r, \omega_n) \\ -f_s(r, \omega_n) & 0 \end{vmatrix} = f_s(r, \omega_n) \begin{vmatrix} 0 & 1 \\ -1 & 0 \end{vmatrix} \quad (2)$$

with only one unknown function to be found. When the solution of the generalized Usadel equations, \hat{f} , differs from (2), some exotic pairing is present.

The full symmetry of the superconducting pairing is characterized by the symmetry of the anomalous Green's function in momentum space (s-wave, p-wave, *etc.*), spin space (spin-singlet or spin-triplet) and with respect to the Matsubara frequency ω_n . It is known that only s-wave correlations can survive in the dirty limit [12] - accordingly the momentum-averaged functions in (1) have only one spatial argument r . Together with the general symmetry properties of the anomalous Green's function, [13] matrix \hat{f} is in general a superposition of the spin-singlet component (2) with f_s being an even function of ω_n , and three spin-triplet components

$$f_1(r, \omega_n) \begin{vmatrix} 1 & 0 \\ 0 & 0 \end{vmatrix}, \quad f_2(r, \omega_n) \begin{vmatrix} 0 & 1 \\ 1 & 0 \end{vmatrix}, \quad f_3(r, \omega_n) \begin{vmatrix} 0 & 0 \\ 0 & 1 \end{vmatrix} \quad (3)$$

with $f_{1,2,3}$ being odd in ω_n . The odd-in-frequency spin-triplet pairing was first considered by Berezinskii.[14]

Solutions of the Usadel equations in hybrid systems with F and S layers show that triplet components of \hat{f} are generated near the F/S boundaries and decay into both the ferromagnetic and superconducting materials. When the boundaries are sufficiently close to each other, the triplet component propagates over the whole system and can lead to new interesting effects.

The property of the spin-triplet components $f_{1,2,3}(\omega_n) = -f_{1,2,3}(-\omega_n)$ means that their presence is not easy to observe. For example, the order parameter Δ is related to the sum $\sum_{n=-\infty}^{n=+\infty} \hat{f}(\omega_n)$ in which all contributions of the odd functions $f_{1,2,3}$ cancel. However, there are phenomena where the presence of the spin-triplet pairing plays a crucial role. One of them is the effect of the T_c dependence on the mutual orientation of magnetizations in the F/S/F structure. Another one is the predicted long-range proximity effect based on the spin-triplet component, which should lead to a Josephson current in F/S/F/S structures with anomalously thick F-layers.[10] The latter is relevant for experimental results of Ref. [5].

2 F/S/F superconducting switch

The F/S/F structures were proposed in Refs. [15] and [16] (an F/F/S structure with similar properties was proposed earlier in Ref. [17]). In both cases F layers suppress the T_c of the S layer, but the magnitude of the suppression

depends on the relative magnetization orientation of the two F layers. The superconducting transition temperature of the middle layer is denoted T_c^P for the configuration with parallel (P) magnetizations of the F layers, and T_c^{AP} for the one with antiparallel (AP) magnetizations. Relative magnetization orientation of the F layers can be controlled by a weak magnetic field H provided one of the F layers is pinned, *i.e.* by proximity to an antiferromagnet (AF) (spin-valve setting). The field necessary to switch the structure between parallel and antiparallel configurations can be small so that by itself it would be insufficient to influence the superconductivity of the middle layer. In theory papers [15, 16] it was proposed that at temperature T between the T_c^P and T_c^{AP} switching between P and AP magnetic configurations of the F/S/F system will result in switching between the superconducting and normal states of the middle layer. A schematic of such an F/S/F proximity switch device is illustrated in Fig. 1.

Solution of the Usadel equations in certain limits [15, 16] shows that $T_c^{AP} > T_c^P$ and $\Delta T_c = T_c^{AP} - T_c^P$ is non-negligible only when the thickness of the superconducting layer d_S is not much larger than the superconducting coherence length ξ_S . For larger d_S the temperature difference decays as $\exp(-d_S/\xi_S)$. Usually this result is explained qualitatively by saying that when the size of the Cooper pairs ξ_S is larger than d_S , they feel a pair-breaking effect proportional to the average magnetization of the two F layers. According to that logic, one should naturally observe some cancellation of pair-breaking in the AP state. One can say that a Cooper pair, consisting of two electrons with opposite spin, puts the spin-up electron into the F layer with up magnetization and the spin-down electron into the F layer with down magnetization. Thus both electrons are less disturbed by the magnetic layers and so the suppression of T_c is smaller than in the P configuration. This argument, however, should be taken with a grain of salt. For example, it was shown in Ref. [18] for a model system, that while $T_c^{AP} > T_c^P$ holds, it is also true that at $T = 0$ the system in the P configuration has a larger order parameter $\Delta^P > \Delta^{AP}$ (see also Refs. [19, 20, 21]), contradicting the above mentioned reasoning.

It is important to note that the T_c dependence on the magnetic configuration would not exist, at least in the dirty limit, if only singlet superconducting correlations were present. This is because the singlet anomalous Green's function carries no information about the direction of the magnetization which suppressed it. Thus the left F/S interface would not know about the magnetization direction on the right F/S interface, and the angle between magnetizations would not enter into the solution of Usadel equations. In this case one could only expect a stronger suppression of T_c in the F/S/F trilayer compared to the F/S bilayer due to the additional hostile interface. In reality, the presence of magnetic layers changes the nature of the Cooper pairs in the S layer. The usual spin-singlet pairs are modified and acquire an admixture of spin-triplet nature. Now the coefficients of the triplet components (3) define a vector direction of the spin orientation of the pair. The interaction of a spin-triplet pair with the F layer then does depend on the angle between the spin

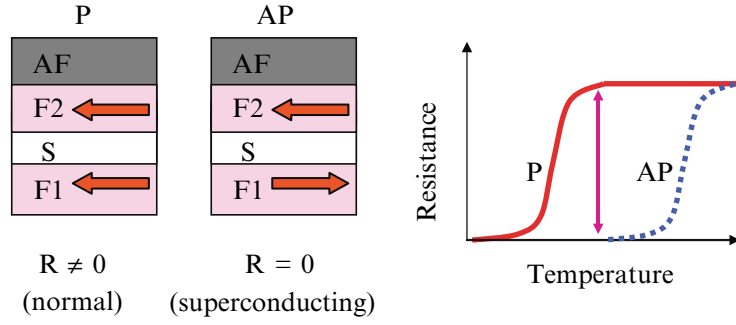


Fig. 1. Schematic structure of an F/S/F/AF proximity switch device. As shown by the arrow, resistance can change from a finite value to zero at $T_c^P < T < T_c^{AP}$.

of the pair and the magnetization of the F layer. Thus the effect discussed here is made possible.

Experimentally the difference ΔT_c was first observed in an all-metallic system in Ref. [8]. The analogous phenomena with insulating F layers was reported much earlier. [22, 23] In the following, we summarize our experimental and theoretical work on the all-metallic system.

3 Experiment

We chose dilute ferromagnetic $\text{Cu}_x\text{Ni}_{1-x}$ alloys ($x \leq 0.6$) as the F layer. CuNi was similarly used previously for the study of S/F/S junctions [4, 24] and S/F bilayers, [25] since its weak ferromagnetism is less devastating to superconductivity than for pure Ni. A sputtering target of $x = 0.4$ was made by pressing a mixture of Cu and Ni powders. The Curie temperature, T_C , of our sputtered CuNi films is ~ 70 K based on the T -dependence of the magnetization, $M(T)$. Magnetic hysteresis measurements at 5 K show a coercive field, H_c , of ~ 100 Oe. According to the dependence of T_C on x for $\text{Cu}_x\text{Ni}_{1-x}$ alloys, [26] the Cu compositions of the thin films are expected to be 0.47 (instead of $x = 0.4$), which is slightly different from the target composition.

In order to get well defined P and AP alignments between the two CuNi layers, we initially employed an exchange-biased spin-valve stack of CuNi/Nb/CuNi/ $\text{Fe}_{50}\text{Mn}_{50}$. The AF $\text{Fe}_{50}\text{Mn}_{50}$ layer pins the magnetization of the adjacent CuNi layer via exchange bias so that it remains fixed in weak magnetic fields that can reorient the magnetization of the “free” CuNi layer, allowing control of the P and AP configurations of the two F layers. However, a problem we encountered was that we could not get a well-defined AP region due to the rather large H_c of the CuNi layer compared to the exchange-bias field, H_E . H_c of the CuNi layer is about 100 Oe and the H_E is

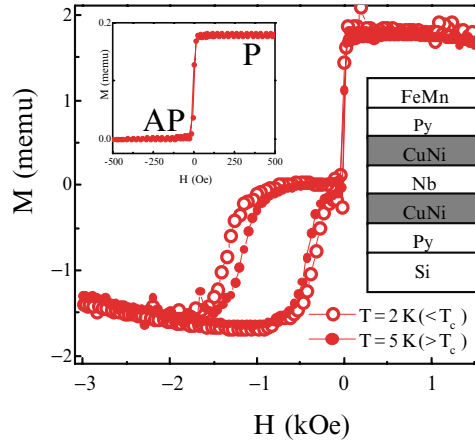


Fig. 2. $M(H)$ of $\text{Py}(4 \text{ nm})/\text{Cu}_{0.47}\text{Ni}_{0.53}(5)/\text{Nb}(18)/\text{CuNi}(5)/\text{Py}(4)/\text{FeMn}(6)$. Empty and filled circles denote data measured at $T = 2 \text{ K} (< T_c)$ and $T = 5 \text{ K} (> T_c)$, respectively. A minor loop measured between $\pm 500 \text{ Oe}$ and the structure of an exchange-biased spin valve, $\text{Py}/\text{CuNi}/\text{Nb}/\text{CuNi}/\text{Py}/\text{FeMn}$, are shown in the inset.

only about $150 \sim 200 \text{ Oe}$. Therefore, the two hysteresis curves of the free and pinned CuNi layers overlap. To solve this problem, we inserted a soft ferromagnetic layer of permalloy ($\text{Py} = \text{Ni}_{82}\text{Fe}_{18}$) adjacent to the CuNi layers to yield $\text{Py}/\text{CuNi}/\text{Nb}/\text{CuNi}/\text{Py}/\text{Fe}_{50}\text{Mn}_{50}$ multilayers, as shown in the inset of Fig. 2. Introduction of the Py layer decreases H_c of the CuNi layer and creates a range of fields where an AP alignment of the two CuNi layers is well defined. Coupling with the soft layer significantly reduces the field required to switch the hard layer. A multilayer, starting with the bottom Py and ending with the FeMn layer, was deposited onto a Si substrate using a chamber with a base pressure of 10^{-8} Torr and an Ar pressure of $1.5 \sim 4 \text{ mTorr}$. To set the exchange bias, the multilayers were heated to 370 K and cooled through the Neel temperature of the FeMn layer in a magnetic field of 1 T . Figure 2 shows the $M(H)$ curves of $\text{Py}(4 \text{ nm})/\text{Cu}_{0.47}\text{Ni}_{0.53}(5)/\text{Nb}(18)/\text{CuNi}(5)/\text{Py}(4)/\text{FeMn}(6)$ measured at $5 \text{ K} (> T_c \approx 2.81 \text{ K})$ and $2 \text{ K} (< T_c)$. The hysteresis loop of the top CuNi/Py layer is shifted due to the exchange bias between the Py and FeMn layers. The hysteresis loops measured in the normal and S-state do not show much difference and both have well-defined P and AP configurations. A minor loop measured between $\pm 500 \text{ Oe}$ is shown in the inset, where P and AP states between two CuNi layers are well defined. [27] The fact that the net magnetization value at the AP configuration is zero also suggests that the

top and bottom Py/CuNi layers are aligned in opposite directions and the magnetizations cancel.

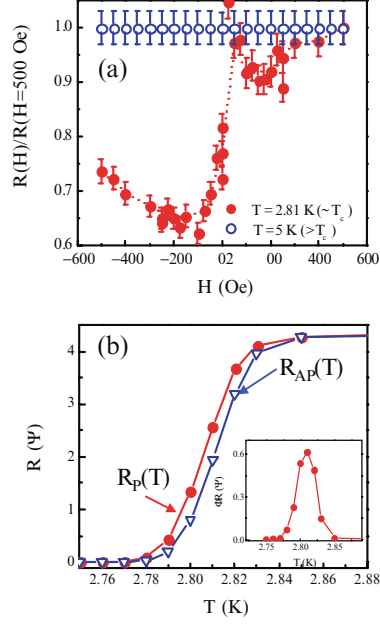


Fig. 3. (a) $R(H)/R(H = 500 \text{ Oe})$ curves at $T = 5 \text{ K}$ ($> T_c$) and $T = 2.81 \text{ K}$ ($\sim T_c$) and (b) $R_P(H = 300 \text{ Oe}, T)$ and $R_{AP}(H = -300 \text{ Oe}, T)$ for Py(4 nm)/Cu_{0.47}Ni_{0.53}(5)/Nb(18)/CuNi(5)/Py(4)/FeMn(6). $\Delta R(T) = R_P(T) - R_{AP}(T)$ is shown in the inset of (b).

Figure 3(a) shows the resistance as a function of H , $R(H)$, data of the Py(4 nm)/Cu_{0.47}Ni_{0.53}(5)/Nb(18)/CuNi(5)/Py(4)/FeMn(6) measured both at $T > T_c$ (5 K) and $T \sim T_c$ (2.81 K) and normalized at $R(H = 500 \text{ Oe})$. For $T > T_c$, the S-layer is in the normal state and $R(H)$ does not change between $\pm 500 \text{ Oe}$, indicating that R is not affected by whether the two CuNi layers are aligned P or AP. However, when the S-layer enters into the superconducting state at $T \leq T_c$, $R(H)$ shows a dramatic change when alternating the configuration of the two CuNi layers between P and AP. We observe that R decreases when the field goes from positive (P configuration) to negative (AP configuration): $R_{AP} < R_P$, where R_P and R_{AP} are the resistances measured at $H = 300 \text{ Oe}$ and $H = -300 \text{ Oe}$, respectively. The sign of this change is consistent with the fact that the AP configuration has a higher T_c . Indeed, in the idealized situation of infinitely sharp superconducting transitions, theoretical calculations [15, 16]

predict that R would decrease from a finite value to zero in a T -region between T_c^{AP} and T_c^P , as illustrated in Fig. 1. However, only a small reduction in the resistance is observed, and there is an $\sim 25\%$ change of R ($[(R(H = 300 \text{ Oe}) - R(H = -300 \text{ Oe}))/R(H = 500 \text{ Oe})] \times 100\%$) upon switching from P to AP alignment.

We also made T -dependence measurements of $R_P(T) = R(H = 300 \text{ Oe}, T)$ and $R_{AP}(T) = R(H = -300 \text{ Oe}, T)$. As shown in the $M(H)$ curve in the inset of Fig. 2, 300 Oe is enough to create a single domain configuration, so that we can neglect the magnetic stray-field effect which exists only at the edge of the sample in our case. It is important to note that the methodology of making measurements at fixed T while reversing the field ensures the accuracy of the ΔR values: there is virtually no T drift during the magnetization switch. The $R_P(T)$ and $R_{AP}(T)$ curves themselves are shown in Fig. 3(b). From ΔR value at the middle of the transition and the slope of $R_P(T)$ [or $R_{AP}(T)$], we find $\Delta T_c \approx 6 \text{ mK}$ for $t_{CuNi} = 5 \text{ nm}$ and $t_{Nb} = 18 \text{ nm}$. Since the ΔT_c value is smaller than the width of superconducting transition, we were not able to observe a system going from normal in the P configuration to fully superconducting in the AP configuration. However, it is important to note that the width of superconducting transition (from 10 - 90%) in the experimental data is quite small ($\sim 35 \text{ mK}$) even though it is larger than the ΔT_c value. Thus improved sample quality cannot decrease the transition width much more.

4 Numeric solution of Usadel equations

As mentioned in the introduction, the proximity effect in F/S hybrid systems is usually described by Usadel equations valid in the limit of a small mean free path. [15, 16, 28, 25, 29] Analytic solutions for F/S/F structures were obtained in Refs. [15, 16, 30] and significantly different values of T_c^{AP} and T_c^P were predicted. This is in sharp contrast with experimental results [8] that however did verify the inequality $T_c^{AP} > T_c^P$. The significance of such discrepancy is not immediately clear: all analytic calculations [15, 16, 30] used certain approximations (either a thin S-layer approximation or a “single-mode” approximation) to solve the Usadel equations. In a “single-mode” approximation, W_n in Eq. (7) is approximately independent on n . The actual experiments of Ref. [8] were performed on a structure with $d_S \approx \xi_S$. Thus neither of the approximations is suitable for their description. This is even more true if one recalls that the F-layers were deliberately fabricated from a weak ferromagnet; so $\hbar \gg \omega_{n*}$ used in “single-mode” approximation, where E_{ex} is the band splitting parameter in F-layer, may not be valid either. Hence, a numeric solution is required to compare theory and experiment in a meaningful way.

We found how T_c can be calculated using an extension of the numerical method of Fominov *et al.* [25, 29] This method was originally proposed to calculate T_c of the F/S bilayer structures. Its extension to the case of an F/S/F trilayer in the P configuration is straightforward, but application to

the AP configuration requires consideration. Below we summarize the key points of the original method and describe its modification.

The strength of the superconducting interaction is characterized by the transition temperature of the single S layer without F layers, T_{cs} . The ferromagnetic layers are modelled by introducing spin split bands described by the mean field exchange constant, h . First, it can be shown that for collinear magnetic configurations the f_1 and f_3 triplet components vanish. The f_2 component is non-zero and can be proven to satisfy a special property: $f_2 \sim if_s$. As a result functions $f_{\uparrow\downarrow}$ and $f_{\downarrow\uparrow}$ have the form

$$\begin{aligned} f_{\uparrow\downarrow} &= f_s + if_3 = F(\omega_n), \\ f_{\downarrow\uparrow} &= -f_s + if_3 = -F^*(\omega_n). \end{aligned}$$

Therefore it is enough to solve just one complex equation for F , instead of the original four equations for $f_{\sigma_1\sigma_2}$. This equation has a form

$$\xi^2(x)\pi T_{cs}F''(x, \omega_n) - (|\omega_n| + ih(x)\text{sgn}(\omega_n))F(x, \omega_n) + \Delta(x) = 0, \quad (4)$$

with self-consistency condition on the order parameter

$$\begin{aligned} \Delta(x) \log\left(\frac{T_{cs}}{T}\right) &= \pi T \sum_{\omega_n} \frac{\Delta(x)}{|\omega_n|} - F(x, \omega_n) \\ &= 2\pi T \sum_{\omega_n > 0} \frac{\Delta(x)}{|\omega_n|} - \text{Re}\{F(x, \omega_n)\}, \end{aligned} \quad (5)$$

where ξ is piece-wise constant in the S and F layers, expressed through the diffusion coefficients D_S and D_F , respectively:

$$\begin{aligned} \xi_S &= \sqrt{D_S/(2\pi T_{cs})}, \\ \xi_F &= \sqrt{D_F/(2\pi T_{cs})}. \end{aligned}$$

The band splitting parameter h_i ($i = 1, 2$) is non-zero only in the $F_{1,2}$ layers and comes with positive sign for up and negative for down-direction of the magnetization.

On the outer boundaries of the magnetic layers the function F satisfies a boundary condition

$$\frac{dF}{dx} = 0.$$

The interaction between the magnetic and superconducting layers is given by the S/F boundary conditions derived by Kupriyanov and Lukichev. [31] On the F_i/S ($i = 1, 2$) boundaries

$$\begin{aligned} \gamma \xi_F \left(\frac{dF_F}{dx} \right)_i &= \xi_S \left(\frac{dF_S}{dx} \right)_i, \\ (-1)^{i+1} \gamma_b \xi_F \left(\frac{dF_F}{dx} \right)_i &= F_{Si} - F_{Fi}, \end{aligned} \quad (6)$$

where F_F and F_S denote the function on the ferromagnetic and superconducting sides of the F/S junction, and γ , γ_b characterize the band structure mismatch and boundary transparency.

The method of Fominov *et al.* [25, 29] was formulated for the case of an F/S bilayer. Following it, Eq. (4) is first solved analytically in the F layers and for the f_3 component in the S layer. This is possible because in all these cases the equation is uniform. The order parameter Δ is zero in the F layers and has only singlet component in the S layer. After that, the boundary condition (6) - there is only one F/S ($i = 1$) boundary in this case - can be re-expressed through the f_s part of the anomalous function on the S layer side only

$$\xi_S f'_s(r, \omega_n) = W(\omega_n) f_s(r, \omega_n) \quad (7)$$

with real $W(\omega_n)$ (see Refs. [25, 29]). At the boundary with the vacuum

$$f'_s = 0. \quad (8)$$

Since self-consistency condition (5) is also formulated in terms of f_s , we get a closed system of two equations on a real function f_s which is solved numerically.

Following the same route for an F/S/F structure, we solve equations analytically in the F layers and for f_3 in the S layer. The important step is the realization that, if the $F_{1,2}$ layers and two F/S boundaries are identical, $f_s(r, \omega_n)$ is symmetric in space with respect to the center of the S layer in both collinear magnetic configurations. This result is trivial in the P configuration, but is somewhat unexpected in the AP one. In contrast, the triplet component $f_3(r, \omega_n)$ is symmetric in the P and anti-symmetric in the AP configuration.

The symmetry of f_s enables utilization of the method of Fominov *et al.* [25, 29] The trilayer is now equivalent to a bilayer with S layer of effective thickness $d_S^{eff} = d_S/2$, and, after some algebra, it is possible to reduce (6) to an effective counterpart of the condition (7)

$$\xi_S f'_{si}(r, \omega_n) = W_{[P/AP]}(\omega_n) f_{si}(r, \omega_n), \quad (9)$$

with

$$W_{[P/AP]} = \gamma \frac{A_{[P/AP]}(\gamma_b + \text{Re}[B]) + \gamma}{A_{[P/AP]}|\gamma_b + B|^2 + \gamma(\gamma_b + \text{Re}[B])}, \quad (10)$$

where

$$\begin{aligned} A_{[P]} &= k_S(\omega_n) \xi_S \tanh(k_S(\omega_n) d_S/2), \\ A_{[AP]} &= k_S(\omega_n) \xi_S \coth(k_S(\omega_n) d_S/2), \\ k_S(\omega_n) &= \frac{1}{\xi_S} \sqrt{\frac{|\omega_n|}{\pi T_{cs}}}, \end{aligned} \quad (11)$$

and

$$B = \frac{1}{\xi_F k_F(\omega_n) \tanh(d_F k_F(\omega_n))}, \quad (12)$$

$$k_F(\omega_n) = \frac{1}{\xi_F} \sqrt{\frac{|\omega_n| + i|h| \text{sgn}(\omega_n)}{\pi T_{cs}}},$$

with d_F being the thickness of identical F layers. Examination of Eq. (10) shows that the only difference between the P and the AP arrangements comes from $A_{[P]} \neq A_{[AP]}$. As expected, we find $W_{[P]}$ to be identical to the one found for the F/S bilayer with S layer of half thickness (compare with Refs. [25] and [29]). The AP case gives a new result. Substituting Eq. (10) instead of (7) into the numeric procedure of Fominov *et al.* [25, 29] we obtain T_c^P and T_c^{AP} for the actual parameters of our F/S/F hybrids.

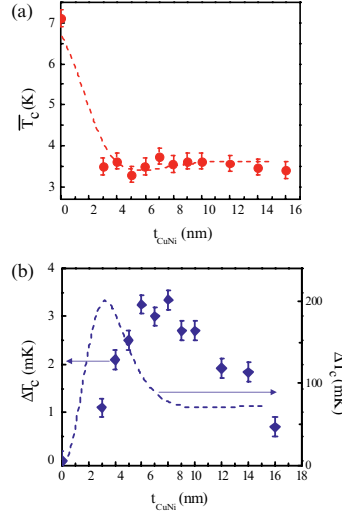


Fig. 4. (a) $\overline{T}_c(t_{\text{CuNi}})$ for Py(4 nm)/Cu_{0.49}Ni_{0.51}(t_{CuNi})/Nb(19)/CuNi(t_{CuNi})/Py(4)/FeMn(6). $\Delta T_c(t_{\text{CuNi}})$ is shown in (b). Experimental data and theoretical calculations are plotted as symbols and dashed lines, respectively.

The results for $\overline{T}_c = (T_c^P + T_c^{AP})/2$ and ΔT_c are shown in Fig. 4. We attempted to fit the experimental data for the F/S/F structure studied in Ref. [8]. The fit parameters are $d_S = 19$ nm, $\gamma = 0.135$, $\gamma_b = 0.3$, and

$h/k_B = 110$ K. The behavior of $\overline{T_c}$ shows agreement between the experimental data and theoretical calculations. However, the result for ΔT_c with γ_b and h obtained from the fitting of experimental $\overline{T_c}$ shows only qualitative agreement between the theoretical and experimental ΔT_c . Even with a numeric procedure that uses no approximations, there is a large discrepancy in the magnitude of ΔT_c . Inversely, when we tried to fit the experimental ΔT_c with the present theory, we could not get γ_b and h fitting both the magnitude and the peak position of ΔT_c simultaneously. Furthermore, the discrepancy of the experimental and theoretical $\overline{T_c}$ is noticeable when we use the parameters obtained from the fit of the experimental ΔT_c . Therefore, we were not able to fit both $\overline{T_c}$ and ΔT_c by varying two unknown parameters γ_b and h . We would like to contrast this result with the case of a thin superconductor ($d_S \ll \xi_S$), where such a fit is always possible. [32] Such is the difference between the $d_S \sim \xi_S$ experimental situation of Ref. [8] and the thin superconductor limit.

5 Discussion

The small value of ΔT_c experimentally measured in Ref. 8 compared to the theoretical prediction could be due to several reasons, even within the framework of theory based on the Usadel equations. Firstly, there is only a small region in d_F giving a large value of ΔT_c , for example $d_F \sim 0.5 \sqrt{4\hbar D_F/I}$. [15, 33] Therefore, d_F and d_S should be optimized to get a large value of ΔT_c . Secondly, as mentioned previously, the interface transparency of the S/F layers has a large effect on the behavior of T_c and ΔT_c . For example, when the interface transparency decreases, ΔT_c becomes smaller. [15, 33] Since the interface transparency is affected by the interface quality of the sample, the absolute value of ΔT_c will strongly depend on the CuNi/Nb interface. A better understanding and control of the interface of our samples will be necessary. Thirdly, the two CuNi layers may not be identical. This asymmetry makes the value of ΔT_c smaller since the cancellation of the pair-breaking effect will not be perfect in AP alignment if the two CuNi layers are not the same. Fourthly, the contribution from the Py layer adjacent to the CuNi layer should be taken into account especially for samples with thin CuNi layers. Finally, local mechanical strain and compositional fluctuations can have a strong effect on the magnetic behavior of the CuNi layers, whose net composition is close to the onset of ferromagnetism. Further quantitative explanation of the data remains a challenge for future research.

6 Conclusions

In summary we showed experimental results and theoretical calculations on magnetization orientation dependence of superconductor critical temperature in F/S/F all-metallic structures. This effect is based on the emergence of a small admixture of spin-triplet superconductivity in the hybrid

superconductor-ferromagnet structures. We showed that the proposed effect exists, but the observed magnitude is even smaller than the prediction based on the numeric solution of the Usadel equations with no approximations involved. Reconciling theory and experiment is a challenge for the future.

Acknowledgements.— The work at Argonne National Laboratory is supported by the U. S. Department of Energy Division of Basic Energy Science-Material Science under contract No. W-31-109-ENG-38. C.-Y. You is supported by National R&D Project for Nano Science and Technology of the Ministry of Science and Technology of Korea (M1-0214-00-0001).

References

1. Z. Radović, M. Ledvij, L. Dobrosavljević-Grujić, A. I. Buzdin, and J. R. Clem, Phys. Rev. B **44**, 759 (1991) and references therein.
2. A. I. Buzdin and M. Yu. Kupriyanov, JETP Lett. **25**, 290 (1991); A. I. Buzdin, B. Bujicic, and M. Yu. Kupriyanov, Sov. Phys. JETP **74**, 124 (1992).
3. C. L. Chien and D. H. Reich, J. Magn. Magn. Mater. **200**, 83 (1999) and references therein.
4. V. V. Ryazanov, V. A. Oboznov, A. Yu. Rusanov, A. V. Veretennikov, A. A. Golubov, and J. Aarts, Phys. Rev. Lett. **86**, 2427 (2001).
5. V. T. Petrashov, I. A. Sosnin, I. Cox, A. Parsons, and C. Troadec, Phys. Rev. Lett. **83**, 3281 (1999).
6. J. S. Jiang, D. Davidovic, Daniel H. Reich, and C. L. Chien, Phys. Rev. Lett. **74**, 314 (1995).
7. L. Lazar, K. Westerholt, H. Zabel, L. R. Tagirov, Yu. V. Goryunov, N. N. Garifyanov, and I. A. Garifullin, Phys. Rev. B **61**, 3711 (2000).
8. J. Y. Gu, C.-Y. You, J. S. Jiang, J. Pearson, Ya. B. Bazaliy, and S. D. Bader, Phys. Rev. Lett. **89**, 267001 (2002).
9. F. S. Bergeret, K. B. Efetov, and A. I. Larkin, Phys. Rev. B **62**, 11872 (2000).
10. A. F. Volkov, F. S. Bergeret, and K. B. Efetov, Phys. Rev. Lett. **90**, 117006 (2003); F. S. Bergeret, A. F. Volkov, and K. B. Efetov, Phys. Rev. B **68**, 064513 (2003).
11. Ya. V. Fominov, A. A. Golubov, M. Yu. Kupriyanov, JETP Letters **77**, 510 (2003) (*Pis'ma v ZhETF*, **77**, 609).
12. K. D. Usadel, Phys. Rev. Lett. **25**, 507 (1970).
13. A. A. Abrikosov, L. P. Gorkov, and I. E. Dzialoshinskii, “Methods of Quantum Field Theory in Statistical Physics” (Dover Publications), 1963.
14. V. L. Berezinskii, JETP **20**, 287 (1974).
15. L. R. Tagirov, Phys. Rev. Lett. **83**, 2058 (1999).
16. A. I. Buzdin, A. V. Vedyayev, and N. V. Ryzhanova, Europhysics Lett. **48**, 686 (1999).
17. Sangjun Oh, D. Youm, and M. R. Beasley, App. Phys. Lett. **71**, 2376 (1997).
18. A. Buzdin and M. Daumens, Europhysics Letters **64**, 510 (2003).
19. R. Melin, J. Phys. Condens. Matter **13**, 6445 (2001).
20. V. Apinyan, R. Melin, Eur. Phys. J. B **25**, 373 (2002).
21. H. Jirari, R. Melin, N. Stefanakis, cond-mat/0204610 (2002).
22. G. Deutscher and F. Meunier, Phys. Rev. Lett. **22**, 395 (1969).

23. J. J. Houser, Phys. Rev. Lett. **23**, 374 (1969).
24. A. Rusanov *et al.*, Physica C **369**, 300 (2002).
25. Ya. V. Fominov, N. M. Chtchelkatchev, and A. A. Golubov, cond-mat/0202280; JETP. Lett. **74**, 96 (2001).
26. S. A. Ahern, M. J. C. Martin, and W. Sucksmith, Proc. R. Soc. London Ser. A **248**, 145 (1958).
27. X-ray resonant magnetic scattering measurements of the Ni and F signals have verified that the coupled CuNi and Py layers switch in tandem and that the switching of the pinned and free CuNi/Py layers are well separated; J. W. Freeland (unpublished).
28. E. A. Demler, G. B. Arnold, and M. R. Beasley, Phys. Rev. B **55**, 15174 (1997).
29. Ya. V. Fominov, N. M. Chtchelkatchev, and A. A. Golubov, Phys. Rev. B **66**, 014507 (2002).
30. I. Baladié, A. I. Buzdin, N. V. Ryzhanova, and A. V. Vedyayev, Phys. Rev. B **63**, 054518 (2001).
31. M. Yu. Kupriyanov and V. F. Lukichev, Zh. Eksp. Teor. Fiz. **94**, 139 (1988) (Sov. Phys. JETP **67**, 1163 (1988)).
32. A. Buzdin, private communication.
33. C. -Y. You, Ya. B. Bazaliy, J. Y. Gu, S. D. Bader, S.-J. Oh, and L. M. Litvak (submitted).

STM Spectroscopy of the Local Density of States in Normal Metal - Superconductor Systems

L. Créton, A. Gupta, N. Moussy, B. Pannetier, and H. Courtois

Centre de Recherches sur les Très Basses Températures - C.N.R.S., in convention with Université Joseph Fourier, 25 Avenue des Martyrs, 38042 Grenoble Cedex, France courtoih@grenoble.cnrs.fr

Summary. At the contact with a Superconductor, the electrons from a Normal metal are Andreev-reflected. This modifies the normal metal electronic properties in the vicinity of the interface, including the local density of states (LDOS). A gap of reduced width (a mini-gap) is expected in the normal metal if its size is small as compared to the phase-breaking length. Otherwise, a pseudo-gap is expected. We performed the local spectroscopy of Normal-metal-Superconductor (N-S) structures with the help of a very low temperature (60 mK) Scanning Tunneling Microscope (STM). Both structures with a lateral and with a bilayer geometry were investigated. By comparing the experimental spectra with the predictions of the quasi-classical theory, we found a good agreement in many cases but also some clear discrepancies, especially in the mini-gap regime.

1 Introduction

In a normal metal (N) coupled to a superconductor (S), superconducting properties are locally induced by the proximity effect. The characteristic energy scale of this proximity superconductivity is given by the minimum of the bulk superconductor energy gap Δ and the Thouless energy ϵ_c :

$$\epsilon_c = \frac{\hbar D}{L^2} \quad (1)$$

which is equal to \hbar over the diffusion time L^2/D of an electron over the sample length L . Here D is the diffusion coefficient in the normal metal.

In order to get a physical understanding of this effect, one has to consider the microscopic mechanism of the Andreev reflection at the N-S interface [1]. An electron arriving on the interface from the normal metal side cannot

enter the superconductor if its energy lies within the energy gap Δ of the superconductor density of states. In order to enter the superconductor, this electron has to form an electron pair with another electron from the normal metal. A Cooper pair is then transferred in the superconductor. This process is often described as the retro-reflection of a hole in the normal metal. The incident electron and retro-reflected hole phases are correlated and coupled to the superconducting condensate phase [2]. In terms of excitation energy, the electron and the hole have the same energy: there is no energy transfer through an N-S interface. In terms of electronic particles, these two electron states have symmetric energies relative to the Fermi level at the energy E_F . One should not make the trivial error to refer here to “electron-hole pairs” which is a fully irrelevant concept here. The total charge of the pair is $2e$. In classical terms, the electron exists before the reflection, the hole exists after. One should rather use the term of Andreev pairs introduced in Ref. [3]. The Andreev reflection of an electron will therefore be described as the absorption of an Andreev pair of two electrons from the normal metal into the superconductor. It may be more interesting to consider the reverse effect, where two phase-correlated electrons are injected in the normal metal. This Andreev pair does not hold with the help of an attraction between electrons in the normal metal, but only because of a boundary effect, at the N-S interface.

The question of the decay length of superconducting correlations in the normal metal is an important issue. It is not correct to consider the thermal length $L_T = \sqrt{\hbar D/k_B T}$ as the general coherence length of Andreev pairs. In fact, the coherence length of an Andreev pair depends on its energy ϵ . The key point is that due to the $E(k)$ dispersion relation, the two electronic component of an Andreev pair do not have the same wave-vector k magnitude. As the momentum transfer perpendicular to the interface has to be zero, the parallel component of the hole and the electron wave-vectors will be different. This induces an angle of order ϵ/E_F between the two trajectories, the Fermi level being used as the reference $\epsilon = 0$. Although small, this difference also results in a phase shift between the two components of an Andreev pair with $\epsilon \neq 0$. This phase shift becomes of order one when the position of the two electrons is separated by a distance of order the Fermi wave-length. At this point, the Andreev pair is broken. This happens at a characteristic time \hbar/ϵ which corresponds to a characteristic length scale:

$$L_\epsilon = \sqrt{\frac{\hbar D}{\epsilon}}. \quad (2)$$

The thermal length L_T coincides with L_ϵ at $\epsilon \simeq k_B T$. A striking fact is also that the coherence length L_ϵ seems to diverge at the Fermi level ($\epsilon = 0$). At non-zero temperature, this naive prediction is of course hindered by the unavoidable phase-breaking events due to phonons or magnetic impurities. A physical consequence of the long-range coherence of low-energy Andreev pairs is the persistence of large magneto-resistance oscillations of Andreev interferometers and their decay with temperature T as $1/T$ [3]. In terms of energy, the Andreev pairs coherence condition $L < L_\epsilon$ can be recast as $\epsilon < \epsilon_c$,

which means that pairs with an energy below the Thouless energy $\epsilon_c = \hbar D/L^2$ remain coherent over the sample length L .

The superconducting properties induced in the normal metal manifest themselves in many different ways, including energy-dependent transport properties and a modification of the local density of states. For instance, the conductance of a normal conductor connected to a superconducting electrode shows a striking re-entrant behavior [4]. At non-zero temperature and/or bias, the conductance of the normal metal is enhanced as compared to the normal-state. At zero temperature and zero bias, the expected conductance coincides with the normal-state value. The conductance has therefore a non-monotonous behavior.

As compared to transport experiments, local density of states measurements have the strong advantage to bring a local physical quantity, which is not integrated over a full sample length. The energy dependence of the local density of states brings an exhaustive information on the phase-coherent coupling of electron states to the superconducting interface. In the diffusive regime, the prediction is that the local density of states should show a fully opened gap (a mini-gap) in the case of a closed normal metal system coupled to a superconductor [5, 6, 7, 8]. Indeed, in a closed system, every electronic trajectory should couple to the superconducting interface. This will be the case of a normal metal of finite length, in practice smaller than the phase-breaking length. In an open system, for example with a very long normal metal, not every electron state will Andreev-reflect at the interface within the coherence time \hbar/ϵ , except if one considers an energy which is infinitely close to the Fermi level $\epsilon = 0$. This will induce a pseudo-gap behavior in the density of states: the density of states will be zero only at the Fermi level and will be proportional to the energy close to it. The predicted width of the mini- or the pseudo-gap is again the Thouless energy, since Andreev pairs with a larger energy will loose correlation before diffusing through the whole normal metal length. The same distinction is expected in coherent ballistic cavities [9]. In chaotic cavities, every trajectory will reach the superconducting interface, even-though it may be after a very long diffusion time. A mini-gap is therefore expected. In an integrable cavity, some closed-loop trajectories will never hit it, which makes expect a pseudo-gap.

The local density of states was probed in N-S bilayers using tunneling spectroscopy in thin film junctions [10], and in lateral N-S structures with solid tunnel junctions [11, 12]. More local studies are welcome in order to overcome the unavoidable spatial averaging of such conventional experiments. Indeed, the Scanning Tunneling Microscopy (STM) in the spectroscopy mode enables one to measure the very local density of states under the tip. Due to the technical complexity of (very-low-temperature STM, the local study of mesoscopic superconductors is still in its infancy. Inoue and Takayanagi measured the tunneling spectra of a Nb-InAs-Nb system at 4.2 K [13]. Pioneering work by Tessmer *et al.* focused on the proximity effect in Au nano-sized islands on top of a NbSe₂ sample [14]. Levi et al. studied complex Ni-Cu-NbTi

multi-filamentary superconducting wires [15]. Recently, a NbSe₂ crystal covered with Au [16] was also investigated.

In our recent experiments, we have been able to combine the very-low temperature ($T \ll 1$ K) conditions with the local probe technique. This guarantees a much improved energy resolution, and therefore the possibility to probe the proximity effect on a larger length scale, together with a high spatial resolution. The geometry of a STM tip generally results in a low resistance for the tunnel probe so that no (dynamical) Coulomb blockade should interfere with the spectroscopy experiments. Our very low temperature STM works at 60 mK in a dilution refrigerator [17]. It features both an atomic resolution and a large scanning range of $6 \times 6 \mu\text{m}^2$ at low temperature. In the spectroscopy mode, this STM has shown an unprecedented energy resolution of $36 \mu\text{eV}$. This corresponds to an effective temperature of 210 mK which had to be introduced in the BCS fit of the spectroscopy data for plain Al and Nb layers. These fits were performed without any inelastic scattering parameter [18], which means that this effective temperature is actually a maximum value. With this apparatus, we have investigated two different types of N-S structures: the junction between a superconducting dot and a normal metal film, N-S bilayers with a thick superconductor and a normal metal of varying thickness.

2 Theoretical description

The proximity effect in diffusive metals can be described by the quasiclassical theory based on the Usadel equations [5, 6, 7, 8]. In the usual θ parametrization, the complex angle $\theta(\epsilon, x)$ is related to the pair amplitude as $F(\epsilon, x) = -i \sin \theta(\epsilon, x)$. The local density of states is expressed as:

$$n(r, \epsilon) = n_0 \Re[\cos \theta(r, \epsilon)]. \quad (3)$$

The Usadel equations in one dimension write:

$$\begin{cases} \frac{1}{2} \hbar D_S \frac{\partial \theta^2}{\partial x} + i \epsilon \sin \theta + \Delta(r) \cos \theta = 0 & \text{in } S \\ \frac{1}{2} \hbar D_N \frac{\partial \theta^2}{\partial x} + i \epsilon \sin \theta = 0 & \text{in } N \end{cases} \quad (4)$$

where D_N and D_S are the diffusion coefficients in N and S respectively. The inelastic and spin-flip rates were neglected. The gap $\Delta(r)$ in S is self consistently defined by:

$$\Delta(r) = n_0 V_{eff} \int_0^{\hbar \omega_D} \tanh\left(\frac{\epsilon}{2k_B T}\right) \Im[\sin \theta] d\epsilon, \quad (5)$$

where n_0 is the electron density, V_{eff} is the local interaction parameter and ω_D is the Debye frequency. In the case of a perfect transparency, the boundary

conditions at the N-S interface include the continuity of θ at the interface and the spectral current conservation:

$$\sigma_S \frac{\partial \theta}{\partial x_{x=0^-}} = \sigma_N \frac{\partial \theta}{\partial x_{x=0^+}}, \quad (6)$$

where σ_S and σ_N are the conductivity in S and N respectively. In this work, we benefited from the numerical code developed by W. Belzig *et al.* [5], which solves the Usadel equation for a quasi-1D N-S junction and calculates the local density of states. The relevant theoretical parameters are the gap Δ of the S metal, the mismatch parameter

$$\gamma = \frac{\sigma_N \xi_S}{\sigma_S \xi_N} \quad (7)$$

and the thicknesses of the N and S layers in units of the characteristic lengths:

$$\xi_N = \sqrt{\frac{\hbar D_N}{2\Delta}}; \quad \xi_S = \sqrt{\frac{\hbar D_S}{2\Delta}} \quad (8)$$

respectively. Whereas the length ξ_S is close to the usual superconducting coherence length, the length ξ_N does not stand for a coherence length of electron pairs in the normal metal.

3 Local spectroscopy close to a N-S junction

In this section, we will describe the spatially-resolved spectroscopy studies we performed on a lateral N-S junction [19]. These samples were made by successive in-situ evaporation of Nb (Superconducting below about 9 K) and Au (Normal metal). First, the Si sample substrate was introduced in the UHV evaporator with a patterned Si membrane clamped on it. This 5 μm -thick Si membrane was previously patterned by e-beam lithography and deep Reactive Ion Etching. An array of circular holes with a periodicity of 4 μm and a diameter of about 1.5 μm were drilled throughout the membrane. During Nb evaporation, the Si membrane acted as a mechanical mask, so that only dots of Nb are deposited on the substrate. After deposition of 40 nm of Nb, the mask was removed in situ and an uniform layer of 20 nm of Cu or Au was deposited. The pressure was below 10^{-8} mbar during the few minutes between the two evaporations. This provides a highly transparent Nb-Au interface. Let us point out that no lithography or two-step deposition procedure was needed here, so that the Nb-Au interface is actually as clean as possible.

Figure 1b shows an STM image of the Nb-Au sample at 60 mK. Two Nb dots are clearly visible. The relief of the Nb dots is rather smooth. This is due to both the thickness of the mask and the residual distance between the substrate and the mask. We performed several series of spectroscopies as a function of distance from the center of a Nb dot by traveling along

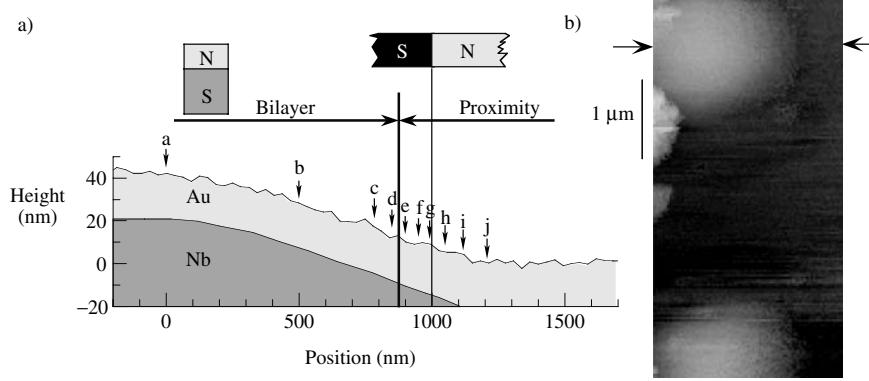


Fig. 1. a: Profile of the sample surface extracted from image b) (line indicated by the two arrows) together with a schematics of the sample geometry. Note that the vertical scale has been expanded by a factor of about 10 compared to the horizontal one. The locations where the spectra of Fig. 2a were measured are indicated, as well as the domains of application of the two geometry models used in the calculations (shown in Fig. 2b). In the “Bilayer” region, the sample is modeled by a series of (vertical) N-S bilayers, the thickness of $S = \text{Nb}$ being given by the measured profile. In the “Proximity” region, the sample is modeled by a single (horizontal) N-S region. b: $2.6 \times 5 \mu\text{m}^2$ STM image at 60 mK captured with a 10 mV bias voltage and a 30 pA tunnel current. Two circular Nb dots are visible.

one line. During each series, the displacement speed was limited to 10 nm/s and the scanning direction was kept fixed in order to reduce the piezoelectric hysteresis. Figure 2a shows a representative selection of spectra taken during a single series. The surface profile of the same line is shown in Fig. 1a. Labeled arrows indicate the position of the spectra shown in Fig. 2. In the center of the Nb island (curve a), the density of states exhibits a clear gap, which is reminiscent of a BCS behavior. Compared to the bulk Nb gap value $\Delta_{\text{Nb}} \simeq 1.4$ meV, the measured gap is significantly reduced. This behavior is consistent with the measured critical temperature $T_c = 3$ K at the superconductivity onset. As we move away from the Nb dot center (curves b to d), the density of states first continues to exhibit a fully developed but reduced gap. This remains approximately true up to close to the curve e, which shows a clear pseudo-gap: the density of states goes approximately linearly to zero at the Fermi level. As the tip is moved further away (spectra e to j), the pseudo-gap width is reduced.

In order to analyze easily our experimental results, we modeled the different parts of our structures as quasi-1D junctions. On top of the Nb dot, we locally model the sample as an uniform bilayer of Nb and Au, see Figure 1b. Note that the vertical magnification by a factor of about 10 may make the reader underestimate the validity of this approach. In the remaining region labeled “Proximity”, we model our sample as a single horizontal N-S junction,

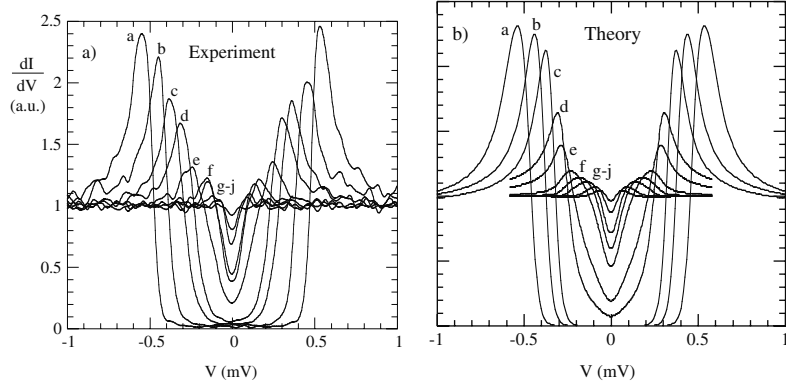


Fig. 2. a: Experimental spectra measured on locations a to j (see Fig. 1a) during a single scan along one line. The tunnel resistance was about $12 \text{ M}\Omega$ during the spectroscopies. b: Theoretical spectra calculated with the Usadel equations. The actual geometry was modeled as a series of N-S bilayers (curves a to d) and a single lateral N-S junction (curves e to j). An effective temperature of 210 mK was introduced. In the bilayer region, the measured thickness of the Nb layer ($d_S = 40, 21, 15$ and 11 nm in a, b, c and d respectively) in units of $\xi_S = 27 \text{ nm}$ was introduced in the calculation together with the fixed Au layer thickness $d_N = 20 \text{ nm} = 0.3\xi_N$. In the proximity-effect region, the distance from the interface was a free fit parameter (see Fig. 3b).

the interface position being *a posteriori* determined by the comparison with the theory.

Let us first consider the “Bilayer” region. The sample is locally modeled as a quasi-1D N-S junction with a constant length of N metal and a locally varying length of S metal. A fully-developed gap is predicted, in agreement with the experiment. We assumed a perfect interface transparency and no inelastic or spin-flip scattering. By fitting the curve a, a good set of values was found to be $\gamma = 1.1$, $\Delta = 0.82 \text{ meV}$, $d_S = 1.5\xi_S$ and $d_N = 0.3\xi_N$. The γ parameter value matches within the experimental accuracy the estimation of 1.2 based on the measured transport properties of the N and S layers. The magnitude of Δ is significantly smaller than the Nb bulk value, which we attribute to the small Nb thickness [20] and the special conditions of Nb evaporation. As the Nb and Au layers thicknesses are known, we can extract the length scales $\xi_S = 27 \text{ nm}$ and $\xi_N = 67 \text{ nm}$, in qualitative agreement with the respective expected values 41 nm and 55 nm . Curves for locations b to d in the “Bilayer” region were subsequently calculated by taking into account the fixed Au thickness $d_N = 20 \text{ nm} = 0.3\xi_N$ and the measured Nb layer thickness in units of ξ_S . As expected, the mini-gap amplitude is reduced as the thickness of the Nb layer decreases, the Au layer thickness being constant. In the calculated curves (shown in Fig. 2b), we introduced an effective temperature $T = 210 \text{ mK}$ in order to account for the experimental accuracy [17]. The agreement

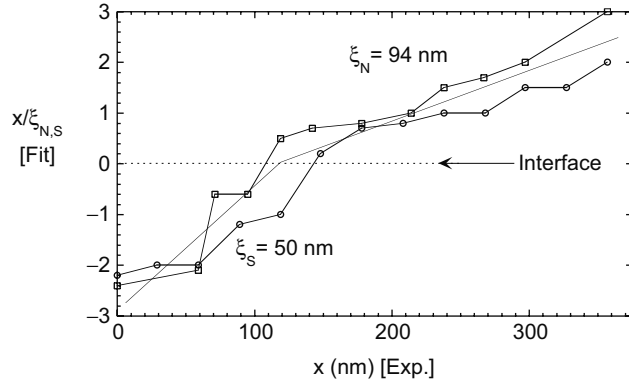


Fig. 3. Comparison of the fit-derived distance from the interface with the actual (measured) position. Two data series taken on two different lines are shown and identified by squares and triangles symbols. The slopes of the adjusted lines give the length scales values $\xi_S = 50$ nm and $\xi_N = 94$ nm.

is very good, as both the mini-gap amplitude and the spectra shape are well described.

In the “Proximity” region, the measured spectra (curve e and beyond) show a filling of the density of states near the Fermi level and a peak shape that are not compatible with a bilayer model. This pseudo-gap behavior is the signature of the proximity effect in a N-S junction with a long normal metal N. In this “Proximity” region, we described the sample as a single infinite N-S junction extending laterally. We used the same γ parameter as in the “Bilayer” region. Again we consider a perfect interface transparency and zero inelastic and spin-flip scattering. In order to describe successfully the data, we had to assume a reduced gap value $\Delta' = 0.27$ meV. Compared to the value in the bilayer region, this reduced value may be understood as the effective gap of the Nb-Au dot treated as a whole. The experimental curves e to j were fitted within this model by considering the tip position as a free parameter.

The validity of our description can be checked in Fig. 3 where we compare the actual position of the acquired spectra to the position extracted from the fit, in units of the relevant characteristic length. The data points follow a monotonous behavior, but with a significant scattering. From the slope of the mean line we can draw through the data points on the N side (top part of Fig. 3), we can extract the value $\xi_N = 94$ nm. This corresponds exactly to the estimation based on the gap Δ' and the measured mean free path of 16 nm in Au. On the S side (bottom part of Fig. 3), the estimated length is $\xi_S = 50$ nm. Taking into account the reduced gap Δ' , it corresponds to a mean free path of 4.5 nm which is half the value estimated from transport properties of similar samples. In fact, it should be considered more as a property of the Nb-Au layer at its border than a property of the bare Nb film.

The location of the interface can be accessed from the fitting procedure. It appears that the interface is situated at an estimated Nb thickness of 6 nm. This means that the Nb layer is not superconducting when it is thinner than 6 nm. This behavior is expected in respect of the getter properties of Nb during evaporation. In Fig. 3, the scatter in the fitted position compared to the actual position can be envisioned as a signature of the extreme locality of the STM measurement. It is indeed visible from our whole set of data that the measured spectrum often changed abruptly as the surface is scanned. Some of these events are really local at the nanometer scale and show anomalies presumably related to point-like impurities. The other events feature step-like evolutions which may be related to local scattering centers in the sample, like grain boundaries.

The experimental data compares therefore favorably with the spectra calculated from the Usadel equations [5], assuming a very simple geometrical model of the complex sample geometry. The same data were also successfully described with the Bogoliubov-de Gennes equations [21]. Vinet *et al.* performed a similar spatially-resolved spectroscopy of Nb-Au structures patterned by lithography [22]. Again a good agreement with the quasi-classical theory based on the Usadel equations was obtained.

4 Anomalous density of states in N-S bilayers

In the following, we will present measurements of the local density of states at the N metal surface of S-N bilayers with a varying N metal thickness [23]. In these samples, the superconducting layer was thick enough that the superconducting gap was not depressed. The achieved high ratio $\Delta/k_B T$ enabled us to study with a high accuracy the mini-gap regime. In particular, we will focus on the case of a long Normal metal ($L \gg \xi_N$) which was not investigated before. This new approach made us unveil a new phenomenon, namely a non-zero density of states appearing in the vicinity of the Fermi level together with clear sub-gap structures, and an anomalous mini-gap width dependence with the N metal length.

We fabricated simultaneously a series of Nb-Au bilayers, with a fixed Nb thickness and a varying Au thickness, on a single ($6 \times 40 \text{ mm}^2$) Si substrate. The Nb layer thickness was chosen to be significantly larger than the coherence length ξ_S in order to avoid any effect due to the finite thickness of the superconductor. For varying the Au thickness, another Si wafer was used as a mask and moved in situ above the Si substrate. After depositing the 120 nm Nb film, the Au film (from 10 to 260 nm) was deposited within 15 minutes at a pressure below 10^{-8} mbar. These conditions minimize the interface contamination and should preserve the best Nb-Au interface transparency. The full Si wafer with the bilayer films thus obtained (see Fig. 4a) was cleaved in air to separate the different samples. Individual Au (260 nm) and Nb (120 nm)

layers were characterized by transport measurements. The calculated values for the characteristic length scales are $\xi_s = 23.2$ and $\xi_n = 60.8$ nm.

Each bilayer sample was cooled separately in the STM, with a freshly cut Pt-Ir wire used as the STM tip. A STM image of the 72 nm Au sample at very low temperature (100 mK) is shown in Fig. 4b. We observe a polycrystalline structure with a grain size of about 50 nm. The same grain size was observed in every sample, except in the thinnest one (10 nm). Moreover, this value is consistent with the measured elastic mean free path $l_{e,n} = 36$ nm in the 260 nm sample. The rms surface roughness is 3.4 nm. Thus our Au films are in clearly in the diffusive regime, except for the smaller thicknesses where ballistic effects may occur. On every sample, we acquired series of $I(V)$ tunnel characteristics, at a tunnel resistance of 5 to 12 $M\Omega$, and at numerous places in order to check reproducibility. The acquired spectra were actually very reproducible over a sample surface. The $I(V)$ data was numerically differentiated to obtain the differential conductance $dI/dV(V)$, which gives the LDOS at the energy eV with an accuracy limited by the thermal smearing. A selection of tunneling spectra is shown in Fig. 4. The spectra are flat at large bias voltages ($|V| \gg 2.5$ meV) and have been normalized to make this conductance as 1.

For the bilayer with the smallest Au thickness (10 nm), the spectrum qualitatively resembles a BCS spectrum with a gap amplitude very close to the expected bulk Nb gap: $\Delta/e \sim 1.5$ meV. For the larger thicknesses, the spectra shows a mini-gap that reduces in width with increasing Au thickness. For large Au thicknesses, there is a small dip at Δ/e which actually implies that the superconducting gap in the bulk of Nb is not significantly influenced by the Au. Inside the mini-gap, the density of states is strikingly different from zero and features a few sub-gap structures. The observed sub-gap features do not scale with the bulk Nb energy gap Δ , as their energy position evolves with the normal metal length L_n . The mean LDOS close to the Fermi level ($V = 0$) monotonously increases with the Au thickness. This effect is therefore not a ballistic one which would be restricted to the smaller thicknesses. Let us point out that the high energy resolution of our STM [17] rules out the thermal smearing as a cause of such a large (up to 50%) zero bias conductance.

We compared our data to the solutions of the Usadel equations with the help of the numerical code from W. Belzig *et al.* [5]. Again, we considered the interface transparency as perfect and we took into account a thermal smearing with an effective temperature of 210 mK. We adjusted the calculation parameters to fit the tunneling spectra. Fig. 5 displays a comparison of experimental spectra with two sets of calculated curves. In order to recover the observed LDOS peaks amplitude and position, we had to assume a mismatch parameter γ value of 0.6 instead of 2.6 as estimated from the transport measurements, keeping the other parameters matching precisely the measured values. This discrepancy may be related to the Nb-Au interface roughness which is expected to affect the Andreev reflection rate [8].

We first assumed that the inelastic and spin-flip scattering lengths are much larger than the Au layer thickness, so that we can neglect these processes

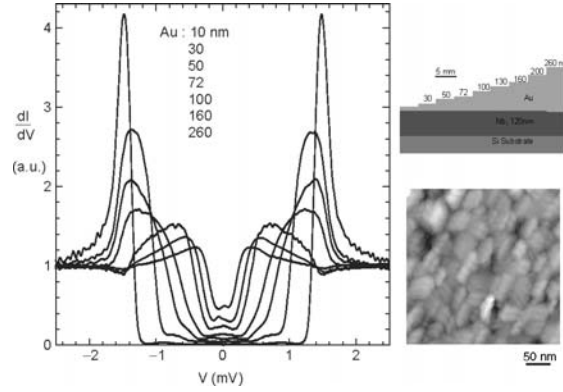


Fig. 4. Left: Tunneling density of states measured at 60 mK at the Au surface of Nb-Au bilayer samples with a varying Au thickness L_n . Data from the 130 and 200 nm samples are not shown for ease of reading. Right, top: Schematic cross section of the full Nb-Au bilayers sample. Right, bottom: STM image ($410 \times 410 \text{ nm}^2$) at 100 mK of the sample with a Au thickness of 72 nm. The rms roughness for this image is 3.4 nm.

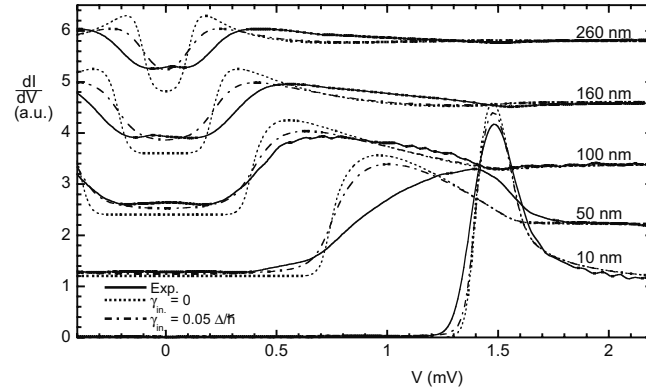


Fig. 5. Comparison of the experimental data for $L_n = 10; 50; 100; 160$ and 260 nm (full line) with the calculated spectra. The calculation parameters are $L_s/\xi_s = 5.17$, $\Delta = 1.57 \text{ meV}$, $T = 210 \text{ mK}$, $\gamma = 0.6$, $r_B = 0$, and $\xi_n = 60.8 \text{ nm}$. The dotted line curve stands for $\gamma_{in} = 0$ and the dashed line curve for $\gamma_{in} = 0.05 \Delta/\hbar$. The curves have been evenly shifted for clarity.

(Fig. 5 dotted lines). The overall spectra shapes are qualitatively reproduced, except for the peak of the 50 nm spectra which is noticeably different from the experimental data. At large L_n , the predicted mini-gap is clearly smaller than in the experiment. Changing the $\xi_{n,s}$ values or introducing a small interface resistance in the calculation did not improve the fit. We tried to take into account the dependence of the elastic mean free path with the normal metal thickness L_n , and hence the related variation of the characteristic length ξ_n

and of the mismatch parameter γ with L_n . This modified only slightly the calculated spectra in the regime $L_n < 100$ nm. Obviously, we always obtain a fully opened gap with a zero LDOS at the Fermi level. This is in clear disagreement with our experimental results, where we always get a non-zero conductance at zero bias.

With the hope to obtain a better fit, we included a non-zero inelastic scattering rate in the calculation parameters (Fig. 5 dashed lines). We achieved a good agreement of the calculated LDOS with the measured one, but only at the precise Fermi level, by choosing $\gamma_{in} = 0.05\Delta/\hbar$. This value corresponds to an inelastic mean free path of about 370 nm, which is significantly smaller than the expected value of about 2 μm . At large thicknesses, the calculated mini-gap remains smaller than in the experiment. Fitting the mini-gap width requires a significant modification of the calculation parameters such that the calculated LDOS close to the Fermi level also diminishes. This makes the disagreement between the experimental data and calculated LDOS even stronger for a fixed value of γ_{in} . We also tried to include a spin-flip scattering [11, 22] or a small interface resistance in the calculation, but it did not improve the fit.

The observed LDOS in N-S bilayers, especially its amplitude at the Fermi level and the mini-gap width evolution, cannot be described by the quasi-classical theory, even after assuming an extremely strong phase-breaking scattering. Our observations are somewhat reminiscent of some unexplained features reported on the LDOS of presumably quite disordered 20 nm N metal ridges lying over a Nb surface [22]. There also, a clear filling of the LDOS at the Fermi level was observed in the absence of any mini-gap width evolution. Let us point out that both this and our systems are far from the strongly disordered regime where a non-zero LDOS for all energies is predicted [25]. Rather, our films have the typical polycrystalline structure of a weakly disordered thin film. The elastic diffusion in the N metal is not homogenous as in an amorphous metal but controlled by the interfaces between ballistic grains. The possible confinement of electron states within a grain can have serious effects on the LDOS in the proximity superconductivity regime of interest here. A significant fraction of electron states may be sufficiently decoupled from the N-S interface to avoid any Andreev reflection. These states would thus remain insensitive to the superconductivity in the S layer and contribute fully to the LDOS.

5 Conclusion

In conclusion, we have probed the local density of states in the vicinity of various N-S structures [19, 23] at very low temperature. The samples with a lateral geometry (and a reduced gap) showed a good agreement between the experiment and the quasi-classical theory. In contrast, N-S bilayers with a

thick N layer feature an anomalous mini-gap width evolution and a non-zero density of states background within the mini-gap.

In our opinion, this new effect was not observed before because previous studies either did not feature the relevant thickness range and a confined geometry where the mini-gap enables a clear observation of additional low-energy single particle states [19, 22], or were carried out at a higher temperature with insufficient energy resolution in the measured LDOS [16]. These features may be related to the precise granular structure of the normal metal, including the growth mechanisms of the Au layer, but should be observable in other similar diffusive hybrid structures. In this respect, it would be very interesting to investigate new samples with a better control of the normal metal nanostructure.

Acknowledgements. — We thank W. Belzig for sharing his numerical code and acknowledge support from the ACI “Nanostructures” program.

References

1. A. F. Andreev, *Sov. Phys. JETP* **19**, 1228 (1964).
2. C. W. J. Beenakker, cond-mat/9909293
3. H. Courtois, Ph. Gandit, D. Mailly and B. Pannetier, *Phys. Rev. Lett.* **76**, 130 (1996).
4. H. Courtois, P. Charlat, Ph. Gandit, D. Mailly and B. Pannetier, *J. of Low Temp. Phys.* **116**, 187 (1999), and references therein.
5. W. Belzig, C. Bruder, and G. Schön, *Phys. Rev. B* **54**, 9443 (1996).
6. A. A. Golubov and M. Yu. Kupriyanov, *J. Low. Temp. Phys.* **61**, 83 (1988).
7. F. Zhou, P. Charlat, B. Spivak and B. Pannetier, *J. of Low Temp. Phys.* **110**, 841 (1998).
8. S. Pilgram, W. Belzig, and C. Bruder, *Phys. Rev. B* **62**, 12462 (2000).
9. J. A. Melsen, P. W. Brouwer, K. M. Frahm and C. W. J. Beenakker, *Europhys. Lett.* **35**, 7 (1996).
10. D. H. Prothero, *Phil. Mag.* **26**, 829 (1973).
11. S. Guéron, H. Pothier, N. O. Birge, D. Estève, and M.H. Devoret, *Phys. Rev. Lett.* **77**, 3025 (1996).
12. M. Sillanpää, T. Heikkilä, R. K. Lindell and P. J. Hakonen, *Europhys. Lett.* **56**, 590 (2001).
13. K. Inoue and H. Takayanagi, *Phys. Rev. B* **43**, 6214 (1991).
14. S. H. Tessmer, M. B. Tarlie, D. J. van Harlingen, D. L. Maslov and P. M. Goldbart, *Phys. Rev. Lett.* **77**, 924 (1996).
15. Y. Levi, O. Millo, N. D. Rizzo, D. E. Prober and L. R. Motowidlo, *Phys. Rev. B* **58**, 15128 (1998).
16. A. D Truscott, R. C. Dynes and L. F. Schneemeyer, *Phys. Rev. Lett.* **83**, 1014 (1999).
17. N. Moussy, H. Courtois and B. Pannetier, *Rev. Sci.Instrum.* **72**, 128 (2001).
18. R. C. Dynes, V. Narayamurti and J. P. Garno, *Phys. Rev. Lett.* **41**, 1509 (1978).
19. N. Moussy, H. Courtois, and B. Pannetier, *Europhys. Lett.* **55**, 861 (2001).
20. S. I. Park and T. H. Geballe, *Physica* **135B**, 108 (1985).

21. K. Halterman and O. T. Valls, *Phys. Rev. B* **66**, 224516 (2002).
22. M. Vinet, C. Chapelier, and F. Lefloch, *Phys. Rev. B* **63**, 165420 (2001).
23. A. K. Gupta, L. Créton, N. Moussy, B. Pannetier and H. Courtois, *Phys. Rev. B* to appear (2004).
24. K. Fuchs, *Proc. Cambridge Philos. Soc.* **11**, 1120 (1938).
25. P. M. Ostrovsky, M. A. Skvortsov and M. V. Feigelman, *Phys. Rev. Lett.* **87**, 027002 (2001).

Quantum Tunneling between Paramagnetic and Superconducting States of a Nanometer-Scale Superconducting Grain Placed in a Magnetic Field

A.V. Lopatin and V.M. Vinokur

Materials Science Division, Argonne National Laboratory, Argonne, Illinois 60439, USA lopatin@anl.gov

Summary. We consider the process of quantum tunneling between the superconducting and paramagnetic states of a nanometer-scale superconducting grain placed in a magnetic field. The grain is supposed to be weakly coupled to a normal metallic contact that plays a role of the spin reservoir. Using the instanton method we find the probability of the quantum tunneling process and express it in terms of the applied magnetic field, order parameter of the superconducting grain and conductance of the tunneling junction between the grain and metallic contact.

1 Introduction

In certain geometrically restricted superconductors the Zeeman effect plays a major role in suppression of superconductivity by applied magnetic field. One of examples of such systems is a thin superconducting film placed in a magnetic field applied in a direction parallel to the film; it was shown a long time ago that an Al film with thickness $b \lesssim 5 \text{ nm}$ at low temperatures exhibits the first order phase transition between the superconducting and normal states at field $H \approx 4.8 \text{ T}$. [1, 2] This magnitude is in a good agreement with the theoretical result $H_{spin} = \Delta/\sqrt{2}\mu_B = 4.4 \text{ T}$ [3] ($\Delta_{film} = 0.38 \text{ meV}$) which is obtained by comparing the Zeeman and condensation energies under assumption that the Zeeman pair breaking effect completely dominates the orbital one.

Another example of a system where the Zeeman effect plays a crucial role is a nano-scale superconducting grain: For a dirty grain the orbital pair breaking effect becomes significant at $H_{orb} \sim \Phi_0/(r\sqrt{D/\Delta})$ [4] where $\Phi_0 = hc/2e$, D is the diffusion coefficient and r is the radius of the grain. Comparing H_{orb} with H_{spin} we have

$$\frac{H_{spin}}{H_{orb}} \sim \sqrt{\frac{\Delta}{d}} \sqrt{\frac{l}{r}} \quad (1)$$

with $l = v_F \tau$ being the mean free path and d being the mean level spacing. In case of the grain with ballistic electron transport and diffusive surface scattering the ratio H_{spin}/H_{orb} can be estimated by taking $l \sim r$ in Eq.(1)

$$\frac{H_{spin}}{H_{orb}} \sim \sqrt{\frac{\Delta}{d}}. \quad (2)$$

We see that in case of the ballistic transport the paramagnetic effect is dominant when Δ becomes less than the mean level spacing. Under such condition the grain cannot be considered as a superconductor [5] since Δ loses its physical meaning of the energy gap. This is, probably, the reason why the first order phase transition was not yet observed in experiments with ultra small Al superconducting grains [6]: For the grains with $\Delta \gg d$ ($r \gtrsim 5 \text{ nm}$) the orbital effect dominates leading to the second order phase transition, while for smaller grains $\Delta \ll d$, there is no well defined order parameter and therefore a phase transition of any kind cannot occur.

On the contrary, for a dirty grain from Eq.(1) we see that the paramagnetic limit can be achieved even in case $\Delta \gg d$ if the ratio l/r is small enough.

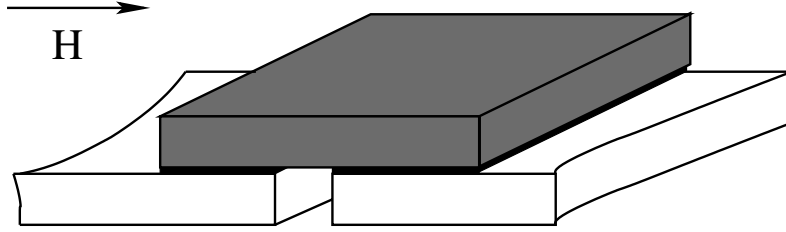


Fig. 1. Schematic picture of a platelet superconducting grain (gray) and two metallic plates separated by the insulating layers (black). The state of the grain can be controlled by measuring the conductance of the grain.

The paramagnetic limit can be also achieved by considering a grain of a special platelet form with thickness b being much less than the area S . Indeed, the orbital field in that case is determined by the smallest size $H_{orb} \sim \Phi_0 / (b \sqrt{D/\Delta})$ while the density of states is determined by the volume $d \sim 1/mk_F S b$ and instead of (1) we have

$$\frac{H_{spin}}{H_{orb}} \sim \sqrt{\frac{\Delta}{d}} \sqrt{\frac{l}{b}} \frac{b}{\sqrt{S}}. \quad (3)$$

From this equation we see that even for ballistic grains ($l/b \sim 1$) the paramagnetic effect can be dominant while $\Delta \gg d$ if the ratio b/\sqrt{S} is sufficiently small.

In the present paper we consider an ultra small superconducting grain placed in a magnetic field assuming that the Zeeman effect dominates the orbital one while the order parameter Δ is larger than the mean level spacing d . According to the written above a clean superconducting grain of platelet geometry or a dirty spherical grain are the possible realizations of such a system. Our goal is to find the probability of quantum tunneling between paramagnetic and superconducting states of the grain. Such quantum tunneling process cannot be entirely described in terms of a Hamiltonian that includes only the superconducting interaction. That is because the paramagnetic and superconducting states are characterized by different values of the total spin, thus some processes allowing for total spin non-conservation must be included in the Hamiltonian. In the present work we assume that the grain is weakly coupled to a normal metallic contact and that this coupling is the dominant mechanism for non-conservation of the total spin of the grain. Schematic picture of a possible experimental set up is shown on Fig. 1. Apart from restrictions on size and shape of a grain described above we also assume that the largest size of the grain is less than the coherence length of a corresponding bulk sample - this makes the problem effectively zero-dimensional in terms of Δ . Our final result for the probability of the quantum tunneling between the superconducting and paramagnetic states is

$$P \sim \exp [N \ln(\beta \delta E G / \Delta_0)] \quad (4)$$

where the numerical coefficient $\beta \approx 1.1$, the factor N is the number of polarized electrons in the paramagnetic state of the grain, G is the conductance of the tunneling junction between the superconducting grain and the metallic plate measured in units e^2/h , Δ_0 is the order parameter of the grain in the superconducting state and $N\delta E$ is the total energy difference between the superconducting and paramagnetic states of the grain. The factor N is of the order of Δ_0/d and it is related with applied magnetic field H and average density of states ν by $N = 2\nu\mu_B H$ with $\mu_B = |e|\hbar/2mc$. The energy difference per one polarized state δE is related with the magnetic field deviation δH from the magnitude at which the thermodynamic phase transition occurs by $\delta E = \mu_B \delta H$. The result (4) is valid only for $\delta E / \Delta_0 \ll 1$, the general case $\Delta_0 \sim \delta E$ is more technically complicated and we leave it for future study.

The paper is organized as follows: In Section II we find the total energy of an isolated grain in applied magnetic field as a function of the total spin of the grain, in section III we write the general expression for the tunneling probability, in section IV we derive the instanton equations which solution is described in sections V-VIII. Our final result is discussed in Section IX. Some details of calculations are presented in the Appendix.

2 Energy of an isolated grain

An isolated superconducting grain can be described by the reduced BCS Hamiltonian with the Zeeman coupling to the magnetic field

$$H_g = \sum_k \psi_k^\dagger [\varepsilon_k - \mu - h\sigma_z] \psi_k - \lambda \sum_{k1, k2} \psi_{k1\uparrow}^\dagger \psi_{k1\downarrow}^\dagger \psi_{k2\downarrow} \psi_{k2\uparrow}, \quad (5)$$

where ψ is a spinor $\psi = (\psi_\uparrow, \psi_\downarrow)$, ε_k are the exact eigenvalues of the non interacting Hamiltonian, μ is the chemical potential and the magnetic field h that is assumed to point along the z - axis is measured in the energy units $h = \mu_B H$.

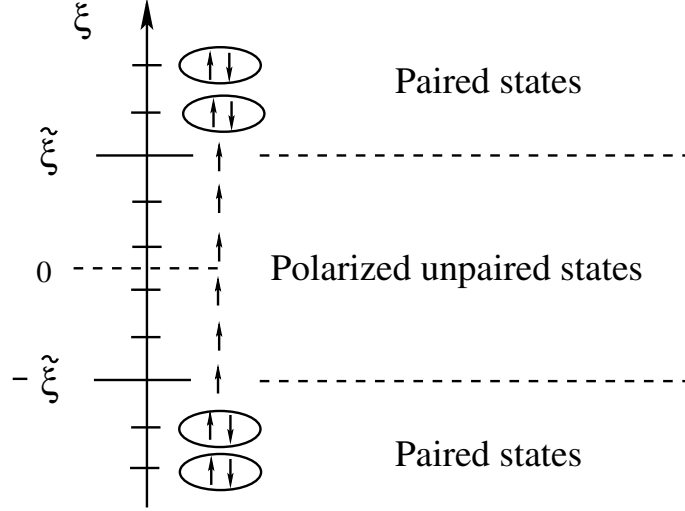


Fig. 2. Schematic presentation of the ground state of the grain in the magnetic field. States with $|\xi| < \tilde{\xi}$ are polarized and unpaired, while the states with $|\xi| > \tilde{\xi}$ are paired and have zero spin.

Since the Hamiltonian (5) conserves the total spin the quantum states of the grain may be characterized by the values of the z -component of the total spin

$$S_z = \frac{1}{2} \sum_k n_{\uparrow k} - n_{\downarrow k}, \quad (6)$$

where $n_\sigma = \langle \psi_\sigma^\dagger \psi_\sigma \rangle$. Therefore the energy of the system can be considered as a function of the total spin S . Technically, the spin can be fixed by introducing the Lagrange multiplier $\tilde{S}_z [\frac{1}{2} \sum_k \psi_k^\dagger \sigma_z \psi_k - S_z]$ into Lagrangian that corresponds to the Hamiltonian (5)

$$\mathcal{L} = -\frac{1}{\lambda} \Delta^* \Delta - \sum_k \psi_k^\dagger [\partial/\partial\tau + \xi_k - \tilde{h}\sigma_z] \psi_k - \Delta \psi_{k\uparrow}^\dagger \psi_{k\downarrow}^\dagger - \Delta^* \psi_{k\downarrow} \psi_{k\uparrow} - \tilde{S}_z S_z, \quad (7)$$

where $\tilde{h} = h + \tilde{S}_z/2$, $\xi_k = \varepsilon_k - \mu$ and the BCS interaction was decoupled with the help of the pair field Δ . In the mean field approximation the action corresponding to the Lagrangian (7) should be at extremum with respect to Δ and \tilde{S}_z , that results in equations defining the order parameter and spin

$$\Delta = \lambda \sum_k f_k, \quad S_z = \sum_k s_{zk}. \quad (8)$$

with $f_k = \langle \psi_{\uparrow k} \psi_{\downarrow k} \rangle$, $f_k^\dagger = \langle \psi_{\downarrow k}^\dagger \psi_{\uparrow k}^\dagger \rangle$ and $s_{zk} = [n_{\uparrow k} - n_{\downarrow k}]/2$. Note, that for a fixed Lagrange multiplier \tilde{h} the energy corresponding to Lagrangian (7) should not be at minimum with respect to Δ , in fact the energy should be stable only with respect to simultaneous variations of Δ and \tilde{h} that leave the total spin conserved. The functions $n = n_\uparrow + n_\downarrow$, s_z and f, f^\dagger can be easily found from the Lagrangian (7): for $\sqrt{\xi^2 + \Delta^2} > |\tilde{h}|$ we obtain

$$n = 1 - \frac{\xi}{\sqrt{\xi^2 + |\Delta|^2}}, \quad f = \frac{\Delta}{2\sqrt{\xi^2 + |\Delta|^2}}, \\ f^\dagger = f^*, \quad s_z = 0, \quad (9)$$

and for $\sqrt{\xi^2 + \Delta^2} < |\tilde{h}|$ we have

$$n = 1, \quad f = f^\dagger = 0, \quad s_z = 1/2. \quad (10)$$

Introducing the energy $\tilde{\xi} = \sqrt{\tilde{h}^2 - \Delta^2}$ we clearly see the physical meaning of Eqs.(9): states with $|\xi| > \tilde{\xi}$ are paired and thus have nonzero f - functions and zero spin (see Fig 2.), while the states with $|\xi| < \tilde{\xi}$ are unpaired having zero f - functions and only one electron per state with spin $s_z = 1/2$. Thus, the total spin in terms of energy $\tilde{\xi}$ is

$$S = N/2 = \frac{1}{2} \sum_{\xi_k} \theta(|\xi_k| - \tilde{\xi}). \quad (11)$$

The energy of the superconducting grain in the mean field approximation is given by

$$E' = \frac{1}{\lambda} \Delta^* \Delta - 2S_z h + \sum_k \xi_k n_k - \Delta^* f_k - \Delta f_k^\dagger. \quad (12)$$

It is convenient to subtract the energy of the normal state in absence of the magnetic field $E_0 = 2 \sum_{\xi < 0} \xi_k$ from Eq. (12) and consider $E = E' - E_0$. Using Eqs. (9,10) we obtain

$$E = \frac{1}{\lambda} \Delta^* \Delta - 2hS_z + \sum_k |\xi_k| - \sum_{|\xi_k| > \tilde{\xi}} \sqrt{\xi_k^2 + |\Delta|^2}. \quad (13)$$

We shall assume that only the levels with $|\xi| < \omega_D$ where $\omega_D \gg \Delta$ is the Debye frequency are paired. Assuming also that the density of states ν is

constant around the Fermi level and choosing Δ to be real from Eq. (8) we obtain

$$\frac{1}{\lambda\nu} = \int_{\tilde{\xi}}^{\omega_D} d\xi \frac{1}{\sqrt{\xi^2 + \Delta^2}} = \ln \frac{2\omega_D}{\tilde{\xi} + \sqrt{\tilde{\xi}^2 + \Delta^2}}. \quad (14)$$

The order parameter Δ_0 in absence of the magnetic field is determined by

$$1/\lambda\nu = \ln 2\omega_D/\Delta_0. \quad (15)$$

Using this equation we can present Eq. (14) in the form

$$\tilde{\xi} + \sqrt{\tilde{\xi}^2 + \Delta^2} = \Delta_0, \quad (16)$$

from which we see that the superconducting state exists only in the region $0 < \tilde{\xi} < \Delta_0/2$, for $\tilde{\xi} > \Delta_0/2$ only paramagnetic state is possible. Finally, for the energy we obtain

$$E/\nu = -\Delta_0^2/2 + 2\tilde{\xi}\Delta_0 - \tilde{\xi}^2 - 2h\tilde{\xi}, \quad \tilde{\xi} < \Delta_0/2, \quad (17)$$

$$E/\nu = -2h\tilde{\xi} + \tilde{\xi}^2, \quad \tilde{\xi} > \Delta_0/2, \quad (18)$$

Under assumption of constant density of states the total spin is related with $\tilde{\xi}$ by $S = N/2 = \nu\tilde{\xi}$.

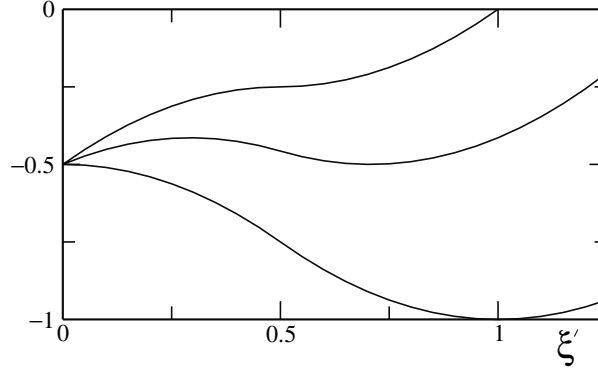


Fig. 3. Dependence of the energy $E/\Delta_0^2\nu$ on a variable $\xi' = \tilde{\xi}/\Delta_0$ which is related with a total spin as $S = \nu\Delta_0\tilde{\xi}$ for different magnetic fields $h = \Delta_0/2, \Delta_0/\sqrt{2}, \Delta_0$ (from top to bottom). The superconducting state corresponds to the region $\xi' < 0.5$.

Dependence of the energy of the grain on $\tilde{\xi}$ is shown on Fig. 3. For the Hamiltonian with no spin relaxation that we have considered so far all the values of $\tilde{\xi}$ correspond to the stable physical states. If one turns on a finite spin relaxation, then only the minima of $E(\tilde{\xi})$ will describe stable or locally stable states. In this case, from Fig. 1 we see that, for $h < \Delta_0/2$ only the

superconducting state ($\tilde{\xi} = 0, \Delta \neq 0$) is stable while for $h > \Delta_0$ only the paramagnetic state is stable. In the intermediate regime $\Delta_0/2 < h < \Delta_0$ both phases are locally stable such that for $h < \Delta_0/\sqrt{2}$ the superconducting state is globally stable and for $h > \Delta_0/\sqrt{2}$ the paramagnetic state is globally stable.

3 Tunneling

The main goal of our study is to develop a theory of quantum tunneling between superconducting and paramagnetic states. This tunneling process cannot be entirely described by the Hamiltonian (5) for the reason that it conserves the total spin of the grain while during the quantum tunneling process the total spin of the grain must change. Thus, some additional processes allowing for non-conservation of the total spin of the grain should be included. We shall consider the simplest case: the superconducting grain is weakly coupled to the normal metallic contact that plays a role of an external spin bath and the spin exchange between the grain and the normal metal is realized by means of electron tunneling. The system of the grain and metal is described by the Hamiltonian

$$\hat{H} = \hat{H}_g + \hat{H}_M + \sum_{k,k'} t_{kk'} [\hat{\psi}_{k\sigma}^\dagger \hat{d}_{k'\sigma} + \hat{d}_{k'\sigma}^\dagger \hat{\psi}_{k\sigma}]. \quad (19)$$

where \hat{H}_g and \hat{H}_M are the Hamiltonians of the grain and metallic contact respectively, \hat{d}^\dagger and \hat{d} are the creation and annihilation operators of electrons that belong to the metal and $t_{kk'}$ is the electron tunneling matrix element between the grain and metal. Electrons that belong to the metallic contact are assumed to be described by the free-fermion Hamiltonian H_M

$$\hat{H}_M = \sum_{k'} \hat{d}_{k'\sigma}^\dagger \zeta_{\sigma k'} \hat{d}_{k'\sigma}.$$

The amplitude of tunneling process between the initial and final states is given by the general formula

$$A = \langle f | T_t e^{-i \int_{t_i}^{t_f} \hat{H}(t) dt} | i \rangle. \quad (20)$$

The Hamiltonian (19) in Eq. (20) is written in the interaction representation: the noninteracting part includes the metal Hamiltonian H_M and the first (free-fermion) term of grain Hamiltonian (5) while the interaction part includes the BCS interaction and electron tunneling between the grain and metal. We shall consider a process of quantum tunneling from pure superconducting state (initial state) to the paramagnetic state with $\Delta = 0$ (see Fig. 4). The electron tunneling between the grain and metal will be treated as a perturbation assuming that the tunneling matrix elements $t_{kk'}$ are weak. During the quantum tunneling process the spin of the grain must change by

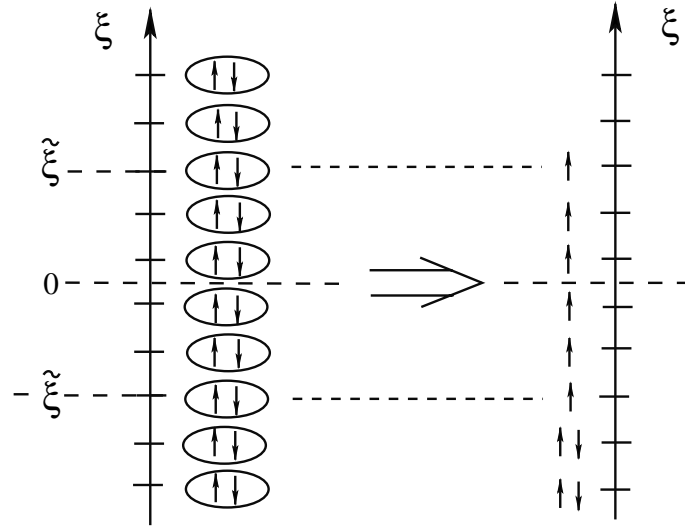


Fig. 4. Ground states of the grain before the quantum tunneling process (left) and after (right). The spin of the grain increases from zero to S during the tunneling process due to the quasiparticle exchange with the metallic plate.

S , thus there must be $N = 2S$ electron tunneling processes between the grain and metal and therefore the first nonzero contribution in expansion in $t_{kk'}$ of Eq. (20) emerges only in the N -th order. Moreover from the analysis of the previous section it is clear that the paired states which are destroyed by the electron tunneling are those with $|\xi| < \tilde{\xi}$. Expanding Eq. (20) in $t_{kk'}$ we have

$$\begin{aligned}
 A = & \langle f | \prod_{|\xi_k| < \tilde{\xi}} \int dt_k T_t e^{-i \int_{t_i}^{t_f} \hat{H}(t) dt} \sum_{k'} t_{kk'} \\
 & \times [\hat{\psi}_{k\sigma}^\dagger(t_k) \hat{d}_{k'\sigma}(t_k) + \hat{d}_{k'\sigma}^\dagger(t_k) \hat{\psi}_{k\sigma}(t_k)] | i \rangle .
 \end{aligned} \quad (21)$$

In the absence of coupling between the grain and metal the initial and final states of the system are the products of corresponding initial and final states of the grain and metal

$$|i\rangle = |i_G\rangle |i_M\rangle, \quad |f\rangle = |f_G\rangle |f_M\rangle, \quad (22)$$

thus in the leading order in $t_{kk'}$ the quantum mechanical average of operators \hat{d} in (21) can be directly implemented. During the tunneling process the z-component of the spin of the grain increases while the z-component of the total spin of the metal decreases. Thus the only relevant processes inside the metal are creation of electrons with spin down and annihilation of electrons (or equivalently creation of holes) with spin up. The corresponding matrix elements are:

$$\langle f_M | d_{k\downarrow}^\dagger(t) | i_M \rangle = e^{i\zeta_{k\downarrow} t}, \quad \zeta_{k\downarrow} > 0 \quad (23)$$

$$\langle f_M | d_{k\uparrow}(t) | i_M \rangle = e^{i\zeta_{k\uparrow} t}, \quad \zeta_{k\uparrow} < 0. \quad (24)$$

The initial state of the metal is the Fermi sea while its final state having N electron/hole excitations is characterized by the set of excitation energies $\zeta_{k'\alpha}^{\{p\}}$ where the index k' labels the quantum number of excitation p . k' labels its quantum number. Assuming a simple model for electron tunneling matrix elements [7]

$$t_{kk'} = t \quad (25)$$

the amplitude of the tunneling process can be written as

$$\begin{aligned} A = t^N \langle f_G | T_t \prod_{|\xi_k| < \bar{\xi}} \int dt_k e^{-i \int_{t_i}^{t_f} \hat{H}(t) dt} \sum_{\text{Per } p(k)} e^{i\zeta_{k'}^{\{p(k)\}} t_k} \\ \times [\hat{\psi}_{k\uparrow}^\dagger(t_k) \theta(-\zeta_{k'}^{\{p(k)\}}) + \hat{\psi}_{k\downarrow}(t_k) \theta(\zeta_{k'}^{\{p(k)\}})] | i_G \rangle \end{aligned} \quad (26)$$

where the sum goes over all excitation permutations $p(k)$. At this step we will simplify the problem further: we shall assume that the typical excitation energy in the metal is much less than Δ_0 . This is always the case if the difference of the energy of the paramagnetic and superconducting states per one polarized electron energy level

$$\delta E = (E_{sup} - E_{par})/N$$

is much less than Δ_0 . In this case in the leading order we can neglect the energies $\zeta_{k'}^{\{p\}}$ in (26) and using the Heisenberg representation we write the amplitude (26) as

$$\begin{aligned} A = N! t^N \langle f_G | \prod_{|\xi_k| < \bar{\xi}} \int dt_k [\hat{\psi}_{k\uparrow}^\dagger(t_k) \theta(-\zeta_{k'}^{\{p(k)\}}) \\ + \hat{\psi}_{k\downarrow}(t_k) \theta(\zeta_{k'}^{\{p(k)\}})] | i_G \rangle, \end{aligned} \quad (27)$$

where a specific permutation $p(k)$ was chosen.

The probability of an elementary process with a given final state (characterized by the set of the excitation energies $\zeta_{k'}^{\{p\}}$) is $A^* A$, thus the whole probability P of the tunneling process should be obtained by integrating $A^* A$ over all possible quantum states of the metal.

$$P \sim \frac{\nu_M^N}{N!} \int d\zeta^{\{1\}} \dots d\zeta^{\{N\}} A^* A \delta(N \delta E - \sum_p |\zeta^{\{p\}}|), \quad (28)$$

where ν_M is the density of states of the metal.

To find the values of A we shall use the instanton method turning to operate with the Euclidean time $t \rightarrow -i\tau$. Taking initial and final times as $\tau_i = -\infty, \tau_f = 0$ we present the amplitude A as

$$A = N! t^N \langle f_G | S(0, -\infty) | i_G \rangle \quad (29)$$

with the evolution operator

$$S(\tau_2, \tau_1) = \prod_{|\xi_k| < \tilde{\xi}} \int_{\tau_1}^{\tau_2} d\tau_k [\hat{\psi}_{k\uparrow}^\dagger(\tau_k) \theta(-\zeta_{k'}^{\{p(k)\}}) + \hat{\psi}_{k\downarrow}(\tau_k) \theta(\zeta_{k'}^{\{p(k)\}})] \quad (30)$$

In principle, the instanton method should be applied to the amplitude A directly, but it is more convenient to consider the product $A^* A$ presenting A^* as

$$A^* = N! t^N \langle i_G | S^\dagger(\infty, 0) | f_G \rangle . \quad (31)$$

and writing the product $A^* A$ as

$$\begin{aligned} \langle i_G | S^\dagger(\infty, 0) | f_G \rangle \langle f_G | S(0, -\infty) | i_G \rangle \\ = \langle i_G | S^\dagger(\infty, 0) S(0, -\infty) | i_G \rangle . \end{aligned} \quad (32)$$

where we used that by construction the Euclidean evolution operator S must bring the system from initial $|i_G\rangle$ to the final $|f_G\rangle$ state: $S|i_G\rangle = |f_G\rangle$. Now the instanton process has the following structure (see Fig. 5.): the evolution begins at $\tau = -\infty$ from the superconducting state, then at $\tau \approx -T$ the system turns into the paramagnetic state and stays there till it turns back to the superconducting state at $\tau \approx T$. The artificial part of process ($\tau > 0$) is the mirror reflection of the “physical” process with $\tau < 0$.

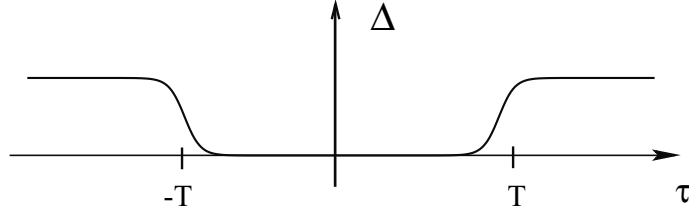


Fig. 5. Dependence of the order parameter Δ on time τ . The region $\tau > 0$ is the mirror reflection of the “physical” region $\tau < 0$. The superconducting state corresponds to the regions $|\tau| > T$ while the paramagnetic one to $|\tau| < T$.

The advantage of this representation is that now the new initial ($\tau = -\infty$) and final ($\tau = \infty$) states are identical and therefore we can use the convenient functional representation for $A^* A$

$$\begin{aligned}
 A^* A &= [N! t^N]^2 \int D\psi^\dagger D\psi e^{\int \mathcal{L} dt} \prod_k \int d\tau_{1k} d\tau_{2k} \\
 &\times \left[\psi_{k\uparrow}(\tau_{1k}) \psi_{k\uparrow}^\dagger(\tau_{2k}) \theta(-\zeta_{k'}^{\{p(k)\}}) \right. \\
 &\quad \left. + \psi_{k\downarrow}^\dagger(\tau_{1k}) \psi_{k\downarrow}(\tau_{2k}) \theta(\zeta_{k'}^{\{p(k)\}}) \right], \tag{33}
 \end{aligned}$$

with the Lagrangian

$$\begin{aligned}
 \mathcal{L} &= -\frac{1}{\lambda} \Delta^* \Delta - \sum_k \psi_k^\dagger [\partial_\tau + \xi_k - h \sigma_z] \psi_k \\
 &\quad - \Delta \psi_{k\uparrow}^\dagger \psi_{k\downarrow}^\dagger - \Delta^* \psi_{k\downarrow} \psi_{k\uparrow}. \tag{34}
 \end{aligned}$$

Note that the integration over the fermionic fields in (33) should be implemented exactly while the assumed integration over $\Delta(\tau)$ will be taken with the saddle point accuracy. Now taking integrals in (28) for the probability we obtain

$$\begin{aligned}
 P &= e^{N \ln(N \delta E t^2 \nu_M)} \int D\psi^\dagger D\psi \prod_k \int d\tau_{1k} d\tau_{2k} \\
 &\times e^{\int \mathcal{L} d\tau} [\psi_{k\uparrow}(\tau_{1k}) \psi_{k\uparrow}^\dagger(\tau_{2k}) + \psi_{k\downarrow}^\dagger(\tau_{1k}) \psi_{k\downarrow}(\tau_{2k})], \tag{35}
 \end{aligned}$$

where we used that $N! = N \ln N - N$ in the limit $N \gg 1$. Finally integrating over the fermionic fields we obtain

$$\begin{aligned}
 \ln P &= N \ln(N \delta E t^2 \nu_M) + \sum_k \text{Tr} \ln[\partial_\tau + \mathcal{H}_k] \\
 &- \frac{1}{\lambda} \int d\tau \Delta^*(\tau) \Delta(\tau) + \sum_k \ln \text{Tr} \int d\tau_1 d\tau_2 \hat{G}_{1k}(\tau_1, \tau_2), \tag{36}
 \end{aligned}$$

where

$$\mathcal{H}_k(\tau) = \begin{bmatrix} \xi_k - h & \Delta(\tau) \\ \Delta^*(\tau) & -\xi_k - h \end{bmatrix}, \tag{37}$$

and the matrix Green function $\hat{G}_1(\tau_1, \tau_2)$ is defined by the equation

$$[\partial_{\tau_1} + \mathcal{H}_k(\tau_1)] \hat{G}_{1k}(\tau_1, \tau_2) = \delta(\tau_1 - \tau_2). \tag{38}$$

This Green function can be written as the average of the Nambu spinors $\tilde{\psi} = (\psi_\uparrow, \psi_\downarrow^\dagger)$ with respect to the Lagrangian (34)

$$\hat{G}_{1k}^{\alpha\beta}(\tau_1, \tau_2) = \langle \tilde{\psi}_k^\alpha(\tau_1) \tilde{\psi}_k^{\beta\dagger}(\tau_2) \rangle_{\mathcal{L}}. \tag{39}$$

For the components of \hat{G}_1 we adopt the standard notations

$$\hat{G}_{1k}(\tau_1, \tau_2) = \begin{bmatrix} G_{1k}(\tau_1, \tau_2) & F_{1k}(\tau_1, \tau_2) \\ F_{1k}^\dagger(\tau_1, \tau_2) & \bar{G}_{1k}(\tau_1, \tau_2) \end{bmatrix}. \tag{40}$$

4 Instanton equations

To find the instanton equations we take the functional derivative of Eq.(36) with respect to Δ^* obtaining

$$\frac{1}{\lambda}\Delta(\tau) = \sum_k f_{1k}(\tau) + f_{2k}(\tau), \quad (41)$$

where the Green function $f_1(\tau) = F_1(\tau, \tau)$ emerges from the variational derivative of $\text{Tr} \ln[\partial_\tau + \mathcal{H}_k]$ in (36) and f_2 emerges from the functional derivative of the Green function \hat{G}_1

$$f_2(\tau) = Z_k^{-1} \frac{\delta}{\delta \Delta^*(\tau)} \text{Tr} \int d\tau_1 d\tau_2 G_{1k}(\tau_1, \tau_2), \quad (42)$$

where $Z_k = \int d\tau_1 d\tau_2 \text{Tr} G_{1k}(\tau_1, \tau_2)$.

The function $f_1(\tau)$ being the equal-time part of $F_1(\tau_1, \tau_2)$ is completely determined by the definition of the Green function (38). But instead of using Eq. (38) it is more convenient to derive equations that define $f_1(\tau)$ entirely in terms of the equal time Green functions

$$\hat{g}_{1k}(\tau) = \begin{bmatrix} g_{1k}(\tau) & f_{1k}(\tau) \\ f_{1k}^\dagger(\tau) & \bar{g}_{1k}(\tau) \end{bmatrix} = \hat{G}_{1k}(\tau, \tau). \quad (43)$$

For that we write Eq.(38) in the form

$$\hat{G}_{1k}(\tau_1, \tau_2)(-\partial_{\tau_2} + \mathcal{H}_k(\tau_2)) = \delta(\tau_1 - \tau_2), \quad (44)$$

where derivative ∂_{τ_2} acts on the left and then we add Eqs. (38, 44) obtaining

$$\partial_\tau \hat{g}_1(\tau) + [\mathcal{H}_0(\tau), \hat{g}_1(\tau)] = 0, \quad (45)$$

where

$$\mathcal{H}_0(\tau) = \begin{bmatrix} \xi_k & \Delta(\tau) \\ \Delta^*(\tau) & -\xi_k \end{bmatrix}. \quad (46)$$

Note that Eqs. (45, 46) do not contain the magnetic field h . Writing Eq. (45) in components we get

$$\partial_\tau \tilde{g}_{1k} + \Delta f_{1k}^\dagger - \Delta^* f_{1k} = 0, \quad (47)$$

$$\partial_\tau f_{1k} + 2\xi f_{1k} - 2\Delta \tilde{g}_{1k} = 0, \quad (48)$$

$$-\partial_\tau f_{1k}^\dagger + 2\xi f_{1k}^\dagger - 2\Delta^* \tilde{g}_{1k} = 0, \quad (49)$$

$$\partial_\tau s_{z1k} = 0, \quad (50)$$

where the variables

$$\tilde{g}_{1k} = [g_{1k} - \bar{g}_{1k}]/2, \quad s_{z1k} = -[g_{1k} + \bar{g}_{1k}]/2, \quad (51)$$

were introduced instead of components g_1 and \bar{g}_1 . Eqs. (47, 48, 49) are very similar to the well known Eilenberger [8] equations and posses the same invariant

$$\tilde{g}_{1k}^2 + f_{1k}^\dagger f_{1k} = \text{const.} \quad (52)$$

Now we turn to the function $f_2(\tau)$: Using the definition of the Green function (38) one can take the variation derivative in (42)) obtaining

$$f_{2k}(\tau) = -\frac{f_k^{II}(\tau)g_k^I(\tau) + \bar{g}_k^{II}(\tau)f_k^I(\tau)}{\int d\tau[g_k^I(\tau) + \bar{g}_k^I(\tau)]} \quad (53)$$

where

$$\hat{g}_k^I(\tau) \equiv \begin{bmatrix} g_k^I(\tau) & f_k^I(\tau) \\ f_k^{\dagger I}(\tau) & \bar{g}_k^I(\tau) \end{bmatrix} = \int d\tau_2 \hat{G}_{1k}(\tau, \tau_2) \quad (54)$$

and

$$\hat{g}_k^{II}(\tau) \equiv \begin{bmatrix} g_k^{II}(\tau) & f_k^{II}(\tau) \\ f_k^{\dagger II}(\tau) & \bar{g}_k^{II}(\tau) \end{bmatrix} = \int d\tau_1 \hat{G}_{1k}(\tau_1, \tau). \quad (55)$$

Analogously we define the function f_2^\dagger as a derivative of $\ln Z_k$ with respect to Δ^*

$$f_{2k}^\dagger(\tau) = -\frac{g_k^{II}(\tau)f_k^{\dagger I}(\tau) + f_k^{\dagger II}(\tau)\bar{g}_k^I(\tau)}{\int d\tau[g_k^I(\tau) + \bar{g}_k^I(\tau)]}. \quad (56)$$

Equations that determine the functions \hat{g}^I and \hat{g}^{II} can be easily found by integrating Eq. (38) over τ_2 and Eq. (44) over τ_1

$$\partial_\tau g_k^I(\tau) + \mathcal{H}_k(\tau)g_k^I(\tau) = 1, \quad (57)$$

$$-\partial_\tau g_k^{II}(\tau) + g_k^{II}(\tau)\mathcal{H}_k(\tau) = 1. \quad (58)$$

5 Boundary conditions

To determine boundary conditions for the functions $\hat{g}_1, f_2, f_2^\dagger$ first we introduce the ‘‘physical’’ equal time matrix Green function

$$\hat{g}_k(\tau) = \begin{bmatrix} g_k(\tau) & f_k(\tau) \\ f_k^\dagger(\tau) & \bar{g}_k(\tau) \end{bmatrix}, \quad (59)$$

which is defined with respect to the evolution operator $S^\dagger S$,

$$\hat{g}_k^{\alpha,\beta}(\tau) = \frac{\langle i_S | S^\dagger(\infty, 0) S(0, \tau) \tilde{\psi}_k^\alpha \tilde{\psi}_k^{\beta\dagger} S(\tau, -\infty) | i_S \rangle}{\langle i_S | S^\dagger(\infty, 0) S(0, -\infty) | i_S \rangle} \quad (60)$$

where negative τ was chosen for concreteness. To find the function $\hat{g}_k(\tau)$ in the functional representation we add the source term $\int d\tau \mu_k^{\alpha\beta}(\tau) \tilde{\psi}_\alpha(\tau) \tilde{\psi}_\beta^\dagger(\tau)$

to the Lagrangian (34) and take the variation derivative of (36) with respect to $\mu_k^{\alpha\beta}(\tau)$ obtaining

$$\hat{g}_k(\tau) = \hat{g}_{1k}(\tau) + \hat{g}_{2k}(\tau), \quad (61)$$

where \hat{g}_{1k} is defined by Eq.(43) and the off-diagonal components of the function

$$\hat{g}_{2k}(\tau) = \begin{bmatrix} g_{2k}(\tau) & f_{2k}(\tau) \\ f_{2k}^\dagger(\tau) & \bar{g}_{2k}(\tau) \end{bmatrix} \quad (62)$$

are defined by Eqs. (53, 56), while the diagonal components are

$$\begin{aligned} g_{2k}(\tau) &= Z_k^{-1} \frac{\delta}{\delta \mu_\uparrow(\tau)} \int d\tau_1 d\tau_2 G_k(\tau_1, \tau_2) \\ &= - \frac{g^{II}(\tau)g^I(\tau) + f^{\dagger II}(\tau)f^I(\tau)}{\int d\tau [g^I(\tau) + \bar{g}^I(\tau)]}, \end{aligned} \quad (63)$$

$$\begin{aligned} \bar{g}_{2k}(\tau) &= Z_k^{-1} \frac{\delta}{\delta \mu_\downarrow(\tau)} \int d\tau_1 d\tau_2 G_k(\tau_1, \tau_2) \\ &= - \frac{\bar{g}^{II}(\tau)\bar{g}^I(\tau) + f^{II}(\tau)f^{\dagger I}(\tau)}{\int d\tau [g^I(\tau) + \bar{g}^I(\tau)]}. \end{aligned} \quad (64)$$

To the extent one can consider an instanton trajectory as a physical process (in fact only the initial and final states of the instanton trajectory have a physical sense) only the function \hat{g} has a physical meaning and therefore the physical requirements for boundary conditions should be applied to the function \hat{g} .

In the superconducting phase ($|\tau| \gg |T|$) this function should coincide with the equilibrium superconducting Green functions

$$\tilde{g}_k = \frac{\xi_k}{2\sqrt{\xi_k^2 + \Delta_0^2}}, \quad f_k = \frac{\Delta_0}{2\sqrt{\xi_k^2 + \Delta_0^2}}, \quad f_k^\dagger = f_k^*, \quad s_z = 0 \quad (65)$$

where the functions \tilde{g} and s_z are defined in a similar way with \tilde{g}_1 and s_{z1}

$$\tilde{g}_k = [g_k - \bar{g}_k]/2, \quad s_{zk} = -[g_k + \bar{g}_k]/2. \quad (66)$$

The function \tilde{g} is directly related with electron density on the level k by $n_k = 1 - 2\tilde{g}_k$ and the function s_{zk} is the z-component of the spin on the level k . Analogously, in the paramagnetic phase the Green function \hat{g} should coincide with the equilibrium Green functions defined by Eqs. (9, 10) with $\Delta = 0$. For the sake of generality (it is also useful for numerical solution) we shall assume that the order parameter in the paramagnetic phase $\Delta_p \neq 0$. Our final results though will be applicable only for $\Delta_p = 0$. Thus, in the paramagnetic phase the boundary conditions for the function $\hat{g}_k(\tau)$ are

$$\tilde{g}_k = \frac{\xi_k}{2\sqrt{\xi_k^2 + \Delta_p^2}}, \quad f_k = \frac{\Delta_p}{2\sqrt{\xi_k^2 + \Delta_p^2}}, \quad f_k^\dagger = f_k^*,$$

$$s_{zk} = 0, \quad \text{for} \quad |\xi_k| > \tilde{\xi} \quad (67)$$

$$\tilde{g}_k = f_k = f_k^\dagger = 0, \quad s_{zk} = 1/2 \quad \text{for} \quad |\xi_k| < \tilde{\xi}. \quad (68)$$

The boundary conditions formulated in Eqs. (65, 67, 68) contain all the physical requirements for the instanton trajectory. Now we need to figure out the boundary conditions for the functions \hat{g}_1, \hat{g}_2 that are consistent with Eqs. (65, 67, 68). We will show below that the function $\hat{g}_2 \rightarrow 0$ in the superconducting region. Thus, at $|\tau| \gg |T|$ the Green function \hat{g}_1 has the same boundary conditions with those defined by Eq. (65) for function \hat{g}_k

$$\tilde{g}_{1k} = \frac{\xi_k}{2\sqrt{\xi_k^2 + \Delta_0^2}}, \quad f_{1k} = \frac{\Delta_0}{2\sqrt{\xi_k^2 + \Delta_0^2}},$$

$$f_{1k}^\dagger = f_{1k}^*, \quad s_{z1k} = 0. \quad (69)$$

One can see that the Green functions defined by Eqs. (69) at the same time are the stationary solutions of Eqs. (47, 48, 49). Boundary conditions (69) also define the value of the invariant (52)

$$\tilde{g}_{1k}^2 + f_{1k}^\dagger f_{1k} = 1/4. \quad (70)$$

In the paramagnetic region $|\tau| \ll |T|$ the boundary conditions for the function \hat{g}_1 are analogous to those defined by Eq.(69)

$$\tilde{g}_{1k} = \frac{\xi_k}{2\sqrt{\xi_k^2 + \Delta_p^2}}, \quad f_{1k} = \frac{\Delta_p}{2\sqrt{\xi_k^2 + \Delta_p^2}},$$

$$f_{1k}^\dagger = f_{1k}^*, \quad s_{z1k} = 0. \quad (71)$$

These are the only possible boundary conditions for the function \hat{g}_1 in the paramagnetic region because (i) in the paramagnetic state the components of the Green function \hat{g}_1 must be the stationary solutions of Eqs. (47, 48, 49) and (ii) Eq. (70) should be satisfied.

Now knowing the boundary conditions for functions \hat{g} and \hat{g}_1 given by Eqs. (67, 68, 71) we finally determine the boundary conditions for \hat{g}_2 in the paramagnetic phase:

$$\tilde{g}_{2k} = -\frac{\xi_k}{2\sqrt{\xi_k^2 + \Delta_p^2}}, \quad f_{2k} = -\frac{\Delta_p}{2\sqrt{\xi_k^2 + \Delta_p^2}},$$

$$f_{2k}^\dagger = f_{2k}^*, \quad s_{z2k} = 1/2. \quad (72)$$

6 Numerical solution for function \hat{g}_1

For a given order parameter configuration $\Delta(\tau)$ the functions $\tilde{g}_{1k}(\tau)$, $f_{1k}(\tau)$, $f_{1k}^\dagger(\tau)$ can be found numerically by solving Eqs. (47-49) supplemented by the boundary conditions (69, 71). Numerical solutions for functions $\tilde{g}_{1k}(\tau)$ and $f_{1k}^{(s)}(\tau) \equiv f_{1k}(\tau) + f_{1k}^\dagger(\tau)$ corresponding to the self-consistent configuration of $\Delta(\tau)$ (see below) in the region $\tau \sim T$ are shown on Fig. 6. Solutions at the left instanton boundary $\tau \sim -T$ can be obtained by the time reversal transformation $\tau \rightarrow -\tau$, $\Delta \rightarrow \Delta^*$, $\tilde{g}_1 \rightarrow \tilde{g}_1$, $f \rightarrow f^\dagger$, $f^\dagger \rightarrow f$ following from Eqs. (47-49). Since we choose the real order parameter $\Delta(\tau)$ the functions $\Delta(\tau)$, $\tilde{g}_{1k}(\tau)$ and $f_{1k}^{(s)}(\tau)$ shown on Fig. 6 are symmetric under time reflection $\tau \rightarrow -\tau$.

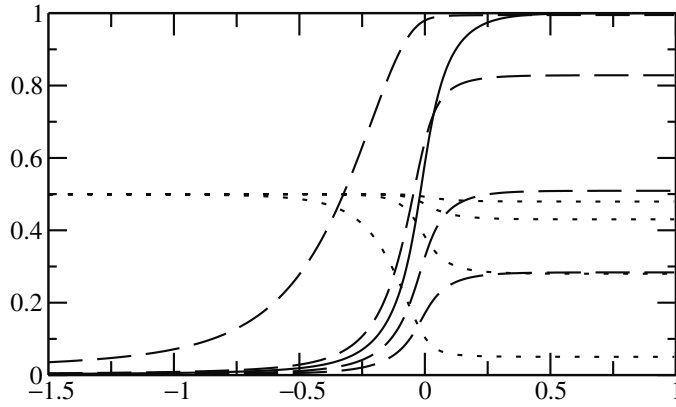


Fig. 6. Order parameter $\Delta(\tau)/\Delta_0$ (solid line) and functions $\tilde{g}_{1k}(\tau)$ (dotted lines) and $f_{1k}^{(s)}(\tau) = f_{1k}(\tau) + f_{1k}^\dagger(\tau)$ (dashed lines) plotted as functions of $(\tau - T)d$ for electron levels $\xi = 3d, 20d, 50d, 100d$. For the functions \tilde{g}_{1k} higher curves correspond to larger ξ_k while for the functions $f_{1k}^{(s)}$ higher curves correspond to lower ξ_k .

7 Asymptotic and boundary conditions of functions \hat{g}^I, \hat{g}^{II}

According to Eqs. (53, 56, 63, 64) the matrix Green function \hat{g}_2 is determined by the matrix Green functions \hat{g}^I and \hat{g}^{II} defined by Eqs. (57, 58). Now our task is to find such solutions of Eqs. (57, 58) that being inserted into Eqs. (53, 56, 63, 64) provide the Green function \hat{g}_2 satisfying the proper boundary conditions found in Sec. 5.

Let us first formulate the ansatz for general form of the functions \hat{g}^I, \hat{g}^{II} and then show that this ansatz leads to the function \hat{g}_2 satisfying all the necessary requirements. The function g^I exponentially grows $\hat{g}^I \sim e^{\lambda_p \tau}$ in the

interval $(-T, T)$ from values of order of $1/\Delta_0$ at $\tau \sim -T$ to exponentially large values at $\tau \sim T$. At $\tau > T$ the function g^I exponentially decrease $\hat{g}^I \sim e^{\lambda_s \tau}$. The corresponding exponents may be easily found from Eq. (57) where we can neglect the r.h.s. since \hat{g}^I is exponentially large in the region $t \sim T$

$$\lambda_p = h - \sqrt{\xi_k^2 + \Delta_p^2} > 0, \quad \lambda_s = h - \sqrt{\xi_k^2 + \Delta_0^2} < 0.$$

In the region $\tau \ll -T$ the function \hat{g}^I is time independent and can be easily found as a stationary solution of Eq. (57)

$$\hat{g}^I = D^{-1} \begin{bmatrix} \xi_k + h & \Delta_0 \\ \Delta_0 & -\xi_k + h \end{bmatrix}, \quad (73)$$

where $D = \xi^2 + \Delta_0^2 - h^2$. The function $g^{II}(\tau)$ has a similar structure but it has a peak at $t \sim -T$ and it grows with exponent $-\lambda_s$ in the region $t < -T$ and decays in the paramagnetic region $-T < \tau < T$ with exponent $-\lambda_p$ to the value of order $1/\Delta_0$ at $\tau \sim T$. In the region $t \gg T$ the function \hat{g}^{II} is the stationary solution of Eq. (58) and it coincides with $\hat{g}^I(\tau \ll -T)$ given by Eq. (73).

Although functions \hat{g}^I, \hat{g}^{II} in the paramagnetic region $-T < \tau < T$ strongly depend on time their products that enter Eqs. (53, 56, 63, 64) do not. Thus the components of the function \hat{g}_2 stay constant in the paramagnetic region as they should. Moreover, the numerators and denominators in Eqs. (53, 56, 63, 64) are of the same order and thus the function \hat{g}_2 is of order one in spite of the fact that functions \hat{g}^I, \hat{g}^{II} are exponentially large. Thus the components of the functions \hat{g}_2 change only on the boundaries $\tau \sim -T, T$ between the paramagnetic and superconducting regions.

Writing Eqs. (57, 58) in components one can see that there is a symmetry relation between the functions g^I and g^{II} under change of time sign $\tau \rightarrow -\tau$: $\Delta \rightarrow \Delta^*$, $g^I \rightarrow g^{II}$, $\bar{g}^I \rightarrow \bar{g}^{II}$, $f^I \rightarrow f^{\dagger II}$, $f^{\dagger II} \rightarrow f^I$. Therefore, since we choose the real order parameter $\Delta(\tau)$, solutions of Eqs. (57, 58) on the left and right boundaries are interrelated and further we shall consider only the right boundary $\tau \sim T$.

Writing Eq. (58) in components one can see that the pairs of functions g^{II}, f^{II} and $\bar{g}^{II}, f^{\dagger II}$ enter this equation separately: Functions g^{II}, f^{II} satisfy

$$\partial_\tau g_k^{II} = (\xi_k - h)g_k^{II} + \Delta f_k^{II} - 1 \quad (74)$$

$$\partial_\tau f_k^{II} = \Delta g_k^{II} - (\xi_k + h)f_k^{II} \quad (75)$$

$$(g_k^{II}, f_k^{II}) = A_k (\xi_k + \sqrt{\xi_k^2 + \Delta_p^2}, \Delta_p) e^{-\lambda_p \tau}, \quad \tau \ll T, \quad (76)$$

while the functions \bar{g} and f^\dagger obey

$$\partial_\tau \bar{g}_k^{II} = -(\xi_k + h)\bar{g}_k^{II} + \Delta f_k^{\dagger II} - 1 \quad (77)$$

$$\partial_\tau f_k^{\dagger II} = (\xi_k - h)f_k^{\dagger II} + \Delta \bar{g}_k^{II} \quad (78)$$

$$(\bar{g}_k^{II}, f_k^{\dagger II}) = \bar{A}_k (-\xi_k + \sqrt{\xi_k^2 + \Delta_p^2}, \Delta_p) e^{-\lambda_p \tau}, \quad \tau \ll T. \quad (79)$$

The coefficients A_k, \bar{A}_k should be found numerically by matching the boundary conditions in the superconducting region defined by Eq. (73).

Since the components of the function \hat{g}^I are exponentially large on the boundary $\tau \sim T$ one can neglect the r.h.s. in Eq. (57). Writing Eq. (57) in components we can separate equations for g^I and $f^{\dagger I}$

$$\partial_\tau g_k^I + (\xi_k - h)g_k^I + \Delta f_k^{\dagger I} = 0 \quad (80)$$

$$\partial_\tau f_k^{\dagger I} - (\xi_k + h)f_k^{\dagger I} + \Delta g_k^I = 0 \quad (81)$$

from equations on \bar{g}^I, f^I

$$\partial_\tau f_k^I + (\xi_k - h)f_k^I + \Delta \bar{g}_k^I = 0 \quad (82)$$

$$\partial_\tau \bar{g}_k^I - (\xi_k + h)\bar{g}_k^I + \Delta f_k^I = 0. \quad (83)$$

Since Eqs. (80-83) are homogeneous they define the pairs of functions $g_k^I, f_k^{\dagger I}$ and \bar{g}_k^I, f_k^I only up to the normalization factors. From Eqs. (53, 56, 63, 64) we see that the overall normalization factor for the functions $g_k^I, f_k^{\dagger I}, \bar{g}_k^I, f_k^I$ gets cancel out and thus we are left with one free parameter to be fixed by the requirements on the boundary conditions on resulting function \hat{g}_{2k} . In the superconducting region $\tau \gg T$ the components of \hat{g}_{2k} decay to zero due to our asymptotic requirements while in the paramagnetic region there are four equations (one for each component of \hat{g}_{2k}) that should be satisfied. Fortunately all these four equations can be shown to be linear dependent, thus we are left with one requirement for which we have one free parameter.

Numerical solution for resulting function \hat{g}_{2k} is presented on Fig. 7. Being able to find numerical solutions for functions f_{1k} and f_{2k} for a given order parameter configuration $\Delta(\tau)$ one can find self-consistent order parameter configuration satisfying to Eq. (41) which is presented on Fig. 6.

8 Action

The probability of the tunneling process is determined by Eq. (36). The last term in this equation can be written in terms of the function $g_k^I(\tau)$ that up to the normalization factor is defined by Eqs. (80, 81)

$$A_1 = \sum_k \ln \text{Tr} \int d\tau \hat{g}_k^I(\tau). \quad (84)$$

To find the normalization factor of the function g^I we need to consider Eq. (57) in the region $\tau \sim -T$ with the proper boundary conditions

$$\partial_\tau g_k^I = 1 - (\xi_k - h)g_k^I - \Delta f_k^{\dagger I} \quad (85)$$

$$\partial_\tau f_k^{\dagger I} = (\xi_k + h)f_k^{\dagger I} - \Delta g_k^I \quad (86)$$

$$(g_k^I, f_k^{\dagger I}) = \tilde{A}_k (\xi_k + \sqrt{\xi_k^2 + |\Delta_p|^2}, \Delta_p) e^{\lambda_p \tau}, \tau \gg -T. \quad (87)$$

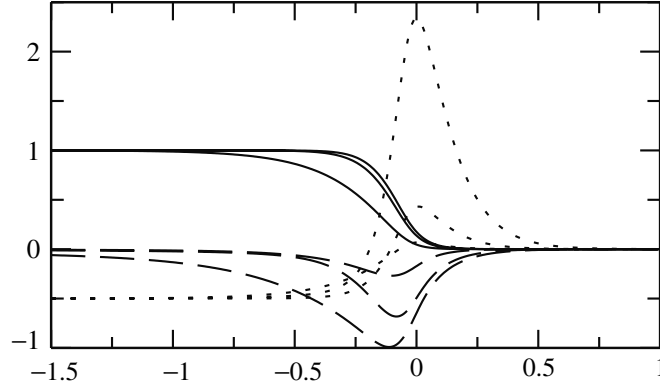


Fig. 7. The solid lines represent dependencies of the doubled quasiparticle spins $2s_k = -(g_{2k} + \bar{g}_{2k})$ on $(\tau - T)d$ for energy levels $\xi = 2d, 8d, 16d$ (higher curves correspond to larger ξ_k). The functions $f_{2k}^{(s)} \equiv f_{2k} + f_{2k}^\dagger$ (higher curves correspond to larger ξ_k) and $2\tilde{g}_{2k} \equiv g_{2k} - \bar{g}_{2k}$ (higher curves correspond to lower ξ_k) are represented by dashed and dotted lines respectively.

Analogous equations for the pair of functions \bar{g}_k^I and f_k^I can be formally obtained from the above equations by the transformation $g \rightarrow \bar{g}, f^\dagger \rightarrow f, \xi \rightarrow -\xi$. The coefficient \bar{A}_k that defines the asymptotic behavior in the region $-T \ll \tau \ll T$ is uniquely defined by the requirement of matching the boundary conditions (69) in the superconducting region $\tau \ll -T$. The normalization constant of the function g_k^I in the region $\tau \sim T$ now is determined by the asymptotic behavior (87).

As we show in the Appendix the third term in Eq. (36) can be written in terms of the functions f_{1k}, f_{1k}^\dagger such that

$$\begin{aligned} A_2 &\equiv -\frac{1}{\lambda} \int d\tau \Delta^*(\tau) \Delta(\tau) + \sum_k \text{Tr} \ln[\partial_\tau + \mathcal{H}_k] \\ &= \int d\tau \left[-\frac{\Delta^2(\tau)}{\lambda} + \frac{\Delta(\tau)}{4} \sum_k \left[\frac{1}{f_{1k}(\tau)} + \frac{1}{f_{1k}^\dagger(\tau)} \right] \right]. \end{aligned} \quad (88)$$

This action should be compared with the action of the superconducting state $\int d\tau E_s$, where E_s is the energy of the superconducting state given by Eq. (12) with $S_z = 0$. Subtracting this term from (88) we get

$$A_2 \rightarrow \int d\tau \left[-E_s - \frac{\Delta(\tau)^2}{\lambda} + \frac{1}{4} \sum_k \left[\frac{\Delta(\tau)}{f_{1k}(\tau)} + \frac{\Delta(\tau)}{f_{1k}^\dagger(\tau)} \right] \right]. \quad (89)$$

Using the Green functions in the superconducting state given by Eq. (69) one can check that the expression under integral in (89) tends to zero in the superconducting region $|\tau| \gg T$.

Now the probability of the tunneling process (36) can be written as

$$\ln P = N \ln(N \delta E t^2 \nu_M) + A_1 + A_2. \quad (90)$$

The probability of the instanton process should not depend on the time difference $2T$ between the boundaries of the instanton processes. Although terms A_1 and A_2 both depend on T one can show that their sum is T independent. Indeed the change of the term A_1 under increase of T

$$\delta A_1 = 2 \sum_{|\xi| < \tilde{\xi}} \lambda_p \delta T \equiv 2 \sum_{|\xi| < \tilde{\xi}} (h - \sqrt{\xi_k^2 + \Delta_p^2}) \delta T, \quad (91)$$

is exactly compensated by the change in the action A_2 . In the limit $\Delta/d \rightarrow \infty$ the sum of the terms A_1 and A_2 can be presented as

$$A_1 + A_2 = N(\ln[\Delta_0^{-2}] + \beta') \quad (92)$$

where $\beta' \approx 4.1$ is a numerical constant, which was found for $N = 40$ levels and $\omega_D/d = 100$. Finally we can present the probability as

$$\ln P \sim N \ln(\beta \delta E G / \Delta_0), \quad (93)$$

where $\beta \approx 1.1$ and G is the dimensionless conductance of the junction between the superconducting grain and metallic plate which for our model is

$$G = 8\pi^2 \nu_G \nu_M t^2, \quad (94)$$

where $\nu_G = N/2\tilde{\xi}$ is the density of states of the grain.

9 Conclusions

In the present paper we have considered the quantum tunneling between paramagnetic and superconducting states of a nano-scale superconducting grain weakly coupled to a normal metallic contact assuming that the quasiparticle tunneling between the grain and metal provides the dominant mechanism for non-conservation of the total spin of the grain. Our final answer (93) can be understood more clearly when written in a form

$$P \sim \left(\frac{\beta \delta E G}{\Delta_0} \right)^N. \quad (95)$$

We see that the factor $(G\delta E)^N \sim (t^2 \nu_G \nu_M \delta E)^N$ represents the probability of tunneling of N electrons or holes from the grain to the metal with δE being the typical energy of one electron (hole) excitation in the metal. Determination of the factor β in (95) requires an application of the instanton method which is capable of careful description of quantum tunneling process between

paramagnetic and superconducting states of the grain (see Figs. 3, 4). Deriving Eq. (93) we assumed that the typical energy of electron (hole) excitation inside the metal $\delta E \ll \Delta_0$, this situation is realized if the magnetic field H is close to the value $H_0 = \Delta_0/\sqrt{2}\mu_B$ at which the thermodynamic first order phase transition takes place: $H - H_0 \ll H_0$.

Although we have considered only the zero temperature case, at finite temperatures $T \ll \delta E$ our result should still hold. In the case $\delta E \ll T \ll \Delta_0$ we expect that the dependence on the applied magnetic field will be saturated by temperature such that one should substitute $\delta E \rightarrow T$ in (93), the coefficient β for this case requires a more advanced study.

Acknowledgements. — We would like to thank Y. Bazaliy, Ya. M. Blanter, E.M. Chudnovsky, D. Feldman, Y.M. Galperin, A.E. Koshelev, A.I. Larkin, K. Matveev, A. Mel'nikov, V.L. Pokrovsky, R. Ramazashvily for useful discussions.

A Appendix. Action A_2

To find the action A_2 , following the method of Ref. [9], we first consider the Green function Eqs. (47-49) and introduce the new variables u_k and v_k

$$g_{1k} = u_k v_k, \quad f_{1k} = u_k^2, \quad f_{1k}^\dagger = -v_k^2 + \frac{1}{4u_k^2}. \quad (96)$$

such that the constraint (52) is identically satisfied. From Eqs. (47-49) we find that the functions u_k and v_k obey the equations

$$\partial_\tau u_k + \xi_k u_k - \Delta v_k = 0, \quad (97)$$

$$\partial_\tau v_k - \xi_k v_k - \Delta^* u_k + \Delta/4u_k^3 = 0 \quad (98)$$

that can also be obtained taking the variational derivative of the functional

$$A'_2 = \sum_k \int d\tau \left[2v_k \partial_\tau u_k + 2\xi_k u_k v_k - \Delta v_k^2 + \Delta^* u_k^2 + \frac{\Delta}{4u_k^2} \right]. \quad (99)$$

Taking the variation derivative of the action A'_2 with respect to Δ and Δ^* we obtain $\sum_k f_{1k}^\dagger$ and $\sum_k f_{1k}$ respectively. Therefore up to the boundary terms the functional (99) should coincide with $\sum_k \text{Tr} \ln[\partial_\tau + \mathcal{H}_k]$. Moreover, the possible boundary terms should vanish because the Green functions of initial $\tau = -\infty$ and final $\tau = \infty$ coincide. Writing the action (99) in terms of the original functions g, f, f^\dagger and using Eqs. (47-49) to bring it into symmetric form for A_2 we finally get

$$A_2 = \int d\tau \left[-\frac{1}{\lambda} \Delta^* \Delta + \sum_k \frac{1}{4} \left[\Delta/f_{1k} + \Delta^*/f_{1k}^\dagger \right] \right]. \quad (100)$$

References

1. R. Meservey, P.M. Tedrow, and P. Fulde, Phys. Rev. Lett. **25**, 1270 (1970).
2. R. Meservey, P.M. Tedrow, Phys. Rep. **238**, 173 (1994).
3. A. M. Clogston, Phys. Rev. Lett., **5**, 464 (1960).
4. A. I. Larkin, Zhurnal Eksperimental'noi i Teoreticheskoi Fiziki **48**, 232 (1965); Sov.Phys. JETP **21**, 153 (1965).
5. P. W. Anderson, J. Phys. Chem. Solids **11**, 28 (1959).
6. C. T. Black, D. C. Ralph, and M. Tinkham **76**, 688 (1996).
7. More realistic choice of random Gaussian correlated tunneling amplitudes t_{k_1, k_2} leads to the same results after averaging over t_{k_1, k_2} .
8. G. Eilenberger, Z. Phys. **214**, 195 (1968).
9. A. V. Lopatin and L. B. Ioffe, Phys. Rev. **B** 6412 (1999).

Domain Wall Superconductivity in Ferromagnetic Superconductors and Hybrid S/F Structures

A. Yu. Aladyshkin¹, A. I. Buzdin², A. A. Fraerman^{1,3}, A. S. Mel'nikov^{1,3},
D. A. Ryzhov^{1,3}, and A. V. Sokolov¹

¹ Institute for Physics of Microstructures, Russian Academy of Sciences 603950,
Nizhny Novgorod, GSP-105, Russia melnikov@ipm.sci-nnov.ru

² Centre de Physique Moleculaire Optique et Hertzienne, Universite Bordeaux
1-UMR 5798, CNRS, F-33405 Talence Cedex, France

³ Argonne National Laboratory, Argonne, Illinois 60439, USA

Summary. On the basis of phenomenological Ginzburg-Landau approach we investigate the problem of order parameter nucleation in a ferromagnetic superconductor and hybrid superconductor - ferromagnetic (S/F) systems with a domain structure in an applied external magnetic field H . We study the interplay between the superconductivity localized at the domain walls and between the domain walls and show that such interplay determines a peculiar nonlinear temperature dependence of the upper critical field. For hybrid S/F systems we also study the possible oscillatory behavior of the critical temperature $T_c(H)$ similar to the Little-Parks effect.

The presence of domains is inherent to ferromagnets and, thus, for systems with coexisting superconducting and magnetic orderings it is important to study the influence of the domains on the superconducting order parameter nucleation (see, e.g., [1] and references therein). The revival of interest to the domain wall superconductivity has been stimulated, in part, by recent investigations of hybrid superconductor/ferromagnetic (S/F) systems, e.g., S/F bilayers or superconducting films with arrays of magnetic dots. The interest to such structures is caused by their large potential for applications (e.g., as switches or systems with a controlled artificial pinning). In many cases such thin film structures consist of a ferromagnetic insulator film and superconducting film deposited on it, or a metallic ferromagnetic and superconducting films separated by a buffer oxide layer. In both situation the proximity effect can be neglected. A nonhomogeneous magnetic field distribution induced by the domain structure in a ferromagnetic layer influences strongly the conditions

of the superconducting order parameter nucleation, and, as a consequence, the hybrid S/F systems reveal a nontrivial phase diagram in an external applied magnetic field \mathbf{H} (see, e.g., [2, 3, 4, 5]). In particular, it was found that depending on the domain structure the temperature dependence of the upper critical field becomes strongly nonlinear near the superconducting critical temperature T_c . Provided the thickness of a superconducting film is rather small as compared with the coherence length ξ , the critical temperature of the superconducting transition as well as the structure of superconducting nuclei should be determined by a two-dimensional distribution of a magnetic field component $B_z(x, y)$ (perpendicular to the superconducting film plane) induced by the domain structure or an array of ferromagnetic particles. Obviously, the highest critical temperature corresponds to the nuclei which appear near the lines of zeros of B_z .

The profile $B_z(x, y)$ is determined by the ratio of two length scales: thickness of a ferromagnetic film D and distance between the domain walls w (hereafter we consider the width of the domain wall to be much less than ξ). Provided the ferromagnetic film is rather thick ($D \gg w$), the magnetic field in a thin superconducting film is almost homogeneous over the domain and shifts the critical temperature of superconductivity nucleation at a value $\Delta T_c^{orb} = (2\pi B_0 \xi_0^2 / \Phi_0) T_{c0}$ due to the orbital mechanism (B_0 is the maximum absolute value of the z -component of the field induced by the ferromagnet). In this case with the decrease in the temperature the superconductivity must firstly appear just above the domain wall due to the mechanism analogous to the one responsible for the surface superconductivity below H_{c3} (see, e.g., [6]). Thus, in this limit the domain walls stimulate the nucleation of the superconducting order parameter. For a thin ferromagnetic film ($D \ll w$) the magnetic field decays with the increase in the distance from the domain wall and almost vanishes inside the domain. In the absence of the external field such domain wall should locally weaken superconductivity as it was discussed by Sonin [7]. The superconducting nucleus in this case should appear far from the domain wall. As we switch on an external magnetic field, we can control the position of the superconducting nucleus suppressing the order parameter inside the domains.

Another reason which explains recent experimental and theoretical activity in the field of domain wall superconductivity is associated with the discovery of ferromagnetic superconductors UGe_2 and $URhGe$ [8] where superconductivity appears in the presence of large exchange field which obviously excludes singlet superconducting pairing. Thus, these compounds are considered as good candidates for superconductivity with triplet pairing. The basic features of the $H - T$ phase diagram and possible re-entrant superconductivity induced by external magnetic field in such compounds can be analyzed within the appropriate version of the Ginzburg–Landau (GL) theory.

The goal of the present paper is to study the unusual nonlinear behavior of the temperature dependence of the upper critical field observed experimentally in hybrid S/F systems and ferromagnetic superconductors using the GL model. We consider a linearized GL equation which is equivalent to

the Schrödinger equation for two – dimensional electronic gas in the presence of some inhomogeneous magnetic field [9]: $-(\nabla + 2\pi i \mathbf{A}/\Phi_0)^2 \Psi = \xi^{-2}(T)\Psi$. Here $\mathbf{A}(\mathbf{r})$ is the vector potential, Φ_0 is the flux quantum, $\xi(T) = \xi_0/\sqrt{1-T/T_{c0}}$, and T_{c0} is the critical temperature of the bulk superconductor at $B = 0$. The lowest eigenvalue $1/\xi^2(T)$ of this Schrödinger-like equation defines the critical temperature T_c of the phase transition into a superconducting state. As for the case of ferromagnetic triplet superconductors like UGe_2 , a nonzero spin of the Cooper pair can be phenomenologically taken into account if we just assume the existence of two order parameters corresponding to different spin orientations and define two different critical temperatures depending on the mutual orientation of Cooper pair spin and ferromagnetic moment. These two components of the order parameter can be viewed, for instance, as the ones corresponding to two different one-dimensional irreducible representations of the symmetry group of the crystal. We also assume that the domain walls are well pinned and do not take account of changes in the domain structure with an increase in H .

Let us start from the one-dimensional case and take a step-like magnetization profile $\mathbf{M} = M(x)\mathbf{z}_0$. Consider first narrow domains ($w \ll D$). An external magnetic field H applied along the z axis results in a partial compensation of magnetic induction in one of the domains. As a result, the critical temperature of superconductor depends non-monotonously on H (see Fig. 1a). Both the critical temperature of superconducting nucleation inside the domain and critical temperature of formation of localized superconductivity should increase up to the external field value equal to the magnetic induction induced by the ferromagnetic moment. So the external magnetic field shrinks the region of the domain wall superconductivity and causes the shift of the S nucleus from the wall.

For UGe_2 we must take account of some additional shift in energy of Cooper pairs corresponding to the shift in T_c for a given order parameter component in different domains due to the exchange interaction. We found that the effect of this exchange field can completely suppress the formation of the localized superconducting nuclei as it produces a rather large shift in critical temperature $\Delta T_c^{ex} > 0.6\Delta T_c^{orb}$ for Cooper pairs with different spin orientation with respect to the magnetic moment.

Let us now consider another possible limit of wide domains ($w \gg D$). As we increase an external magnetic field H the position of a superconducting nucleus shifts from infinity to the domain wall. So at low H the asymptotical behavior of $T_c(H)$ for a nucleus localized near the zero of the total magnetic field appears to be strongly nonlinear: $(T_{c0} - T_c)/\Delta T_c^{orb} \sim (\Phi_0/B_0 D^2)^{1/3} \sin^{4/3}(\pi|H|/(2B_0))$. For rather large fields H the nucleus appears to be localized at the domain wall with T_c given by the expression $(T_c - T_{c0})/\Delta T_c^{orb} = 1 - |H|/B_0$. These asymptotical expressions are in a good agreement with our numerical simulations (see Fig. 1b). The nuclei can be considered as isolated only if their characteristic size is much less than w . Otherwise, we should take account of the interaction of Cooper pair wavefunctions nucleated at different domain walls. The phase diagram for a periodic

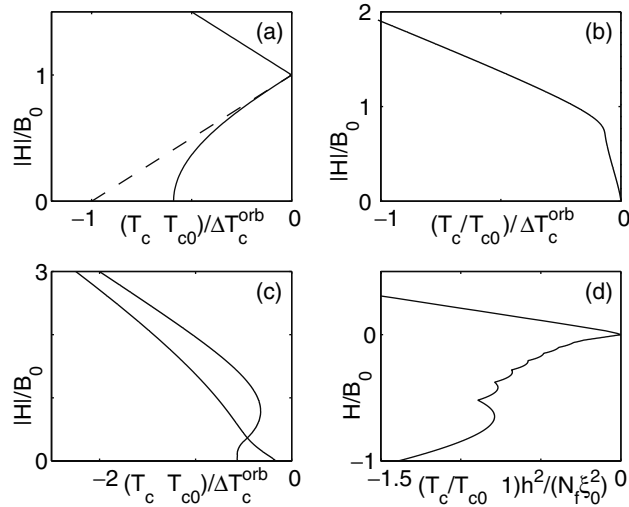


Fig. 1. The $H - T$ phase diagrams for different S/F systems. (a) Structure with narrow domains. The solid (dashed) line corresponds to an isolated superconducting nucleus at the domain boundary (far from the domain boundary). (b) Isolated superconducting nucleus in a structure with wide domains ($B_0 D^2 / \Phi_0 = 25$). (c) Periodic domain structure for $\pi B_0 w^2 / \Phi_0 = 5$ (solid line) and $\pi B_0 w^2 / \Phi_0 = 1$ (dashed line). (d) Ferromagnetic dot over the superconducting film ($N_f = 10$).

step-like distribution of magnetic field induced by the domain structure with the period $2w$ is shown in Fig. 1c. For large values $\pi B_0 w^2 / \Phi_0$ the phase transition line is very close to the one found for an isolated domain boundary, except for the small temperature region close to T_c : $\Delta T \sim 4T_{c0}\xi_0^2/w^2$. For not very large values $\pi B_0 w^2 / \Phi_0 < 2.0$ the critical temperature becomes a monotonic function of the external magnetic field because of the strong overlapping of wavefunctions corresponding to different domain walls. However, even in this case we still observe a change in the slope of the phase transition line (see dashed line in Fig. 1c).

For two-dimensional distributions of magnetization or for magnetic dot arrays a line of $B_z(x, y)$ zeros can form a closed loop. The winding number m of a superconducting nucleus at such loop will be determined by the magnetic flux through the loop. Thus, changing this flux (e.g., increasing an external H field) we can control the winding number. The resulting phase transitions between the multiquantum states with different m can cause the oscillations of T_c similar to the well-known Little-Parks oscillations. A possibility to create multiquantum vortex states in a hybrid S/F system has been previously discussed in [10]. Here we focus only on the oscillatory behavior of $T_c(H)$ in a large area superconducting film caused only by the quantization associated with the characteristics of the inhomogeneous magnetic field produced by ferromagnetic structure. To investigate the details of this oscillatory behavior we consider a particular case of a small ferromagnetic particle with a magnetic

moment $\mathbf{M} = M\mathbf{z}_0$ placed at a height h over the superconducting film. In the limit $H \rightarrow 0$ the nucleation of superconductivity occurs at large distances from the dot and T_c for different m are very close. For large $|H|$ (much larger than the maximum field induced by the dipole) the superconductivity nucleates near the minima of the total field $|B_z|$ and, thus, is localized near the dipole. In the intermediate field region we obtain the oscillatory behavior of T_c with the number of oscillations controlled by the dimensionless parameter $N_f = 4\pi M / (3\sqrt{3}h\Phi_0)$. The resulting dependence $T_c(H)$ for $N_f = 10$ is shown in Fig.1d.

The appearance of the localized superconducting nuclei should result in a broadening of the superconducting transition probed, e.g., by the resistivity measurements. In fact, the beginning of the resistivity decrease with the temperature decrease would correspond to the domain wall superconductivity, while its complete disappearance would signal the bulk superconductivity. Taking, for example, the parameters of *Nb* and typical magnetization $4\pi M \sim 1 - 10 \text{ kOe}$ we obtain a quite strong increase in T_c above a domain wall in a S/F bilayer: $\delta T_c \sim 1 - 3 \text{ K}$. Taking the magnetization $4\pi M \sim 2 \text{ kOe}$ and $dH_{c2}/dT \sim 40 \text{ kOe/K}$ for *UGe₂* we obtain $\max(\delta T_c) \sim 0.02 \text{ K}$. These estimates give us quite measurable temperature intervals. Experimental observation of the $H - T$ phase diagram discussed above for *UGe₂* and *URhGe* could provide arguments in favor of unconventional pairing in these compounds and permit to determine the important parameter τ , describing the ratio of exchange and orbital effects. Taking $M \sim 3 \times 10^{-11} \text{ G} \cdot \text{cm}^3$ and $h \sim 300 \text{ nm}$ for a ferromagnetic particle we obtain $N_f \simeq 10$ and the characteristic scales of T_c oscillations $\Delta H \sim 100 \text{ Oe}$, $\Delta T_c \sim 0.1 \text{ K}$ for a Nb film. Such oscillatory behaviour of T_c has been, in fact, observed experimentally in [2, 5]. A change in a slope of the phase transition curve $T_c(H)$ (which is probably a signature of phenomena discussed above) has been also found in [3] for a Pb film with CoPd particles. The behavior observed in [4] for S/F bilayers with bubble domains is also qualitatively similar to our predictions.

Acknowledgements.— We would like to thank Yu. N. Nozdrin and I. A. Shereshevskii for stimulating discussions. This work was supported, in part, by the US DOE Office of Science under contract No. W-31-109-ENG-38, by the Russian Foundation for Basic Research, Grant No. 03-02-16774, Russian Academy of Sciences under the Program ‘Quantum Macrophysics’, Russian State Fellowship for young doctors of sciences (MD-141.2003.02), ESF ‘Vortex’ Programme, and University of Nizhny Novgorod under the program BRHE and ‘Physics of Solid State Nanostructures’.

References

1. A. I. Buzdin, L. N. Bulaevskii, and S. V. Panyukov, Zh. Eksp. Teor. Phys. **87**, 299 (1984) [Sov. Phys. JETP **60**, 174 (1984)].
2. Y. Otani, B. Pannetier, J. P. Nozières, and D. Givord, Journ. Magn. Magn. Mater. **126**, 622 (1993).

3. M. Lange, M. J. Van Bael, Y. Bruynseraede, and V. V. Moshchalkov, preprint cond-mat/0209101 (2002).
4. M. Lange, M. J. Van Bael, and V. V. Moshchalkov, preprint (2003).
5. D. S. Golubović, W. V. Pogosov, M. Morelle, and V. V. Moshchalkov, *Preprint* cond-mat/0307413 (2003).
6. D. Saint-James, G. Sarma, and E. J. Thomas, *Type-II Superconductivity*, Pergamon Press, New York, 1969.
7. E. B. Sonin, *Pis'ma Zh. Tekh. Phys.* **14**, 1640 (1988) [*Sov. Tech. Phys. Lett.* **14**, 714 (1988)].
8. S. S. Saxena *et al.*, *Nature* **406**, 587 (2000); A. Huxley *et al.*, *Phys. Rev. B* **63**, 144519 (2001); D. Aoki *et al.*, *Nature* **413**, 613 (2001).
9. F. M. Peeters and P. Vasilopoulos, *Phys. Rev. B* **47**, 1466 (1993); I. S. Ibrahim and F. M. Peeters, *Phys. Rev. B* **52**, 17321 (1995); J. Reijniers and F. M. Peeters, *J. Phys.: Condens. Matter* **12**, 9771 (2000).
10. M. V. Milošević *et al.*, *Phys. Rev. B* **66**, 024515 (2002); M. V. Milošević and F. M. Peeters, *Phys. Rev. B* **68**, 024509 (2003).

Rasba Spin-Orbit Interaction in a Ballistic Josephson Junction

I.V. Krive^{1,2}, L.Y. Gorelik¹, R.I. Shekhter¹, and M. Jonson¹

¹ Department of Applied Physics, Chalmers University of Technology and Göteborg University, SE-412 96 Göteborg, Sweden shekhter@fy.chalmers.se

² B. I. Verkin Institute for Low Temperature Physics and Engineering, 47 Lenin Avenue, 61103 Kharkov, Ukraine

Summary. We consider the Josephson effect in a ballistic Superconductor/Quantum Wire/ Superconductor junction. It is shown that the interplay of chiral symmetry breaking generated by Rashba spin-orbit interaction and Zeeman splitting results in the appearance of a Josephson current even in the absence of any phase difference between the superconductors.

1 Introduction

It is well known [1] that electrons confined to a plane (e.g. in MOSFET structures or in heterostructures) experience a strong spin-orbit interaction originating from interface electric field (Rashba spin-orbit interaction). Recently it was shown experimentally that the strength of the Rashba coupling can be controlled by a gate voltage [2]. The Rashba effect leads to various interesting suggestions in spintronics and it has been a subject of active theoretical and experimental studies in recent years (see e.g. Ref. [3] and references therein).

For quasi-1D electron systems the influence of the Rashba interaction on thermodynamic and transport properties of quantum wires were considered in Refs. [4] and [5]. There, it was shown that in the presence of an in-plane confinement potential and spin-orbit interactions the electron spectrum is qualitatively modified. Chiral symmetry, which is usually assumed to be present in QWs, is violated resulting in the appearance of a dispersion asymmetry. To be more precise, the right-moving spin-up (left-moving spin-down) and left-moving spin-up (right-moving spin-down) electrons have different Fermi velocities [4]. This implies that electrons in quantum wires with Rashba interaction are “chiral particles” and their spin projections are correlated with the direction of motion. Being interested in low-energy ($E \ll E_F$) properties of

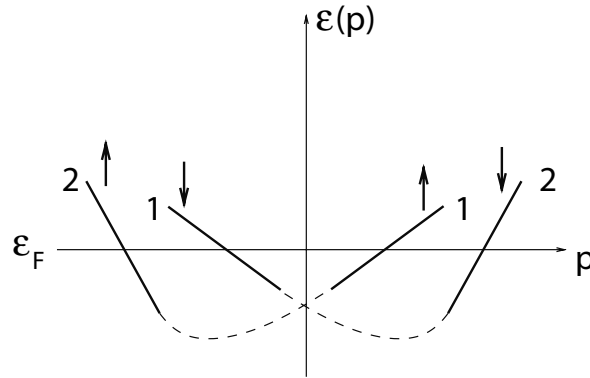


Fig. 1. Schematic energy spectrum of 1D electrons with dispersion asymmetry. The particles with energies close to the Fermi energy ε_F have an almost linear dependence on momentum and are classified by their Fermi velocities (v_{1F} - subband 1, v_{2F} - subband 2).

quantum wires, we can classify these particles as belonging to two subbands (“1” and “2”) characterized by their Fermi velocities (see Fig. 1). Notice that this electron spectrum pertains to a weak or moderate s-o interaction. As it was demonstrated in Ref. [6] for a strong Rashba interaction the projection of electron spin is strongly correlated with the direction of motion and left- and right-moving electrons with the Fermi energy always have opposite spin projections. The unusual spectral properties of electrons in QWs have to show up in situations when spin degrees of freedom are nontrivially involved in the electron dynamics. Here we consider the Josephson current in a long S-QW-S junction for electron spectrum with dispersion asymmetry and large Zeeman splitting. Recently [7] the combined effect of magnetic field and spin-orbit interaction on the Josephson current in a short ballistic junction formed in a 2DEG was studied. Notice that interaction induced dispersion asymmetry in the electron spectrum is a specific property of quasi-one-dimensional geometry [4]. For a pure 2D geometry spin-orbit interaction does not lead to a chiral symmetry breaking and the peculiar effects produced by chiral particles do not manifest themselves in the short and wide SNS junction considered in Ref. [7]. In particular, we show that the combined effect of Rashba and Zeeman interactions results in the appearance of an anomalous Josephson current $J_{an} = J(\varphi = 0)$ in a long S-QW-S junction. For a transparent junction the induced by Rashba and Zeeman interaction supercurrent at low temperatures is a step-like periodic or quasiperiodic function of magnetic field (see Fig. 2). The periodicity depends on the ratio of the Fermi velocities and is controlled by the strength of the spin-orbit interaction. The amplitude of the anomalous current at $T = 0$ is of the order of the critical Josephson current in a long S-N-S junction and it appears abruptly at finite values of Zeeman splitting of the order of the Andreev level spacing (Fig. 2). For a low-transparency

junction ($D \ll 1$), realized by introducing a scattering barrier (impurity) into the normal region, the maximum amplitude of J_{an} at special (resonance) conditions is of the order of \sqrt{D} . Notice that this unusual dependence on transparency, which corresponds to tunneling of a *single* electron through a barrier (its entangled partner resonantly passes through the structure) holds also for the critical Josephson current even in the absence of dispersion asymmetry. This effect can be interpreted as a tunnel splitting of the deGennes - Saint-James bound state [10] shifted by magnetic field to the vicinity of the Fermi level. Analogous effects of giant critical supercurrents in tunnel SIS (“I” stands for insulator) and SINIS structures were discussed in Ref. [8] (see also Ref. [9], where resonance effects are considered for a persistent current in a normal metal ring).

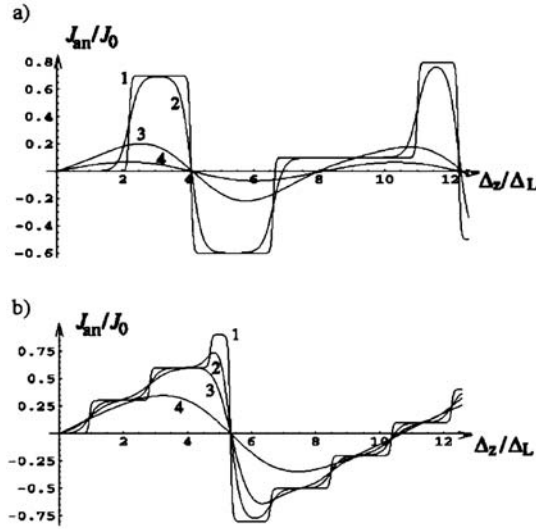


Fig. 2. The dependence of the normalized anomalous Josephson current J_{an}/J_0 ($J_0 = ev_F/L$) on the dimensionless Zeeman splitting Δ_Z/Δ_L ($\Delta_L = \hbar v_F/L$). **a)** asymmetry parameter $\lambda_a = 0.3$. The different plots (1 - 4) correspond to different temperatures $T = (0.1, 0.5, 3, 5) T^*$ where $T^* = \Delta_L/2\pi$. **b)** $\lambda_a = 0.7$; $T = (0.1, 0.5, 1, 3)$.

When the Zeeman splitting vanishes the anomalous supercurrent and all the above described resonance effects disappear. Then, the Josephson current in a low-D junction is small ($\sim D$). What is the influence of dispersion asymmetry on the critical current? There is a general statement [17] that spin-orbit interaction in systems with Aharonov-Bohm geometry suppresses persistent currents. Although the theorem directly concerns normal ring-shaped conductors, it also holds for linear hybrid systems with Andreev mirrors due to the analogy between persistent currents in a normal 1D ring and Josephson currents in a long SNS junction. We show here that the cited statement is not

valid when the spin-orbit interaction is accompanied by a chiral symmetry breaking. Rashba spin-orbit interaction in quantum wires always enhances the critical current.

2 Anomalous Josephson Current

The Josephson current, being an equilibrium supercurrent between two superconductors, can be calculated from the general thermodynamical relation

$$J = \frac{e}{\hbar} \frac{\partial \Omega}{\partial \varphi}, \quad (1)$$

where Ω is the thermodynamic potential of the junction considered and φ is the phase difference between the two superconductors. We have included a factor 2, which usually appears in Eq. (1) in combination with the electric charge, into the definition of Ω . This factor originates from spin degeneracy and in the presence of Zeeman splitting $\Omega = \Omega_{\uparrow} + \Omega_{\downarrow}$ and $\Omega_{\uparrow} \neq \Omega_{\downarrow}$.

In general both the Andreev bound states ($E < |\Delta|$, Δ is the superconducting order parameter) and the continuum scattering states ($E \geq |\Delta|$) contribute to the supercurrent. In two limiting cases - short ($L \ll \xi_0 = \hbar v_F / |\Delta|$, L is the junction length) and long ($L \gg \xi_0$) junctions - only bound states are relevant. This statement is well-known for the case of short junctions (see e.g. Ref. [11] and references therein). For a long junction it has been shown that the Josephson current through a long SNS junction does not depend on $|\Delta|$ at all [12]. Then, one can formally put $|\Delta| \rightarrow \infty$ and sum over all Andreev bound states E_n ($n = 0, \pm 1, \pm 2, \dots$) with the natural assumption that the supercurrent vanishes in the limit $L \rightarrow \infty$. This procedure (analogous to Casimir energy evaluation in quantum field theory, see e.g. Ref. [13]) reproduces all known results for a long ballistic SNS junction. In what follows we will consider only long junctions.

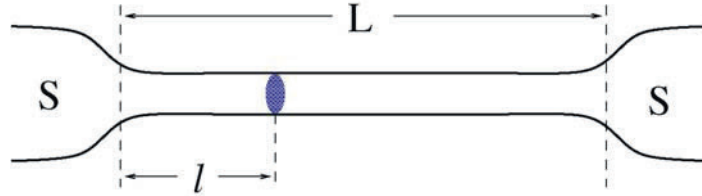


Fig. 3. A long ($L \gg \xi_0$) ballistic S-N-S junction with a scattering barrier (shadow region).

To get analytical results we consider a single barrier junction of length L , where the barrier is located at the point $x = l \leq L$, a distance l is counted

from the left bank of the junction (see Fig. 3). We start with the general equation for Andreev bound state energies expressed in terms of scattering matrices of electrons (\hat{S}_E) and holes (\hat{S}_{-E}^*) in the normal region [14]

$$\det(1 - \alpha_A \hat{S}_E \hat{r}_A \hat{S}_{-E}^* \hat{r}_A^*) = 0, \quad (2)$$

where $\alpha_A = \exp[-2i \arccos(E/|\Delta|)] \simeq -1$ in our case ($E \ll \Delta$) and \hat{r}_A is a diagonal matrix that only depends on the superconducting phases (see Appendix). Since the presence of a magnetic field violates T-symmetry, two channel scattering of spin-1/2 electrons is described by a 4×4 nonsymmetric unitary matrix \hat{S}_E . The scattering potential in our model always changes channel index $1 \Leftrightarrow 2$ (see Fig. 1) because it does not flip electron spin. This allows us to parameterize the scattering matrix by 7 independent real parameters (see Appendix).

After straightforward (although rather lengthy) transformations, Eq. (2) results in the transcendental equation for Andreev level energies of the form

$$\begin{aligned} & \cos[(E + \frac{\eta}{2} \Delta_Z) \delta_L^{(+)}] + R \cos[(E + \frac{\eta}{2} \Delta_Z) \delta_{L-2l}^{(+)}] \\ & + D \cos[(E + \frac{\eta}{2} \Delta_Z) \delta_L^{(-)} + \eta\varphi] = 0. \end{aligned} \quad (3)$$

Here $\Delta_Z = g\mu_B H$ is the Zeeman energy splitting ($g = 2$ for bare electrons), $\eta = \pm 1$, D is the transparency of the junction $D + R = 1$, and

$$\delta_x^{(\pm)} = \frac{x}{\hbar} \left(\frac{1}{v_{1F}} \pm \frac{1}{v_{2F}} \right). \quad (4)$$

In the limit $H = 0$ and $v_{1F} = v_{2F}$ (absence of spin-orbit interaction) Eq. (3) is reduced to a well-known spectral equation for Andreev levels in a long SNS junction with a single barrier [15, 11].

For a transparent junction ($D = 1$) the Andreev bound states are described by two independent sets of energy levels

$$\begin{aligned} E_{n,\eta}^{(1)} &= \pi \Delta_L^{(1)} \left(n + \frac{1}{2} + \eta \frac{\varphi + \chi_1}{2\pi} \right), \\ E_{m,\eta}^{(2)} &= \pi \Delta_L^{(2)} \left(m + \frac{1}{2} + \eta \frac{\varphi - \chi_2}{2\pi} \right), \end{aligned} \quad (5)$$

where $n, m = 0 \pm 1, \pm 2, \dots; \eta = \pm 1$ and $\Delta_L^{(j)} = \hbar v_{jF} / L, \chi_j = \Delta_Z / \Delta_L^{(j)}$. Notice that for a given band index (“1” or “2”) the relative sign between the superconducting phase φ and the magnetic phase χ_j is fixed and it is different for channels “1” and “2”. This is a direct consequence of the chiral properties of the electrons in our model.

Knowing explicitly the energy spectrum Eq. (5), it is straightforward to evaluate the Josephson current. It takes the form

$$J(\varphi, T, H) = \frac{2eT}{\hbar} \sum_{k=1}^{\infty} (-1)^{k+1} \left\{ \frac{\sin k(\varphi + \chi_1)}{\sinh(2\pi kT/\Delta_L^{(1)})} + \frac{\sin k(\varphi - \chi_2)}{\sinh(2\pi kT/\Delta_L^{(2)})} \right\}. \quad (6)$$

It is readily seen from Eq. (6) that an anomalous Josephson current $J_{an} \equiv J(\varphi = 0)$ appears only if both the Zeeman splitting (Δ_Z) and dispersion asymmetry ($v_{1F} \neq v_{2F}$) are nonzero. Here we use the term ‘‘anomalous’’ just to define the supercurrent at $\varphi = 0$. Actually this current is induced by Zeeman splitting in 1D electron system with dispersion asymmetry. The direction (sign) of J_{an} is totally determined by the sign of asymmetry parameter (see Eq. (8)). At high temperatures $T \geq \Delta_L^{(j)}$ anomalous supercurrent is exponentially small. In the low temperature region ($T \ll \Delta_L^{(j)}$) it is a piece-wise constant function of magnetic field represented by the following series

$$J_{an}(H) = \frac{e}{\pi L} \sum_{k=1}^{\infty} \frac{(-1)^{k+1}}{k} (v_{1F} \sin k\chi_1 - v_{2F} \sin k\chi_2). \quad (7)$$

For rational values $v_{1F}/v_{2F} = p/q$ ($p \leq q$ are the integers) J_{an} is a periodic function of magnetic field with period $\delta H = 2\pi q \Delta_L^{(1)}/g\mu_B$, otherwise it is a quasiperiodic function.

It is convenient to introduce the mean Fermi velocity $v_F = (v_{1F} + v_{2F})/2$ and the asymmetry parameter λ_a ,

$$\lambda_a = \frac{v_{1F} - v_{2F}}{v_{1F} + v_{2F}}, \quad (8)$$

which determines the strength of Rashba spin-orbit interaction in a 1D quantum wire. The dependence of the normalized anomalous supercurrent J_{an}/J_0 ($J_0 = ev_F/L$) on the dimensionless Zeeman splitting $\chi \equiv \Delta_Z/\Delta_L$, ($\Delta_L = \hbar v_F/L$) for $\lambda_a = 0.3$ and for different temperatures is shown in Fig. 2a. In the limit of strong asymmetry (this range of parameters, however, seems to be unrealistic [4]), when only one of the two channels (‘‘1’’ or ‘‘2’’) contributes to Eq. (6), the dependence of the anomalous current on the magnetic field becomes analogous to the well-known phase dependence of the Josephson current [16]. The approach to this simple behavior passes via the stages of staircase-like dependencies (see Fig. 2b). Notice that we plotted the figures assuming that $v_{1F} \geq v_{2F}$. The interchange $v_{1F} \leftrightarrow v_{2F}$ makes the supercurrent Eq. (7) change sign.

3 Giant Critical Current in a Magnetically Controlled Low Transparency Junction

Now we consider the limit $D \ll 1$ pertaining to low transparency SNS junctions. As is well known (see e.g. Refs. [15] and [11]), the supercurrent in this

limit for a single barrier junction in the absence of Zeeman and spin-orbit interactions is described by the simple formula $J(\varphi) = J_c \sin \varphi$, where the critical current at low temperatures $T \ll \Delta_L$ is of the order of D ($J_c \sim D e v_F / L$). Interesting physics for low- D junctions appears when resonant electron tunneling occurs. This is, for instance, the case for the symmetric double-barrier ballistic junction considered in Refs. [8] and [11]. There, it was shown that for resonance conditions (realized for a special set of junction lengths) a giant critical supercurrent appears $J_c \propto D_b$, where D_b is the transparency of a *single* barrier. Analogous results were obtained for the persistent current in a ballistic ring with a double barrier [9]. Notice that for the symmetric structure considered in Ref. [8] the normal current (i.e. the current through a double barrier structure with normal leads) at resonance conditions does not depend on barrier transparency at all. It means that for the hybrid structure considered in Ref. [8], the superconductivity actually suppresses electron transport.

We show below that in a magnetically controlled single barrier junction there are conditions when superconductivity in the leads strongly enhances electron transport and a mesoscopic hybrid structure is characterized by a giant critical current $J_c \propto \sqrt{D}$.

We start with the case of a symmetric single barrier junction, when the scattering barrier is situated in the middle of the normal region, i.e. $l = L/2$ in Eq. (3). Then $\delta_{x=0}^{(\pm)} = 0$ and the second cosine term in the spectral equation Eq. (3) is equal to one

$$\cos \left[\left(E + \frac{\eta}{2} \Delta_Z \right) \delta_{L-2l}^{(+)} \right] = 1. \quad (9)$$

When the condition (9) is fulfilled the spectral equation is reduced to the much simpler expression

$$\cos^2 \left[\frac{1}{2} \left(E + \frac{\eta}{2} \Delta_Z \right) \delta_L^{(+)} \right] = D \sin^2 \left[\frac{1}{2} \left(E + \frac{\eta}{2} \Delta_Z \right) \delta_L^{(-)} + \eta \varphi \right]. \quad (10)$$

By using Eq. (10), one can readily evaluate the partial supercurrent $j_{\{\alpha\}}$ characterized by 3 quantum numbers $\{\alpha\} = (n, \eta, \sigma)$ where $n = 0, \pm 1, \pm 2, \dots; \eta, \sigma = \pm 1$

$$\begin{aligned} j_{\{\alpha\}} = \frac{e}{\hbar} \frac{\partial E_{\{\alpha\}}}{\partial \varphi} = -\frac{e\eta\sigma}{\hbar} \sqrt{D} \cos \frac{1}{2} \left[E_{\{\alpha\}} \delta_L^{(-)} + \eta \left(\frac{1}{2} \Delta_Z \delta_L^{(-)} + \varphi \right) \right] \times \\ \left\{ \delta_L^{(+)} \sin \frac{1}{2} \left[\frac{\delta_L^{(+)}}{2} \left(E_{\{\alpha\}} + \frac{\eta}{2} \Delta_Z \right) \right] \right. \\ \left. + \sigma \delta_L^{(-)} \sqrt{D} \cos \frac{1}{2} \left[E_{\{\alpha\}} \delta_L^{(-)} + \eta \left(\frac{1}{2} \Delta_Z \delta_L^{(-)} + \varphi \right) \right] \right\}^{-1}, \quad (11) \end{aligned}$$

where $E_{\{\alpha\}} \equiv E_{n,\eta,\sigma}$ is a solution of Eq. (10). The Josephson current at $T = 0$ is a sum of partial currents over all occupied states.

The resonance current (of order \sqrt{D}) is formed by non-compensated partial currents carried by the Andreev levels in the vicinity of the Fermi energy, i.e. for $E_{\{\alpha\}} = 0^-$ when $D \rightarrow 0$. Such levels exist only for a discrete set of Zeeman splittings

$$\Delta_Z^{(k)} = \frac{2\pi(2k+1)}{\delta_L^{(+)}} , \quad k = 0, 1, 2, \dots \quad (12)$$

At a given $\Delta_Z^{(k)}$ (controlled e.g. by an external local magnetic field) two ($\eta = \pm 1$) Andreev levels contribute to the resonance Josephson current J_r , which can be represented in the form

$$J_r(\varphi) = J_0 \sqrt{D} \frac{1 - \lambda_a^2}{2} \frac{\sin\left(\frac{1}{2}\Delta_Z^{(k)}\delta_L^{(+)}\lambda_a + \varphi\right)}{\left|\sin\frac{1}{2}\left(\frac{1}{2}\Delta_Z^{(k)}\delta_L^{(+)}\lambda_a + \varphi\right)\right|}, \quad (13)$$

where $J_0 = ev_F/L$, and asymmetry parameter λ_a is defined in Eq. (8).

In the absence ($\lambda_a = 0$) of spin-orbit interaction Eq. (13) has the typical form of a resonance Josephson current (see e.g. Ref. [11]) associated with the contribution of a single Andreev level. One can interpret this result as follows. Let us assume for a moment that the potential barrier is infinite. Then, a symmetric SNINS junction (“I” stands for the insulator “layer”) breaks into two identical INS-hybrid structures. In each of the two systems de Gennes-Saint-James energy levels [10] with spacing $2\pi\hbar v_F/L$ are formed. For a finite barrier these levels are split with the characteristic splitting energy $\delta \sim \sqrt{D}\Delta_L \ll \Delta_L$. The tunnel split levels being localized already on the whole length L between the two superconductors are nothing but the Andreev energy levels i.e. they depend on the superconducting phase difference. Although the partial current of a single level is large (of the order of \sqrt{D} , see Ref. [11, 8]), the current carried by a pair of split levels is small ($\sim D$) due to a partial cancellation. A Zeeman splitting of order Δ_L shifts the set of Andreev levels so that the Fermi energy lies in between the split levels. Now only the lower state is occupied and this results in an uncompensated, large Josephson current. In other words only one of the two electrons of the Cooper pairs that form the supercurrent *tunnels* through the barrier. Its entangled partner at resonance conditions passes through the hybrid SFIFS structure (“F” denotes the region with nonzero Zeeman splitting) without backscattering. Since the quantized electron-hole spectrum is formed by Andreev scattering, the resonance structure for a single barrier junction disappears when the leads are in the normal state. Hence, electron transport through a normal region in our case is enhanced by superconductivity.

The effect of chiral symmetry breaking on the physical picture described above is to additionally split the degenerate Andreev levels. A dispersion asymmetry $\lambda_a \neq 0$ lifts the left-right symmetry of electron transport through the junction and splits the doubly degenerated Andreev levels at $\varphi = 0$. This

results in appearance of giant anomalous Josephson current (see Eq. (13)) at $\varphi = 0$.

We saw that it is indispensable that Eq. (9) holds for resonant transport through the single barrier hybrid structure to occur. This equation can be satisfied not only for the symmetric junction considered above. One can easily check that for a fixed value of Zeeman splitting $\Delta_Z^{(k)}$, given by Eq. (12), there is a set of points where a barrier still supports resonant transport. These points, determined by their coordinates $x_m^{(k)}$ counted from the middle of a junction, are (m is the integer)

$$x_m^{(k)} = \pm \frac{m}{2k+1}L, \quad 0 \leq m \leq k + 1/2. \quad (14)$$

The temperature dependence of the \sqrt{D} -currents is determined by the energy scale $\delta \sim \sqrt{D}\Delta_L$ and at temperatures $T_D \geq \delta$, which are much less than Δ_L , all resonance effects are washed out.

4 Influence of Chiral Symmetry Breaking on a Critical Current

There is a general statement [17] that spin-orbit interaction in 1D systems with Aharonov-Bohm geometry produces additional reduction factors in the Fourier expansion of thermodynamic or transport quantities. This statement holds for spin-orbit Hamiltonians for which the transfer matrix is factorized into spin-orbit and spatial parts. In a pure 1D case the spin-orbit interaction is represented by the Hamiltonian $H_{1D}^{(so)} = \alpha_{(so)}\hat{p}_x\sigma_z$, which is the product of spin-dependent and spatial operators, and thus it satisfies the above described requirements. However, as was shown by direct calculation in Ref. [4], spin-orbit interaction of electrons in 1D quantum wires formed in 2DEG by an in-plane confinement potential can not be reduced to the Hamiltonian $H_{1D}^{(so)}$. Instead, a violation of left-right symmetry of 1D electron transport, characterized by a dispersion asymmetry parameter λ_a , appears. We show now that in quantum wires with broken chiral symmetry the spin-orbit interaction enhances persistent current.

There is a close analogy between the Josephson current in a long SNS junction and the persistent current in a normal metal ring. For a long ($L \gg \hbar v_F/|\Delta|$) SNS junction Andreev boundary conditions can be recasted [18] in the form of twisted boundary conditions for chiral (right- or left-moving) fermions on a ring with circumference $2L$ pierced by the magnetic flux $\Phi/\Phi_0 = 1/2 + \varphi/2\pi$, where $\Phi_0 = hc/e$ is the normal flux quantum. Due to this mapping the corresponding formulae for the persistent current in a normal diamagnetic (with odd number of spinless fermions) 1D ring and the formulae for Josephson current coincide up to numerical factors. Here we consider the influence of dispersion asymmetry in electron spectrum on the off-resonance supercurrent

through a single barrier SNS junction (notice that resonance effects disappear in zero magnetic field).

In a low transparency 1D SNS junction the critical current in the presence of dispersion asymmetry is of the form $J_c = f(\lambda_a)Dev_F/L$. To analytically evaluate the function $f(\lambda_a)$ we consider two limiting cases: (i) an asymmetric junction $l = 0$, and (ii) a symmetric junction $l = L/2$.

The first case models a junction with strong normal backscattering at one of the two interfaces. In zero magnetic field the spectral equation, Eq. (3), in the limit considered is reduced to

$$\cos(E\delta_L^{(+)}) \simeq -\frac{D}{2} \cos(E\delta_L^{(-)} + \eta\varphi). \quad (15)$$

The energy spectrum and the partial supercurrents in the limit $D \ll 1$ are

$$E_n^{(0)} = \frac{\pi}{2\delta_L^{(+)}} \left(n + \frac{1}{2} \right), \quad (16)$$

$$j_{n,\eta}^{(a)} = \eta(-1)^{n+1} \frac{e}{\hbar} \frac{D}{2\delta_L^{(+)}} \sin \left[\pi \left(n + \frac{1}{2} \right) \lambda_a + \eta\varphi \right].$$

By summing partial currents over quantum numbers of occupied states ($E_n^{(0)} \leq 0$) at $T = 0$ one gets

$$J^{(a)} = \sum_{n=-1;\eta=\pm 1}^{-\infty} j_{n,\eta}^{(a)} = J_c^{(a)}(\lambda_a) \sin \varphi, \quad J_c^{(a)}(\lambda_a) = \frac{ev_F}{4L} D \frac{1 - \lambda_a^2}{\cos(\pi\lambda_a/2)}. \quad (17)$$

The critical current in the absence of spin-orbit interaction $J_c^{(a)}(0) = Dev_F/4L$ coincides with known results (see e.g. Ref. [11]).

For a symmetric junction the analogous calculation leads to the expression

$$J_c^{(s)}(\lambda_a) = \frac{ev_F}{\pi L} D \frac{\pi\lambda_a(1 - \lambda_a^2)}{\sin(\pi\lambda_a)}, \quad J_c^{(s)}(0) = \frac{ev_F}{\pi L} D. \quad (18)$$

The curves in Fig. 4 demonstrate the dependence of the normalized critical current $J_c^{(a,s)}/J_c^{(a,s)}(0)$ on the spin-orbit parameter λ_a for asymmetric (a) and symmetric (s) junction. We see that the spin-orbit Rashba interaction in quasi-1D quantum wires always enhances the critical current. The qualitative explanation of the unusual impact of chiral symmetry breaking on a critical Josephson current is as follows. The Josephson current (as any other thermodynamic persistent current) is a sum of partial currents of all occupied energy levels. The partial currents of adjacent energy levels are opposite in sign and for chiral invariant systems (i.e. without dispersion asymmetry) they almost perfectly cancel each other to produce a net current of the order of a single level current. When chiral invariance is broken the absolute values of partial currents of adjacent energy levels are different and the cancelation of currents for distant levels is less perfect. It results in an enhancement of the critical Josephson current. The effect is, however, numerically not large.

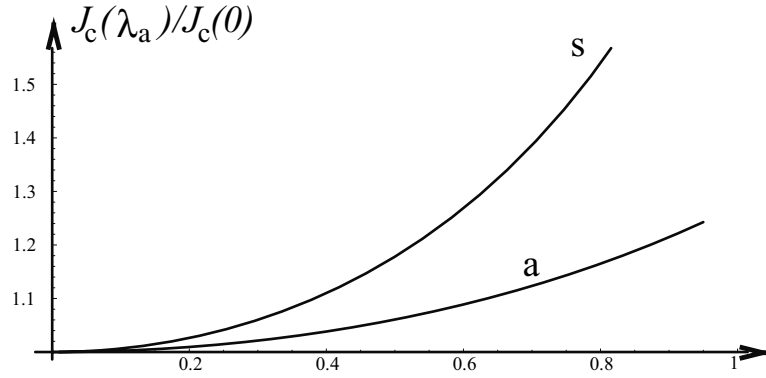


Fig. 4. The dependence of the normalized critical current $J_c(\lambda_a)/J_c(\lambda_a = 0)$ in a low-transparency ($D \ll 1$) S-N-S junction on the parameter of dispersion asymmetry λ_a . The curve labeled by “s” corresponds to the case of symmetric junction ($l = L/2$), the curve “a” describes strongly asymmetric junction ($l = 0$).

5 Conclusion

In quantum wires formed in a two-dimensional electron gas (2DEG) by lateral confinement the Rashba spin-orbit interaction is not reduced to a pure 1D Hamiltonian $H_{1D}^{(so)} = \alpha_{so} \hat{p}_x \sigma_z$. As was shown in Ref. [4] the presence of an in-plane confinement potential qualitatively modifies the energy spectrum of the 1D electrons so that a dispersion asymmetry appears. As a result the chiral symmetry is broken in quantum wires with Rashba coupling. Although the effect was shown [4] not to be numerically large, the breakdown of symmetry leads to qualitatively novel predictions.

We have considered here the influence of dispersion asymmetry and Zeeman splitting on the Josephson current through a superconductor/quantum wire/superconductor junction. We showed that the violation of chiral symmetry in a quantum wire results in qualitatively new effects in a weak superconductivity. In particular, the interplay of Zeeman and Rashba interactions induces a Josephson current through the hybrid 1D structure even in the absence of any phase difference between the superconductors. At low temperatures ($T \ll \hbar v_F/L$) the anomalous supercurrent can be of the order of the critical Josephson current. For a transparent junction with small or moderate dispersion asymmetry (characterized by the dimensionless parameter $\lambda_a = (v_{1F} - v_{2F})/(v_{1F} + v_{2F})$) it appears, as a function of the Zeeman splitting Δ_Z , abruptly at $\Delta_Z \sim \hbar v_F/L$. In a low transparency ($D \ll 1$) junction, the anomalous Josephson current at special (resonance) conditions is of the order of \sqrt{D} . In zero magnetic field the anomalous supercurrent disappears (as it should) since the spin-orbit interaction itself respects T-symmetry. However, the influence of the spin-orbit interaction on the critical Josephson current through a quasi-1D structure is still anomalous. Contrary to what holds

for chiral invariant systems with Aharonov-Bohm geometry where spin-orbit effects suppress persistent currents [17], the breakdown of chiral symmetry results in an enhancement of the supercurrent.

All the phenomena described above are absent in a 2D-junction when the effects of transverse mode quantization are neglected [7]. We have considered the limiting case of a single (transverse) channel because this is the case when the effects induced by a dispersion asymmetry in the electron spectrum are most pronounced. The anomalous supercurrent Eq. (7) is a sign alternating function of the transverse channel index since for neighboring channels the spin projections of chiral states are opposite [4]. Besides, the absolute value of the dispersion asymmetry parameter $\lambda_a^{(j)}$ decreases with transverse-channel number j . So, for a multichannel junction the effects related to a dispersion asymmetry phenomenon will be strongly suppressed and they completely disappear in the pure 2D case.

We evaluated the Josephson current through a S-QW-S junction in a model of noninteracting electrons. In QWs the effects of electron-electron interaction can be significant and here we comment on how interaction effects could modify the obtained results. Electronic properties of 1D QWs are usually described by a Luttinger liquid (LL) model (see e.g. Ref. [19]). The supercurrent in a S-LL-S junction with repulsive e-e interaction strongly depends on the quality of electric contact of a nanowire with the bulk superconductors. For adiabatic contacts when only Andreev scattering takes place at the interfaces the Josephson current through a perfect wire is not renormalized by interaction [18, 21]. For tunnel contacts e-e interaction in a wire renormalizes the barrier transparencies (Kane-Fisher effect [20]) and for repulsive interaction the critical current is strongly suppressed [22].

We are interested in spin-orbit effects in S-QW-S junction. It is reasonable to expect that Eqs. (6), (7) derived for a perfect junction (without normal backscattering) will be valid even for interacting electrons. One could expect also that in a tunneling regime ($D \ll 1$) the interaction effects in Eqs. (13), (17), (18) can be estimated by replacing the bare transparency D by the interaction-renormalized one [18] $D_g \sim D(d/L)^{K_\rho^{-1}-1}$ (here $d \ll L$ is the width of the wire and K_ρ is the LL correlation parameter). In quantum wires formed in 2DEG the Coulomb interaction is not strong and it can be controlled by the gate electrodes. For weakly interacting electrons (a conceivable case for “semiconducting” QWs) when the electron picture of charge transport through a 1D wire is still valid [23], the interaction effects can be really accounted for by replacing the bare transmission coefficient by the renormalized one.

Acknowledgements.— Financial support from the Royal Swedish Academy of sciences (IVK), the Swedish Science Research Council (LIG, RIS) and the Swedish Foundation for Strategic Research (LIG, RIS, MJ) is gratefully acknowledged.

A Appendix

We consider electron transport through a normal region of length L with a local scatterer placed a distance l from the left bank, at point $x = l$. In our two channel chiral model (the term “chiral” here means that left- and right-moving particles with a given Fermi velocity have opposite spin polarizations, see Fig. 1) backscattering by nonmagnetic impurity corresponds to a backward interchannel scattering (“1” \leftrightarrow “2”). In the presence of a magnetic field and interchannel scattering the general 4×4 nonsymmetric S-matrix can be parameterized as follows

$$\hat{S}_E = \begin{pmatrix} |r|\sigma_1 \exp i(\rho_R + \sigma_3\mu_R) & |t|\sigma_3 \exp i(\alpha_R + \sigma_3\eta_R) \\ |t|\sigma_3 \exp i(\alpha_L + \sigma_3\eta_L) & |r|\sigma_1 \exp i(\rho_L + \sigma_3\mu_L) \end{pmatrix}.$$

Here $\sigma_{1,3}$ are the Pauli matrices, $t_{R,L} = |t| \exp(i\eta_{R,L})$, $r_{R,L} = |r| \exp(i\rho_{R,L})$ and $|t|^2 + |r|^2 = 1$. Unitarity of the S-matrix ($SS^\dagger = I$) implies the relations

$$\mu_R + \eta_R = \mu_L + \eta_L, \quad \rho_R + \rho_L = \alpha_R + \alpha_L \quad (19)$$

So, the scattering matrix in our problem is described by 7 independent real parameters. For a point scatterer with energy independent scattering amplitudes (t_0, r_0) one readily gets that $|t|^2 = |t_0|^2 \equiv D$ (D is the junction transparency). The phases are

$$\begin{aligned} \mu_R &= -(L-l)k_-, \quad \rho_R = (L-l)k_+, \quad \eta_R = Lk_-^{\uparrow\downarrow}, \quad \alpha_R = Lk_+^{\uparrow\downarrow} \\ \mu_L &= lk_-, \quad \rho_L = lk_+, \quad \eta_L = Lk_-^{\downarrow\uparrow}, \quad \alpha_L = Lk_+^{\downarrow\uparrow}, \end{aligned} \quad (20)$$

where $k_\pm = k_+^{\uparrow\uparrow} \pm k_+^{\downarrow\downarrow}$, and

$$k_\pm^{\sigma\sigma'} = \frac{1}{2} (k_1^\sigma \pm k_2^{\sigma'}), \quad k_j^\sigma(\pm E) = k_{jF} + \frac{\pm E + \sigma g \mu_B H/2}{\hbar v_{jF}} \quad (21)$$

and k_{jF}, v_{jF} ($j = 1, 2$) are the Fermi momentum and the Fermi velocity in the j -th channel.

The diagonal matrix \hat{r}_A in Eq. (2) takes the form

$$\hat{r}_A = \begin{pmatrix} \exp(i\varphi/2)\hat{I} & 0 \\ 0 & \exp(-i\varphi/2)\hat{I} \end{pmatrix}, \quad (22)$$

where φ is the superconducting phase difference and \hat{I} is 2×2 unit matrix.

References

1. E. I. Rashba, *Fiz.Tverd.Tela (Leningrad)* **2**, 1224 (1960) [*Sov.Phys.Solid.State* **2**, 1109 (1960)]; Y. A. Bychkov, and E. I. Rashba, *J.Phys.C* **17**, 6039 (1984).

2. J. Nitta, T. Akasaki, H. Takayanagi, and T. Enoki, *Phys.Rev.Lett.* **78**, 1335 (1997); D. Grundler, *Phys. Rev. Lett.* **84**, 6074 (2000).
3. F. Mireles, and G. Kirczenow, *Phys. Rev. B* **64**, 024426 (2001).
4. A. V. Moroz, and C. H. Barnes, *Phys. Rev. B* **60**, 14272 (1999).
5. A. V. Moroz, K. V. Samokhin, and C. H. Barnes, *Phys. Rev. B* **62**, 16900 (2000).
6. M. Governale, and U. Zulicke, *Phys. Rev. B* **66**, 073311 (2002).
7. E. V. Bezuglyi, A. S. Rozhavsky, I. D. Vagner, and P. Wyder, *Phys. Rev. B* **66**, 052508 (2002).
8. G. Wendin, and V. S. Shumeiko, *Phys. Rev. B* **53**, R6006 (1996); *Superlattices Microstruct.* **4**, 569 (1996).
9. P. Sandström, and I. V. Krive, *Phys. Rev. B* **56**, 9255 (1997).
10. P. G. de Gennes, and D. Saint-James, *Phys. Lett.* **4**, 151 (1963).
11. P. Samuelsson, J. Lantz, V. S. Shumeiko, and G. Wendin, *Phys. Rev. B* **62**, 1319 (2000).
12. A. Svidzinsky, T. N. Antsygina, and E. N. Bratus', *ZhETF* **61**, 1612 (1971); [*Sov. Phys. JETP* **34**, 860 (1972)].
13. V. M. Mostepanenko, and N. N. Trunov, *The Casimir effect and its Application*, Claredon Press, Oxford (1997).
14. C. W. J. Beenakker, *Phys. Rev. Lett.* **67**, 3836 (1991).
15. P. F. Bagwell, *Phys. Rev. B* **46**, 12573 (1992).
16. I. O. Kulik, *Zh. Eksp. Teor. Fiz.* **57**, 1745 (1969) [*Sov. Phys. JETP* **30**, 944 (1970)].
17. Y. Meir, Y. Gefen, and O. Entin-Wohlman, *Phys. Rev. Lett.* **63**, 798 (1989).
18. D. L. Maslov, M. Stone, P. M. Goldbart, and D. Loss, *Phys. Rev. B* **53**, 1548 (1996).
19. A. O. Gogolin, A. A. Nersesyan and A. M. Tsvelik, *Bosonization and Strongly Correlated Systems*, Cambridge University Press (1998).
20. C. L. Kane, and M. P. A. Fisher, *Phys. Rev. Lett.* **68**, 1220 (1992); *Phys. Rev. B* **46**, 15233 (1992).
21. I. Affleck, J.-S. Caux, and A. Zagoskin, *Phys. Rev. B* **62**, 1433 (2000).
22. R. Fazio, F. W. J. Hekking, and A. A. Odintsov, *Phys. Rev. Lett.* **74**, 1843 (1995).
23. K. A. Matveev, D. Yue, and L. I. Glazman, *Phys. Rev. Lett.* **71**, 3351 (1993).

Manifestation of Triplet Superconductivity in Superconductor-Ferromagnet Structures

F.S. Bergeret¹, A.F. Volkov^{1,2}, and K.B. Efetov^{1,3}

¹ Theoretische Physik III, Ruhr-Universität Bochum, D-44780 Bochum, Germany

² Institute of Radioengineering and Electronics of the Russian Academy of Sciences, 103907 Moscow, Russia

³ L.D. Landau Institute for Theoretical Physics, 117940 Moscow, Russia

Summary. We study proximity effects in a multilayered superconductor/ferromagnet (S/F) structure with arbitrary relative directions of the magnetization \mathbf{M} . If the magnetizations of different layers are collinear the superconducting condensate function induced in the F layers has only a singlet component and a triplet one with a zero projection of the total magnetic moment of the Cooper pairs on the \mathbf{M} direction. In this case the condensate penetrates the F layers over a short length ξ_J determined by the exchange energy J . If the magnetizations \mathbf{M} are not collinear the triplet component has, in addition to the zero projection, the projections ± 1 . The latter component is even in the momentum, odd in the Matsubara frequency and penetrates the F layers over a long distance that increases with decreasing temperature and does not depend on J (spin-orbit interaction limits this length). If the thickness of the F layers is much larger than ξ_J , the Josephson coupling between neighboring S layers is provided only by the triplet component, so that a new type of superconductivity arises in the transverse direction of the structure. The Josephson critical current is positive (negative) for the case of a positive (negative) chirality of the vector \mathbf{M} .

1 Introduction

Multilayered superconductor/ferromagnet (S/F) structures are under an intensive study now (for a recent review see e.g. [1]). The interest in such systems originates from a possibility to find new physical phenomena as well from the hope to construct new devices based on these structures. Although a ferromagnet F attached to a superconductor S is expected to suppress the order parameter in S, under certain conditions superconductivity and ferromagnetism may coexist and exhibit interesting phenomena. In most papers on S/F structures the case of collinear (parallel or antiparallel) orientations

of the magnetization \mathbf{M} was considered. If the magnetization vector \mathbf{M} is not constant in space, as in a domain wall, or if the orientations of \mathbf{M} in different F layers are not collinear to each other, a qualitatively new and interesting effect occurs. For example, if a ferromagnetic wire is attached to a superconductor, a domain wall in the vicinity of the interface can generate a triplet component of the superconducting condensate [2] (a similar case was analyzed in a later work [3]). The existence of the triplet component (TC) has far reaching consequences. It is well known that the singlet component (SC) penetrates into a ferromagnet over the length $\xi_J = \sqrt{D_F/J}$, where D_F is the diffusion coefficient in F . In contrast, it was shown that even for $J \gg T$ the TC penetrated F over a much longer distance $\xi_T = \sqrt{D_F/2\pi T}$. This long-range penetration of the TC might lead to an increase of the conductance of the F wire if the temperature is lowered below T_c [2, 3].

In this report we consider a multilayered S/F structure. Each F layer has a constant magnetization \mathbf{M} but the direction of the \mathbf{M} vector varies from layer to layer. We show that, in this case, the triplet component of the superconducting condensate is also generated and it penetrates the F layers over the long length ξ_T that does not depend on the large exchange energy J at all. If the thickness of the F layers d_F is much larger than ξ_J , then the Josephson coupling between adjacent S layers and, therefore, superconductivity in the transverse direction is due to the TC . In the vicinity of the S/F interface the amplitudes of the SC and TC may be comparable but, unlike the TC , the SC survives in F only over the short distance ξ_J from the S/F interface. In other words, in the multilayered F/S structures with a non-collinear magnetization orientation, a new type of superconductivity arises. The non-dissipative current within the layers is due to the s-wave singlet superconductivity, whereas the transversal supercurrent across the layers is due to the s-wave, triplet superconductivity.

It is important to emphasize (see Ref. [2]) that the TC in this case differs from the TC realized in the superfluid He^3 and, for example, in materials like Sr_2RuO_4 [4]. The triplet-type superconducting condensate we predict here is symmetric in momentum and therefore is insensitive to non-magnetic impurities. It is odd in frequency and is called sometimes odd superconductivity. This type of the pairing has been proposed by Berezinskii in 1975 [5] as a possible candidate for the mechanism of superfluidity in He^3 . However, it turned out that another type of pairing was realized in He^3 : triplet, odd in momentum p (sensitive to ordinary impurities) and even in the Matsubara frequencies ϖ . It is also important to note that while the symmetry of the order parameter Δ in Refs. [4, 5] differs from that of the BCS order parameter, in our case Δ is nonzero only in the S layers and is of the BCS type. It is determined by the amplitude of the singlet component. Since the triplet and singlet components are connected with each other, the TC affects Δ in an indirect way.

Therefore the type of superconductivity analyzed in our paper complements the three known types of superconductivity: s-wave and d-wave singlet superconductivity that occur in ordinary superconductors and in high T_c

superconductors respectively, and the p-wave superconductivity with triplet pairing observed in Sr₂RuO₄.

In addition, the new type of the triplet superconductivity across the *S/F* layers shows another interesting property related to the chirality of the magnetization \mathbf{M} . If the angle of the magnetization rotation 2α across the S_A layer (see Fig. 3) has the same sign as the angle of the \mathbf{M} rotation across the S_B layer, then the critical Josephson current I_c between S_A and S_B is positive. If these angles have different signs, then the critical current I_c is negative and π -state is realized (in this case spontaneous supercurrents arise in the structure). Depending on the chirality an “effective” condensate density in the direction perpendicular to the layers may be both positive and negative.

2 The condensate function in a F/S/F sandwich

In order to get a better understanding of the properties of the superconducting condensate in the presence of the ferromagnetic layers, we consider in this section a simple case of a trilayered F/S/F structure (see Fig. 1). Generalization to a multilayered structures is of no difficulties and will be done in the next section.

In the most general case, when the magnetization vectors \mathbf{M} of the F-layers are non-collinear, the electron Green functions are 4×4 matrices in the particle-hole \otimes spin-space. A very convenient way for the study of proximity effects is the method of quasiclassical Green’s functions [7, 8, 9]. Equations for the quasiclassical Green’s functions \check{g} have been generalized recently to the case of a non-homogeneous exchange field (magnetization) \mathbf{M} [10].

The elements of the matrix \check{g} diagonal in the particle-hole space (i.e proportional to $\hat{\tau}_0$ and $\hat{\tau}_3$) are related to the normal Green’s function, while the off-diagonal elements (proportional to $\hat{\tau}_1$ and $\hat{\tau}_2$) determine the superconducting condensate function \check{f} . In the case under consideration the matrix \check{g} can be expanded in the Pauli matrices in the particle-hole space ($\hat{\tau}_0$ is the unit matrix):

$$\check{g} = \hat{g}_0 \hat{\tau}_0 + \hat{g}_3 \hat{\tau}_3 + \check{f}, \quad (1)$$

where the condensate function is given by

$$\check{f} = \hat{f}_1 i \hat{\tau}_1 + \hat{f}_2 i \hat{\tau}_2. \quad (2)$$

The functions \hat{g}_i and \hat{f}_i are matrices in the spin-space. In the case under consideration the matrices \hat{f}_i can be represented in the form

$$\hat{f}_2(x) = f_0(x) \hat{\sigma}_0 + f_3(x) \hat{\sigma}_3 \quad (3)$$

$$\hat{f}_1(x) = f_1(x) \hat{\sigma}_1 \quad (4)$$

This follows from the equation that determines the Green’s function (see below).

Let us discuss briefly properties of the condensate matrix function \check{f} . According to the definitions of the Green's functions \check{g} the functions $f_i(x)$ are related to following correlation functions

$$\begin{aligned} f_3 &\sim \langle \psi_\uparrow \psi_\downarrow \rangle - \langle \psi_\downarrow \psi_\uparrow \rangle, \\ f_0 &\sim \langle \psi_\uparrow \psi_\downarrow \rangle + \langle \psi_\downarrow \psi_\uparrow \rangle, \\ f_1 &\sim \langle \psi_\uparrow \psi_\uparrow \rangle \sim \langle \psi_\downarrow \psi_\downarrow \rangle. \end{aligned} \quad (5)$$

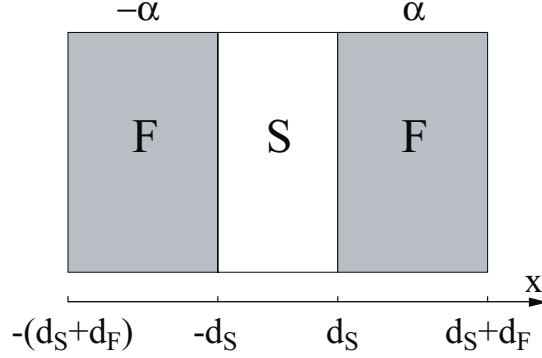


Fig. 1. The F/S/F trilayer. The magnetizations vectors in the F layers make an angle $\pm\alpha$ with the z -axis, respectively

The function f_3 describes the *SC*, while the functions f_0 and f_1 describe the *TC* (see for example Ref. [11]). The function f_0 is proportional to the zero projection of the triplet magnetic moment of the Cooper pairs on the z -axis, whereas the function f_1 corresponds to the projections ± 1 .

It is important that in the absence of an exchange field \mathbf{J} (or magnetization \mathbf{M}) acting on spins, the *SC*, i.e. the function f_3 , exists both in the superconducting and normal (non-magnetic) layers. If J is not equal to zero but is uniform in space and directed along the z -axis, then the part f_0 of the *TC* arises in the structure.

However, both the functions f_3 and f_0 decay very fast in the ferromagnet (over the length ξ_J). The singlet component decays because a strong magnetization makes the spins of a pair be parallel to each other, thus destroying the condensate. The triplet component with the zero projection of the magnetic moment is also destroyed because it is more energetically favorable for the magnetic moment to be parallel to the magnetization.

In order to find the Green's function \check{g} , we consider the diffusive case when the Usadel equation is applicable. This equation can be used provided the condition $J\tau \ll 1$ is satisfied (τ is the momentum relaxation time). Of course, this condition can hardly be satisfied for strong ferromagnets like *Fe* and in this case one should use a more general Eilenberger equation for a quantitative

computation. However, the Usadel equation may give qualitatively reasonable results even in this case.

The Usadel equation is a nonlinear equation for the 4×4 matrix Green's function [15]. The Usadel equation is complemented by the boundary conditions at the S/F interface [12]

$$\gamma (\check{g} \partial_x \check{g})_F = (\check{g} \partial_x \check{g})_S, \quad x = \pm d_S \quad (6)$$

$$2\gamma_b \xi_J (\check{g} \partial_x \check{g})_F = \pm [\check{g}_S, \check{g}_F], \quad x = \pm d_S, \quad (7)$$

where $\gamma = \sigma_F/\sigma_S$, and $\sigma_{S,F}$ are the conductivities of the F and S layers, $\gamma_b = \sigma_F R_b/\xi_J$ is a coefficient characterizing the transmittance of the S/F interface with resistance per unit area R_b .

The Usadel equation can be solved in some limiting cases [15]. In Fig. 2 we present the spatial dependence of the condensate function (singlet and triplet). One can see that the SC penetrates the F layer over a short distance of the order ξ_J whereas the TC penetrates over a long distance $\xi_T = \sqrt{D_F/2\pi T}$. The amplitude of the long-range part of the TC has a maximum at $\alpha = \pi/4$.

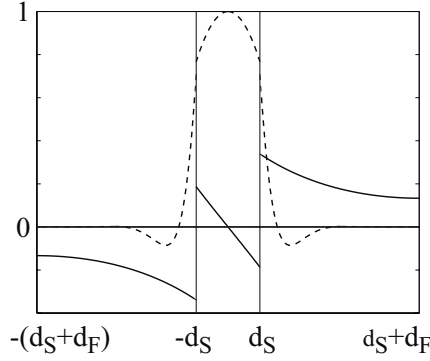


Fig. 2. The spatial dependence of $\text{Im}(\text{SC})$ (dashed line) and the long-range part of $\text{Re}(\text{TC})$ (solid line). We have chosen $\gamma = 0.2$, $J/T_C = 50$, $\gamma_b = 0.05$, $d_F \sqrt{T_C/D_S} = 2$, $d_S \sqrt{T_C/D_S} = 0.4$ and $\alpha = \pi/4$. The discontinuity of the TC at the S/F interface is because the short-range part is not shown in this figure.

3 Josephson Current in a F/S/F/S/F structure

In this section we calculate the Josephson current between the S layers of a FSFSF structure. We assume again that the thickness of the F layers d_F is much larger than ξ_J . In this case the Josephson coupling between the S layers is due to the long range part of the TC. Therefore the supercurrent in the transverse direction is unusual, since it is caused by the triplet component of the condensate that is odd in frequency and even in momentum.

At the same time, the in-plane superconductivity is caused mainly by the ordinary singlet component. Therefore the macroscopic superconductivity due to the Josephson coupling between the layers is an interesting combination of the singlet superconductivity within the layers and the odd triplet superconductivity in the transversal direction.

We will see that the unusual character of the superconductivity in the transversal direction leads to peculiarities of the Josephson effect. For example, if the bias current flows through the terminal superconducting layer S_O and S_A (see Fig. 3), the supercurrent is zero because of the different symmetry of the condensate in S_O and S_A . In order to observe the Josephson effect in this structure the bias current has to pass through the layers S_A and S_B , as shown in Fig. 3. The supercurrent between S_A and S_B is non-zero because each superconductor has its “own” TC and the phase difference φ is finite.

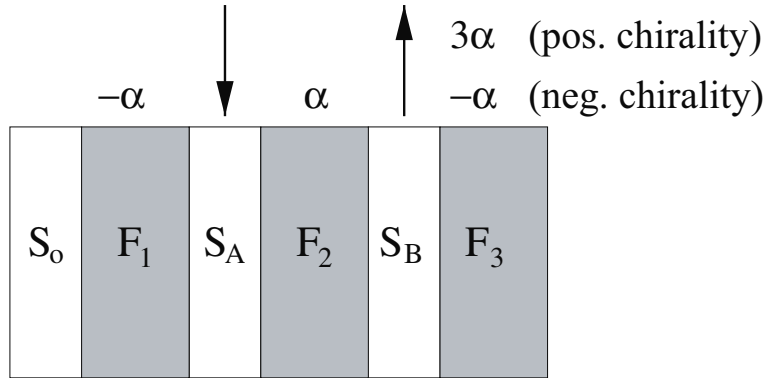


Fig. 3. The multilayered structure considered. The arrows show the bias current. In the case of positive (negative) chirality the magnetization vector \mathbf{M} of the layer F_3 makes an angle 3α ($-\alpha$) with the z -axis, i.e. in the case of positive chirality the vector \mathbf{M} rotates in one direction if we go over from one F layer to another whereas it oscillates in space in the case of negative chirality.

The Josephson current I_S is given by the expression

$$I_S = (L_y L_z) \sigma_F \text{Tr}(\hat{\tau}_3 \hat{\sigma}_0) \sum_{\omega} \check{f} \partial_x \check{f} \quad (8)$$

This current was calculated for the case of small angles α in Ref. [6]. Here $L_y L_z$ is the area of the interface and σ_F is the conductivity of the F layer. The simplest way to calculate the I_S is to assume a weak coupling between the S layers, which corresponds to the case when the condition $d_F > \xi_T$ holds. In this case the long-range part of the TC is given by the sum of two terms each of those is induced by the layers S_A and S_B in Fig. 3:

$$\check{f}(x) = \check{f}_A(x) + \check{S} \cdot \check{U} \cdot \check{f}_B(x - d_S - d_F) \check{U}^+ \cdot \check{S}^+ , \quad (9)$$

where $\check{f}_A(x)$ is the long range part of the TC induced by the layer S_A . If the $S_{A,B}/F$ interfaces are identical as well as the superconductors S_A and S_B , the function \check{f}_B is equal to \check{f}_A if one replace the exponential function $\exp(-\kappa_\omega(x - d_S))$ by $\exp(\kappa_\omega(x - d_S - d_F))$. The phase of the S_A layer is set to be zero and the phase of the S_B is φ . This phase has been taken into account by the gauge transformation performed with the help of the matrix $\check{S} = \hat{\tau}_0 \cos(\varphi/2) + i\hat{\tau}_3 \sin(\varphi/2)$. The magnetizations \mathbf{M} of the layers F_1 and F_2 make an angle $\mp\alpha$ with the z -axis respectively. For the direction of \mathbf{M} in the F_3 we consider two cases: a) the direction of magnetization is $-\alpha$ (negative chirality) or b) 2α (positive chirality). In the latter case the matrix \check{U} in Eq. (9) is given by

$$\check{U} = \hat{\tau}_0 \hat{\sigma}_3 \cos \alpha + i\hat{\tau}_3 \hat{\sigma}_2 \sin \alpha . \quad (10)$$

In the case of negative chirality, \check{U} is the unit matrix and one has to change the sign of α in the expression for the function \check{f}_B (Eq. (9)). In Fig. 4 we show schematically the spatial dependence of $f_1(x)$.

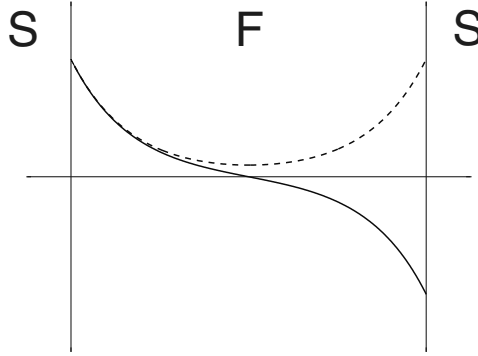


Fig. 4. The spatial dependence of the amplitude of the TC $f_1(x)$ in the case of positive (solid line) and negative (dashed line) chirality.

Using the solution of the Usadel equation [15], one obtains after simple transformations $I_S = I_c \sin \varphi$, where

$$eR_F I_c = \pm 2\pi T \sum_{\omega} \kappa_{\omega} d_F b_1^2(\alpha) (1 + \tan^2 \alpha) e^{-d_F \kappa_{\omega}} , \quad (11)$$

where the sign “+” (“-”) corresponds to the positive (negative) chirality. In the case of negative chirality the critical current is negative (π -contact). The negative Josephson coupling is due to the TC and can be realized in S/F structures with negative chirality. This gives a unique opportunity to switch experimentally between the 0 and π -contacts by changing the angles of the mutual magnetization of the layers.

If the orientation of \mathbf{M} is parallel ($\alpha = 0$) or antiparallel ($\alpha = \pi/2$) the amplitude of the triplet component is zero and therefore there is no coupling between the neighboring S layers, i.e. $I_c = 0$. For any other angle between the magnetizations the amplitude of the TC is finite. This leads to a non-zero critical current. At $\alpha = \pi/4$ (perpendicular orientation of \mathbf{M}) I_c reaches its maximum value. The weak coupling assumption ($d_F > \xi_T$) leads to an exponential decay of I_c with increasing d_F (Eq. (11)). In the case $d_F \leq \xi_T$, Eq. (11) is not valid. One can easily obtain I_c for the case of an arbitrary d_F and small α . It turns out that in this case Eq. (11) remains valid if the exponential factor $\exp(-\kappa_\omega d_F)$ is replaced by $\cosh^{-2}(\kappa_\omega d_F/2)$.

In order to estimate the value of the critical current I_c , we use Eq. (11). If d_F exceeds the length ξ_T (for example $d_F/\xi_T = 2$) only the term with $n = 0$ (i.e. $\omega = \pi T_c^*$) is important in the sum. In this case one obtains

$$\frac{eR_F I_c}{T_c^*} = \frac{4}{\pi} \left(\frac{\Delta}{T_c^*} \right)^2 e^{-\kappa_T d_F} C, \quad (12)$$

where the factor C can be easily expressed in terms of M_\pm , T_\pm , etc. Thus, C depends on many parameters such as γ , γ_b , κ_J , etc. We estimate C for values of these parameters similar to those which were used in Ref. [13]: $\gamma_b = 0.5$, $\gamma = 0.1$, $d_S \kappa_S = 0.4$, $d_F \kappa_\omega = 1.5$, $\kappa_\omega/\kappa_S = 3$. We get $C = 10^{-2} - 10^{-3}$ for $\kappa_J d_S = 5 - 10$. The expression (12) for I_c also contains the parameters $(\Delta/T_c^*)^2$ and $\exp(-d_F \kappa_T)$ which are also small. We note however that if $d_F \leq \xi_T$, the exponential function is replaced by a numerical factor of the order of 1. The factor $(\Delta/T_c^*)^2$ is also of the order 1 if the temperature is not close to T_c^* . Taking $\sigma_F^{-1} = 60 \mu\Omega \cdot \text{cm}$ (cf. Ref. [13]) and $d_F \sim \xi_T \sim 200$ nm we obtain $I_c \sim 10^4 - 10^5$ A.cm $^{-2}$; that is, the critical current is a measurable quantity (see experimental work [14]) and the detection of the TC is possible.

4 Conclusion

We studied odd, s-wave, triplet superconductivity that may arise in S/F multilayered structures with a non-collinear orientation of magnetizations. It was assumed that the orientation of the magnetization is not affected by the superconductivity (e.g. the energy of the magnetic anisotropy is much larger than the superconducting energy). The analysis was carried out in the dirty limit ($J\tau \ll 1$) when the Usadel equation is applicable.

It was shown that for all values of α the condensate function consists of a singlet (SC) and a triplet (TC) components. Even in the case of a homogenous magnetization ($\alpha = 0$), in addition to the SC, the TC with the zero projection onto the z axis arises. In this case, both the SC and the TC decay in the F layers over a short distance given by $\xi_J = \sqrt{D_F/J}$. If the magnetization vectors \mathbf{M} are not collinear $\alpha \neq 0, \pi/2$, all projections of the TC appear, in particular, those with non-zero projection on the z -axis. In this case, the TC

penetrates the F layer over a long distance $\xi_T = \sqrt{D_F/2\pi T}$. In the presence of spin-orbit interaction this penetration length is given by $\min(\xi_{so}, \xi_T)$, where $\xi_{so} = \sqrt{\tau_{so} D_F}$. Generally, this length may be much larger than ξ_J .

Thus, if the condition $d_F \gg \xi_J$ is fulfilled the Josephson coupling between neighboring S layers is only due to the TC. Therefore in this case a new type of superconductivity may arise in the multilayered structures with non-collinear magnetizations. The supercurrent within each S layer is caused by the SC, whereas the supercurrent across the layers is caused by the triplet condensate, which is odd in the frequency ω and even in the momentum.

The TC in our case is completely different from the triplet condensate found in Sr_2RuO_4 [4]. In the latter case one has a p -wave, even in ω , triplet superconductivity, which is suppressed by impurity scattering. In contrast, the TC we have considered is not affected by non-magnetic impurities. The reason for the existence of the long-range TC is the fact that if $\alpha \neq 0$, the SC and the TC are coupled and, in addition to $\kappa_{\pm} = \xi_J^{-1}(1 \pm i)$, the eigenvalue $\kappa_T = \xi_T^{-1}$ appears. The latter corresponds to the long-range penetration of the TC in the ferromagnet.

The triplet superconductivity in S/F structures possesses an interesting property: the Josephson current depends on the chirality of the magnetization \mathbf{M} : If the \mathbf{M} vector rotates in only one direction (the positive chirality) the critical current I_c is positive. If the direction of the \mathbf{M} vector oscillates in space (the negative chirality) then $I_c < 0$. In the latter case spontaneously circulating currents must arise in the structure. This result can be explained as follows: if the chirality is positive the averaged \mathbf{M} vector $\langle \mathbf{M} \rangle$ is zero and the S/F structure behaves as a superconductor with anisotropic properties (the singlet superconductivity along the layers and the triplet superconductivity across them). In the case of the negative chirality the average in space yields a non-zero magnetization $\langle \mathbf{M} \rangle \neq 0$. In such a superconductor with a build-in magnetic moment the circulating currents arise as they arise in superconductors of the second type in the mixed state.

It would be interesting to carry out experiments on S/F structures with non-collinear magnetization in order to observe this new type of superconductivity. As follows from a semiquantitative analysis, the best conditions to observe the Josephson critical current caused by the TC are high interface transparency (small γ_b) and low temperatures. These conditions are a bit beyond our quantitative study. Nevertheless, all qualitative features predicted here (angle dependence, etc) should remain in a general case when one has to deal with the non-linear Usadel equation.

Acknowledgements.— We would like to thank SFB 491 and the German-Israeli Foundation (GIF) for a financial support.

References

1. Yu.A. Izyumov, Yu.N. Proshin, and M.G. Khusainov, *Uspekhi Fiz. Nauk* **172**, 113 (2002).
2. F.S. Bergeret, A.F. Volkov and K.B. Efetov, *Phys. Rev. Lett.* **86**, 4096 (2001).
3. A. Kadigrobov, R.I. Shekhter, and M. Jonson, *Europhys. Lett.* **54**, 394 (2001).
4. A.P. Mackenzie, R.K.W. Haselwimmer, A.W. Tayler, G.G. Lonzarich, Y. Mori, S. Nishizaki, and Y. Maeno, *Phys. Rev. Lett.* **80**, 161 (1998)
5. V.L. Berezinskii, *JETP Lett.* **20**, 287 (1975).
6. F.S. Bergeret, A.F. Volkov and K.B. Efetov, *Phys. Rev. Lett.* **90**, 117006 (2003).
7. G. Eilenberger, *Z. Phys.* **214**, 195 (1968).
8. A.I. Larkin, Yu.N. Ovchinnikov, *JETP* **26**, 1200 (1968).
9. K.L. Usadel, *Phys. Rev. Lett* **25**, 507 (1970).
10. F.S. Bergeret, K.B. Efetov, and A.I. Larkin, *Phys. Rev. B* **62**, 11872 (2000).
11. A.J. Leggett, *Rev. Mod. Phys.* **47**, 331 Section VII (1975).
12. A.V. Zaitsev, *Sov. Phys. JETP* **59**, 863 (1984); M.Y. Kupriyanov and V.F. Lukichev, *Sov. Phys. JETP* **64**, 139 (1988).
13. Ya. V. Fominov, N.M. Chtchelkatchev and A.A. Golubov, *Phys. Rev. B* **66**,14507 (2002).
14. V.V. Ryazanov et al., *Phys. Rev. Lett.* **86**, 2427 (2001); T. Kontos et al. *Phys. Rev. Lett* **89**, 137007 (2002); Y. Blum et al., *Phys. Rev. Lett.* **89**, 187004 (2002).
15. F.S. Bergeret, A.F. Volkov, and K.B. Efetov, *Phys. Rev. B* **68**, 064513 (2003).

Noise and Fluctuation Phenomena

Phase Dependent Current Statistics in a Short-Arm Andreev Interferometer

E.V. Bezuglyi^{1,3}, E.N. Bratus¹, V.S. Shumeiko², and V.M. Vinokur³

¹ Institute for Low Temperature Physics and Engineering, Kharkov 61103, Ukraine

² Chalmers University of Technology, Gothenburg S-41296,
Swedeneugene@fy.chalmers.se

³ Materials Science Division, Argonne National Laboratory, Argonne IL 60439,
USA

Summary. We calculate analytically the full counting statistics for a short normally conducting diffusive wire connecting a normal reservoir and a short superconductor-normal metal-superconductor junction, at arbitrary applied voltages and temperatures. The cumulant-generating function oscillates with the phase difference ϕ across the junction and approaches the normal-state value at $\phi = \pi$. At $T = 0$ and at applied voltage much smaller than the proximity gap Δ_ϕ , the current noise P_I doubles and the third current cumulant C_3 is 4 times larger compared to the normal state; at $eV \gg \Delta_\phi$ they acquire large excess components. At the gap edge, $eV = \Delta_\phi$, the differential shot noise dP_I/dV exhibits sharp peak, while the differential Fano factor dP_I/dI turns to zero along with the differential resistance, which reflects the transmission resonance associated with the singularity of the density of states. At nonzero temperature, C_3 shows a non-monotonous voltage dependence with a dip near $eV = \Delta_\phi$; the zero-bias slope of $C_3(V)$ is much larger (up to 5 times) than at the zero temperature.

During last few years the statistics of quantum and thermal fluctuations of the electric current in mesoscopic systems has been attracted a rapidly growing attention. It was recognized that measuring the fluctuation properties of mesoscopic conductors provide unique and important information about correlations and statistics of charge carriers, the information that is not accessible through conventional conductance measurements. An adequate and powerful theoretical approach to the fluctuations was built on the concept of full counting statistics (FCS), i.e., the statistics of the number of particles transferred through the conductor. The concept of FCS, which appeared first in quantum optics, was extended to normal electron systems [1] and then successfully applied to superconducting structures [2].

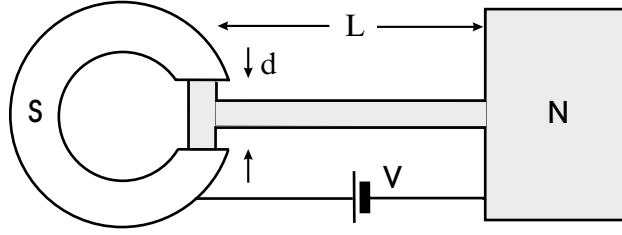


Fig. 1. A model of Andreev interferometer. A diffusive wire of the length L connects a normal reservoir (N) and short SNS junction of the length d ; magnetic flux Φ threads a superconducting loop (S) of the interferometer.

The basic problem of the FCS is to calculate a probability $P_{t_0}(N)$ for N particles to pass a system during an observation time t_0 . Equivalently, one can find a cumulant generating function (CGF) $S(\chi)$,

$$\exp[-S(\chi)] = \sum_N P_{t_0}(N) \exp(iN\chi), \quad (1)$$

which determines the current correlation functions as follows:

$$C_n \equiv \frac{1}{e^n} \int_0^{t_0} dt_1 \dots \int_0^{t_0} dt_n \langle \langle \hat{I}(t_1) \dots \hat{I}(t_n) \rangle \rangle = -(\partial/i\partial\chi)^n S(\chi)|_{\chi=0}, \quad (2)$$

where $\langle \langle \dots \rangle \rangle$ denotes the irreducible part (cumulant) of a correlation function. The first two cumulants, $C_1 = \bar{N} \equiv \sum_N N P_{t_0}(N)$ and $C_2 = \overline{(N - \bar{N})^2}$, correspond to the average current $I = (e/t_0)C_1$ and noise power $P_I = (2e^2/t_0)C_2$. Intense studies of the current noise have led to a number of interesting results concerning statistical correlations in the current transport (for a review, see Ref. [3]), and the effective charge q_{eff} transferred during an elementary transport event. The third cumulant $C_3 = \overline{(N - \bar{N})^3}$ has recently attracted a special interest as the lowest-order correlation function which is not disguised by equilibrium fluctuations [4]. First measurements of $C_3(V)$ in the tunnel junction [5] have revealed a high sensitivity of this cumulant to an electromagnetic environment [6].

In normal metal (N)/superconducting (S) hybrid structures, the basic mechanism of charge transport at subgap energies, $E < \Delta$, is due to Andreev reflection of quasiparticles at the NS boundary [7], i.e., conversion of electrons incident from the normal side of the junction to retroreflected holes, accompanied by escape of Cooper pairs into the superconductor. During an elementary Andreev reflection event, the effective charge transferred through the NS interface is twice the electron charge, $q_{eff} = 2e$. This charge doubling strongly affects the current statistics in the NS junctions. For example, it leads to a factor of two increase in the magnitude of a zero-bias shot noise in the NS junctions as compared to that in normal ones [2, 8]. At finite biases, the effective charge becomes dependent on the applied voltage [9, 10], due to variations of the size of the proximity region near the NS boundary, where the quantum coherence holds between the electrons and retroreflected holes.

In the Andreev interferometers (see Fig. 1), the phase relations between the electron and hole wavefunctions in the normal wire can be controlled by the magnetic flux enclosed by a superconducting loop, which results in the periodic dependence of transport characteristics of the interferometer on the superconducting phase difference ϕ across the SNS junction. Initially, the oscillations of the conductance were investigated both experimentally (see a review in Ref. [11]) and theoretically [12], and, more recently, the oscillations in the current noise were reported [10].

Motivated by the growing interest in high-order correlation functions, we develop in the present Paper a systematic approach to full statistics of charge transport in Andreev interferometers. We adopt several simplifying assumptions, which enables us to present an analytical solution for the CGF and, without a loss of generality, to clearly demonstrate essential features of coherent effects in the current statistics in NS structures. Our approach is based on the extended Keldysh-Green technique [13, 14], in which the CGF is determined by the equation

$$(-ie/t_0)\partial S/\partial\chi = I(\chi), \quad I(\chi) = \frac{1}{8e} \int dE \text{Tr} \check{\tau}_K \check{I}, \quad \check{\tau}_K = \sigma_z \tau_x. \quad (3)$$

The Pauli matrices σ (τ) operate in the Nambu (Keldysh) space. The counting current $I(\chi)$ is to be found from the quantum kinetic equations [15] for the 4×4 matrix Keldysh-Green function \check{G} in the mesoscopic normal region of the interferometer confined between the reservoirs,

$$\sigma_N [\sigma_z E, \check{G}] = i\hbar \mathcal{D} \partial \check{I}, \quad \check{I} = \sigma_N \check{G} \partial \check{G}, \quad \check{G}^2 = \check{1}, \quad (4)$$

where \mathcal{D} is the diffusion coefficient, ∂ denotes spatial derivative, and σ_N is the normal conductivity per unit length. The counting field χ is introduced via a modified boundary condition involving the gauge transformation of the local-equilibrium function \check{G}_R , e.g., in the right (R) normal reservoir,

$$\check{G}_R(\chi) = \exp(i\chi \check{\tau}_K/2) \check{G}_R \exp(-i\chi \check{\tau}_K/2). \quad (5)$$

A brief overview of this technique in the particular case of normal structures is given in the Appendix.

For a multi-terminal structure of Fig. 1, the solution of Eq. (4) has to be found separately in each arm of the interferometer, taking into account the matching condition following from the Kirchhoff's rule for partial counting currents at the node [16]. The problem simplifies if the junction length d is much smaller than the length L of the interferometer wire (or, more precisely, in the case where the wire resistance dominates the net interferometer resistance). In this case, the wire weakly affects the spectrum of the junction [17], which thus can be considered as an effective left (L) reservoir. Correspondingly, the function \check{G}_L which imposes the boundary condition to Eq. (4) at the junction node, is to be constructed from the Green and distribution functions taken at the middle of a closed equilibrium SNS junction.

Furthermore, if d is much smaller than the coherence length $\xi_0 = \sqrt{\hbar D/\Delta}$, these Green functions take the BCS form, with the phase-dependent proximity gap $\Delta_\phi = \Delta|\cos(\phi/2)|$ [18]. This results in the BCS-like singularity at the gap edge in the density of states (DOS) of the normal wire and suppression of the DOS at $E < \Delta_\phi$. Within such model, the problem of current statistics in the Andreev interferometer reduces to the calculation of the CGF for an NS junction with the effective order parameter Δ_ϕ in the superconducting reservoir.

Proceeding with this calculation, we encounter a common technical difficulty, namely, the violation of the standard triangle form of \check{G} in the Keldysh space which results from the gauge transformation in Eq. (5). In such a situation, Eq. (4) cannot be decomposed into the Usadel equation for the Green's functions and the kinetic equations for the distribution functions, and therefore the well developed methods for solving Keldysh-Green's equations quite cannot be applied. This is the reason why the FCS problem in the NS structures requires generally a numerical analysis of the whole 4×4 matrix boundary problem; such an analysis has been carried out so far only in the limit of small characteristic energies $\{eV, T\} \ll \Delta$ [9, 10].

In some particular cases, however, the analytical solution to this problem can be attained by the methods of the generalized circuit theory [19, 20]. Within this approach, the CGF for a mesoscopic connector between two reservoirs is expressed in terms of the distribution $\rho(T)$ of the transparencies of the conduction channels,

$$S(\chi) = \frac{gt_0}{4e^2} \int dE \int_0^1 dT \rho(T) \text{Tr} \ln \check{W}(E, T, \chi), \quad (6)$$

$$\check{W} = 1 + (T/4)(\{\check{G}_L, \check{G}_R(\chi)\} - 2), \quad (7)$$

where g is the connector conductivity. Eq. (6) generally applies to the normally conducting structures with arbitrary $\rho(T)$. It was also applied to the superconducting tunnel junctions [21] and point contacts [20, 22] with a singular transparency distribution localized at the junction transparency. In general NS structures, the statistics of conducting modes, in contrast to their behavior in normal structures [23, 24], do not reduce to statistics of transparencies - due to dephasing between the electron and hole wavefunctions described by the left-hand side (lhs) of Eq. (4) - but requires the knowledge of full scattering matrices. However, if the characteristic energies are much smaller than the Thouless energy, $\{eV, T\} \ll E_{Th} = \hbar D/L^2$, the dephasing term in Eq. (4) can be neglected, and the transparency statistics for a normal wire [23] can be applied to the NS structure. In long junctions, $L \gg \xi_0$, where the Thouless energy is small, $E_{Th} \ll \Delta$, the quasiparticle spectrum is structureless at small energies, $E \ll E_{Th}$, which results in linear voltage dependence of the CGF and, correspondingly, of all cumulants at $eV \ll E_{Th}$ [14]. In the opposite limit, $eV \gg E_{Th}$, the CGF for a long junction can be found within the so-called "incoherent" approximation [25], by neglecting the contribution of

the coherent proximity region. The calculations in Refs. [14] and [25] lead to the conclusion that the FCS exhibits the reentrance effect: In both limits, $eV \ll E_{Th}$ and $eV \gg E_{Th}$, it is described by the same expression for $S(\chi)$. An interesting situation occurs in NS junctions with opaque interfaces dominating the net resistance [26]. In this case, the crossover between the coherent and incoherent transport regimes occurs at very small voltage of the order of the inverse dwell time of quasiparticles confined between the interface barriers.

In our work we focus on short NS junctions with the length smaller than ξ_0 and, correspondingly, with large Thouless energy, $E_{Th} \gg \Delta_\phi$. In such situation, the energy region of negligibly small dephasing, $E \ll E_{Th}$, overlaps with the region $E \gg \Delta_\phi$, in which the NS junction behaves as the normal system. This enables us to apply Eq. (6) and the transparency statistics for diffusive normal conductor at arbitrary voltages and temperatures, and obtain the analytical solution of the FCS problem in the full range of V and T .

The calculation of the integrand in Eq. (6) is performed as follows. The Keldysh-Green function $G_R(\chi)$ in the normal reservoir is traceless in the Keldysh space and therefore it can be expanded over the Pauli matrices τ as

$$\check{G}_R(\chi) = \boldsymbol{\tau}(\mathbf{g}_1 + \sigma_z \mathbf{g}_z), \quad \mathbf{g}_1 \mathbf{g}_z = 0, \quad \mathbf{g}_1^2 + \mathbf{g}_z^2 = 1, \quad \boldsymbol{\tau} = (\tau_x, \tau_y, \tau_z), \quad (8)$$

where the vectors $\mathbf{g}_{1,z}(\chi)$ are expressed through the local-equilibrium distribution functions in the voltage biased electrode. In the subgap energy region, $E < \Delta_\phi$, the function \check{G}_L at the junction node is the unity matrix in the Keldysh space proportional to the Nambu matrix Green's function \hat{g} ,

$$\check{G}_L = \hat{g} = \sigma_y \exp(\sigma_x \theta_\phi), \quad \hat{g}^2 = 1, \quad \theta_\phi = \operatorname{arctanh}(E/\Delta_\phi). \quad (9)$$

Then the calculation of the trace in the Nambu space in Eq. (7) is reduced to the summation over the eigenvalues $\sigma = \pm 1$ of the matrix \hat{g} ,

$$\operatorname{Tr} \ln \check{W} = \sum_\sigma \operatorname{Tr}_\tau \ln \check{W}_\sigma, \quad \check{W}_\sigma = a + \boldsymbol{\tau} \mathbf{b}, \quad (10)$$

$$a = 1 - T/2, \quad \mathbf{b} = (T/2)(\sigma \mathbf{g}_1 - i \mathbf{g}_z \sinh \theta_\phi). \quad (11)$$

Noticing that any 2×2 matrix can be presented in exponential form as

$$\check{W}_\sigma = \exp(\ln w + \varphi \check{p}), \quad (12)$$

$$w^2 = a^2 - \mathbf{b}^2, \quad \cosh \varphi = a/w, \quad \check{p} = \boldsymbol{\tau} \mathbf{b}/w \sinh \varphi, \quad \operatorname{Tr} \check{p} = 0, \quad (13)$$

where w is independent of σ due to orthogonality of the vectors \mathbf{g}_1 and \mathbf{g}_z , one easily obtains $\operatorname{Tr}_\tau \ln \check{W}_\sigma = \ln w^2$ and $\operatorname{Tr} \ln \check{W} = 2 \ln w^2$. At $E > \Delta_\phi$, the function G_L is traceless in the Keldysh space,

$$\check{G}_L = \hat{g}(\boldsymbol{\tau} \mathbf{g}_L), \quad \hat{g} = \sigma_z \exp(\sigma_x \theta_\phi), \quad \theta_\phi = \operatorname{arctanh}(\Delta_\phi/E), \quad (14)$$

where the vector \mathbf{g}_L is constructed from the equilibrium distribution function at zero potential. In this case, the 4×4 matrix \check{W} has the form $\check{W} = a + \boldsymbol{\sigma} \mathbf{b}$, where a and \mathbf{b}^2 are scalars,

$$a = 1 - (T/2)(1 - \mathbf{g}_L \mathbf{g}_z \cosh \theta_\phi), \quad (15)$$

$$\mathbf{b}^2 = (T/2)^2 [(\mathbf{g}_L \mathbf{g}_1)^2 - (\mathbf{g}_L \times \mathbf{g}_z)^2 \sinh^2 \theta_\phi], \quad (16)$$

therefore it can also be transformed to the exponent form similar to Eqs. (12) and (13), with the traceless matrix $\check{p} = \boldsymbol{\sigma} \mathbf{b} / w \sinh \varphi$. Following this line, we obtain $\text{Tr} \ln \check{W} = 2 \ln w^2$, and then, integrating over T in Eq. (6), we arrive at the final expressions for the CGF

$$S(\chi) = \frac{gt_0}{4e^2} \int_0^\infty dE S(E, \chi), \quad S(E, \chi) = \begin{cases} 2\theta^2, & E < \Delta_\phi, \\ \theta_+^2 + \theta_-^2, & E > \Delta_\phi, \end{cases} \quad (17)$$

where the quantities θ and θ_\pm are given by explicit relations,

$$Z(0) \cosh^2 \theta = Z(2\chi) \cosh^2 \theta_\phi, \quad (18)$$

$$Z(0) \cosh \theta_\pm = [Z(\chi) + \cos \chi - 1] \cosh \theta_\phi \pm \tanh \frac{\epsilon}{2} [\sinh p - \sinh(p - i\chi) - i \sin \chi] \left(1 - \frac{\cosh \epsilon + 1}{\cosh p - 1} \sinh^2 \theta_\phi\right)^{1/2}, \quad (19)$$

$$\theta_\phi = \text{arctanh} \left[(\Delta_\phi / E)^{\text{sgn}(E - \Delta_\phi)} \right], \quad (20)$$

$$Z(\chi) = \cosh(\epsilon) + \cosh(p - i\chi), \quad \epsilon = E/T, \quad p = eV/T. \quad (21)$$

By using Eqs. (2) and (17)-(21), one can obtain analytical expressions for all cumulants. At zero temperature, the calculation essentially simplifies. Indeed, at $T \rightarrow 0$ and $E > eV$, the dominating terms in Eqs. (18)-(21) are proportional to $\exp(\epsilon)$, and therefore θ and θ_\pm are equal to θ_ϕ . This implies that the CGF is independent of the counting field at these energies, and all cumulants turn to zero. At $E < eV$, the terms with $\exp(p - in\chi)$ dominate, and we arrive at simple relations,

$$\cosh \theta = e^{-i\chi} \cosh \theta_\phi, \quad \cosh \theta_\pm = e^{-i\chi} \cosh \theta_\phi \pm (e^{-i\chi} - 1). \quad (22)$$

At subgap voltage, $eV < \Delta_\phi$, when the charge transport at $T = 0$ is only due to the Andreev reflection, the current I , the shot noise power P_I , and the third cumulant C_3 read

$$I = I_\Delta q(z), \quad q(z) = \int_0^z \frac{dx}{x} \text{arctanh} x, \quad P_I = 2e [I - I_\Delta f(z^{-1})], \quad (23)$$

$$C_3 = \bar{N} - \frac{\bar{N}_\Delta}{2z^2} [(5z^2 - 3)f(z^{-1}) + z], \quad I_\Delta = \frac{g\Delta_\phi}{e}, \quad \bar{N}_\Delta = \frac{I_\Delta t_0}{e}, \quad (24)$$

$$f(z) = (1/2)[z - (z^2 - 1)\text{arctanh} z^{-1}], \quad z = eV/\Delta_\phi. \quad (25)$$

At small voltages, $eV \ll \Delta_\phi$, the magnitude of the shot noise doubles, $P_I = (4/3)eI$, and $C_3 = 4\bar{N}/15$ is four times larger compared to the normal case [8, 2, 27, 1]. When the voltage increases and exceeds the gap edge, $eV > \Delta_\phi$, the normal electron processes at the energies $E > \Delta_\phi$ begin to contribute

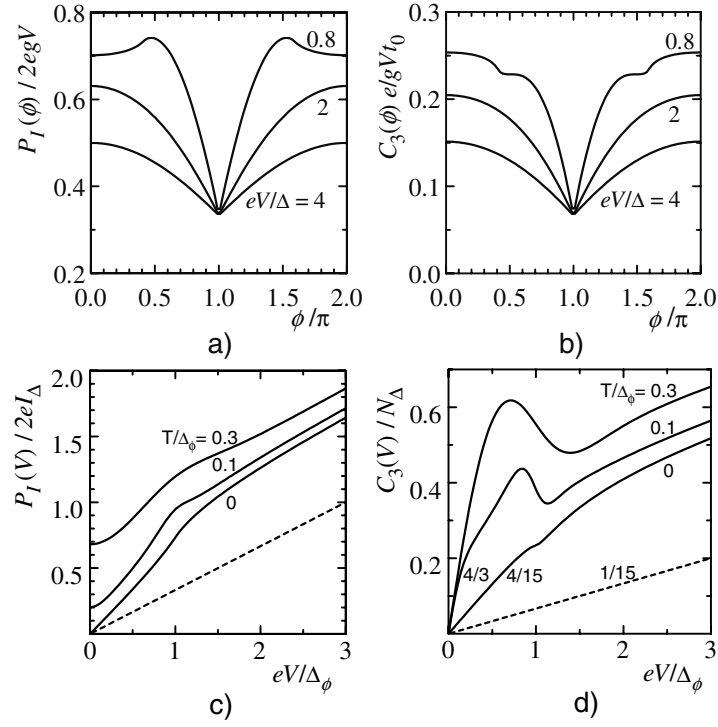


Fig. 2. Shot noise power and third cumulant vs superconducting phase (a, b) at different voltages and $T = 0$, and vs voltage at different temperatures (c, d). Dashed lines denote voltage dependencies in the normal state at $T = 0$. In the panel (d), zero-bias slopes of the normalized $C_3(V)$ are indicated.

to the charge transport, providing the normal-state voltage dependencies of the cumulants at $eV \gg \Delta_\phi$. At large voltage, the Andreev reflected particles produce voltage-independent excess components of the cumulants,

$$I = I_N - I_\Delta f(z) + I^{\text{ex}}, \quad P_I = 2eI_\Delta(z^2 - 1)f(z) + P_I^{\text{ex}}, \quad I_N = gV, \quad (26)$$

$$C_3 = \frac{\bar{N}_\Delta}{2}(z + 1) \left\{ (z - 1) [8z/3 - (8z^2 - 3)f(z)] - 1/3 \right\} + C_3^{\text{ex}}, \quad (27)$$

$$I^{\text{ex}} = (I_\Delta/2)(\pi^2/4 - 1), \quad P_I^{\text{ex}} = 2eI^{\text{ex}}, \quad C_3^{\text{ex}} = (\bar{N}_\Delta/2)(\pi^2/4 - 4/3). \quad (28)$$

At nonzero temperatures, $T \neq 0$, we calculate the cumulant spectral densities $I(E)$, $P(E)$ and $C(E)$ defined as

$$I = I_\Delta \int_0^\infty dE I(E), \quad P_I = 2eI_\Delta \int_0^\infty dE P(E), \quad C_3 = \bar{N}_\Delta \int_0^\infty dE C(E). \quad (29)$$

Here $I(E) = f_1 \sinh p / Z(0)$, and the functions $P(E)$ and $C(E)$ at $E < \Delta_\phi$ read

$$P(E) = \frac{2}{Z^2(0)} [2Qf_1 + (1 - f_2) \sinh^2 p], \quad Q = 1 + \cosh \epsilon \cosh p, \quad (30)$$

$$C(E) = \frac{\sinh p}{Z^3(0)} \{4f_1 \sinh^2 \epsilon + (2f_2 + 3f_3) \sinh^2 p + 2Q [3(1 - f_2) - 2f_1]\}, \quad (31)$$

whereas at $E > \Delta_\phi$ they are given by equations,

$$P(E) = \frac{2}{Z^2(0)} \left[Q \left(1 + 2f_1 - 2f_2 \frac{\cosh p - 1}{\cosh \epsilon + 1} \right) + \sinh^2 p - Z(0) \right], \quad (32)$$

$$C(E) = \frac{\sinh p}{Z^3(0)(1 + \cosh \epsilon)} \left\{ 4f_1(1 + \cosh \epsilon)(Q + \sinh^2 \epsilon) \right. \\ \left. + 3[Z(0)(1 - 2f_3) + Q(4(1 - f_2 + f_3 \cosh \epsilon) + 3 \cosh \epsilon - 2f_3)] \right. \\ \left. + \sinh^2 \epsilon(2f_3 - \cosh \epsilon + (3 - 5 \cosh p)f_2) \right\} + f_2(5 \cosh \epsilon - 1) \sinh^2 p, \quad (33)$$

In Eqs. (30)-(33), the functions

$$f_1 = \theta_\phi \coth \theta_\phi, \quad f_2 = (f_1 - 1) / \sinh^2 \theta_\phi, \quad f_3 = (f_2 - 1/3) / \sinh^2 \theta_\phi. \quad (34)$$

describe energy variation of quasiparticle spectrum which is most essential in the vicinity of the gap edge Δ_ϕ .

As shown in Fig. 2,(a,b), the cumulants oscillate with the phase and exhibit deep minima at $\phi \bmod 2\pi = \pi$, when the gap closes and the cumulants approach their normal values. When the proximity gap Δ_ϕ approaches eV , $P_I(\phi)$ exhibits a peak, while $C_3(\phi)$ shows a step-like structure. Shown in Fig. 2,(c,d) are voltage dependence of the cumulants for different temperatures plotted as functions of variables that provide the universality of the curves for any ϕ . As the temperature increases, the current noise approaches finite value at $eV = 0$ due to thermal fluctuations, and exhibits quadratic dependence on the applied voltage at $eV \ll T$. Within the intermediate voltage region, $T < eV < \Delta_\phi$, $P_I(V)$ becomes linear with doubled slope produced by the Andreev reflected particles, and at $eV > \Delta_\phi$, the slope turns to its normal-metal value. A considerable excess noise at large voltages is contributed by both the thermal fluctuations and Andreev reflection. A more interesting behavior is discovered for the third cumulant. At nonzero temperature, the zero-bias slope of the normalized $C_3(V)$ is much larger than at zero temperature (up to the factor 5 which is similar to the normal structures [4]), approaching the value 4/3. At larger voltages, $T < eV < \Delta_\phi$, the slope of $C_3(V)$ returns to the value 4/15 found for $T = 0$. At $eV \sim \Delta_\phi$, the curve $C_3(V)$ shows \mathcal{N} -like feature, and finally, at $eV > \Delta_\phi$, it approaches a straight line with the (normal-state) slope 1/15. Such a behavior indicates that C_3 acquires anomalously large thermal component at voltage $eV \sim \Delta_\phi$, which, however, rapidly decreases at $eV > \Delta_\phi$ and/or $T > \Delta_\phi$ towards the normal metal level.

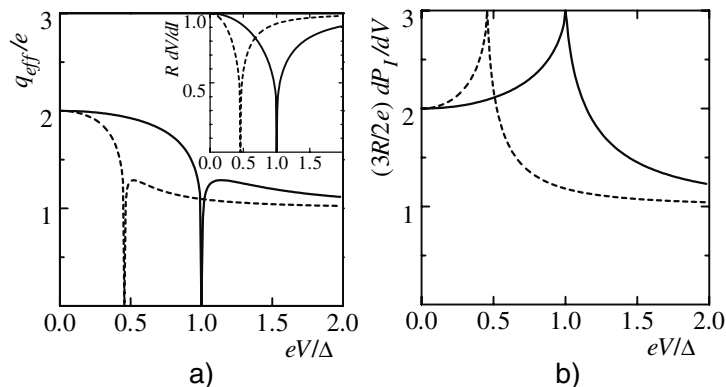


Fig. 3. Effective transferred charge (a), differential noise (b), and differential resistance (inset) vs voltage at $\phi = 0$ (solid lines) and $\phi = 0.7\pi$ (dashed lines), $T = 0$.

The singularity in the DOS at the proximity gap edge produces interesting features of the differential transport characteristics of the interferometer shown in Fig. 3. First, we note that the differential resistance $R_d = dV/dI$ turns to zero at $eV = \Delta_\phi$ (see inset in Fig. 3,a), which is explained by full transmission of the NS junction at the resonant energy Δ_ϕ . Correspondingly, the differential Fano factor $dP_I/dI = R_d(dP_I/dV)$, which is commonly interpreted as effective transferred charge, $q_{\text{eff}} = (3/2)dP_I/dI$, also turns to zero, $q_{\text{eff}} = 0e$, while the differential noise normalized in a similar way, $(3R/2) dP_I/dV$, shows a large peak of the height $3e$. Thus we conclude that none of these quantities can be unambiguously associated with the physical elementary transferred charge, but they rather reflect the energy variation of the transmission characteristics. Similar effects have been predicted for an NS structure with opaque interfaces [26] where a considerable enhancement of dP_I/dV and suppression of dP_I/dI occur, however, at small applied voltage determined by large dwell time of quasiparticles.

It is instructive to compare our analytical results for short-arm interferometers with that obtained numerically for long NS junctions with a small minigap $E_g \sim E_{Th} \ll \Delta$. The results are qualitatively similar: in long junctions, q_{eff} is equal to $2e$ at $eV \ll E_g$ and has a minimum at $eV \approx E_g(\phi)$, which moves towards small voltage when at $\phi \rightarrow \pi$ [10]; the differential noise is also non-monotonous and approaches maximum at $eV \approx 5E_{Th}$ [9]. After this comparison we see that the proximity gap Δ_ϕ in short junctions plays the role of the minigap E_g in long junctions and determines the feature in the effective charge, though this feature at $eV \sim E_g$ in long junctions is much less pronounced. However, as noted above, a qualitative difference of long junctions is the existence of an intermediate incoherent voltage region $E_g \ll eV \ll \Delta$, where both the effective charge and the normalized differential noise have the value $2e$, and their crossover to e occurs only at $eV \geq \Delta$ [28].

In conclusion, we have studied the full counting statistics of a normal diffusive wire confined between the normal electrode and SNS junction controlled by the magnetic flux through a superconducting loop (Andreev interferometer). Assuming the size of the mesoscopic structure to be much smaller than the coherence length, we calculated analytically the cumulant-generating function for arbitrary applied voltage and temperature. We studied in detail the second (the current noise) and the third cumulants. Both quantities oscillate with the phase difference across the junction and show non-monotonous voltage dependence in the vicinity of the proximity gap edge, which reflects resonant transmission of the structure at the singularity of the density of states.

This work was supported by the U.S. Department of Energy, Office of Science under contract No. W-31-109-ENG-38.

In this Appendix we outline, for reference purposes, the procedure and summarize the results of calculation of the CGF for a diffusive connector between normal reservoirs, by using the extended Keldysh-Green's technique. For generality, we consider a diffusive wire interrupted by tunnel barriers, which enables us to present several original results and to examine various limiting situations.

In normal systems, the matrices \check{G} and \check{I} are traceless in the Keldysh space and therefore they can be expressed through 3-vectors with the components diagonal in the Nambu space, $\check{G} = \mathbf{g}\boldsymbol{\tau}$, $\check{I} = \mathbf{I}\boldsymbol{\tau}$, where $\boldsymbol{\tau}$ is the vector of the matrices τ , and $\mathbf{g}^2 = 1$. Since the lhs of Eq. (4) turns to zero in normal systems, the formal solution of Eq. (4) for the matrix current density \check{I}_N in each segment of the wire can be easily obtained,

$$\begin{aligned}\check{I}_N &= g_N \ln \check{G}_1 \check{G}_2 = g_N \ln[\mathbf{g}_1 \mathbf{g}_2 + i\boldsymbol{\tau}(\mathbf{g}_1 \times \mathbf{g}_2)] = \boldsymbol{\tau} \mathbf{I}_N, \\ \mathbf{I}_N &= i g_N \mathbf{p} \phi_N, \quad \phi_N = \arccos \mathbf{g}_1 \mathbf{g}_2,\end{aligned}\quad (35)$$

where g_N is the conductivity of the wire segment, $\check{G}_{1,2}$ are the Green's functions at the left and right segment edges, respectively, ϕ_N is the angle between the (complex) unit vectors \mathbf{g}_1 and \mathbf{g}_2 , and $\mathbf{p} = (\mathbf{g}_L \times \mathbf{g}_R) / \sin \phi_N$ is the unit vector perpendicular to \mathbf{g}_1 and \mathbf{g}_2 .

The matrix current \check{I}_B through the tunnel barrier can be expressed in terms of Green functions \check{G}_- and \check{G}_+ at the left and right sides of the barrier by using the boundary condition [29],

$$\begin{aligned}\check{I}_{B-} = \check{I}_{B+} &= \frac{g_B}{2} [\check{G}_-, \check{G}_+] = \boldsymbol{\tau} \mathbf{I}_B, \\ \mathbf{I}_B &= i g_B \mathbf{p} \sin \phi_B, \quad \phi_B = \arccos \mathbf{g}_- \mathbf{g}_+, \end{aligned}\quad (36)$$

where $\mathbf{p} = (\mathbf{g}_- \times \mathbf{g}_+) / \sin \phi_B$ and g_B is the barrier conductance.

The conservation of the matrix current along the connector, $\check{I} = \text{const}$, following from Eq. (4) and the boundary condition in Eq. (36), results in conservation of the vector current, $\mathbf{I} = \mathbf{I}_N = \mathbf{I}_B = \text{const}$. This implies that for all elements of the connector, the unit vectors \mathbf{p} coincide, therefore the

Green's vectors \mathbf{g} lie in plane, and the vector \mathbf{p} can be constructed from known Green's vectors \mathbf{g}_L and \mathbf{g}_R in the reservoirs, $\mathbf{p} = (\mathbf{g}_L \times \mathbf{g}_R) / \sin \phi$, where ϕ is the angle between \mathbf{g}_L and \mathbf{g}_R ,

$$\begin{aligned} \phi &= \arccos[1 + P_{-+}(e^{i\chi} - 1) + P_{+-}(e^{-i\chi} - 1)], \\ P_{\sigma\sigma'} &= n_\sigma(1 - n_{\sigma'}), \quad n_- = n_F(E), \quad n_+ = n_F(E + eV). \end{aligned} \quad (37)$$

From the current conservation, we also conclude that all elements are characterized by a single variable η ,

$$g_B \sin \phi_B = g_N \phi_N = g\eta = \text{const}, \quad (38)$$

where the normalization constant g is chosen to be equal to the conductance of the whole connector. Thus, the vector current is given by equation,

$$\mathbf{I} = \frac{ig\eta}{\sin \phi} (\mathbf{g}_L \times \mathbf{g}_R). \quad (39)$$

The planar rotation of the Green's vector results in the additivity of the angles between all consecutive vectors \mathbf{g} , therefore the sum of these angles is equal to ϕ ,

$$\sum_{\text{wires}} \phi_N + \sum_{\text{barriers}} \phi_B = \phi = \arccos(\mathbf{g}_L \mathbf{g}_R), \quad (40)$$

which leads to the equation for the parameter $\eta(\phi)$,

$$\gamma_N \eta + \sum_k \arcsin(\gamma_k \eta) = \phi, \quad \gamma_N = R_N/R, \quad \gamma_k = R_k/R, \quad \gamma_N + \sum_k \gamma_k = 1, \quad (41)$$

where R_N is the net resistance of all wires, R_k is the resistance of the k -th barrier, and $R = g^{-1}$.

By using the definitions in Eq. (3), we obtain the counting electric current $I(\chi)$ and the CGF,

$$I(\chi) = \frac{1}{2e} \int_0^\infty dE \text{Tr} \sigma_z \mathbf{I}_x = \frac{ig}{2e} \int_0^\infty dE \text{Tr} \frac{\sigma_z \eta}{\sin \phi} (\mathbf{g}_L \times \mathbf{g}_R)_x, \quad (42)$$

$$S(\chi) = \frac{gt_0}{4e^2} \int dE \text{Tr} \left[r_N \eta^2 / 2 + \sum_k \left(1 - \sqrt{1 - r_k^2 \eta^2} \right) / r_k \right], \quad (43)$$

We note that the statistics is insensitive to the position of the barriers and depends only on the barrier resistances and the net resistance of the diffusive part of the connector. In the absence of barriers, $r_k \rightarrow 0$, the CGF reads

$$\begin{aligned} S(\chi) &= \frac{gt_0}{4e^2} \int dE \phi^2 \\ &= \frac{gt_0}{4e^2} \int dE \arccos^2 \left[1 + P_{-+}(e^{i\chi} - 1) + P_{+-}(e^{-i\chi} - 1) \right]. \end{aligned} \quad (44)$$

At zero temperature, the integration over energy in Eq. (43) can be explicitly performed,

$$S(\chi) = \frac{\bar{N}}{2} \left[r_N \eta^2 / 2 + \sum_k \left(1 - \sqrt{1 - r_k^2 \eta^2} \right) / r_k \right], \quad (45)$$

where $\bar{N} = gVt_0/e$. From Eq. (45) we find the Fano factor F in the shot noise power $P_I = eFI$,

$$F = (2/3)(1 + 2B_3), \quad B_n = \sum_k r_k^n, \quad (46)$$

which varies between the Poissonian value $F = 2$ for the tunnel connector and $1/3$ -suppressed value, $F = 2/3$, in the absence of barriers. The third cumulant C_3 varies between \bar{N} for Poissonian statistics in the single barrier case and $\bar{N}/15$ for a diffusive conductor,

$$C_3(V, 0) = (\bar{N}/15) [1 + 10B_3(1 + 4B_3) - 36B_5]. \quad (47)$$

It is interesting to note that Eq. (41) can be easily transformed into equation for the transparency distribution $\rho(\mathbb{T})$, by making use of the relation of the generalized circuit theory between the counting current $I(\chi)$ and the matrix current \check{I} following from Eqs. (6) and (3),

$$I(\chi) = \frac{1}{4e} \int_0^\infty dE \text{Tr} \tau_x \sigma_z \check{I}, \quad \check{I} = \frac{g}{2} \int_0^1 d\mathbb{T} \rho(\mathbb{T}) \mathbb{T} [\check{G}_L, \check{G}_R(\chi)] \check{W}^{-1}. \quad (48)$$

Rewriting these equations in the vector representation, comparing them with Eq. (42), and introducing the variable $z = (1 - \mathbf{g}_L \mathbf{g}_R)/2$, we obtain the equation for $\rho(\mathbb{T})$,

$$\int_0^1 \frac{\mathbb{T} d\mathbb{T} \rho(\mathbb{T})}{1 - z\mathbb{T}} = \frac{\eta}{2\sqrt{z(1-z)}}, \quad (49)$$

where η obeys Eq. (41) with the function $\phi(z) = 2 \arcsin \sqrt{z}$ in the right-hand side (rhs). The solution of Eq. (49) has the form $\rho(\mathbb{T}) = \text{Re} \eta / 2\pi \mathbb{T} \sqrt{1 - \mathbb{T}}$, where $\eta(\mathbb{T})$ is the solution of Eq. (41) with the function $\pi + 2i \text{arccosh}(1/\sqrt{\mathbb{T}})$ in the rhs [24].

In some limiting cases, one can obtain an analytical solution of Eq. (41). In particular, if the number M of the barriers is large, $M \gg 1$, then the resistance of each barrier is small compared to the net resistance, $R_k \ll R$. In this case, the approximate solution of Eq. (41) is $\eta = \phi$, and the CGF coincides with that for diffusive wire, Eq. (44). In the tunnel limit, when the resistance of each barrier much exceeds the net resistance of diffusive segments, $R_k \gg R_N$, the first term in Eq. (41) can be neglected. Then an analytical expression for the parameter η and the CGF at arbitrary M can be obtained in the case of equivalent barriers, $r_k = 1/M$,

$$\eta = M \sin \frac{\phi}{M}, \quad S(\chi) = \bar{N} M^2 \sin^2 \frac{\arccos e^{i\chi/2}}{M}, \quad (50)$$

when the Fano factor is given by $F = (2/3)(1 + 2/M^2)$. In the limit of large number of the barriers, $M \gg 1$, we return to the diffusive statistics, while for single-barrier structure, $M = 1$, we obtain Poissonian statistics, $S(\chi) = \bar{N}(e^{i\chi} - 1)$.

At arbitrary temperature, the cumulants can be found analytically by asymptotic expansion in Eqs. (41), (43) over small η and χ . In particular, the noise power,

$$P_I(V, T) = \frac{4T}{3R} \left[(1 + 2B_3) \frac{p}{2} \coth \frac{p}{2} + 2(1 - B_3) \right], \quad (51)$$

exhibits crossover between the shot noise at $T \ll eV$ and the Johnson thermal noise $P_T = 4T/R$ at large temperature, $T \gg eV$. The voltage dependence of the third cumulant,

$$C_3(V, T) = C_3(V, 0) + \frac{2}{5} \bar{N} (1 - 10B_3^2 + 9B_5) \frac{\sinh p - p}{p \sinh^2(p/2)}, \quad (52)$$

is linear in both limits and approaches $(\bar{N}/3)(1 + 2B_3)$ at high temperatures. In the absence of barriers, $B_n = 0$, Eq. (52) reproduces the result of a modified kinetic theory of fluctuations for a diffusive wire [4].

In order to access FCS in multi-terminal structures, which consist of a set of connectors attached between several normal electrodes and a diffusive island (node) with negligibly small resistance, separate counting fields χ_α and parameters η_α are to be introduced in each arm [16],

$$\mathbf{I}_\alpha = i\xi_\alpha(\mathbf{g}_\alpha \times \mathbf{g}_c), \quad \xi_\alpha = g_\alpha \eta_\alpha / \sin \phi_\alpha. \quad (53)$$

The quantities η_α obey the equations similar to Eq. (41), with the angles $\phi_\alpha = \arccos(\mathbf{g}_\alpha \mathbf{g}_c)$ in the rhs, where the Green's vector \mathbf{g}_c at the node can be found from the current conservation law, $\sum_\alpha \mathbf{I}_\alpha = 0$,

$$\mathbf{g}_c = \mathbf{G} / \sqrt{\mathbf{G}^2}, \quad \mathbf{G} = \sum_\alpha \xi_\alpha \mathbf{g}_\alpha. \quad (54)$$

According to Eq. (54), the vector \mathbf{g}_c depends on all counting fields χ_α , which reflects cross-correlations between the currents in different connectors. For the system of tunnel connectors, where the quantities ξ_α are equal to the conductances g_α and therefore become independent of χ , the CGF at zero temperature can be explicitly evaluated [21],

$$S\{\chi\} = \frac{Vt_0}{2e} G \sqrt{1 + 4 \sum_\alpha \bar{g}_V \bar{g}_\alpha (e^{i\chi_\alpha} - 1)}, \quad \bar{g}_\alpha = g_\alpha / G, \quad G = \sum_\beta g_\beta, \quad (55)$$

where the index V denotes the voltage biased electrode.

For arbitrary connectors, the cumulants can be found from asymptotic solutions of the equations for η_α and \mathbf{g}_c at small χ_α . For instance, the partial

current through α -th connector is $I_\alpha = Vg_\alpha\bar{g}_V$, and the Fano factors defined as $F_{\alpha\beta} = (2ei/I_\alpha)(\partial I_\alpha\{\chi\}/\partial\chi_\beta)_{\chi=0}$ read

$$F_{\alpha\beta} = \left(2 - \frac{4}{3}\bar{g}_V\right)\delta_{\alpha\beta} - \frac{4}{3}\bar{g}_\beta \left[1 + \bar{g}_V(B_{3\alpha} + B_{3\beta}) - B_{3V}(1 - \bar{g}_V)^2 - \bar{g}_V \sum_{\gamma \neq V} \bar{g}_\gamma B_{3\gamma}\right]. \quad (56)$$

The diagonal elements $F_{\alpha\alpha}$ of the matrix $F_{\alpha\beta}$ have the meaning of the Fano factors for the shot noise in α -th connector and may vary between 2/3 and 2. For large number of the terminals, when the normalized conductances \bar{g}_α become small, they approach Poissonian value $F_{\alpha\alpha} = 2$. The cross-correlators $F_{\alpha\beta}$ ($\alpha \neq \beta$) between the currents in different terminals are negative due to Pauli principle [28]. In a particular case of diffusive connectors ($B_\alpha = 0$), Eq. (56) reproduces the result of Ref. [30] for a so-called star-shaped geometry.

References

1. L.S. Levitov and G.B. Lesovik, JETP Lett. **58**, 230 (1993); H. Lee, L.S. Levitov, and A.Yu. Yakovets, Phys. Rev. B **51**, 4079 (1995); L.S. Levitov, H.W. Lee, and G.B. Lesovik, J. Math. Phys. **37**, 4845 (1996).
2. B.A. Muzykantskii and D.E. Khmel'nitskii, Physica B **203**, 233 (1994).
3. Ya.M. Blanter and M. Büttiker, Phys. Rep. **336**, 1 (2000).
4. K.E. Nagaev, Phys. Rev. B **66**, 075334 (2002); D.B. Gutman and Yu. Gefen, *ibid.* **68**, 035302 (2003).
5. B. Reulet, J. Senzier, and D.E. Prober, cond-mat/0302084, Phys. Rev. Lett. **91**, 196601 (2003).
6. C.W.J. Beenakker, M. Kindermann, and Yu.V. Nazarov, Phys. Rev. Lett. **90**, 176802 (2003).
7. A.F. Andreev, Sov. Phys. JETP **19**, 1228 (1964).
8. V.A. Khlus, Sov. Phys. JETP **66**, 1243 (1987); M.J.M. de Jong and C.W.J. Beenakker, Phys. Rev. B **49**, 16070 (1994).
9. W. Belzig and Yu.V. Nazarov, Phys. Rev. Lett. **87**, 067006 (2001); M.P.V. Steinberg and T.T. Heikkilä, Phys. Rev. B **66**, 144504 (2002).
10. B. Reulet, A.A. Kozhevnikov, D.E. Prober, W. Belzig, and Yu.V. Nazarov, Phys. Rev. Lett. **90**, 066601 (2003).
11. C.J. Lambert and R. Raimondi, J. Phys.: Condens. Matter **10**, 901 (1998).
12. F.W.J. Hekking and Yu.V. Nazarov, Phys. Rev. Lett. **71**, 1625 (1993); H. Nakano and H. Takayanagi, Phys. Rev. B **47**, 7986 (1993).
13. Yu.V. Nazarov, Ann. Phys. (Leipzig) **8**, SI-193 (1999).
14. W. Belzig, in *Quantum Noise in Mesoscopic Physics*, ed. by Yu.V. Nazarov, NATO Science Series **97**, 463 (2003).
15. A.I. Larkin, and Yu.N. Ovchinnikov, Sov. Phys. JETP **41**, 960 (1975); **46**, 155 (1977).
16. Yu.V. Nazarov and D.A. Bagrets, Phys. Rev. Lett. **88**, 196801 (2002).
17. T.T. Heikkilä, J. Särkkä, and F.K. Wilhelm, Phys. Rev. B **66**, 184513 (2002); E.V. Bezuglyi, V.S. Shumeiko, and G. Wendin, *ibid.* **68**, 134506 (2003).
18. I.O. Kulik and A.N. Omelyanchouk, JETP Lett. **21**, 96 (1975).

19. Yu.V. Nazarov, *Superlatt. Microstruct.* **25**, 1221 (1999).
20. W. Belzig and Yu.V. Nazarov, *Phys. Rev. Lett.* **87**, 197006 (2001).
21. J. Börlin, W. Belzig, and C. Bruder, *Phys. Rev. Lett.* **88**, 197001 (2002).
22. J.C. Cuevas and W. Belzig, *Phys. Rev. Lett.* **91**, 187001 (2003); G. Johansson, P. Samuelsson, and Å. Ingeman, *Phys. Rev. Lett.* **91**, 187002 (2003).
23. O.N. Dorokhov, *JETP Lett.* **36**, 318 (1982); *Solid State Comm.* **51**, 381 (1984); P.A. Mello, P. Pereyra, and N. Kumar, *Ann. Phys.* **181**, 290 (1988).
24. Yu.V. Nazarov, *Phys. Rev. Lett.* **73**, 136 (1994); W. Belzig, A. Brataas, Yu.V. Nazarov, and G.E.W. Bauer, *Phys. Rev. B* **62**, 9726 (2000).
25. W. Belzig and P. Samuelsson, *Europhys. Lett.* **64**, 253 (2003).
26. P. Samuelsson, *Phys. Rev. B* **67**, 054508 (2003).
27. K.E. Nagaev, *Phys. Lett. A* **169**, 103 (1992); C.W.J. Beenakker and M. Büttiker, *Phys. Rev. B* **46**, 1889 (1992).
28. K.E. Nagaev and M. Büttiker, *Phys. Rev. B* **63**, 081301 (2001).
29. M.Yu. Kupriyanov and V.F. Lukichev, *Sov. Phys. JETP* **67**, 89 (1988).
30. E.V. Sukhorukov and D. Loss, *Phys. Rev. Lett.* **80**, 4959 (1998); *Phys. Rev. B* **59**, 13054 (1999).

Semiclassical Theory of Higher Cumulants of Noise

K.E. Nagaev

Institute of Radioengineering and Electronics, Russian Academy of Sciences,
Mokhovaya ulica 11, 125009 Moscow, Russia nag@cplire.ru

Summary. The semiclassical Boltzmann–Langevin method is extended to calculations of higher cumulants of current. Its efficiency is demonstrated for mesoscopic diffusive contacts and chaotic cavities. We show that in addition to a dispersion at the inverse RC time characteristic of charge relaxation, higher cumulants of noise have a low-frequency dispersion at the inverse dwell time of electrons in the system.

Higher-order correlations of current became a subject of interest for theorists since early nineties. This work was pioneered by Levitov and Lesovik [1], who discovered that the charge transmitted through a single-channel quantum contact obeys a binomial distribution. Based on their quantum-mechanical formulas, higher cumulants of current were calculated for a variety of multichannel phase-coherent systems [2, 3, 4]. Meanwhile a wide class of these systems, like diffusive conductors and chaotic cavities, allows a semiclassical description of their average transport properties and second cumulant of noise [5, 6]. Hence it is of interest to have a fully semiclassical theory for higher cumulants of noise in these systems too. Very recently, such a theory was developed in a number of papers and here we give a brief overview of it.

The basis for the semiclassical description of kinetics is the existence of two well separated time scales, one of which describes a “slow” classical evolution of the system and the other describes “fast” quantum processes. For example, the collision integral in the Boltzmann equation may be written as local in time because quantum-mechanical scattering is assumed to be fast as compared to the evolution of the distribution function.

The second cumulants of noise are conveniently described by the Boltzmann–Langevin equation [5]

$$\left[\frac{\partial}{\partial t} + \mathbf{v} \frac{\partial}{\partial \mathbf{r}} + e \mathbf{E} \mathbf{v} \frac{\partial}{\partial \varepsilon} \right] \delta f(\mathbf{p}, \mathbf{r}, t) + \delta I = -e \delta \mathbf{E} \mathbf{v} \frac{\partial f}{\partial \varepsilon} + J^{ext}, \quad (1)$$

where δI is the linearized collision integral and J^{ext} is the Langevin source that accounts for the randomness of electron scattering. Because of a short duration of scattering events, the Langevin sources are δ -correlated in time. Furthermore, since different scattering events are independent, the scattering between each pair of states presents a Poissonian process whose cumulants of any order are proportional to its average rate

$$J(\mathbf{p} \rightarrow \mathbf{p}') = W(\mathbf{p}, \mathbf{p}')f(\mathbf{p}, \mathbf{r}, t)[1 - f(\mathbf{p}', \mathbf{r}, t)]. \quad (2)$$

Hence the cumulants of extraneous sources of the corresponding order related with randomness of scattering may be written as the sums of incoming and outgoing scattering fluxes taken with appropriate signs. For example, the second cumulant is given by [5]

$$\begin{aligned} \langle\langle J^{ext}(\mathbf{p}_1, \mathbf{r}_1, t_1)J^{ext}(\mathbf{p}_2, \mathbf{r}_2, t_2) \rangle\rangle &= \delta(\mathbf{r}_1 - \mathbf{r}_2)\delta(t_1 - t_2) \left\{ \delta_{\mathbf{p}_1\mathbf{p}_2} \right. \\ &\times \sum_{\mathbf{p}'} [J(\mathbf{p}_1 \rightarrow \mathbf{p}') + J(\mathbf{p}' \rightarrow \mathbf{p}_1)] - J(\mathbf{p}_1 \rightarrow \mathbf{p}_2) - J(\mathbf{p}_2 \rightarrow \mathbf{p}_1) \left. \right\}. \quad (3) \end{aligned}$$

Similar expressions are valid for the third and fourth cumulants [7]. However to obtain higher cumulants of δf , it is insufficient to multiply the corresponding number of solutions of Eq. (1) and average the product using the corresponding cumulant of Langevin sources. The point is that the second cumulant of Langevin sources (3) as well as their higher cumulants are functionals of the distribution function and hence may also fluctuate. As the characteristic time for the variations of fluctuations δf is much longer than the correlation time of Langevin sources, their cumulants adiabatically follow δf . On the other hand, δf is correlated with other measurable fluctuations. This results in additional correlations, which may be termed “cascade” because lower-order correlators of Langevin sources contribute to higher-order cumulants of measurable quantities. Symbolically, the expression for the cascade correction to the third cumulant of current may be written in a form [7]

$$\Delta\langle\langle I_1 I_2 I_3 \rangle\rangle = P_{123} \left\{ \frac{\delta\langle\langle I_1 I_2 \rangle\rangle}{\delta f_4} \langle\delta f_4 \delta I_3 \rangle \right\}, \quad (4)$$

where P_{123} denotes a summation over all inequivalent permutations of indices (123) and $\delta\langle\langle \dots \rangle\rangle/\delta f_4$ denotes a functional derivative with respect to $f(\varepsilon_4, \mathbf{r}_4, t_4)$. The products imply a convolution over the arguments of the distribution functions with repeating indices. The expressions for higher cumulants are conveniently presented in a diagrammatic form (see Fig. 1). All diagrams present graphs whose outer vertices correspond to different instances of the fluctuating quantity and whose inner vertices correspond either to cumulants of extraneous sources or their functional derivatives. As there should be no back-action of higher cumulants on the lower cumulants, all diagrams

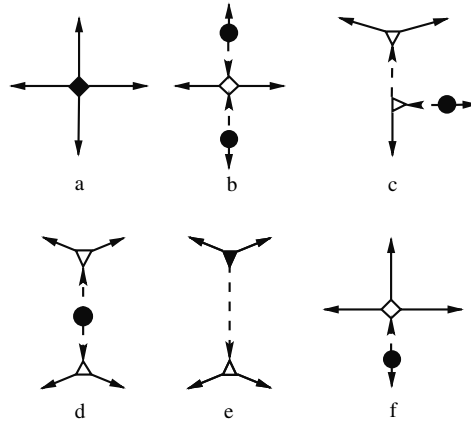


Fig. 1. The contributions to the fourth cumulant of the current. Dashed lines correspond to fluctuations of the distribution function. Full circles, triangles and squares correspond to the second, third, and fourth cumulants of extraneous currents. The empty triangles and squares present their functional derivatives.

are singly connected and their number is strictly limited for a cumulant of a given order. Hence any diagram for the n th cumulant of the fluctuating quantity may be obtained from a diagram of order $m < n$ by inserting one of its outer vertices into one of the inner vertices of a diagram of order $n - m + 1$. A summation over all inequivalent permutations of the outer vertices should be performed.

As an application of this formalism, consider the third and fourth cumulants of current in a voltage-biased diffusive-metal contact. In this case, the direct contributions from the third and fourth cumulants of Langevin sources are negligibly small because these cumulants are proportional to the inverse elastic scattering time τ^{-1} and each solution of the Boltzmann–Langevin equation gives an additional factor of τ , so that the cumulants of transport current would be proportional to τ^3 instead of τ . Hence all higher cumulants of current for diffusive contacts are dominated by diagrams constructed of the second cumulant of Langevin sources and its functional derivatives. As a result, one obtains the low-frequency Fourier transform of the third cumulant in the form

$$P_3(0, 0) = \frac{1}{15} \frac{e}{R} \frac{eV \cosh(eV/T) + 12T \sinh(eV/T) - 13eV}{\cosh(eV/T) - 1}. \quad (5)$$

This expression coincides exactly with previous quantum-mechanical results [8] and gives $P_3 = (1/15)e^2 I$ at high voltages $eV \gg T$ and $P_3 = (1/3)e^2 I$ at low voltages $eV \ll T$. The resulting expression for the fourth cumulant reads

$$P_4(0, 0, 0) = -\frac{1}{420} \frac{e^2}{R} \frac{1}{\sinh^3(eV/2T)} \left[eV \cosh\left(\frac{3eV}{2T}\right) \right]$$

$$-20T \sinh\left(\frac{3eV}{2T}\right) - 313eV \cosh\left(\frac{eV}{2T}\right) + 684T \sinh\left(\frac{eV}{2T}\right) \Big]. \quad (6)$$

In the high-voltage regime it gives $P_4 = -(1/105)e^3I$ in agreement with the corresponding quantum-mechanical expression [4]. Moreover, the terms of cascade expansion can be directly mapped on the Keldysh diagrams for the same cumulants in diffusive metals.

Now we show that the validity of the cascade Langevin approach extends beyond the limits of validity of Boltzmann equation. Consider a frequency-dependent noise in a chaotic cavity, i.e. in a metallic island of irregular shape connected to the electrodes L, R via two quantum point contacts of conductances $G_{L,R} \gg e^2/h$ and arbitrary transparencies $\Gamma_{L,R}$. As the dwell time of an electron in the cavity $\tau_D = e^2 N_F / (G_L + G_R)$ is much larger than the time of flight through the cavity, the electrons in the cavity lose memory of their initial phase and are described by an energy-dependent distribution function $f(\varepsilon, t)$. The fluctuations of the electric current in the left and right contacts are given by equations

$$\delta I_{L,R} = \int d\varepsilon \left[(\tilde{I}_{L,R})_\varepsilon + \frac{1}{e} G_{L,R} \delta f(\varepsilon) \right], \quad (7)$$

where $(\tilde{I}_L)_\varepsilon$ and $(\tilde{I}_R)_\varepsilon$ are the energy-resolved random extraneous currents generated by the left and right contacts. The fluctuation of the distribution function $\delta f(\varepsilon)$ obeys a kinetic equation

$$\left(\frac{\partial}{\partial t} + \frac{1}{\tau_D} \right) \delta f(\varepsilon, t) = -e \frac{\partial \delta U}{\partial t} \frac{\partial f}{\partial \varepsilon} - \frac{1}{e N_F} [(\tilde{I}_L)_\varepsilon + (\tilde{I}_R)_\varepsilon], \quad (8)$$

where $\tau_D = e^2 N_F / (G_L + G_R)$ is the dwell time of an electron in the cavity, N_F is the density of states in it, and δU is a fluctuation of the electric potential of the cavity. This fluctuation is obtained from the charge-conservation law

$$\frac{\partial \delta U}{\partial t} = \frac{1}{C} \frac{\partial \delta Q}{\partial t} = -\frac{1}{C} \int d\varepsilon [(\tilde{I}_L)_\varepsilon + (\tilde{I}_R)_\varepsilon], \quad (9)$$

where C is the electrostatic capacitance of the cavity. Equations (7) - (9) suggest that different parts of δf are described by different time scales. The relaxation of electrically neutral fluctuations is described by the characteristic time τ_D , whereas the fluctuations of charge are described by $\tau_Q = [(G_L + G_R)/C + 1/\tau_D]^{-1}$, which is much shorter than τ_D for good conductors.

If the distribution function of electrons in the cavity $f(\varepsilon, t)$ were not allowed to fluctuate, the contacts would be independent generators of current noise whose zero-frequency energy-resolved cumulants $\langle\langle \tilde{I}_{L,R}^n \rangle\rangle_\varepsilon$ could be obtained from a quantum-mechanical formula

$$\langle\langle \tilde{I}_{L,R}^n \rangle\rangle_\varepsilon = \frac{G_{L,R}}{\Gamma_{L,R}} \frac{\partial^n}{\partial \chi^n} \ln \{ 1 + \Gamma_{L,R} f_{L,R}(\varepsilon) [1 - f(\varepsilon)] (e^{-\varepsilon \chi} - 1) \}$$

$$+ \Gamma_{L,R} f(\varepsilon) [1 - f_{L,R}(\varepsilon)] (e^{\varepsilon x} - 1) \Big|_{x=0}. \quad (10)$$

If the voltage is high enough, the noise of isolated contacts can be considered as white at frequencies at which the distribution function f fluctuates. This allows us to consider the contacts as independent generators of white noise, whose intensity is determined by the instantaneous distribution function of electrons in the cavity. Based on this time-scale separation, we perform a recursive expansion of higher cumulants of current in terms of its lower cumulants. In the low-frequency limit, the expressions for the third and fourth cumulants coincide with those obtained by quantum-mechanical methods for arbitrary ratio of conductances G_L/G_R and transparencies $\Gamma_{L,R}$ [9]. Very recently, the same recursive relations were obtained as a saddle-point expansion of a stochastic path integral [10].

Consider now the frequency dependence of the third cumulant. We will be interested in the case of a good conductor where the charge-relaxation time τ_Q is much shorter than the dwell time τ_D . Unlike the second cumulant of current, the third cumulant $P_3(\omega_1, \omega_2)$ in general exhibits a strong dispersion at $\omega_{1,2} \sim 1/\tau_D$ [11]. For symmetry reasons, this dispersion vanishes for symmetric cavities and cavities with two tunnel or two ballistic contacts. The shape of $P_3(\omega_1, \omega_2)$ essentially depends on the parameters of the contacts. In particular, for a cavity with one tunnel and one ballistic contact with equal conductances $G_L = G_R = G$ it exhibits a non-monotonic behavior as one goes from $\omega_1 = \omega_2 = 0$ to high frequencies. A relatively simple analytical expression for this case may be obtained if $\tau_D \gg \tau_Q$ and one of the frequencies is zero:

$$P_3(\omega, 0) = -\frac{1}{32} e^2 I \frac{1 + 2\tau_D^2 \omega^2 + \tau_D^2 \tau_Q^2 \omega^4}{(1 + \omega^2 \tau_D^2)(1 + \omega^2 \tau_Q^2)^2}. \quad (11)$$

The $P_3(\omega, 0)$ curve shows a clear minimum at $\omega \sim (\tau_D \tau_Q)^{-1/2}$ and the amplitude of its variation tends to $P_3(0, 0)$ as $\tau_Q/\tau_D \rightarrow 0$.

In summary, we demonstrated a semiclassical method for calculating higher cumulants of noise in systems with a large time-scale separation. This method is not restricted to zero frequencies and allows an inclusion of inelastic processes. Its validity has been rigorously substantiated for diffusive conductors and semiclassical chaotic cavities. By using this method, we have shown that the third cumulant of current in normal-metal mesoscopic systems may exhibit a strong dispersion at frequencies much smaller than the charge-relaxation time of the system. The variations of the cumulant may be of the order of its zero-frequency value even if the number of quantum channels in the system is large.

Acknowledgements.— This work was supported by the Russian Foundation for Basic Research, Grant No. 01-02-17220, INTAS (project 0014, open call 2001), and by the Russian Science Support Foundation.

References

1. L. S. Levitov and G. B. Lesovik, *Pis'ma Zh. Eksp. Teor. Fiz.* **58**, 225 (1993) [*JETP Lett.* **58**, 230 (1993)].
2. R. A. Jalabert, J.-L. Pichard, and C. W. J. Beenakker, *Europhys. Lett.* **27**, 255 (1994).
3. H. U. Baranger and P. Mello, *Phys. Rev. Lett.* **73**, 142 (1994).
4. H. Lee, L. S. Levitov, and A. Yu. Yakovets, *Phys. Rev. B* **51**, 4079 (1995).
5. Sh. M. Kogan and A. Ya. Shul'man, *Zh. Eksp. Teor. Fiz.* **56**, 862 (1969) [*Sov. Phys. JETP* **29**, 467 (1969)].
6. S. V. Gantsevich, V. L. Gurevich, and R. Katilius, *Zh. Eksp. Teor. Fiz.* **57**, 503 (1969) [*Sov. Phys. JETP* **30**, 276 (1970)].
7. K. E. Nagaev, *Phys. Rev. B* **66**, 075334 (2002).
8. D. B. Gutman and Y. Gefen, *cond-mat/0201007*.
9. K. E. Nagaev, P. Samuelsson, and S. Pilgram, *Phys. Rev. B* **66**, 195318 (2002).
10. S. Pilgram, A. N. Jordan, E. V. Sukhorukov, and M. Büttiker, *Phys. Rev. Lett.* **90**, 206801 (2003).
11. K. E. Nagaev, S. Pilgram, and M. Büttiker, *Phys. Rev. B* **70**, 045304 (2004).

Josephson Junctions as Threshold Detectors for Full Counting Statistics

Jens Tobiska and Yuli V. Nazarov

Department of NanoScience, Delft University of Technology, 2628 CJ Delft, The Netherlands Y.V.Nazarov@tn.tudelft.nl

Summary. We discuss how threshold detectors can be used for a direct measurement of the full counting statistics (FCS) of current fluctuations and how to implement Josephson junctions in this respect. We propose a scheme to characterize the full counting statistics from the current dependence of the escape rate measured. We illustrate the scheme with explicit results for tunnel, diffusive and quasi-ballistic mesoscopic conductors.

Quantum noise in electron transport is an actively developing field. Noise measurements provide exclusive information about microscopic mechanisms of the transport that can hardly be obtained by other means [1, 2]. Still, the experiments in the field neither match the intensive theoretical development nor gather *all* information about electric fluctuation. Indeed, the concept of full counting statistics pioneered in [3] allows one to predict the non-Gaussian distribution function of the current measured during a time interval τ , $P_\tau(I)$. This distribution is characterized by an infinite set of cumulants $\ll I^n \gg$. A traditional noise measurement only assesses the second cumulant of this set discarding the rest. Recent pioneering work reports a successful measurement of the third cumulant [4], but there is a long way to go if one measured the cumulants one by one. It would be advantageous to measure the distribution function directly and thus to get all cumulants at once, thereby collecting the wealth of information being currently discarded.

Why is such a measurement difficult? The probabilities to measure correspond to big deviations of the current from its average value, $|I - \langle I \rangle| \simeq \langle I \rangle$, and are therefore exponentially small. For instance, in the shot noise regime $P_\tau(I) \simeq \exp(-\langle I \rangle \mathcal{G}(I/\langle I \rangle) \tau/e)$, $\mathcal{G}(I/\langle I \rangle) \simeq 1$ being the function to characterize. One has to concentrate on very rare measurement outcomes that occur with probability $\exp(-\langle I \rangle \tau/e) \approx 0$. Such measurements can only be carried out with *threshold detectors* that discriminate these rare events. Let us discuss

an *ideal* threshold detector that measures the current during the time interval τ , and gives a signal if the current measured exceeds the threshold current I_{th} . The signal probability will then be proportional to $P_\tau(I_{\text{th}})$. To give a realistic illustration, a detector that measures a tunnel junction with $\langle I \rangle = 10$ pA in the time interval $\tau = 10^{-6}$ s would go off once an hour if $I_{\text{th}} = 2\langle I \rangle$ and once in 10^{-4} s if $I_{\text{th}} = 1.5\langle I \rangle$. Therefore, if one measures the rate of the detector signals as a function of I_{th} , one directly assesses the full counting statistics.

Albeit realistic detectors are not ideal. There are three important factors that can either hinder the interpretation of such a measurement or even prevent the measurement: (i) a realistic detector hardly measures the current averaged over a certain time interval τ . It is *dispersive*, being usually more sensitive to longer and smaller current fluctuations rather than to bigger and shorter ones. (ii) The detector may produce a significant feedback on the system measured when it starts to signal, thereby disrupting its noise properties. (iii) The detector could just go off by itself, for instance, due to quantum tunneling.

A Josephson junction seems to be a natural threshold detector for current fluctuations. It can be viewed as a particle in a washboard potential [5], the superconducting phase difference ϕ across the junction corresponding to the particle's coordinate. The junction is in zero-voltage state provided the current does not exceed the critical value corresponding to the critical tilt of the washboard potential. ϕ is trapped in one of the minima of the potential, which is separated by a barrier from the neighboring one. A current fluctuation that exceeds the critical threshold sets ϕ into motion and the junction gives a signal—a voltage pulse that lasts till ϕ is retrapped in a different minimum.

In this paper we address the feasibility of Josephson junction systems for measuring the FCS of a mesoscopic conductor. Our results are as follows. The Josephson junction is a realistic detector, all three factors mentioned are in play. Albeit one can measure FCS provided the width of the barrier $\phi_0 \gg 1$. This can be realized by connecting several Josephson junctions in series. Under these conditions, the third factor is of no importance and the first and second factor do not hinder the unambiguous correspondence between FCS and the escape rate of the junction as a function of I_{th} . These theoretical results open the way to direct experimental observation of FCS.

The circuit under consideration consists of a normal coherent conductor with conductance G in series with the Josephson junction(system) (Fig. 1). The system is biased with voltage source $V \gg k_{\text{B}}T/e$. This assures that the normal conductor is in the shot noise regime. In addition, we inject extra current I_{b} that controls the slope of the Josephson washboard potential.

If fluctuations are neglected, this system can be described with the celebrated model of resistively shunted junction [5]. The normal conductor is a source of non-gaussian current fluctuations that instantly tilt the washboard potential and can lead to an escape of ϕ from the minimum. The escape gives rise to an observable voltage pulse. The escape rate in the same or similar systems has been studied for a variety of noise sources and potentials [6, 7, 8, 9].

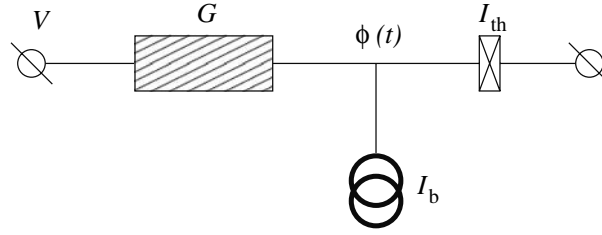


Fig. 1. A voltage biased mesoscopic conductor with conductance G provides the noise source for a threshold detector which is characterized by its threshold current I_{th} . I_b is an additional current bias.

To our knowledge, the non-Gaussian noise sources that are characterized by FCS were not addressed yet.

To proceed, we begin with the fully quantum mechanical description of the system in terms of a Keldysh action for a single variable ϕ [10, 9], that incorporates information about FCS of the normal conductor and the properties of the Josephson junction. We calculate the escape rate by considering saddle-point trajectories of the action, A , that connect the potential minimum with the nearest potential maximum. With exponential accuracy, the rate is given by $\Gamma \simeq \exp(-\text{Im}A/\hbar)$.

The action consists of two terms, $A = A_J + A_N$, corresponding to the elements of the circuit. We denote by ϕ^\pm the phases on the forward/backward parts of the Keldysh contour and also use symmetrized combinations of these $\phi, \chi = (\phi^+ \pm \phi^-)/2$. The junction part reads in a standard way [10]:

$$A_J = \int dt \left(U(\phi^+(t)) - \frac{\hbar^2 C}{8e^2} \dot{\phi}^{+2}(t) \right) - \{\phi^+ \leftrightarrow \phi^-\}, \quad (1)$$

C being the self-capacitance of the junction, $U(\phi)$ being the Josephson energy with the current bias term included: $-U(\phi) = (\hbar/2e)(I_c \cos \phi + I_b \phi)$ for a single junction. Further we concentrate on overdamped junctions where $C \ll G^2 \hbar / (2eI_c)$ and neglect the capacitance term. The normal conductor part we write following [11] in quasi-stationary approximation

$$A_N = \frac{i\hbar}{2e} G \int dt (V - \frac{\hbar}{2e} \dot{\phi}(t)) S(\chi(t)); \quad (2)$$

where S characterizes the FCS and the preceding factor is just the voltage drop over the normal conductor. A coherent conductor can be presented by a set of transmission eigenvalues T_n and S is given by Levitov's formula [3]

$$S(\chi) = \frac{G_Q}{G} \sum_n \ln(1 + T_n(e^{i\chi} - 1)), \quad (3)$$

G_Q being the conductance quantum. Concrete forms of $S(\chi)$ for specific conductors will be given below. At $\chi \rightarrow 0$, S can be expanded in χ ,

$S \approx i\chi - \chi^2 F/2$, F being the Fano factor that describes the suppression of shot noise in comparison with the Poisson value [1].

This quasi-stationary approximation is only valid if the typical time τ of the motion along the saddle-point trajectory is long in comparison with \hbar/eV , that is, $eV\tau \gg \hbar$. To check the validity of this, we precede the results with simple qualitative estimations.

Let us consider an arbitrary barrier with the width ϕ_0 and height $U_0 \simeq (\hbar/e)I_{\text{th}}\phi_0$. The detection time can be estimated equating the potential energy term and the term with $\dot{\phi}$, $G\phi_0(\hbar/e)^2\chi/\tau \simeq U_0\chi/\phi_0$, χ being a typical value along the trajectory. This gives $\tau \simeq (\hbar/eV)\phi_0(I_f/I_{\text{th}})$. The quasi-stationary approximation thus holds provided $I_f \equiv GV \gg I_{\text{th}}/\phi_0$. Let us estimate χ by equating the term which is quadratic in χ and the potential term. This gives $\chi \simeq I_{\text{th}}/I_f$ if $I_{\text{th}} \ll I_f$, $\chi \simeq 1$ otherwise. We see that if $\phi_0 < 1$ then $\chi \ll 1$. The latter implies that $S(\chi)$ can be expanded near $\chi = 0$ and only the first two cumulants are relevant: no chance to see the effect of FCS. However, if $\phi_0 \gg 1$, χ can become of the order of unity without violating the quasi-stationary approximation, and one can observe the FCS. The quasi-stationary approximation remains valid for $\chi < \phi_0$.

The resulting rate can be estimated as $\log \Gamma \simeq \phi_0(G/G_Q)\chi$. If $\phi_0 < 1$, this reduces to $\log \Gamma \simeq \phi_0(G/G_Q)I_{\text{th}}/I_f$. In the opposite limit, the estimation for the rate reads $\log \Gamma \simeq \phi_0(G/G_Q)F(I_{\text{th}}/I_f)$, F being a dimensionless function $\simeq 1$. It is important to note that these expressions match the quantum tunneling rate $\log \Gamma_{\hbar} \simeq U_0\tau/\hbar \simeq (G/G_Q)\phi_0^2$ provided $eV\tau \simeq \hbar$. Therefore the quasi-stationary approximation is valid when the quantum tunneling rate is negligible and the third factor mentioned in the introduction is not relevant. For equilibrium systems, the situation corresponds to the well-known crossover between thermally activated and quantum processes at $k_B T\tau \simeq \hbar$ [9].

We proceed with the quantitative solution. The trajectories we are looking at start at $t \rightarrow -\infty$ in the minimum of the potential with $\phi = \phi_{\text{min}}$, $\chi = 0$ and approach the maximum $\phi = \phi_{\text{max}}$, $\chi = 0$ at $t \rightarrow \infty$. They obey the equations of motion

$$0 = \frac{\partial}{\partial \chi} \left[U(\phi^+(t)) - U(\phi^-(t)) + \frac{i\hbar}{2e}G(V - \frac{\hbar}{2e}\dot{\phi}(t))S(\chi(t)) \right], \quad (4)$$

$$0 = \frac{\partial}{\partial \phi} [U(\phi^+(t)) - U(\phi^-(t))] + i\left(\frac{\hbar}{2e}\right)^2 G\chi \frac{\partial S}{\partial \chi}. \quad (5)$$

It is important to note that these equations have a simple integral of motion

$$i(U(\phi^+) - U(\phi^-)) + \frac{\hbar}{2e}I_f S(\chi) = \mathcal{I} \quad (6)$$

$\mathcal{I} = 0$ for saddle-point trajectories of interest. The full action along the trajectory then reads

$$-\frac{2e^2}{\hbar^2 G}A = \int dt \dot{\phi} S(\chi) = \int_{\phi_{\text{min}}}^{\phi_{\text{max}}} d\phi S(\chi(\phi)) \quad (7)$$

where in the last relation χ is expressed in terms of ϕ by means of Eq. 6.

Let us start with the results for $\phi_0 \simeq 1$. In this case, one expands the action in terms of χ keeping terms of the first and second order only. This immediately yields $\chi = i4e(\partial U/\partial\phi)/(\hbar FI_f)$. The general answer for the escape rate can be obtained at any shape of the barrier and reads:

$$\Gamma \simeq \exp\left(-\frac{U_{\max} - U_{\min}}{k_B T^*}\right); \quad k_B T^* = eVF/2 \quad (8)$$

This is thermal activation with an effective temperature given by the noise in the normal conductor. A similar effect of noise was envisaged in a recent article [12] for the phase diffusion regime.

Let us now consider the more interesting case $\phi_0 \gg 1$. The simplest realization of such a barrier comprises $N \gg 1$ Josephson junctions connected in series, this gives $U(\phi) = NI_c \sin(\phi/N)$, $\phi_0 \simeq N$. However, this system is formally metastable: the vortices can traverse the junction providing phase slips $\Delta\phi = 2\pi$. To eliminate this, one would increase the barrier for the vortex formation, for instance, by making several parallel chains of junctions. This would further complicate the concrete function $U(\phi)$. We notice that any function $U(\phi)$ can be approximated by a cubic parabola if the tilting of the washboard potential is close to the critical value. This is why we choose the cubic parabola form

$$\frac{\partial U}{\partial\phi} = \frac{\hbar}{2e} I_{\text{th}} \left[1 - \left(\frac{\phi}{\phi_0} \right)^2 \right], \quad (9)$$

for actual calculations. It is convenient to require that the barrier does not change if we change I_f . This can be done by a corresponding change of I_b . To simplify this further, we notice that $\chi \ll \phi_0$ so that

$$U(\phi^+) - U(\phi^-) \approx \chi \frac{\partial U}{\partial\phi}. \quad (10)$$

Substitution into Eq. 6 gives ϕ in terms of χ

$$\phi = \phi_0 \sqrt{1 + \frac{I_f}{I_{\text{th}}} \left(\frac{S(\chi)}{i\chi} - 1 \right)}. \quad (11)$$

Combining this with Eq. 7, we obtain the escape rates as a function of I_{th}/I_f for any given FCS.

To stress similarities and differences with thermal activation, we present the results in the form of Arrhenius-like plots. We plot $\log \Gamma$ in units of $(G/G_Q)\phi_0$ versus the dimensionless I_{th}/I_f . Thermal activation with the effective temperature given by (8) would give a straight line (dashed lines in the plot). By virtue of our approach, the rates should exceed the quantum limit $\log \Gamma_{\hbar} \simeq (G/G_Q)\phi_0^2$. This means that the rates should saturate at this value provided $I_f \rightarrow 0$. For each choice of $S(\chi)$ we plot two curves

corresponding to two possible signs of V with respect to the current via the junction. For forward bias, the barrier is crossed when the fluctuating current is smaller than the average current. For backward bias, the barrier is crossed if the fluctuating current is bigger than the average value. The difference between two curves thus reflects the asymmetry of the current distribution with respect to the average current. In Fig. 2, left panel, we present

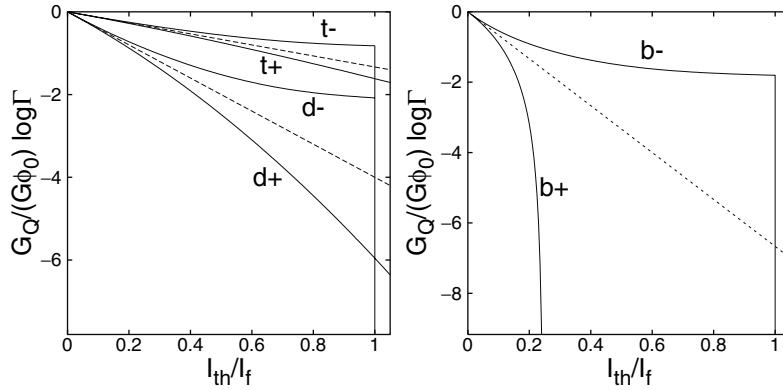


Fig. 2. Escape rates versus I_{th}/I_f for a tunnel (t), diffusive (d) and ballistic (b) mesoscopic conductor. “+”/“−” refers to forward/backward bias respectively. Dashed lines correspond to the rates due to Gaussian noise.

the results for a tunnel junction ($S_t(\chi) = e^{i\chi} - 1$) and a diffusive conductor ($S_d(\chi) = (1/4)\text{arccosh}^2(2e^{i\chi} - 1)$) [13]. All curves approach the dashed thermal activation lines at $I_f \gg I_{th}$. Since the tunnel junction is more noisy ($F = 1$ versus $F = 1/3$ for a diffusive conductor), it generally provides higher escape rates. However, the difference in functional form of the rates remains pronounced even upon rescaling with factor 3. The most pronounced feature of the backward bias curves is a plateau at $I_f \rightarrow I_{th}$ with subsequent drop to very small escape rates $\simeq \Gamma_{\hbar}$ (beyond the vertical scale of the plot). This is because the current distribution is restricted: shot noise current is always of the same sign as the average current.

A quasi-ballistic conductor presents two peculiarities of this kind. We choose the transmissions of all channels to be the same, $T_0 = 0.8$, $S_b(\chi) = (1/T_0) \ln(1 + T_0(e^{i\chi} - 1))$. In this case, the current distribution is restricted from both sides: the maximum current fluctuation can not exceed the ballistic limit $I_1 = I_f/T_0$. From this we conclude that the barrier can not be crossed at forward bias if $I_{th} > (1/T_0 - 1)I_f = 0.25I_f$, as seen in the right panel of Fig. 2. The rate becomes increasingly smaller upon approaching this threshold.

There is an unambiguous correspondence between the rates as a function of I_f/I_{th} and S , that is given by Eqs. (7), (11) and can be used to characterize the FCS from the rates measured. However, this relation is implicit and more

complicated than that of an ideal detector. Apparently, this complication is due to the first and second factor mentioned in the introduction. To look at it in more detail, we compute the optimal current and voltage fluctuations that switch the detector.

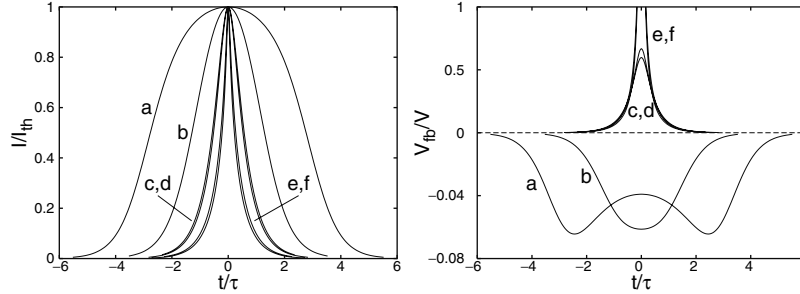


Fig. 3. Optimal current fluctuations (left panel) and feedback voltage (right panel) versus time for different conductors and different values of I_{th}/I_f . Each line corresponds to one point on the curves in figure 2. Note the different voltage scales. The labels stand for (branch| I_{th}/I_f): (a) $b+|1/5$, (b) $b+|1/10$, (c) $t-|1/3$, (d) $d-|1/3$, (e) $d-|2/3$, (f) $t-|2/3$.

The optimal current fluctuations are plotted in the left panel of Fig. 3 for different conductors and I_f . The curves are symmetric owing to the symmetry of the cubic parabola potential. Common features are that they all reach the threshold current at maximum and their time spread is of the order of τ . Still, the spread, shape, and most importantly, the integral of the current over time, varies significantly from curve to curve. This proves that the detector in use is dispersive and suffers from the first factor mentioned in the introduction.

The third factor is also in play. When ϕ moves, crossing the potential barrier, the resulting voltage changes the voltage drop over the normal conductor thereby affecting the current fluctuations in there. This feedback voltage V_{fb} is negative for forward bias and positive for negative one. We see from the evolution equations that

$$\frac{V_{fb}}{V} \equiv -\frac{\hbar\dot{\phi}}{2eV} = \frac{S(\chi(t))}{\chi(t)} \frac{\partial\chi}{\partial S(\chi(t))} - 1, \quad (12)$$

so the change in the voltage drop across the junction is quite significant if $\chi \simeq 1$. We check that the negative feedback can never change the sign of the voltage for $S(\chi)$ in use. The right panel of Fig. 3 presents voltage fluctuations corresponding to the current fluctuations on the left panel. Interestingly, the positive feedback can be very big on the plateau at the backward bias (curves e, f). In this case, the detector seeks to optimize the rare fluctuation where almost no current is flowing in the normal conductor. The probability of such fluctuations is increased upon increasing the voltage drop over the conductor

so that the detector provides the extra voltage required. Eventually, the feedback can be reduced with an extra resistive shunt over the Josephson junction. However, this would decrease τ and reduce the region of applicability of our results.

To conclude, we proved that Josephson junctions can be used as threshold detectors for non-Gaussian noise produced by coherent conductors. Our theoretical results facilitate a new type of electric noise measurement: direct measurement of full counting statistics of the transferred charge.

Acknowledgements.— This work was supported by the Dutch Foundation for Fundamental Research on Matter (FOM).

References

1. Y. M. Blanter and M. Büttiker, Phys. Rep. **336**, 1 (2000).
2. *Quantum Noise in Mesoscopic Physics*, eds. Y. V. Nazarov, vol. 97 of NATO Science Series, Kluwer Academic Publishers, Dordrecht, the Netherlands, 2003.
3. L. S. Levitov and G. B. Lesovik, Journ. Math. Phys. **37**, 10 (1996).
4. B. Reulet, J. Senzier, and D. E. Prober, Phys. Rev. Lett. **91**, 196601 (2003).
5. M. Tinkham, *Introduction to Superconductivity*, McGraw-Hill, New York, (1996), 2nd ed.
6. H. A. Kramers, Physica **7**, 284 (1940).
7. T. A. Fulton and L. N. Dunkleberger, Phys. Rev. B **9**, 4760 (1974).
8. M. Büttiker, E. P. Harris, and R. Landauer, Phys. Rev. B **28**, 1268 (1983).
9. A. I. Larkin and Y. N. Ovchinnikov, JETP Lett. **37**, 382 (1983).
10. G. Schön and A. D. Zaikin, Phys. Rep. **198**, 237 (1990).
11. M. Kindermann and Y. V. Nazarov, in [2], pp. 403–427, cond-mat/0303590.
12. H. Grabert and G.-L. Ingold, Europhys. Lett. **58**, 429 (2002).
13. D. A. Bagrets and Y. V. Nazarov, in [2], pp. 429–462, cond-mat/0301505.

Energy Dependence of Current Noise in Superconducting/Normal Metal Junctions

M. Houzet¹ and F. Pistolesi²

¹ Commissariat à l'Énergie Atomique, DSM, Département de Recherche
Fondamentale sur la Matière Condensée, SPSMS, F-38054 Grenoble, France

² Laboratoire de Physique et Modélisation des Milieux Condensés, CNRS-UJF
B.P. 166, F-38042 Grenoble, France fabio.pistolesi@grenoble.cnrs.fr

Summary. Interference of electronic waves undergoing Andreev reflection in diffusive conductors determines the energy profile of the conductance on the scale of the Thouless energy. A similar dependence exists in the current noise, but its behavior is known only in few limiting cases. We consider a metallic diffusive wire connected to a superconducting reservoir through an interface characterized by an arbitrary distribution of channel transparencies. Within the quasiclassical theory for current fluctuations we provide a general expression for the energy dependence of the current noise. We calculate analytically the quantum interference corrections to the semiclassical result.

1 Introduction

Interference of electronic waves in metallic disordered conductors is responsible for weak localization corrections to the conductance [1]. If these are neglected, the probability of transferring an electron through the diffusive medium is given by the sum of the *modulus squared* of the quantum probability amplitudes for crossing the sample along all possible paths. This probability is denoted as semiclassical, since quantum mechanics is necessary only for establishing the probability for following each path independently of the phases of the quantum amplitudes. In superconducting/normal metal hybrid structures, interference contributions are not corrections, they may actually *dominate* the above defined semiclassical result for temperatures and voltages smaller than the superconducting gap. This is seen experimentally as an energy dependence of the conductance on the scale of the Thouless energy. Indeed, the energy dependence comes from the small wavevector mismatch, linear in the energy of the excitations, between the electron and the Andreev

reflected hole. This is responsible for the phase difference in the amplitudes for two different paths leading to interference. The effect is well known and explicit predictions and measurements exist for a number of systems [2, 3, 4].

Interference strongly affects the current noise too [5]. The largest effects are expected in the tunneling limit, when the transparency of the barrier is small and its resistance is much larger than the resistance of the diffusive normal region. Then, the conductance has a strong non linear dependence at low bias (reflectionless tunneling) [2, 3]. This is actually the case, but the zero-temperature noise (or shot noise) does not give any additional information on the system since it is simply proportional to the current, as shown quite generally in Ref. [6]. In the more interesting case of a diffusive metal wire in contact with a superconductor through an interface of conductance G_B much larger than the wire conductance G_D , Belzig and Nazarov [7] found that the differential shot noise, dS/dV , shows a reentrant behavior, as a function of the voltage bias, *similar*, but not *identical*, to the conductance one. (The extension of the Boltzman-Langevin approach to the coherent regime in Ref. [8] neglects this difference.) In order to compare quantitatively with actual experiments [9, 10, 11] and to gain more insight in the interference phenomenon, it is necessary to obtain the energy dependence of noise in more general situations. The numerical method used in Ref. [7] is, in principle, suitable to treat more general cases, notably the case when $G_D \sim G_B$, but only if all channel transparencies, $\{\Gamma_n\}$, that characterize the interface are small. In Ref. [12] we presented an analytical solution for the diffusion-type differential equation for the noise within the theory of current fluctuations [13] in the quasiclassical dirty limit [7]. It allows to treat the general case of arbitrary values for $\{\Gamma_n\}$ and G_B/G_D . In the present paper we present the minimal set of equations necessary to obtain the noise. We then exploit them to obtain closed analytical expressions for the noise at large energy.

2 Equations to obtain the noise

In Ref. [12] we have developed an analytical theory to calculate the current noise in a diffusive wire of length L , diffusive constant D , and conductance G_D . The wire is connected to a normal reservoir on one side through a transparent interface and to a superconducting one on the other side through an arbitrary interface characterized by a set of channel transparencies $\{\Gamma_n\}$. Let us summarize in a compact form the equations necessary to obtain the noise. These equations are obtained by exploiting the semiclassical theory proposed by Nazarov [14] to calculate the full counting statistics of charge transfer [13]. Details are given in Ref. [12].

The first step consists in obtaining the conductance G . For that we need $f_T(x)$ and $\theta(x)$ (x varies between 0 and L), parameterizing respectively the fermion distribution and the superconducting correlations. $\theta = \theta_1 + i\theta_2$ is a complex parameter that satisfies the equation

$$\hbar D \theta''(x) + 2i\varepsilon \sinh \theta(x) = 0, \quad (1)$$

with boundary conditions [15] $\theta(L) = 0$ and $\theta'(0) = H[\theta(0)]$, where

$$H[\theta] = \frac{i}{Lr} \left\langle \frac{\cosh \theta}{1 + \frac{\Gamma}{2} (i \sinh \theta - 1)} \right\rangle. \quad (2)$$

We defined $\langle \psi(\Gamma) \rangle \equiv \sum_n \Gamma_n \psi(\Gamma_n) / \sum_n \Gamma_n$, $G_B = (2e^2/h) \sum_n \Gamma_n$, and $r = G_D/G_B$. For f_T we have the simpler equation $(\cosh^2 \theta_1(x) f_T'(x))' = 0$ with boundary conditions $f_T(L) = f_{T0}$ and

$$f_T'(0) = \frac{f_T(0) \theta_1'(0)}{\cosh \theta_1(0) \sinh \theta_1(0)}. \quad (3)$$

Here $f_{T0} = f_- - f_+$, $f_{\pm}(\varepsilon) = f(\varepsilon \pm eV)$, f is the Fermi function at temperature T , and V is the voltage bias. Then the current is $I = 1/(2e) \int d\varepsilon \mathcal{G}(\varepsilon) f_{T0}(\varepsilon)$ with [2]

$$\mathcal{G}(\varepsilon) = G_D \left[\mathcal{D}^{-1}(\varepsilon) + \frac{\tanh \theta_1(0)}{L \theta_1'(0)} \right]^{-1} \quad (4)$$

and $\mathcal{D}^{-1}(\varepsilon) = 1/L \int_0^L ds / \cosh^2 \theta_1(s)$. At low temperatures, $k_B T \ll eV$, $G(V) = \mathcal{G}(eV)$ is the differential conductance. Similar equations have been recently exploited in Ref. [16] to discuss the conductance.

To obtain the noise we need an additional parameter $a(x)$. It parameterizes the first correction in the counting field to the Usadel Green's function. Other parameters intervene, but we do not need them to calculate the noise [12].

The complex parameter $a = a_1 + ia_2$ satisfies the following linear differential equation:

$$\hbar D a''(x) + 2i\varepsilon a(x) \cosh \theta(x) = -2E_T \frac{\sinh \theta_1(x)}{\cosh^3 \theta_1(x)} \frac{G(\varepsilon)^2}{G_D^2}, \quad (5)$$

with $E_T = \hbar D/L^2$ the Thouless energy. The boundary conditions are $a(L) = 0$ and $L a'(0) = \alpha a(0)/r + \beta/r$ with

$$\alpha = \left\langle \frac{i \sinh \theta - \Gamma(i \sinh \theta - 1)/2}{[1 + \Gamma(i \sinh \theta - 1)/2]^2} \right\rangle \quad (6)$$

$$\beta = \frac{ic^2}{8} \left\langle \frac{2\Gamma^2 \cosh \theta^* + 8(\Gamma - 1) \cosh \theta - 2i\Gamma(\Gamma - 2) \sinh \theta \cosh \theta^*}{|1 + \Gamma(i \sinh \theta - 1)/2|^2 (1 + \Gamma(i \sinh \theta - 1)/2)} \right\rangle,$$

both evaluated at $x = 0$. The low frequency noise is finally given by:

$$S = \int d\varepsilon \mathcal{G}(\varepsilon) \{1 - f_{L0}^2(\varepsilon) - [1 - \mathcal{F}(\varepsilon)] f_{T0}^2(\varepsilon)\}, \quad (7)$$

where

$$\mathcal{F}(\varepsilon) = \frac{2}{3}(1 + c^3) + \frac{2\mathcal{G}}{G_D} \int_0^1 \frac{\sinh \theta_1 a_1}{\cosh^3 \theta_1} ds - \frac{G_D a_1'(0) c^2}{\mathcal{G} \tanh \theta_1(0)} - \frac{2a_1(0)c}{\sinh 2\theta_1(0)}, \quad (8)$$

with $c = 1 - \mathcal{G}(\varepsilon)/[G_D \mathcal{D}(\varepsilon)]$ and $f_{L0} = 1 - f_+ - f_-$.

We have now all the ingredients to calculate explicitly the noise for arbitrary values of the ratio r , of the energy ε , and of the transparency set $\{\Gamma_n\}$.

3 Large energy limit for $r \neq 0$

Let us now study the large energy (or incoherent) limit. We will actually find an analytical expression for the quantum corrections. Indeed if $r \neq 0$ for $\varepsilon \gg E_T$ the parameter θ vanishes like $1/\sqrt{\varepsilon}$, it is thus convenient to set up the following expansion:

$$\theta(x) = \frac{\theta^{(0)}(x)}{k} + \frac{\theta^{(1)}(x)}{k^2} + \frac{\theta^{(2)}(x)}{k^3} + \dots \tag{9}$$

where we introduced the large parameter $k = \sqrt{\varepsilon/E_T}$. We can now substitute (9) into (1) and the boundary conditions. In collecting terms of the same order in $1/k$ one has to take care that each derivative with respect to x introduces an additional k factor. At lowest order we obtain

$$\theta^{(m)''}(\tilde{x}) + 2ik^2 \theta^{(m)} = 0 \tag{10}$$

$$\theta^{(2)''}(\tilde{x}) + 2ik^2 [\theta^{(2)} + \theta^{(0)3}/3!] = 0, \tag{11}$$

where $m = 0, 1$ and $\tilde{x} = x/L$. For the boundary conditions we have $\theta^{(m)}(L) = 0$ for all m , $\theta^{(0)'} = kH(0)$, $\theta^{(1)'} = kH'(0)\theta^{(0)}$, and $\theta^{(2)'} = kH'(0)\theta^{(1)} + kH''(0)\theta^{(0)2}/2$. To obtain the conductance to order $1/k^2$ we need also the boundary condition for $\theta^{(3)'}$, but we do not need to solve the associated differential equation. Solving the differential equations (10) and (11) and substituting the result into Eq. (4) we obtain for the conductance up to second order in $1/k$ the following expression:

$$G = \frac{H'}{1+H'} + \frac{H'H''}{2k(1+H')^2} + \frac{H'H''(2H'+2H'^2-HH'')}{4k^2(1+H')^4} + \dots \tag{12}$$

Equation (12) holds for any distribution of channel transparency, it suffices to calculate the appropriate averages for H , H' , and H'' .

The procedure to obtain the noise is similar. This time we need an expansion of the parameter a which has the same form of (9). Actually the differential equation for $a^{(0)}$ and $a^{(1)}$ coincide with those for $\theta^{(0)}$. The equation for $a^{(2)}$ reads:

$$a^{(2)''}(\tilde{x}) + 2ik^2 a^{(2)} = -2k^2 [ia^{(0)}\theta^{(0)2} + f_{T0}G^2\theta_1^{(0)}]. \tag{13}$$

The boundary conditions for a read: $a^{(0)'} + k\beta^{(0)}/r = 0$, $a^{(1)'} + k[\alpha^{(0)}a^{(0)} + \beta^{(1)}/r] = 0$, and $a^{(2)'} + k[\alpha^{(0)}a^{(1)} + \alpha^{(1)}a^{(0)} + \beta^{(2)}/r] = 0$, where $\alpha = \alpha^{(0)} +$

$\alpha^{(1)}/k + \dots$ and $\beta = \beta^{(0)} + \beta^{(1)}/k + \dots$. Substituting these expressions into (8) we can obtain the differential Fano factor $\mathcal{F}(\varepsilon) = (dS/dV)(\varepsilon)/2eG(\varepsilon)$. The lowest order, i.e. the incoherent contribution, has a simple form:

$$\mathcal{F}_{inc} = \frac{2}{3} \left[1 + (2 - 3 \frac{\langle \frac{\Gamma^3}{(2-\Gamma)^4} \rangle}{\langle \frac{\Gamma}{(2-\Gamma)^2} \rangle}) \frac{G_D^3}{(G_D + 2G_B \langle \frac{\Gamma}{(2-\Gamma)^2} \rangle)^3} \right]. \quad (14)$$

This can be understood by a comparison with the classical calculation of Ref. [17] for a wire connected to normal reservoirs. Eq. (14) coincide with the Fano factor given there when the substitution $e \rightarrow 2e$, $G_D \rightarrow G_D/2$ and $\Gamma_n \rightarrow \Gamma_n^A = \Gamma_n^2/(2 - \Gamma_n)^2$ are performed. This is consistent with the expectation that phase coherence becomes irrelevant at high energy (see also the discussion in Ref. [18]).

The expression for the quantum correction to (14) is cumbersome in the general case and we will not present it. A simpler expression is obtained when all transparencies are the same ($\Gamma_n = \Gamma$):

$$\mathcal{F}^{(1)} = \frac{2r^2(\Gamma - 2)^2}{[r(\Gamma - 2)^2 + 2\Gamma]^4} [\Gamma(\Gamma - 2)(r(\Gamma - 2)(\Gamma^2 + 12\Gamma - 12) - 64) - 64]$$

and $\mathcal{F}(\varepsilon) = \mathcal{F}_{inc} + \mathcal{F}^{(1)}/\sqrt{\varepsilon/E_T}$.

4 Conclusions

We presented a theory to calculate the energy dependence of the noise in a wire connecting a normal with a superconducting reservoir. The theory allows to obtain closed analytical expressions in different relevant limits. We considered here in some details the large energy case. The classical incoherent result appears for energy much larger than the Thouless energy. Quantum corrections are explicitly evaluated when all transparencies have the same value.

References

1. B. L. Altshuler and A. G. Aronov, in *Electron-electron interactions in disordered systems*, Eds. A. L. Efros and M. Pollak, (North-Holland, Amsterdam) (1985).
2. A. F. Volkov, A. V. Zaitsev, and T. M. Klapwijk, *Physica C* **210**, 21 (1993).
3. F. W. J. Hekking and Yu. V. Nazarov, *Phys. Rev. Lett.* **71**, 1625 (1993).
4. C. W. J. Beenakker, *Rev. Mod. Phys.* **69**, 731 (1997).
5. Ya. M. Blanter and M. Büttiker, *Phys. Rep.* **336** 1 (2001).
6. F. Pistolesi, G. Bignon, and F. W. J. Hekking, *cond-mat/0303165* (unpublished).
7. W. Belzig and Yu. V. Nazarov, *Phys. Rev. Lett.* **87**, 067006 (2001).

8. M. Houzet and V. P. Mineev, *Phys. Rev. B* **67**, 184524 (2003).
9. X. Jehl, M. Sanquer, R. Calemczuk, and D. Mailly, *Nature* **405**, 50 (2000).
10. A. A. Kozhevnikov, R. J. Schoelkopf, and D. E. Prober, *Phys. Rev. Lett.* **84**, 3398 (2000).
11. F. Lefloch, C. Hoffmann, M. Sanquer, and D. Quirion, *Phys. Rev. Lett.* **90**, 067002 (2003).
12. M. Houzet and F. Pistolesi, (unpublished).
13. L. S. Levitov, H. W. Lee, and G. B. Lesovik, *J. Math. Phys.* **37**, 4845 (1996).
14. Yu. V. Nazarov, *Superlatt. Microstruct.* **25**, 1221 (1999).
15. A. V. Zaitsev, *Sov. Phys. JETP* **59**, 1163 (1984).
16. Y. Tanaka, A. A. Golubov, and S. Kashiwaya, *cond-mat/0212019* (unpublished).
17. M. J. M. de Jong and C. W. J. Beenakker, *Physica A* **230**, 219 (1996).
18. P. Samuelsson and M. Büttiker, *Phys. Rev. B* **66**, 201306 (2002).

Measurement of the Third Moment of Voltage Fluctuations in a Tunnel Junction

B. Reulet^{1,2}, J. Senzier¹, L. Spietz¹, C.M. Wilson¹, and D.E. Prober¹

¹ Departments of Applied Physics and Physics, Yale University, New Haven CT 06520-8284, USA

² Laboratoire de Physique des Solides, UMR8502, bât 510 Université Paris-Sud, 91405 ORSAY, France

1 Introduction

Transport studies provide a powerful tool for investigating electronic properties of a conductor. The $I(V)$ characteristic (or the differential resistance $R_{diff} = dV/dI$) contains partial information on the mechanisms responsible for conduction. A much more complete description of transport in the steady state, and further information on the conduction mechanisms, is given by the probability distribution of the current P , which describes both dc current I and the fluctuations $\delta I = I(t) - I$. The current fluctuations can be characterized by the moments of the probability distribution P of order two and higher. However, until now only the second moment has been measured in the many systems studied [1]. In this article we report the first measurements of the third moment of the voltage fluctuations across a conductor, $\langle \delta V^3 \rangle$, where $\delta V = V(t) - V$ represents the voltage fluctuations around the dc voltage V (see also [2]); $\langle \cdot \rangle$ stands for time averaging, or equivalently for averaging over the distribution P . Below we relate $\langle \delta V^3 \rangle$ to $\langle \delta I^3 \rangle$. Our experimental setup is such that the sample is current biased at dc and low frequency but the electromagnetic environment has an impedance $\sim 50 \Omega$ within the detection bandwidth, 10 MHz to 1.2 GHz. Our results are in agreement with a recent theory that considers the strong effect of the electromagnetic environment of the sample [3]. Moreover, we show that certain of these environmental effects can be dramatically reduced by signal propagation delays from the sample to the amplifier.

We present the theoretical overview first for the case of voltage bias [1]. In a junction with a low transparency barrier (which corresponds to our samples) biased by a dc voltage V , the current noise spectral density (related to the

second moment) is given for low frequency by: $S_{I^2} = eGV \coth(eV/2k_B T)$ [4] (in A^2/Hz), where e is the electron charge and G is the conductance. Only at high voltage $eV \gg k_B T$ does this reduce to the Poisson result $S_{I^2} = eI$ [4]. The spectral density of the third moment of the current fluctuations in a voltage biased tunnel junction of low transparency is calculated to be: $S_{I^3} = e^2GV$, independent of temperature [5, 6]. By considering how the Fourier components can combine to give a dc signal, we find that $\langle \delta I^3 \rangle = 3S_{I^3}(f_2 - 2f_1)^2$, where the detection bandwidth is from f_1 to f_2 . We have experimentally confirmed this unusual dependence on f_1 and f_2 (data not reported here, see [2]).

We next consider the effects of the sample's electromagnetic environment (contacts, leads, amplifier, etc.); the sample is no longer voltage biased. The environment emits noise, inducing fluctuations of the voltage across the sample, which in turn modify the probability distribution P . Moreover, due to the finite impedance of the environment, the noise emitted by the sample itself induces also voltage fluctuations. We consider the circuit depicted in the inset of Fig. 2, at first neglecting time delay along the coaxial cable. The noise of the sample of resistance R is modeled by a current generator i . The voltage δV is measured across a resistor R_0 , which has a current generator i_0 of noise spectral density S_{i_0} . One has $\delta V = -R_D(i + i_0)$ with $R_D = RR_0/(R + R_0)$ (R in parallel with R_0). It has been recently predicted that the third moment of P is significantly modified by the environment [3], leading to a spectral density:

$$S_{V^3} = -R_D^3 S_{I^3} + 3R_D^4 S_{i_0} \frac{dS_{I^2}}{dV} + 3R_D^4 S_{I^2} \frac{dS_{I^2}}{dV} \quad (1)$$

The first term on the right is like that of the second moment. The negative sign results from an increasing sample current giving a reduced voltage. Our detection method is insensitive to S_{i_0} . The environment noise i_0 induces voltage fluctuations $\delta V = -R_D i_0$ across the sample. These modify the sample's noise S_{I^2} (which depends on $V(t)$) as $-R_D i_0 dS_{I^2}/dV$, to first order in δV . This is the origin of the second term. The sample's own current fluctuations also modify the sample voltage to contribute similarly, giving the last term of Eq. (1). We present below a simple derivation of how to include the effect of propagation time in the coaxial cable, which dramatically affects S_{V^3} .

2 Experimental setup and results

Two samples have been studied. Both are tunnel junctions made of Al/Al oxide/Al, using the double angle evaporation technique [7]. In sample A (made by C. Wilson), the bottom and top Al films are 50 nm thick. The bottom electrode was oxidized for 2 hours in pure O_2 at a pressure of 500 mTorr. The junction area is $15 \mu m^2$. In sample B (made by L. Spietz), the films are 120 nm and 300 nm thick, oxidation was for 10 min, and the junction area is $5.6 \mu m^2$.

We have measured $\delta V(t)^3$ in real time (see Fig. 1). The resistance of the sample is close to 50Ω , and thus is well matched to the coaxial cable and amplifier. After amplification at room temperature the signal is separated into four equal branches, each of which carries a signal proportional to $\delta V(t)$. A mixer multiplies two of the branches, giving $\delta V^2(t)$; a second mixer multiplies this result with another branch. The output of this second mixer, $\delta V^3(t)$, is then low pass filtered, to give a signal which we refer to as D. Ideally D is simply proportional to S_{V^3} , where the constant of proportionality depends on mixer gains and frequency bandwidth. The last branch is connected to a square-law crystal detector, which produces a voltage X proportional to the the rf power it receives: the noise of the sample $\langle \delta V^2 \rangle$ plus the noise of the amplifiers. The dc current I through the sample is swept slowly. We record $D(I)$ and $X(I)$; these are averaged numerically. This detection scheme has the advantage of the large bandwidth it provides (~ 1 GHz), which is crucial for the measurement. We deduce $S_{V^3} \propto (D(I) - D(-I))/2$. The magnitude and sign of $\langle \delta V^3 \rangle$ is obtained from measurements of D when the sample is replaced by a programmable function generator.

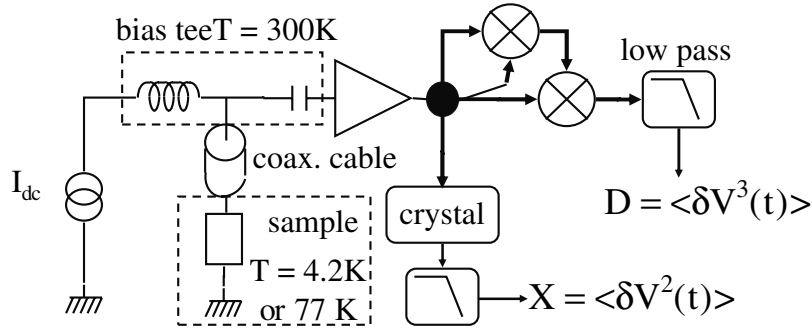


Fig. 1. (a) Schematic of the experimental setup.

Sample A was measured at $T = 4.2\text{K}$. Its total resistance (tunnel junction + contacts) is 62.6Ω . The resistance R_A of the junction is extracted from the fit of S_{V^2} as a function of $eV/k_B T$, with V the voltage drop across the junction. We find $R_A = 49.6 \Omega$. R_{diff} is voltage independent to within 1%. The gain of the amplification chain has been calibrated by replacing the sample by a macroscopic 50Ω resistor whose temperature was varied. We find $\eta = 1$ with a precision of a few percent for both samples. $S_{V^3}(eV/k_B T)$ for $|V| \leq 10$ mV is shown in Fig. 2 (top); these data were averaged for 12 days.

Sample B was measured at $T = 4.2$ K, 77 K and 290 K. The resistance of the junction $R_B = 86 \Omega$ is almost temperature independent. The contribution of the contacts is $\sim 1 \Omega$. In Fig. 2 (middle and bottom panels) the averaging time for each trace was 16 hours.

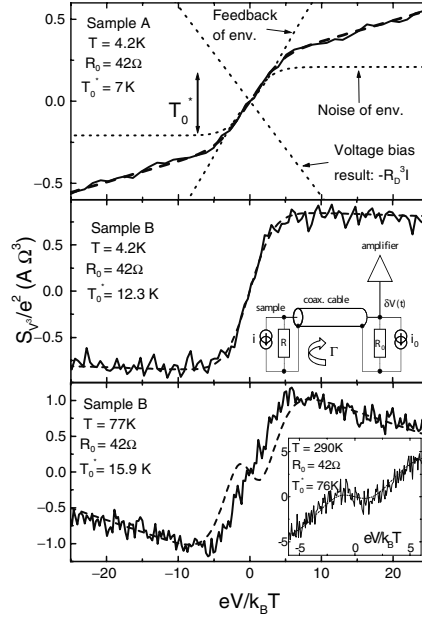


Fig. 2. Measurement of $S_{V3}(eV/k_B T)$ (solid lines). The dashed lines corresponds to the best fit with Eq. (1). The dotted lines in the top plot correspond to the different contributions to S_{V3} (see text). Inset of the middle plot: schematics of the equivalent circuit used for the theoretical model.

3 Interpretation

To analyze our results, consider again the circuit in the inset of Fig. 2, a simplified equivalent of our setup. $R_0 \sim 50 \Omega$ is the input impedance of the amplifier, which is connected to the sample through a coaxial cable of impedance R_0 (i.e., matched to the amplifier). The sample's voltage reflection coefficient is $\Gamma = (R - R_0)/(R + R_0)$. In the analysis we present next we neglect the influence of the contact resistance and impedance mismatch of the amplifier, but we have included it when computing the theory to compare to the data. The voltage $\delta V(t)$ measured by the amplifier at time t arises from three contributions: i) the noise emitted by the amplifier at time t : $R_0 i_0(t)/2$; half of i_0 enters the cable. ii) the noise emitted by the sample (at time $t - \Delta t$, where Δt is the propagation delay along the cable) that couples into the cable: $(1 - \Gamma)Ri(t - \Delta t)/2$; iii) the noise emitted by the amplifier at time $t - 2\Delta t$ that is reflected by the sample: $\Gamma R_0 i_0(t - 2\Delta t)/2$; thus,

$$\delta V(t) = -\frac{R_0}{2} [i_0(t) + \Gamma i_0(t - 2\Delta t)] - \frac{R}{2} (1 - \Gamma) i(t - \Delta t) \quad (2)$$

For $\Delta t = 0$, Eq. (2) reduces to $\delta V = -R_D(i + i_0)$ with $R_D = RR_0/(R + R_0)$. Thus, $\langle \delta V^3 \rangle = -R_D^3 (\langle i^3 \rangle + 3 \langle i^2 i_0 \rangle + 3 \langle i i_0^2 \rangle + \langle i_0^3 \rangle)$ for $\Delta t = 0$. In this equation the term $\langle i^2 i_0 \rangle$ leads to the second term on the right of Eq. (1). The term $\langle i^3 \rangle$ yields the first term of Eq. (1), and, due to the sample noise modulating its own voltage, the third term of Eq. (1) as well. The terms $\langle i_0^3 \rangle$ and $\langle i i_0^2 \rangle$ are zero. The result for $\Delta t = 0$ corresponds to Eq. (1), which is a particular case of Eq. (12b) of Ref. [3].

The finite propagation time does affect the correlator $\langle i^2 i_0 \rangle$. The term $S_{i_0^2}$ in Eq. (1) has to be replaced by $(\Gamma S_{i_0^2} + S_{i_0(t)i_0(t-2\Delta t)})/(1 + \Gamma)$, where $S_{i_0(t)i_0(t-2\Delta t)}$ is the spectral density corresponding to the correlator $\langle i_0(t)i_0(t-2\Delta t) \rangle$. For long enough Δt this term vanishes, since $i_0(t)$ and $i_0(t-2\Delta t)$ are uncorrelated. Thus, the effect of the propagation time is to renormalize the noise temperature of the environment $T_0 = R_0 S_{i_0^2}/(2k_B)$ into $T_0^* = T_0 \Gamma/(1 + \Gamma)$.

We now check whether Eq. (1), with $S_{I^3} = e^2 I$ and modified as above to account for finite propagation time, can explain our data. The unknown parameters are the resistance R_0 and the effective environment noise temperature T_0^* . We checked that the impedance of the samples was frequency independent up to 1.2 GHz within 5%. Fig. 2 shows the best fits to the theory, Eq. (1), for all our data. The four curves lead to $R_0 = 42 \Omega$, in agreement with the fact that the electromagnetic environment (amplifier, bias tee, coaxial cable, sample holder) was identical for the two samples. We have measured the impedance Z_{env} seen by the sample. Due to impedance mismatch between the amplifier and the cable, there are standing waves along the cable. This causes Z_{env} to be complex with a phase that varies with frequency. We measured that the modulus $|Z_{env}|$ varies between 30 Ω and 70 Ω within the detection bandwidth, in reasonable agreement with $R_0 = 42 \Omega$ extracted from the fits.

We have measured directly the noise emitted by the room temperature amplifier; we find $T_0 \sim 100$ K. The cable of length ~ 2 m corresponds to Δt being large for the bandwidth we used. As a consequence, the relevant noise temperature to be used to explain the data is T_0^* . For sample A, $\Gamma = 0.11$; including the contact resistance and cable attenuation one expects $T_0^* = 5$ K; for sample B, $\Gamma = 0.26$ and one expects $T_0^* = 21$ K. A much shorter cable was used for $T = 290$ K, and the reduction of T_0 is not as significant. These numbers are in reasonably good agreement with the values of T_0^* deduced from the fits (see Fig. 2), and certainly agree with the trend seen for the two samples. Clearly $T_0^* \ll T_0$ for the long cable.

Our data are consistent with a third moment of current fluctuations S_{I^3} being independent of T between 4K and 300K when the sample is voltage biased, as predicted for a tunnel junction. We have also clearly demonstrated the effect of the environment, through its noise and impedance (data not reported here, see [2]). This is of prime importance for designing future measurements on samples with unknown third moment.

Acknowledgements.— We thank C. Beenakker, W. Belzig, M. Büttiker, A. Clerck, M. Devoret, Y. Gefen, S. Girvin, N. Hengartner, M. Kindermann, L. Levitov, A. Mukherjee, Y. Nazarov and P.-E. Roche for useful discussions. This work was supported by NSF DMR 0072022.

References

1. Y.M. Blanter and M. Büttiker, Phys. Rep. **336**, 1 (2000).
2. B. Reulet, J. Senzier and D.E. Prober, cond-mat/0302084.
3. C.W.J. Beenakker, M. Kindermann and Yu V. Nazarov, Phys. Rev. Lett. **90**, 176802 (2003).
4. One often finds $S_{I^2} = 2eI$ in the literature. The factor 2 corresponds to the contributions of positive and negative frequencies.
5. L.S. Levitov, H. Lee and G.B. Lesovik, J. Math. Phys. **37**, 4845 (1996).
6. L.S. Levitov and M. Reznikov, cond-mat/0111057
7. T.A. Fulton and G.J. Dolan, Phys. Rev. Lett. **59**, 109 (1987).

Shot Noise in Mesoscopic Transport Through Localised States

A.K. Savchenko

School of Physics, University of Exeter, Stocker Road, Exeter, EX4 4QL, United Kingdom
A.K.Savchenko@ex.ac.uk

Summary. We show how shot noise can be used for studies of hopping and resonant tunneling between localized electron states. In *hopping*, shot noise is seen to be suppressed compared with its classical Poisson value $S_I = 2eI$ (I is the average current) and depends on the geometry of current paths and the distribution of the barriers between the states. In *resonant tunneling* through a single impurity an unusual enhancement of shot noise is observed. It has been established that a considerable increase of noise can occur due to interaction between resonant tunneling channels.

1 Introduction

In the past few years much attention has been drawn to the properties of shot noise in mesoscopic structures. So far experimental studies have been primarily concentrated on ballistic and diffusive systems, with only few exceptions [1, 2] where shot noise in electron tunneling or hopping was investigated.

In this work we have studied shot noise in hopping in short, *mesoscopic* barriers, where the condition $L/L_c < 1$ is realized (L_c is the correlation length of the hopping network). We have found that the result depends on the geometry of the sample [3]. The Fano factor $F = S_I/2eI$ for a wide sample (2D geometry) is found to be smaller than for a narrow (1D geometry) sample. We explain this by the reconstruction of the hopping network in the 2D case [4, 5]: in a short sample the current is carried by a set of most conductive hopping chains.

With decreasing further the sample length and temperature, resonant tunneling (RT) through a single localized state can be seen. It has been predicted that in this case the suppression factor F is equal to $(\Gamma_L^2 + \Gamma_R^2) / (\Gamma_L + \Gamma_R)^2$ [6], where $\Gamma_{L,R}$ are the leak rates from the state to the left and right contacts.

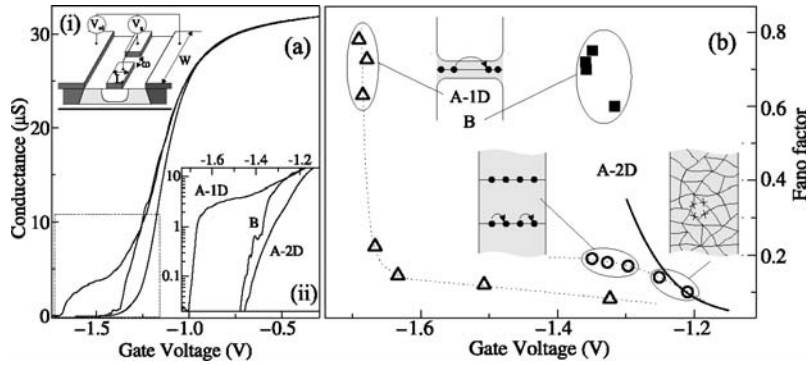


Fig. 1. (a) Conductance as a function of the gate voltage for 2D and 1D configurations at $T = 4.2$ K. Insets: (i) Cross-section of the transistor structure. (ii) Enlarged $G(V_g)$ near the pinch-off. (b) Fano factor for different samples with a schematic representation of hopping paths in each case. Small crosses show dominant hops. The solid line shows the $(L/L_c)^{-1}$ dependence and dotted lines are guides to the eye.

In our study of shot noise in resonant tunneling we have observed significant enhancement of shot noise [7]. We have proved that this effect is caused by the Coulomb interaction between two parallel resonant tunneling channels.

The experiment has been carried out on a n -GaAs MESFET consisting of a GaAs layer of $0.15 \mu\text{m}$ (donor concentration $N_d = 10^{17} \text{cm}^{-3}$). On the top of the GaAs layer Au gates are deposited with dimensions $L = 0.4$, $W = 4 \mu\text{m}$, and $L = 0.2$, $W = 20 \mu\text{m}$, Fig. 1a (i). By applying a negative gate voltage, V_g , a lateral potential barrier is formed between the ohmic contacts (source and drain). Some gates contain a split of width $\omega = 0.3, 0.4 \mu\text{m}$ with the aim to define a one-dimensional hopping channel.

2 Hopping

We have studied two gates on the same structure ($L = 0.4 \mu\text{m}$ and $W = 4 \mu\text{m}$) with splits of different width: $\omega = 0.3 \mu\text{m}$ (sample A) and $\omega = 0.4 \mu\text{m}$ (sample B). The sample with the narrow split shows different behaviour from one cooldown to another: two-dimensional (referred to as A-2D) and one-dimensional (A-1D), Fig. 1a. In the 1D configuration where the position of the conducting hopping chain is determined by the position of the split electron transport through the split is seen in Fig. 1a (ii) as a characteristic bend in the conductance. The second sample (B) has $G(V_g)$ that does not look similar to either of the two curves of the sample A. To determine the characteristic length L_c in the structure at different gate voltages, we have measured the T -dependence of the conductance of sample A in its 2D configuration.

We have measured the cross-correlated spectrum $S_I(I_{sd})$ [3]. In order to find the Fano factor we used the following fit $S_I(I_{sd}) = F2eI_{sd} \coth\left(\frac{FeV_{sd}}{2k_B T}\right) - 4k_B T G_S$, where G_S is the ohmic conductance [8, 9].

The Fano factor as a function of gate voltage for different structures is shown in Fig. 1b. In the 2D case the Fano factor slowly increases from 0.1 to 0.2 with decreasing V_g . According to the $N = 1/F$ -barrier model this change corresponds to a decrease in the number of dominant hops from 10 to 5. In the range V_g from -1.34 to 1.18 V we find agreement between the Fano factor and the number of the hard hops $N = L/L_c$. With depleting the conducting channel L_c increases and approaches L , while the Fano factor shows a saturation around $F \sim 0.2$. The difference between $(L/L_c)^{-1}$ and F confirms that electron transport at these gate voltages is determined by chains of hops [5, 4].

In A-1D sample the 1D channel is only formed at $V_g < -1.3$ V, Fig. 1a. In the range of V_g from -1.32 to -1.63 V, F increases from 0.07 to 0.15 which corresponds to $N \simeq 1/F = 7$. With further increasing negative gate voltage ($V_g < -1.65$ V) the Fano factor in Fig. 1b rapidly increases to 0.8. In this case, as the distribution of the resistances of these hops is exponentially broad, only a single hop dominates the whole conductance of the 1D channel, so that the Fano factor is close to 1.

For sample B the measurements of shot noise in the range of V_g from -1.36 V to -1.31 V have shown an increase of F from 0.6 to 0.8, Fig. 1b (sample B). This large value of the Fano factor compared with $F \sim 0.2$ expected for 2D hopping implies that hopping in this sample occurs through the 1D split and is dominated by one or two hard hops.

3 Resonant tunneling

Shot noise in the case of resonant tunneling through a single impurity has been studied on a 2D sample with the gate length $0.2 \mu\text{m}$ and width $20 \mu\text{m}$. Fig. 2a shows the increase of the amplitude of the peaks with decreasing T , which is a typical feature of RT through an impurity. The box in Fig. 2b indicates the range of V_g where shot noise has been studied at $1.85 \text{ K} < T < 4.2 \text{ K}$. In Fig. 2c (inset) an example of the shot noise spectrum is shown at a gate voltage near the RT peak in Fig. 2b.

Fig. 2c shows the dependence of the shot noise power on V_{sd} at two temperatures. At small biases ($V_{sd} < 3 \text{ mV}$) a pronounced peak in noise is observed, with an unexpectedly large Fano factor $F > 1$. At large biases ($V_{sd} > 3 \text{ mV}$), shot noise decreases to a conventional sub-Poisson value, $F \sim 0.6$. The figure shows the dependence $S_I(V_{sd})$ with different F plotted using the phenomenological expression for shot noise for RT through a single impurity $S_I = F2eI_{sd} \coth\left(\frac{eV_{sd}}{2k_B T}\right) - F4k_B T G_S$. We have established that this increase of shot noise appears not only at small V_{sd} , but also in a specific range

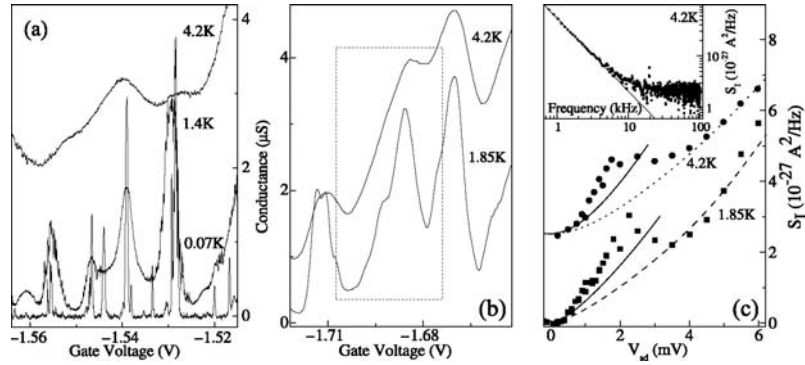


Fig. 2. (a) Typical RT peaks in the ohmic conductance. (b) Conductance peaks in the region of V_g where the current noise has been measured. (c) Shot noise power as a function of V_{sd} : at $V_g = -1.6945$ V for $T = 1.85$ K and $V_g = -1.696$ for $T = 4.2$ K. Lines show the dependencies $S_I(V_{sd})$ expected for resonant tunneling through a single impurity, with $F = 1$ (solid), $F = 0.63$ (dashed), and $F = 0.52$ (dotted). Inset: Excess noise spectrum at $V_g = -1.696$ V and $V_{sd} = 1.5$ mV.

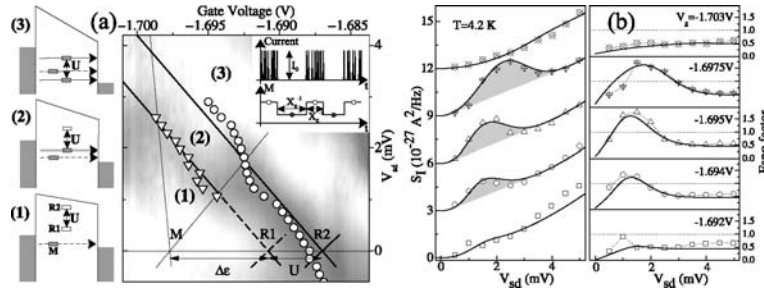


Fig. 3. (a) Left panel: Energy diagrams of the two impurities for different positive V_{sd} : $V_{sd}^{(1)} < V_{sd}^{(2)} < V_{sd}^{(3)}$. Inset: Schematic representation of the modulation of the current through R by modulator M . Main part: Grey-scale plot of the differential conductance as a function of V_g and V_{sd} at $T = 1.85$ K (darker regions correspond to higher differential conductance, background hopping contribution is subtracted). Lines show the positions of the conductance peaks of R and M obtained from the analysis. (b) Shot noise and the corresponding Fano factor as a functions of source-drain bias at different gate voltages. Solid lines show the results of the numerical calculation.

of V_g . It has been shown in [7] that the region V_{sd} - V_g with enhanced shot noise corresponds to the resonant current carried by two interacting impurities.

Consider two spatially close impurity levels, R and M , separated in the energy scale by $\Delta\epsilon$. If impurity M gets charged, the level R is shifted upwards by the Coulomb energy, Fig. 3a (diagram 1). Thus, depending on the occupation of M impurity R can be in two states: $R1$ or $R2$. If V_{sd} is small

enough, state $R2$ is above the Fermi level in the left contact, Fig. 3a (diagram 2). Hence, electrons are transferred via $R1$ with the rates $\Gamma_{L,R}$ only when M is empty. Let us assume that, impurity M (modulator) gets charged with rate X_c and empties with rate X_e . If $X_{e,c} \ll \Gamma_{L,R}$, the contribution of M to the total current is negligible, but the current through impurity R jumps randomly between two values: zero and I_0 , Fig. 3a (inset). If the bias is further increased, the upper state $R2$ is shifted down into the conducting energy strip and the modulation of the current via impurity R vanishes, Fig. 3a (diagram 3).

In such a modulation regime, the corresponding Fano factor can be written as $F = \frac{\Gamma_L^2 + \Gamma_R^2}{(\Gamma_L + \Gamma_R)^2} + 2 \frac{\Gamma_L \Gamma_R}{\Gamma_L + \Gamma_R} \frac{X_c}{(X_e + X_c)^2}$. The first term in this expression describes the conventional (suppressed) Fano factor for one-impurity RT [6], whereas the second term gives an enhancement of F . The generalisation of this simple model for any relation between X and Γ is based on the master equation formalism [6, 10]. As a result of the calculations, the current and the Fano factor are obtained as functions of the energy positions of the two impurities which are shifted with changing V_{sd} and V_g .

By measuring the differential conductance as a function of V_g and V_{sd} we have shown that the increase of shot noise occurs exactly in the region of V_g - V_{sd} where two interacting impurities carry the current in a correlated way, region 2 in Fig. 3a. In Fig. 3a at small V_{sd} a cross-like feature is clearly seen near point $R2$ – the exact positions of the maxima of the conductance peaks of this line are indicated by circles. With increasing V_{sd} , however, a new parallel line $R1$ appears at $V_g \approx -1.694$ V and $V_{sd} \approx 1$ mV. This happens when the line $R2$ enters the central area of cross M – the maxima of the conductance peaks of the new line are shown by triangles. In Fig. 3b current noise and the Fano factor are presented as functions of V_{sd} for different V_g . One can see that the modulation of the current occurs in region (2) of the central area of cross M , between lines $R1$ and $R2$.

For a quantitative analysis we have taken into account that in our experiment resonant tunneling via state R exists in parallel with the background hopping. Then the total Fano factor has to be expressed as $F = (F_{RT}I_{RT} + F_B I_B) / (I_{RT} + I_B)$, where F_{RT} , F_B and I_{RT} , I_B are the Fano factors and currents for RT and hopping, respectively. The numerical results have been fitted to the experimental data, Fig. 3b. The fitting parameters are $\hbar\Gamma_L \simeq 394$ μeV , $\hbar\Gamma_R \simeq 9.8$ μeV , $\hbar X_e \simeq 0.08$ μeV , $\hbar X_c \simeq 0.16$ μeV , $\Delta\varepsilon = 1$ meV, and $F_B = 0.45$. The coefficients in the linear relation between the energy levels M , R and V_{sd} , V_g have also been found to match both the experimental data in Fig. 3b and the position of lines $R1$ and $R2$ in Fig. 3a. One can see that the model gives good agreement with the experiment.

References

1. H. Birk, M.J.M. de Jong, and C. Schönenberger, *Phys. Rev. Lett.* **75**, 1610 (1995).
2. V.V. Kuznetsov, E.E. Mendez, G.L. Snider, E.T. Croke, *Phys. Rev. Lett.* **85**, 397 (2000).
3. S.H. Roshko, S.S. Safonov, A.K. Savchenko, W.R. Tribe, E.H. Linfield, *Physica E* **12**, 861 (2001).
4. M.E. Raikh and A.N. Ruzin. in *Mesoscopic Phenomena in Solids*, eds B.L. Altshuler, P.A. Lee, and R.A. Webb (Elsevier Science, Amsterdam, 1991).
5. A.O. Orlov, M.E. Raikh, I.M. Ruzin, and A.K. Savchenko, *Sov. Phys. JETP* **69**, 1229 (1989).
6. Y.V. Nazarov and J.J.R. Struben, *Phys. Rev. B* **53**, 15466 (1996).
7. S.S. Safonov, A.K. Savchenko, D.A. Bagrets, O.N. Jouravlev, Y.V. Nazarov, E.H. Linfield, D.A. Ritchie, *Phys. Rev. Lett.* (accepted for publication, 2003).
8. A. van der Ziel. *Noise in Solid State Devices and Circuits*. (Wiley, New York, 1986).
9. A.N. Korotkov and K.K. Likharev, *Phys. Rev. B* **61**, 15975 (2000).
10. L.I. Glazman and K.A. Matveev, *Sov. Phys. JETP* **67**, 1276 (1988).

Single Electron Physics

Single Particle Transport in Disordered Andreev Wires

N.B. Kopnin¹, A.S. Mel'nikov², and V.M. Vinokur³

¹ L. D. Landau Institute for Theoretical Physics, Russian Academy of Sciences, 117940 Moscow, Russia kopnin@boojum.hut.fi

² Institute for Physics of Microstructures, Russian Academy of Sciences, 603950, Nizhny Novgorod, GSP-105, Russia

³ Materials Science Division, Argonne National Laboratory, Argonne, Illinois 60439, USA

Summary. We study how the single-electron transport in clean Andreev wires is affected by a weak disorder introduced by impurity scattering. The transport has two contributions, one is the Andreev diffusion inversely proportional to the mean free path ℓ and the other is the drift along the transverse modes that increases with increasing ℓ . This behavior leads to a peculiar re-entrant localization as a function of the mean free path.

1 Introduction

Transport of electrons along conducting wires surrounded by insulators have been studied for several decades; mechanisms of the transport phenomena involved are nowadays well understood (see [1, 2, 3] for review). In the ballistic regime where the mean free path is much longer than the wire lengths, $\ell \gg d$, the conductance is given by the Sharvin expression, $G = (e^2/\pi\hbar)N$, where $N \sim (k_F a)^2$ is the number of transverse modes, a is the wire radius, $a \ll d$, and k_F is the Fermi wave vector. For a shorter mean free path $\ell \ll d$, a diffusion controlled transport is obtained with the ohmic behavior of the conductance, $G \sim (e^2/\pi\hbar)N\ell/d$, neglecting the weak localization interference between scattered electronic waves. With a further decrease in the ratio ℓ/d , the ohmic behavior breaks down due to the localization effects when $\ell/d < N^{-1}$: the conductance appears to decay exponentially [4].

The picture above is essentially based on the assumption that electrons are confined inside the wire by the insulating gap in the material around the wire being reflected from the wall. Another way to confine electrons within

a normal wire is to place the wire of a radius a much larger than the coherence length ξ into a superconducting environment. Due to the presence of a superconducting gap Δ the density of states outside the normal wire tends to zero for excitation energies $\epsilon < \Delta$, thus the low-energy electronic states are confined in the transverse direction of the normal metal channel. The nature of these states is determined by the particle-hole Andreev reflection processes at the superconducting/normal-metal (SN) boundaries. If the usual (with a large momentum transfer) reflection processes at the SN boundaries can be ignored, we refer to such a normal conducting region *inside* a superconducting environment as to an ‘‘Andreev wire’’. An Andreev wire can be connected through bulk normal-metal leads to an external measuring circuit. Note that our definition of Andreev wire differs from that used, e.g., in Ref. [5] where it was applied for a normal conductor in an insulating environment, *connected* to superconducting leads. A simple way to create Andreev wires is to introduce vortex lines in a type-II superconductor by applying a magnetic field. Andreev wires can be manufactured artificially in the form of normal channels in a superconducting matrix, using modern nano-fabrication techniques employed also for producing a wider class of hybrid SN structures (Andreev interferometers [6] and billiards [7]). From the experimental point of view, the most important difference between an Andreev wire and a normal channel surrounded by an insulator is that measurements of the thermal conductance are more appropriate than those of electrical conductance to probe the single electron transport in an Andreev wire because the single-particle part of the charge transport is short-circuited by the superflow.

2 Transport Properties

Usually, the electronic thermal conductance κ can be calculated from the Wiedemann – Franz law, $\kappa \sim TG/e^2$. However, as shown in Ref.[8, 9] for the ballistic limit $\ell \gg d$, this law gives a wrong result for Andreev wires if one uses an expression for G obtained for a wire surrounded by an insulator. Andreev processes strongly suppress the single electron transport for all quasiparticle trajectories except for those which have momenta almost parallel to the wire thus avoiding Andreev reflection at the walls. The resulting expression for the thermal conductance

$$\kappa_{bal} \sim (T/\hbar)(k_F a)^2 (a^2/d^2). \quad (1)$$

appears to be much smaller than what can be derived from the Sharvin expression for G . This conductance decreases rapidly with increasing d and finally saturates at a yet smaller Landauer-like expression [9]

$$\kappa_L \sim (T/\hbar)(k_F a)^2 (v_g/v_F) \sim (T/\hbar)(k_F a)^2 (T/E_F) \quad (2)$$

that is proportional to a non-quasiclassical group velocity of a slow drift of particles along the transverse modes (Andreev states in the wire) $v_g = \hbar^{-1} \partial \epsilon_{k_z} / \partial k_z \sim \epsilon / p_F$ much smaller than v_F .

Here we report how the single electron transport in Andreev wires at low temperatures $T \ll T_c$ is affected by a weak disorder introduced by impurity scattering assuming that inelastic processes are negligible. The Andreev wire is clean in the sense that the mean free path ℓ is much longer than the wire diameter, $\ell \gg a$.

We find that disorder modifies both the free motion of particles and the drift along the Andreev states. Let us discuss these two mechanisms in turn. Consider a quasiparticle propagating within the wire along a trajectory that bounces from the normal/superconducting walls at both its ends. Neglecting the slow drift, the distributions of particles and holes are equal at the wall due to the Andreev reflection. If quasiparticle scattering is absent, the distributions remain equal throughout the wire, thus there is no net single-particle transport associated with these trajectories. In the presence of scattering, the distributions of particles and holes deviate from each other by an amount proportional to the probability of scattering, a/ℓ . In the presence of a gradient of the distribution function produced by the temperature difference at the ends of the wire, the electronic thermal conductance becomes

$$\kappa_A = A(T/\hbar)(k_F a)^2(a^2/\ell d) \quad (3)$$

where $A \sim \ln(\ell/a)$. It is different from the standard expression for the electronic thermal conductance in a diffusive normal wire

$$\kappa \sim (T/\hbar)(k_F a)^2(\ell/d). \quad (4)$$

The counter-intuitive behavior of the single-particle conductance Eq. (3) which *increases* with *decreasing* ℓ was first predicted by Andreev [10]. Comparing Eq. (3) with the ballistic ($\ell \gg d$) expression Eq. (1) we see that disorder with $\ell \ll d$ stimulates the single-particle transport by opening of new single-particle conducting modes that are blocked by Andreev reflections in the ballistic limit. The conductance reaches its maximum when the mean free path decreases down to $\ell \sim a$, after which the distinction between the usual and the Andreev diffusion is lost and Eq. (3) transforms into Eq. (4) for a dirty wire (see [11] for the particular case of vortex lines).

The drift along Andreev bound states with a group velocity v_g , which is due to a small non-quasiclassical particle-hole asymmetry, is also modified by disorder. We demonstrate that the characteristic mean free path $\ell_{\text{drift}} \sim v_g \tau$ relevant for the drift transport is considerably shorter than the usual mean free path ℓ . For $\ell_{\text{drift}} \ll d$, the thermal conductance associated with the disorder-modified drift is *proportional* to the mean free path with a qualitative behavior

$$\kappa_L \sim (T/\hbar)(k_F a)^2(v_g/v_F)^2(\ell/d). \quad (5)$$

It saturates at the ballistic Landauer expression Eq. (2) for enormously long $\ell \gg (v_F/v_g)d$, i.e., when $\ell_{\text{drift}} \gg d$.

The total single-particle transport of a clean Andreev wire contains two contributions: one is the Andreev diffusion decreasing as ℓ^{-1} and the other

is the diffusive drift that increases with increasing ℓ . Introducing an effective number of transverse modes $N = \kappa\hbar/T$ we have

$$N \sim (k_F a)^2 \left[A \left(\frac{a^2}{\ell d} \right) + B \left(\frac{v_g}{v_F} \right)^2 \frac{\ell}{d} \right] \quad (6)$$

where $B \sim 1$. The number of modes has a minimum as a function of ℓ . This behavior gives rise to a peculiar re-entrant localization as a function of the mean free path: for a long enough Andreev wire, the quasiparticles with $\epsilon < \Delta$ may become localized not only in a dirty limit for a short mean free path $\ell < d(k_F a)^{-2}$ but also in a clean limit for a long mean free path $\ell \sim a(v_F/v_g)$ if the length of the wire is $d > d_c$ where $d_c \sim a(k_F a)^2(v_g/v_F)$. In the latter case, an increase or decrease in ℓ can lead to re-opening of the conduction via the Landauer drift or Andreev diffusion, respectively.

3 Conclusions

In conclusion, we mention that the effects of disorder on the kinetics of quasiparticles confined in an insulator/normal-metal/superconductor (INS) hybrid structure due to Andreev reflections was first considered in Ref. [12] within a model where the disorder is provided by irregularities on the I/N boundary through the normal scattering of quasiparticles.

Acknowledgements.— This work was supported in part by the US DOE Office of Science under contract No. W-31-109-ENG-38, by Russian Foundation for Basic Research, the Program “Quantum Macrophysics” of the Russian Academy of Sciences, Russian State Fellowship for young doctors of science, and NATO Collaborative Linkage Grant No. PST.CLG.978122. A.S.M. is grateful to the Low Temperature Laboratory at the Helsinki University of Technology for hospitality.

References

1. Y. Imry, *Introduction to Mesoscopic Physics*, Oxford University Press (Oxford, 1997).
2. S. Datta, *Electronic Transport in Mesoscopic Systems*, Cambridge University Press (Cambridge, 1995).
3. C. W. J. Beenakker, *Rev. Mod. Phys.* **69**, 731 (1997).
4. D. J. Thouless, *Phys. Rev. Lett.* **39**, 1167 (1977).
5. B. Reulet, A. A. Kozhevnikov, D. E. Prober, W. Belzig, and Yu. V. Nazarov, *Phys. Rev. Lett.* **90**, 066601 (2003).
6. D. Esteve et al., in: *Mesoscopic Electron Transport* edited by L. L. Sohn, L. P. Kouwenhoven, and G. Schon, NATO ASI Series E345, Kluwer Academic Publishers (Kluwer, Dordrecht, 1997).
7. I. Kosztin, D. L. Maslov, and P. M. Goldbart, *Phys. Rev. Lett.* **75**, 1735 (1995).

8. A. S. Mel'nikov and V. M. Vinokur, *Nature*, **415**, 60 (2002); *Phys. Rev. B* **65**, 224514 (2002).
9. N. B. Kopnin, A. S. Mel'nikov and V. M. Vinokur, cond-mat/0302540; *Phys. Rev. B*, to be published (2003).
10. A. F. Andreev, *Zh. Eksp. Teor. Fiz.* **47**, 2222 (1964) [*Sov. Phys. JETP* **20**, 1490 (1965)].
11. N. B. Kopnin, *Zh. Eksp. Teor. Fiz.* **69**, 364 (1975) [*Sov. Phys. JETP*, **42**, 186 (1975)].
12. A. V. Shytov, P. A. Lee, and L. S. Levitov, *Usp. Fiz. Nauk* **168**, 222 (1998) [*Physics–Uspekhi*, **41**, 207 (1998)].

Two-Channel Kondo Effect in a Modified Single Electron Transistor

Yuval Oreg

Department of Condensed Matter Physics, Weizmann Institute of Science, Rehovot, 76100, Israel yuval.oreg@weizmann.ac.il

Summary. We suggest a simple system of two electron droplets which should display two-channel Kondo behavior at experimentally-accessible temperatures. Stabilization of the two-channel Kondo fixed point requires fine control of the electrochemical potential in each droplet, which can be achieved by adjusting voltages on nearby gate electrodes. We study the conditions for obtaining this type of two-channel Kondo behavior, discuss the experimentally-observable consequences, and explore the generalization to the multi-channel Kondo case.¹

1 Introduction

The single-channel Kondo (1CK) effect has been studied for decades in metals with magnetic impurities [1]. The same phenomenon has recently been observed in the novel context of semiconductor nanostructures containing no magnetic impurities: here, an electron droplet with a degenerate ground state assumes the role of a magnetic impurity, and nearby electron reservoirs act as the surrounding normal metal [2, 3, 4, 5, 6, 7]. These semiconductor systems are extremely flexible. The electron droplet's shape and size are determined by lithographic patterning, and its occupancy, energy levels, and coupling to external reservoirs can be precisely measured, and even tuned *in-situ* using gate voltages. This unique tunability has enabled the first precision measurements of Kondo temperature as a function of system parameters, yielding an excellent match to theory [4, 8]. Experiments on semiconductor nanostructures have also accessed new regimes, notably the low-temperature unitary limit [5], Kondo effect out of equilibrium [9], and the single mixed-valence impurity [4]. These experiments have even introduced exotic varieties of Kondo

¹ This manuscript is a copy of Yuval Oreg and David Goldhaber-Gordon Phys. Rev. Lett. 90, 136602 (2003). Copyright (2003) by the American Physical Society.

effect never seen in bulk studies, such as magnetic field-induced Kondo [10, 11] and two-impurity Kondo [12]. As with conventional 1CK, each of these systems displays an interesting many-body resonance. However, at very low T we can describe each system simply as a Fermi liquid superimposed with a resonance [13]; *i.e.*, there is no non-Fermi liquid ground state.

Studying two-channel Kondo (2CK) effect [14, 15, 16, 17, 18] in semiconductor nanostructures could be even more intriguing. In 2CK, a twofold degenerate system such as a local spin is antiferromagnetically coupled to not one, but two independent electron reservoirs. Since the reservoirs do not communicate, each attempts to screen the local spin, resulting in overall overscreening. Unlike 1CK, this system exhibits fascinating low-energy non-Fermi-liquid behavior [19, 20]. Yet there have been no conclusive experimental observations of 2CK [14, 16, 21]. Indeed, in contrast to single-channel Kondo, 2CK effect is not likely to occur in ordinary metals with magnetic impurities, due to intrinsic channel anisotropy [22]. Ralph reported observation of 2CK, with local near-degeneracies associated with atomic tunneling in a disordered metal rather than the traditional spin. The observed behavior is striking, but its physical origin has remained controversial [16, 21].

2 Model and Results

In this paper we argue that a simple configuration of two electron droplets (see Fig. 1) attached to conducting leads can exhibit 2CK correlations [19, 20], retaining non-Fermi-liquid (NFL) behavior at low temperature.

The relevant fixed point is stabilized at low temperature by fine tuning the voltage on just one gate electrode. Near a 2CK fixed point, quantities such as specific heat, entropy and spin susceptibility [20] behave differently than they would in a Fermi liquid. The conductance through our model system should exhibit an anomalous power-law dependence on temperature, deviating from its $T = 0$ value as \sqrt{T} [20] rather than T^2 . The simplicity of the structure and the ability to tune system parameters offer hope for detailed study of the NFL realm, including non-thermodynamic quantities such as transmission phase [23], noise [24], pumping [25], and tunneling density of states.

In our model, a small central electron droplet (denoted by d) hosts a single level of energy ε_{ds} , which can be empty, or occupied by electrons of either or both spin directions $s = \uparrow, \downarrow$. Henceforth we refer to this droplet as *small dot d*. The spin of the (singly-occupied) small dot d serves as the local degeneracy needed for 2CK. Connected to small dot d by tunneling are two conducting leads, plus an additional, much larger dot. In the large dot we neglect the discreteness of single-particle energy levels, while retaining a finite Coulomb energy. Thus, this dot behaves as a ‘‘Coulomb-interacting lead’’; we refer to it as *large dot m*.

For fixed number of electrons: n_m on dot- m and n_d on dot- d , the electrostatic energy $E_{n_d}^{n_m} \equiv E_{n_d}^{n_m}(\mathcal{V}_m, \mathcal{V}_d)$ is:

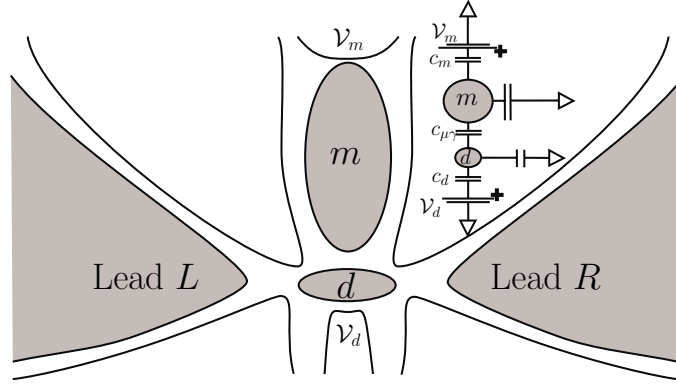


Fig. 1. A proposed realization of the two-channel Kondo (2CK) model. Two non-interacting leads (L and R) and a large dot m are attached to a single-level small dot d . If dot d is occupied by a single electron, it can flip its spin by virtually hopping the electron onto either dot m or the leads, and then returning an electron with opposite spin to dot d . Dot m and the leads thus serve as the two distinct screening channels required to produce the 2CK effect. Crucially, when kT is smaller than the charging energy of dot m , Coulomb blockade blocks transfer of electrons between the leads and dot m . Fine tuning of the voltage \mathcal{V}_m (and/or \mathcal{V}_d) can equalize the coupling to the two channels, stabilizing the 2CK fixed point.

$$E_{n_d}^{n_m} = U (n_d - \mathcal{N}_d)^2 + u_m (n_d + \alpha n_m - \mathcal{N})^2, \quad (1)$$

where $U \equiv e^2/(2\tilde{C}_d) \gg u_m \equiv e^2/(2\tilde{C}_m - c_\mu^2/\tilde{C}_d)$, $|e|\mathcal{N}_d \equiv c_d\mathcal{V}_d$, $|e|\mathcal{N} \equiv c_m\mathcal{V}_m + c_dc_\mu/\tilde{C}_m\mathcal{V}_d$ and $\alpha \equiv c_\mu/\tilde{C}_d \lesssim 1$. Here $\tilde{C}_{m(d)}$ is the *total* capacitance of dot $m(d)$. See Fig. 1 for definitions of the other capacitances. Note that the parameter \mathcal{N}_d controls the number of electrons on the small dot while \mathcal{N} controls the total number of electrons on both dots combined. Since dot m is large we may assume that \tilde{C}_m is much larger than all other capacitances.

To write down the full Hamiltonian H of the model system, it is useful to perform a transformation on the operators L_{ks} and R_{ks} for electrons in leads L and R , respectively [26]. We define $\psi_{ks} = \cos\theta L_{ks} + \sin\theta R_{ks}$, $\phi_{ks} = \cos\theta R_{ks} - \sin\theta L_{ks}$, $\tan\theta = V_R/V_L$, $V_\psi = \sqrt{|V_L|^2 + |V_R|^2}$. Without loss of generality we take the coupling constants V_i , $i = L, R, m$, to be real. With these definitions, the new effective lead ψ couples to the small dot d , but the effective lead ϕ does not couple:

$$H = \sum_{i=\phi,\psi,m;ks} \varepsilon_{iks} i_{ks}^\dagger i_{ks} + \sum_s \varepsilon_{ds} d_s^\dagger d_s + E_{n_m}^{n_d} + V_m \sum_{ks} m_{ks}^\dagger d_s + V_\psi \sum_{ks} \psi_{ks}^\dagger d_s + \text{h.c.}, \quad (2)$$

To obtain a 2CK fixed point we assume that \mathcal{V}_d is tuned to make the average occupancy of the small dot $n_d = 1$, creating a local spin- $\frac{1}{2}$. We further

assume that $D, U \gg u_m$, with D a cutoff of order the Fermi energy [27]. With decreasing temperature the system evolves through several stages. Formally, we integrate out the fast variables progressively in the renormalization group (RG) sense. Details of this calculation will be published elsewhere.

For $kT > U$, charge fluctuations on both the small and large dots are possible. Haldane showed [8] that in this regime only the level energy ε_d is renormalized, while the couplings to the leads remain the same. For $kT \lesssim U$ we may perform the Schrieffer-Wolff transformation. In this transformation charge fluctuations on the small dot are eliminated, and the effect of virtual electron hopping is simply to flip the spin on the small dot. Our Anderson-like Hamiltonian is mapped onto a 1CK Hamiltonian. In the present case we have four possible spin flip events. Two are diagonal processes in which an electron hops onto dot d from lead ψ (large dot m) and then an electron with opposite spin hops off to the same lead ψ (large dot m). And two are off-diagonal processes in which an electron hops onto dot d from lead ψ (large dot m) and then an electron with opposite spin hops off to large dot m (lead ψ). (Four “hole” processes, in which an electron first hops *from* the dot to lead ψ or large dot m , are also possible). As T decreases further, so long as $kT > u_m$ charge fluctuations on large dot m are allowed and the system flows according to the single channel Kondo RG laws [8]. However, for $kT < u_m$ charge fluctuations on the large dot are not possible and off-diagonal hopping is suppressed. Diagonal spin flip events remain possible. In this regime we obtain the standard two-channel Kondo model [20], with an additional free channel ϕ which decouples from the rest of the system [see also Eq. (8)]. The diagonal exchange coupling constants (at scale U) are:

$$\begin{aligned}\tilde{J}_{mm}(\mathcal{V}_m, \mathcal{V}_d) &\equiv \Gamma_m \left[\frac{1}{E_0^1 - E_1^0} + \frac{1}{E_2^{-1} - E_1^0} \right]; \\ \tilde{J}_{\psi\psi}(\mathcal{V}_m, \mathcal{V}_d) &\equiv \Gamma_\psi \left[\frac{1}{E_2^0 - E_1^0} + \frac{1}{E_0^0 - E_1^0} \right].\end{aligned}\quad (3)$$

Here $\Gamma_{m(\psi)} = |V_{m(\psi)}|^2 \nu_{m(\psi)}$ is the rate of tunneling between dot d and dot m (effective lead ψ); and E_{nd}^{nm} are defined in Eq. (1). To obtain a 2CK fixed point we tune \mathcal{V}_m and \mathcal{V}_d to make \tilde{J}_{mm} , the antiferromagnetic coupling of dot d to dot m , equal to $\tilde{J}_{\psi\psi}$, the antiferromagnetic coupling of dot d to the leads. Eq. (3) and the ratio $\gamma \equiv \Gamma_m/\Gamma_\psi$ define a curve in the $\mathcal{V}_m, \mathcal{V}_d$ plane. In Fig. 2 we show these “2CK lines” for two different values of γ , both of order 1. On these lines 2CK physics should be realized at low T . We did not consider in Fig. 2 the renormalization of the parameters at scales below U , which may modify the detailed shape of the curves.

The 2CK fixed point can be reached experimentally by a three-step procedure: First, fix \mathcal{V}_d to give one electron (or an odd number of electrons) in the small dot. Second, tune γ to roughly 1 by adjusting the individual tunneling rates. No great precision is required in this step. Finally, fine-tune \mathcal{V}_m so that

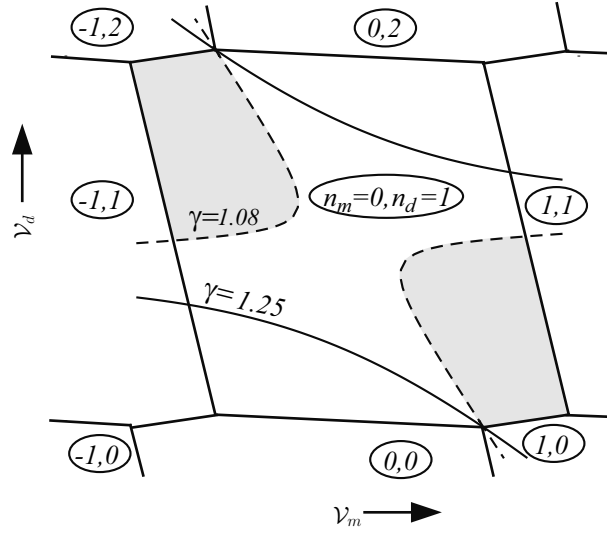


Fig. 2. The number of electrons on dots m and d are functions of the gate voltages \mathcal{V}_m and \mathcal{V}_d . Within the central hexagon, dot d is singly-occupied, a prerequisite for observation of Kondo effect. Curves superimposed on this hexagon (“2CK lines”) map where in the $\mathcal{V}_m, \mathcal{V}_d$ plane the two-channel Kondo (2CK) effect is realized for two different values of the coupling ratio $\gamma \equiv \Gamma_m/\Gamma_\psi$ — each value gives rise to a pair of disjoint curves. As illustrated for $\gamma = 1.08$ (dashed) these two curves divide the hexagon into three regions with distinct low-temperature fixed points. On the curves, the 2CK effect is realized and the deviation of the inter-lead differential conductance from its $T \rightarrow 0, \mathcal{V}_{LR} \rightarrow 0$ limit $G(0,0)$ is $\propto \sqrt{\max(T, \mathcal{V}_{LR})}$ [Eq. (4)]. In the shaded regions at top left and bottom right, dot m “wins”, forming an exclusive 1CK resonance with dot d , and driving $G(T, \mathcal{V}_{LR})$ close to zero [Eq. (5)]. By contrast, in the large unshaded region, leads L and R “win” giving rise to familiar Fermi-liquid behavior $G(0,0) - G(T, \mathcal{V}_{LR}) \propto [\max(T, \mathcal{V}_{LR})]^2$, [Eq. (6)]. With increasing γ , the regions where dot m wins grow and merge, while the region where the leads win shrinks and splits.

$\tilde{J}_{mm}(\mathcal{V}_m, \mathcal{V}_d) = \tilde{J}_{\psi\psi}(\mathcal{V}_m, \mathcal{V}_d)$. In Fig. 2 this corresponds to tuning \mathcal{V}_m until we hit a 2CK line for our given value of γ .

The current I between the left and right leads can be measured as a function of T , and as a function of \mathcal{V}_{LR} , the bias applied between leads L and R (see Fig. 1). Drawing on the extensive literature of 2CK physics [14] we can predict the qualitative behavior of the I - \mathcal{V}_{LR} curve through the dot, for different values of the gate voltages $\mathcal{V}_m, \mathcal{V}_d$ that scan the hexagon of Fig. 2. On the 2CK lines (see Fig. 2) in the unitary limit — $T, \mathcal{V}_{LR} \ll$ Kondo temperature $T_K \cong \sqrt{U\Gamma_m}/2 e^{-1/\tilde{J}_{mm}(\mathcal{V}_m, \mathcal{V}_d)}$ — the differential conductance $G(T, \mathcal{V}_{LR}) \equiv dI/d\mathcal{V}_{LR}$ should approach its limiting value $G(0,0)$ as

$$2CK: G(0,0) - G(T, \mathcal{V}_{LR}) \propto \sqrt{\max(\mathcal{V}_{LR}, kT)}. \quad (4)$$

In the symmetric case $V_L = V_R$, we get $G(0,0) = G_K \equiv e^2/h$, half the maximal value of $G(0,0)$ in the 1CK effect [5, 7].

In the part of the hexagon where $\tilde{J}_{mm} > \tilde{J}_{\psi\psi}$ (shaded, for $\gamma = 1.08$), at low T the electrons in dot m screen the spin of dot d , while the leads are decoupled. In the RG sense $\tilde{J}_{\psi\psi}$ flows to zero, so that dot m “wins” over the leads and forms a 1CK state with dot d . In this case $dI/d\mathcal{V}_{LR}$ is small and given by

$$\text{Large dot wins: } G(T, \mathcal{V}_{LR}) \propto [\max(\mathcal{V}_{LR}, kT)]^2. \quad (5)$$

In contrast, in the unshaded part of the hexagon in Fig. 2, where $\tilde{J}_{mm} < \tilde{J}_{\psi\psi}$, dot m decouples from dot d at low T , leaving the leads to form a 1CK resonance with dot d and

$$\text{Leads win: } G(0,0) - G(T, \mathcal{V}_{LR}) \propto [\max(\mathcal{V}_{LR}, kT)]^2, \quad (6)$$

where $G(0,0) = 2G_K$ for $V_L = V_R$.

At sufficiently low temperature the finite level spacing Δ_m in dot m will cut off the RG flow of the coupling constants [28]. We cannot make Δ_m infinitesimal as we must retain a finite Coulomb blockade energy [29] $u_m > kT$. However, the ratio between charging energy and level spacing can be made large, allowing 2CK behavior to be observed over an order of magnitude in temperature before the system finally flows to the 1CK fixed point.

The above discussion can be generalized to include $M - 1$ large dots, resulting in an M -channel Kondo (MCK) model, which may be possible (though challenging) to realize experimentally for $M > 2$.

To describe this system we use the model Hamiltonian:

$$H = \sum_{aks} \varepsilon_{aks} a_{ks}^\dagger a_{ks} + \sum_a u_a (n_a - \mathcal{N}_a)^2 + \sum_s \varepsilon_d d_s^\dagger d_s + U n_{d\uparrow} n_{d\downarrow} + \sum_{ks} V_{ak}^* a_{ks}^\dagger d_s + \text{h.c.} \quad (7)$$

Here a_{ks} is the annihilation operator of an electron in state k , with spin s and energy ε_{aks} on large dot a . $a = 1, \dots, M$, $n_a = \sum_{ks} a_{ks}^\dagger a_{ks}$, and the parameter \mathcal{N}_a sets dot a 's equilibrium occupancy.

The physical role of the u_a terms is clear: at low temperatures they forbid processes in which charge is ultimately transferred from one large dot to another. Spin flip events — e.g. when an electron hops onto the small dot and then an electron with opposite spin hops off the small dot to the same large dot — remain possible and under appropriate conditions lead to a MCK fixed point.

After integrating out energies larger than U [8], we perform the Schrieffer-Wolff transformation [30] and find that the second line of Eq. (7) is transformed to

$$\sum_{ab,kq} J_{ab}^{kq} \left[S^+ s_{ab}^{-kq} + S^- s_{ab}^{+kq} + 2S^z s_{ab}^{zkq} \right], \quad (8)$$

$S^\pm = d_{\uparrow(\downarrow)}^\dagger d_{\downarrow(\uparrow)}$, $2S^z = d_{\uparrow}^\dagger d_{\uparrow} - d_{\downarrow}^\dagger d_{\downarrow}$, $s_{ab}^{\pm kq} = a_{k\uparrow(\downarrow)}^\dagger b_{q\downarrow(\uparrow)}$ and $2s_{ab}^{zkq} = \frac{1}{2} a_{k\uparrow}^\dagger b_{q\uparrow} - a_{k\downarrow}^\dagger b_{q\downarrow}$. With $V_{aq} = V_{bk} \equiv V$, and assuming that $\varepsilon_{a(b)qs} \approx \varepsilon_{a(b)F}$, where $\varepsilon_{a(b)F}$ is the last empty (occupied) level in dot a (b), we find:

$$J_{ab}^{kq} = J_{ab} = |V|^2 \frac{U + u_b^- + u_a^+}{[U + \varepsilon_d + u_b^-] [u_a^+ - \varepsilon_d]}, \quad (9)$$

where $u_p^\pm = u_p [1 \pm 2(n_p - \mathcal{N}_p)] \pm \varepsilon_{pF}$, $p = a, b$. For $-1/2 < \mathcal{N}_p - n_p + (\mu - \varepsilon_{pF})/(2u_p) < 1/2$ there are n_p electrons in dot p , where μ is the electrochemical potential of a reference reservoir. Particle-hole symmetry may be absent in the large dots, so in general $J_{ab} \neq J_{ba}$.

At $kT > \max\{u_{ab}\}$ the system evolves according to the 1CK RG flow, where $u_{ab} = (u_a^+ + u_b^-)(1 - \delta_{ab})$. At $kT < \min\{u_{ab}\}$, $a \neq b$, the off-diagonal processes describing transfer of an electron from dot b to dot a are exponentially suppressed as $J_{ab} = J_{ab}^0 e^{u_{ab}/(4kT)}$. Notice that $u_{aa} = 0$, since the charge on dot a is not changed when an electron hops from dot a onto dot d and then back to the same dot a . At $kT < \min\{u_{ab}\}$ only the diagonal terms of J_{ab} do not flow to zero. Assuming that we are not at a degeneracy point where $u_{ab} = 0$, an easy condition to avoid, the RG equations are identical to the MCK RG equations [22]. As in the case of classic MCK, our NFL fixed point is unstable to the introduction of channel anisotropy. If one of the coupling constants is larger than the others, the corresponding channel alone screens the local spin and forms a Kondo resonance while the other channels are decoupled from the local spin. In our model we can tune all the \mathcal{N}_a to achieve $J_{aa} = J$ for all a .

Gate voltages capacitively control the energy of the last occupied level in each large dot, so excitations in each large dot will be around a different Fermi energy. This does not modify the RG equations, but does affect certain physical properties such as the small dot density of states at finite energies. A similar situation occurs in the discussion of 2CK in a dot out of equilibrium [15, 18].

3 Conclusions

In conclusion, if a small dot is coupled to two (or more) electron reservoirs, Coulomb blockade can suppress inter-reservoir charge transfer at low temperatures. Electrostatic gates provide the tunability needed to stabilize a 2CK fixed point, resulting in observable NFL behavior. Softer suppressions of inter-reservoir tunneling could also work in place of Coulomb blockade. For example, the reservoirs could be conductors with large impedance [31], one-dimensional Luttinger liquids [32] or conductors with strongly-interacting charge carriers.

Finally, while the channel asymmetry parameter is relevant in the RG sense, for realistically well-matched channel couplings we expect that the system will remain near the 2CK fixed point, and will show NFL behavior, over a wide range of temperatures.

Acknowledgements.— It is our pleasure to acknowledge useful discussions with Natan Andrei, Michel Devoret, Leonid Glazman, Gabi Kotliar, Leo Kouwenhoven, Yigal Meir, Ron Potok, Arcadi Shechter, Alex Silva, Ned Wingreen, and especially Avi Schiller. This work was supported by DIP grant c-7.1, by ISF grant 160/01-1, and by Stanford University.

References

1. A. C. Hewson, *The Kondo Problem to Heavy Fermions* (Cambridge University Press, Cambridge, 1993).
2. D. Goldhaber-Gordon, H. Shtrikman, D. Mahalu, D. Abusch-Magder, U. Meirav, and M. A. Kastner, *Nature* **391**, 156 (1998).
3. S. M. Cronenwett, T. H. Oosterkamp, and L. P. Kouwenhoven, *Science* **540**, 281 (1998).
4. D. Goldhaber-Gordon, J. Göres, M. A. Kastner, H. Shtrikman, D. Mahalu, and U. Meirav, *Phys. Rev. Lett.* **81**, 5225 (1998).
5. W. G. van der Wiel *et al.* *Science* **289**, 2105 (2000).
6. J. Nygard, D. H. Cobden, and P. E. Lindelof, *Nature* **408**, 342 (2000).
7. W. Liang, M. Bockrath, and H. Park, *Phys. Rev. Lett.* **88**, 126801 (2002).
8. F. D. M. Haldane, *Phys. Rev. Lett.* **40**, 416 (1978).
9. S. De Franceschi *et al.* *cond-mat/0203146* (2002).
10. S. Sasaki *et al.* *Nature* **764**, 405 (2000).
11. M. Pustilnik, Y. Avishai, and K. Kikoin, *Phys. Rev. Lett.* **84**, 1756 (2000), and M. Pustilnik and L. I. Glazman *Phys. Rev. B* **64** 045328 (2001).
12. H. Jeong, A. M. Chang, and M. R. Melloch, *Science* **293**, 2221 (2001).
13. P. Nozières, *J. Low Temp. Phys.* **17**, 31 (1974).
14. D. Cox and A. Zawadowski, *Advances in Physics* **47**, 599 (1998), *cond-mat/9704103*.
15. We emphasize that our proposal differs from other suggested experimental realizations of the 2CK effect [16, 17], in that our local degeneracy comes from spin rather than charge or some other two-level system. Our mapping differs from that of [17] in several essential ways: we consider a system with fixed electron number in what would otherwise be a Coulomb valley, not a charge degeneracy point; our Kondo temperature is set by the charging energy of a small dot; and we do not require single-mode coupling between the dot and leads. Our 2CK effect is realized at equilibrium, avoiding decoherence and suppression of 2CK by voltage-driven current [18].
16. D. C. Ralph and R. A. Buhrman, *Phys. Rev. Lett.* **69**, 2118 (1992), and *Phys. Rev. B* **51**, 3554 (1995); and D. C. Ralph *et al.* *Phys. Rev. Lett.* **72**, 1064 (1994).
17. K. A. Matveev, *Phys. Rev. B* **51**, 1743 (1995).
18. A. Rosch, J. Kroha, and P. Wölffe, *Phys. Rev. Lett.* **87**, 156802 (2001).
19. N. Andrei and C. Destri *Phys. Rev. Lett.* **52**, 364 (1984); P. B. Wiegmann and A. M. Tsvelick *Z. Phys. B* **54**, 201 (1985)

20. I. Affleck and A. W. W. Ludwig, Phys. Rev. B **48**, 7297 (1993).
21. N. S. Wingreen, B. L. Altshuler, and Y. Meir, Phys. Rev. Lett. **75**, 769 (1995), see also Ralph *et al.* Reply *ibid* 770 and Wingreen *et al.* Erratum *ibid* 81, 4280 (1998).
22. P. Nozieres and A. Blandin, J. Physique **41**, 193 (1980).
23. U. Gerland *et al.* Phys. Rev. Lett. **84**, 3710 (2000), and Y. Ji *et al.* Science **290**, 779 (2000).
24. R. de Picciotto *et al.* Nature **389**, 162 (1997).
25. M. Switkes *et al.* Science **283**, 1907 (1999).
26. L. I. Glazman and M. E. Raikh, Sov. Phys. Lett. **47**, 452 (1988), *pis'ma Zh. Eksp. Teor. Fiz.* **47**, 378-380 (1988).
27. In semiconductor structures, generally $D > U$. We will assume this here, but relaxing this assumption has no significant impact on our conclusions.
28. W. B. Thimm, J. Kroha, and J. von Delft, Phys. Rev. Lett. **82**, 2143 (1999).
29. Our Kondo temperature is set by parameters of the small dot. For small (large) dot of diameter $100nm(2\mu m)$ in a GaAs/AlGaAs heterostructure, it is possible to achieve $u_m \sim 3K > T_K \sim 1K \gg \Delta_m \sim 50mK$.
30. J. R. Schrieffer and P. A. Wolff, Phys. Rev. **149**, 491 (1966).
31. M. H. Devoret *et al.* Phys. Rev. Lett. **64**, 1824 (1990).
32. M. Fabrizio and A. O. Gogolin, Phys. Rev. B. **51**, 17827 (1995).

Spin-Dependent Transport of Electrons in a Shuttle Structure

L.Y. Gorelik¹, S.I. Kulinich^{1,2}, and R.I. Shekhter¹, M. Jonson¹,
and V.M. Vinokur³

¹ Department of Applied Physics, Chalmers University of Technology and
Göteborg University, SE-412 96 Göteborg, Sweden shekhter@fy.chalmers.se

² B. I. Verkin Institute for Low Temperature Physics and Engineering, 47 Lenin
Avenue, 61103 Kharkov, Ukraine

³ Materials Science Division, Argonne National Laboratory, 9700 South Cass Ave,
Argonne, Illinois 60439, USA

Summary. We consider “shuttling” of spin-polarized electrons between two magnetic electrodes (half-metals) by a movable dot with a single electronic level. If the magnetization of the electrodes is antiparallel we show that the transmittance of the system can be changed by orders of magnitude if an external magnetic field, perpendicular to the polarization of the electronic spins, is applied. A giant magnetotransmittance effect can be achieved for weak external fields of order $1 \div 10$ Oe.

1 Introduction

Metal-organic nanocomposite materials are interesting from the point of view of the “bottom-up” approach to building future electronic devices. The ability of the organic parts of the composite materials to identify and latch on to other organic molecules is the basis for the possible self assembly of nanoscale devices, while the metallic components provide mechanical robustness and improve the electrical conductance.

Such composite materials are heteroelastic in the sense that the mechanical rigidity of the organic and metallic components are very different. This allows for a special type of deformation, where hard metallic components embedded in a soft organic matrix can be rearranged in space at a low deformation energy cost associated with stretching and compressing the soft matrix. Strong Coulomb forces, due to accumulation of electronic charge in embedded nanoscale metallic particles, can be a source of such mechanical deformations. This leads to a scenario where the transport of electric charge,

possibly due to tunneling of electrons between metal particles, becomes a complex nano-electromechanical phenomenon, involving an interplay of electronic and mechanical degrees of freedom [1]. Such an interplay can lead to new physics, as was recently demonstrated theoretically for the simplest possible structure — a Nanoelectromechanical single-electron transistor. The electromechanical instability predicted to occur in this device at large enough bias voltage was shown to provide a new mechanism of charge transport [2]. This mechanism can be viewed as a “shuttling” of single electrons by a metallic island — a Coulomb dot — suspended between two metal electrodes. The predicted instability leads to a periodic motion of the island between the electrodes shuttling charge from one to the other.

The shuttle instability appears to be a rather general phenomenon. It has, e.g., been shown to occur even for extremely small suspended metallic particles (or molecules) for which the coherent quantum dynamics of the tunneling electrons [3] or even the quantum dynamics of the mechanical vibration [4, 5, 6, 7] become essential. Nanomechanical transport of electronic charge can, however, occur without any such instability, e.g., in an externally driven device containing a cantilever vibrating at frequencies of order 100 MHz. A small metallic island attached to the tip of the vibrating cantilever may shuttle electrons between metallic leads as has recently been demonstrated [8]. Further experiments with magnetic and superconducting externally driven shuttles as suggested in [9], seem to be a natural extension of this work. Fullerene-based nanomechanical structures [10] are also of considerable interest.

The possibility to place transition-metal atoms or ions inside organic molecules introduces a new “magnetic” degree of freedom that allows the electronic spins to be coupled to mechanical and charge degrees of freedom [12]. By manipulating the interaction between the spin and external magnetic fields and/or the internal interaction in magnetic materials, spin-controlled nano-electromechanics may be achieved. An inverse phenomenon — a nanomechanical manipulation of nanomagnets — was suggested earlier in [11]. A magnetic field, by inducing the spin of electrons to rotate (precess) at a certain frequency, provides a clock for studying the shuttle dynamics and a basis for a dc spectroscopy of the corresponding nanomechanical vibrations.

A particularly interesting situation arises when electrons are shuttled between electrodes that are half-metals. A half-metal is a material that not only has a net magnetization as do ferromagnets, but all the electrons are in the same spin state — the material is fully spin-polarized. Examples of such materials can be found among the perovskite manganese oxides, a class of materials that show an intrinsic, so called “colossal magnetoresistance” effect at high magnetic fields (of order 10÷100 kOe) [13]. A large magnetoresistance effect at lower magnetic fields has been observed in layered tunnel structures where two thin perovskite manganese oxide films are separated by a tunnel barrier [13, 14, 15, 16]. Here the spin polarization of electronic states crucially affects the tunneling between the magnetic electrodes. This is because electrons that can be extracted from the source electrode have their spins aligned in

a definite direction, while electrons that can be injected into the drain electrode must also have their spins aligned — possibly in a different direction. Clearly the tunneling probability and hence the resistance must be strongly dependent on the relative orientation of the magnetization of the two electrodes. An external magnetic field aligns the magnetization direction of the two films at different field strengths, so that the relative magnetization can be changed between high- and low resistance configurations. A change in the resistance of trilayer devices by factors of order 2-5 have in this way been induced by magnetic fields of order 200 Oe [14, 15, 16]. The required field strength is determined by the coercivities of the magnetic layers. This makes it difficult to use a tunneling device of the described type for sensing very low magnetic fields. In this paper we propose a new functional principle — spin-dependent shuttling of electrons — for low-magnetic field sensing purposes. We will show that this principle can lead to a giant magnetoresistance effect in external fields as low as $1\div 10$ Oe.

The new idea which we propose to pursue is to use the external magnetic field to manipulate the *spin of shuttled electrons* rather than the magnetization of the leads. The possibility to “trap” electrons on a nanomechanical shuttle (decoupled from the magnetic leads) during quite a long time on the scale of the time it takes an electron to tunnel on/off the shuttle makes it possible for even a weak external field to rotate the electron’s spin to a significant degree. Such a rotation allows the spin of an electron, loaded onto the shuttle from the spin-polarized source electrode, to be reoriented in order to allow the electron finally to tunnel from the shuttle to the spin-polarized drain lead. As we will show below, the magnetic field induced spin-rotation of shuttled electrons is a very sensitive nanomechanical mechanism for a giant magnetoresistance (GMR) effect.

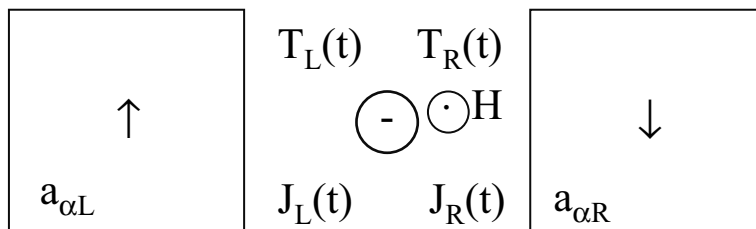


Fig. 1. Schematic view of the nanomechanical GMR device: a movable dot with a single electron level couples to the leads due to tunneling of electrons, described by the tunneling probability amplitudes $T_{L,R}(t)$, and due to the exchange interaction whose strength is denoted by $J_{L,R}(t)$. An external magnetic field H is oriented perpendicular to the direction of the magnetization in the leads (arrows).

2 Formulation of the Problem. General Expression for the Current

A schematic view of the nanomechanical GMR device to be considered is presented in Fig. 1. Two fully spin-polarized magnets with fully spin-polarized electrons serve as source and drain electrodes in a tunneling device. In this paper we will consider the situation when the electrodes have exactly opposite polarization. A mechanically movable quantum dot (described by a time-dependent displacement $x(t)$), where a single energy level is available for electrons, performs forced harmonic oscillations with period $T = 2\pi/\omega$ between the leads. The external magnetic field is perpendicular to the orientation of the magnetization in both leads.

The Hamiltonian that governs the dynamical evolution of the system is

$$\begin{aligned} \hat{\mathcal{H}}(t) = & \varepsilon_0(a_{\uparrow}^{\dagger}a_{\uparrow} + a_{\downarrow}^{\dagger}a_{\downarrow}) + \sum_{\alpha} (\varepsilon_{\alpha}a_{\alpha,L}^{\dagger}a_{\alpha,L} + \varepsilon_{\alpha}a_{\alpha,R}^{\dagger}a_{\alpha,R}) \\ & - J_L(t)(a_{\uparrow}^{\dagger}a_{\uparrow} - a_{\downarrow}^{\dagger}a_{\downarrow}) - J_R(t)(a_{\downarrow}^{\dagger}a_{\downarrow} - a_{\uparrow}^{\dagger}a_{\uparrow}) - (g\mu H/2)(a_{\uparrow}^{\dagger}a_{\downarrow} + a_{\downarrow}^{\dagger}a_{\uparrow}) \\ & + T_L(t) \sum_{\alpha} (a_{\alpha,L}^{\dagger}a_{\uparrow} + a_{\uparrow}^{\dagger}a_{\alpha,L}) + T_R(t) \sum_{\alpha} (a_{\alpha,R}^{\dagger}a_{\downarrow} + a_{\downarrow}^{\dagger}a_{\alpha,R}), \end{aligned} \quad (1)$$

where $a_{\alpha,L(R)}^{\dagger}, (a_{\alpha,L(R)})$ are the creation (annihilation) operators of electrons with the energy ε_{α} on the left (right) lead (we have suppressed the spin indices for the electronic states in the leads due to the assumption of full spin polarization), $a_{\uparrow(\downarrow)}^{\dagger}, (a_{\uparrow(\downarrow)})$ are the creation (annihilation) operators on the dot, ε_0 is the energy of the on-dot level, $J_{L(R)}(t) \equiv J_{L(R)}(x(t))$ are the exchange interactions between the on-grain electron and the left (right) lead, $\Lambda_{L(R)}(t) \equiv \Lambda_{L(R)}(x(t))$ are the tunnel coupling amplitudes, g is the gyromagnetic ratio and μ is the Bohr magneton.

The single-electron density matrix describing electronic transport between the leads may be presented in the form:

$$\hat{\rho} = \sum_{\alpha} w_{\alpha,L} |\Psi^{\alpha,L}\rangle \langle \Psi^{\alpha,L}| + \sum_{\alpha} w_{\alpha,R} |\Psi^{\alpha,R}\rangle \langle \Psi^{\alpha,R}|. \quad (2)$$

Here $|\Psi^{\alpha,L}\rangle$ are single-electron states that obey the time-dependent Schrödinger ($\hbar = 1$) equation with a Hamiltonian given by Eq. (1). The initial condition has the form

$$|\Psi^{\alpha,L(R)}(t \rightarrow -\infty)\rangle = |\alpha, L(R)\rangle \exp(-i\varepsilon_{\alpha}t),$$

where $|\alpha, L(R)\rangle$ is a single-electron state on the left (right) lead with energy ε_{α} .

We will suppose that the internal relaxation in the leads is fast enough to lead to equilibrium distributions of the electrons. This means that $w_{\alpha,L(R)} = f(\varepsilon_{\alpha} \mp V/2)$ (where $f(\varepsilon)$ is the Fermi distribution function) and V is the applied voltage.

The problem at hand is greatly simplified if one considers the large bias-voltage limit

$$|V - \varepsilon_0| \gg \nu \Lambda_{max}^2, \quad (3)$$

where ν is the density of states on the leads. The restriction(3) does not allow us to consider a narrow transition region of voltages from the zero-current regime at $V < \varepsilon_0 - \nu \Lambda_{max}^2$ to the fully transmissive (in the absence of spin polarization effects) regime at $V > \varepsilon_0 + \nu \Lambda_{max}^2$. However, it covers the in practise most important case when the fully transmissive junction is strongly affected by electronic spin-polarization. Therefore, in our further considerations we will take $w_{\alpha,L} = 1$, $w_{\alpha,R} = 0$ and $\varepsilon_0 = 0$.

We will calculate the average current, I , through the system from the relation

$$I = \frac{1}{T} \int_0^T dt Tr \{ \hat{\rho} \hat{j} \}, \quad (4)$$

$$\hat{j} = e \frac{\partial \hat{N}_R}{\partial t} = ie [\hat{\mathcal{H}}, \hat{N}_R] = ie T_R(t) \sum_{\alpha} (a_{\downarrow}^{\dagger} a_{\alpha,R} - a_{\alpha,R}^{\dagger} a_{\downarrow}),$$

where \hat{N} is the electron number operator for the right lead, $\hat{N} = \sum_{\alpha} a_{\alpha,R}^{\dagger} a_{\alpha,R}$.

In general, the state $|\Psi^{\alpha,L}\rangle$ can be expressed as

$$|\Psi^{\alpha,L}(t)\rangle = c_{\uparrow}^{\alpha}(t) |\uparrow\rangle + c_{\downarrow}^{\alpha}(t) |\downarrow\rangle + \sum_{\beta} (c_L^{\alpha,\beta}(t) |\beta, L\rangle + c_R^{\alpha,\beta}(t) |\beta, R\rangle), \quad (5)$$

Thus the problem is reduced to determining the coefficients $c_{R(L)}^{\alpha,\beta}$ and $c_{\downarrow(\uparrow)}^{\alpha}$.

At this point it is convenient to introduce the bi-vectors

$$\mathbf{c}^{\alpha} = \begin{pmatrix} c_{\uparrow}^{\alpha} \\ c_{\downarrow}^{\alpha} \end{pmatrix}, \quad \mathbf{e}_1 = \begin{pmatrix} 1 \\ 0 \end{pmatrix}, \quad \text{and} \quad \mathbf{e}_2 = \begin{pmatrix} 0 \\ 1 \end{pmatrix},$$

so that the coefficients $c_{R(L)}^{\alpha,\beta}$ can be expressed as (see Appendix 1)

$$c_L^{\alpha,\beta} = e^{-i\varepsilon_{\beta}t} \delta_{\alpha\beta} - i \int_{-\infty}^t dt' e^{i\varepsilon_{\beta}(t-t')} T_L(t') (\mathbf{e}_1, \mathbf{c}^{\alpha}(t')),$$

$$c_R^{\alpha,\beta} = -i \int_{-\infty}^t dt' e^{i\varepsilon_{\beta}(t-t')} T_R(t') (\mathbf{e}_2, \mathbf{c}^{\alpha}(t')).$$

Here (\mathbf{a}, \mathbf{b}) is the inner product of two bi-vectors. As shown in Appendix 1, by using the wide band approximation (i.e. by taking the electron density of states in the leads ν to be constant) the equation for the bi-vectors \mathbf{c}^{α} takes the form

$$i \frac{\partial \mathbf{c}^{\alpha}}{\partial t} = \hat{R}(t) \mathbf{c}^{\alpha} + \mathbf{f}^{\alpha}(t). \quad (6)$$

Here $\mathbf{f}^{\alpha}(t) = T_L(t) e^{-i\varepsilon_{\alpha}t} \mathbf{e}_1$ and the matrix $\hat{R}(t)$ is

$$\hat{R}(t) = \begin{pmatrix} -J(t) - i\Gamma_L(t)/2 & -g\mu H/2 \\ -g\mu H/2 & J(t) - i\Gamma_R(t)/2 \end{pmatrix}, \quad (7)$$

where $J(t) = J_L(t) - J_R(t)$ and $\Gamma_{L(R)}(t) = 2\pi\nu\Lambda_{L(R)}^2(t)$ is the level width.

The formal solution of Eq. (6) can be written in the form

$$\mathbf{c}^\alpha(t) = -i \int_{-\infty}^t dt' \hat{L}(t, t') \mathbf{f}^\alpha(t'), \quad (8)$$

where the ‘‘evolution’’ operator $\hat{L}(t, t')$, ($\hat{L}(t, t) = \hat{I}$), is defined as the solution of the equation

$$i \frac{\partial \hat{L}(t, t')}{\partial t} = \hat{R}(t) \hat{L}(t, t'), \quad (9)$$

and obeys the multiplicative and periodicity properties,

$$\hat{L}(t, t') = \hat{L}(t, t'') \hat{L}(t'', t'), \quad \hat{L}(t+T, t'+T) = \hat{L}(t, t'). \quad (10)$$

Using Eq. (8) together with Eq. (4), one can write the average current on the form

$$I = \frac{e}{T} \int_0^T dt \Gamma_R(t) \int_{-\infty}^t dt' \Gamma_L(t') |\hat{L}_{21}(t, t')|^2, \quad (11)$$

where $\hat{L}_{21}(t, t') = (\mathbf{e}_2, \hat{L}(t, t') \mathbf{e}_1)$.

Since the probability amplitude for tunneling is exponentially sensitive to the position of the dot, the maximum of the tunnel exchange interaction between an electron on the dot and an electron in one lead occurs when the tunneling coupling to the other lead is negligible. This is why we will assume the following property of tunneling amplitude $\Lambda_{L,R}(t)$ to be fulfilled:

$$T_L(t)T_R(t) = 0, \quad T_L(t), T_R(t) \neq 0 \quad (12)$$

This assumption allows us to divide the time interval $(0, T)$ into the intervals $(0, \tau) + (\tau, T/2) + (T/2, T/2 + \tau) + (T/2 + \tau, T)$. We suppose that $T_L(t) \neq 0$ (but $H = 0$) only in the time interval $(0, \tau)$ (and, analogously, $T_R(t) \equiv T_L(t + T/2) \neq 0$ in the time interval $(T/2, T/2 + \tau)$). Using this approximation together with the properties (10) of the operator $\hat{L}(t, t')$, we arrive at the following expression for the average current (Appendix 2):

$$I = \frac{e}{T} (1 - e^{-\Gamma})^2 \sum_{n=0}^{\infty} |(\mathbf{e}_2, \hat{L}(T/2, \tau) \hat{L}^n \mathbf{e}_1)|^2. \quad (13)$$

Here $\hat{L} \equiv \hat{L}(T + \tau, \tau)$ and

$$\Gamma = 2\pi\nu \int_0^\tau dt T_L^2(t) \quad (14)$$

is the tunneling rate. Consequently, in order to calculate the average current it is necessary to investigate the properties of the evolution operator \hat{L} . It follows from its definition that

$$\begin{aligned}\hat{L} &= \hat{L}(T+\tau, T)\hat{L}(T, T/2+\tau)\hat{L}(T/2+\tau, T/2)\hat{L}(T/2, \tau) \\ &= e^{-(1+\sigma_3)\Gamma/4+i\sigma_3\Phi_0}\hat{L}(T, T/2+\tau)e^{-(1-\sigma_3)\Gamma/4-i\sigma_3\Phi_0}\hat{L}(T/2, \tau),\end{aligned}\quad (15)$$

where $\Phi_0 = \int_0^\tau dt J(t)$. From the symmetry properties of the operator $\hat{R}(T/2+\tau < t < T)$,

$$\hat{R}^\dagger = \hat{R}, \sigma_2 \hat{R}^* = -\hat{R}, \sigma_3 \hat{R}(-t) = -\hat{R}(t)\sigma_3$$

it follows that the operator $\hat{U} \equiv \hat{L}(T, T/2+\tau)$ has the form

$$\hat{U} = \begin{pmatrix} \sqrt{1-\gamma^2} & i\gamma e^{i\varphi} \\ i\gamma e^{-i\varphi} & \sqrt{1-\gamma^2} \end{pmatrix}\quad (16)$$

In addition to this, $\hat{L}(T/2, \tau) = \sigma_1 \hat{U} \sigma_1$. As a result, the operator \hat{L} can be expressed as

$$\hat{L} = e^{-\Gamma/2} \left(e^{-\sigma_3 \Gamma/4 + i\Phi_0 \sigma_3} \hat{U} \sigma_1 \right)^2. \quad (17)$$

Proceeding with the analysis we (i) calculate the eigenvalues λ_i and eigenvectors \mathbf{b}_i of the operator \hat{L} of Eq. (17); $\hat{L}\mathbf{b}_i = \lambda_i\mathbf{b}_i$, (ii) substitute the expansion $\mathbf{e}_i = a_{ji}\mathbf{b}_j$ (where $(a)^{-1} = (\mathbf{e}_i, \mathbf{b}_j)$) into Eq. (13) and calculate the average current. The result is

$$I = \frac{e\kappa}{T} \sinh \Gamma/2 \frac{\cosh \Gamma/2 + \cos 2\vartheta}{\sinh^2 \Gamma/2 + \kappa(1 + \cos 2\vartheta \cosh \Gamma/2)}, \quad (18)$$

where $\vartheta = \varphi + \Phi_0$, $\kappa = 2\gamma^2/(1+\gamma^2)$. Equation (18) for the average current is our main result.

3 Calculation of the Current in Limit of Strong and Weak Exchange Coupling between the Dot and the Leads

Although the result (18) for the tunnel current is both transparent and compact, it is in general a rather complicated problem to find the magnetic field dependence of the coefficient κ , which depends on the probability amplitude γ for flipping the spin of shuttled electrons. Three different time scales are involved in the spin dynamics of a shuttled electron. They correspond to three characteristic frequencies: (i) the frequency of spin rotation, determined by the tunnel exchange interaction with the magnetic leads; (ii) the frequency of spin rotation in the external magnetic field, and (iii) the frequency of shuttle vibrations. Different regimes occur depending on the relation between these time scales. Here we will consider two limiting cases, where a simple solution of the problem can be found. Those are the limits of weak $J_{L(R)} \ll \mu H$ and strong $J_{L(R)} \gg \mu H$ exchange interactions with the leads.

3.1 Weak exchange interaction

In the limit $J_{L(R)} \ll \mu H$ one may neglect the influence of the magnetic leads on the on-dot electron spin dynamics. In this case the matrix \hat{U} given by Eq. (16) can easily be calculated and Eq. (18) reduces to

$$I = \frac{2e}{T} \frac{\sin^2 \vartheta/2 \tanh \Gamma/4}{\sin^2 \vartheta/2 + \tanh^2 \Gamma/4}, \quad (19)$$

where $\vartheta = g\mu \int_{\tau}^{T/2} dt H$ is the rotation angle of the spin in the external field.

Two different scales for the external magnetic field determine the magneto-transmittance in this limit. One scale is associated with the width of the resonant magnetic field dependence (see the denominator in Eq. (19)). This scale is (restoring dimension)

$$\delta H \simeq \Gamma \frac{\hbar\omega}{g\mu}, \quad (20)$$

where ω is the shuttle vibration frequency. The second scale,

$$\Delta H \simeq \frac{\hbar\omega}{g\mu}, \quad (21)$$

comes from the periodic function $\sin^2 \vartheta/2$ that enters Eq. (19). The magnetic-field dependence of the current is presented in Fig. 2a. Dips in the transmittance of width δH appear periodically as the magnetic field is varied, the period being Δ . This amounts to a giant magneto-transmittance effect. It is interesting to notice that by measuring the period of the variations in $I(H)$ one can in principle determine the shuttle vibration frequency. This amounts to a dc method for spectroscopy of the nanomechanical vibrations. Equation (21) gives a simple relation between the vibration frequency and the period of the current variations. The physical meaning of this relation is very simple: every time when $\omega/\Omega = n + 1/2$ (Ω is the spin precession frequency in a magnetic field) the shuttled electron is able to fully flip its spin to remove the ‘‘spin-blockade’’ of tunneling between spin polarized leads having their magnetization in opposite directions.

3.2 Strong Dot-Leads Exchange Interaction

A strong magnetic coupling to the leads, $J_{max} \gg \mu H$, preserves the electron spin polarization, preventing spin-flips of shuttled electrons due to an external magnetic field. However, if the magnetization of the two leads are in opposite directions, the exchange coupling to the leads have different sign. Therefore, the exchange couplings to the two leads tend to cancel out when the dot is in the middle of the junction. Hence the strong exchange interaction affecting a dot electron depends on time and periodically changes sign, being arbitrary

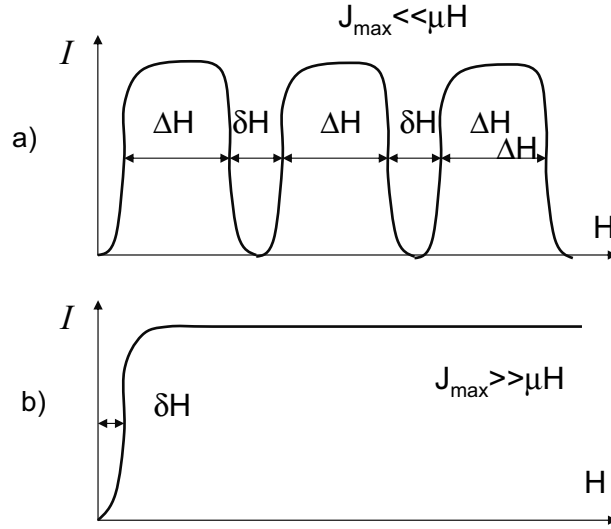


Fig. 2. Magnetic-field dependence of the transmittance of the device shown in Fig. 1 for the limiting cases of a) weak and b) strong exchange coupling between dot and leads. The period ΔH and the width δH of the “dips” are given by Eqs. (21) and (20) for case a) and δH is given by Eq. (24) for the case b).

small close to the time of sign reversal. In Fig. 3 the on-dot electronic energy levels for spins parallel and antiparallel to the lead magnetization are presented as a function of time. The effect of an external magnetic field is in the limit $J_{L(R)} \gg \mu H$ negligible almost everywhere, except in the vicinity of the level crossing. At this “time point”, which we denote t_{LZ} , the external magnetic field removes the degeneracy and a gap is formed in the spectrum (dashed curve). The probability of electronic spin-flip in this case is determined by the probability of a Landau-Zener reflection from the gap formed by the magnetic field (in this case a Landau-Zener transition across the gap is a mechanism for backscattering of the electron, since this is the channel where the electronic spin is preserved). The matrix \hat{U} can readily be expressed in terms of Landau-Zener scattering amplitudes. The amplitude and phase of electronic spin-flip is given by $\varphi = \varphi_0 + \Phi_1$, φ_0 is the Landau-Zener phase shift,

$$\Phi_1 = \int_{\tau}^{T/2-\tau} dt J(t) \quad (22)$$

and γ^2 is the probability of the Landau-Zener “backward” scattering,

$$\gamma^2 = 1 - \exp \left[-\frac{\pi(\mu H)^2}{J'(t_{LZ})} \right]. \quad (23)$$

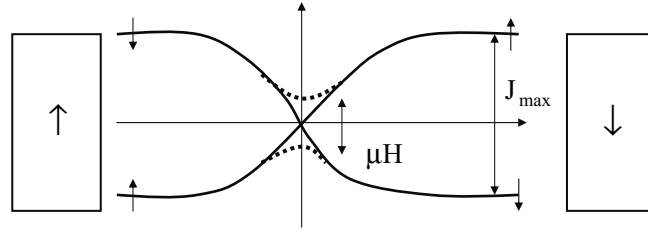


Fig. 3. On-dot energy levels for spin-up and spin-down electron states as a function of the position of the dot. Level crossing in the middle of the device is removed by an external magnetic field.

Schematical view of $I(H)$ dependence is presented on a Fig. 2b. The width δH of the minimum in $I(H)$ dependence can be found directly from Eqs. (18), (23),

$$\delta H = \frac{\pi g \mu}{\sqrt{J_0 \hbar \omega}}, \quad (24)$$

where $J_0 = \min (J_{L(R)}(t))$.

4 Conclusion

The analysis presented above demonstrates the possibility of a giant magneto-transmittance effect caused by shuttling of spin-polarized electrons between magnetic source- and drain electrodes. The sensitivity of the shuttle current to an external magnetic field is determined, according to Eq. (20), by the transparency of the tunnel barriers. By diminishing the tunneling transmittance one can increase the sensitivity of the device to an external magnetic field. The necessity to have a measurable current determines the limit of this sensitivity. In the low transparency limit, $\Gamma \ll 1$, the current through the device can be estimated as $I \simeq e\Gamma\omega$. If one denotes the critical field that determines the sensitivity of the device by H_{cr} , one finds from Eq. (20) that $H_{cr} \simeq \delta H$. The critical field can now be expressed in terms of the current transmitted through the device as

$$H_{cr}(Oe) \simeq \frac{\hbar I}{e\mu g} \simeq \frac{g_0}{g} (3 \times 10^2) I(nA), \quad (25)$$

where $g_0 (= 2)$ is the gyromagnetic ratio for the free electrons. For $I \simeq 10^{-1} \div 10^{-2}$ nA and $g_0/g \simeq 1/3$ this gives a range $H_{cr} \simeq 1 \div 10$ Oe. A further increase in sensitivity would follow if one could use a shuttle with several (N) electronic levels involved in the tunneling process. The critical magnetic field would then be inversely proportional to the number of levels, $H_{cr}(N) = H_{cr}(N=1)/N$.

Acknowledgements.— Financial support from the Royal Swedish Academy of sciences (SIK), the Swedish Science Research Council (LIG, RIS) and

the Swedish Foundation for Strategic Research (LIG, RIS, MJ) is gratefully acknowledged. Support from the U.S. Department of Energy (Basic Energy Science, Contract No W-31-109-ENG-38) is gratefully acknowledged.

A Appendix 1

The Schrödinger equation results in equations for the coefficients $c_{R(L)}^{\alpha\beta}, c_{\uparrow(1)}^{\alpha}$:

$$\begin{aligned} i\frac{\partial c_{\uparrow}^{\alpha}}{\partial t} &= -J(t)c_{\uparrow}^{\alpha} - (g\mu H/2)c_{\downarrow}^{\alpha} + T_L(t)\sum_{\beta}c_L^{\alpha\beta}(t), \\ i\frac{\partial c_{\downarrow}^{\alpha}}{\partial t} &= J(t)c_{\uparrow}^{\alpha} - (g\mu H/2)c_{\downarrow}^{\alpha} + T_R(t)\sum_{\beta}c_R^{\alpha\beta}(t), \\ i\frac{\partial c_L^{\alpha\beta}}{\partial t} &= \varepsilon_{\beta}c_L^{\alpha\beta} + T_L(t)c_{\uparrow}^{\alpha}(t), \\ i\frac{\partial c_R^{\alpha\beta}}{\partial t} &= \varepsilon_{\beta}c_R^{\alpha\beta} + T_R(t)c_{\downarrow}^{\alpha}(t). \end{aligned} \quad (26)$$

As it follows from the last two equations (together with the initial conditions)

$$\begin{aligned} c_L^{\alpha\beta}(t) &= e^{-i\varepsilon_{\beta}t}\delta_{\alpha\beta} - i\int_{-\infty}^t dt' e^{i\varepsilon_{\beta}(t'-t)}T_L(t')c_{\uparrow}^{\alpha}(t'), \\ c_R^{\alpha\beta}(t) &= -i\int_{-\infty}^t dt' e^{i\varepsilon_{\beta}(t'-t)}T_R(t')c_{\downarrow}^{\alpha}(t'). \end{aligned} \quad (27)$$

Therefore, for the $\sum_{\beta}c_R^{\alpha\beta}(t)$ one gets

$$\sum_{\beta}c_R^{\alpha\beta}(t) = -i\int_{-\infty}^t dt'T_R(t')c_{\downarrow}^{\alpha}(t')\sum_{\beta}e^{i\varepsilon_{\beta}(t'-t)}.$$

In wide-band approximation we suppose $\nu(\varepsilon) = \text{const}$, therefore $\sum_{\beta}e^{i\varepsilon_{\beta}(t'-t)} = 2\pi\nu\delta(t'-t)$ and

$$\sum_{\beta}c_R^{\alpha\beta}(t) = -i\pi\nu T_R(t)c_{\downarrow}^{\alpha}. \quad (28)$$

Analogously,

$$\sum_{\beta}c_L^{\alpha\beta}(t) = e^{-i\varepsilon_{\alpha}t} - i\pi\nu T_L(t)c_{\uparrow}^{\alpha}. \quad (29)$$

Substitute the expressions, Eqs. (28), (29), to the first two equations (26), one get the equation Eq. (6) for the bi-vector \mathbf{c}^{α} .

B Appendix 2

Under our approximation we can change the integration limits in Eq. (11):

$$\begin{aligned} I &= \frac{e}{T} \int_0^T dt \Gamma_R(t) \int_{-\infty}^t dt' \Gamma_L(t') |\hat{L}_{21}(t, t')|^2 \\ &= \frac{e}{T} \int_{T/2}^{T/2+\tau} dt \Gamma_R(t) \int_{-\infty}^{\tau} dt' \Gamma_L(t') |\hat{L}_{21}(t, t')|^2. \end{aligned} \quad (30)$$

Beside this, in the time moments $T/2 < t < T/2 + \tau$ $\hat{L}(t, T/2)$ is a diagonal matrix. Therefore $\hat{L}_{21}(t, t') = \hat{L}_{22}(t, T/2) \hat{L}_{21}(T/2, t')$. As a consequence, the integral in the expression for the average current, Eq. (30), is factorized:

$$I = \frac{e}{T} \int_{T/2}^{T/2+\tau} dt \Gamma_R(t) |\hat{L}_{22}(t, T/2)|^2 \int_{-\infty}^{\tau} dt' \Gamma_L(t') |\hat{L}_{21}(T/2, t')|^2. \quad (31)$$

The first integral in Eq. (31) is easy to calculate. Having in mind that ($T/2 < t < T/2 + \tau$) $|\hat{L}_{22}(t, T/2)|^2 = \exp\left[-\int_{T/2}^t dt \Gamma_R(t)\right]$, one gets

$$\int_{T/2}^{T/2+\tau} dt \Gamma_R(t) |\hat{L}_{22}(t, T/2)|^2 = 1 - e^{-\Gamma}, \quad (32)$$

where quantity Γ is defined in Eq. (14).

The calculation of the second integral in Eq. (31) can be done in the same manner. One has the set of equalities,

$$\begin{aligned} \int_{-\infty}^{\tau} \Gamma_L(t) |\hat{L}_{21}(T/2, t)|^2 &= \sum_{n=0}^{\infty} \int_{-nT}^{-nT+\tau} dt \Gamma_L(t) |\hat{L}_{21}(T/2, t)|^2 \\ &= \sum_{n=0}^{\infty} \int_0^{\tau} dt \Gamma_L(t) |(\mathbf{e}_2, \hat{L}(T/2, \tau) \hat{L}(\tau, t - nT) \mathbf{e}_1)|^2. \end{aligned} \quad (33)$$

For the quantity $\hat{L}(\tau, t - nT) = \hat{L}(\tau + nT, t)$ one has

$$\hat{L}(\tau + nT, t) = \hat{L}(\tau + nT, \tau + (n-1)T) \dots \hat{L}(\tau, t) = \hat{L}^n(\tau + T, \tau) \hat{L}(\tau, t). \quad (34)$$

Therefore,

$$\int_{-\infty}^{\tau} dt \Gamma_L(t) |\hat{L}_{21}(T/2, t)|^2 = \sum_{n=0}^{\infty} \int_0^{\tau} dt \Gamma_L(t) |(\mathbf{e}_2, \hat{L}(T/2, \tau) \hat{L}^n \hat{L}(\tau, t) \mathbf{e}_1)|^2. \quad (35)$$

Integral over t in Eq. (35) can be taken similarly to ones in Eq. (32) and, as a result, one gets the Eq. (13) for the average current.

References

1. R. I. Shekhter, Yu. Galperin, L. Y. Gorelik *et al.*, *J. Phys.: Condens. Matter* **15** R441(2003).
2. L. Y. Gorelik, A. Isacsson, M. V. Voinova *et al.*, *Phys. Rev. Lett.* **80**, 4526 (1998).
3. D. Fedorets, L. Y. Gorelik, R. I. Shekhter, and M. Jonson, *Europhys. Lett.* **58**, 99 (2002).
4. D. Fedorets, L. Y. Gorelik, R. I. Shekhter, and M. Jonson, cond-mat/0311105, *Phys. Rev. Lett.* **92**, 166801 (2004).
5. D. Fedorets, L. Y. Gorelik, R. I. Shekhter, and M. Jonson, cond-mat/0212561 (unpublished).
6. T. Novotny, A. Donarini, and A.-P. Jauho, *Phys. Rev. Lett.* **90**, 256801 (2003).
7. D. Fedorets, *Phys. Rev. B* **68**, 033106 (2003).
8. A. Erbe, C. Weiss, W. Zwirger and R. H. Blick, *Phys. Rev. Lett.* **87**, 096106 (2001).
9. D. V. Scheibe, A. Erbe and R. H. Blick, *New J. Phys.* **4**, 86 (2002).
10. H. Park, J. Park, A. K. L. Lim, E. H. Anderson, A. P. Alivisatos, and P. L. McEuen, *Nature* **407**, 57 (2000).
11. L. Y. Gorelik, R. I. Shekhter, V. M. Vinokur *et al.*, *Phys. Rev. Lett.* **91**, 088301 (2003).
12. J. Park, A. Pasupathy, J. I. Goldsmith *et al.*, *Nature* **417**, 722 (2002).
13. “Colossal Magnetoresistive Oxides” ed. by Y. Tokura (Gordon and Breach Science Publishers, Amsterdam, 2000).
14. J. Z. Sun, W. J. Gallagher, P. R. Duncombe *et al.*, *Appl. Phys. Lett.* **69**, 3266 (1996).
15. J. Z. Sun, L. Krusin-Elbaum, P. R. Duncombe *et al.*, *Appl. Phys. Lett.* **70**, 1769 (1997).
16. Yu Lu *et al.*, *Phys. Rev. B* **54**, R8357 (1996).

Index

- adiabaticity, 9
- Aharonov-Bohm interferometer, 3, 77
- Andreev interferometer, 241
- Andreev reflection, 173, 271, 293
- Andreev wires, 291
- anomalous magnetoresistance, 67

- backward scattering, 95
- Berry phase, 9
- boson-vortex duality, 83
- bosonization, 147

- carbon nanotubes, 47, 141, 147
- charge density wave, 91
- charge-imbalance, 57
- chiral symmetry, 215
- condensate of Cooper pairs, 84
- conductance, 147
- conductivity of granular metals, 29
- correlation function, 92
- Coulomb blockade, 47
- Coulomb drag, 119
- Coulomb interaction, 96, 141
- current rectification, 147

- density of states of granular metals, 27
- differential resistance, 57
- diffusive wire, 241
- disorder, 91, 291
- disordered quantum systems, 92
- dissipative dynamics, 9
- domain wall superconductivity, 209

- domain walls, 209
- drag resistance, 119
- dynamic resistance, 39

- electron-radiation interaction, 77
- exact ground state, 103

- F/S/F trilayer, 159
- ferromagnet/superconductor, 57, 159, 209, 229
- forward scattering, 99, 120
- full counting statistics, 241, 263

- giant magnetoresistance, 307
- Ginzburg-Landau approach, 209
- granular metals, 27
- granular superconductor, 83

- half-metals, 307
- Hartree approximation, 147
- higher cumulants, 257
- higher-order correlations, 257
- hopping, 283
- hybrid system, 159, 209, 217, 242, 271

- impurity scattering, 147, 291
- instanton method, 187
- interference in nanostructures, 3
- interwire backscattering, 119

- Josephson effect, 215
- Josephson junctions, 263
- Josephson tunneling, 215

- Kosterlitz-Thouless transition, 101
- Lamb shift, 9
- Landau-Zener transition, 9, 307
- Langevin equation, 257
- lattice potential, 92
- Little-Parks effect, 209
- localization transition, 91
- localized impurity states, 283
- Luttinger liquids, 91, 119, 141, 147
- magnetization switching, 39
- magnetoresistance, 67
- memory effects, 68
- mesoscopic conductors, 241
- mesoscopic rings, 77
- molecular electronics, 307
- multi channel Kondo effect, 297
- multilayered S/F structure, 229
- nanoelectromechanical systems, 47
- noise, 257, 271
- Non-Fermi Liquid, 297
- nonequilibrium noise, 257
- one-dimensional electronic systems, 91, 129
- orbital magnetic moments, 77
- proximity effect, 159, 173, 229, 271
- quantum dot, 3, 141, 297
- quantum noise, 263
- quantum phase transition, 85, 91
- quantum tunneling, 187
- quantum wires, 92, 119, 129, 141, 215
- qubit, 9
- Rashba effect, 215
- ratchets, 147
- re-entrant localization, 291
- renormalization group, 91, 141
- replica Hamiltonian, 98
- resonant transmission, 3
- resonant tunneling, 141, 283, 307
- S/N/S junction, 241
- SC/PM states, 187
- Shot noise, 283
- shuttling of electrons, 307
- single-electron transport, 291
- spin density wave, 91
- spin-charge separation, 129
- spin-dependent tunneling, 307
- spin-orbit interaction, 215
- spin-polarized, 57
- STM spectroscopy, 173
- strong pinning, 103
- superconducting grain, 189
- superconducting hybrid systems, 271
- superconductor-insulator transition, 83
- superconductor/normal metal, 173
- third moment, 277
- transport in granular metals, 27
- trilayered F/S/F structure, 231
- triplet superconductivity, 229
- tunnel conductance, 29
- tunnel junction, 129, 187, 277
- tunneling spectrum, 129
- two-dimensional electron gas, 67, 84, 215
- Usadel equations, 176, 271
- voltage fluctuations, 277
- weak localization, 271
- Zeeman coupling, 189
- Zeeman splitting, 57, 215